Alma Mater Studiorum – Università di Bologna

DOTTORATO DI RICERCA IN

INGEGNERIA CIVILE, CHIMICA, AMBIENTALE E DEI MATERIALI

Ciclo XXX

Settore Concorsuale: 08/B3 Tecnica delle costruzioni

Settore Scientifico Disciplinare: ICAR/09 Tecnica delle costruzioni

STRUCTURAL HEALTH MONITORING AND DAMAGE IDENTIFICATION USING MODAL FLEXIBILITY-BASED APPROACHES FROM OUTPUT-ONLY VIBRATION DATA

Presentata da: Giacomo Bernagozzi

Coordinatore Dottorato

prof. Luca Vittuari

Supervisore

prof. ing. Pier Paolo Diotallevi

Co-supervisori

ing. Luca Landi

ing. Carla Sandri

Co-supervisori (periodi di ricerca all'estero)

prof. Raimondo Betti

prof. Carlos Ventura

Esame finale anno 2018

Abstract

STRUCTURAL HEALTH MONITORING AND DAMAGE IDENTIFICATION USING MODAL FLEXIBILITY-BASED APPROACHES FROM OUTPUT-ONLY VIBRATION DATA

Giacomo Bernagozzi

An area of research in civil engineering that has received increasing attention in recent years concerns the application of vibration-based health monitoring and damage detection techniques on structures under ambient vibrations. The dissertation presents research investigations that were carried out in this field, by focusing mainly on building structures and on techniques that belong to a subclass of the modal flexibility (MF)-based methodologies for damage detection. According to these techniques, modal flexibility-based models of structures are estimated from vibration tests, and then, by applying inspection loads to such models, structural deflections are determined and used for detecting damage. Three main problems are addressed in the thesis. 1) In modal testing and identification of real-life structures not all the modes can be usually identified. MF-based deflections are thus estimated using incomplete modal models, leading to truncation effects. To address this problem, approaches are proposed to predict and reduce the truncation effects on MF-based deflections of building structures. 2) In the literature the damage detection methods based on MF-based deflections have been mainly developed for building structures that can be modeled as plane structures. In an attempt to extend these existing methodologies to more complex structures, research investigations were carried out on simple rectangular “box type” 3D building structures characterized by either plan-symmetric or plan-asymmetric configurations. 3) Modal flexibility can be only determined when mass-normalized mode shapes are available. However, such scaled mode shapes can not be directly estimated from output-only data. To address this problem, a MF-based approach for damage detection in building structures that can be applied directly on output-only data with minimal or no a-priori information on the masses is proposed. For all three analyzed problems, numerical simulations and experimental output-only vibration tests conducted on frame building structures were used to demonstrate the effectiveness of the proposed approaches.

Contents

List of Abbreviations

DSF	=	damage sensitive feature
EMA	=	experimental modal analysis
$eMAC_{id}$	=	error on MAC_{id}
ID	=	interstory drift
LPF	=	load participation factor
MAC	=	modal assurance criterion
MAC_{id}	=	modal assurance criterion applied to vectors of interstory drifts
MD	=	Mahalanobis distance
MD_{id}	=	Mahalanobis distance between vectors of interstory drifts
MF	=	modal flexibility
MPF	=	mass participation factor
MPL	=	mass proportional load
MPL-PF	=	mass proportional load participation factor
OMA	=	operational modal analysis
PFM	=	proportional flexibility matrix
PMM	=	proportional mass matrix
PSIL	=	positive shear inspection load
SHM	=	structural health monitoring
UL	=	uniform load
UL-PF	=	uniform load participation factor

Acknowledgments

First and foremost, I would like to express my sincere gratitude to my advisor Prof. Ing. Pier Paolo Diotallevi for introducing me to the exciting topics of structural health monitoring and modal testing, for being a wise guide in my research, and for the valuable suggestions and the critical questions on my work. I am also extremely grateful to Prof. Diotallevi for giving me the great opportunity and the support for attending important international events related to my research topic throughout the doctoral course.

I would like to express my sincere gratitude to my co-advisor Dr. Ing. Luca Landi for the valuable suggestions, for the patience and the time dedicated to me when we have read and proofread together some of the works carried out during my doctoral path, and for his great help in many situations.

I would like to express my sincere gratitude to my co-advisor Dott. Ing. Carla Sandri for the support and the valuable advice. She was the first who motivated me to pursue a doctoral path, and I am extremely grateful for her encouragement.

I would like to express my sincere gratitude to my co-advisor Prof. Raimondo Betti for giving me the opportunity of spending a research and study period at Columbia University, for his guidance, for the valuable suggestions and the critical questions on my work, and for his great hospitality when I arrived at Columbia. I am also extremely grateful to Prof. Betti for giving me the great chance of performing experimental tests in the Carleton Laboratory during the study period at Columbia, and for his great support and his assistance during these tests. I am also sincerely grateful to Prof. Betti for the opportunity and the support that he has given to me to attend the EMI 2017 conference to present the work done during the study period at Columbia.

I would like to express my sincere gratitude to my co-advisor Prof. Carlos Ventura for giving me the opportunity of spending a research and study period at the University of British Columbia (UBC), for his guidance and his wise suggestions, and for his kind hospitality when I arrived at UBC. Since the first time I met him during his pre-conference

OMA course at the 6th IOMAC and since the beginning of the study period at UBC he motivated me to approach and learn the basic concepts of the practice of performing vibration tests. I am extremely grateful to Prof. Ventura for the teachings he gave to me on this practice and for giving me the great chance of participating to the experimental program related to the ambient vibration tests on the "Yellow Frame" that was ongoing at UBC during the study period that I spent there.

I would like to thank Dr. Suparno Mukhopadhyay for his insightful comments and observations on the research investigations that are presented in Chapter 6 of the thesis, and for the very interesting conversations that we had on the work at the EMI 2017 conference together with Prof. Betti. I would also like to thank all the people that provided their assistance during the vibration tests performed at the Carleton Laboratory of Columbia University (see Chapter 6), especially Dr. Adrian Brügger and Dr. Matthew Sloane.

I would like to thank Dr. Yavuz Kaya for his valuable suggestions on the work done during the study period at UBC, for his help in the organization of this study period, and for his great hospitality when I arrived at UBC. I would like to thank Dr. Saeid Allahdadian for his great support during our collaboration related to the execution of the ambient vibration tests on the "Yellow Frame" at UBC (see Chapter 5). I would also like to thank all the other people that provided their assistance during these ambient vibration tests, especially Dr. Yuxin Pan. Finally, I would like to thank Dr. Martin Turek for giving me information about the frame structure.

There are many other people met at the University of Bologna or during the research periods abroad at Columbia University and at the University of British Columbia that helped me in various ways. The help and the support from all of them is gratefully acknowledged.

I would like to thank all the members of the IASC-ASCE Task Group for Structural Health Monitoring for having made the experimental data related to their benchmark studies publicly available for the research community (such data are used in Chapter 4).

I would like to thank all the people that organized the vibration test performed during the pre-conference OMA course at the 6th IOMAC (see Appendix A), especially Prof. Manuel López Aenlle, Dr. Pelayo Fernández Fernández, Prof. Svend Gade, and Prof. Carlos Ventura. I would also like to thank all the participants of the mentioned OMA course that collaborated with me in the execution of the vibration test, especially Oscar Ramírez and Guillermo Fernandez-Lorenzo.

I would like to thank Prof. Hilmi Luş and Prof. Álvaro Cunha for their time dedicated to review and evaluate the present thesis, for their comments and suggestions.

Finally, I would like to express my deepest gratitude to my parents for their unconditional love, for their support, and for their encouragement to pursue my doctoral studies. I also would like to thank all my closest friends and all the people that supported and helped me during the doctoral path.

Dedicated to my family

Chapter 1

Introduction

This dissertation was developed in the field of Structural Health Monitoring (SHM). One of the most comprehensive definitions of the subject was provided in the editorial letter that opened the first volume of the international journal Structural Health Monitoring. According to the letter this definition is as follows: "*Structural Health Monitoring (SHM) is the continuous or regular monitoring of the condition of a structure or system using built-in or autonomous sensory systems, and any resultant intervention to preserve structural integrity"* [Chang, Prosser & Schulz, 2002].

Structural Health Monitoring is a multidisciplinary field where both technological and scientific disciplines are involved. As evident in the above-mentioned definition, any SHM strategy is based on the use of a system of sensors that is able to measure and collect experimental data on the structure. The recorded data are then analyzed to extract meaningful information about the structural systems that can be used to monitor and evaluate the condition of the structure over time. Over the last few decades the technologies and the techniques of SHM have been investigated and applied on different types of structural systems, including civil, mechanical, and aerospace structures.

One of the main goals that can be pursued using a SHM strategy is to detect damage in structural systems. As reported in [Farrar & Worden, 2013], "*damage can be defined as changes introduced into a system, either intentionally or unintentionally, that adversely affect the current or future performance of that system*". In addition to

the definition of damage, another definition is introduced herein to describe the general process of damage detection. As also reported in [Farrar & Worden, 2013], "*failure occurs when the damage progresses to a point where the system can no longer perform its intended function*". The main objective of the damage detection techniques in SHM is thus to detect damage in structures at the earliest possible stages, so that adequate actions and interventions can be adopted to prevent the failure of the structural system.

As evident from the definition of SHM reported in [Chang, Prosser & Schulz, 2002], the SHM process includes not only the phases related to the data acquisition and the data analysis. An important part of the SHM process is related to the actions that are undertaken (on the basis of information/feedback obtained through the monitoring process) to preserve the health of the structure and to guarantee the safety of the structure during its whole life. Such interventions can be, for example, retrofit interventions to be adopted when the structure has experienced a relevant damage, or minor interventions to be executed on a regular basis (i.e. structural maintenance). It is clear that, in general, an SHM process can provide important information that can be used to support the decision-making about the interventions and to plan maintenance programs. These aspects can be though as a second general objective that can be pursued with the SHM strategies. The integration of the SHM strategies in the operation of planning maintenance programs is the main idea behind the so-called condition-based maintenance. When adopting such approach, two main advantages should be obtained using information obtained from the monitoring system: the costs of the intervention should be minimized, and the efficacy of the interventions should be maximized.

There are several other objectives that can be pursued using SHM strategies. Among them, a third objective has to be mentioned. The techniques and the tools used in SHM can be also used to verify if the structural system has been constructed as designed. First of all, by adopting this strategy some actions can be undertaken in the cases in which discrepancies are present between the structure that was designed and the structure that was constructed. Secondly, this operation of comparing the constructed structure against the structure that was designed can lead to the definition of a realistic and refined model of the structure. This model might also be very useful

for the SHM purposes that have been already mentioned in the previous paragraphs (e.g. damage detection).

Among the different objectives that can be pursued using SHM strategies, damage detection is the one that has received (and is currently receiving) most of the attention of researchers. This objective of SHM is also the one that is mainly addressed in the present dissertation. Before going further, it is also important to underline that the types of structures that are considered in the present thesis are civil structures.

An important application of the SHM strategies in civil structures is related, for example, to the investigation and the verification of the condition of the structure after an extreme event, such as an earthquake. After this event some of the questions that usually arise are the following: is there damage in the structure? Is the structure safe and it can be reoccupied? As reported in [Farrar & Worden, 2013], there are currently no quantifiable and experimental-based methods that can provide a rapid response to such questions after a major earthquake has occurred. In this context, as also reported in [Farrar & Worden, 2013], it is expected that in the near future SHM strategies could play a fundamental role and could be used as a tool to integrate the current post-earthquake damage evaluation procedures based on visual inspection.

For a general structural system and in addition to visual inspection, one way of detecting damage is to use Non-Destructive Evaluation (NDE) techniques based on the execution of localized experiments on the structures [Doebling et al., 1996; Farrar & Worden, 2013]. Such localized investigations can be performed on the structure by adopting, for example, the following technologies: ultrasonic testing, acoustic emission, magnetic field inspections, thermography, radiography, etc. However, referring to civil structures (especially large-scale structures), performing such localized experiments for NDE on the whole structures can be very time-consuming operations, which might also be associated to prohibitive costs.

For the above-mentioned reasons, the need of having techniques that can be used to perform, according to the expressions adopted in [Farrar & Worden, 2013], a “quantitative”, “global”, and fast damage detection on the whole structures has emerged in recent years. To attain this objective many researches have been carried out (and are currently on going) to try to detect damage in structures by the analysis

of the vibration responses and the vibration characteristics of the structures. In the field of structural health monitoring, the methods and the techniques that adopt this strategy are indicated as vibration-based approaches for damage detection. Such approaches are the focus of the present dissertation.

The techniques for vibration-based damage detection are valuable tools that can complement the traditional procedures based on visual inspection. Such techniques can be very useful, for example, in the following cases: 1) the case in which the damage may not be evident and observable using visual inspection (for example, if the damage is hidden inside the structure); 2) the case in which not all the parts of the structure are easily accessible. In general, as will be discussed later in this chapter, the vibration-based techniques can be used not only to detect the existence of the damage, but also to have an idea of the region of the structure that has experienced damage (this operation is usually referred to as damage localization). Obtaining such information on the location of the damage is an extremely useful achievement that can be used to perform in such damaged regions of the structure more refined analyses based, for example, on localized experiments of non-destructive evaluation.

1.1 Vibration-based damage detection

In vibration-based approaches for SHM and damage detection, the types of data that have to be monitored and recorded are vibration responses of the structures. The fundamental idea behind these approaches is that damage can induce modifications in the dynamic and mechanical characteristics of the structure. For example, a structure can experience a local reduction in the stiffness due to some unexpected loading conditions, and this modification (i.e. damage) might alter the vibration responses of the structure. All the vibration-based damage detection techniques thus aim to extract information on the dynamic and mechanical properties of the structures from the vibration measurements, and they also aim to detect eventual changes in such properties that can be associated to the presence of damage in the structure.

Referring to civil structures (such as bridge or building structures) that are tested in-situ, obtaining measurements of the vibration responses of such structures is an operation that can be performed using sensors, such as accelerometric sensors

(piezoelectric or force-balance accelerometers). Referring to the type of excitations, it is in general convenient to measure the vibration responses of the structures associated with ambient inputs. In such case the structures are excited by natural excitations such as wind loads, traffic loads, or microtremors. In this kind of testing, as reported in [Brincker & Ventura, 2015], the measurements can be taken during the normal operating conditions of the structures without interrupting their functionality during the testing phases. It is evident that this type of vibration testing is an extremely convenient approach in the context of a vibration-based damage detection and SHM strategy. In fact, a monitoring system can be permanently installed on the structure, and then ambient vibration measurements can be recorded (for example, at regular intervals of time or continuously).

As reported in [Farrar & Worden, 2013], it is implicit that in any damage detection strategy at least two different states of the structures have to be compared: one of the two states is assumed as the healthy or undamaged state (which is also indicated as baseline state or baseline condition); the other state is the state considered in the inspection stage, and it is the one that is potentially damaged. In general, if the results of the damage detection process show that the structural state in the inspection phase is similar to the baseline state, then the state related to the inspection phase is classified as healthy; otherwise, if any modifications that can be associated to the presence of damage are detected, then the state related to the inspection phase is classified as damaged.

Due to the nature of the damage detection problem and as explained in the work by [Farrar & Worden, 2013], the process of damage detection can be seen as a pattern recognition problem. In fact, the problem described in previous paragraph can be seen as one of the simplest pattern recognition problems - i.e. performing a binary decision and classifying the system in the inspection phase as healthy or damaged. On the basis of this recently developed paradigm in SHM [Farrar & Worden, 2013], several techniques in vibration-based damage detection were borrowed from the field of statistical pattern recognition implemented with machine learning algorithms. This discipline is a well-established and mature discipline and, as reported in [Farrar & Worden, 2013], it has the main objective of associating generic data set with different and possible options of labels. This basically means that the approach aims at

classifying the data set. According to a generic machine learning process, at first the algorithm learns information about the system starting from an initial data set (which is called the training data set); then, data sets acquired in a later stage (which are called testing data sets) are analyzed and classified on the basis of the trained model and on the basis of information learned by the algorithm in the first phase.

If one interprets the phase of data acquisition in a vibration-based damage detection strategy under the paradigm of the machine learning approaches, two different situations can be considered. In the first situation, the training data set can be composed by vibration data that is related both to the undamaged and to the damaged structures, and the association between the data and the two possible states is known. This situation is indicated in the context of machine learning as supervised learning mode [Farrar & Worden, 2013]. In the second situation, the training data set is composed by vibration data that is only related to the structure that is undamaged. This situation is indicated in the context of machine learning as unsupervised learning mode [Farrar & Worden, 2013].

As reported in [Farrar & Worden, 2013], unsupervised approaches in SHM are more convenient than supervised approaches. In fact, for the second approaches (i.e. the supervised approaches) data related to the damaged structure are needed to form the training data set. Such data might be available when the SHM strategies are applied to mechanical structures. For example, for a generic type of machine that is produced in series, historical data of previous failures that happened in one component of the machine may be available. On the contrary, when the monitoring process is applied on existing civil structures, it is in general not possible to have vibration data that are related to a damaged state at the beginning of the monitoring phase. Of course, one can not artificially induce damage in the structure to obtain such kind of data.

Vibration-based damage detection strategies that, according to the interpretation of the process in the framework of machine learning, are developed using an unsupervised approach are the strategies that are considered in the present thesis. On one side, in fact, as reported in [Farrar & Worden, 2013], unsupervised approaches should be always considered for damage detection purposes whenever

possible; on the other side, these approaches are in general the only option that can be selected for civil structures.

An overview of a generic vibration-based damage detection process based on the paradigm of the "unsupervised approaches" is reported in the flow chart presented in Fig. 1.1. This process is mainly composed of three parts: data acquisition, feature extraction, and feature discrimination.

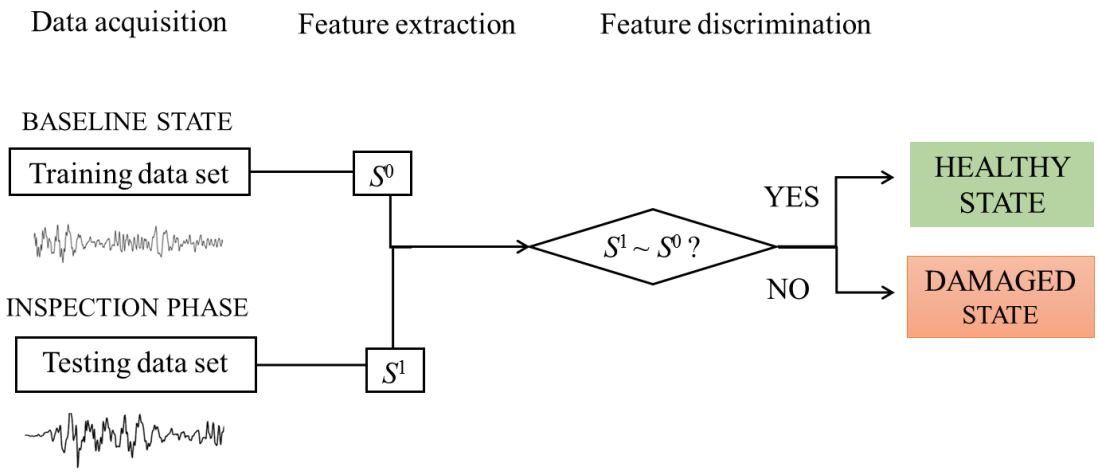

Figure 1.1. Overview of a generic vibration-based damage detection process.

Referring to the process of data acquisition (i.e. the first part of the flow chart), vibration data of the structure are acquired at first in the state of the structure that is assumed as healthy (baseline state). These data are used to form the training data set. In a later stage during the inspection phase, new vibration data are acquired, and these data form the testing data set.

The second part of the flow chart is defined as feature extraction, and it is related to the process of extracting the so-called damage sensitive features. According to the definition provided in [Farrar & Worden, 2013], "*a damage sensitive feature (DSF) is some quantity extracted from the measured system response data that indicates the presence (or not) of damage in a structure*".

The third part of the flow chart is defined as feature discrimination. This part is related to the process of comparing the DSFs obtained from the training data set

(baseline state) with the DSFs obtained from the testing data set. This part of the process has the objective of classifying the structure considered in the inspection stage as healthy or damaged. The comparison between the damage sensitive features related to the two different states is usually performed by defining a metric. As stated in [Farrar & Worden, 2013], a metric is a quantity that is able to measure the similarity or the difference between the DSFs. In practical applications, it is usually of interest to define metrics that are able to measure the departure of the DSFs in the possibly damaged state from the DSFs related to the baseline state.

According to [Farrar & Worden, 2013], in the context of the unsupervised approaches for vibration-based damage detection, an important class of methods for feature discrimination are the methods that belong to the field of outlier analysis [Barnett & Lewis, 1994], as indicated in the statistics community. This field is also known as novelty or anomaly detection in the context of the machine learning community. The simplest way of adopting these techniques, which also give in general an indication of how these techniques work, is to construct a statistical model of the system using the data that is related to the baseline structure. Then, the features extracted from the testing data set are compared with respect to the above-mentioned statistical model, and any deviation, in a statistical sense, from the original model is considered as a structural modification that can be associated to the presence of damage.

Detecting the existence of damage is not the sole achievement that can be obtained using a vibration-based damage detection strategy. The different achievement levels that can be obtained from the process were defined in the work by [Rytter, 1993], and subsequently revisited in the work by [Farrar & Worden, 2013]. These achievement levels were classified, as reported in Fig. 1.2, into five different levels. According to the first level the damage detection method gives an indication of the existence of damage in the structure. In the second level, the method gives information about the approximate and probable location of the damage on the structure. According to the third level the damage can be classified (i.e. the type of the damage can be determined). In the fourth level, the method can provide an estimate of the amount of damage that is present in the structure (i.e. damage quantification). Finally, the fifth level is related to the estimation of the residual life of the structure.

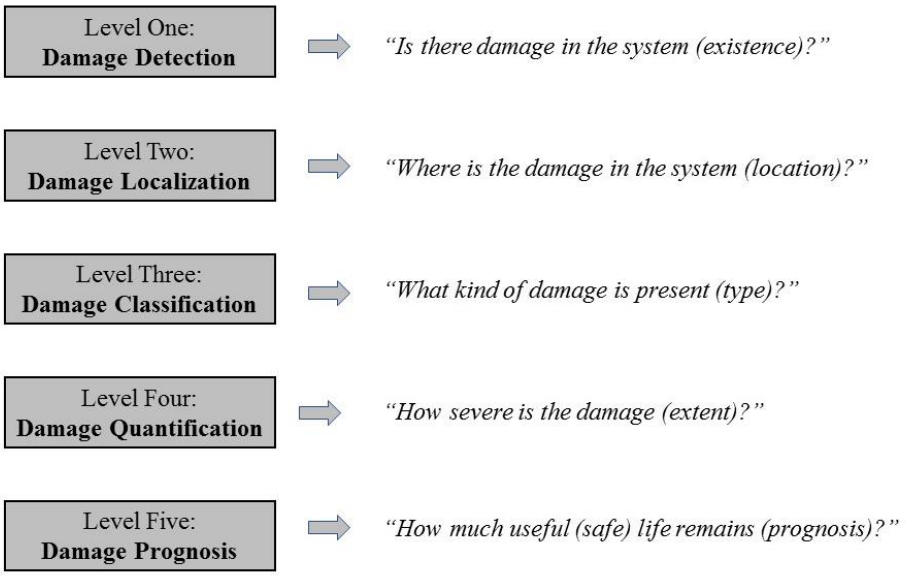

Figure 1.2. Achievement levels in damage assessment
(defined in [Farrar & Worden, 2013]).

As highlighted by [Farrar & Worden, 2013], an important aspect that has to be considered in the applications of vibration-based damage detection on real-life structures, especially civil structures, is that, during the monitoring phase, these structures can experience changing operational and environmental conditions. Referring to the latter, among the different variables that can be associated to changing environmental conditions, temperature is probably the one that is more relevant. Referring to the former, changing operational conditions can be associated to variations of the masses in the structure (that, for example, are due to the variations of the payloads). Changing operational and environmental conditions might affect in general the vibration responses of the structures, and it is thus important that such changes introduced into the system are not considered as modifications that are due to damage.

To conclude this section, it is important to underline that some axioms have been introduced in recent years in the field of Structural Health Monitoring (SHM). These fundamental axioms represent an important contribution for the definition of the subject, and they were presented in the works by [Worden et al., 2007; Farrar & Worden, 2013]. These axioms are as follows:

Axiom I: "All materials have inherent flaws or defects".

Axiom II: "The assessment of damage requires a comparison between two system states".

Axiom III: "Identifying the existence and location of damage can be done in an unsupervised learning mode, but identifying the type of damage present and the damage severity can generally only be done in a supervised learning mode".

Axiom IVa: "Sensors cannot measure damage. Feature extraction through signal processing and statistical classification is necessary to convert sensor data into damage information".

Axiom IVb: "Without intelligent feature extraction, the more sensitive a measurement is to damage, the more sensitive it is to changing operational and environmental conditions".

Axiom V: "The length- and time-scales associated with damage initiation and evolution dictate the required properties of the SHM sensing system".

Axiom VI: "There is a trade-off between the sensitivity to damage of an algorithm and its noise rejection capability".

Axiom VII: "The size of damage that can be detected from changes in system dynamics is inversely proportional to the frequency range of excitation".

The methods for damage detection that are considered in the present dissertation will be analyzed and interpreted under the general framework for vibration-based SHM and damage detection that is based on these axioms.

1.2 An overview of the vibration-based damage detection techniques available in the literature

As already mentioned in previous sections, the field related to the vibration-based structural health monitoring techniques applied for damage detection purposes is an extremely multidisciplinary field. In this context a large number of techniques can be applied, and in general several of such techniques were originally formulated in fields different from the field of SHM. For this reason, it is difficult to have a unique and exhaustive classification of all the techniques that can be employed in vibration-based damage detection. Moreover, the different techniques in general are related to one of the different phases of the damage detection process (e.g. extraction of the damage sensitive features, discrimination of such features etc.). The different techniques that are applied in the mentioned different phases can thus be combined together, and this leads to an exponential increase in the number of the different approaches that can be adopted.

In the literature the vibration-based damage detection methods are in general classified depending on the quantities and the types of information that are extracted from the vibration data and considered as damage sensitive features (i.e. the second phase of the damage detection process, as reported in Fig. 1.1). It is worth noting that this phase of the process is also the one that in general has received (and it is currently receiving) most of the attention of the research carried out in this field [Farrar & Worden, 2013]. According to the work by [Farrar & Worden, 2013], where the techniques are classified as a function of the damage sensitive features, such techniques can be grouped into different classes. Examples of such classes are the following, and each class includes methods that are:

1) based on signal statistics or features obtained using signal processing techniques
2) based on modal properties and features derived from modal properties
3) based on Finite Element Model (FEM) updating
4) based on time series models
5) other methods.

Another distinction can be made between the different techniques: it is possible to make a distinction between the non-model-based approaches and the model-based approaches [Alvin et al., 2003]. Methods that belong to the first type (i.e. the non-model-based approaches) determine and detect eventual changes and structural modifications using directly the vibration response signals of the structure [Alvin et al., 2003]. Approaches that belong to the second type (i.e. the model-based approaches, which are also indicated in the literature as inverse modelling approaches [Farrar & Worden, 2013]) are based on the determination of a physics-based model of the structure starting from the measured vibration data [Alvin et al., 2003; Farrar & Worden, 2013].

The methods that are based on the calculation of statistical properties of the structural response signals or on the extraction through signal processing techniques of the damage sensitive features (i.e. first class of methods reported in the above mentioned bulleted list) belong to the non-model-based approaches. On the contrary, the methods based on the identification of the dynamic properties of the structures (which are usually defined in terms of the modal parameters, i.e. natural frequencies, modal damping ratios, and mode shapes) or on the use of model updating approaches to define an accurate finite element model of the structure (i.e. second and third classes of methods) belong to the model-based approaches. Finally, the methods based on time series models, which are individuated as the fourth class of methods and which are based on the estimation of the coefficients of autoregressive models from the measured time series, can also be classified as model-based techniques. However, as discussed in [Farrar & Worden, 2013], one drawback of such techniques is that it is difficult to assign a physical meaning to the above-mentioned coefficients and to the changes detected using such approaches.

The general approach taken in this thesis is to consider damage detection techniques that are model-based and specifically physics-based techniques. In particular, as shown later in this section and in next section, the thesis focuses on techniques that are based on the extraction of the modal properties of the structures from vibration data and on the use of features derived from such modal properties to perform the damage detection. To adopt this model-based approach for damage detection, the techniques of the structural identification [Juang, 1994; Alvin et al.,

2003], and specifically of the modal identification [Ewins, 2000; Brincker & Ventura, 2015] are thus considered as part of the damage detection process.

Structural identification, according to the definition proposed in [ASCE, 2013], is "*the process of creating and updating a physics-based model of a structure based on its dynamic measured response which will be used for assessment of structure's health and performance"*. It is evident from this definition that the main goal of structural identification is to obtain a physics-based model of the structure. In general, the process is carried out by identifying this model of the structure starting from the measurements of input and output vibration data (i.e. from the measurements of the inputs that excite the structure and from the responses of the structure to such excitations). In particular, the basic principle behind all the identification techniques is that the model of the structure identified from the data has to minimize the difference between the responses predicted by that model and the experimental vibration data. This basic principle is clearly evident in a second definition of structural identification that was formulated in the work by [Doebling et al., 2000] and that is presented herein: structural identification can be defined as *"the parametric correlation of structural response characteristics predicted by a mathematical model with analogous quantities derived from experimental measurement"*. It is worth noting that most of the approaches that are adopted in structural identification, especially the ones that work in time domain, belong to the more general field of system identification [Ljung, 1987; Soderstrom & Stoica, 2001; Guidorzi, 2003]. Structural identification can thus be considered as the application of the system identification to dynamic systems that are structural systems.

Several structural identification methods were specifically formulated and developed with the objective of determining the dynamic modal properties of the structures (i.e. the modal parameters defined in terms of natural frequencies, modal damping ratios, and mode shapes). Such specific structural identification techniques are thus indicated as modal identification techniques. At this point it is important to underline one crucial aspect that is related to civil structures tested under ambient vibrations, for example, in the context of a vibration-based monitoring strategy. It is in general not possible to have reliable measurements of the natural inputs (e.g. wind loads, traffic loads, microtremors etc.) that excite the structure. In ambient vibration

tests it is possible in general to record only the structural responses of the structure. For this reason, one of the major issues that the modal identification techniques have to address when applied in such case is the fact that the calculations have to be performed starting from the structural vibration responses only and without the knowledge of the input excitations. This particular type of modal identification is thus indicated in the literature as output-only modal identification. In the last decades several research efforts have been dedicated to solving the output-only identification problem, and, nowadays, there exist robust techniques and algorithms that can be applied to estimate the modal parameters of a structure from output-only vibration data. It is worth noting that output-only modal identification (as well as structural identification) refers in general to the phase of processing the vibration data through adequate algorithms and techniques. This processing phase is only one phase of the different phases that are needed in the more general process of testing structures under ambient vibrations (which is the process that starts from the planning and the execution of the vibration test and ends with the determination of the dynamic properties of the structure). This way of testing structures has emerged in recent years as a mature discipline and engineering field, and it is indicated as Operational Modal Analysis (OMA) [Brincker & Ventura, 2015].

In the modal-based approaches for damage detection, the modal parameters extracted from the data (or other features derived from the modal parameters) are considered as damage sensitive features and used to detect eventual structural modifications that can be associated to a damaged state. The fundamental principle behind the use of such approaches for damage detection, is that damage in structures can lead to modifications in the mechanical and energy dissipation characteristics of the structures [Farrar & Worden, 2013], and thus, the vibration responses of the structures and the related modal parameters are in general affected by such structural modifications. It is worth noting that modal parameters extracted from vibration data can also be used to update a finite element model (FEM) of the structure. This procedure is usually performed using optimization techniques able to minimize a cost function that evaluates the discrepancies between the parameters related to the analytical model and the analogous quantities estimated from the data. As already

mentioned in this section, such approaches can also be used for damage detection purposes.

1.2.1 Modal-based and modal flexibility-based techniques for damage detection: a brief literature review

A brief literature review of the main techniques and damage sensitive features that can be considered in modal-based damage detection is presented in this section. Advantages and disadvantages of the different approaches are discussed, and the methods that represent the focus of the present dissertation are introduced. For an extensive and more comprehensive literature review of all the modal-based approaches in damage detection and of other methods that belong to classes different from the class of the modal-based approaches, the reader is referred to the literature reviews presented in the works by [Doebling et al., 1996; Sohn et al., 2003; Farrar & Worden, 2013] and to the comparative studies done by [Fan & Qiao, 2011; Sabatino & Ervin, 2015].

In the first approaches that were developed for modal-based damage detection the basic modal properties of the structures (e.g. natural frequencies and mode shapes) were considered as damage sensitive features, and different criteria were investigated to quantify the differences on such quantities. If one assumes that damage can induce a reduction in the local stiffness of some parts of the structure, it is clear that eventual structural modifications induced by the damage can be detected by analyzing the shifts in the natural frequencies of the structure. Many researches have been carried out by applying this criterion and, as reported in [Farrar & Worden, 2013], one of the earliest applications of this approach was found in the work by [Cawley & Adams, 1979], where the frequency shifts were used to detect damage in composite materials. It is evident that this criterion, where a single scalar for each structural mode (i.e. the natural frequency) is considered as a damage indicator, can not be used in general to obtain an achievement level in damage assessment higher that the mere detection of the existence of damage [Farrar & Worden, 2013].

To overcome the above-mentioned limitation of the method based on natural frequencies, later approaches started to consider mode shapes as damage sensitive features. Mode shape vectors, in fact, are quantities that are defined with reference to the geometry of the structure, and thus they can be used theoretically for damage localization. Again, if one assumes that damage is associated to a local reduction in the structural stiffness, then the analysis of the changes in the components of the mode shape vectors can provide information about the localization of such damage (this approach is the so-called change-in-mode-shapes method). In addition to this criterion based on the evaluation of the changes in mode shapes components, other criteria were defined and investigated in an attempt to find more systematic ways for comparing the mode shape vectors.

The Modal Assurance Criterion (MAC), for example, is a criterion that was formulated to evaluate the degree of correlation between mode shape vectors [Allemang & Brown, 1982]. Just after its definition, this criterion became very popular in modal identification and modal testing. Several applications, in fact, can be found in the literature were this criterion is used to compare analytical and experimental modal vectors for purposes of model validation and modal updating [Ewins, 2000]. In addition, the criterion was used in the context of vibration-based damage detection to compare mode shape vectors of the undamaged structure with the corresponding ones of the possibly damaged structure. As reported in [Farrar & Worden, 2013], one of the earliest applications of this damage detection approach was found in the work by [West, 1984], where damage in the body flap of a shuttle space orbiter was detected. It is worth noting, however, that since the Modal Assurance Criterion evaluates the degree of correlation between modal vectors, spatial information present in such vectors is compressed to a single scalar. Again, as already observed for the change-in-natural-frequency method, the MAC can be used in general only to detect the existence of damage in a structure (first achievement level according to [Rytter, 1993]).

For the above-mentioned reason, other approaches were investigated and proposed in the literature to localize damage in structures using mode shapes vectors. For example, [Lieven and Ewins, 1988] proposed a modified version of the Modal Assurance Criterion (MAC) that is defined as Coordinate Modal Assurance Criterion

(CoMAC). In such modified version of the MAC, the degree of correlation is not evaluated between vectors that are mode shape vectors related to a single structural mode (as done in the MAC). In the CoMAC criterion the degree of correlation is evaluated between vectors that are composed by the components of the different mode shapes related to the same spatial location. Another approach was presented in the work by [Yuen, 1985], and this approach is based on the evaluation of the so-called Yuen function, which combines both mode shape vectors and natural frequencies. This function, in fact, evaluates the coordinate-by-coordinate difference between the modal vectors in the possibly damaged and undamaged states, but before performing such operation (which is very similar to the one adopted in the basic change-in-mode shape method) each modal vector is scalarly divided by the corresponding natural frequency.

All the methods discussed so far (i.e. the methods that consider the basic modal properties as damage sensitive features) are affected by a general limitation. In fact, as observed in [Farrar & Worden, 2013], the low frequency modes of the structures (i.e. the first modes which are the modes that can be more easily identified in a vibration test) are quite insensitive to local damage in structures. For this reason, research efforts were spent to find features derived from basic modal properties that are more sensitive to local damage in structures. To reach such objective, more complex modal-based methods were developed. Example of such more complex methods, which are described in the following, are the ones based on the evaluation of the mode shape curvature, the modal strain energy, and the modal flexibility.

The methods based on the evaluation of the mode shape curvature and the modal strain energy were both developed for structures that are mainly characterized by a flexural/bending behavior. The first approach was developed by [Pandey et al, 1991], and, according to this method, the damage localization is performed by evaluating eventual variations in the second derivative (i.e. the curvature) of the mode shape profiles. This method is based on the premise that the curvature of mode shape profiles is more sensitive to damage than the displacement components of the mode shapes. In fact, the curvature of the displacement profile of a beam-like structure is proportional to the inverse of the flexural stiffness. Thus, in general, a reduction in the flexural stiffness of that structure lead to an increase in the curvature of the

displacement profile. The second approach (i.e. the one based on the evaluation of the modal strain energy) was presented and verified in the works by [Stubbs et al., 1992; Stubbs et al., 1995]. This method is based on the premise that when a structure experiences a damage (such as a local stiffness reduction), the distribution of the strain energy in the damaged state is altered with respect to the distribution of the strain energy in the undamaged state. According to the method, the modal strain energy is defined as the strain energy that is present in a structure when it deforms with the profile of one of the mode shapes. The damage localization is thus performed by the analysis of the variation of the modal strain energy in different regions of the structure.

Most of the features and metrics presented so far use the individual modal parameters of a single structural mode to perform the damage detection. If one again interprets damage as a local reduction in the stiffness of the structure, this means that information related to damage (which in such case is a mechanical quantity) is decomposed into different contributions that are related to the different structural modes. Referring to this point it is important to underline that in general the identified modal parameters, in terms of natural frequencies and mode shapes, can be also used to obtain an estimate of the mechanical parameters of the structures, for example, the stiffness (or flexibility) coefficients of the different parts of the structure. This operation can be performed in modal identification if mass-normalized mode shapes of the structures are available, and it is based on the principle of cumulating the contribution of the different structural modes to estimate the stiffness (or flexibility) matrices of the structures.

It is important to underline that in modal testing and identification of structures, and especially considering civil structures, not all the structural modes can be identified. Generally, only the first lower structural modes are identified. This means that modal information extracted from the test is in general incomplete, and thus the estimates of the stiffness (or flexibility) matrices of the structure derived from the test are approximated with respect to the corresponding true matrices. Several researches were carried out in the literature to solve the above-mentioned inverse problem on real structures. As already mentioned, the operation can be performed in two different ways: on one side, by estimating the stiffness matrix of the structure; on the other side, by estimating the flexibility matrix. As reported in the work related to

the theory of incomplete modal models by [Berman & Flannelly, 1971], the contribution of the first lower modes in the flexibility matrix is higher with respect to the contribution of the same modes in the stiffness matrix. This principle was extensively analyzed and verified in the literature [Gao & Spencer, 2002; Duan et al., 2005; Koo et al., 2010], and the conclusion drawn from all the studies is that estimating flexibility matrices from identified modal data is a preferable approach than estimating stiffness matrices. This is because in general accurate estimates of the flexibility matrix can be obtained using only the first lower modes. This principle is discussed more in detail in Chapter 3 of the dissertation, where it is shown how experimental flexibility matrices of structures can be estimated starting from vibration data and specifically from modal parameters. These matrices are usually indicated as modal flexibility matrices.

Estimating modal flexibility matrices from vibration data is the main operation performed in all the modal flexibility (MF)-based methods for damage detection. Due to the above-mentioned property of the modal flexibility matrix, such methods have emerged as an important class of methods in vibration-based damage detection (VBDD), and they can be considered as the most advanced techniques in modal-based damage detection. A great advantage of all the modal flexibility-based approaches is that a model of the structure is estimated directly from the vibration data. This experimentally-derived model of the structure is the modal flexibility matrix, and it is an important source of information for damage detection purposes. In fact, as demonstrated in the work by [Zhao & DeWolf, 1999], where sensitivity studies were performed on mass-spring numerical models, the coefficients of the modal flexibility matrices are more sensitive to damage than the modal parameters individually (i.e. natural frequencies and components of the mode shapes). Moreover, since in the modal flexibility-based methods for damage detection an attempt is made to estimate the mechanical properties of the structure, such approaches are theoretically suitable to perform a quantification of the extent of damage (i.e. the fourth achievement level according to the classification formulated by [Rytter, 1993]). This achievement is, on the contrary, much more difficult to be obtained if the damage quantification is performed by considering the modal parameters individually.

The modal flexibility-based methods for vibration-based damage detection can be grouped into three main classes, where each class includes methods that are:

1) based on the evaluation of the change-in-flexibility matrix
2) based on a decomposition of the change-in-flexibility matrix
3) based on the estimation of structural deflections from modal flexibility matrices
4) other methods.

One of the earliest approaches in modal flexibility-based damage detection is the so-called change-in-flexibility method. This method was presented for the first time in the works by [Pandey & Biswas, 1994; Pandey & Biswas, 1995], and it is based on the estimation of the modal flexibility matrices of the structures both in the undamaged and in the damaged states. Then, these two matrices are subtracted to obtain the change-in-flexibility matrix, which is used as a metric to localize the damage. This operation is done by analyzing the components of the change-in-flexibility matrix. The degree-of-freedom of the structure that is detected as the one closest to the damage location is the DOF that corresponds to the column of the change-in-flexibility matrix where the maximum variation is present. In the works by [Pandey and Biswas, 1994; Pandey and Biswas, 1995] the approach was verified on beam-like structures, considering both analytical and experimental analyses. The experimental verification was conducted on various wide-flange steel beams that were tested through an impact hammer. Saw cuts in the flange of such steel beams were created to artificially introduce damage in the structure.

Two methods belong to the group of the modal flexibility-based methods that are based on a decomposition of the change-in-flexibility matrix. The first one is the Damage Locating Vector (DLV) method, which was proposed in the work by [Bernal, 2002]. The method was formulated to localize damage in a generic structural system, and similarly to the method described in previous paragraph, it is based at first on the determination of the change-in-flexibility matrix. The basic idea behind the DLV method is to compute a set of load vectors that if applied to the structure induce a zero stress field in the elements of the structure that are damaged. On the basis of this analysis and due to the property of these load vectors, the damaged elements can be

identified. Such load vectors are obtained by computing the null space of the change in flexibility matrix, and this operation is performed numerically through a singular value decomposition of that matrix. The DLV approach was verified through numerical simulations performed on a truss structure [Bernal, 2002]. The analytical model of this truss structure was excited by white noise inputs, and the identification of the structural modes was performed using input-output modal identification techniques. This method, which was originally formulated to be applied starting from the results of the input-output modal identification, was also extended to the case of the output-only modal identification [Bernal, 2001; Bernal & Gunes, 2002]. This version of the method extended to the output-only case is termed Stochastic Damage Locating Vector (SDLV). Other techniques than can be applied with the same purpose (i.e. applying the DLV method using output-only vibration data) were also presented in the works by [Duan et al., 2005; Duan et al., 2007]. More details on these techniques formulated by [Bernal, 2001; Bernal & Gunes, 2002; Duan et al., 2005; Duan et al., 2007] will be presented later in this chapter in the section related to the definition of the objectives of the thesis.

Another method that is based on a decomposition of the change-in-flexibility matrix (i.e. the second group of modal flexibility-based methods reported in the above-mentioned bulleted list) was defined in the work by [Yang & Liu, 2009]. This method is based on the eigenparameter decomposition of the change in flexibility matrix, and it can be used both for damage localization and for damage quantification. In the work by [Yang & Liu, 2009], the validity of the methodology was demonstrated on three different structural systems using numerical simulations.

The third group of modal flexibility-based methods reported in the above-mentioned classification is composed by the methods based on the evaluation of structural deflections starting from experimental modal flexibility matrices. These deflections are thus indicated as modal flexibility-based deflections, and they are calculated by applying special loads termed “inspection loads” to models of structures identified through vibration tests (i.e. modal flexibility matrices). It is worth noting that such inspection loads are not real loads that are effectively applied to the structures. These loads are only introduced in the calculations related to the damage detection process.

Some of the earliest approaches related to the application of techniques based on the estimation of deflections from modal flexibility matrices can be found in the works by [Zhang, 1993; Zhang & Aktan, 1995; Zhang & Aktan, 1998]. As defined in such works, the uniform load (UL) surface is the deflection profile that can be calculated from experimentally-derived modal flexibility matrices by applying a uniform load at all the degree-of-freedoms of a structure. This load is defined as a vector composed by components that are all equal to one. As observed in the works by [Zhang, 1993; Zhang & Aktan, 1995; Zhang & Aktan, 1998], the uniform load deflection evaluated from modal flexibility is an important source of information in vibration-based structural identification and damage detection. In fact, the components of such deflection can be considered as damage-sensitive features, and eventual modifications of these features, when at least two structural states are compared, can be associated to structural damage, such as a stiffness reduction. A modified version of the uniform load surface method was also presented in the work by [Zhang & Aktan, 1995]. According to this modified version of the method, the second derivative (i.e. the curvature) of the uniform load surface is evaluated, and the values of the deflection curvature are considered as damage-sensitive-features for damage localization. This approach was verified by the authors by performing numerical simulations on a three-span bridge structure.

It is worth noting that these methods based on the calculation of the uniform load deflections [Zhang, 1993; Zhang & Aktan, 1995; Zhang & Aktan, 1998] were introduced approximately at the same time in which the change-in flexibility method was presented [Pandey & Biswas, 1994; Pandey & Biswas, 1995]. These two methods have several similarities, and they are based on a similar formulation. The methods based on modal flexibility-based deflections in fact can be considered as methods that were directly derived from the methods based on modal flexibility matrices only. However, an important aspect related to the two methods and which shows the advantages of using structural deflections (instead of modal flexibility matrices in the damage detection process) has to be highlighted. As already mentioned, in vibration testing and modal identification of structures, especially civil structures, not all the modes can be identified. Then, the use of incomplete modal models [Berman & Flannelly, 1971] for assembling modal flexibility matrices leads to inevitable errors,

which are defined, according to [Zhang & Aktan, 1998], as flexibility truncation errors or modal truncation errors. These errors are thus generated by the fact that only a limited number of structural modes is considered in the calculations. The errors present in the modal flexibility matrices affect, of course, also the modal flexibility-based deflections which are calculated from these matrices. The above-mentioned important aspect related to modal flexibility matrices and structural deflections is that, as demonstrated in the works by [Zhang, 1993; Zhang & Aktan, 1995; Zhang & Aktan, 1998], the components of the uniform load deflections are in general less sensitive to modal truncation errors than the components of the modal flexibility matrices. In addition, as also shown in [Zhang & Aktan, 1998], the components of the uniform load deflections are also less sensitive to experimental errors than the components of the modal flexibility matrices. Such experimental errors are always present on features derived from an experimental test, and, referring to vibration tests, these errors are mainly due to the inevitable noise that is present in the measurements. Uncertainties thus affect the modal parameters of structures that are identified from the data, and these uncertainties on the modal parameters then propagate to modal flexibility matrices and modal flexibility-based deflections. These two above-mentioned properties of the uniform load deflections were demonstrated in the works by [Zhang, 1993; Zhang & Aktan, 1995; Zhang & Aktan, 1998] using both numerical and experimental analyses on a three-span bridge structure. It is worth noting that this structure is the same structure that was used to verify the damage detection approach based on uniform load deflections [Zhang & Aktan, 1995].

Several other applications where the uniform load deflections are used for the assessment of the condition of structures and for damage detection can be found in the literature. For example, in the work by [Catbas et al., 2006] uniform load deflections were employed to detect and localize damage in two real-life bridge structures. One of the two bridges was tested using traditional input-output testing, while the second bridge was tested under ambient vibrations. In another work by [Catbas et al., 2008] the two damage detection methodologies based, respectively, on the evaluation of the displacements of the uniform load deflections and the curvature of the uniform load deflections were compared using the experimental data of a laboratory bridge model. The authors showed that for beam-like structures the method

based on the evaluation of the curvature of the deflections can be advantageous in the cases in which changes due to damage are not detected using the displacements of the deflections. However, the authors also highlighted the fact that non-negligible numerical errors may be introduced in the calculations when the curvature of the deflections is evaluated.

The method based on the evaluation of uniform load deflections [Zhang, 1993; Zhang & Aktan, 1995; Zhang & Aktan, 1998] was taken one step further in the work by [Koo et al., 2008]. In this last work a methodology for damage localization in beam-like structures was presented. The main difference between the approach based on uniform load deflections and the more recent approach proposed in [Koo et al., 2008], is that in this last work a more rigorous procedure to map the changes in the modal flexibility-based deflections with the locations of the damage is adopted. The main idea behind the approach is that, by applying to the structures special loads termed Positive Bending Inspection Loads (PBIL), there exists an explicit relationship between the changes in the modal flexibility based-deflections and the damage (e.g. localized stiffness reductions in the structure). It is worth noting that such PBIL loads are not necessarily uniform loads, and they depend on the geometry of the bridge (for example, they depend on the number of the spans and on the boundary conditions of the bridge). The validity of the approach was demonstrated using both numerical simulations and experimental tests conducted on a two-span steel continuous beam.

Recently, the damage detection approaches based on the evaluation of modal flexibility-based deflections have been also applied on building structures. In the work by [Koo et al., 2010] a method for output-only damage detection in shear building structures was presented. Then, in later works by the same authors [Koo et al., 2011; Sung et al., 2012] the method was improved further. According to this method, the modal flexibility-based deflections of a shear building structure are calculated by applying to the structure (i.e. to an experimentally-derived model of the structure based on the modal flexibility matrix) special loads, termed Positive Shear Inspection Loads (PSIL) [Koo et al., 2010; Koo et al., 2011; Sung et al., 2012]. These loads are special loads that induce positive shear forces in each story of the shear building structure. As will be explained in detail in next section where the objectives of the thesis are outlined, this method is frequently mentioned through all the present

dissertation. For this reason and even if the proposed terminology was not used in the original work that introduced the method, this method is denoted in the present dissertation as PSIL method.

It is worth noting that among the different positive shear inspection loads that can be chosen and applied to the shear building structure, in the works by [Koo et al., 2010; Koo et al., 2011; Sung et al., 2012] it is suggested to use a uniform load. This is the same load adopted in the uniform load surface method [Zhang, 1993; Zhang & Aktan, 1995; Zhang & Aktan, 1998], which was on the contrary developed mainly for bridge structures. There exists, however, an important difference between the two approaches. According to the uniform load surface method, the components of the deflections are considered as damage-sensitive features. On the contrary, in the PSIL method, which was specifically developed for shear building structures, after computing the modal flexibility-based deflections, an additional operation has to be made in the calculations. In fact, the interstory drifts associated to such deflections are evaluated and considered as damage-sensitive features. Once the modal flexibility-based interstory drifts of the structure have been evaluated both in the undamaged and in the possibly damaged states, these parameters can be used for the localization of damage. The method in fact is able to identify the stories of the structure that have been affected by damage (e.g. a story stiffness reduction). One important characteristic of the PSIL method is that this operation of feature discrimination (where the features are the interstory drifts) is performed using criteria that are taken from the field of outlier analysis (which are also known as techniques for novelty detection). As already mentioned, these novelty detection techniques are the most effective and simplest techniques that can be used for feature discrimination in the framework of a vibration-based damage detection strategy that is based, according to the machine learning interpretation [Farrar & Worden, 2013], on an unsupervised learning mode.

The PSIL method was verified in the works by [Koo et al., 2010; Koo et al., 2011; Sung et al., 2012] using both numerical simulations and experimental vibration tests on frame building structures. In the works by [Koo et al., 2010; Koo et al., 2011], a 5-story frame building structure tested using a shaking table is considered. In these tests the damage was simulated by substituting some columns of the frame structure

with other columns with a reduced cross-section. In the work by [Sung et al., 2012], a 5-story full-scale shear building tested using shaker excitations is considered and used to apply the PSIL method. In such case the damage was simulated by modifying the stiffness of a spring member that was positioned in the bracing system of one story of the structure.

It is important to underline that the PSIL method was developed for shear building structures that can be modeled as plane structures. For this reason, the experimental verifications, performed using a laboratory frame building structure [Koo et al., 2010; Koo et al., 2011] or a full-scale shear building [Sung et al., 2012], were conducted by considering structures with a plan-symmetric configuration both in the pristine and in the damaged states. Moreover, the tests were performed using uniaxial excitations both in the shake table tests and in the shaker tests. In this way the structures were tested only in one prevalent direction, and 2D analyses were performed to estimate the modal flexibility matrices and the modal flexibility-based deflections of the structures in that direction. It is also worth noting that both in the shake table and shaker tests the structures were excited by white noise input signals. Then, these input excitations were not considered in the analyses, and the modal parameters of the structures were obtained using output-only modal identification techniques. This choice was done to mimic the situation that one has to analyze when real-structures are tested under ambient vibrations. As already mentioned, to assemble modal flexibility matrices mass-normalized mode shapes are required. However, one drawback in output-only modal identification is that mass-normalized mode shapes can not be directly obtained using output-only vibration data. In the works by [Koo et al., 2010; Koo et al., 2011; Sung et al., 2012] where the PSIL method is presented, the authors have used the system mass matrix of the structure to mass-normalize the mode shapes identified using the output-only modal identification. This mass matrix of the structure was thus estimated a-priori, and it is not a quantity that was derived from the data. These characteristics of the PSIL method (i.e. the fact that the method was developed for plane structures and the fact that an a-priori estimation of the mass matrix was used to normalize the mode shapes in output-only identification) are aspects that are particularly relevant in the present dissertation. These aspects will be

specifically addressed later in this chapter in the Section 1.3 where the objectives of the thesis are outlined.

As claimed by the authors in [Koo et al., 2010; Sung et al., 2012], one of the main advantages of the PSIL method is that for the considered structures (i.e. shear building structures) there exists an explicit relationship between damage (e.g. a story stiffness reduction) and the changes in the modal flexibility-based deflections that are used to localize the damage. This property makes the method very effective in localizing the damaged stories of shear building structures. To show the effectiveness of the PSIL method, the technique was compared with other modal-based damage detection techniques. As reported in [Koo et al., 2010; Sung et al., 2012], the PSIL method has shown better performances than both the method based on mode shape curvature [Pandey et al, 1991] and the method based on the modal strain energy [Stubbs et al., 1992; Stubbs et al., 1995] in the damage localization on shear building structures.

A comparison between a technique that is almost equivalent to the PSIL method and other damage detection techniques is also shown in the work by [Zhang et al., 2013]. In this work the approach based on the evaluation of the modal flexibility-based deflections was used to detect and localize damage in a steel frame structure. The structure and the vibration data used in this work are benchmark studies for SHM and damage detection in building structures, which are known in the literature as IASC-ASCE benchmark studies [Dyke et al., 2003; Ventura et al., 2003; Dyke, 2011]. The mentioned benchmark structure was tested using various types of excitations (impact hammer, electrodynamic shaker, and ambient vibrations), and in the work by [Zhang et al., 2013] the impact hammer tests were analyzed. The damage detection was carried out by performing a 2D analysis and by estimating the uniform load deflections of the structure. Then, the interstory drifts of the structure were evaluated (which is the same approach adopted in the PSIL method). As shown by the results presented in [Zhang et al., 2013], the technique based on the evaluation of the interstory drifts has shown better performance than the method based on the evaluation of the curvature of the uniform load deflections [Zhang & Aktan, 1995] in the damage localization performed on the building structure.

As shown in the works by [Koo et al., 2011; Sung et al., 2012], the PSIL method can be used not only for damage localization, but also for damage quantification. This is an aspect that was not included in the first version of the PSIL method presented in [Koo et al., 2010]. A great advantage of the PSIL method is that the damage quantification (i.e. a quantification of the stiffness reduction that a story might have experienced as an effect of damage) can be carried out using simple algebraic operations on the interstory drifts calculated from the modal flexibility-based deflections. As reported in [Koo et al., 2011], performing the damage quantification using the PSIL method is much more advantageous than using FEM updating procedures, which are traditionally used for damage quantification. On one side, in fact, the PSIL method does not require a FEM model of the structure. On the other side, the calculations that have to be performed using the PSIL method are much simpler than any finite element model updating procedure (which is based in general on the use of optimization techniques).

1.3 Focus and objectives of the work

The present dissertation focuses on the methods for vibration-based damage detection that are based on the determination of structural deflections starting from experimentally-derived modal flexibility-based models of structures subjected to vibration tests. As already mentioned in previous section and as graphically depicted in Fig. 1.3, these methods are a sub class of the modal flexibility-based methods for damage detection.

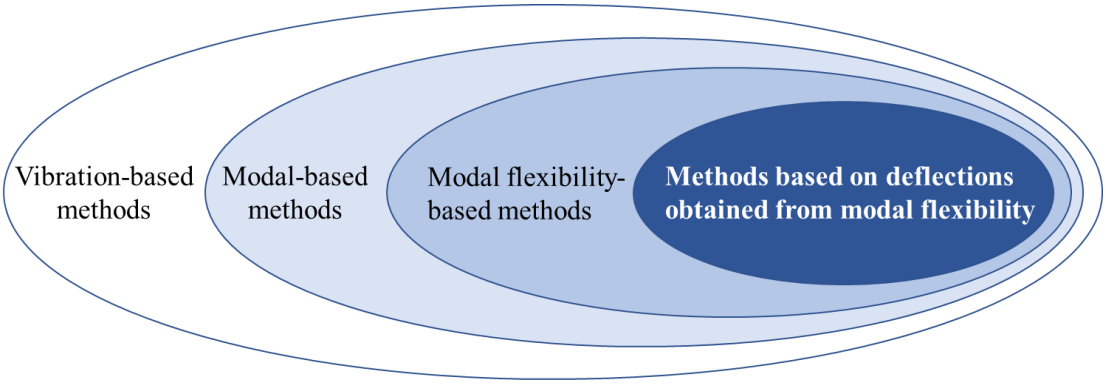

Figure 1.3. Diagrammatic representation of the damage detection methods considered in the thesis.

Vibration-based techniques for structural identification and damage assessment have been investigated in the civil engineering community since the early 1980s [Farrar & Worden, 2013]. However, as evident in the literature [Doebling et al., 1996; Sohn et al., 2003; Farrar & Worden, 2013] and as explicitly reported in the works by [Koo et al., 2010; Koo et al., 2011; Sung et al., 2012], the great majority of the damage detection studies were performed on bridge structures. Fewer studies were conducted on building structures.

In light of this premise, the present dissertation focuses mainly on building structures and on the application of the modal flexibility-based techniques for damage detection on such structures. Referring to the structural identification, the thesis focuses especially on the application of the output-only modal identification techniques. These techniques are considered as a tool that is integrated in the damage detection process, and these techniques were selected because they can be specifically applied on the data of structures tested under ambient vibrations. Referring to the damage detection methods, the Positive Shear Inspection Load method [Koo et al., 2010] for output-only damage detection in building structures is considered in the thesis as the reference method and the starting point for the development of most of the research investigations. As already mentioned in previous section, the PSIL method can be thought as an evolution of the uniform load surface (ULS) method [Zhang & Aktan, 1998], originally developed for bridge structures, to the case of building structures.

Three main problems are considered in the dissertation. These problems have been defined and analyzed after having recognized potential research gaps in the literature. Such research gaps were the starting points for most of the research investigations presented in this dissertation. The three problems and the research investigations that were undertaken to address these problems are presented in the following.

1.3.1 Problem and objective no. 1

The first main problem considered in the thesis is related to the fact that modal flexibility matrices and thus modal flexibility-based deflections of real-life structures subjected to vibration tests are in general estimated using incomplete modal models. As already discussed in previous section, in fact, in modal testing and identification of civil structures not all the structural modes can be identified. This is especially true for structures tested under ambient vibrations. The input in such case has a wide frequency content, however, since the test is performed using exclusively natural excitations, some structural modes may not be excited, and they may not be identified [Brincker & Ventura, 2015]. In addition, in vibration testing of structures extracting the high-order modes is in general more difficult than extracting the low-order modes. As already mentioned in previous section, using a limited number of modes to assemble the modal flexibility matrices generates errors that are indicated as flexibility or modal truncation errors, and these errors also affect the modal flexibility-based deflections. The study of these errors on modal flexibility matrices and related deflections is defined in the literature, according to [Zhang & Aktan, 1998], as modal truncation error analysis. This analysis aims to investigate how many modes need to be included in the calculations in order to obtain good estimates of the modal flexibility matrices and the modal flexibility-based deflections derived from experimental data. As discussed in previous paragraphs, the effect of the modal truncation errors is reduced by adopting the approach based on the estimation of modal flexibility matrices (instead of estimating stiffness matrices). Moreover, as demonstrated in the work by [Zhang & Aktan, 1998], the components of the uniform load deflections are less sensitive to modal truncation errors than the components of the modal flexibility matrices.

The first main objective of the thesis is to continue the investigations in this area of research on the topic of modal truncation error analysis, by focusing on modal flexibility-based deflections of building structures. In particular, the objective is to study the truncation errors that are introduced when the modal flexibility-based deflections of the structures are calculated using a limited number of modes and by considering the case of generic inspection loads. In the literature, on the contrary, it

was found that these analyses have been performed mainly on modal flexibility-based deflections evaluated for a uniform load.

The research investigations carried out on this topic were developed with two main purposes. On one side, an approach was proposed to predict the truncation effects expected on the modal flexibility-based deflections due to a generic inspection load. As shown in detail in Chapter 4 of the present dissertation, advantage of the proposed approach is that an indication of the expected truncation effects is obtained using only the subset of structural modes that are identified and included in the calculations of the truncated modal flexibility-based deflections. On the other side, inspection loads different from the uniform load were considered and applied on flexibility-based models of building structures with the aim of reducing the truncation errors on the modal flexibility-based deflections.

1.3.2 Problem and objective no. 2

As already mentioned in Section 1.2.1, the Positive Shear Inspection Load (PSIL) method for vibration-based damage detection in shear building structures was formulated for structures that can be modeled mainly as plane structures. The method, in fact, was verified and applied by the authors that presented the methodology through vibration tests on frame building structures with symmetric configurations (both in the pristine and in the damaged states). As already mentioned, these vibration tests were performed using uniaxial excitations in shaking table tests [Koo et al., 2010; Koo et al., 2011] or shaker tests [Sung et al., 2012]. Then, 2D analyses were performed to estimate the modal flexibility matrices and the modal flexibility-based deflections of the structures in the direction considered in the vibration tests.

Of course, in practice one might have to deal with structures that are more complex than structures which can be modeled as plane structures. Real-life building structures can be characterized, for example, by a generic distribution of the stiffness and the mass of the different stories. Alternatively, even if the structure considered in the damage detection process as the pristine structure is plan symmetric, the structure can then experience a damage in a generic position of any story. The structure in the

damaged state can thus be a plan asymmetric structure, which can not be modeled as a plane structure.

In light of this premise, it is clear that it is of interest to have a damage detection technique that can be applied on a 3D building structure. This represents the second main problem addressed in the thesis, and an attempt was made to extend the Positive Shear Inspection Load (PSIL) method so that it can be applied on structures that can not be modeled as plane structures. The research investigations carried out with reference to this problem were performed by considering simple rectangular "box type" 3D building structures [Brincker & Ventura, 2015]. In particular, ambient vibration tests were planned and then executed on a 3D steel frame structure to carry out the above-mentioned research investigations. The data of these ambient vibrations tests were used to localize and quantify single- and multiple- damage in the 3D steel frame structure, and such damaged conditions were created by imposing local stiffness reductions in the members of the structure.

1.3.3 Problem and objective no. 3

As already mentioned in Section 1.2.1, it is important to underline that modal flexibility can be estimated only when mass-normalized mode shapes are available. Mass-normalized mode shapes can be obtained from the data of forced vibration tests (using input-output modal identification techniques) when there exists at least one actuator-sensor pair [De Angelis et al., 2002], i.e. a driving-point measurement is acquired in the test [Farrar & Worden, 2013]. This means that the scaling factors on the mode shapes can be obtained from vibration data when in the experimental test setup the actuator and one sensor are located in the same position on the structure. On the contrary, when an operational modal analysis (i.e., an output-only modal identification) is performed starting, for example, from ambient vibration data of a structure (i.e. the case of interest for the present dissertation), only arbitrarily-scaled mode shapes can be obtained from the data. This is because no information about the exciting inputs are in general available in ambient vibration tests. As reported in [Duan et al., 2005], flexibility matrices are not readily available and can not be estimated directly from the vibration data when the output-only modal identification

is applied. This represents a drawback that is common to all the modal flexibility-based approaches when applied in the important case of structures under ambient vibrations [Brincker & Ventura, 2015].

Before discussing the third main objective of the thesis, a brief overview on how this modal scaling problem in output-only modal identification has been addressed in the literature is presented.

The mass normalization of the mode shapes can be carried out in the framework of an ambient vibration test using the strategies that belong to the classes of the so called "mass change methods" [Parloo et al, 2003; Brincker & Andersen, 2003; Bernal, 2004; Aenlle et al., 2010] and the "mass-stiffness change methods" [Khatibi et al., 2012; Lopez-Aenlle et al., 2012]. According to these techniques, an ambient vibration test is performed at first on the original structure. Then, the test is repeated by applying modifications in the mass and/or in the stiffness of the structure. These modifications have to be known and quantified, and they represent a piece of information required to perform the mode shape scaling. These strategies are absolutely suitable to solve the problem of modal scaling in output-only identification. However, as reported in [Brincker & Ventura, 2015], it might be challenging in practice to apply such known mass/stiffness modifications on civil structures, especially large civil structures. Moreover, these strategies can be convenient strategies for the cases in which few ambient vibration tests have to be performed on the structure, while they might not be a practical solution to be applied in the context of ambient vibration monitoring for damage detection purposes.

An alternative approach was presented in the work by [Aenlle & Brincker, 2013] where a FEM model is used to mass normalize the mode shapes derived from output-only vibration tests. This last approach is similar to the strategy that was adopted in the work by [Koo et al., 2010; Koo et al., 2011; Sung et al., 2012], where the Positive Shear Inspection Load (PSIL) method for output-only damage detection in building structures was presented. As already mentioned in Section 1.2.1, in the works by [Koo et al., 2010; Koo et al., 2011; Sung et al., 2012] the mass normalization of the mode shapes obtained from output-only modal identification was carried out using an a-priori estimate of the system mass matrix.

In light of this premise, the third objective of the thesis is to propose, on the basis of the theory behind the PSIL method [Koo et al., 2010; Koo et al., 2011; Sung et al., 2012], a modal-flexibility based approach for output-only damage detection in building structures that can be applied with minimal or no a-priori information on the structural masses. This is thus an attempt to make the damage detection process based on modal flexibility-based deflections independent as much as possible from an a-priori estimate of the mass matrix of the structure (required on the contrary in the PSIL method).

A similar problem was investigated by some authors [Bernal, 2001; Bernal & Gunes, 2002; Duan et al., 2005; Duan et al., 2007] in the context of another damage detection method - i.e. the Damage Locating Vector (DLV) method [Bernal, 2002], which has been already described in Section 1.2.1. In the works by [Bernal, 2001; Bernal & Gunes, 2002; Duan et al., 2005; Duan et al., 2007] strategies to extend the DLV method, originally formulated to be applied in input-output identification, to the case of output-only identification were investigated.

Two procedures that were presented in the works by [Bernal, 2001; Duan et al., 2005] represented the starting point for the research investigations that were carried out in the context of the third main problem considered in the thesis. The above-mentioned procedures can be used to obtain the distribution of the masses of a structure (i.e. a mass matrix proportional to the corresponding true mass matrix) starting from output-only vibration data and from the results of the output-only modal identification. Then, the proportional mass matrix can be used to assemble matrices that are proportional to the corresponding true flexibility matrices (such matrices are defined as proportional flexibility matrices). The proportional flexibility matrices are finally adopted (instead of the true flexibility matrices) to perform the damage detection using the Damage Locating Vector (DLV) method. These procedures, presented in the works by [Bernal, 2001; Duan et al., 2005] and originally formulated to be applied with the DLV method, were adapted and integrated into the framework of the Positive Shear Inspection Load method for damage detection in building structures, according to the approach proposed in the present dissertation.

1.4 Organization of the thesis

In this first chapter an introduction to the topics of vibration-based structural health monitoring and damage detection is provided together with the description of the objectives of the thesis. To conclude this chapter, the organization of the thesis is presented. The organization of the thesis is also shown in the diagrammatic scheme reported in Fig. 1.4.

The thesis is organized into two main parts. The first part concerns the presentation of the theoretical background, and it is composed by this first chapter, by the second chapter, and by the third chapter. The second chapter is an introduction to the topics of modal testing and modal identification. After discussing the motivations for which ambient vibration tests, instead of a traditional input/output forced vibration tests, can be more convenient ways for testing civil structures, an overview of the fundamental assumptions and principles in operational modal analysis (and output-only modal identification) is presented. Then, a brief review of the different output-only modal identification techniques that can be applied to estimate the modal parameters of structures tested under ambient vibrations is presented, and the output-only modal identification techniques that are applied in thesis are introduced. The third chapter is dedicated to the description of the existing modal flexibility-based approaches that are considered in the thesis (i.e. state-of-the-art approaches). After introducing how the modal flexibility matrices and the modal flexibility-based deflections of structural systems can be estimated from vibration tests (and, specifically, from identified modal parameters), the chapter presents in detail the steps and the theory related to the Positive Shear Inspection Load (PSIL) method [Koo et al., 2010] for vibration-based damage detection in shear building structures.

The second part of the thesis presents the research investigations that were carried out and the approaches that were developed to address the three main problems considered in the thesis (i.e. the problems discussed in Section 1.3). This second part of the thesis is composed by the fourth, the fifth, and the sixth chapters, which correspond, respectively, to the first, the second, and the third problems discussed in Section 1.3. The fourth chapter presents the research investigations carried out on the topic of truncation error analysis on modal flexibility-based deflections of building

structures. The fifth chapter presents the research investigations carried out in an attempt to extend the PSIL method, originally formulated for building structures that can be modeled as plane structures, to the case of more complex structures (by considering simple rectangular "box type" 3D buildings). The sixth chapter presents the modal flexibility-based approach that is proposed for detecting damage in building structures starting from output-only vibration data and with minimal or no a-priori information on the structural masses.

Finally, the seventh chapter presents the conclusions drawn for each of the three main problems addressed in the thesis and the directions for future research. An appendix is also reported at the end of the thesis, and in this appendix a description of the main steps of the output-only modal identification techniques adopted in the thesis is provided. Moreover, in the appendix some numerical and experimental case studies where the output-only modal identification techniques were applied are presented.

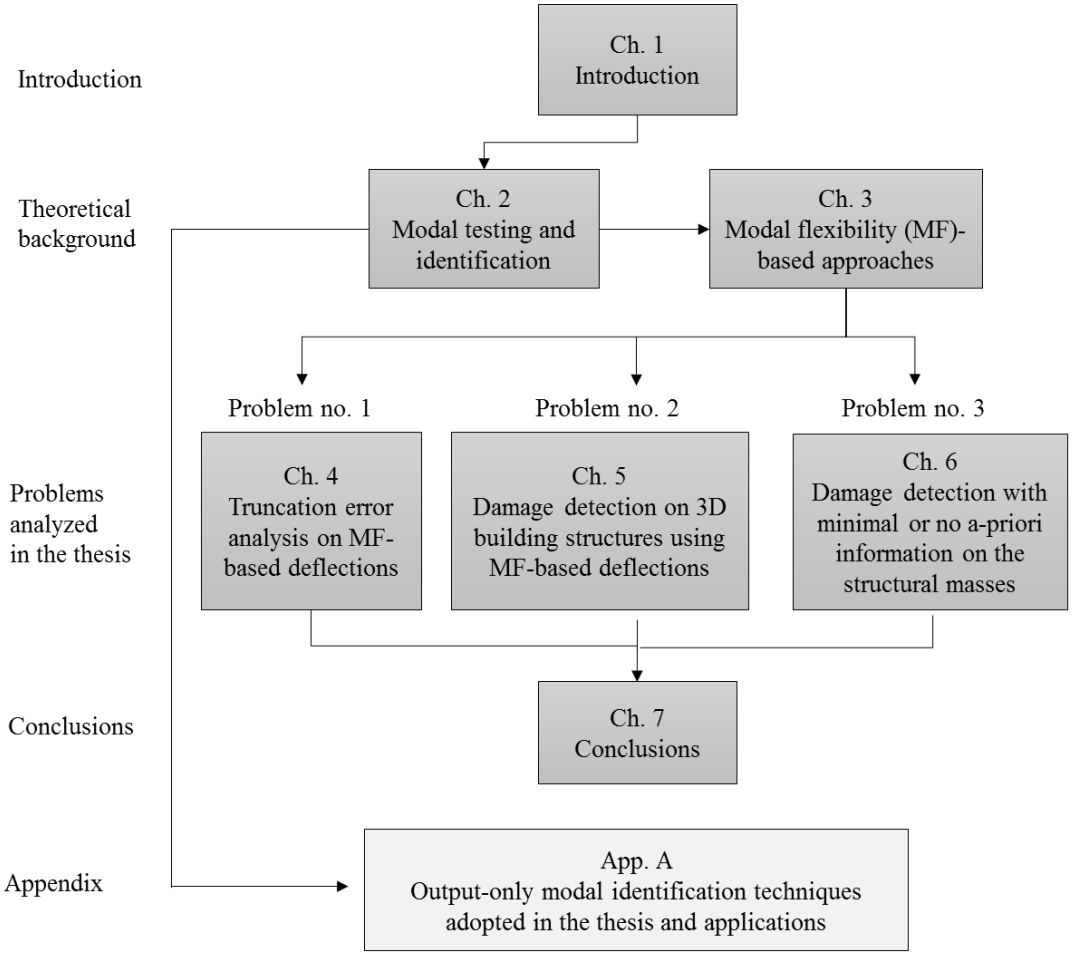

Figure 1.4. Diagrammatic representation of the organization of the thesis.

Chapter 2

Modal testing and identification

Modal analysis can be defined, according to [He & Fu, 2001], as "*the process of determining the inherent dynamic characteristics of a system in forms of natural frequencies, damping factors and mode shapes, and using them to formulate a mathematical model for its dynamic behaviour*". This operation can be performed either starting from an analytical model of a structure or starting from vibration data acquired in an experimental test performed on a structure. The first type of modal analysis is usually referred to as an analytical modal analysis, while the second one is an experimental modal analysis. In this second type of modal analysis after performing a vibration test, the modal properties of the structure are estimated from the data using the techniques of the modal identification. It is worth noting that this second type of modal analysis is the one that is mainly considered in the present dissertation.

In recent years a distinction has been made between two types of modal analysis that can be used for testing structures. The traditional or classical type of modal testing based on controlled input forces (where both the input forces and the output vibration responses are measured) is usually referred to as an Experimental Modal Analysis (EMA). On the contrary, the process of performing a vibration test and the subsequent modal identification process for a structure tested under

operational forces (by measuring only the output vibration responses) is indicated as Operational Modal Analysis (OMA). In this second type of modal analysis the structures are tested by measuring the responses due to ambient or natural excitations, and this is the type of testing that is mainly considered in the present dissertation.

2.1 From Experimental Modal Analysis (EMA) to Operational Modal Analysis (OMA) of civil structures

This section provides at first a very short introduction on the topic of Experimental Modal Analysis (EMA). Then, this section shows the motivations for which Operational Modal Analysis (OMA) tests, instead of traditional EMA tests, can be more convenient ways for testing civil structures, especially when large civil structures are considered [Cunha & Caetano, 2005; Brincker & Ventura, 2015].

Experimental modal analysis, as already mentioned, is the traditional or classical way of testing structures based on controlled or artificial input forces. This way of testing is also indicated as forced vibration testing. However, applying forces to a structure for a certain period of time is not the only option that can be used to excite the structure. Motion in a structure can be induced, for example, by perturbing its original position of static equilibrium and by imposing an initial displacement or an initial velocity in one or more points of the structure. As reported in [Brincker & Ventura, 2015], in fact, when any type of artificial input or excitation is applied to the structure a forced vibration test is performed.

Depending on the types of excitations that are applied, the modal testing techniques can be classified into different groups. As extensively described in the literature [Ewins, 2000; Brincker & Ventura, 2015], some of the most popular testing techniques that can be used to excite a structure using artificial inputs are the following:

- *Shaker tests*

  In this type of testing, shakers are used to apply forces on the structure for a certain period of time. In shaker tests it is possible in general to measure the

input forces applied to the structure, by adopting criteria and procedures that depends on the specific excitation device that is used. Examples of such excitation devices are, for example, mechanical shakers, electromagnetic shakers, or hydraulic exciters.

- *Hammer tests*

  In this type of testing an hammer is used to excite the structure, and the impact of the hammer generates a transient load. Typically, the excitation, in terms of the applied force, is measured using a load cell (i.e. a force transducer installed on the hammer). Since the impact of the hammer acts on the structure for a very short period of time and due to the impulse-momentum theorem, the operation of exciting the structure through the impact of an hammer means basically to impose an initial velocity to the structure. After the impact the structure vibrates under free vibrations until it returns to the initial static equilibrium. This type of testing is commonly adopted in the field of mechanical engineering, but it can be also applied on civil engineering structures. Of course, in this second case hammers with adequate characteristics and dimensions have to be adopted, depending on the size of the structure. However, this type of testing is in general not adequate for very large civil structures, as also discussed later in this section.

- *Step relaxation tests*

  In this kind of testing, an initial temporary static deformation is imposed on the structure. The initial deflection can be imposed, for example, using a steel cable, and by measuring the applied static force using a load cell in the cable. Alternatively, a dead weight can be attached to the structure to impose the initial deflection. Then, the initial static load is suddenly removed, for example, by cutting the cable or by removing the dead weight. In this way the structure starts vibrating under free vibrations. The response of the structure can be recorded until the structure reaches the unperturbed static equilibrium (i.e. the original configuration that the structure had before the initial imposed deflection). The responses (for example, in terms of accelerations) of the structure under free

vibrations are the so-called free decays of the structure. These tests are also known in the literature as pull-back or quick-release tests [Brincker & Ventura, 2015], and they are often used for testing large civil structures.

Just after having induced motion in the structure using, for example, one of the above-mentioned techniques, the structural responses are measured. In a vibration test this operation is typically performed using accelerometric sensors that are connected to a data acquisition system, and by measuring the responses, in terms of accelerations, of several points of the structure. There exists a wide variety of accelerometers that can be used to acquire dynamic response measurements. As extensively discussed in [Maia et al., 1997; Cunha & Caetano, 2005], the accelerometers can be classified into four different categories, depending on the specific physical mechanism on which the devices are based (i.e. piezoelectric, piezoresistive, capacitive, and force balance accelerometers). It is worth noting that, as reported in [Cunha & Caetano, 2005], most of the piezoelectric accelerometers are not suitable to measure responses in the range of the low frequencies (which is often the frequency range where the natural frequencies of large civil structures are contained). On the contrary, the other three types of accelerometers (i.e. piezoresistive, capacitive, and force balance accelerometers) are more suitable to measure responses in the low frequency range.

After having acquired the vibration measurements (i.e. input forces and output response data), in experimental modal analysis the modal properties of the tested structures are extracted using modal identification techniques. Numerous well-established modal identification techniques are available in the literature to perform this operation. Such techniques are classified and extensively described in the classical books on experimental modal analysis such as [Maia et al., 1997; Ewins, 2000]. An overview and a description of the different modal analysis techniques is also reported in the review paper by [Cunha & Caetano, 2005]. In this section, only a few of the well-established modal identification techniques are mentioned. Moreover, the main criteria that can be used to classify and understand in broad terms how the different techniques work are reported herein.

The different modal identification techniques can be classified using the following criteria and as function of the following variables:

- the domain where the analysis is performed (i.e. time domain or frequency domain). When the analysis is performed in frequency domain, the modal properties of the structures are typically extracted from the Frequency Response Functions (FRF). Such functions are estimated between each point of the structure where a response is acquired in the test and the location where the excitation is applied. Alternatively, if the analysis is performed in time domain, the extraction of the modal parameters is typically performed after estimating the Impulse Response Functions (IRF);

- the number of modes that are obtained by a single modal extraction. On the basis of this criterion a distinction can be made between methods based on an SDOF formulation and methods based on an MDOF formulation;

- the number of input and output signals that are processed simultaneously in the analysis. On the basis of this criterion a distinction can be made between the following types of methods: single-input single-output (SISO) methods, single-input multiple-output (SIMO) methods, multiple-input multiple-output (MIMO) methods, multiple-input single-output (MISO) methods. It is worth noting that SIMO methods are also indicated in the literature as "global" methods, while MIMO methods are also indicated as "polyreference" methods.

Referring to the methods that work in frequency domain, the earliest approaches that were developed are methods based on an SDOF formulation. Such methods are, for example, the Peak Picking method [Bishop & Gladwell, 1963] and the Maximum Frequency Spacing method [Kennedy & Pancu, 1947]. This last method is also known as Circle fit method [Ewins, 2000]. Other existing methods that work in frequency domain are based on an MDOF formulation. Examples of such methods are the Rational Fraction Polynomial (RFP) [Richardson & Formenti, 1982], and the Complex Exponential in frequency domain (CEFD) [Schmerr, 1982].

All the methods that work in time domain are in general based on an MDOF formulation. One of the earliest methods that was developed in time domain is the Complex Exponential (CE) method [Spitznogle & Quazi, 1970], which is a SISO method. Subsequently, more refined and complex versions of the CE method were developed (e.g. the SIMO or global version termed Least Square Complex Exponential (LSCE) [Brown et al., 1979], and the MIMO version termed Polyreference Complex Exponential (PRCE) [Vold & Rocklin, 1982]). Other methods that work in time domain are, for example, the Ibrahim Time Domain (ITD) [Ibrahim & Mikulcik, 1973; Ibrahim & Mikulcik, 1977], which is a SIMO method, or the Eigensystem Realization Algorithm [Juang & Pappa, 1985; Juang, 1994], which is a MIMO method. The time-domain modal identification can be also performed using methods based on Auto-Regressive Moving-Average (ARMA) models [Gersch, 1970].

It is worth noting that some of the above-mentioned traditional EMA methods (both related to time and frequency domains) will be discussed more in detail in Section 2.2.2 which, on the contrary, presents a brief literature review and the main characteristics of the Operational Modal Analysis (OMA) techniques that can be applied starting from output-only vibration data (i.e. ambient vibration data). As will be clarified in next sections, in fact, most of the output-only modal identification techniques were derived starting from the traditional input-output techniques.

To conclude this very short overview of the main principles and techniques in experimental modal analysis, a final remark must be made on the results that can be obtained from a modal test. Referring to this aspect, a five-level classification was formulated by the [Dynamic Testing Agency, 1993], and this classification is also reported in [Ewins, 2000]. In this classification each level corresponds to a type of modal testing characterized by a specific degree of complexity and for which certain achievements can be obtained. In particular, the levels are ordered from the first level to the fifth level: the higher the order of the level, the more complete is the experimental modal model that can be obtained from the test.

The classification mentioned in the previous paragraph is reported below [Ewins, 2000], and the results that can be obtained according to the different levels are also schematically shown in Fig. 2.1.

Level 0: "estimation of natural frequencies and damping factors; response levels measured at few points; very short test times."

Level 1: "estimation of natural frequencies and damping factors; mode shapes defined qualitatively rather than quantitatively."

Level 2: "measurements of all modal parameters suitable for tabulation and mode shape display, albeit un-normalised."

Level 3: "measurements of all modal parameters, including normalised mode shapes; full quality checks performed and model usable for model validation."

Level 4: "measurements of all modal parameters and residual effects for out-of-range modes; full quality checks performed and model usable for all response-based applications, including modification, coupling and response predictions."

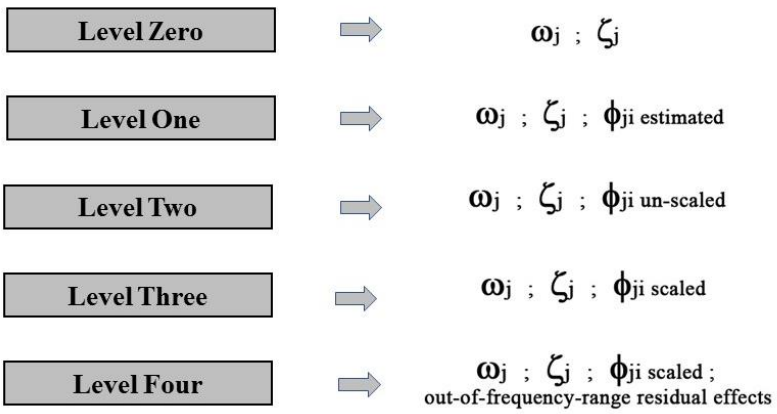

Figure 2.1. Achievement levels in modal testing (defined in [Ewins, 2000]).

Referring to civil engineering structures, the traditional way of testing structures (i.e. performing an experimental modal analysis using artificial and controlled excitations) tends nowadays to be replaced by the more innovative way of testing structures under operational forces (i.e. performing an operational modal analysis). The motivations behind this choice of performing OMA tests instead of EMA tests on civil structures are extensively reported in the works by [Cunha & Caetano, 2005; Brincker & Ventura, 2015], and they can be summarized as follows.

On one side, there are several disadvantages and drawbacks that are connected to the execution of an EMA test on civil structures. First of all, using artificial excitations it is difficult in general to excite civil structures, especially large-scale civil structures, with sufficient energy and at the low frequencies (i.e. at the frequencies related to the first structural modes) [Cunha & Caetano, 2005]. Secondly, to perform an EMA vibration test of a civil structure the functionality of the structure has to be usually interrupted. It is worth noting that this drawback is not present, on the contrary, in OMA tests. As discussed later in next section, in fact, operational forces are the excitations that are used in OMA tests, and thus some of the operational forces may also derive from the actions connected to the use of the structure. Finally, in EMA testing applied on civil structures, damage can be induced on the structure if the artificial excitation is not controlled in a proper manner. This situation, as reported in [Brincker & Ventura, 2015], can occur, for example, when a large civil structure is tested using a hammer with a large mass (using a hammer with a large mass is the only option for many practical cases, and it is required to excite the structure with sufficient energy). If special care is not adopted in such situation, the hammer can cause local damage in the structure.

On the other side, the possibility of performing OMA tests instead of EMA tests on civil structures is due to the developments that were gained in recent years in the technologies related to sensors and data acquisition systems [Cunha & Caetano, 2005]. The developments in such technologies lead to the possibility of measuring the vibration responses of civil structures tested under ambient vibrations. In general, the responses of structures under ambient vibrations are much lower than the responses of structures that are tested using controlled forces. For example, as reported in [Brincker & Ventura, 2015], the acceleration responses of a structure tested under

ambient vibrations are typically of the order of 10-100 milli-g's. This means that the sensors that are used for acquiring operational vibration measurements have to be characterized by a sensitivity that is in general much higher than the sensitivity of the sensors that are used in forced vibration tests.

Before concluding this section, two other advantages of OMA tests applied on civil structures must be highlighted. The application of OMA testing techniques, especially for large complex structures, is an operation that is characterized in general by economic costs that are lower than the ones associated with traditional EMA testing techniques. In addition, the preparation of the testing setup in OMA tests on civil structures is an operation that is in general more rapid with respect to the corresponding operation executed in the context of traditional EMA tests [Brincker & Ventura, 2015].

2.2 Operational Modal Analysis (OMA)

Operational Modal Analysis (OMA), as reported in [Brincker & Ventura, 2015], is the engineering field that aims to determine the modal properties of a dynamic system, assumed as linear and time-invariant, from vibration data of its normal operating responses. The OMA testing techniques can be applied in many areas and fields related to structural engineering [Brincker et al., 2003]. Among these different areas, the OMA techniques can be applied in civil engineering, for example on building structures that are tested under ambient vibrations.

The first ambient vibration tests on building structures, as reported in [Brincker & Ventura, 2015], were performed by D.S. Carter in 1935. He performed several tests on building structures in California after that these structures were subjected to the Long Beach earthquake. Carter applied very basic OMA techniques to extract the natural modes of such building structures. It is worth noting, however, that in general (i.e. referring not only to building structures) operational modal analysis started to become a well-established field not until the early 1990s.

In next sections, following closely the work by [Brincker & Ventura, 2015], a brief overview of the fundamental principles in operational modal analysis and a brief literature review of the main OMA identification techniques are presented.

2.2.1 OMA testing techniques: an overview of the fundamental assumptions and principles

During normal operating conditions (i.e. the case of an OMA test) a civil structure, such as a building structure, is subjected to ambient vibrations that are induced by natural excitations. Examples of such natural excitations are the following: wind, traffic loads, microtremors from the ground, vibrations induced by occupants or machineries that are present in the structure, etc. [Brincker & Ventura, 2015]. It is in general not possible to measure such input excitations, and in an OMA test only the vibration responses of the structure due to such loads are measured. These measured data are then used to estimate the modal properties of the structure (i.e. natural frequencies, modal damping ratios, and mode shapes).

As already mentioned, the input excitations are unmeasured. However, for a generic structure that is tested under ambient vibrations, the natural excitations tend to have in general the following characteristics [Brincker & Ventura, 2015]:

- the natural excitations have approximately white noise characteristics. This means that the excitations are random, characterized by a wide frequency content, and the frequency spectrum of such excitations is approximately flat in a specific frequency range.
- the natural excitations are multiple inputs that act simultaneously all over the structure.
- the natural excitations tend to have stationary characteristics.

It is important to underline that the quality of the results that can be obtained using the OMA testing and identification techniques depends in general on how much the input excitations tend to have the above-mentioned characteristics. This means that the best conditions (from an OMA point of view) to extract the modal properties of a structure starting from the vibration responses are the following:

- all or at least most of the natural frequencies of the tested structure are contained in the frequency range of the input excitations. In this way, all the prevalent modes of the structure are excited. Moreover, since the natural excitation is characterized

by an approximately flat spectrum, the structural system is not excited at any specific or dominant frequency.

- the vibrations responses are generated by multiple inputs that act all over the entire structure, and that are weakly- or un- correlated inputs at different spatial locations.
- the vibrations responses are generated by inputs that are stationary.

In the OMA process the unmeasured input signals are thus considered as white noise signals. Of course, this is an idealization, because in practice the inputs will never be exactly white noise signals with a perfectly flat spectrum. As reported in [Brincker & Ventura, 2015], the inputs that act as a load on the structure are in general colored (i.e. they do not have a perfectly flat spectrum). These inputs are in any case suitable exciting inputs which generate responses that can be used to perform the OMA analysis, because of the following interpretation (discussed in [Brincker & Ventura, 2015]).

The real inputs acting on the structural system (i.e. the colored loads) can be considered as the output of a virtual system (defined as a loading filter) which receives, as input, loads that have exactly white noise characteristics [Brincker & Ventura, 2015]. This concept is shown in Fig. 2.2. The virtual system (i.e. the loading filter) and the real system (i.e. the structural system) can then be considered together to form a combined system. This combined system, as shown in Fig. 2.2., receives, as input, white noise loads, and gives in output the measured responses. Under this interpretation, it is clear that, when OMA is applied starting from the measured structural responses by assuming that the unmeasured inputs are white noise signals, the identified quantities are the modal properties of the above-mentioned combined system (which is composed by the loading filter and the structural system). Referring to this interpretation, one important point is that, as demonstrated in [Ibrahim et al., 1996] and as also reported in [Brincker & Ventura, 2015], including a loading filter in the system (identified in OMA) does not alter the modes of the true structural system. On one side, this means that the modes of the true structural system are contained in the set of the modes of the combined system that are identified from the data. On the other side, however, this means that the number of modes of the combined

system might be in general higher than the modes of the true system. In fact, additional modes might be introduced in the combined system due to the presence of the loading filter. In the OMA identification process, it is thus important to separate modes that might be related to the loading conditions from the natural modes of the structure (i.e. the true structural modes). Of course, in the OMA identification process, as well as in the EMA identification process, there are also computational not physical modes that are due to the presence of noise on the measurements. These modes must be separated from the natural modes of the structure, as well.

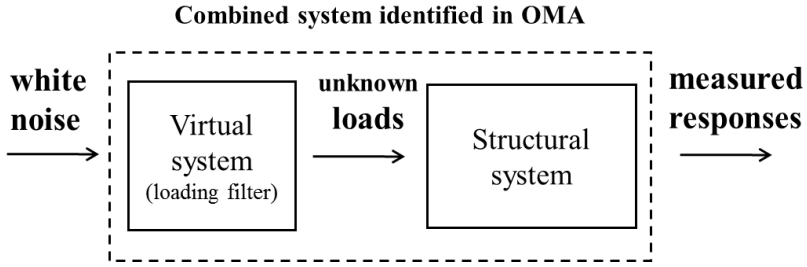

Figure 2.2. Combined system identified in Operational Modal Analysis (OMA).

In any OMA identification process, assumptions are made not only on the unmeasured natural excitations. Assumptions are also made on the structural system that is considered in the vibration test and on the measured vibration responses. On one side, as already mentioned at the beginning of this section, it is assumed that the considered dynamic system is linear and time invariant. On the other side, referring to the measured vibration responses, two main assumptions are made:

- the vibration responses are stationary;

- the distribution of the random responses of the structure is Gaussian and such responses have a zero mean.

Referring to the first of the two above-mentioned assumptions and to guarantee that the vibration responses are stationary, it is important, as reported in [Brincker & Ventura, 2015], that the structure is time invariant. Of course, if the structure is not time invariant, then the responses will not be in general stationary. If the above-mentioned assumption on the structural system is valid (i.e. the system is time invariant), it is clear that the responses are stationary if the natural excitations are stationary (which is an assumption that is made on the inputs).

Referring to the second of the two above-mentioned assumptions made on the responses, two observations, reported in [Brincker & Ventura, 2015], must be mentioned. Firstly, the condition of having response signals with a zero mean is in general something that can be guaranteed in any case by performing signal processing operations on the recorded data - for example, direct current (DC) offsets that might be present in the measurements can be removed by performing a detrending operation. This means that if the recorded signals have not a zero mean, this condition can be guaranteed in the data analysis. Secondly, the assumption of having random responses with a distribution that is approximately Gaussian is in general fulfilled for structures tested under ambient vibrations. In fact, as extensively shown in [Brincker & Ventura, 2015], the random responses of a structure due to white noise inputs have a distribution that is approximately Gaussian independently from the distribution of applied random inputs[1]. In other words, this means that the applied loads might have a distribution which is non-Gaussian, but the random responses due to such loads have in general a Gaussian distribution.

The process of a typical Operational Modal Analysis (OMA) test is mainly composed by the following phases[2]:

(1) test planning and preparation of the test setup;

(2) measurement of the structural responses using accelerometric sensors and a data acquisition system;

(3) check of the quality of the acquired data;

(4) data analysis based on signal processing;

(5) application of the techniques of the output-only modal identification to extract the natural modes of the structure;

(6) validation of the identified modal model.

[1] This principle is justified by the central limit theorem, as shown in [Brincker & Ventura, 2015].

[2] General concepts related to the phases from no. 1 to no. 4 are presented in this section, while an overview of the different OMA techniques that can be applied on the data (phase no. 5) are presented in Section 2.2.2. An overview of the main criteria that can be applied for modal validation (phase no. 6) is provided in Section A.3 of Appendix A (after presenting the steps of the OMA techniques that are applied in the thesis).

One important aspect that must be discussed in the planning phase of an ambient vibration test is related to the position of the accelerometric sensors. In particular, the number, the location, and the orientation of the sensors have to be defined. In many practical cases the number of the sensors available for the test is lower than the number of the points (i.e. the DOFs) of the structure where one wants to take the measurements. Of course, in fact, the higher the number of the sensors, the higher the costs that are associated with the instrumentations. In such practical situations, the test can be performed using a limited number of sensors by adopting the following strategy. The test can be performed using both reference and roving sensors: the reference sensors are sensors with a fixed position during the whole test, while the roving sensors are sensors that are moved throughout the structures during the test. This means that at first the ambient vibration measurements can be acquired for a first layout of the reference and the roving sensors (first data set). Then, the roving sensors are moved in locations that are different from the ones considered for acquiring the first data set, while the position of the reference sensors is unaltered. Using this new layout of the sensors, the test is repeated (second data set). This operation is repeated by obtaining several data sets until the measurements have been acquired for all the points (i.e. the DOFs) of the structure that are of interest for the test.

The modal parameters that are characterized by a spatial location are the mode shapes. Thus, merging the results of the operational modal analysis (in terms of mode shape components) obtained from the different data sets is an operation that can be performed for ambient vibration tests executed using the above-mentioned strategy. In this way, even if the test is performed using a limited number of sensors, mode shapes with components defined at all the points considered in the different test setups can be obtained. This operation, of course, can be performed if the reference sensors are fixed during the whole test and if data from these sensors are available in all the data sets.

For a building structure tested under ambient vibrations the sensors that are typically used are, for example, force balance accelerometers. As reported in [Cunha & Caetano, 2005], such sensors can be used to measure accelerations in the low frequency range (e.g. 0-50 Hz), and they are insensitive to high frequency vibrations.

It is clear that force balance accelerometers are sensors suitable for performing ambient vibration tests in civil engineering, since the natural frequencies of civil structures are typically in the above-mentioned low frequency range.

A typical layout of the sensors for an ambient vibration test performed on a simple rectangular "box type" building structure is reported in Fig. 2.3. According to [Brincker & Ventura, 2015], the layout reported in Fig. 2.3 is the layout that one should adopt when the test is performed using as few sensors as possible. In particular, the green arrows reported in Fig. 2.3 are the reference sensors, while the red arrows are roving sensors. The minimum number of the sensors required in the test is thus equal to five, where two sensors are reference sensors while three sensors are roving sensors. According to [Brincker & Ventura, 2015], several observations can be made on the layout of the sensors reported in Fig. 2.3.

First of all, referring to simple rectangular "box type" building structures that are subjected to ambient vibration tests, only the horizontal displacements of the mode shapes are usually estimated, while the vertical modal displacements are usually neglected [Brincker & Ventura, 2015]. This explains why, according to the layout reported in Fig. 2.3, the acceleration response measurements are taken only in the horizontal direction. Moreover, under the assumption of having floors with a rigid-body in-plane behavior, the disposition of the roving sensors reported in Fig. 2.3 (i.e. three sensors whose directions do not converge to a unique point) is a typical disposition that can be used to estimate mode shapes characterized by horizontal displacement components in the two prevalent directions and rotational components. The above-mentioned rotations are, of course, around the vertical axis and can be obtained starting from two modal displacements estimated in the same direction but in different corners of the structure.

The second observation is that, as shown by the green arrows reported in Fig. 2.3, it is convenient to have the reference sensors at the top story of the building. This choice related to the reference sensors is made to avoid positions that can be possible nodes of the mode shapes (e.g. positions at the intermediate stories of the building).

A final observation on the layout reported in Fig. 2.3 is the following: if one wants to estimate the components of the mode shapes at all stories of the structure

using the layout reported in Fig. 2.3, the number of the required test setups (and thus the number of the data sets to be acquired) is equal to the number of the stories of the structure. In each setup the roving sensors (red arrows) are positioned on a different story of the structure. Of course, if the number of sensors that can be used in the test is higher than the number of sensors reported in Fig. 2.3 (i.e. more sensors are available), then the number of the required test setups can be lower. In general, the higher the number of the sensors, the lower the number of the test setups required to perform the OMA analysis.

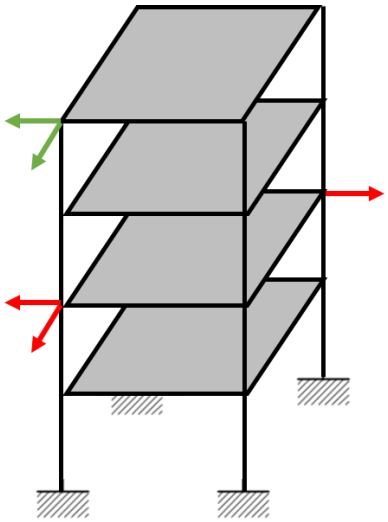

Figure 2.3. Typical OMA measurement plan in a building structure (green arrows: reference sensors; red arrows: roving sensors).

When an OMA test is performed and ambient vibration measurements are recorded, two fundamental aspects must be considered. First of all, it is important to acquire enough data - i.e. response measurements with an adequate length of time (details and indications on the minimum length of time of the measurements will be provided later in this section). Secondly, it is important to acquire measurements characterized by a good quality. As extensively discussed in [Rainieri & Fabbrocino, 2014; Brincker & Ventura, 2015], in fact, good results can be obtained in the estimation of the modal parameters of the structures only if the quality of the acquired data is satisfactory. Otherwise, if the quality of the data is not good enough, then

performing the modal extraction using any output-only identification technique will be a really complex task (which will provide in the majority of the cases to non-satisfactory or erroneous results).

The quality of the ambient vibration measurements can be checked by performing some operations on the acquired data. First of all, it is important to take a look at the acquired time histories to avoid problems that are typically related to wrong settings in the data acquisition system. For example, one should check that the signals are not clipped or if there is excessive noise on the measurements. Secondly, one should check if eventual outliers are present in the recorded vibration data, such as spikes, dropouts, etc. This operation can be performed not only by visually inspecting the measurements, but also by computing some statistical parameters (such as the mean or the standard deviation of portions of the acquired signals). Finally, it is also possible to check the validity of the assumptions that are usually made in OMA on the vibration responses of the structures (as discussed in previous paragraphs). For example, one can check if the measured responses are signals characterized by approximately a Gaussian distribution[3].

In a typical OMA process after having acquired the vibration data, checked the quality of the data, and performed some signal processing operations on the data (for example, operations of detrending, decimation, filtering, etc.), the extraction of the modal properties is performed using the techniques of the output-only modal identification. There exist several and well-established techniques that can be used to extract the modal properties from output-only vibration data, and some of these techniques will be described in next section (where a brief literature review of the different OMA identification techniques is presented).

The OMA identification analysis can be performed either in time domain or in frequency domain. When one performs the OMA identification in time domain, the analysis is usually performed by evaluating correlation functions starting from the measured time histories. On the contrary, when the analysis is performed in frequency

[3] An example of analyses performed to check the quality of ambient vibration measurements will be presented in Chapter 5, where the OMA results of an ambient vibration test performed on a steel frame structure will be discussed.

domain, spectral density functions are in general estimated from the acquired response signals.

The correlation function for a time signal $x(t)$ can be calculated as follows

$$R_{xx}(\tau) = E[\ (x(t)\ \ x(t+\tau)\ ] \tag{2.1}$$

where E [·] is the operator used to indicate the expected value and the parameter τ is a time lag that is used to introduce a shift in the time history. This function evaluates how points of the signal $x(t)$ separated by the time lag τ are correlated. Since the correlation function reported in Eq. (2.1) is calculated between the signal $x(t)$ and the same signal shifted-in-time, this function is properly an auto-correlation function. On the contrary, when the correlation function is evaluated starting from two signals $x(t)$ and $y(t)$, it is properly a cross-correlation function and it is defined as follows

$$R_{xy}(\tau) = E[\ (x(t)\ \ y(t+\tau)\ ] \tag{2.2}$$

The spectral density function is the discrete Fourier transform of the correlation function. Thus, the auto and cross spectral density functions (usually indicated in the literature as $S_{xx}(f)$ and $S_{xy}(f)$, respectively) form with the auto and cross correlation functions ($R_{xx}(\tau)$ and $R_{xy}(\tau)$, respectively), Fourier transform pairs.

In the OMA identification process the correlation functions (or the spectral density functions) are evaluated between the different signals of the acquired vibration measurements. Referring to the correlation functions, two important assumptions are made on these functions in OMA. First of all, when the correlation functions are evaluated from random response signals, it is assumed that all the information about the modal properties of the structures are extracted from these random signals and included in the correlation functions. As shown in [Brincker & Ventura, 2015], this property is a direct consequence of dealing with structural responses that are random signals with a zero mean and a Gaussian distribution. The second assumption is that it is possible to consider the correlation functions as the free decays of the structural system (where, as already mentioned, the free decay is the response of the structure

under free vibrations)[4]. This second assumption implies that all the classical EMA modal identification techniques that can be applied starting from free decays (or starting from impulse response functions) can be also used in the context of the output-only modal identification starting from correlation functions. In the same way, it is clear that many traditional input-output identification methods based on the evaluation of frequency response functions can be converted to the output-only case and can be applied starting from spectral density functions [Brincker & Ventura, 2015].

As already mentioned, when an OMA test is performed, it is important not only to acquire measurements characterized by a good data quality, it is also important to acquire enough data. In other words, it is necessary to obtain response measurements with an adequate length of time. In general, the longer are the recorded time histories, the better are the OMA results. However, in practical applications it is of course necessary to have a way for estimating the length of time of the measurements that should be considered in the test. According to [Brincker & Ventura, 2015], this required length of time of the measurements (indicated as T_{tot}) can be determined as follows. To define the parameter T_{tot}, one has to estimate at first the maximum correlation time that is present in the responses. This quantity is also defined as the memory time of the system (T_{mem}), and it is assumed that this quantity depends on the first mode of the structure (i.e. the mode that has the lowest natural frequency) [Brincker & Ventura, 2015]. As already mentioned, in OMA the correlation functions can be considered as free decays of the structure. Thus, in theory the autocorrelation function of the first modal coordinate[5] is proportional to

$$R(\tau) = e^{-\zeta_1 \omega_1 \tau} \cos(\omega_{d,1} t) \tag{2.3}$$

where ζ_1, ω_1 are the modal damping ratio and the natural circular frequency of the first mode, while $\omega_{d,1}$ is the damped natural frequency of the first mode defined as

[4] More details about this assumption, which is a fundamental assumption in OMA, are presented in the Appendix A where the Natural Excitation technique [James et al., 1993] is presented.

[5] Details on how to obtain correlation functions in modal coordinates are provided in Section A.2 of the Appendix A, where the main steps of the Frequency Domain Decomposition (FDD) method [Brincker, Zhang & Andersen, 2001] are presented.

$\omega_{d,1} = \omega_1\sqrt{1-\zeta_1^2}$. According to [Brincker & Ventura, 2015], the memory time of the system T_{mem} is the time lag τ for which

$$\zeta_1\omega_1 T_{mem} = \pi \tag{2.4}$$

In particular, the memory time of the system T_{mem} has the following property: after a time lag equal to T_{mem} the autocorrelation function expressed by Eq. (2.3) is reduced to approximately 4% [6]. Starting from Eq. (2.4), the memory time of the system T_{mem} can be expressed as

$$T_{mem} = \frac{1}{2\,\zeta_1 f_1} \tag{2.5}$$

where the natural frequency of the first mode f_1 is introduced instead of the natural circular frequency ω_1 (with $\omega_1 = 2\pi\, f_1$). Finally, according to [Brincker & Ventura, 2015], to guarantee that accurate estimates of the correlation functions (or the spectral density functions) are obtained from the data, the minimum length of time of the measurements is considered as 20 times the memory time of the system T_{mem}. The length of time of the measurements T_{tot} is thus

$$T_{tot} > 20\; T_{mem} = \frac{10}{\zeta_1\, f_1} \tag{2.6}$$

This last equation expresses the minimum length of time required for acquiring ambient vibration measurements according to [Brincker & Ventura, 2015]. However, more conservative indications are prescribed in the "Guidelines for the Measurement of Vibrations and Evaluation of Their Effects on Buildings" [ANSI S2.47, 1990], as discussed in [Brincker & Ventura, 2015], as well. According to the indications reported in ANSI S2.47, the length of time of the measurements should be at least

$$T_{tot} > \frac{200}{\zeta_1\, f_1} \tag{2.7}$$

To conclude this section, the two main drawbacks that characterize an OMA test are discussed. It is worth noting that these two drawbacks have been already mentioned in Chapter 1 to introduce the problems and the objectives that are mainly considered in the thesis.

[6] This result can be explained by considering that the exponential function in Eq. (2.3) evaluated for $\tau = 0$ is $e^0 = 1$, while $e^{-\pi}$ is approximately equal to 0.04.

First of all, since in OMA the input excitations can not be measured, mass normalized mode shapes can not be estimated directly from the vibration response data of an ambient vibration test [Brincker & Ventura, 2015]. In other words, the modal model that can be estimated in OMA is not a scaled modal model. Referring to the achievement levels in modal testing, defined in the classification made by [Dynamic Testing Agency, 1993] and shown in Section 2.1, in OMA only the level no. 2 can be obtained. This limitation, however, can be overcome using additional modal scaling techniques [Parloo et al, 2003; Brincker & Andersen, 2003; Bernal, 2004; Aenlle et al., 2010; Khatibi et al., 2012; Lopez-Aenlle et al., 2012], as already discussed in Section 1.3 of Chapter 1.

The second main drawback in OMA is due to the fact that the test is performed using exclusively the ambient or natural excitations: even if the inputs in general tend to have some common characteristics (as discussed in this section), there are always sources of variability in the inputs, which can not be, of course, controlled. For this reason, in OMA some structural modes may not be adequately excited, and thus they might not be identified.

It is worth noting that the two above-mentioned drawbacks are in general not present in EMA tests, which are based on controlled input excitations and where such inputs excitations are measured. In any case and as shown in the literature [Rainieri & Fabbrocino, 2014; Brincker & Ventura, 2015], if one compares advantages and disadvantages of EMA and OMA when applied to civil structures, the latter remains a more convenient way for performing vibration tests on such structures.

2.2.2 OMA identification techniques: a brief literature review

As already mentioned in previous section, there exist several well-established techniques for output-only modal identification that can be applied in OMA testing. In this section a brief literature review of the most efficient and popular OMA identification techniques is presented. For an extensive and more comprehensive literature review of all the OMA identification techniques and for more details about each technique, the reader is referred to the books published on the topic of operational

modal analysis by [Rainieri & Fabbrocino, 2014; Brincker & Ventura, 2015] and in the review papers by [Cunha & Caetano, 2005; Zhang, 2005; Masjedian & Keshmiri, 2009].

The OMA analysis, as already mentioned, can be performed either in time domain or in frequency domain. Thus, the OMA techniques can be divided in two groups depending on the domain in which the calculations are performed (i.e. time or frequency domain). The first group of techniques (time domain techniques) deals with response time histories or correlation functions, while the second group (frequency domain techniques) deals with spectral density functions. The distinction between working in time domain or frequency domain seems to be immaterial if one considers that in general any signal can be represented either in time domain or in frequency domain [Rainieri & Fabbrocino, 2014]. Notwithstanding this observation, from a practical point of view there are some differences between the time domain and the frequency domain identification techniques, and these differences must be mentioned.

The main advantage of frequency-domain methods is that dealing with spectral density functions is a natural way to obtain a decomposition and a separation of the different structural modes in the different frequency ranges. On the contrary, in time domain methods when considering either the response time histories or the correlation functions all the structural modes contribute to such signals at any time, and this represents one drawback of the time domain methods [Brincker & Ventura, 2015]. Time-domain methods, however, have the advantage that the data used for the identification (e.g. correlation functions) are characterized by minimum bias and minimum errors. On the contrary, this is, in general, not true for the frequency-domain methods where bias can be present in the estimated spectral density functions [Brincker & Ventura, 2015]. Typical errors that may occur in the transformation of signals from time to frequency domain (for example, errors due to leakage or aliasing effects etc.) are, of course, not present when one works directly in time domain.

Referring to the OMA identification techniques, another distinction is between parametric and non-parametric methods. The main characteristic of the parametric methods is that a model is fitted into the data, while, on the contrary, this operation is not performed using the non-parametric methods. Thus, the parametric methods are

more complex methods with respect to the non-parametric methods [Rainieri & Fabbrocino, 2014]. It is worth noting that, in general, all the time domain methods are parametric methods, while frequency domain methods can be either non-parametric or parametric.

2.2.2.1 Time-domain OMA techniques

This section presents some of the most common OMA identification techniques that can be applied in time domain. A description of the main characteristics of each technique is provided.

- Modal identification using AR and ARMA models

In the field of system identification [Ljung, 1987; Soderstrom & Stoica, 2001; Guidorzi, 2003], Auto Regressive (AR) models belong to the general class of the models that adopt an input-output representation to describe the dynamics of the system. This representation is one of the simplest ways to describe a dynamic system[7], and it is theoretically the most suitable type of model that can be used for system identification from input/output data. The specific characteristic of AR models is, however, that they do not consider any observable inputs, and thus they are generally used to model time series [Guidorzi, 2003]. In the context of OMA, the identification using AR models can be performed by estimating at first the correlation functions, and then by determining the autoregressive coefficients that describe the dynamics of the system.

Auto Regressive Moving Average (ARMA) models represent a more refined and complex version of the AR models. In addition to the autoregressive (AR) part of the model (which describes the dynamics of the system), in ARMA models a moving average (MA) is also introduced and used to model the noise [Rainieri & Fabbrocino, 2014]. In the context of OMA, the identification using ARMA models can be

[7] An alterative and different representation of a dynamic system is, for example, the input-state-representation, or state-space representation, which will be introduced later in this section where other time-domain OMA techniques are described (e.g. Eigensystem Realization Algorithm or Stochastic Subspace Identification).

performed directly using the response vibration measurements. This represents one difference with respect to the technique based on AR models, where, on the contrary and as already mentioned, it is necessary to estimate the correlation functions from the recorded data. It is worth noting, however, that methods based on ARMA models require in general a very long calculation time, and, when applying these methods, a nonlinear optimization problem has to be solved. This implies that possible problems, such as convergence problems, may arise in the calculations. Due to these drawbacks, these techniques based on ARMA models are not commonly used in the field of operational modal analysis [Rainieri & Fabbrocino, 2014; Brincker & Ventura, 2015].

- Ibrahim Time Domain (ITD) method

The Ibrahim Time Domain [Ibrahim & Mikulcik, 1973; Ibrahim & Mikulcik, 1977] is a method that was originally formulated in the context of the traditional or classical modal identification and that can be applied starting from free decays. Then, the technique was combined with the Random Decrement (RD) technique, originally developed at NASA by [Cole, 1973], to extend the methodology to the case of output-only modal identification, as shown in the work by [Ibrahim, 1977].

In OMA the Random Decrement technique can be considered as a pre-processing technique. As reported in [Brincker & Ventura, 2015], the RD technique is a fast and simple way for estimating correlation functions, using an approach that is alternative to the direct estimation method based on the definition of the correlation functions. The functions estimated using the RD technique are properly indicated as random decrement functions, and the technique is able to transform stochastic signals (such ambient vibration response measurements) into deterministic signals with a decaying sinusoidal trend. The operation of removing the stochastic components in the signals is performed through an averaging process between different portions of the original signal. These segments are selected by imposing some triggering conditions, which are used to determine the initial points of the segments used in the averaging process. It is worth mentioning that applications of the RD technique in OMA are presented in the works by [Asmussen et al., 1998; Rodrigues & Brincker, 2005].

- Eigensystem Realization Algorithm (ERA)

The Eigensystem Realization Algorithm (ERA) is a modal identification technique that was presented for the first time in the work by [Juang & Pappa, 1985] and that is extensively described in other later works [Juang, 1994; Juang & Phan, 2001].

It is important to underline that the ERA method has a theoretical formulation that was developed in the framework of the system and control theory. The method adopts an input-state-output representation to model the dynamics of the structural system (which is also known in the literature as state space model). State space models are widely used in system and control theory, and they have the advantage that are capable of controlling complex systems in a computationally efficient way [De Schutter, 2000]. One of the main theoretical developments that contributed to the definition of the ERA method [Juang & Pappa, 1985] are the studies that were performed by [Ho & Kalman, 1966] in the field of the system realization theory and, specifically, on the concept of the minimal realization of linear time-invariant systems. On the basis of the above-mentioned work, the ERA technique was then formulated to solve structural system identification problems and, specifically, to determine the dynamic properties of the structures (i.e. to perform a modal identification).

In its original formulation the Eigensystem Realization Algorithm (ERA) is based on the identification of a state space model of a structure, assumed as linear and time-invariant, starting from experimental measurements of the free decays of the structure. The modal parameters of the structure are then determined by performing an eigenvalue analysis starting from the state space model identified from the data. The ERA method can be also applied starting from input/output vibration measurements. In such case, for example, the impulse response functions are estimated at first from the input/output data, and then the ERA method is applied. For the input-output case, it is worth mentioning that an alternative approach is to integrate the ERA method with the Observer Kalman Filter Identification (OKID) technique[8] [Juang et al., 1993; Juang, 1994].

[8] This input/output procedure based on the integration between the ERA method and the OKID technique was also extended to the case of output only identification, and it is indicated as Output-Only Observer Kalman Filter Identification (O^3KID) [Vicario et al., 2015].

The Eigensystem Realization Algorithm (ERA) was applied starting from output-only vibration measurements in the work of [James et al., 1993], where the Natural Excitation technique (NExT) was presented. According to this technique, the correlation functions are estimated at first (using the direct estimation method based on the definition of the correlation functions). Then, according to the NExT technique, the ERA method is applied starting from the correlation functions and assuming such functions as free decays[9]. As reported in [Brincker & Ventura, 2015], the work by [James et al., 1993] provided a very important contribution since such work is one of the first attempt to justify (both from the theoretical point of view and in the applications) the use of correlation functions instead of free decays. This concept, as already mentioned in previous section, is one of the main assumptions in OMA [Brincker & Ventura, 2015].

It is worth mentioning that other techniques (different from the direct estimation method) can be applied to estimate the correlation functions, and thus these techniques can be also used to complement the Eigensystem Realization Algorithm (ERA) in the output-only case. One of these techniques has been already mentioned in this section, and it is the Random Decrement technique. Alternatively, instead of using the direct method to compute the correlation functions, the spectral density functions can be estimated at first, and then the correlation functions in time domain can be determined through an inverse Fast Fourier Transform (FFT) of the spectral density functions estimated in frequency domain. However, as reported in [Brincker & Ventura, 2015], using the direct estimation method to obtain the correlation functions should always be considered as the preferable option. The other techniques for estimating correlation functions should be taken into account only in the cases in which, for example, it is necessary to minimize the time of the calculations.

[9] It is worth noting that in the literature the NExT technique was not applied exclusively using the ERA method, but also using other traditional time-domain modal identification techniques (all these approaches are indicated in the literature as NExT-type procedures [Rainieri & Fabbrocino, 2014]). For this reason, in the present dissertation the approach based on the use of the NExT technique and the ERA method is also indicated as the NExT-ERA approach.

- Stochastic Subspace Identification (SSI) methods

The Stochastic Subspace Identification (SSI) methods represent another class of time domain methods that can be applied in OMA. These subspace-based methods for system identification were presented in the work of [Van Overschee and De Moor, 1996], and then they were adopted and applied in the field of modal identification [Peeters et al., 1995; Peeters & De Roeck, 1999]. Similarly to the ERA method, these techniques are based on concepts related to the system and control theory.

In OMA two different versions of the Stochastic Subspace Identification (SSI) method can be adopted: the covariance-driven SSI and the data-driven SSI. The covariance-driven SSI (which is also known as correlation-driven SSI) is a method that can be applied starting from correlation functions estimated from the response measurements. It is worth noting that the covariance-driven SSI is almost equivalent to the Eigensystem Realization Algorithm (ERA) applied starting from correlation functions (according to the NExT technique). The data-driven SSI, on the contrary, is a method that can be applied directly starting from the vibration response measurements, without the need to perform a preliminary and separate operation to estimate the correlation functions. In the data-driven SSI, in fact, the operation of calculating the correlation functions is an operation that is integrated and performed implicitly in the steps of the algorithm. As reported in [Rainieri & Fabbrocino, 2014], the results, in terms of the modal parameter estimates, that can be obtained using the covariance-driven SSI or the data-driven SSI are characterized by similar accuracy.

2.2.2.2 Frequency-domain OMA techniques

This section presents a description of some of the most common OMA identification techniques that can be applied in frequency domain.

- Basic Frequency Domain (BFD) method

One of the earliest frequency domain approaches is the Basic Frequency Domain (BFD) method. This method is also known as “classical frequency-domain approach”, as reported in [Brincker & Ventura, 2015], or “peak picking” method, as reported in

[Rainieri & Fabbrocino, 2014]. The BFD method can be considered as one of the simplest OMA approaches. The method, in fact, is very similar to the peak picking technique available in traditional modal analysis and applied on frequency response functions. In the case of output only data, the peak picking technique is applied on the auto and cross spectral density functions computed from the response measurements. The method can be applied if lightly damped structures are considered and if the modes of such structures are well separated. As reported in [Brincker & Ventura, 2015], one practical implementation of the BFD method was developed by [Felber, 1993], and then this implementation was used to analyze the data of OMA tests performed on civil engineering structures.

- Frequency Domain Decomposition (FDD) method

The Frequency Domain Decomposition (FDD) method [Brincker, Zhang & Andersen, 2001] can be considered as an extension of the Basic Frequency Domain (BFD) method. Similarly to the BFD method, the FDD method is a non-parametric approach. However, the FDD method is a method that is more complex than the BDF method, and, in particular, the FDD method overcome some of the limitations of the BDF method. Two important characteristics of the FDD method are the following: the method is able to analyze cases with closely spaced modes, and the method is easy to be implemented.

According to the steps of the FDD method, at first the auto and cross spectral density functions are evaluated for all the response measurements (i.e. for all the channels). Such spectral density functions are assembled in the so-called spectral density matrix, and then a singular value decomposition is performed on such matrix. One important feature of the FDD method is that plotting the singular values (computed from the SVD of the spectral density matrix) as a function of the frequency is a convenient way to analyze simultaneously all the information related to the different measurements [Brincker & Ventura, 2015]. It is worth noting that the FDD method is similar to the traditional modal analysis approach based on the Complex Modal Indicator Function (CMIF) [Shih et al., 1988]. This last approach is based on a singular value decomposition of the frequency response function (FRF) matrix.

The FDD method can be used to identify natural frequencies and mode shapes. On the contrary, it is not possible to have estimates of the modal damping ratios usign the FDD method. To overcome this shortcoming, an improved version of the technique - i.e. the Enhanced Frequency Domain Decomposition (EFDD) - was developed [Brincker, Ventura & Andersen, 2001]. This improved version of the FDD method is also able to provide estimates of the modal damping ratios.

2.3 Output-only modal identification techniques adopted in the thesis and applications

The output-only modal identification techniques that are adopted in the thesis are the Eigensystem Realization Algorithm (ERA) [Juang & Pappa, 1985; Juang, 1994], applied in the output-only case according to the Natural Excitation technique (NExT) [James et al., 1993], and the Frequency Domain Decomposition (FDD) [Brincker, Zhang & Andersen, 2001]. Such techniques were used as a tool for extracting the modal parameters of the structures considered in the thesis. The modal parameters identified from vibration responses were then used to estimate the modal flexibility of the considered structures, according to the general modal flexibility-based approach that is presented in next chapter (i.e. Chapter 3).

The description of the main steps and the analytical formulation of the two well-known OMA techniques that are applied in the thesis are reported in Appendix A. In particular, in Section A.1 the main steps of the Eigensystem Realization Algorithm (ERA) applied according to the Natural Excitation technique (NExT) are presented, while the main steps of the Frequency Domain Decomposition (FDD) method are shown in Section A.2. In the remainder of Appendix A, some numerical and experimental case studies are presented, and in these case studies the two above-mentioned output-only modal identification techniques were applied.

Chapter 3

Modal flexibility and modal flexibility-based deflections for structural identification and damage detection

This chapter introduces the theory behind the modal flexibility-based techniques for structural identification and damage detection that represented the starting point for most of the research investigations presented in the thesis. These modal flexibility-based techniques are the Uniform Load Surface method [Zhang, 1993; Zhang & Aktan, 1995; Zhang & Aktan, 1998] and the Positive Shear Inspection Load method [Koo et al., 2010; Koo et al, 2011; Sung et al., 2012]. As already mentioned in Chapter 1, the first approach was developed mainly for bridge structures, while the second approach was specifically developed for building structures.

In the first part of the chapter, the general procedure that can be adopted to estimate modal flexibility matrices of MDOF structural systems from vibration data is outlined. Then, it is shown how structural deflections can be computed from the modal flexibility matrices. These two operations are present both in the Uniform Load Surface method and in the Positive Shear Inspection Load method. In the final part of the chapter the theory behind the Positive Shear Inspection Load method for vibration-based damage detection in building structures is presented.

3.1 Estimation of modal flexibility matrices from vibration data

In this section it is shown how the modal flexibility matrix of an MDOF structural system can be estimated starting from vibration data. To derive the analytical expressions needed to perform this operation, the continuous-time second-order equation of motion of a generic *n*-DOF damped structure under free vibrations is considered

$$\mathbf{M}\,\ddot{\mathbf{x}}(\mathrm{t}) + \boldsymbol{\mathcal{C}}\,\dot{\mathbf{x}}(\mathrm{t}) + \mathbf{K}\,\mathbf{x}(\mathrm{t}) = \mathbf{0} \tag{3.1}$$

where $\boldsymbol{x}(t)_{n\times 1}$ is the displacement vector and $\boldsymbol{M}_{n\times n}$, $\boldsymbol{\mathcal{C}}_{n\times n}$, $\boldsymbol{K}_{n\times n}$ are the mass, damping and stiffness matrices, respectively. As reported in [Alvin et al., 2003], the undamped portion of this equation of motion can be decoupled if the equation is expressed in the modal space. This operation can be done by substituting the displacement vector $\boldsymbol{x}(t)$ in Eq. (3.1) with the following expression

$$\mathbf{x}(\mathrm{t}) = \boldsymbol{\Phi}\ \boldsymbol{q}(t) \tag{3.2}$$

where $\boldsymbol{q}(t)$ are the displacements expressed in modal coordinates and $\boldsymbol{\Phi}_{n\times n}$ is a matrix that contains mass-orthogonal and mass-normalized real mode shapes. This matrix is derived from the generalized eigenvalue problem associated with the undamped portion of the system

$$\mathbf{K}\,\boldsymbol{\Phi} = \mathbf{M}\,\boldsymbol{\Phi}\,\boldsymbol{\Lambda} \tag{3.3}$$

where $\boldsymbol{\Lambda}_{n\times n}$ is the spectral matrix associated to the above-mentioned eigenvalue problem. By substituting Eq. (3.2) into Eq. (3.1), the following expression can be derived

$$\mathbf{M}\,\boldsymbol{\Phi}\,\ddot{\boldsymbol{q}}(\mathrm{t}) + \boldsymbol{\mathcal{C}}\,\boldsymbol{\Phi}\,\dot{\boldsymbol{q}}(\mathrm{t}) + \mathbf{K}\,\boldsymbol{\Phi}\,\boldsymbol{q}(\mathrm{t}) = \mathbf{0} \tag{3.4}$$

Then, by pre-multiplying Eq. (3.4) by the term $\boldsymbol{\Phi}^{\mathbf{T}}$, the following equation is obtained

$$\ddot{\boldsymbol{q}}(\mathrm{t}) + \boldsymbol{\Theta}\,\dot{\boldsymbol{q}}(\mathrm{t}) + \boldsymbol{\Lambda}\ \boldsymbol{q}(\mathrm{t}) = 0 \tag{3.5}$$

with

$$\boldsymbol{\Phi}^{\mathbf{T}}\,\mathbf{M}\,\boldsymbol{\Phi} = \mathbf{I} \tag{3.6}$$

$$\boldsymbol{\Phi}^{\mathbf{T}}\,\mathbf{K}\,\boldsymbol{\Phi} = \boldsymbol{\Lambda} \tag{3.7}$$

$$\boldsymbol{\Phi}^{\mathbf{T}}\,\boldsymbol{\mathcal{C}}\,\boldsymbol{\Phi} = \boldsymbol{\Theta} \tag{3.8}$$

In these last equations $\mathbf{I}_{n\times n}$ is the identity matrix and $\mathbf{\Lambda}_{n\times n}$ is a matrix that contains the square of the natural circular frequencies ω_i^2 of the structure on the main diagonal - i.e. $\mathbf{\Lambda} = \text{diag}\{\omega_i^2\}$ for $i = 1 \ldots n$.

It is worth noting that, for a generic system with a generic damping behavior, only the undamped portion of the system can be decoupled using the above-mentioned modal transformation. In fact, only the matrices $\mathbf{I}_{n\times n}$ and $\mathbf{\Lambda}_{n\times n}$ are diagonal matrices, while the matrix $\mathbf{\Theta}$ is not necessarily diagonal. Only if the damping behavior of the system can be modeled using a proportional damping model (for example, a Rayleigh damping model such that $\boldsymbol{\mathcal{C}} = \alpha\,\mathbf{M} + \beta\,\mathbf{K}$ where α, β are scalar quantities, or a more general model such that $\boldsymbol{\mathcal{C}} = \sum \alpha_i\,\mathbf{M}^{-1}\,\mathbf{K}^i$ where α_i is scalar quantity) [Alvin et al., 2003], then the second order equation of motion can be completely decoupled and the matrix $\mathbf{\Theta}$ is also diagonal

$$\mathbf{\Phi}^{\mathbf{T}}\,\boldsymbol{\mathcal{C}}\,\mathbf{\Phi} = \mathbf{\Theta} = \text{diag}\{2\,\zeta_i\,\omega_i\} \quad \text{with } i = 1,\ldots, n \tag{3.9}$$

In this last equation the term ζ_i is the modal damping ratio related to the generic *i*-th mode of the structure. It is worth noting, however, that, as shown later in this section, having the knowledge of the modal damping ratios related to the modes of the structure is not necessary for the estimation of the modal flexibility matrix.

By reformulating Eq. (3.7), the stiffness matrix of an undamped or classically-damped MDOF structure can be expressed as a function of the natural frequencies and the mass-normalized real mode shapes

$$\boldsymbol{K} = \mathbf{\Phi}^{-T}\,\mathbf{\Lambda}\,\mathbf{\Phi}^{-1} \tag{3.10}$$

The flexibility matrix **F** of the structure is the inverse of the stiffness matrix, thus the flexibility matrix can be expressed in terms of the modal parameters using the following equation

$$\boldsymbol{F} = \mathbf{\Phi}\,\mathbf{\Lambda}^{-1}\,\mathbf{\Phi}^{T} \tag{3.11}$$

which is derived by inverting both sides of Eq. (3.10).

If the modal parameters (in terms of natural frequencies and mass-normalized mode shapes) of a structure are extracted using modal identification techniques from the data of a vibration test, theoretically both Eq. (3.10) and Eq. (3.11) can be used to

obtain, respectively, an estimate of the stiffness matrix or the flexibility matrix of the structure. From a practical point of view, however, there exists, an important difference between performing the above-mentioned operations by considering the stiffness matrix or the flexibility matrix, as extensively described in the literature [Berman & Flannelly, 1971; Duan et al., 2005; Koo et al., 2010]. To show this important aspect, let us explicitly introduce the terms ω_i^2, i.e. the square of the natural circular frequency related to the *i*-th mode, in Eqs. (3.10, 3.11)

$$\boldsymbol{K} = \boldsymbol{\Phi}^{-T} \begin{bmatrix} \ddots & & \\ & \omega_i^2 & \\ & & \ddots \end{bmatrix} \boldsymbol{\Phi}^{-1} \tag{3.12}$$

$$\boldsymbol{F} = \boldsymbol{\Phi} \begin{bmatrix} \ddots & & \\ & \frac{1}{\omega_i^2} & \\ & & \ddots \end{bmatrix} \boldsymbol{\Phi}^{T} \tag{3.13}$$

It is evident in Eqs. (3.12, 3.13) that while in the stiffness matrix the influence of the *i*-th mode depends on the term ω_i^2, in the flexibility matrix the influence of the *i*-th mode depends on the term $\frac{1}{\omega_i^2}$. This property related to the above-mentioned equations plays an important role in the choice of one formulation or the other when dealing with a vibration test. In fact, from a vibration test the first lower modes are generally identified, while it is more difficult to extract the high-order modes. Of course, the first modes of the structure are characterized by the lower values of the natural frequencies. This means that the contribution of the lower modes in the flexibility matrix is higher with respect to the contribution of the same modes in the stiffness matrix [Berman & Flannelly, 1971]. This result was also shown in the work by [Gao & Spencer, 2002], where numerical simulations were performed on a 40 DOFs planar truss using eigenvalue analyses.

In light of this premise, it is clear that estimating flexibility matrices from identified modal parameters is a more convenient approach than estimating stiffness matrices. When this advantageous operation is performed, the flexibility matrix is usually indicated as modal flexibility matrix [Zhang & Aktan, 1998]. The modal flexibility matrix has also the advantage that it can be easily assembled using a limited number of modes. In fact, Eq. (3.13), which is expressed in terms of all the modal

parameters of the structure (i.e. both the matrices $\boldsymbol{\Phi}$ and $\boldsymbol{\Lambda}$ have dimensions equal to $n \times n$), can be reformulated in terms of truncated matrices, as follows

$$\boldsymbol{F_r} = \boldsymbol{\Phi_r}\, \boldsymbol{\Lambda_r^{-1}}\, \boldsymbol{\Phi_r^T} \tag{3.14}$$

where r is the number of the modes included in the calculation with $r \leq n$, $\boldsymbol{\Phi_r}_{\,n\times r}$ is a modal matrix formed by r columns and each column contains a mass-normalized mode shape vector, $\boldsymbol{\Lambda_r}_{\,r\times r}$ is a diagonal spectral matrix which contains the square of the first r natural circular frequencies ω_i^2 on the main diagonal, i=1…r is the mode index, and n is the number of the DOFs. It is worth noting that dealing with a limited number of modes (thus dealing with modal and spectral matrices that have reduced dimensions with respect to the corresponding matrices assembled using all the modal parameters) is an operation that can be easily handled in the equation of the modal flexibility matrix (3.14). On the contrary, if one uses a limited number of modes to assemble the stiffness matrix (according to Eq. 3.10), then pseudo-inverse operations have to be performed to deal with the mode shape matrix assembled using r modes, which is a rectangular matrix. This matrix, in fact, needs to be inverted according to the equation of the stiffness matrix expressed as a function of the modal parameters (Eq. 3.10).

The equation of the modal flexibility matrix (Eq. 3.14) can be expressed in terms of the individual components of the mode shapes $\phi_{j,i}$ - with j =1 … n (DOF index) and i = 1… r (mode index) - and the natural circular frequencies ω_i as follows

$$\boldsymbol{F_r} = \begin{bmatrix} \sum_{i=1}^{r} \frac{\phi_{n,i}{}^2}{\omega_i^2} & \sum_{i=1}^{r} \frac{\phi_{n,i}\phi_{n-1,i}}{\omega_i^2} & \cdots & \cdots & \sum_{i=1}^{r} \frac{\phi_{n,i}\phi_{1,i}}{\omega_i^2} \\ \sum_{i=1}^{r} \frac{\phi_{n-1,i}\phi_{n,i}}{\omega_i^2} & \sum_{i=1}^{r} \frac{\phi_{n-1,i}{}^2}{\omega_i^2} & \ddots & \ddots & \vdots \\ \vdots & \ddots & \ddots & \ddots & \vdots \\ \vdots & \ddots & \ddots & \ddots & \\ \sum_{i=1}^{r} \frac{\phi_{1,i}\phi_{n,i}}{\omega_i^2} & \cdots & \cdots & & \sum_{i=1}^{r} \frac{\phi_{1,i}{}^2}{\omega_i^2} \end{bmatrix} \tag{3.15}$$

where each component of the matrix $\boldsymbol{F_r}$ is

$$f_{j,k} = \sum_{i=1}^{r} \frac{\phi_{j,i}\,\phi_{k,i}}{\omega_i^2} \qquad \text{with } j,k = 1\ldots n \tag{3.16}$$

It is evident from this formulation that the flexibility matrix $\boldsymbol{F_r}$ is assembled using the contributions of the different modes, and these contributions are summed together for i = 1 ... r.

If all the modes are considered (i.e. $r=n$) and if we assume to be in the ideal case in which we are dealing with exact modal parameters (for example, the modal identification is applied on noiseless vibration data), then the static flexibility matrix $\boldsymbol{F_n}$ is obtained using Eq. (3.14), where the subscript n indicates that all the modes are considered. On the contrary, if $r < n$ the components of the modal flexibility matrix are approximated with respect to the corresponding exact components of the static flexibility matrix [Berman & Flannelly, 1971]. As reported in [Doebling et al., 1996], the difference between the two terms (i.e. the modal flexibility obtained using a limited number of modes and the static flexibility) is indicated in the literature as residual flexibility. This last term is related to the contribution of the modes that are not included in the calculations. Moreover, according to [Zhang & Aktan, 1998] and as anticipated in Chapter 1, the errors that are introduced when computing the modal flexibility matrix using a limited number of modes are indicated in the literature as modal truncation errors. As shown later in this chapter, these modal truncation errors also affect the deflections that are calculated from the modal flexibility matrices, and this is an aspect that will be addressed specifically in Chapter 4. Referring to the modal truncation errors, it is worth noting that in general accurate estimates of the modal flexibility matrices can be obtained using the first lower modes of the structures. In any case, as discussed in this section, the modal truncation errors introduced in the computation of the modal flexibility matrix using a limited number of modes are lower than the modal truncation errors introduced in the evaluation of the stiffness matrix using the same subset of structural modes.

The modal flexibility matrix has some interesting properties that are summarized herein according to the more extensive description presented in [Zhang & Aktan, 1998]. First of all, each term in the summation that is present in Eq. (3.16) – i.e. the expression of a generic component in the modal flexibility matrix – is independent from the global sign of the i-th mode shape (i.e. it does not change if the mode shape is multiplied by -1). This is because the contribution of the i-th mode to the component of the flexibility matrix located in the position (j,k) contains the product $\phi_{j,i} \times \phi_{k,i}$, where $\phi_{j,i}$, $\phi_{k,i}$ are, respectively, the j-th and the k-th components of the i-th mode shape vector. The second property of the modal flexibility matrix, which derives directly from the first property, is that only the diagonal components of

the matrix are always positive quantities. This is evident in Eq. (3.15) where each *i*-th contribution to the diagonal components of the matrix contains the square of one mode shape component at the numerator and the square of the natural circular frequency at the denominator. A third property, reported in the work by [Zhang & Aktan, 1998], is that the lower modes have a major contribution in the modal flexibility than the higher modes (this property has been already discussed in this section and derives from the fact that each term in the summation present in Eq. 3.16 has the square of the natural circular frequency ω_i^2 at the denominator).

A final remark, reported in the work by [Zhang & Aktan, 1998] referring to the properties of the modal flexibility matrices, is that particular care should be taken when assembling these matrices in case of structures with closely spaced modes. This is a common situation that can be encountered in practice (for example, when a building structure, characterized by a symmetric plan and similar values of the story stiffness in the two prevalent directions, is tested). Dealing with closely spaced modes in modal identification is a problem that in general can be reasonably handled if a multiple input test (which, as discussed in Chapter 2, is generally the case for structures tested under ambient vibrations) and suitable modal identification techniques are considered. One of the techniques that are suitable to deal with closely space modes is, for example, the Frequency Domain Decomposition (FDD) [Brincker & Ventura, 2015], as discussed in Chapter 2. However, as described in [Brincker & Aenlle, 2015; Brincker, 2015], the case of closely spaced modes inherits some relevant properties from the theoretical case of the repeated eigenvalues in structural dynamics (i.e. the case in which a structure, described through an analytical model, has two natural frequencies that are identical). One of these properties is that, according to the dynamic characteristic equations of an undamped system, the orthogonality relation between two modes characterized by the same eigenfrequencies is not assured [Brincker & Aenlle, 2015; Brincker, 2015]. A similar property may thus be related to identified closely spaced modes, and issues may arise if modes characterized by such property are employed to calculate the modal flexibility matrix using Eq. (3.14). In fact, dealing with mode shapes that are orthogonal with respect to the mass matrix of the structure is one of the assumptions that are made (as shown in this section) to derive the equations of the stiffness/flexibility matrices expressed as a function of the

modal parameters of the structure (starting from the general equation of motion of a damped system under free vibrations). With reference to the problem of assembling modal flexibility matrices in the case of closely spaces modes it is worth noting, however, that there exist examples in the literature where the modal flexibilities were adequately estimated in these special situations. One of these examples is reported in work by [Hogue et al., 1991], where a reinforced concrete bridge was subjected to vibration tests: the bridge was excited by the impact of a weight that was dropped on the bridge deck. In this experimental case study, the modal flexibility coefficients of the bridge structure were adequately estimated even in presence of several closely spaced modes.

3.2 Estimation of modal flexibility-based deflections from vibration data

Once the modal flexibility matrix of a generic structure has been estimated from vibration data, such matrix can be considered as an experimentally-derived model of the structure and used to calculate the deflection of the structure due to a generic applied load. This deflection is indicated in the literature as a modal flexibility-based deflection. This operation of estimating modal flexibility-based deflections has to be performed according to both the Uniform Load Surface method [Zhang, 1993; Zhang & Aktan, 1995; Zhang & Aktan, 1998] and the Positive Shear Inspection Load method [Koo et al., 2010; Koo et al, 2011; Sung et al., 2012] for damage detection. According to these methods, the applied loads are indicated as "inspection loads" because the resulting deflections are considered as important sources of information to evaluate the condition of the structure. It is worth noting that, as already mentioned in Chapter 1, the inspection loads are loads that are not effectively acting on the real structure that was tested. These loads are applied only in a second phase related exclusively to the data analysis and that is different from the testing phase, as evident in Fig. 3.1.

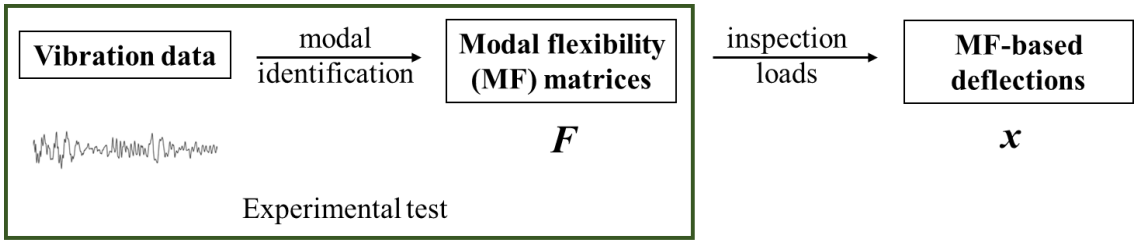

Figure 3.1. Estimation of modal flexibility-based deflections from vibration data

The deflection of a generic MDOF structure due to a generic load $\boldsymbol{p}_{n\times 1}$ can be determined starting from the modal flexibility matrix $\boldsymbol{F_r}$ assembled using r modes (Eq. 3.14) as follows

$$\boldsymbol{x_{p,r}} = \boldsymbol{F_r}\,\boldsymbol{p} \tag{3.17}$$

where $\boldsymbol{p} = [p_n \;\; p_{n-1} \;\; \dots \;\; p_1]^T$ is a generic inspection load. Considering that the modal flexibility matrix can be expressed in terms of the modal parameters as shown in Eq. (3.15), each displacement components of the deflection can be expressed as follows

$$x_{p,r,j} = \sum_{i=1}^{r} \frac{\phi_{j,i}}{\omega_i^2}\left(\phi_{n,i}p_n + \phi_{n-1,i}p_{n-1} + \cdots + \phi_{1,i}p_1\right) \tag{3.18}$$

According to the Uniform Load Surface method for vibration-based damage detection [Zhang & Aktan, 1998], a uniform load (UL) $\boldsymbol{u} = [1 \;\; 1 \;\; \dots \;\; 1]^T$ is selected as the inspection load. This inspection load is characterized by unit values that act as a load at each DOF of the structure. It is worth noting that adopting a uniform load as the inspection load is a choice that should also be made according to the Positive Shear Inspection Load method [Koo et al., 2010] for damage detection in building structures (as shown in Section 3.3).

In light of this premise, the deflection of an MDOF structure calculated starting from the modal flexibility matrix $\boldsymbol{F_r}$ and due to a uniform load $\boldsymbol{u}$ (i.e. the uniform load surface according to [Zhang & Aktan, 1998]) is expressed as

$$\boldsymbol{x_{u,r}} = \boldsymbol{F_r}\,\boldsymbol{u} \tag{3.19}$$

where the j-th component of the deflection vector $\boldsymbol{x_{u,r}}$ is

$$x_{u,r,j} = \sum_{i=1}^{r} \frac{\phi_{j,i}}{\omega_i^2}\left(\phi_{n,i} + \phi_{n-1,i} + \cdots + \phi_{1,i}\right) = \sum_{i=1}^{r} \frac{\phi_{j,i}\sum_{k=1}^{n}\phi_{k,i}}{\omega_i^2} \tag{3.20}$$

As reported in [Zhang & Aktan, 1998], some interesting observations can be formulated on the uniform load deflection. First of all, the contribution of a single mode in Eq. (3.20) does not depend on the global sign of the mode shape (i.e. it does not change if the mode shape is multiplied by -1). This is a propriety that was already observed for the contribution of each single mode in each component of the modal flexibility matrix (Eq. 3.16). However, if one compares Eq. (3.16) and Eq. (3.20), an important difference is evident between the two equations. The generic mode shape component $\phi_{k,i}$ present in Eq. (3.16), which is related to the modal flexibility, is substituted in Eq. (3.20), which is related to the uniform load modal flexibility-based deflection, by the term $\sum_{k=1}^{n} \phi_{k,i}$. For the sake of convenience and by introducing a different notation with respect to the original one presented in [Zhang & Aktan, 1998], the term $\sum_{k=1}^{n} \phi_{k,i}$ present in Eq. (3.20) is indicated herein as s_i, and Eq. (3.20) is reformulated as

$$x_{u,r,j} = \sum_{i=1}^{r} \frac{\phi_{j,i}}{\omega_i^2} s_i \tag{3.21}$$

According to [Zhang & Aktan, 1998], the term s_i is the summation of all the coefficients of the *i*-th mode shape, and it can be considered as the contribution of that mode. In general, higher values of the term s_i are obtained for the lower modes of the structure. For this reason, by considering an increasing number of modes included in the calculation, the convergence of each component of the UL deflection to the exact solution (i.e. the deflection calculated starting from the theoretical static flexibility matrix) is more rapid with respect to each component of the modal flexibility matrix. As already mentioned, this is due to the presence in Eq. (3.21) of the term $s_i = \sum_{k=1}^{n} \phi_{k,i}$ and implies that the components of the uniform load deflections are less sensitive to modal truncation errors than the components of the modal flexibility matrices. This property was shown in the work by [Zhang & Aktan, 1998] through numerical analyses performed both on a 10 DOF mass-spring model and on a FEM model of a bridge structure.

According to [Zhang & Aktan, 1998], a third property related to the components of the UL deflection is that such components are less sensitive to experimental errors than the components of the modal flexibility matrix. For example, experimental errors can be due to uncertainties that affect the mode shape components

estimated from vibration measurements, which are, in turn, affected by inevitable noise. The above-mentioned property derives from the fact that the operation of double summation present in Eq. (3.20) acts as a way of averaging random errors that affect the components of the mode shapes. This double summation effect is, on the contrary, not present in the equation of the generic component of the modal flexibility matrix (Eq. 3.16).

These properties of the uniform load deflection, formulated by [Zhang & Aktan, 1998] in the framework of the uniform load surface method, highlight some of the advantages of considering the modal flexibility-based deflections, instead of the modal flexibility matrices, as sources of information for structural identification and damage detection purposes. Estimating the deflections of structures starting from modal flexibility matrices also represents the core of the calculations that have to be performed according to the Positive Shear Inspection Load method [Koo et al., 2010] for damage detection in building structures. This method is presented in detail in next section.

3.3 Damage detection using modal flexibility-based deflections due to Positive Shear Inspection Loads (PSIL): a state-of-the-art approach

This section presents the method that was recently developed for the detection of damage in building structures tested under ambient vibrations. The method was firstly presented in the work by [Koo et al., 2010]. Then, further improvements of the technique were presented in later works [Koo et al., 2011; Sung et al., 2012]. As shown in this section, the method is based on the estimation of the modal flexibility-based deflections of building structures. These deflections are calculated from experimentally-derived modal flexibility matrices of the structures by applying special loads termed Positive Shear Inspection Loads (PSIL). As already mentioned in Chapter 1 and for the sake of brevity, the method is denoted in the present dissertation as PSIL method (even if this terminology was not used in the work by [Koo et al., 2010] to indicate the approach). According to the methodology, the operation of estimating modal flexibility-based deflections has to be done at first using

the vibration data of the structure assumed as the pristine or undamaged structure (i.e. the baseline state). Then, the same operation is repeated using the data obtained from the structure in the inspection stage (i.e. the possibly damaged state). Eventual changes in such deflections are used to localize and quantify damage in the structure. The types of damage the PSIL method can deal with are mainly reductions in the stiffness of one or more stories of building structures.

The PSIL method was formulated with reference mainly to building structures that can be modeled as plane shear-type building structures. A practical example of such structures is a frame building structure characterized by horizontal elements (e.g. beams) which can be supposed as infinitely stiff in comparison to the vertical elements (e.g. columns), as shown in Fig. 3.2. The equations and the analytical formulation of the method were thus obtained starting from a shear-type model of a building structure.

According to [Koo et al., 2010], the method can be applied if horizontal acceleration measurements are available at all the stories of the structure that is tested under ambient vibrations (Fig. 3.2a). As already mentioned, the method was formulated for structures that can be modeled as plane shear buildings, which are structures characterized by a number of the degree-of-freedoms (DOFs) that is equal to the number of the stories. Since we are dealing with a plane structure, at least one measurement of horizontal accelerations is required at each story. Of course, all the measurements have to be acquired in the same direction of the structure, which is the direction that is considered in the 2D analysis. In addition, it is evident that according to the methodology there is a one-to-one correspondence between the number of the DOFs of the idealized model of the structure and the number of the measurements.

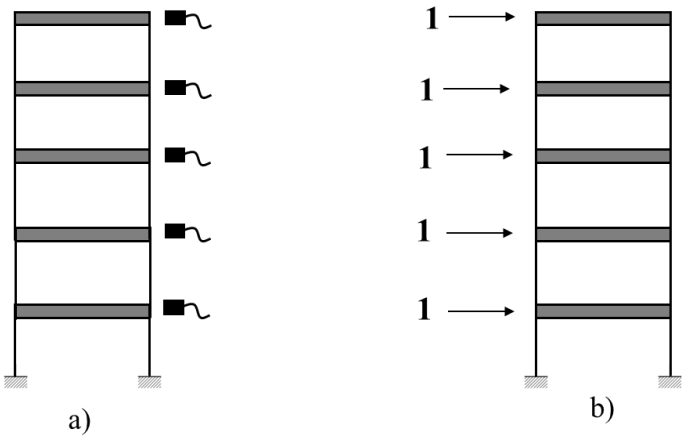

Figure 3.2. Shear building structures: a) location of the sensors; b) application of a uniform load as the Positive Shear Inspection Load (PSIL).

In the experimental applications that were performed by the authors that proposed the methodology [Koo et al., 2010; Koo et al., 2011; Sung et al., 2012], it is assumed that, not only the acceleration measurements, but also the sensors are available at all the stories of the structure. Referring to this point, it is worth noting, however, that having sensors at all the stories is not the only option that can be adopted to obtain acceleration measurements at all the stories. In fact, as discussed in Chapter 2, one option that is alternative to the case of having sensors at all the stories is to acquire multiple data sets of the ambient vibration measurements by adopting both reference and roving sensors (i.e. fixed and moving sensors) [Brincker & Ventura, 2015]. In this last case, the number of the sensors needed to apply the damage detection approach can thus be lower than the number of the stories of the structure.

The main steps of the PSIL damage detection methodology (as shown in Fig. 3.3) are presented herein. Then, in the second part of this section the analytical and rigorous demonstration of the validity of the approach for shear building structures, as formulated in the work by [Koo et al., 2010], is provided. As evident in the flow chart of Fig. 3.3, the main part of the calculations follows two different paths. On one side, the calculations are performed for the structure that is assumed as the pristine or undamaged structure (path on the left-hand side in Fig. 3.3, where B stands for baseline state). On the other side, the calculations are performed for the possibly

damaged structure that is considered in the inspection stage (path on the right-hand side in Fig. 3.3, where I denotes the state related to the inspection stage).

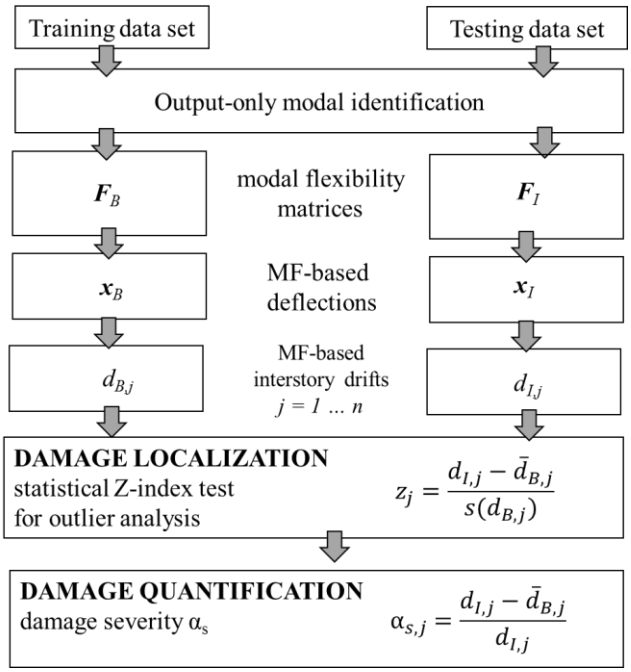

Figure 3.3. Flow chart of the Positive Shear Inspection Load (PSIL) method for damage detection in building structures.

The methodology is applied starting from the response measurements of the building structure tested under ambient vibrations. These vibration data are divided into two groups: the first data set is related to the undamaged structure (acquired in the baseline state), while the second group is related to the possibly damaged structure (acquired in the inspection stage). As reported in Fig. 3.3, the data set are indicated as the training and the testing data sets, according to the terminology used in the pattern recognition framework for SHM [Farrar & Worden, 2013]. It is worth noting that this alternative terminology was not used by the authors that proposed the methodology. The alternative terminology is adopted in the present dissertation because an attempt is made to interpret and discuss the validity of the PSIL method in the framework of the general theory for vibration-based damage detection (and the related fundamental axioms for SHM, as reported in Chapter 1) recently presented in the important work of [Farrar & Worden, 2013].

In the first step of the methodology any output-only modal identification technique can be applied to estimate the modal parameters of the structure starting from the recorded ambient vibration data. In the second step modal flexibility matrices of the structures are assembled. As already mentioned in Section 3.1, to perform this operation mass-normalized mode shapes are required. However, in output-only modal identification only arbitrarily-scaled mode shapes can be obtained. The modal masses are in fact not directly available in OMA because, as reported in [Brincker & Ventura, 2015], the input forces are not measured, and thus it is not possible to have a relationship between the input forces and the structural responses (which is, on the contrary, available in classical experimental modal analysis). The mass normalization of the mode shapes in output-only modal identification can be carried out using the methods that belong to the class of the "mass change methods" [Parloo et al, 2003; Brincker & Andersen, 2003; Bernal, 2004; Aenlle et al., 2010]. The mass changes that have to be applied on the structure, according to such techniques, have to be adequate for the considered structure, and these changes have to be quantified and known. However, as already discussed in Chapter 1, it migth be challenging in practice to apply to the structure such mass modifications. The use of the added mass methods is indicated as a possible strategy to perform the mass normalization of the mode shapes in the work related to the PSIL method [Koo et al., 2010]. However, an alternative option is suggested in the work of [Koo et al., 2010] and used in this work to carry out the numerical and experimental analyses related to the verification of the approach: the system mass matrix of the shear building structure is estimated a-priori, and then this estimated mass matrix of the structure is used to mass normalize the mode shapes [Koo et al., 2010; Koo et al., 2011; Sung et al., 2012].

In light of this premise, the modal flexibility matrix $\boldsymbol{F_r}_{n\times n}$ of the building structure, according to the PSIL method, can be assembled from identified modes as follows

$$\boldsymbol{F_r} = \boldsymbol{\Psi_r}\, \boldsymbol{\Lambda_r^{-1}} (\boldsymbol{\Psi_r^T}\, \mathbf{M}\, \boldsymbol{\Psi_r})^{-1}\, \boldsymbol{\Psi_r^T} \tag{3.22}$$

where $\boldsymbol{\Psi_r}_{n\times r}$ is the arbitrarily-scaled mode shape matrix, $\boldsymbol{\Lambda_r}_{r\times r}$ is a matrix with the square of the natural circular frequencies ω_i^2 on the main diagonal, $\boldsymbol{M}_{n\times n}$ is the mass matrix of the structure that is estimated a-priori (which is a diagonal matrix for a plane

shear building), *n* is the total number of the DOFs of the structure (i.e. the number of the stories for a plane shear building), and *r* is the number of the modes included in the calculations. As already discussed in Section 3.1, not all the modes of the structure can be identified in practice, and thus the modal flexibility matrices are usually assembled using a limited number of modes (i.e. $r \leq n$).

It is worth noting that Eq. (3.22), expressed in terms of arbitrarily-scaled mode shapes, is equivalent to Eq. (3.14), which is expressed in terms of mass-normalized mode shapes. In fact, the modal mass μ_i related to the *i*-th mode is

$$\mu_i = \boldsymbol{\psi}_i^T \, \mathbf{M} \, \boldsymbol{\psi}_i \tag{3.23}$$

where $\boldsymbol{\psi}_i$ is the arbitrarily-scaled mode shape vector related to the *i*-th mode. The relationship between this vector and the corresponding mass-normalized mode shape vector $\boldsymbol{\phi}_i$ is

$$\boldsymbol{\phi}_i = \frac{1}{\sqrt{\mu_i}} \boldsymbol{\psi}_i \tag{3.24}$$

The above-mentioned operation of modal scaling is implicitly performed in Eq. (3.22), where the operation of the mass normalization of the arbitrarily-scaled mode shapes is expressed using a matrix formulation.

In the third step of the methodology, the modal flexibility-based deflections of the structure are computed. As already shown in Eq. (3.17), this operation is performed by multiplying the modal flexibility matrix $\boldsymbol{F}_r$ by an inspection load $\boldsymbol{p}_{n\times 1}$ – i.e. $\boldsymbol{x}_r = \boldsymbol{F}_r \, \boldsymbol{p}$. According to [Koo et al., 2010], the applied inspection load is defined as a Positive Shear Inspection Load (PSIL). As suggested by the acronym, this PSIL is a load that induces positive shear forces in each story of the structure [Koo et al., 2010]. Considering loads with such characteristics is required to correctly apply the damage detection methodology (as also demonstrated later in Section 3.3.1.2). In the original work that proposed the PSIL method [Koo et al., 2010], it is suggested to consider a uniform load vector $\boldsymbol{p} = [1 \;\; 1 \;\; \ldots \;\; 1]^T$ as the positive shear inspection load (Fig. 3.2b). It is worth noting that this load is the same load that is applied to evaluate the modal flexibility-based deflections according to the Uniform Load Surface method [Zhang & Aktan, 1998]. However, it is important to underline that, as shown

analytically in Section 3.3.1.2, in the PSIL method selecting a uniform load as the inspection load is not the only option that can be considered.

In the fourth step of the methodology, the interstory drifts of the building structure are calculated starting from the modal flexibility-based deflections. The *j*-th modal flexibility-based interstory drift $d_{r,j}$ can be evaluated as follows

$$d_{r,j} = \begin{cases} x_{r,j} - x_{r,j-1} & for\ j = 2..n \\ x_{r,j} & for\ j = 1 \end{cases} \tag{3.25}$$

All the calculations related to the PSIL method described so far (i.e. performing the output-only modal identification and then estimating the modal flexibility matrices, the modal flexibility-based deflections, and the interstory drifts) have to be performed both for the undamaged and for the possibly damaged structures. The modal flexibility-based interstory drifts of the structure are in fact considered as damage-sensitive features (DSFs), and they are used both for the localization and the quantification of eventual damage present in the shear building structure.

The localization of the damaged stories (i.e. stories where, for example, a reduction of the story stiffness has occurred as an effect of the damage) can be performed by analyzing the changes in the modal flexibility-based interstory drifts. As indicated in [Koo et al., 2010], a story in a shear building can be classified as damaged (i.e. the damage can be localized) if

$$\Delta d_j = d_{I,j} - d_{B,j} > 0 \qquad \text{under a PSIL load} \tag{3.26}$$

where $d_{B,j}$ and $d_{I,j}$ are, respectively, the interstory drifts estimated for the structure in the baseline state and for the structure related to the inspection stage. On the contrary, if a story in a shear building structure is undamaged then the damage-induced MF-based interstory drifts is theoretically equal to zero – i.e.

$$\Delta d_j = d_{I,j} - d_{B,j} = 0 \qquad \text{under a PSIL load} \tag{3.27}$$

It is worth noting that the above-mentioned relationship is valid (i.e. Δd_j for an undamaged story is equal to zero) in the ideal case in which there are no uncertainties on the considered damage sensitive features and in the ideal case in which such quantities are estimated using all the modes of the structure. Referring to this last point, of course, in practice the modal flexibility matrices and the quantities derived

from these matrices are estimated using a limited number of modes, and thus inevitable approximations are introduced in the calculations. In any case, the modal flexibility matrices used for damage detection purposes are usually assembled using the same number of the identified modes (i.e. $r_I = r_B = r$). Under this assumption and for the sake of convenience, the subscript r is omitted in Eqs. (3.26, 3.27). It is worth noting that in the present thesis this choice made on the notation is adopted in all the equations where a parameter related to an undamaged structure is compared with the one related to a possibly damaged structure.

Of course, the modal flexibility-based interstory drifts estimated from experimental data are affected by uncertainties. On one side, in fact, the uncertainties that affect the identified modal parameters propagate to the modal flexibility matrices and the related derivatives (i.e. deflections and interstory drifts). On the other side, additional uncertainties might be introduced in the calculations because the mass matrix of the structure (used to normalize the mode shapes) is estimated a-priori. To deal with the uncertainties that affect the DSFs (i.e. the interstory drifts), the localization of eventual damaged stories is performed, according to [Koo et al., 2010] using a statistical approach. A basic premise in the considered approach is that the amount of the recorded vibration data related to the undamaged structure is larger than the data related to the inspection phase (this is a strategy commonly adopted in the majority of the vibration-based damage detection techniques). In this way, the training data set can be subdivided in different portions, and each of these portions of the data is used to extract a damage sensitive feature. According to [Koo et al., 2010], an index z_j is then adopted to perform the damage localization. This index is defined as follows

$$z_j = \frac{d_{I,j} - \bar{d}_{B,j}}{s(d_{B,j})} \tag{3.28}$$

where $\bar{d}_{j,B}$ and $s(d_{B,j})$ are, respectively, the sample mean and the sample standard deviation of the interstory drifts $d_{B,j,i}$ calculated for the baseline state using the training data set (for $i = 1 \ldots p$ where p = no. of DSFs extracted from the training data set), and $d_{I,j}$ is the interstory drift estimated in the inspection phase using the testing data set. Under the simplified assumption that the variable z_j is normally distributed,

the *j*-th story of the structure is labelled as damaged if the following statistical test is satisfied

$$z_j > z^{TH} \tag{3.29}$$

where z^{TH} is a threshold value for the z index. On the contrary, the *j*-th story of the structure is considered as undamaged if

$$z_j \leq z^{TH} \tag{3.30}$$

The value of the threshold z^{TH} is a user choice, and for example, as suggested in [Koo et al., 2010; Koo et al., 2011], $z^{TH} = 2.5$ can be selected. This threshold is used to obtain a quantification of the minimum difference, between the mean of the interstory drifts in the baseline state and the drift in the state related to the inspection phase, that is required to classify a story as damaged. In particular, according to the formulation of the z index and under the simplified assumption that z_j is approximately normally distributed, this minimum difference is quantified as a multiple of the standard deviation of the drifts in the baseline state. The number of standard deviations considered to quantify this minimum difference is indicated by the value of the selected threshold.

Once a story is identified as damaged using the z index test (Eqs. 3.28, 3.29), the PSIL method can be also used to quantify such damage. This operation can be done by evaluating the damage severity α_s, as defined in [Sung et al., 2012; Koo et al., 2011]. This parameter is a relative index ($0 \leq \alpha_s < 1$) that quantifies the relative portion of the story stiffness that is lost due to the damage. The damage severity α_s for the *j*-th story is expressed as

$$\alpha_{s,j} = \frac{d_{I,j} - \bar{d}_{B,j}}{d_{I,j}} \tag{3.31}$$

The parameter $\alpha_{s,j}$ is theoretically equal to zero if the story is not damaged, while it is equal to one if the story is completely damaged [Sung et al., 2012; Koo et al, 2011]. Of course, both the two situations are ideal cases. On one side, the damage severity has to be calculated only when the story has already been identified as damaged usign the z index. For this reason, the damage severity will never be zero. On the other side, having a damage severity equal to one implies that all the story stiffness is lost due to the damage, and of course this is only a theoretical case.

3.3.1 Theory behind the PSIL method

3.3.1.1 General relationship between damage and modal flexibility-based deflections

This section presents the analytical formulation that is needed to show the validity of the PSIL method and of all the calculations discussed in previous section. This analytical formulation is summarized herein following the original and more extensive formulation that was presented in [Koo et al., 2010]. According to [Koo et al., 2010], the problem is formulated at first for a generic MDOF structural system, and then in a second stage the equations are expressed specifically for a shear building structure. The objective of the first part is to derive the general expression of the so-called damage-induced deflection [Koo et al., 2010]. In other words, the objective is to derive an analytical relationship between damage (which can be present in structures as a stiffness reduction) and the changes in the modal flexibility-based deflections.

The formulation is derived considering stiffness and flexibility matrices of a generic structure that are exact analytical models (i.e. they are not matrices assembled from experimentally-derived modal parameters). Let us consider an undamaged structure (i.e. a structure in the baseline state) characterized by a stiffness matrix $\boldsymbol{K_B}$. The relationship between the deflection $\boldsymbol{x_B}$ and the generic load $\boldsymbol{p}$ is as follows

$$\boldsymbol{K_B}\,\boldsymbol{x_B} = \boldsymbol{p} \tag{3.32}$$

A similar relationship can be expressed for the structure considered in the inspection stage of the damage detection process, assuming that this structure is damaged

$$\boldsymbol{K_I}\,\boldsymbol{x_I} = \boldsymbol{p} \tag{3.33}$$

where $\boldsymbol{K_I}$ is the stiffness matrix of the damaged structure. The damage is here modeled as a reduction in the stiffness matrix of the baseline structure equal to $\Delta\boldsymbol{K}$, according to the following equation

$$\boldsymbol{K_I} = \boldsymbol{K_B} - \Delta\boldsymbol{K} \tag{3.34}$$

In light of this premise, the relationship between the deflection of the undamaged structure and the one of the damaged structure is as follows

$$\boldsymbol{x_I} = \boldsymbol{x_B} + \Delta\boldsymbol{x} \tag{3.35}$$

where the term $\Delta \boldsymbol{x}$, according to [Koo et al., 2010], is defined as the damage-induced deflection. By introducing Eqs. (3.34, 3.35) in Eq. (3.33), this last equation can be thus reformulated as

$$(\boldsymbol{K_B} - \Delta \boldsymbol{K}) (\boldsymbol{x_B} + \Delta \boldsymbol{x}) = \boldsymbol{p} \tag{3.36}$$

Then, by subtracting Eq. (3.32) from Eq. (3.36) the general expression of the damage-induced deflection can be obtained

$$\Delta \boldsymbol{x} = (\boldsymbol{K_B} - \Delta \boldsymbol{K})^{-1} \Delta \boldsymbol{K}\, \boldsymbol{x_B} = \boldsymbol{F_I}\, \Delta \boldsymbol{K}\, \boldsymbol{x_B} \tag{3.37}$$

The damage-induced deflection is the difference between the deflections in the damaged and in the undamaged states, and it is in general a non-zero vector because it is assumed that a stiffness modification is present between the two structural states.

According to [Koo et al., 2010], it can be recognized that the term $(\boldsymbol{K_B} - \Delta \boldsymbol{K})^{-1}$ is equal to the flexibility matrix of the damaged structure $\boldsymbol{F_I}$. Moreover, according to the interpretation provided in [Koo et al., 2010], the term $\Delta \boldsymbol{K}\, \boldsymbol{x_B}$ that is present in Eq. (3.37) can be considered as a load, and it is indicated as $\Delta \boldsymbol{p}$ where

$$\Delta \boldsymbol{p} = \Delta \boldsymbol{K}\, \boldsymbol{x_B} \tag{3.38}$$

In this way, by substituting Eq. (3.38) in Eq. (3.37), this last equation becomes

$$\Delta \boldsymbol{x} = \boldsymbol{F_I}\, \Delta \boldsymbol{p} \tag{3.39}$$

The term $\Delta \boldsymbol{p}$ is a load different from the original inspection load $\boldsymbol{p}$. As evident in Eq. (3.39) and as defined in [Koo et al., 2010], this load $\Delta \boldsymbol{p}$ is such that if applied to the damaged structure, it produces the damage-induced deflection $\Delta \boldsymbol{x}$. As reported in [Koo et al., 2010], this force is indicated as the "lost resisting force by the damage".

3.3.1.2 Damage-induced deflection for a shear building structure

According to the formulation presented in [Koo et al., 2010], the relationships defined for a generic MDOF structure in previous section are then specified for a shear building structure. In particular, by considering a shear building which experiences damage (modeled as a proportional reduction in the story stiffness of one story), the objective is to evaluate at first the expression of the term $\Delta \boldsymbol{p}$ (i.e. the "lost resisting

force by the damage" according to Eq. 3.38). Then, the second objective is to evaluate for such structure the values and the characteristics of the damage-induced deflection $\Delta \boldsymbol{x}$ (according to Eq. 3.39). It is worth noting that the analytical formulation adopted in this section to express the model of a shear building structure is slightly different with respect to the one adopted in [Koo et al., 2010]. However, using this different formulation does not substantially alter the approach and the theory behind the PSIL method.

Let us consider a plane shear building structure composed by *n* stories and modeled with *n* DOFs. The model of such structure can be defined in terms of the stiffness matrix $\boldsymbol{K}_{n\times n}$ and the mass matrix $\boldsymbol{M}_{n\times n}$

$$\boldsymbol{K} = \begin{bmatrix} k_n & -k_n & 0 & \cdots & \cdots & \cdots & \cdots & 0 \\ -k_n & k_n + k_{n-1} & \ddots & 0 & & & & \vdots \\ 0 & \ddots & \ddots & \ddots & 0 & & & \vdots \\ \vdots & 0 & \ddots & k_{j+1} + k_j & -k_j & 0 & & \vdots \\ \vdots & & 0 & -k_j & k_j + k_{j-1} & \ddots & 0 & \vdots \\ \vdots & & & 0 & \ddots & \ddots & \ddots & 0 \\ \vdots & & & & 0 & \ddots & k_3 + k_2 & -k_2 \\ 0 & \cdots & \cdots & \cdots & \cdots & 0 & -k_2 & k_2 + k_1 \end{bmatrix} \tag{3.40}$$

$$\boldsymbol{M} = \begin{bmatrix} m_n & 0 & \cdots & \cdots & 0 \\ 0 & \ddots & 0 & \ddots & \vdots \\ \vdots & 0 & m_j & 0 & \vdots \\ \vdots & \ddots & 0 & \ddots & 0 \\ 0 & \cdots & \cdots & 0 & m_1 \end{bmatrix} \tag{3.41}$$

where k_j is the story stiffness of the *j*-th story and m_j is the mass of the *j*-th DOF with $j = 1 \ldots n$. In the same way, the flexibility matrix $\boldsymbol{F}_{n\times n}$ of the shear building structure can be defined in terms of the *j*-th interstory flexibility f_j as follows

$$\boldsymbol{F} = \begin{bmatrix} f_n + \cdots + f_j + \cdots + f_1 & \cdots & f_j + \cdots + f_1 & \vdots & f_1 \\ \cdots & \ddots & \vdots & \vdots & f_1 \\ f_j + \cdots + f_1 & \cdots & f_j + \cdots + f_1 & \vdots & f_1 \\ \cdots & \cdots & \cdots & \ddots & f_1 \\ f_1 & f_1 & f_1 & f_1 & f_1 \end{bmatrix} \tag{3.42}$$

The model of the shear building structure is then specified for the undamaged and the damaged states, where the damaged structure is characterized by a proportional reduction in the story stiffness of the *k*-th story. According to the notation used in previous section, the stiffness matrix of the undamaged structure is $\boldsymbol{K_B}$, while the

stiffness matrix of the damaged structure is $\boldsymbol{K_I}$. For a shear building structure, the change-in-stiffness matrix $\Delta\boldsymbol{K}$ can be expressed as follows

$$\Delta\boldsymbol{K} = \begin{bmatrix} 0 & \cdots & 0 & \cdots & \cdots & \cdots & \cdots & 0 \\ \vdots & & \vdots & & & & & \vdots \\ 0 & \cdots & 0 & \cdots & \cdots & & & \vdots \\ \vdots & & & \alpha_{s,k}\, k_{B,j} & -\alpha_{s,k}\, k_{B,j} & \vdots & & \vdots \\ \vdots & & \vdots & -\alpha_{s,k}\, k_{B,j} & \alpha_{s,k}\, k_{B,j} & & & \vdots \\ \vdots & & & \cdots & \cdots & 0 & \cdots & 0 \\ \vdots & & & & & \vdots & & \vdots \\ 0 & \cdots & \cdots & \cdots & \cdots & 0 & \cdots & 0 \end{bmatrix} \tag{3.43}$$

where $\alpha_{s,k}$ is a damage index ($0 < \alpha_{s,k} < 1$) that is used to model the reduction in the story stiffness at the *k*-th story.

The change-in-stiffness matrix can be used to evaluate the "lost resisting force by the damage" (i.e. the term $\Delta\boldsymbol{p}$, according to Eq. 3.38) for the shear building. In addition to the term $\Delta\boldsymbol{K}$, the other term that is present in Eq. (3.38) is the modal flexibility-based deflection of the structure in the undamaged state $\boldsymbol{x_B}$. This deflection can be evaluated for a generic load $\boldsymbol{p}$ as

$$\boldsymbol{x_B} = \boldsymbol{F_B}\, \boldsymbol{p} \tag{3.44}$$

where $\boldsymbol{F_B}$ is the flexibility matrix of the shear building in the undamaged state. It is worth noting that at this point no assumptions are made on the values assumed by the loads included in the vector $\boldsymbol{p}$. By substituting Eqs. (3.43, 3.44) in Eq. (3.38) the "lost resisting force by the damage" for the shear building can be evaluated as follows

$$\Delta\boldsymbol{p} = \begin{bmatrix} 0 & \cdots & 0 & \cdots & \cdots & \cdots & \cdots & 0 \\ \vdots & & \vdots & & & & & \vdots \\ 0 & \cdots & 0 & \cdots & \cdots & & & \vdots \\ \vdots & & & \alpha_{s,k}\, k_{B,j} & -\alpha_{s,k}\, k_{B,j} & \vdots & & \vdots \\ \vdots & & \vdots & -\alpha_{s,k}\, k_{B,j} & \alpha_{s,k}\, k_{B,j} & & & \vdots \\ \vdots & & & \cdots & \cdots & 0 & \cdots & 0 \\ \vdots & & & & & \vdots & & \vdots \\ 0 & \cdots & \cdots & \cdots & \cdots & 0 & \cdots & 0 \end{bmatrix} \begin{bmatrix} x_{B,n} \\ \vdots \\ \vdots \\ x_{B,k} \\ x_{B,k-1} \\ \vdots \\ \vdots \\ x_{B,1} \end{bmatrix} = \begin{bmatrix} 0 \\ \vdots \\ 0 \\ \Delta p_k \\ -\Delta p_k \\ 0 \\ \vdots \\ 0 \end{bmatrix} \tag{3.45}$$

where the term Δp_k is

$$\Delta p_k = \alpha_{s,k}\, k_{B,j}\, (x_{B,k} - x_{B,k-1}) \tag{3.46}$$

According to [Koo et al., 2010] and as indicated in Eq. (3.39), this force $\Delta\boldsymbol{p}$ is the force that if applied to the damaged structure produces the damage-induced deflection

$\Delta \boldsymbol{x}$. As observed in the work by [Koo et al., 2010], for a shear building structure this force acts only at the damaged story (i.e. at the *k*-th story in such case) and it is a self-equilibrated force. These characteristics of the force $\Delta \boldsymbol{p}$ are also depicted in Fig. 3.4c, which shows a graphical exemplification of the basic principle that is behind the theory of the PSIL method and its related damage detection strategy.

For a shear building structure, it is thus evident that the damage-induced deflection occurs only at the damaged story. This result can be obtained by substituting the force $\Delta \boldsymbol{p}$ obtained for a shear building (i.e. Eq. 3.45) in Eq. (3.39). The resulting damage-induced deflection $\Delta \boldsymbol{x}$ is reported in Fig. 3.4d: the deflection is characterized by an inter-story deflection at the *k*-th story (which is the damaged story), while the inter-story deflection at the other stories (i.e. undamaged stories) is equal to zero.

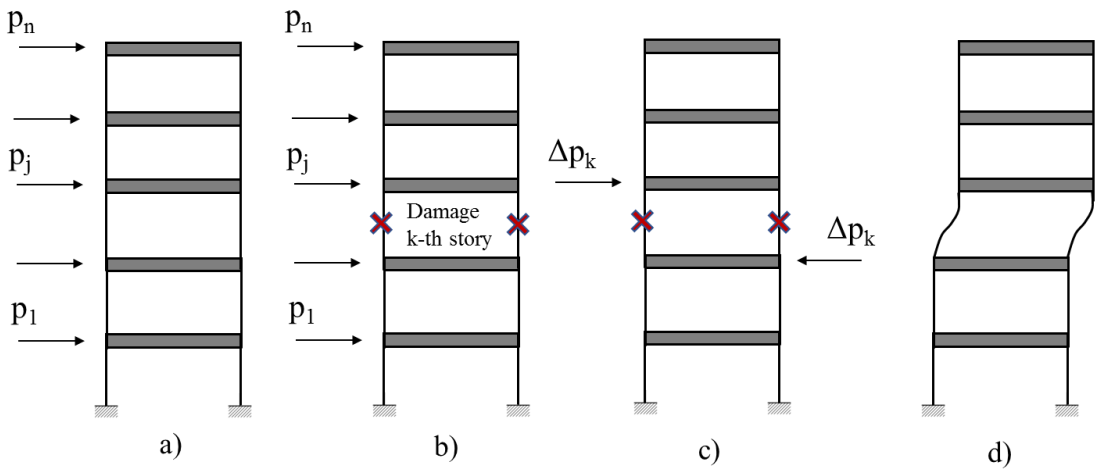

Figure 3.4. Exemplification of the damage detection process based on the PSIL method: a) PSIL applied on the undamaged structure; b) PSIL load applied on the damaged structure; c) load Δp_k that applied on the damaged structure produces the damage-induced deflection; d) damage-induced deflection.

Under the interpretation provided in [Koo et al., 2010] and summarized in this section, it is clear how the PSIL method for damage detection works. As reported in [Koo et al., 2010; Sung et al., 2012], the above-mentioned feature of the method (i.e. the fact that the damage-induced inter-story deflection occurs only at the damaged stories and not at the undamaged stories) plays a key role in the damage localization. It is thus evident the reason for which damage in shear buildings can be localized by analyzing the variations of the modal flexibility-based interstory drifts between the undamaged and the possibly damaged states (according to the criteria reported in Section 3.3 and Eqs. 3.28, 3.31). In fact, as shown analytically in this section, there exists an explicit relationship between damage (modeled as a proportional story stiffness reduction) and the damage sensitive features (i.e. the interstory drifts). This principle is a central pillar of the PSIL method [Koo et al., 2010].

As reported in [Koo et al., 2010], an important observation must be made on the applied inspection load $\boldsymbol{p}$. If one analyzes the term Δp_k (which produces the damage-induced deflection) using Eq. (3.46), it is clear that this term depends on the term $\alpha_{s,k}\, k_{B,j}$ (which is non-zero if there is damage in the structure, as assumed) and the term $(x_{B,k} - x_{B,k-1})$. This last term is the interstory drift $d_{B,k}$ of the undamaged structure at the *k*-th story, which of course is non-zero if the story shear V_k at the *k*-th story of the structure generated by the applied inspection load $\boldsymbol{p}$ is non-zero. On the basis of these observations and to guarantee that for any position in the structure of the damage the force $\Delta\boldsymbol{p}$ is a non-zero vector, it is important to impose a condition on the applied inspection load $\boldsymbol{p}$. As reported in [Koo et al., 2010], the applied inspection load has to be a Positive Shear Inspection Load (PSIL), which is defined as a load that produces a positive shear force in each story of the shear building structure. If this requirement is not guaranteed (e.g. the shear force produced by the inspection load $\boldsymbol{p}$ at the *k*-th story is zero), then the term Δp_k present in the force vector $\Delta\boldsymbol{p}$ is zero even if the *k*-th story is damaged. This of course implies that also the damage-induced deflection at the *k*-th story is zero (even if the *k*-th story is damaged), and thus the damage in such case is not detectable.

As reported in [Koo et al., 2010], different loads can be selected as the PSIL inspection load $\boldsymbol{p}$. One of the simplest options, can be, for example, a load with a unit

value only at the top floor of the shear building structure. However, the authors that proposed the PSIL method suggest considering a uniform load as the PSIL load – i.e. a load $\boldsymbol{p} = [1 \quad 1 \quad ... \quad 1]^T$ (as already discussed in Section 3.3). In fact, as reported in [Koo et al., 2010], a uniform load can be a better choice than a load with a unit value only at the top floor, for example, for the case in which the sensor located at the top floor is corrupted by an amount of noise that is higher than the other sensors. In such case the column that corresponds to the top DOF of the structure in the flexibility matrix might be affected by higher uncertainties. Then, when the load with a unit value only at the top floor is applied, such uncertainties propagates directly to the modal flexibility-based deflection. On the contrary, by applying a uniform load the uncertainties related to one column of the flexibility matrix can be averaged in the calculations and thus reduced when the modal flexibility-based deflection is evaluated. This observation, reported in [Koo et al., 2010], is in agreement with the observation formulated by [Zhang & Aktan, 1998] and that was already discussed in Section 3.2. According to [Zhang & Aktan, 1998], in fact the components of the uniform load deflection are in general less sensitive to experimental errors than the components of the modal flexibility matrix.

In this final part of the section, the validity of the expression that can be used to quantify the amount of damage present in one story of the structure (i.e. the damage severity $\alpha_{s,j}$ presented in Eq. 3.31 and Section 3.3) is demonstrated. This demonstration is performed using the analytical formulation developed in this section for a shear building structure.

Let us consider the expression of the damage-induced deflection (Eq. 3.39) by specifying all the terms for a shear building structure. Moreover, let us consider again that the structure is damaged only at the *k*-th story, and thus the damage-induced deflection occurs only at that story. By considering only the *k*-th story, Eq. (3.39) can be reformulated as follows

$$\left(x_{I,k} - x_{I,k-1} \right) - \left(x_{B,k} - x_{B,k-1} \right) = f_{I,k}\, \Delta p_k \tag{3.47}$$

Then, Eq. (3.46) is substituted in Eq. (3.47), and all the terms in Eq. (3.47) that are the difference between the *k*-th and (*k* - 1)-th components of the deflections (both in

the undamaged and in the damaged states) are substituted by the corresponding interstory drifts. Eq. (3.47) can thus be reformulated as

$$d_{I,k} - d_{B,k} = f_{I,k}\, \alpha_{s,k}\, k_{B,j}\, d_{B,k} \tag{3.48}$$

According to the PSIL method [Koo et al., 2010], the inspection load $\boldsymbol{p}$ is applied both to the undamaged and the damaged structures. For this reason, the shear force that this load induces at the *k*-th story in both two structures is equal. In light of this premise, it is clear that the following relationship is valid

$$k_{B,j}\, d_{B,k} = k_{I,j}\, d_{I,k} \tag{3.49}$$

From Eq. (3.49) the term $k_{B,j}$ can be derived and then substituted in Eq. (3.48). By performing this operation both the flexibility and the stiffness coefficients present in Eq. (3.48) cancel out, and the equation can be reformulated as follows

$$d_{I,k} - d_{B,k} = \alpha_{s,k}\, d_{I,k} \tag{3.50}$$

From this last equation the parameter $\alpha_{s,k}$ can be derived, and the same expression of the damage severity that is reported in Section 3.3 (Eq. 3.31) is obtained. It is worth noting that the only difference between Eq. (3.31) and Eq. (3.50) is the following: in the equation that has to be applied in the experimental case (i.e. Eq. 3.31) the modal flexibility-based interstory drift related to the baseline state is the mean value of the different estimates of the drifts that are obtained from the training data set.

3.3.2 Additional comments with respect to the original formulation of the PSIL method presented by Koo et al. [2010]

Some additional comments and considerations that are not reported in the original formulation of the Positive Shear Inspection Load method proposed by [Koo et al., 2010; Koo et al., 2011; Sung et al., 2012] are presented in this section. Firstly, the PSIL technique is analyzed under the general framework for vibration-based damage detection that has been theorized by [Farrar & Worden, 2013] and that is based on the axioms for SHM presented in Chapter 1. Then, some analytical investigations that were performed on the basis of the theory behind the original formulation of the PSIL method will be presented.

As shown in Section 3.3, according to the PSIL method a statistical test based on the evaluation of the z index (Eq. 3.28) is performed to localize the damaged stories in shear building structures. This statistical test based on the z index is one of the basic approaches that can be adopted in the field of univariate outlier analysis [Barnett & Lewis, 1994]. As already mentioned in Chapter 1, adopting these techniques, which are also known as novelty detection techniques, is the most convenient way for performing a feature discrimination in the framework of a vibration-based damage detection strategy that is based, according to the machine learning interpretation [Farrar & Worden, 2013], on an unsupervised learning mode. The Positive Shear Inspection Load method can be thus considered as a method that adopts a damage detection strategy that is based on an unsupervised learning mode. In fact, only vibration data related to the undamaged structure have to be available to form the training data set.

Let us consider the III axiom for SHM reported in [Worden et al., 2007] by focusing on the following part of this axiom "*Identifying the location of damage can be done in an unsupervised learning mode".* By considering the PSIL method as a strategy based on an unsupervised learning mode, it is clear that the fact that according to the PSIL method damage can be localized using the statistical test based on the z index is in agreement with the above-mentioned part of the III axiom.

The III axiom for SHM [Worden et al., 2007] also states that "*identifying the damage severity can generally only be done in a supervised learning mode.".* This second part of the axiom seems not to be in agreement with the principles and the theory behind the PSIL method (according to the PSIL method in fact the modal flexibility-based interstory drifts of shear building structures are used for the estimation of the damage severity - Eq. 3.31). This contradiction is, however, only apparent. In the PSIL method the damage quantification is performed only after that the damage has been already localized (i.e. a story in a structure has been already labelled as damaged). In fact, the equation to evaluate the damage severity (Eq. 3.31) can be correctly applied only if it is known that the modal flexibility-based interstory drift in the inspection phase is associated to a story that is classified as damaged. In other words, this means that, when the damage quantification is performed, the structure (and the related data set) in the inspection phase is already classified as

damaged, and this is the same information that one has before performing the analysis in the supervised approaches (where, differently from the considered PSIL method, vibration data related to the damaged states are also present in the training data set). In light of this interpretation, there is no contradiction between the part of the III axiom that refers to the damage quantification [Worden et al., 2007] and the PSIL method.

In the work by [Sung et al., 2012], as already mentioned in Chapter 1, damage was detected using the PSIL method on a 5-story full-scale shear building. This structure was tested using shaker excitations, and a stiffness reduction was imposed at the first story of the structure (by modifying the stiffness of a spring member that was positioned in the bracing system). In the above-mentioned work and referring to the above-mentioned structure, the authors provided an estimate of the minimum amount of damage (i.e. the minimum interstory stiffness reduction) that can be detected using the Positive Shear Inspection Load method. For the considered structure and the considered story (the first one) the minimum value of the damage severity (defined according to the PSIL method) is approximately 0.05 (i.e. 5%). The procedure used to obtain the estimate of the minimum damage severity that can be detected using the PSIL method [Sung et al., 2012] is here reported, to show an important property of the method.

The formula of the z index related to the generic *j*-th story of the shear building structure (Eq. 3.28) can be reformulated to express the interstory drift in the inspection phase as follows

$$d_{I,j,min} = \bar{d}_{B,j} + s\left(d_{B,j}\right) z^{TH} \tag{3.51}$$

where the value of the threshold for the z index z^{TH} (e.g. z^{TH} = 2.5 according to [Sung et al., 2012]) is introduced. The term $d_{I,j,min}$ is the minimum drift for which the *j*-th story of the shear building is classified as damaged. This value depends on the mean of the interstory drifts in the undamaged state ($\bar{d}_{B,j}$), the dispersion (i.e. the standard deviation $s\left(d_{B,j}\right)$) related to such quantities affected by uncertainties, and the value of the threshold z^{TH}. The value of the drift in the inspection phase expressed by Eq. (3.51) can then be substituted in the equation of the damage severity (Eq. 3.31)

$$\alpha_{s,j,min} = \frac{d_{I,j,min} - \bar{d}_{B,j}}{d_{I,j,min}} \tag{3.52}$$

According to [Sung et al., 2012], the quantity $\alpha_{s,j,min}$ is the minimum value of the damage severity that can be detected using the PSIL method at the *j*-th story of the structure. Some observations can be formulated on Eqs. (3.51, 3.52) to derive a general property of the PSIL technique. The higher the uncertainties on the interstory drifts related to the baseline state, the higher the dispersion $s(d_{B,j})$ on such parameters. On the contrary, it can be assumed that the mean value of these interstory drifts is not altered and does not depend on the uncertainties related to such parameters. In this situation, it is clear that if the dispersion on the interstory drifts in the baseline state increases, then higher values of the minimum damage severity that can be detected using the PSIL method are obtained. This property of the PSIL method is strictly related to the concept expressed by the VI axiom for SHM formulated by [Worden et al., 2007]. This axiom is as follows: "*There is a trade-off between the sensitivity to damage of an algorithm and its noise rejection capability*.". It is worth noting that, as reported in [Farrar & Worden, 2013], all the methods that adopt outlier analysis or novelty detection techniques (thus including the PSIL method) are characterized by the property expressed by the VI axiom for SHM.

In the work by [Koo et al., 2010] the general expression of the damage-induced deflection (Eqs. 3.37, 3.39) is derived (as shown in Section 3.3.1.1). In particular, according to the interpretation formulated by [Koo et al., 2010], a relationship was found between the damage-induced deflection $\Delta\boldsymbol{x}$ and the so-called "lost resisting force by the damage" $\Delta\boldsymbol{p}$. In this section, this analytical formulation is developed further to show how the damage-induced deflection can be also related to the change-in-flexibility matrix $\Delta\boldsymbol{F}$. This property can be easily shown, as follows. Eq. (3.17) is evaluated both for the undamaged and the possibly damaged structures, and then the two equations are substituted in Eq. (3.35). In this way, the damage-induced deflection can be expressed as

$$\Delta\boldsymbol{x} = \boldsymbol{x_I} - \boldsymbol{x_B} = (\boldsymbol{F_I} - \boldsymbol{F_B})\ \boldsymbol{p} = \Delta\boldsymbol{F}\,\boldsymbol{p} \tag{3.53}$$

where $\Delta\boldsymbol{F}$ is the change-in-flexibility matrix.

This formulation can be also derived starting from the original equation of the damage-induced deflection proposed by [Koo et al., 2010]. To perform this operation, let us consider one general relationship that is valid for the stiffness and flexibility matrices of both the undamaged and the damaged structures. This formulation was found in the work by [Yang & Liu, 2009] where, as already discussed in Chapter 1, a damage detection method based on an eigenparameter decomposition of the change-in-flexibility matrix is presented. The relationship found in the work by [Yang & Liu, 2009] is the following

$$\boldsymbol{F_B}\,\boldsymbol{K_B} = \boldsymbol{F_I}\,\boldsymbol{K_I} \tag{3.54}$$

Of course, since the stiffness matrix is the inverse of the flexibility matrix, both sides of Eq. (3.54) are equal to the identity matrix **I**. According to [Yang & Liu, 2009], the following two general expressions that relate the stiffness/flexibility matrices in the undamaged and in the damaged states can be considered

$$\boldsymbol{K_B} = \boldsymbol{K_I} + \Delta\boldsymbol{K} \tag{3.55}$$

$$\boldsymbol{F_I} = \boldsymbol{F_B} + \Delta\boldsymbol{F} \tag{3.56}$$

If the two above-mentioned expressions are substituted in Eq. (3.54), then according to [Yang & Liu, 2009], the following expression is obtained

$$\Delta\boldsymbol{F}\,\boldsymbol{K_I} = \boldsymbol{F_B}\,\Delta\boldsymbol{K} \tag{3.57}$$

It can be recognized that the term on the right-hand side of Eq. (3.57) is similar to the term that is present in the expression of the damage-induced deflection formulated by [Koo et al., 2010] – i.e. Eq. (3.37). However, in Eq. (3.57) the undamaged flexibility matrix $\boldsymbol{F_B}$ is considered, while the damaged flexibility matrix $\boldsymbol{F_I}$ is present in Eq. (3.37).

For the purpose of carrying on the passages of the proposed analytical formulation, it is shown, however, that an equation alternative to the one obtained by [Yang & Liu, 2009] (Eq. 3.57) can be derived. According to the proposed analytical formulation, Eqs. (3.55, 3.56) can be reformulated as follows

$$\boldsymbol{K_I} = \boldsymbol{K_B} - \Delta\boldsymbol{K} \tag{3.58}$$

$$\boldsymbol{F_B} = \boldsymbol{F_I} - \Delta\boldsymbol{F} \tag{3.59}$$

If the two above-mentioned expressions are substituted in Eq. (3.54), then the following expression can be obtained

$$\Delta \boldsymbol{F}\, \boldsymbol{K_B} = \boldsymbol{F_I}\, \Delta \boldsymbol{K} \tag{3.60}$$

At this point it can be recognized that the term on the right-hand side of Eq. (3.60) is also present in the expression of the damage-induced deflections formulated by [Koo et al., 2010] – Eq. (3.37). By considering the general expression of the deflection in the undamaged state $\boldsymbol{x_B} = \boldsymbol{F_B}\, \boldsymbol{p}$, Eq. (3.37) can be reformulated as follows

$$\Delta \boldsymbol{x} = \boldsymbol{F_I}\ \Delta \boldsymbol{K}\, \boldsymbol{F_B}\, \boldsymbol{p} \tag{3.61}$$

Finally, Eq. (3.60), which was derived by reinterpreting the original relationship proposed in [Yang & Liu, 2009], can be substituted into Eq. (3.61) to obtain the relationship between the damage-induced deflection and the change-in-flexibility matrix

$$\Delta \boldsymbol{x} = \Delta \boldsymbol{F}\ \boldsymbol{p} \tag{3.62}$$

In this way, the above-mentioned relationship is derived starting directly from the original formulation that was proposed in the work by [Koo et al., 2010] – Eq. (3.37). According to the proposed interpretation, the damage-induced deflection can thus be seen as the matrix product between the change-in-flexibility matrix and the inspection load vector.

This final part of the section presents an analytical representation that is alternative with respect to the formulation adopted in the work by [Koo et al., 2010] to calculate the modal flexibility-based interstory drifts and the damage-induced interstory drifts of shear building structures. In the work by [Koo et al., 2010], these operations are expressed using an index notation and by considering the interstory drifts of each story of the structure (Eqs. 3.25, 3.26). However, these operations can also be expressed using a vector representation, as described herein. This alternative formulation will be adopted in the damage detection approach that is proposed in Chapter 6.

According to the proposed representation, the modal flexibility-based interstory drifts of a shear building structure can be collected in a vector indicated as

$\boldsymbol{d}_{n\times 1}$. This vector can be obtained starting from the modal flexibility-based deflection $\boldsymbol{x}$ of the shear building structure using the following equation

$$\boldsymbol{d} = \boldsymbol{T}\,\boldsymbol{x} \tag{3.63}$$

where $\boldsymbol{T}_{\mathrm{n\times n}}$ is a transformation matrix defined as follows

$$\boldsymbol{T} = \begin{bmatrix} 1 & -1 & 0 & \cdots & 0 \\ 0 & 1 & -1 & \ddots & \vdots \\ \vdots & \ddots & \ddots & \ddots & 0 \\ \vdots & \ddots & \ddots & \ddots & -1 \\ 0 & \cdots & \cdots & 0 & 1 \end{bmatrix} \tag{3.64}$$

It is worth noting that in the vector $\boldsymbol{d}$ the modal flexibility-based interstory drifts are ordered from the top story of the building structure to the bottom story, and the matrix $\boldsymbol{T}$ was assembled accordingly. Eq. (3.63) can be considered as a matrix representation that is alternative with respect to Eq. (3.25), reported in the work by [Koo et al., 2010]. In the same way, the equivalent vector representation of Eq. (3.26), reported in the work by [Koo et al., 2010], is

$$\boldsymbol{\Delta d} = \boldsymbol{d_I} - \boldsymbol{d_B} \tag{3.65}$$

where the vector $\boldsymbol{\Delta d}$ can be considered as the vector of the damage-induced modal flexibility-based interstory drifts of the structure. By substituting Eq. (3.17) in Eq. (3.63) and then by substituting Eq. (3.63), evaluated both for the undamaged and for the possibly damaged structures, in Eq. (3.65), the vector of the damage-induced interstory drifts can be expressed as

$$\boldsymbol{\Delta d} = \boldsymbol{T}\,(\boldsymbol{F_I} - \boldsymbol{F_B})\,\boldsymbol{p} = \boldsymbol{T}\,\Delta\boldsymbol{F}\,\boldsymbol{p} \tag{3.66}$$

In this way, it is shown that the vector of the damage-induced modal flexibility-based interstory drifts of a shear building structure can be expressed as a function of the change-in-flexibility matrix $\Delta\boldsymbol{F}$. As already mentioned, these matrix representations (which do not substantially alter the original formulation of the PSIL method) will be adopted in the formulation of the damage detection approach that is proposed in Chapter 6.

Chapter 4

Truncation error analysis on modal flexibility-based deflections

This chapter presents the research investigations that were carried out on the topic of modal truncation error analysis by considering the truncation errors on the modal flexibility-based deflections[1]. As reported in the Section 1.3 of Chapter 1 where the objectives of the thesis are introduced, this problem represents the first main problem that was considered in the thesis (indicated as "problem no. 1").

At the beginning of the chapter in Section 4.1 (an introductory section), it is shown how the problem of modal truncation error analysis has been addressed in the literature (by considering the truncation errors both on modal flexibility matrices and on modal flexibility-based deflections due to a uniform inspection load). Then, in the first part of the chapter, an approach is proposed to have an indication of the truncation effects that are expected on the modal flexibility-based deflections of building structures calculated by applying a generic inspection load. As shown in detail in

[1] Some of the contents of this chapter are presented in a paper co-authored with Dr. Landi and Prof. Diotallevi that is published in the journal Engineering Structures.

Bernagozzi G, Landi L, Diotallevi PP. Truncation error analysis on modal flexibility-based deflections: application to mass regular and irregular structures. *Engineering Structures*, 2017; 142 (1): 192–210. DOI: 10.1016/j.engstruct.2017.03.057

Section 4.2 where this approach is presented, one of the main advantages of the proposed approach is that the prediction of the expected truncation effects is obtained using only the subset of the structural modes that are identified and included in the calculations of the truncated modal flexibility-based deflections. The validation of the proposed approach was carried out, as shown in Section 4.3, using both numerical simulations and experimental data of a steel frame structure that was tested under ambient vibrations.

In the second part of the chapter (i.e. in Section 4.4), inspection loads different from the uniform load were taken into account. Among the different loads that were considered, one load was selected and applied on flexibility-based models of building structures with the aim of reducing the truncation errors on the modal flexibility-based deflections.

4.1 Modal Truncation Error Analysis (TEA) in the literature

Truncation error analysis, according to [Zhang & Aktan, 1998], is the study of the errors that are introduced when the modal flexibility matrices or the modal flexibility-based deflections of a generic MDOF structure are evaluated using a limited number of structural modes, instead of all the modes. Referring to modal flexibility-based deflections, it is worth noting that the truncation error analyses presented in the work by [Zhang & Aktan, 1998] are focused on structural deflections calculated by applying to the structure a uniform load. This choice was presumably made because the truncation error studies performed by [Zhang & Aktan, 1998] were done in the framework of the uniform load surface method for vibration-based damage detection.

Truncation error analysis aims to investigate how many modes need to be included in the calculations in order to obtain good estimates of the modal flexibility matrices and the modal flexibility-based deflections derived from experimental data. This analysis is commonly adopted in pretest design using analytical or numerical models. In the context of an experimental or operational modal analysis, these studies can be used for example to determine the frequency range that has to be investigated during the vibration test. In this way by selecting the adequate frequency range that has to be tested, a subset of structural modes, predetermined using the truncation

analysis and that leads to negligible truncation errors on the modal flexibility matrices, should be theoretically identified from the vibration data. As reported in [Brincker & Ventura, 2015], in any procedure of operation modal analysis the frequency range that is investigated is related to the minimum and maximum frequencies that are measured. Selecting the maximum frequency is often the most challenging choice. In particular, the sampling frequency that is selected for acquiring the data is the parameter that is related, according to the Nyquist theorem, to the maximum frequency that can be investigated during the test. Of course, this choice of the maximum frequency to be measured in the test depends on the maximum natural frequency related to the structural modes that are of interest.

As indicated in the work by [Zhang & Aktan, 1998], there exist three main approaches that can be adopted to perform a truncation error analysis on modal flexibility matrices and modal flexibility-based deflections:

1) the first approach is to consider a number of modes such that the cumulative mass participation factor of the structure is higher than a selected threshold;
2) the second approach is to directly compare the components of the modal flexibility matrices assembled using a limited number of modes (i.e. the truncated matrices) with the components of the exact matrices;
3) the third approach is equal to the second approach, but the components of the uniform load deflections are considered instead of the components of the modal flexibility matrices.

In the work by [Zhang & Aktan, 1998] a series of analyses were performed using the second and the third approaches by considering a 10 DOF mass-spring model and a FEM model of a three-span bridge. As already mentioned in Chapter 3, the authors demonstrated that the components of the uniform load deflections are less sensitive to modal truncation errors than the components of the modal flexibility matrices. It is worth noting that the first approach proposed by [Zhang & Aktan, 1998] (i.e. the one based on the evaluation of the cumulative mass participation factor) was not applied in the numerical analyses presented by the authors.

Since the general objective that is pursued in this chapter is to study the truncation errors on the modal flexibility-based deflections, the first and the third

approaches proposed by [Zhang & Aktan, 1998] are analyzed in detail, while the second approach is not considered.

According to the first approach proposed by [Zhang & Aktan, 1998], the analysis of the truncation errors introduced on modal flexibility matrices and uniform load deflections (assembled using a limited number of modes equal to *r* with *r* < n) can be performed by evaluating the cumulative mass participation factor (MPF) of the structure $\mu_r = \sum_{i=1}^{r} \mu_{(i)}$ for the considered *r* modes. This cumulative mass participation factor can be then compared against a selected threshold (for example, a threshold value equal to 90%). It is worth noting that, according to the notation used in the other chapters of the thesis, *n* is the number of the DOFs of a generic MDOF structure and this parameter is also equal to the total number of the modes of the structure.

If a structure with a diagonal mass matrix and mass-normalized mode shapes are considered, the mass participation factor related to the *i*-th mode of the structure can be evaluated as

$$\mu_{(i)} = \frac{\Gamma_i^{\,2}}{\boldsymbol{\Gamma}^T \boldsymbol{\Gamma}} \tag{4.1}$$

where $\Gamma_i = \sum_{j=1}^{n} m_j \phi_{j,i}$ is the modal participation factor related to the *i*-th mode of the structure. In addition, in this case it is worth noting that the denominator of Eq. (4.1) is $\boldsymbol{\Gamma}^T \boldsymbol{\Gamma} = m_{tot} = \sum_{j=1}^{n} m_j$, where m_{tot} is the total mass of the structure and m_j is the mass related to the *j*-th DOF.

According to the third approach proposed by [Zhang & Aktan, 1998], the truncation error analysis on modal flexibility-based deflections can be performed by directly comparing the truncated components of such deflections with the true components assembled using all the structural modes. The relative error on the *j*-th displacement component of the modal flexibility-based deflection due to the uniform load and assembled using *r* modes can be evaluated as

$$\varepsilon_{x,u,r}^{j} = \frac{x_{u,r,j} - x_{u,n,j}}{x_{u,n,j}} \tag{4.2}$$

where, according to the formulation presented in Chapter 3, $x_{u,n,j}$ is the exact displacement computed from the static flexibility matrix $\boldsymbol{F_n}$ and $x_{u,r,j}$ is the truncated

displacement computed from the modal flexibility matrix $\boldsymbol{F_r}$. It is worth noting that there exists an important difference between the first and the third approaches for truncation error analysis. In the third approach the relative error is computed by comparing the truncated and the exact solutions, where the exact solution can be considered as the solution obtained using all the modes of the structure. On the contrary, the evaluation of the cumulative mass participation factor (according to the first approach) is performed by considering only the subset of structural modes included in the calculation of the truncated deflections, and thus in this truncation error approach having the knowledge of all the modes of the structure is not required.

As shown in next section, the approach for truncation error analysis presented in this thesis can be considered as an extension and a generalization of the first approach proposed by [Zhang & Aktan, 1998]. However, in the numerical and experimental truncation error analyses presented in this chapter, the third criterion proposed in the work by [Zhang & Aktan, 1998] was also be applied. Moreover, this third criterion was also developed further with the objective of defining criteria that are able to quantify the truncation errors expected on the whole modal flexibility-based deflections using a unique single parameter (i.e. a parameter that is related to the whole deflection and not to the single components of the deflection). To attain this objective, the root-mean-square (RMS) criterion can be applied to all the single-DOF truncation errors $\varepsilon_{x,u,r}^{j}$ as follows

$$\varepsilon_{x,u,r}^{RMS} = \sqrt{\frac{1}{n}\sum_{j=1}^{n} {\varepsilon_{x,u,r}^{j}}^{2}} \tag{4.3}$$

or, alternatively, the maximum of the single-DOF truncation errors on the modal flexibility-based deflection, in terms of absolute values, can be evaluated as

$$\varepsilon_{x,u,r}^{MAX} = \max\left|\varepsilon_{x,u,r}^{j}\right| \tag{4.4}$$

It is worth noting that the criteria expressed by Eqs. (4.2, 4.3, and 4.4) are adopted in the present chapter of the dissertation to evaluate the truncation errors on modal flexibility-based deflections that are calculated for loads with generic distributions. These criteria are not applied only on deflections due to uniform loads as done, on the contrary, in the work by [Zhang & Aktan, 1998].

4.2 Proposed approach for modal TEA using the Load Participation Factor

In this section an approach for truncation error analysis that is applicable on modal flexibility-based deflections of structural systems subjected to a generic load is presented. As shown in this section, this approach is based on the definition of a parameter that quantifies the relative contribution of each mode to the modal flexibility-based deflection. This proposed parameter is termed load participation factor (LPF).

The load participation factor is specifically developed for modal flexibility-based deflections that are evaluated for a generic load, since, differently from the mass participation factor, the proposed load participation factor depends not only on the mode shapes and the masses of the structure. The load participation factor depends also on the applied load. These considerations will be clarified by the analytical formulation presented in this section.

In any case, similarly to the mass participation factor, the proposed approach based on load participation factor does not imply a direct comparison between the truncated and the exact components of the modal flexibility-based deflections. To apply the two approaches (based, respectively, on the proposed load participation factor and on the mass participation factor proposed by [Zhang & Aktan, 1998]), in fact, only the knowledge of the subset of structural modes that are included in the truncated solution is required. Due to this important property of the proposed approach, and as will be clarified later in this chapter, the approach based on load participation factor was developed and can be used to obtain an a-priori indication of the truncation effects expected on the modal flexibility-based deflections.

The proposed approach based on load participation factor, which is valid for modal flexibility-based deflections due to a generic load, was investigated when the preliminary observation that follows was recognized. Let us consider the expression of each component of the uniform load deflection that was already presented in Chapter 3

$$x_{u,r,j} = \sum_{i=1}^{r} \frac{\phi_{j,i} \sum_{k=1}^{n} \phi_{k,i}}{\omega_i^2} = \sum_{i=1}^{r} \frac{\phi_{j,i}}{\omega_i^2} s_i \tag{4.5}$$

On the one side, in this equation each term related to the *i*-th mode depends on the modal contribution s_i, which, as already discussed in Chapter 3, is the summation of the components of the *i*-th mode shape (i.e. $s_i = \sum_{k=1}^{n} \phi_{k,i}$). On the other side, the truncation error approach based on the cumulative mass participation factor (i.e. the first approach proposed by [Zhang & Aktan, 1998]) involves the participation factor Γ_i, which is a term where both the structural masses and the mode shape components are included (i.e. $\Gamma_i = \sum_{j=1}^{n} m_j \phi_{j,i}$).

As already discussed in Chapter 3, the deflection $\boldsymbol{x_{p,r}}$ of a generic MDOF structure due to a generic load $\boldsymbol{p}$ can be determined starting from the modal flexibility matrix $\boldsymbol{F_r}$ assembled using *r* modes as follows

$$\boldsymbol{x_{p,r}} = \boldsymbol{F_r}\, \boldsymbol{p} \tag{4.6}$$

Before going further, it should be mentioned that the approach for truncation error analysis presented in this chapter was formulated with reference mainly to plane structures and by considering the modal flexibility-based deflections of these structures in one prevalent direction (which is the direction of the applied load). The *j*-th component of the deflection is expressed as

$$x_{p,r,j} = \sum_{i=1}^{r} \frac{\phi_{j,i}}{\omega_i^2} \left(\sum_{k=1}^{n} p_k\, \phi_{k,i} \right) = \sum_{i=1}^{r} \frac{\phi_{j,i}}{\omega_i^2} c_{p,i} \tag{4.7}$$

where the term $c_{p,i} = \sum_{k=1}^{n} p_k\, \phi_{k,i}$ is introduced. This term $c_{p,i}$ can be interpreted as the work done by the external load $\boldsymbol{p}$ for the modal displacements of the *i*-th mode shape $\boldsymbol{\phi_i}$. It is clear by comparing Eq. (4.7) with Eq. (4.5) that if, instead of a generic load $\boldsymbol{p}$, the uniform load $\boldsymbol{u} = [1 \;\; 1 \;\; ... \;\; 1]^T$ is considered, than the term $c_{p,i}$ becomes equal to s_i.

If one considers Eq. (4.6), it is evident that all the errors that affect the modal flexibility-based deflection are due to the presence of the truncated modal flexibility matrix $\boldsymbol{F_r}$, while no truncation errors are of course present in the load term $\boldsymbol{p}$. In light of this premise, a manipulation of Eq. (4.6) is performed, and this operation represents a fundamental step for the derivation of the proposed approach for truncation error analysis. In fact, the expression for computing the modal flexibility-based deflection

using *r* modes – i.e. Eq. (4.6) – can be reformulated by considering the static flexibility matrix $\boldsymbol{F_n}$ and an *r*-mode equivalent load $\boldsymbol{p_r}$ such that

$$\boldsymbol{x_{p,r}} = \boldsymbol{F_n}\,\boldsymbol{p_r} \tag{4.8}$$

In this way, all the truncation errors are included in the load $\boldsymbol{p_r}$ and not in the flexibility matrix, which in such case is the exact flexibility matrix. The *r*-mode equivalent load $\boldsymbol{p_r}$ is thus defined as the load that applied to the exact flexibility matrix $\boldsymbol{F_n}$ produces the truncated modal flexibility-based deflection $\boldsymbol{x_{p,r}}$. This is the same deflection that can be obtained using the truncated flexibility matrix $\boldsymbol{F_r}$ and the generic load $\boldsymbol{p}$. By comparing the terms on the right-hand side in Eqs. (4.6) and (4.8), the *r*-mode equivalent load can be obtained as follows

$$\boldsymbol{p_r} = \boldsymbol{F_n}^{-1}\boldsymbol{F_r}\,\boldsymbol{p} \tag{4.9}$$

At this point it is important to remember that the modal flexibility matrix is assembled using the contribution of each single mode $\boldsymbol{F_{(i)}}$ where $\boldsymbol{F_{(i)}} = \boldsymbol{\phi_i}\,\frac{1}{\omega_i^2}\,\boldsymbol{\phi_i^T}$. This means that the modal flexibility matrix can be expressed as $\boldsymbol{F_r} = \sum_{i=1}^{r}\boldsymbol{F_{(i)}}$.

By adopting the same approach, the *r*-mode equivalent load can be expressed as $\boldsymbol{p_r} = \sum_{i=1}^{r}\boldsymbol{p_{(i)}}$, where $\boldsymbol{p_{(i)}}$ is a single-mode equivalent load defined as

$$\boldsymbol{p_{(i)}} = \boldsymbol{F_n}^{-1}\boldsymbol{F_{(i)}}\,\boldsymbol{p} \tag{4.10}$$

The objective is then to simplify the expression of the single-mode equivalent load $\boldsymbol{p_{(i)}}$ in order to express this load as a function of the modal parameters of the structure. To perform this operation the fundamental equation that was presented in Chapter 3 and that can be used to assemble modal flexibility matrices starting from mass normalized mode shapes and natural frequencies of the structures is considered – i.e.

$$\boldsymbol{F_r} = \boldsymbol{\Phi_r}\,\boldsymbol{\Lambda_r^{-1}}\,\boldsymbol{\Phi_r^T} \tag{4.11}$$

Substituting Eq. (4.11) evaluated for *r*=*n* in place of $\boldsymbol{F_n}$ in Eq. (4.10) and substituting Eq. (4.11) evaluated for the *i*-th mode only – i.e. $\boldsymbol{F_{(i)}} = \boldsymbol{\phi_i}\,\frac{1}{\omega_i^2}\,\boldsymbol{\phi_i^T}$ – in Eq. (4.10), the single-mode equivalent load can be reformulated as follows

$$\boldsymbol{p_{(i)}} = \boldsymbol{\Phi_n^{-T}}\boldsymbol{\Lambda}\boldsymbol{\Phi_n^{-1}}\boldsymbol{\phi_i}\,\frac{1}{\omega_i^2}\,\boldsymbol{\phi_i^T}\,\boldsymbol{p} \tag{4.12}$$

Some of the matrix operations that are reported in Eq. (4.12) can be simplified as follows. First of all, due to the orthogonality relationships of the mode shapes with respect to the mass matrix – i.e. $\boldsymbol{\Phi_n^T M\ \Phi_n = I}$, where $\boldsymbol{M}_{\ n\times n}$ is the mass matrix and $\boldsymbol{I}_{\ n\times n}$ is the identity matrix – the following relationships are valid

$$\boldsymbol{\Phi_n^{-T} = M\Phi_n} \tag{4.13}$$

$$\boldsymbol{\Phi_n^{-1} = \Phi_n^T M} \tag{4.14}$$

These two equations are substituted in Eq. (4.12), which can be reformulated as

$$\boldsymbol{p_{(i)} = M\Phi_n\ \Lambda\ \Phi_n^T M\ \phi_i\ \frac{1}{\omega_i^2}\ \phi_i^T\ p} \tag{4.15}$$

Other operations can be performed in Eq. (4.15) to simplify the equation. Again, due to the orthogonality relationships of the mode shapes with respect to the mass matrix the following relationship is valid

$$\boldsymbol{\Phi_n^T M\ \phi_i = h_i} \tag{4.16}$$

where the $\boldsymbol{h_i}$ is a $n \times 1$ vector defined as

$$\boldsymbol{h_i} = \begin{bmatrix} 0 \\ \vdots \\ 0 \\ 1_i \\ 0 \\ \vdots \\ 0 \end{bmatrix} \tag{4.17}$$

The vector $\boldsymbol{h_i}$ is a vector with all zero except for a value equal to one at the position of the vector that is equal to i, where i is the mode index related to the single-mode equivalent load $\boldsymbol{p_{(i)}}$. By substituting Eq. (4.16) into Eq. (4.15), this last equation can be reformulated as

$$\boldsymbol{p_{(i)} = M\Phi_n\ \Lambda\ h_i \frac{1}{\omega_i^2}\ \phi_i^T\ p} \tag{4.18}$$

Then, by analyzing the term $\boldsymbol{\Lambda\ h_i \frac{1}{\omega_i^2}}$ included in Eq. (4.18), it can be recognized that for any value of the mode index i, the contribution to the single-mode equivalent load $\boldsymbol{p_{(i)}}$ of the natural frequencies of the structure is zero. This is because such natural frequencies cancel out, as evident in the following relationship

$$\boldsymbol{\Lambda}\, \boldsymbol{h_i} \frac{1}{\omega_i^2} = \boldsymbol{h_i} \tag{4.19}$$

By substituting Eq. (4.19) into Eq. (4.18) this last equation can be reformulated as

$$\boldsymbol{p_{(i)}} = \boldsymbol{M \Phi_n}\, \boldsymbol{h_i}\, \boldsymbol{\phi_i^T}\, \boldsymbol{p} \tag{4.20}$$

Then, by analyzing the term $\boldsymbol{\Phi_n}\, \boldsymbol{h_i}$ included in Eq. (4.20), another simplification can be performed – i.e.

$$\boldsymbol{\Phi_n}\, \boldsymbol{h_i} = \boldsymbol{\phi_i} \tag{4.21}$$

By substituting Eq. (4.21) into Eq. (4.20), this last equation can be finally reformulated as

$$\boldsymbol{p_{(i)}} = \boldsymbol{M}\, \boldsymbol{\phi_i}\, \boldsymbol{\phi_i^T}\, \boldsymbol{p} \tag{4.22}$$

The final result is that the single-mode equivalent load $\boldsymbol{p_{(i)}}$ is independent from the natural circular frequency ω_i, and it depends only on the mass matrix $\boldsymbol{M}$, the i-th mode shape $\boldsymbol{\phi_i}$, and the applied load $\boldsymbol{p}$.

By considering structures with a diagonal mass matrix and by introducing an index notation instead of a matrix formulation, each element of the modal load vector $\boldsymbol{p_{(i)}}$ is expressed as

$$p_{(i),j} = m_j \phi_{j,i} \left(\sum_{k=1}^{n} p_k\, \phi_{k,i} \right) = m_j \phi_{j,i} c_{p,i} \tag{4.23}$$

At this point, according to the proposed approach for truncation error analysis, it is of interest to quantify the contribution of each mode to the modal flexibility-based deflection due to a generic load. This operation is done using the single-mode equivalent load $\boldsymbol{p_{(i)}}$ and using an approach that is based on the same concept that is used traditionally in structural dynamics to obtain the mass participation factor of a generic mode of the structure.

According to the proposed approach, the contribution of each mode to the deflection is evaluated as the summation of all the components of the single-mode equivalent load $\boldsymbol{p_{(i)}}$, and then this summation is divided (i.e. normalized) by the summation of all the components of the applied load $\boldsymbol{p}$. Such contribution of each mode to the deflection is termed load participation factor (LPF). The load participation

factor (LPF) – i.e. the normalized modal contribution of each mode in the modal decomposition of the applied load $\boldsymbol{p}$ – is thus expressed as

$$\chi_{p,(i)} = \frac{p_{(i),TOT}}{p_{TOT}} = \frac{c_{p,i}\,\Gamma_i}{\boldsymbol{c_p^T}\,\boldsymbol{\Gamma}} \tag{4.24}$$

where $p_{TOT} = \sum_{j=1}^{n} p_j$ is the summation of all the components of the assumed load $\boldsymbol{p}$ and $p_{(i),TOT} = \sum_{j=1}^{n} p_{(i),j}$ is the summation of all the components of the single-mode equivalent load $\boldsymbol{p_{(i)}}$. Due to Eq. (4.23), this last term is also expressed as

$$p_{(i),TOT} = \sum_{j=1}^{n} m_j \phi_{j,i} c_{p,i} = c_{p,i} \sum_{j=1}^{n} m_j \phi_{j,i} = c_{p,i}\,\Gamma_i \tag{4.25}$$

Moreover, it can be demonstrated that the total load p_{TOT} – i.e. the sum of the components of the applied load $\boldsymbol{p}$ – is the scalar product between the vectors $\boldsymbol{c_p}$ and $\boldsymbol{\Gamma}$, which contain the terms $c_{p,i}$ and Γ_i respectively – i.e.

$$p_{TOT} = \boldsymbol{c_p^T}\,\boldsymbol{\Gamma} \tag{4.26}$$

The validity of Eq. (4.26) can be demonstrated as follows. First of all, let us analyze the two terms $\boldsymbol{c_p}$ and $\boldsymbol{\Gamma}$. The vector $\boldsymbol{c_p}$, which contains the scalar products between the load $\boldsymbol{p}$ and each mode shape, and the vector $\boldsymbol{\Gamma}$, which contains the modal participation factors, can be expressed as

$$\boldsymbol{c_p^T} = \boldsymbol{p^T \Phi_n} \tag{4.27}$$

$$\boldsymbol{\Gamma} = \boldsymbol{\Phi_n^T M\, I} \tag{4.28}$$

where $\boldsymbol{I}_{n\times 1}$ is a vector of all ones. Using Eqs. (4.27, 4.28), the scalar product between $\boldsymbol{c_p}$ and $\boldsymbol{\Gamma}$ can be thus expressed as

$$\boldsymbol{c_p^T\,\Gamma} = \boldsymbol{p^T \Phi_n\, \Phi_n^T M\, I} = \boldsymbol{p^T I} = p_{TOT} \tag{4.29}$$

where the expression $\boldsymbol{\Phi_n\, \Phi_n^T} = \boldsymbol{M^{-1}}$ is valid due to the fact that mass normalized mode shapes are considered. As evident in Eq. (4.29), the scalar product between the vectors $\boldsymbol{c_p}$ and $\boldsymbol{\Gamma}$ is thus equal to the total load.

By substituting Eqs. (4.25, 4.26) into Eq. (4.24), the load participation factor can be reformulated as follows

$$\chi_{p,(i)} = \frac{c_{p,i}\,\Gamma_i}{\boldsymbol{c_p^T}\,\boldsymbol{\Gamma}} \tag{4.30}$$

It is worth noting that this last formulation of the proposed load participation factor has a structure that is very similar with the respect to the structure of Eq. (4.1) which is used to calculate the mass participation factor.

As described in previous section, the mass participation factors of the single modes are cumulated in order to evaluate the cumulative mass participation factor. By adopting a similar concept, the cumulative load participation factor can be defined. This cumulative load participation factor is the contribution of the first *r* modes in the modal decomposition of the applied load $\boldsymbol{p}$ and is defined as

$$\chi_{p,r} = \frac{p_{r,TOT}}{p_{TOT}} = \sum_{i=1}^{r} \chi_{p,(i)} = \frac{\sum_{i=1}^{r} c_{p,i}\,\Gamma_i}{\boldsymbol{c_p}^T\,\boldsymbol{\Gamma}} \tag{4.31}$$

where $p_{r,TOT} = \sum_{j=1}^{n} p_{r,j} = \sum_{i=1}^{r} p_{(i),TOT}$ is the summation of all the components of the *r*-mode equivalent load $\boldsymbol{p_r}$.

Two important observations must be formulated on the proposed cumulative load participation factor. First of all, according to Eq. (4.8), implicit in the definition of the *r*-mode equivalent load is the concept that all the truncation errors are included in that load. For this reason, it is expected that the proposed cumulative LPF, evaluated for the first *r* modes and starting from the *r*-mode equivalent load, is also related to the contribution of such modes to the modal flexibility-based deflection. The second observation is that if all the modes are included when the cumulative load participation factor is determined (i.e. *r* = *n*), then the cumulative LPF becomes $\chi_{p,r} = 1$.

In light of this premise and according to the proposed approach, it is clear that the overall truncation error that occurs on the whole modal flexibility-based deflection (evaluated using the first *r* modes) can be related to the cumulative LPF of the modes (from *r+1* to *n*) that are not included in the calculation. This last contribution can be evaluated as follows

$$\bar{\chi}_{p,r} = 1 - \chi_{p,r} \tag{4.32}$$

which is an expression derived from the above-mentioned property related to the cumulative LPF evaluated for all the structural modes (i.e. $\chi_{p,n} = 1$ for *r* = *n*). It is important to underline that using such approach, the contribution of the missing modes

(from *r+1* to *n*) is determined using only the modes (from 1 to *r*) that are used to assemble the truncated deflection.

Two additional modifications of Eq. (4.32) have to be introduced to derive the final expression of the cumulative LPF that has to be used according to the proposed approach for truncation error analysis.

First of all, it is important to underline the following general principle that is valid for any problem where an approximated solution is considered instead of the exact one. If the missing contribution to a target solution is positive, the related truncation error is necessarily negative (and vice versa). Thus, according to the proposed approach the overall truncation error on the whole modal flexibility-based deflection can be related to the term $\chi_{p,r} - 1$, computed from Eq. (4.32) by changing the sign of $\bar{\chi}_{p,r}$.

Secondly, as already mentioned in this section, the objective of the proposed approach is to define a parameter that can be used to obtain an a-priori indication of the truncation effects expected on the whole modal flexibility-based deflections, when such deflections are evaluated using only the first *r* structural modes. As shown in Section 4.1 and if the target solution is known (i.e. the deflection obtained using all the modes is known), the calculation of such overall truncation error on the deflection can be done using the RMS criterion or by evaluating the maximum of the single-DOF truncation errors (in terms of absolute values), according to Eqs. (4.3) and (4.4). According to these criteria, the truncation errors on the deflection are quantities that are always positive. On the contrary, the term $\chi_{p,r} - 1$, derived using the approach presented in this section, can assume both positive and negative values. To obtain a parameter that quantifies the truncation errors on the deflections and that assumes values that are always positive, the above-mentioned term can be properly considered with the absolute value, i.e. $|\chi_{p,r} - 1|$.

4.2.1 Derivation of analytical expressions for TEA on modal flexibility-based deflections of shear building structures

In this section the problem of evaluating the truncation errors that affect the modal flexibility-based deflections is specifically addressed for shear building structures. In particular, analytical expressions that can be used to determine the modal truncation errors on the modal flexibility-based interstory drifts of shear building structures are presented. These analytical expressions are valid for a generic load applied to the shear building structure. It is worth noting that these types of structures have been already introduced in Chapter 3 where the Positive Shear Inspection Load (PSIL) method for vibration-based damage detection was presented.

The derivation of the above-mentioned analytical expressions was done by considering two different strategies for the evaluation of the modal flexibility-based interstory drifts of shear building structures. According to the first strategy, the formulation presented in previous section for the evaluation of modal flexibility-based deflections of a generic plane MDOF structure is specified for a shear building structure. According to the second strategy, the interstory drifts are derived starting from the dynamic characteristic equations of an undamped MDOF structural system, expressed in terms of the flexibility matrix, and taking advantage of the special topology of the flexibility matrix of a shear building structure.

The first strategy for the derivation of the modal flexibility-based interstory drifts is considered herein. Referring to an *n*-story building structure modeled as an *n*-DOF shear-type system, if $\boldsymbol{x_{p,r}}$ is the modal flexibility-based displacement profile due to a generic load $\boldsymbol{p}$ and computed using *r* modes, the vector of the interstory drifts $\boldsymbol{d_{p,r}}$ can be calculated, as already discussed in Chapter 3, as

$$d_{p,r,j} = \begin{cases} x_{p,r,j} - x_{p,r,j-1} & \text{for } j=2\ldots n \\ x_{p,r,j} & \text{for } j=1 \end{cases} \tag{4.33}$$

The expression of the modal flexibility-based displacement $x_{p,r,j}$ that, according to Eq. (4.7), was presented for a generic plane MDOF structure, is of course also valid for a shear building structure and can be modified using Eq. (4.33) to obtain the expression of the interstory drifts. In this way, the *j*-th modal flexibility-based interstory drift calculated using *r* modes is expressed as

$$d_{p,r,j} = \sum_{i=1}^{r} \frac{\Delta\phi_{j,i}}{\omega_i^2} \left(\sum_{k=1}^{n} p_k \, \phi_{k,i} \right) = \sum_{i=1}^{r} \frac{\Delta\phi_{j,i}}{\omega_i^2} c_{p,i} \tag{4.34}$$

where $\Delta\phi_{j,i}$ is defined as follows

$$\Delta\phi_{j,i} = \begin{cases} \phi_{j,i} - \phi_{j-1,i} & \text{for } j=2 \ldots n \\ \phi_{j,i} & \text{for } j=1 \end{cases} \tag{4.35}$$

An additional notation, which will be useful later in this section, is introduced in Eq. (4.34). Each term related to the *i*-th mode in the summation of Eq. (4.34) is indicated as $d_{p,(i),j}$ – i.e.

$$d_{p,(i),j} = \frac{\Delta\phi_{j,i}}{\omega_i^2} c_{p,i} \tag{4.36}$$

This last equation is the contribution of the single *i*-th mode to the modal flexibility-based interstory drift of the *j*-th story.

Then, the second strategy for the derivation of the interstory drifts of shear building structures is considered. As already mentioned, this second approach starts from the dynamic characteristic equations of an undamped MDOF structural system, expressed in terms of the flexibility matrix, and takes advantage of the special structure of the flexibility matrix for a shear building structure. Before proceeding with the description of the analytical formulation, it is worth noting that this formulation is basically the dual of the formulation that was presented in the work by [Wang et al., 2007]. This work, where the problem was formulated with reference to the dynamic characteristic equations of an undamped MDOF structural system expressed in terms of the stiffness matrix, was the starting point for the development of the formulation presented in this section.

The dynamic characteristic equations of an undamped MDOF structural system, which in the first section of Chapter 3 was expressed in terms of the stiffness and the mass matrices, is here reformulated using the flexibility matrix $\boldsymbol{F}$ and the mass matrix $\boldsymbol{M}$. These equations are expressed as

$$\boldsymbol{F}\,\boldsymbol{M}\,\boldsymbol{\phi_i} = \frac{1}{\omega_i^2}\,\boldsymbol{\phi_i} \tag{4.37}$$

By considering the flexibility matrix of a plane shear building model, as already defined in Chapter 3 and in which the *j*-th interstory flexibility is f_j, and by considering a diagonal mass matrix, Eq. (4.37) can be specified as follows

$$\begin{bmatrix} f_n+\cdots+f_j+\cdots+f_1 & \cdots & f_j+\cdots+f_1 & \vdots & f_1 \\ \cdots & \ddots & \vdots & \vdots & f_1 \\ f_j+\cdots+f_1 & \cdots & f_j+\cdots+f_1 & \vdots & f_1 \\ \cdots & \cdots & \cdots & \ddots & f_1 \\ f_1 & f_1 & f_1 & f_1 & f_1 \end{bmatrix} \begin{bmatrix} m_n & 0 & \cdots & \cdots & 0 \\ 0 & \ddots & 0 & \ddots & \vdots \\ \vdots & 0 & m_j & 0 & \vdots \\ \vdots & \ddots & 0 & \ddots & 0 \\ 0 & \cdots & \cdots & 0 & m_1 \end{bmatrix} \begin{pmatrix} \phi_{n,i} \\ \vdots \\ \phi_{j,i} \\ \vdots \\ \phi_{1,i} \end{pmatrix} = \frac{1}{\omega_i^2} \begin{pmatrix} \phi_{n,i} \\ \vdots \\ \phi_{j,i} \\ \vdots \\ \phi_{1,i} \end{pmatrix} \quad (4.38)$$

Due to the special structure of the flexibility matrix for a shear building structure, the flexibility coefficients can be expressed in terms of the modal parameters and the structural masses. As evident in Eq. (4.38), in fact, the last row of the flexibility matrix of a shear building contains only the coefficient f_1, which is the flexibility coefficient of the first story of the shear building. This means that the coefficient f_1 can be derived directly from the last equation of the above-mentioned system of equations, as follows

$$f_1^{(i)} = \frac{\phi_{1,i}}{\omega_i^2} \frac{1}{\sum_{k=1}^{n} m_k \, \phi_{k,i}} \quad (4.39)$$

Moreover, as also evident in Eq. (4.38), there is another important characteristic of the matrix $\boldsymbol{F}$ that must be considered and that derives directly from the special topology of the flexibility matrix for a shear building structure. In this matrix, each j-th row contains all the flexibility coefficients that are present in the (j-1)-th row (i.e. the coefficients $f_1 \ \ldots \ f_{j-1}$ present in the row just below the j-th row) plus the coefficient f_j. This means that starting from the expression of the coefficient f_1 (Eq. 4.39) all the other flexibility coefficients for $j = 2 \ \ldots \ n$ can be derived as follows

$$f_j^{(i)} = \frac{\phi_{j,i} - \phi_{j-1,i}}{\omega_i^2} \frac{1}{\sum_{k=j}^{n} m_k \, \phi_{k,i}} \quad (4.40)$$

The j-th flexibility coefficient of a shear building structure can thus be expressed in terms of the modal parameters of the i-th mode only and the structural masses as

$$f_j^{(i)} = \frac{\Delta\phi_{j,i}}{\omega_i^2} \frac{1}{\sum_{k=j}^{n} m_k \, \phi_{k,i}} \quad (4.41)$$

where $\Delta\phi_{j,i}$ is defined according to Eq. (4.35). The formulation expressed by Eq. (4.41) is valid using the modal parameters of any mode i and for any normalization of the mode shape. The notation with the superscript (i) adopted in Eqs. (4.39, 4.40, 4.41) indicates that the exact flexibility coefficient $f_j^{(i)}$ is expressed in terms of the i-th mode only. Here the term "exact" is introduced to indicate that this quantity is not

affected by modal truncation errors, even if the calculations are performed using only one structural mode[2].

To derive the interstory drifts using the second strategy, as mentioned in previous paragraphs, it is important to remember that the *j*-th interstory drift of a shear building structure due to the application of a generic load $\boldsymbol{p}$ can be evaluated as

$$d_{p,j} = f_j \, V_j \tag{4.42}$$

where V_j is the external shear-force at the *j*-th interstory and f_j is the static flexibility coefficient of the *j*-th interstory. If Eq. (4.41) is substituted into Eq. (4.42), the *j*-th interstory drift can be evaluated as

$$d_{p,j}^{(i)} = f_j^{(i)} \, V_j = \frac{\Delta\phi_{j,i}}{\omega_i^2} \frac{V_j}{\sum_{k=j}^{n} m_k \, \phi_{k,i}} = \frac{\Delta\phi_{j,i}}{\omega_i^2} \frac{V_j}{g_i^{j,UP}} \tag{4.43}$$

where again the notation with the superscript (*i*) is introduced to indicate that the interstory drift is exact (i.e. non- truncated) and expressed as a function of the *i*-th mode only. It is worth noting that the term $g_i^{j,UP} = \sum_{k=j}^{n} m_k \, \phi_{k,i}$ is also introduced in Eq. (4.43) to simply the notation in the equation. This term is defined as the portion of the participation factor Γ_i extended only to the DOFs of the shear building structure that are above the selected *j*-th story.

Two different strategies have been described so far to evaluate the modal flexibility-based interstory drifts of shear building structures. In the first strategy modal flexibility matrices were assembled using a number of modes equal to *r*, and the interstory drifts related to the modal flexibility-based deflections were evaluated. This strategy provides a solution that is a truncated solution and depends on the number of the considered modes. The second strategy takes advantage of the topology

[2] A general observation must be made on the approach discussed in the text to obtain the flexibility coefficients of shear building structures (i.e. the approach expressed by Eq. 4.41). This approach is used in this section to derive the analytical expressions for evaluating the truncation errors on the modal flexibility-based interstory drifts of shear building structures. This approach, however, is not used in the thesis to estimate, starting from vibration data, the flexibility coefficients (or flexibility matrices) of building structures, because implicit in the above-mentioned approach is the operation of forcing the flexibility matrix to have the topology of the matrix related to a shear-type system. In the thesis the estimation, starting from vibration data, of flexibility matrices of building structures is performed using the formulation valid for any type of structural system (see Section 3.1), which is the same approach adopted in the Uniform Load Surface method [Zhang & Aktan, 1998] and in the Positive Shear Inspection Load method [Koo et al., 2010].

of the flexibility matrix for shear building structures, and an exact solution (which is not affected by modal truncation errors) is obtained for the interstory drifts (which are expressed as a function of the modal parameters of one structural mode).

The basic idea used to derive analytical expressions that can be adopted for the evaluation of the modal truncation errors that affect the modal flexibility-based interstory drifts of shear buildings is to compare the two above-mentioned solutions (i.e. the truncated and the exact solutions). The derivation of such analytical expressions was done as follows. At first, the contributions of the different modes to the modal flexibility-based interstory drifts of the shear building structure were derived. Then, the analytical expression for evaluating the related truncation errors was determined.

The relative contribution $\alpha^{j}_{d,p,(i)}$ of the i-th mode in the estimation of the j-th modal flexibility-based interstory drift is the ratio between the truncated solution $d_{p,(i),j}$ computed using the i-th mode (Eq. 4.36) and the exact solution $d^{(i)}_{p,j}$ expressed in terms of the i-th mode only (Eq. 4.43)

$$\alpha^{j}_{d,p,(i)} = \frac{d_{p,(i),j}}{d^{(i)}_{p,j}} = \frac{\frac{\Delta\phi_{j,i}}{\omega_i^2} c_{p,i}}{\frac{\Delta\phi_{j,i}}{\omega_i^2}\frac{V_j}{g_i^{j,UP}}} = \frac{c_{p,i}\, g_i^{j,UP}}{V_j} \tag{4.44}$$

As evident in Eq. (4.44), the terms $\Delta\phi_{j,i}$ and ω_i^2 are present both in the truncated solution $d_{p,(i),j}$ and in the exact solution $d^{(i)}_{p,j}$. This means that these terms present both at the numerator and at the denominator of Eq. (4.44) cancel out.

Instead of considering the contribution of a single mode to the j-th modal flexibility-based interstory drift, the relative contribution of the first r modes can be expressed as

$$\alpha^{j}_{d,p,r} = \sum_{i=1}^{r} \alpha^{j}_{d,p,(i)} = \frac{\sum_{i=1}^{r} c_{p,i}\, g_i^{j,UP}}{V_j} \tag{4.45}$$

which is the sum from 1 to r of the contribution of the single modes $\alpha^{j}_{d,p,(i)}$.

As already discussed in previous section, where the approach valid for a generic MDOF structure was presented, if all the modes are included in the evaluation

of the *j*-th modal flexibility based interstory drift (i.e. $r = n$), the exact solution is derived. This means that the relative contribution of these n modes is $\alpha_{d,p,n}^{j} = 1$. Using this last property, if the first r modes are known, the relative contribution to the *j*-th interstory drift of the missing (n - r) modes, which is indicated as $\bar{\alpha}_{d,p,r}^{j}$, can be computed as $\bar{\alpha}_{d,p,r}^{j} = 1 - \alpha_{d,p,r}^{j}$.

At this point it is important to introduce the general principle already discussed in previous section with reference to any problem where an approximated solution is considered (instead of the exact one). This principle is as follows: if the missing contribution to a target solution is positive, the related truncation error is necessarily negative (and vice versa). Due to this general principle, the truncation error $\varepsilon_{d,p,r}^{j}$ on the *j*-th modal flexibility-based interstory drift can be evaluated by changing the sign of $\bar{\alpha}_{d,p,r}^{j}$, which is the expression of the relative contribution to the drift of the missing (n - r) modes. The analytical expression that can be used to calculate the modal truncation error that affects the *j*-th modal flexibility-based interstory drift of a shear building subjected to a generic load is thus

$$\varepsilon_{d,p,r}^{j} = \alpha_{d,p,r}^{j} - 1 = \frac{\sum_{i=1}^{r} c_{p,i}\, g_i^{j,UP}}{V_j} - 1 \tag{4.46}$$

The analysis of this expression (for the evaluation of the truncation errors) when applied to the first (i.e. the lower) story of a shear building structure is a special case that deserves further investigations. In particular, two observations can be formulated about the formula expressed by Eq. (4.46) when applied for j=1 (i.e. when is applied to evaluate the truncation error that affects the first interstory drift of the structure). It is worth noting that, of course, for a building structure the interstory drift of the first story is equal to the absolute displacement of the first story, and thus the following observations are also valid for the first DOF displacement.

Firstly, the term $g_i^{j,UP} = \sum_{k=j}^{n} m_k\, \phi_{k,i}$ present in Eq. (4.46) evaluated for j=1 ($g_i^{1,UP}$) is equal to the participation factor Γ_i. Secondly, the story shear induced by the external load vector $\boldsymbol{p}$ at the first story of the shear building structure is equal to the sum of all the loads applied at each story of the structure. This implies that $V_1 = p_{TOT} = \boldsymbol{c}_{\boldsymbol{p}}^{T}\, \boldsymbol{\Gamma}$, according to Eq. (4.26).

Starting from these two observations and as shown in the following, a relationship was found between the analytical expression in Eq. (4.46) evaluated for the special case of the first interstory drift (or first DOF displacement) of the shear building and the approach based on the load participation factor presented in previous section (and derived starting from the expression of the modal flexibility-based deflections of a generic MDOF structure). In fact, the relative contribution $\alpha^1_{d,p,(i)}$ of the *i*-th mode to the first interstory drift of a shear building structure is equal to the proposed load participation factor $\chi_{p,(i)}$ (Eq. 4.24). Similarly, the contribution of the first *r* modes $\alpha^1_{d,p,r}$ to the same interstory drift is equal to the cumulative load participation factor $\chi_{p,r}$ (Eq. 4.31). This is clear if Eq. (4.45) is evaluated for *j*=1 and by considering that, according to the two above-mentioned observations, the term $g_i^{1,UP} = \Gamma_i$ and the term $V_1 = p_{TOT} = \boldsymbol{c_p^T}\,\boldsymbol{\Gamma}$.

For these reasons and due to Eq. (4.46), the truncation error on the first MF-based interstory drift (evaluated using *r* modes) of a shear building structure can be expressed as

$$\varepsilon^1_{d,p,r} = \alpha^1_{d,p,r} - 1 = \chi_{p,r} - 1 \tag{4.47}$$

This truncation error $\varepsilon^1_{d,p,r}$, which is of course equal to the error $\varepsilon^1_{x,p,r}$ related to the first DOF displacement of the structure, is thus explicitly related to the cumulative load participation factor of the modes that are not included in the calculation. Finally, if the error evaluated using Eq. (4.47) is considered in terms of the absolute value, then the same parameter that was obtained at the end of previous section is derived – i.e. $\left|\chi_{p,r} - 1\right|$.

The findings of this section can thus be summarized as follows. At first, the analytical expression for evaluating the truncation errors on the interstory drifts computed from modal flexibility-based deflections due to a generic load applied to shear building structures was derived. Then, for the special case of the displacement related to the first DOF (i.e. the lowest one) of shear building structures the same expression for truncation error analysis that was proposed according to the approach presented in previous section was analytically derived. The approach presented in

previous section was derived, on the contrary, starting from the expression of the modal flexibility-based deflections of a generic MDOF structure.

One important observation must be made referring to the displacement of the first DOF of a shear building structure. If the modal flexibility-based deflection of the shear building structure is evaluated, for example, for a generic positive shear inspection load (as defined in Chapter 3 in the section that presents the PSIL method for damage detection), the displacement of the first DOF is, in general, the lowest one among the displacements of all the DOFs. For this reason and as shown by the numerical and experimental analyses presented in the next sections of this chapter, the modal truncation effects have a significant impact on the displacement of this DOF.

4.3 Verification of the proposed approach for TEA based on Load Participation Factor

This section presents the numerical and experimental analyses that were carried out to verify the approach for truncation error analysis based on the evaluation of the Load Participation Factor (LPF) and proposed in Section 4.2 of the present chapter.

The strategy adopted for the verification of the proposed approach is the following. On one side, the load participation factors $\chi_{p,r}$ are calculated, according to Eq. (4.31), for the structural modes that are included in the computation of the truncated modal flexibility-based deflections, and then the terms $|\chi_{p,r} - 1|$ are considered as a-priori indications of the truncation effects expected on such deflections. On the other side, the percent truncation errors on the modally truncated deflections are calculated using the third approach proposed in the work by [Zhang & Aktan, 1998] (Eq. 4.2) and the related criteria proposed in Section 4.1 for the evaluation of the overall truncation error that affect the whole deflection (i.e. the criteria based on the calculation of the RMS error and the maximum error - Eqs. 4.3,4.4). It is worth noting that, as already mentioned, these last approaches (i.e. Eqs. 4.2,4.3,4.4) are based on a comparison between the truncated and the non-truncated deflections. For this reason, the truncation errors calculated using such approaches

represent reference solutions that are used for the verification of the proposed approach based on load participation factor.

The analyses were performed on modal flexibility-based deflections calculated both using numerical simulations on structural models and for an experimental vibration test. In the first case, the analyses were performed on discrete models of plane frame building structures, which can be reduced to systems of lumped masses and springs. In the second case, a steel frame structure tested under ambient vibrations was considered. This structure and the related vibration data are benchmark studies for SHM and damage detection, which, as already mentioned in Chapter 1, are known in the literature as IASC-ASCE benchmark studies [Dyke et al., 2003; Ventura et al., 2003; Dyke, 2011].

4.3.1 Numerical verification of the LPF-based approach

A six-story reinforced concrete (RC) plane frame building modeled as a shear building structure (Fig. 4.1) was considered in the numerical analyses performed to verify the approach for truncation error study based on the LPF. This frame is constituted by three spans, and four columns with a rectangular section of 0.5×0.5 m are located at each story. The elastic modulus of the concrete is E = 3×10^{10} N/m^2. The beams of the structure are supposed to be infinitely stiff in comparison to the columns, and the stiffness of each story is equal to k_j=2.29×10^5 kN/m for j=1 … n with n =6. The stiffness matrix of the structure is as follows

$$\boldsymbol{K} = \begin{bmatrix} k_6 & -k_6 & 0 & \cdots & \cdots & 0 \\ -k_6 & k_6+k_5 & -k_5 & \ddots & & \vdots \\ 0 & -k_5 & k_5+k_4 & -k_4 & \ddots & \vdots \\ \vdots & \ddots & -k_4 & k_4+k_3 & -k_3 & 0 \\ \vdots & & \ddots & -k_3 & k_3+k_2 & -k_2 \\ 0 & \cdots & \cdots & 0 & -k_2 & k_2+k_1 \end{bmatrix} \tag{4.48}$$

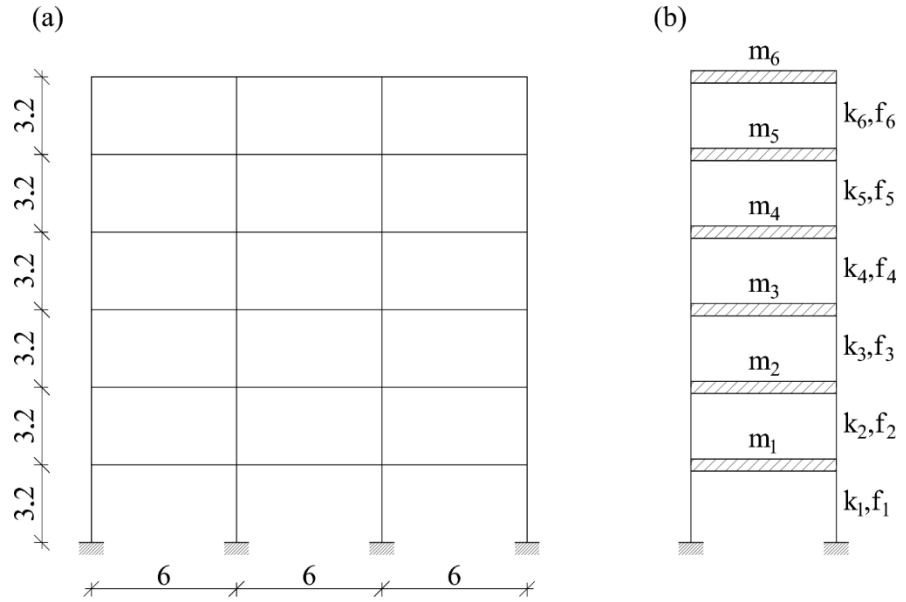

Figure 4.1. Six-story plane frame building (dimensions in m) (a) and shear building model (b) [Bernagozzi et al., 2017a].

Parametric studies were conducted on undamped models of the shear building structure to consider several structural configurations characterized by different distributions of both the structural masses and the loads applied for the evaluation of the modal flexibility-based deflections. The reason for choosing these parameters as variables in the parametric studies is that, as shown in Eq. (4.24), the proposed load participation factor depends both on the masses and on the loads.

The strategy adopted to perform the parametric studies on the shear building structure is based on Monte Carlo simulations. As reported in Fig. 4.2a, the mass of the *j*-th story of the shear building structure is equal to $m_j = \delta_j \, m_{ref}$ where m_{ref} = 100 kN s^2/m, and the generic force applied at each DOF to compute the deflection is $p_j = \beta_j \, p_{ref}$ where p_{ref} = 100 kN. The mass matrix of the structure and the applied loads are thus defined as follows

$$\boldsymbol{M} = \begin{bmatrix} \delta_6 \, m_{ref} & 0 & \cdots & \cdots & \cdots & 0 \\ 0 & \delta_5 \, m_{ref} & \ddots & & & \vdots \\ \vdots & \ddots & \delta_4 \, m_{ref} & \ddots & & \vdots \\ \vdots & & \ddots & \delta_3 \, m_{ref} & \ddots & \vdots \\ \vdots & & & \ddots & \delta_2 \, m_{ref} & 0 \\ 0 & \cdots & \cdots & \cdots & 0 & \delta_1 \, m_{ref} \end{bmatrix} \tag{4.49}$$

$$\boldsymbol{p} = \begin{bmatrix} \beta_6 p_{ref} & \beta_5 p_{ref} & \beta_4 p_{ref} & \beta_3 p_{ref} & \beta_2 p_{ref} & \beta_1 p_{ref} \end{bmatrix}^T \tag{4.50}$$

In the Monte Carlo simulation both the coefficients δ_j, which are the story mass ratios, and the coefficients β_j, which are the single-DOF load ratios, are considered as random variables. For each run of the simulation, these parameters are generated using the pseudo-random integer generator (i.e. using the Matlab command "randi" [MATLAB]), and they are uniformly distributed in the range from 1 to 5.

Two observations must be made on the distributions of the loads and the structural masses considered in the simulation. First of all, referring to the loads, it is worth mentioning that all the random loads generated in the Monte Carlo simulation are loads that induce positive shear forces at all the stories of the shear building structure. In fact, the values of the loads are always positive, and they were applied only in one direction, as evident in Fig. 4.2a. This basically means that all the story shears have the same sign. As already defined in Chapter 3, where the PSIL method for damage detection [Koo et al., 2010] was presented, the loads adopted in the Monte Carlo simulation presented herein can be considered as Positive Shear Inspection Loads (PSIL). In the work by [Koo et al., 2010], the authors suggest using a uniform load as the positive shear inspection load. However, the objective of the present chapter, where the damage detection is not directly involved, is to verify the proposed approach for truncation error study based on LPF, thus random distributions of these positive shear inspection loads were considered. Loads that are not PSIL loads were not considered in the analyses since such loads are not usually considered in the procedures of vibration-based condition assessment and damage detection for building structures.

Referring to the structural masses of the shear building model and as already mentioned, the random distributions of the masses are characterized by story mass ratios that are in the range from 1 to 5. Such distributions correspond in some cases to realistic situations, in other cases to more rare structural configurations. In any case, such distributions were considered in the truncation error study to have a complete insight of the tendencies of the results.

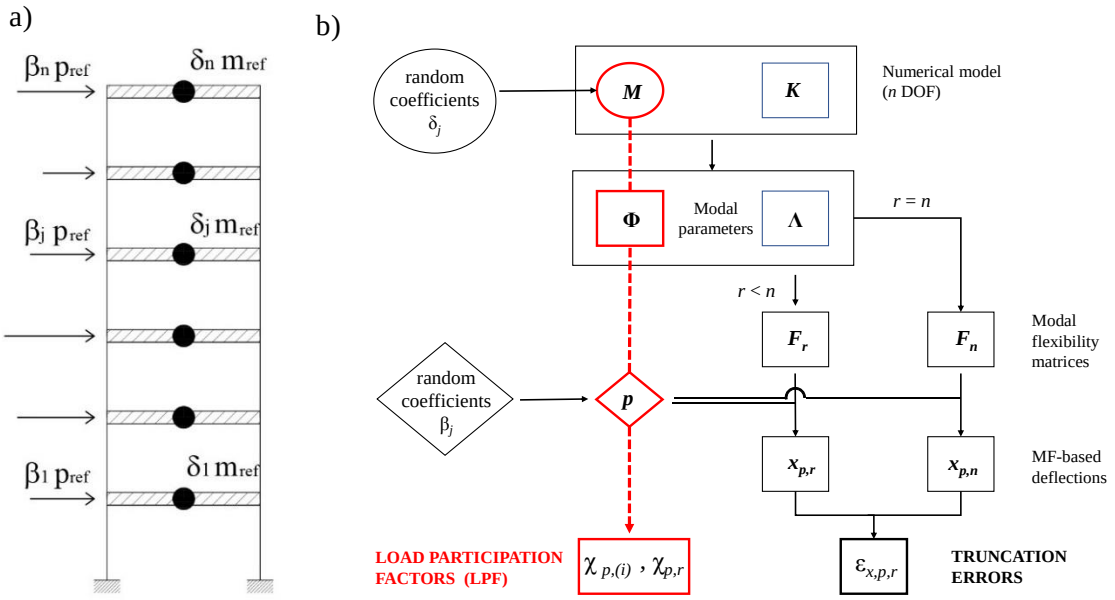

Figure 4.2. Numerical simulation on a shear building structure: random variables considered in the Monte Carlo simulation (a) flow chart of the analysis (b) [Bernagozzi et al., 2017a]

The calculations performed in each run of the Monte Carlo simulation are outlined in the flow chart reported in Fig. 4.2b, and these calculations can be summarized according to the following steps. In the first step, the mass matrix of the structure is assembled using the coefficients δ_j generated using the pseudo-random integer generator. This mass matrix $\boldsymbol{M}$ and the stiffness matrix $\boldsymbol{K}$ (this last matrix is fixed in all the simulations) form the undamped model of the shear building. In the second step, an eigenvector analysis is performed on this undamped $\boldsymbol{M}$ $\boldsymbol{K}$ numerical model of the structure to compute natural frequencies and mode shapes (such mode shapes are then normalized using the mass matrix of the structure). In the third step, one PSIL load $\boldsymbol{p}$ with a distribution defined by the random coefficients β_j is generated. At this point, as reported in Fig. 4.2b, the calculations follow two different paths. On one side, the load participation factors of the different modes (for $i = 1 \ldots r$) and the cumulative LPF of the first r modes are calculated using Eqs. (4.24) and (4.31), respectively. This is the red path highlighted in Fig. 4.2b, and it is worth mentioning, again, that to perform this operation only the subset of r modes (with $r < n$) is considered. On the other side, as shown in Fig. 4.2b, the modal flexibility matrix is assembled using r modes and the truncated MF-based deflection is calculated by applying the load $\boldsymbol{p}$. The displacements of this truncated deflection are compared with

the true displacements of the exact deflection obtained for $r = n$. The truncation errors at each DOF are calculated using Eq. (4.2) and the overall truncation errors are calculated using Eqs. (4.3,4.4). In each run of the Monte Carlo simulation, to have a complete insight of the tendencies of the results, the calculations are performed considering all the possible subsets of structural modes to be included in the computation of the truncated deflection. This means that the parameter r assumes all the values from 1 to n - 1. Of course, the case $r = n$ is not considered in the Monte Carlo simulation since in such case there are no truncation errors.

An example of the modal flexibility-based deflections calculated by applying a load vector $\boldsymbol{\beta}\, p_{ref}$ - where $\boldsymbol{\beta} = [\ 1\ 3\ 1\ 3\ 1\ 1]^T$ - to the shear building structure characterized by a mass distribution $\boldsymbol{\delta}\, m_{ref}$ - where $\boldsymbol{\delta} = [3\ 1\ 3\ 1\ 1\ 1]^T$ - is shown in Fig. 4.3a. Each deflection is calculated for a different subset of included modes (for $r = 1 \ldots n$). It is evident that, as expected, the displacement profile obtained for r=1 shows the major discrepancies with respect to the true deflection obtained for r=6. As shown in Fig. 4.3b and especially for r=1 and r=2, the maximum values of the percent truncation errors, in terms of absolute values, occur at the first DOF of the structure (j=1). As already mentioned in previous section, the first DOF of a shear building structure is the one that is affected in general by significant truncation effects on the modal flexibility-based deflection due to a positive shear inspection load. As also shown in Fig. 4.3b, if higher modes are included (e.g. for $r \geq 3$), the truncation errors along the height of the building are almost of the same order.

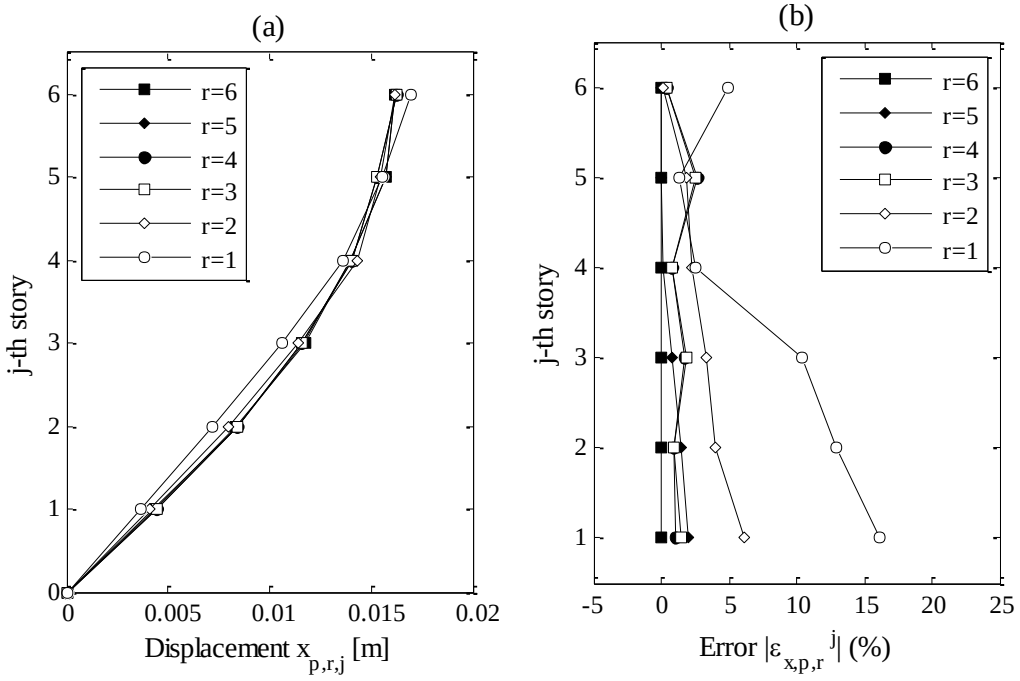

Figure 4.3. MF-based deflections of the shear building structure with a generic distribution of the masses and for a generic load: (a) displacements;
(b) truncation errors [Bernagozzi et al., 2017a].

The Monte Carlo method was applied by performing 500 runs of the procedure outlined in Fig. 4.2b. At the end of all the simulations, the cumulative load participation factors (which represent the prediction of the truncation effects) and the truncation errors (which represent the reference solutions) were compared by means of correlation analysis. This analysis was performed by calculating the correlation coefficient and by evaluating the linear regression between the two different data sets that are compared. According to the first approach for truncation error analysis mentioned in the work by [Zhang & Aktan, 1998] and in addition to the calculations reported in Fig. 4.2b, the cumulative mass participation factors μ_r were also determined and compared with respect to the truncation errors.

The results of the correlation analysis performed at the end of the Monte Carlo simulation are presented in Fig. 4.4 for the case r=1 - i.e. when only the first mode is considered in the calculation of the truncated deflections. Results obtained for all the subsets of modes included in the calculations (i.e. for $r = 1 \dots n$) will be discussed later in this section. In particular, in the scatter plots on the left-hand side of Fig. 4.4 the truncation errors and the terms $|\chi_{p,r} - 1|$ (i.e. the cumulative load participation factors of the modes not included in the calculation of the truncated deflections, derived from the LPFs of the included modes) are reported on the y-axis and the x-axis, respectively. On the contrary, the factors $|\mu_r - 1|$ (i.e. the cumulative mass participation factors of the modes not included in the calculations of the truncated deflections) are compared with the truncation errors in the scatter plots on the right-hand side of Fig. 4.4. It is worth noting that Figs. 4.4a, 4.4b, Figs. 4.4c, 4.4d, and Figs. 4.4e, 4.4f refer to the first DOF errors, the maximum errors, and the root-mean-square errors, respectively (which are evaluated using Eqs. 4.2, 4.3 and 4.4, respectively).

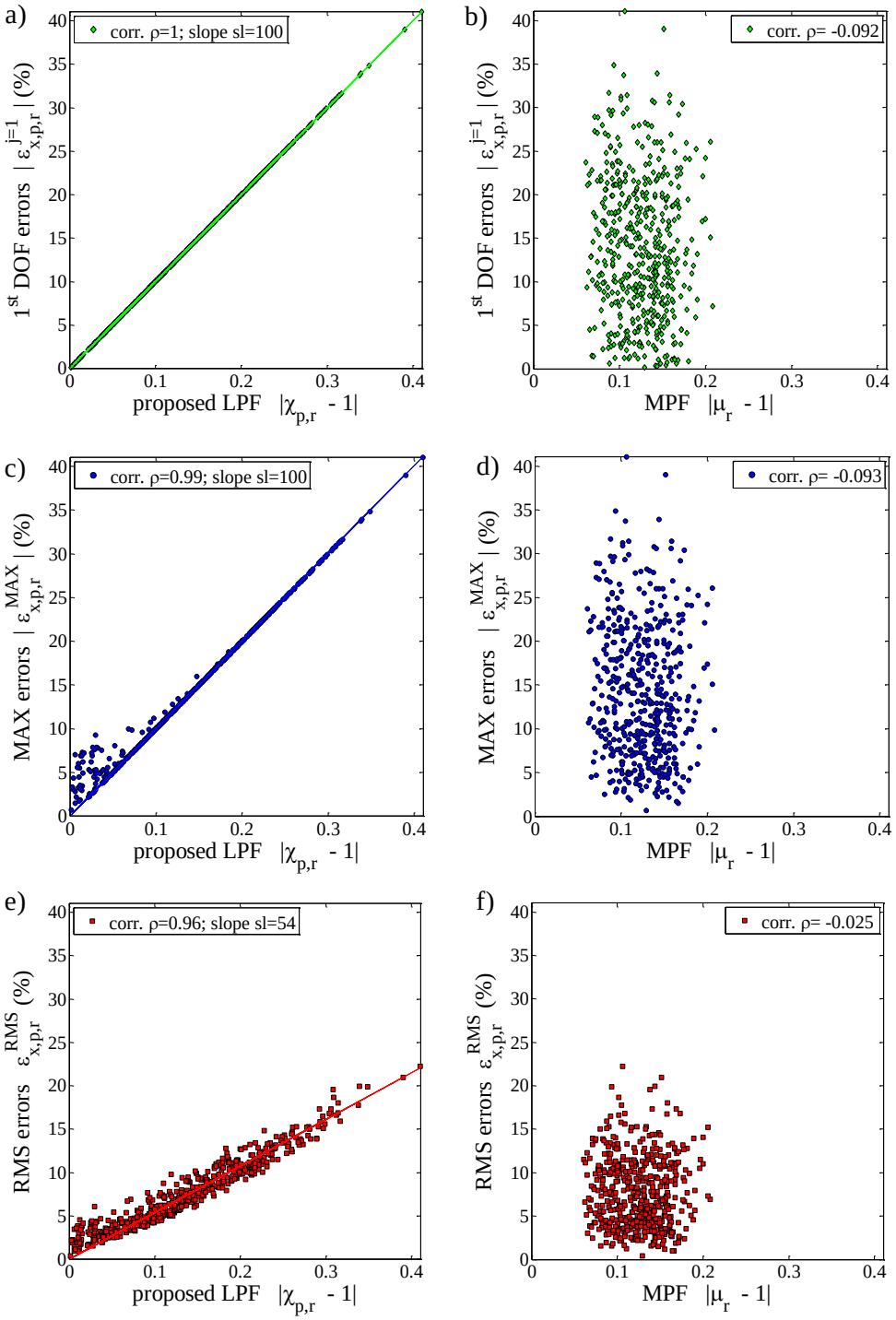

Figure 4.4. Correlation analysis on the truncation errors of the shear building structure for *r* = 1: correlation with the proposed Load Participation Factor (a, c, e); correlation with the Mass Participation Factor (b, d, f) [Bernagozzi et al., 2017a]

First of all, an important observation must be made on the results presented in Fig. 4.4. Referring to the load participation factors and as shown in Figs 4.4a, 4.4c, and 4.4e, very high values of the correlation coefficients ρ were found between the cumulative LPFs of the modes not included in the calculations (i.e. the terms $|\chi_{p,r} - 1|$) and the truncation errors. On the contrary, as evident in Figs 4.4b, 4.4d, and 4.4f, referring to the mass participation factors and for the considered structural cases characterized by random distributions of both the masses and the applied loads, there is no correlation between the cumulative mass participation factors of the modes not included in the calculations (i.e. the terms $|\mu_r - 1|$) and the truncation errors. The correlation coefficients reported in Figs 4.4b, 4.4d, and 4.4f are, in fact, very close to zero.

Referring to the load participation factors, the following observations can be made on the results presented on the left-hand side of Fig. 4.4, where the LPFs are compared with the truncation errors evaluated using different criteria (i.e. first DOF errors, the maximum errors, and the root-mean-square errors).

As evident in Fig. 4.4a, there is an exact relationship between the truncation errors related to the first DOF displacement of the shear building structure and the term $|\chi_{p,r} - 1|$ based on the LPF. In fact, the correlation coefficient is ρ=1. In addition, the linear regression that passes through the origin has a slope $sl = 100$ (or equivalent to 1 if relative errors are considered instead of percent errors). This result confirms the findings that were described in Section 4.2.1. In this last section, in fact, the analytical expression that can be used to evaluate the truncation errors on the modal flexibility-based interstory drifts of shear buildings is derived. Then, it is also shown that if the first story is considered (a special case), the expression for the evaluation of the error on the interstory drift (which is equal to the first DOF displacement) becomes equal to the expression adopted in the proposed approach for truncation error analysis based on LPFs (i.e. the expression $|\chi_{p,r} - 1|$).

In Figs. 4.4c, 4.4e the proposed load participation factors are compared with the overall truncation errors evaluated on the whole modal flexibility-based deflections. As evident in Fig. 4.4c, by comparing the maximum errors with the LPFs, it is evident that, differently from the case of the first DOF errors, an exact linear

relationship is not present anymore. However, a very high correlation (i.e. ρ=0.99) was found between the maximum errors and the LPFs calculated for the 500 simulations performed on the considered shear building structure. In addition, the slope of the linear regression is also equal to 100 (Fig. 4.4c). This result suggests that the proposed load participation factors can be used to predict the maximum truncation errors expected on the modal flexibility-based deflections of shear buildings due to positive shear inspection loads. This result will be confirmed and discussed more in detail in next section, which deals with the experimental verification of the approach.

The root-mean-square errors are compared with the LPFs in Fig. 4.4e, and a correlation coefficient equal to 0.96 was found in this case. This means that the proposed load participation factors are also correlated with the truncation errors averaged for the whole deflection using the RMS criterion. However, the slope of the linear regression obtained in such case is remarkably lower than the slope of the linear regression obtained in the previous case where the maximum truncation errors were considered (Fig. 4.4c). The RMS errors are, of course, lower than the maximum errors.

The results presented in Fig. 4.4 were obtained for the case r=1. However, all the observations on the correlation between the LPFs and the truncation errors formulated in the case r=1 are also confirmed if higher modes are included in the calculation of the modal flexibility-based deflections. This is shown by the results of the same analyses performed by considering all the possible subsets of modes included in the calculations (i.e. for $r = 1 \ldots n-1$). These results are shown in Figs. 4.5, 4.6, and 4.7 where the LPFs are compared with the first DOF errors, the maximum errors, and the root-mean-square errors, respectively.

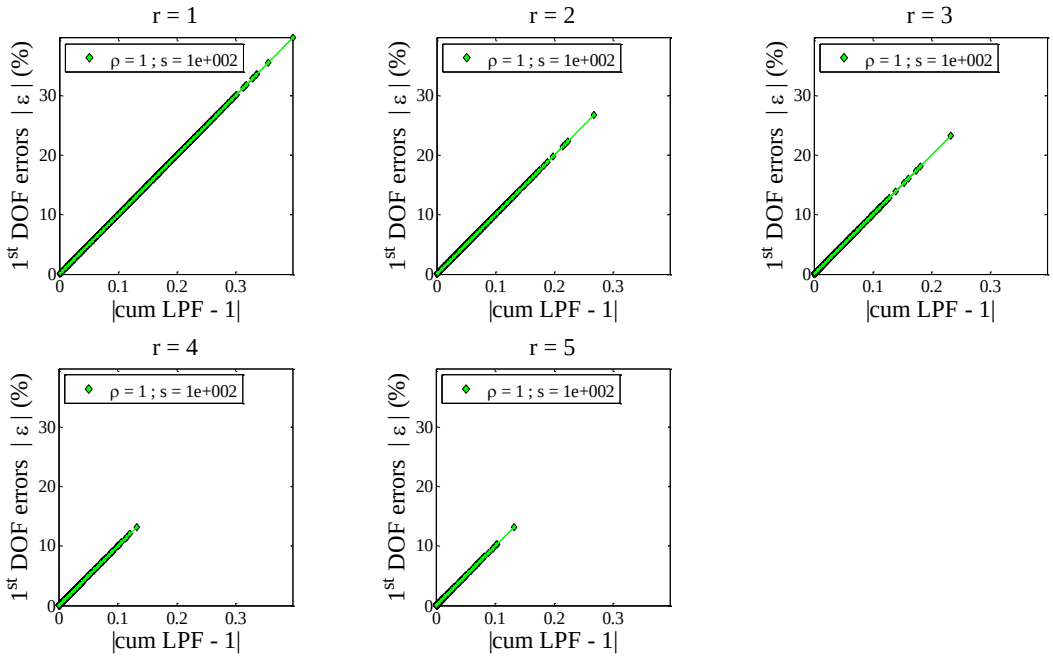

Figure 4.5. Correlation analysis between the 1st DOF truncation errors and the proposed Load Participation Factor: *r* =1, 2, 3, 4, 5 (shear building model).

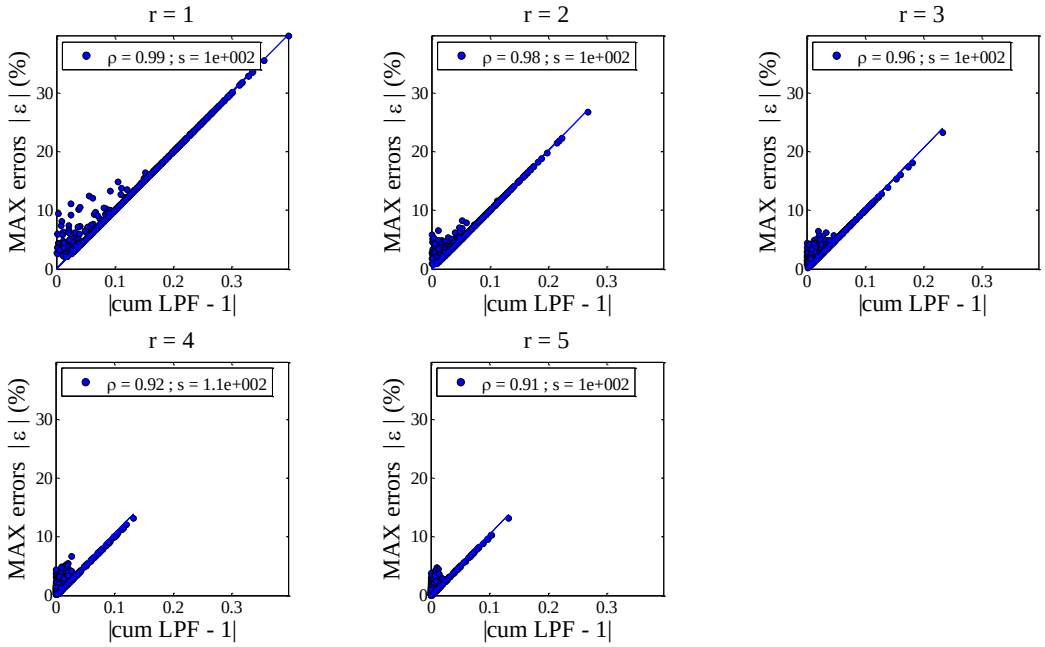

Figure 4.6. Correlation analysis between the maximum truncation errors and the proposed Load Participation Factor: *r* =1, 2, 3, 4, 5 (shear building model)

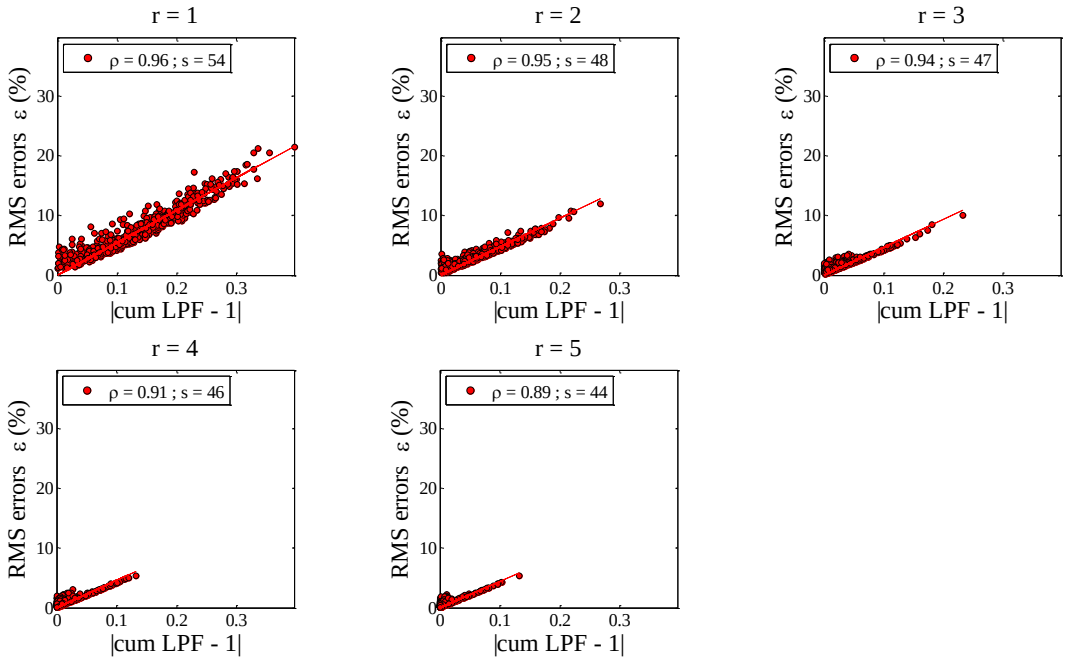

Figure 4.7. Correlation analysis between the RMS truncation errors and the proposed Load Participation Factor: *r* =1, 2, 3, 4, 5 (shear building model)

Of course, as evident in Figs. 4.5, 4.6, and 4.7, the higher the number of the modes included in the calculation of the modal flexibility-based deflections (i.e. the higher the parameter *r*), the lower the truncations errors.

4.3.2 Experimental verification of the LPF-based approach

This section presents the experimental verification of the proposed approach for truncation error analysis based on load participation factor. This verification was performed on a steel frame structure that was tested under ambient vibrations. The ambient vibration responses of the structure were analyzed by means of an output-only modal identification algorithm, and an experimental model of the structure (i.e. the modal flexibility matrix) was derived from the data. Then, parametric studies based on Monte Carlo simulation were performed on such experimental model to determine the modal flexibility based-deflections of the structure due to a large number of positive shear inspection loads with random distributions. The strategy

adopted in the experimental verification of the proposed LPF-based approach will be discussed more in detail later in this section.

The ambient vibration data used in the truncation error analysis presented in this section belong to experimental phase (i.e. phase II) of the benchmark studies for vibration-based damage detection that were sponsored by the IASC-ASCE Task Group for Structural Health Monitoring [Dyke et al., 2003; Ventura et al., 2003; Dyke, 2011][3]. The data related to these tests were made available for the research community [Dyke, 2011]. The tests of these benchmark studies were performed on a one-third scale, four-story, two-bay by two-bay steel frame structure located at the Earthquake Engineering Research Laboratory of the University of British Columbia, Vancouver, Canada. The tests were performed on August 4–7, 2002, using three types of excitations (i.e. impact hammer, electrodynamic shaker, and ambient vibrations). A simplified representation of the geometry of the structure is reported in Fig. 4.8. As already mentioned, these benchmark studies were performed for damage detection purposes. For this reason, the structure was tested at first in its original configuration (which is assumed as the undamaged configuration). Then, the structure was tested again by considering other configurations where damage was artificially introduced (for example, by introducing in the structure some local reductions of the stiffness). As schematically represented in Fig. 4.8a, diagonal wall braces are present in the bays of the structure, and in the damaged configurations of the benchmark study some braces of the structure were removed. Alternatively, the damage configurations were created by loosening the bolts of some beam-column connections [Dyke et al., 2003].

As already mentioned, the damage detection is not involved in the truncation error analyses presented in this chapter, thus only one structural configuration among the different ones that were tested in the benchmark study was selected. This configuration is the first of the tested configurations (i.e. the original fully braced structure, also indicated as the undamaged structure). Moreover, it is also worth noting that, among the different types of tests executed in the benchmark study, only the ambient vibration data were considered in the present analyses.

[3] The work done by the IASC-ASCE Task Group on the benchmark studies for Structural Health Monitoring [Dyke et al., 2003; Ventura et al., 2003; Dyke, 2011] is gratefully acknowledged.

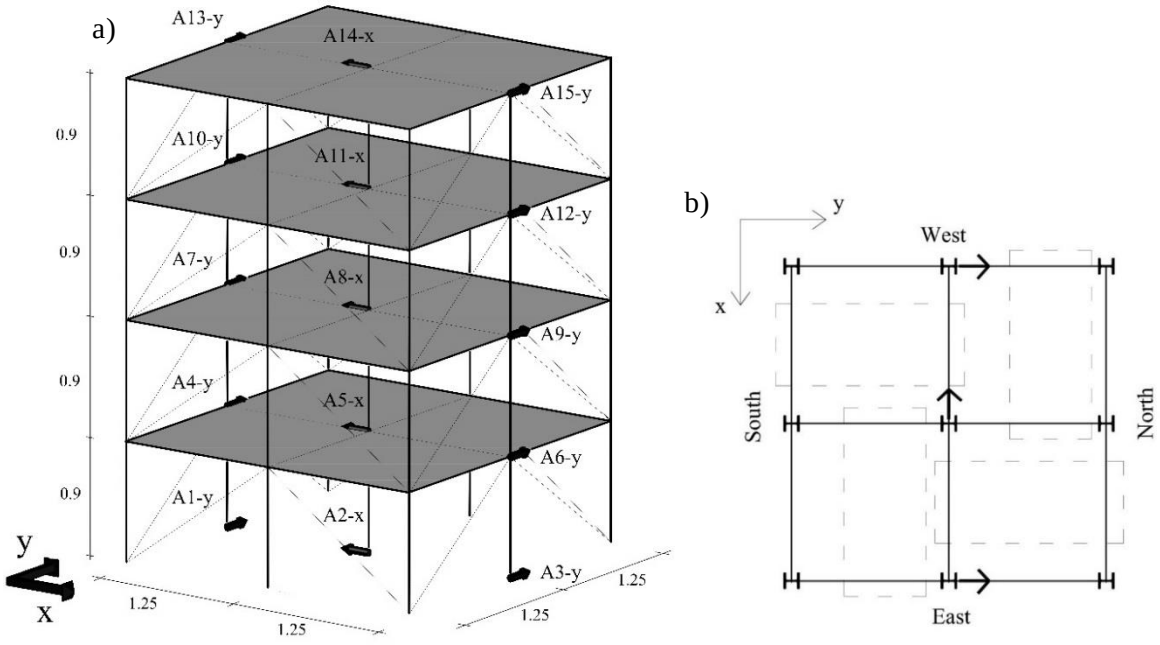

Figure 4.8. IASC-ASCE benchmark structure: (a) 3D view with accelerometer locations (dimensions in m); (b) plan view [Bernagozzi et al., 2017a].

In the ambient vibration test performed on the steel frame structure, fifteen force-balance acceleration sensors, schematically represented in Fig. 4.8a, were used to collect the responses of the structure due to the ambient excitations. As reported in [Dyke, 2011], the measurements have a length of time of 300 s and a sampling frequency of 200 Hz.

As reported in Section 4.2, the proposed approach for truncation error analysis by load participation factors has been formulated with reference mainly to plane structures and by considering the modal flexibility-based deflections of such structures in one prevalent direction. As demonstrated by the following observations, the experimental case study that was selected is suitable for the verification of this proposed approach.

Among the different configurations that were tested in the benchmark study, the one that was considered for the experimental verification of the proposed approach is characterized by a plan-symmetric distribution of the story stiffness at each level. Another relevant information about the geometry of the structure is the following: during the ambient vibration test, as reported in [Dyke et al., 2003], four steel plates

were positioned at each level of the structure to make the mass distribution of the structure reasonably realistic (these four steel plates are schematically shown in Fig. 4.8b). These four steel plates were positioned in a configuration that is slightly plan-asymmetric since the plates aligned to the west-east direction were shifted towards north direction. However, the coupling effects on the structural modes induced by this disposition of the masses are very small, as shown in the work by [Ching & Beck, 2004] where the results of the modal identification applied on the data of the experimental benchmark study are shown. Under the simplified assumption of neglecting the mentioned small coupling effects, the steel frame structure can thus be considered as a suitable case study for the verification of the LPF-based approach, which, as already mentioned, is proposed for structures that can be modeled as plane structures.

Two prevalent directions characterize the benchmark structure, and the structure is composed by columns and beams that have double T sections (B100×9 and S75×11, respectively) [Dyke et al., 2003]. As shown in Fig. 4.8b and according to the orientation of the column sections, the x axis is the weak direction of the structure, while the y axis is the strong direction. Moreover, if one compares the structural rigidities of the columns and the beams in both directions, it can be observed that a simplified modeling, such as a 4-DOF shear-type modeling, is much more valid for the weak direction (i.e. the x direction) of the structure with respect to the strong direction (i.e. the y direction). The steel frame structure in the weak or x direction has thus a structural behavior that is similar to the behavior of the structure that was considered in the numerical analysis presented in previous section (i.e. the 6-story shear building structure). For the above-mentioned reasons, a 2D analysis was performed on the steel frame structure tested under ambient vibrations by considering only the weak or x direction of the structure (Fig. 4.8b). The ambient vibration measurements provided in the benchmark study, as already mentioned, were acquired using fifteen acceleration sensors. However, in the present study only the data acquired with the sensors located in the center of the structure and aligned to the x direction (i.e. the sensors A14-x, A11-x, A8-x, A5-x, A2-x reported in Fig. 4.8a) were analyzed and used to estimate the modal flexibility of the structure in the weak or x direction.

The calculations that were performed to verify the proposed truncation error approach (based on load participation factor) using the ambient vibration data of the benchmark structure are reported in the flow chart presented in Fig. 4.9. The different steps that were considered are the following.

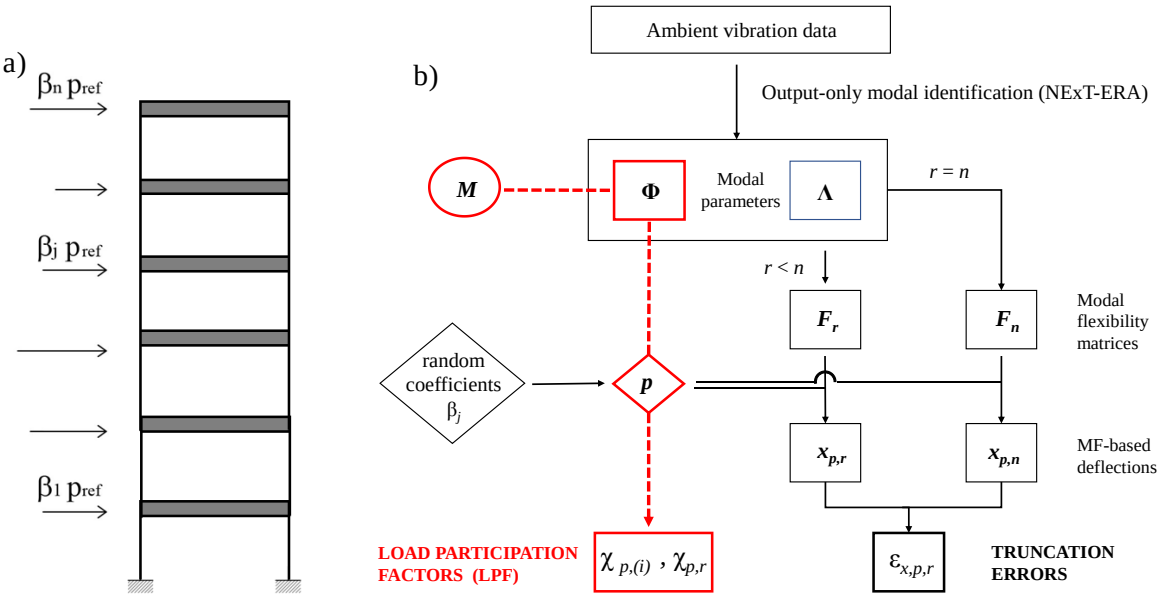

Figure 4.9. Verification of the approach starting from experimental data: random variables considered in the Monte Carlo simulation (a) flow chart of the analysis (b) (adapted from [Bernagozzi et al., 2017a])

In the first step, the ambient vibration data were analyzed using an output-only modal identification technique to obtain the modal parameters of the benchmark structure. In particular, the Natural Excitation technique [James et al., 1993] combined with the Eigensystem Realization Algorithm [Juang & Pappa, 1985], which as already discussed in Chapter 2 is a time-domain identification algorithm, was applied. Natural frequencies, modal damping ratios, and mode shapes of the first four modes of the structure in the considered direction (i.e. x direction) are reported in Table 4.1, where the mode shapes are normalized to a maximum value of unity. It is worth noting that for this experimental case study, these four modes represent all the principal modes that characterize the dynamic behavior of the structure in the considered direction. In fact, as already mentioned, the structure in the weak direction (i.e. x direction) can be reasonably modeled as 4-DOF shear building structure. As discussed later in this

section referring to the other steps of the calculations, the fact that all the principal modes of the structure in the considered direction were identified is a fundamental aspect for the verification of the LPF-based approach using experimental data.

Mode i	Natural frequency f_i (Hz)	Modal damping ratio ζ_i (%)	Mode shape components $\psi_{j,i}$ for each DOF j			
			$\psi_{4,i}$	$\psi_{3,i}$	$\psi_{2,i}$	$\psi_{1,i}$
I	7.49	0.77	1.000	0.838	0.630	0.418
II	19.89	0.54	-0.989	-0.052	1.000	0.964
III	25.31	0.26	0.453	-0.610	-0.272	1.000
IV	28.21	0.23	0.532	-0.991	1.000	-0.954

Table 4.1. Modal parameters of the IASC-ASCE benchmark structure (undamaged configuration) identified from ambient vibration data of the acceleration sensors in x direction [Bernagozzi et al., 2017a]

Then, the system mass matrix of the benchmark structure was estimated on the basis of the information available about the experimental test [Dyke et al., 2003; Dyke, 2011], and it was used to obtain mass-normalized mode shapes (which are, in turn, required to assemble the modal flexibility matrices). This matrix is composed by the masses that participate to the translational motion of the structure in the weak (or x) direction, and it is as follows

$$\boldsymbol{M} = \begin{bmatrix} m_4 & 0 & 0 & 0 \\ 0 & m_3 & 0 & 0 \\ 0 & 0 & m_2 & 0 \\ 0 & 0 & 0 & m_1 \end{bmatrix} \tag{4.51}$$

where m_4 = 1583.27 kg and $m_3 = m_2 = m_1$ = 2079.24 kg. It is worth noting, that as already discussed in Chapter 3, this simple modal scaling approach (adopted in the present analysis) is the same approach that was adopted in the work by [Koo et al., 2010] where the Positive Shear Inspection Load method for output-only damage detection was presented.

In a second step, the parametric study based on the Monte Carlo method (already applied to the numerical model of the 6-story shear building structure) was

also carried out in this experimental case study related to the benchmark structure. It is worth mentioning that the first two steps of the procedure applied to the numerical model of the shear building structure, as described in previous section and outlined in Fig. 4.2b (i.e. assembling an undamped model of the structure with random distributions of the masses and computing the modal parameters using eigenvector analysis) are substituted in this experimental case study by the application of the output-only modal identification algorithm (i.e. NExT-ERA) on the ambient vibration data (Fig. 4.9b). There is one important difference between the strategy adopted for the verification of the LPF-based approach through the numerical model and the verification on the real structure. Referring to the former, when the Monte Carlo method was applied on the numerical model the eigenvalue analysis was repeated for each configuration characterized by a different distribution of the structural masses. On the contrary, in the experimental case study the masses of the structure are fixed (i.e. the structural masses considered in the calculations are the real masses of the structure), and the modal parameters were identified only once from the ambient vibration data. In any case, in the experimental case study in each run of the Monte Carlo method the positive shear inspection loads applied to calculate the modal flexibility-based deflections are varied, and they have different distributions (Fig. 4.9a). They are, in fact, assembled using the same strategy applied on the shear building model (i.e. by generating through the pseudo-random integer generator [MATLAB] random coefficients β_j in the range from 1 to 5).

As already done in the analysis related to the numerical model, when the Monte Carlo method was applied in the experimental case study the calculations were performed following two different strategies (i.e. the two paths shown in Fig. 4.9b). On one side, the cumulative load participation factor of the first r modes of the structure was calculated using Eq. (4.31), which as already mentioned represents the prediction of the truncation effects expected on the modal flexibility-based deflection assembled using such r modes. On the other side, the modal flexibility matrices of the benchmark structure in x direction and the modal flexibility-based deflections due to the PSIL load with a random distribution were calculated considering both a subset of identified modes (i.e. for $r = 1 \dots n - 1$) and all the modes (i.e. $r = n = 4$). In particular, the deflection obtained by including all the structural modes in the calculations was

considered as the "exact" or target deflection. The term "exact" is used in such case to indicate a quantity that is not affected by modal truncation effects (of course, there are in any case uncertainties on the deflection that derive from the identification process applied on real noisy vibration data). Finally, the percent truncation errors were determined by comparing the target deflection (r=n=4) and the truncated deflections (r = 1,2, and 3) using Eqs. (4.2, 4.3, 4.4).

An example of the structural deflections of the benchmark structure obtained by applying a load vector $\boldsymbol{\beta}\, p_{ref}$ - where $\boldsymbol{\beta}$ = [1 3 1 3] ^{T} and p_{ref} = 10 kN - is reported in Fig. 4.10a. It is worth noting that for the applied positive shear inspection load the maximum errors on the single components of the modal flexibility-based deflections occur at the first lower DOF of the structure for all the analyzed cases r=1, r=2, and r=3 (as evident in Fig. 4.10b). This result confirms the findings that were obtained from the simulation performed on the numerical model.

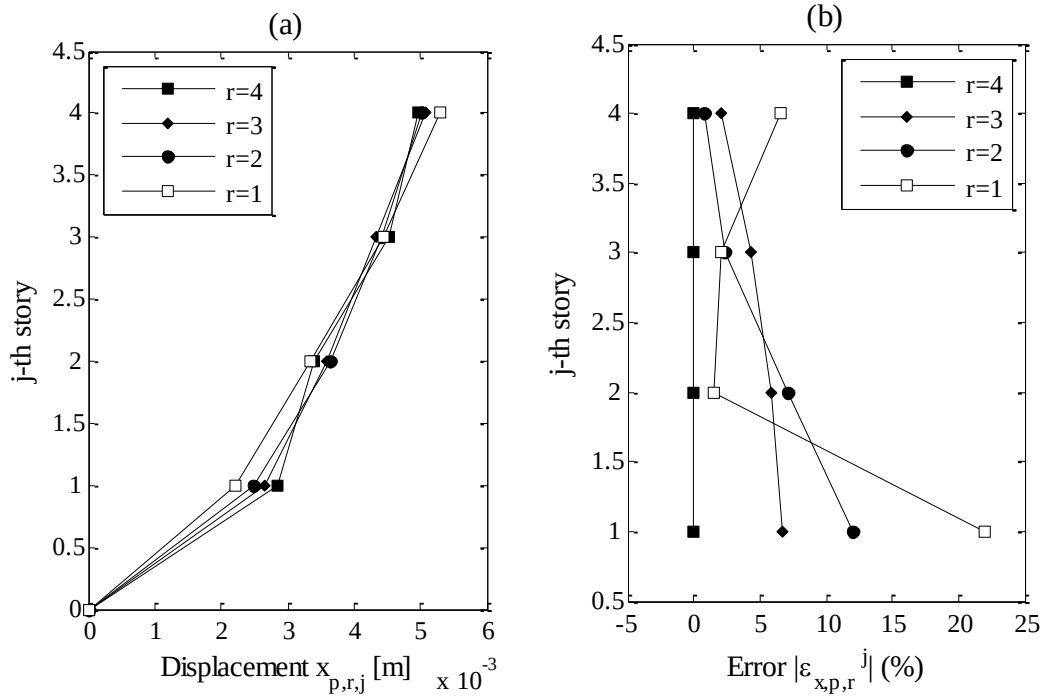

Figure 4.10. MF-based deflections of the IASC-ASCE benchmark structure for a generic load – 2D analysis in x direction: (a) displacements;
(b) truncation errors [Bernagozzi et al., 2017a].

As already done in the numerical simulation performed on the shear building model, 500 runs of the Monte Carlo method were also carried out by considering the experimental model of the benchmark structure. Then, at the end of the calculations the cumulative load participation factors of the modes not included in the computation of the truncated modal flexibility-based deflections (assumed as the predictions of the truncation effects) and the truncation errors (assumed as the reference solutions) were compared using the correlation analysis. As already done in Section 4.3.1, this analysis is based on the evaluation of the correlation coefficient and the linear regression between the two data sets that are compared.

The results of the correlation analysis are presented in Figs. 4.11, 4.12, and 4.13, where the cumulative load participation factors are compared with the 1st DOF errors, the maximum errors, and the root-mean-square errors, respectively. Each figure shows the results obtained for a number of included modes equal to r=1 (Figs. 4.11a, 4.12a, 4.13a), r=2 (Figs. 4.11b, 4.12b, 4.13b), and r=3 (Figs. 4.11c, 4.12c, 4.13c).

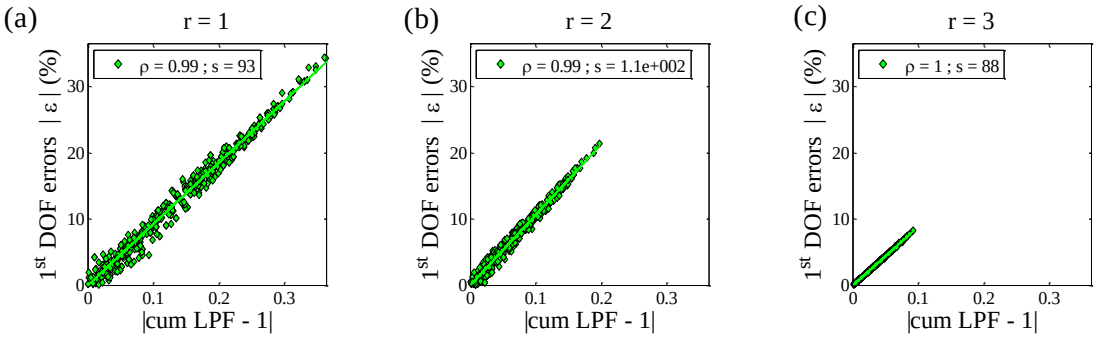

Figure 4.11. Correlation analysis between the 1st DOF truncation errors of the IASC-ASCE benchmark structure and the proposed Load Participation Factor: (a) r=1; (b) r=2; (c) r=3.

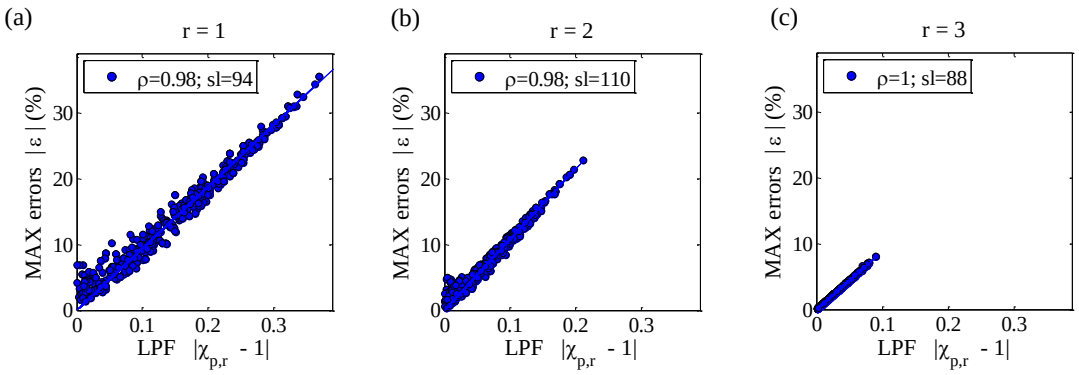

Figure 4.12. Correlation analysis between the maximum truncation errors of the IASC-ASCE benchmark structure and the proposed Load Participation Factor: (a) r=1; (b) r=2; (c) r=3 [Bernagozzi et al., 2017a].

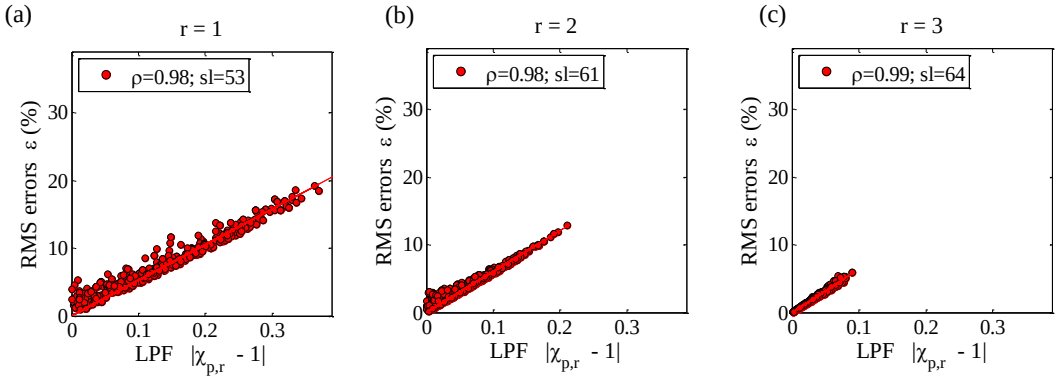

Figure 4.13. Correlation analysis between the RMS truncation errors of the IASC-ASCE benchmark structure and the proposed Load Participation Factor: (a) r=1; (b) r=2; (c) r=3 [Bernagozzi et al., 2017a].

Referring to the results related to the 1st DOF truncation errors (Fig. 4.11), very high values of the correlation coefficients ρ were obtained between the cumulative load participation factors and these truncation errors. Moreover, the slopes of the linear regression evaluated between the LPFs and the errors for the different cases r=1,2,3 were found to be similar to the values obtained for the shear building analytical model with maximum differences of approximately 10%. There are thus small discrepancies between the results obtained for the numerical model and for the experimental case study. As discussed in Section 4.2.1, in fact, an exact analytical relationship was found between the term $|\chi_{p,r} - 1|$ (i.e. the cumulative load participation factor of the missing modes) and the error on the first DOF displacement of a plane

shear building structure. This exact relationship was verified through the numerical simulation performed in previous section, as evident in Figs. 4.4a and 4.5. In the experimental case study, on the contrary, an exact relationship between the two terms was not found (as evident in Fig. 4.11 the points are not exactly aligned to the bisection of the plot). However, this effect obtained in the experimental case study is expected and can be justified by the following two observations. On one side, in fact, the modal parameters related to the experimental case study are affected by inevitable uncertainties that derive from the fact that the modal identification is applied on real noisy vibration data. On the other side, some modeling assumptions have been made on the analyzed benchmark structure - i.e. 1) a simplified shear-type modeling for the structure in the considered x direction was assumed; 2) a 2D analysis was performed under the assumption of neglecting the small coupling effects induced on the structural modes by the mass distribution of the structure which is slightly plan-asymmetric. As shown by the good agreement between the numerical and the experimental results these assumptions can be considered as valid, but of course some modelling approximations are inevitably introduced.

Referring to the results related to the maximum and the RMS truncation errors (Fig. 4.12, 4.13), high values of the correlation coefficients ρ were obtained between the cumulative load participation factors and these truncation errors, as already found in the numerical simulation performed on the plane shear building. Considering the correlation between the LPFs and the maximum errors (Fig. 4.12), the slopes of the linear regression for the different cases r=1,2,3 were found to be similar to the values obtained for the shear building analytical model with maximum differences of approximately 10% (which is the same results obtained in the experimental case study in the correlation between the 1st DOF errors and the LPFs). Considering the RMS errors (Fig. 4.13), the slopes of the linear regression for r=1,2,3 are remarkably lower than the ones related to the maximum errors, as already found and discussed for the analytical shear building model.

Finally, it is worth noting that in this section (related to the experimental case study), and differently from the previous section, the correlation analysis between the truncation errors and the cumulative mass participation factors (first approach for truncation error analysis mentioned in the work by [Zhang & Aktan, 1998]) is not

presented. However, one observation can be made on the relationship between the mass participation factors and the truncation errors in the context of the experimental case study. The fundamental point behind the observation is that the masses of the benchmark structure are fixed, and in each run of the Monte Carlo method applied on the experimental model only the loads are varied. For this reason, the cumulative mass participation factors of the structure are fixed for all the calculations that were performed. On the contrary, the truncation errors depend also on the applied load, and, as evident from the results presented in this section, different values of the errors were obtained for the different runs of the Monte Carlo method. In light of this premise, it is clear that a positive correlation can not be found between one parameter that is fixed (i.e. the cumulative mass participation factor) and another parameter that is varied (i.e. the truncation error).

The results obtained by analyzing the experimental case study (i.e. IASC-ASCE benchmark structure) have thus confirmed the outcomes that were found through numerical simulations on the analytical models of a 6-story plane shear building structure. The following two observations can be formulated to summarize the main findings of the analyses performed on the two building structures.

Firstly, the approach based on the evaluation of the load participation factors is able to provide an estimate of the maximum truncation errors expected on modal flexibility-based deflections of shear building structures that are evaluated using a limited number of structural modes and by applying to the structure positive shear inspection loads with arbitrary distributions. The main advantage of the approach is that the prediction of the error is obtained using only information about the structural modes included in the computation of the truncated deflections.

Secondly, the results showed that the root-mean-square (RMS) errors are in general lower than the maximum errors, but these RMS errors are also correlated with the proposed load participation factors. Thus, if two different structural cases are considered (e.g. two structures with different mass distributions but the same stiffness distribution and/or two different loading conditions), the load participation factors can be used to predict which is the case with the higher RMS truncation error, expected on the deflection.

4.4 Reduction of the truncation errors on modal flexibility-based deflections

The second part of this chapter presents the research investigations that were carried out in an attempt to reduce the truncation errors that affect the modal flexibility-based deflections calculated by applying a uniform load to shear building structures. As demonstrated by the analyses presented in this section, in fact, these truncation errors on the uniform load deflections can not be in general considered as negligible especially for structures with mass irregularities. The uniform load was considered because, as already mentioned in Chapter 3, this load is the inspection load that is generally applied in the procedures of vibration-based damage detection and condition assessment based on modal flexibility-based deflections (e.g. the Uniform Load Surface method [Zhang & Aktan, 1998] and the Positive Shear Inspection Load method [Koo et al., 2010]).

The objective of this second part of the chapter is thus different from the objective related to the first part. In previous sections, in fact, the objective was to obtain an a-priori indication of the truncation effects expected on the modal flexibility-based deflections. In this second part the truncation errors that affect the uniform load (UL) deflections are evaluated, and an alternative strategy to compute the modal flexibility-based deflections is investigated to obtain truncation errors on such deflections that are lower than the ones of the UL deflections. This alternative strategy implies the application of inspection loads that are different from the uniform load. As discussed later in this section, among the different alternative loads that were considered in the initial phase of the research, interesting results were obtained by applying a load that is proportional to the mass distribution of the structure to evaluate the modal flexibility-based deflections. This load is indicated in the present thesis as mass proportional load (MPL).

This second part of the chapter is thus dedicated, at first, to the definition of the above-mentioned mass proportional load and to the discussion of the special properties of such load. Then, numerical analyses performed on a shear building structure are presented. The mass proportional load is compared with the uniform load, by evaluating the corresponding truncation errors on modal flexibility-based

deflections and modal flexibility-based interstory drifts of building structures characterized by mass irregularities.

4.4.1 Definition of the Mass Proportional Load (MPL)

In the initial phase of the research inspection loads that are proportional to one mode shape of the structure were taken into account, and the application of such loads to modal flexibility-based models of structures was investigated analytically. However, such types of loads were not considered suitable and convenient loads to be applied in the procedures of structural identification and condition assessment that are based on the evaluation of modal flexibility-based deflections. To justify the above-mentioned observation let us consider the following ideal case.

A structure characterized by a diagonal mass matrix (for example, a plane shear building structure) is considered, and the modal flexibility-based deflection of such structure is evaluated by applying a vector load that is defined as follows

$$\boldsymbol{p} = a\, \boldsymbol{M}\, \boldsymbol{\phi_i} \tag{4.52}$$

where $\boldsymbol{M}$ is the mass matrix of the structure, $\boldsymbol{\phi_i}$ is the *i*-th mass normalized mode shape, and a is a scalar that represents a constant acceleration equal to one. If the load expressed in Eq. (4.52) is substituted in Eq. (4.6), the modal flexibility-based deflection of the structure due to such load can be obtained

$$\boldsymbol{x_{p,r}} = a\ \boldsymbol{F_r}\, \boldsymbol{M}\, \boldsymbol{\phi_i} \tag{4.53}$$

Some operations can be performed in Eq. (4.53) to simplify the terms that are present in such equation. Eq. (4.11) can be substituted in Eq. (4.53), and this last equation can be reformulated as

$$\boldsymbol{x_{p,r}} = a\ \boldsymbol{\Phi_r}\, \boldsymbol{\Lambda_r^{-1}}\, \boldsymbol{\Phi_r^T}\, \boldsymbol{M}\, \boldsymbol{\phi_i} \tag{4.54}$$

Due to the orthogonality relationships of the mode shapes with respect to the mass matrix the following relationship is valid

$$\boldsymbol{\Phi_r^T M}\, \boldsymbol{\phi_i} = \boldsymbol{h_i} \tag{4.55}$$

where the $\boldsymbol{h_i}$ is a $r \times 1$ vector defined as

$$\boldsymbol{h_i} = \begin{bmatrix} 0 \\ \vdots \\ 0 \\ 1_i \\ 0 \\ \vdots \\ 0 \end{bmatrix} \tag{4.56}$$

The vector $\boldsymbol{h_i}$ is a vector with all zero except for a value equal to one at the position of the vector that is equal to *i*, where *i* is the mode index related to mode that was considered in the equation of the applied inspection load (i.e. Eq. 4.52). By substituting Eq. (4.55) into Eq. (4.53), this last equation can be reformulated as follows

$$\boldsymbol{x_{p,r}} = a \ \boldsymbol{\Phi_r} \boldsymbol{\Lambda_r^{-1}} \boldsymbol{h_i} \tag{4.57}$$

As already mentioned in Chapter 3 where the expression of the modal flexibility matrix was firstly introduced, the matrix $\boldsymbol{\Lambda_r}$ is a $r \times r$ matrix which contains the square of the first *r* natural circular frequencies ω_i^2 of the structure on the main diagonal. It is thus clear that the following relationship is valid

$$\boldsymbol{\Lambda_r^{-1}} \boldsymbol{h_i} = \boldsymbol{q_i} \tag{4.58}$$

where the $\boldsymbol{q_i}$ is a $r \times 1$ vector defined as

$$\boldsymbol{q_i} = \begin{bmatrix} 0 \\ \vdots \\ 0 \\ (\frac{1}{\omega_i^2})_i \\ 0 \\ \vdots \\ 0 \end{bmatrix} \tag{4.59}$$

The vector $\boldsymbol{q_i}$ is a vector with all zero except for a value equal to $1/\omega_i^2$ at the position of the vector that is equal to *i*. By substituting Eq. (4.58) into Eq. (4.57), this last equation can be reformulated as follows

$$\boldsymbol{x_{p,r}} = a \ \boldsymbol{\Phi_r} \boldsymbol{q_i} \tag{4.60}$$

Then, by performing the matrix product between the $n \times r$ truncated mode shape matrix $\boldsymbol{\Phi_r}$ and the vector $\boldsymbol{q_i}$, the final expression of the modal flexibility-based deflection due to the load defined in Eq. (4.52) can be obtained

$$\boldsymbol{x_{p,r}} = a \ \frac{1}{\omega_i^2} \ \boldsymbol{\phi_i} \tag{4.61}$$

where $\boldsymbol{\phi_i}$ is the vector of the i-th mass normalized mode shape. This mode shape is the same mode shape that was considered in the equation of the applied inspection load (i.e. Eq. 4.52). As evident in Eq. (4.61), the deflection is proportional to the considered mode shape (the vectors of the two quantities are in fact related by scalar quantities). Thus, for a structure with a diagonal mass matrix, if a load where each component is the product between the mass of each DOF and each DOF component of one mode shape (Eq. 4.52) is considered, then the modal flexibility-based deflection evaluated for such load is proportional to that mode shape.

A similar result is obtained by applying a load that is proportional to one mode shape vector (in such case the values of the masses are not included in the load). If one repeats the above-mentioned calculations for such load, then the modal orthogonality relationships of the mode shapes with respect to the mass matrix can not be used to simplify the expression of the modal flexibility-based deflection (as done, on the contrary, in previous paragraphs). In any case, it is evident that if a load proportional to one mode shape vector is applied, then the contribution of that mode to the modal flexibility-based deflection will be dominating and the resulting deflection will be in general approximately proportional to that mode shape.

In light of the above-mentioned analytical investigations, inspection loads that are proportional to the mode shapes of the structure were not considered as convenient loads to be applied in the procedures of structural identification and condition assessment that are based on the evaluation of modal flexibility-based deflections. Such loads, in fact, strongly increase the contribution of the mode (selected to assemble the inspection load) in the modal flexibility-based deflection. This characteristic is not in agreement with the general principle that is behind any modal flexibility-based approach – i.e. the contributions of the different structural modes are cumulated to obtain the best achievable estimate of the flexibility of the structure (and this principle is also valid, of course, if one considers the modal flexibility-based deflections instead of the modal flexibility matrices). Considering the contribution of the different structural modes instead of only one single mode is, for example, one of the motivations for which, as already discussed in Chapter 1, in modal-based damage

detection the modal flexibility-based approaches are in general preferred with respect to the approaches based on the modal properties of single-modes.

A final observation can be made on the inspection loads that are proportional to the mode shapes by considering the specific case of plane shear building structures. Except when considering the first mode of a shear building, a load that is proportional to a mode shape might not be a positive shear inspection load.

After having examined the properties of loads that are proportional to the mode shapes of the structure, another strategy was investigated to estimate the modal flexibility-based deflections. According to this second strategy, a load that is proportional to the mass distribution of the structure is selected as the inspection load, and the modal flexibility-based deflections are evaluated for this mass proportional load (MPL). For structures characterized by a diagonal mass matrix (for example, a plane shear building structure), the mass proportional load, indicated as $\boldsymbol{p^m}$, can be expressed as

$$\boldsymbol{p^m} = \boldsymbol{M}\,\boldsymbol{a} \tag{4.62}$$

where $\boldsymbol{M}$ is the mass matrix of the structure and $\boldsymbol{a}$ is a unitary acceleration vector with constant term a assumed equal to one.

If the mass proportional load defined in Eq. (4.62) is substituted into the expression of the modal flexibility-based deflection of a generic MDOF structure due to a generic load (Eq. 4.6), the deflection of the structure due to the mass proportional load evaluated using the first *r* modes is

$$\boldsymbol{x_{m,r}} = \boldsymbol{F_r}\,\boldsymbol{p^m} \tag{4.63}$$

and each component of the deflection vector is

$$x_{m,r,j} = a\sum_{i=1}^{r}\frac{\phi_{j,i}}{\omega_i^2}\left(\sum_{k=1}^{n} m_k\,\phi_{k,i}\right) = a\sum_{i=1}^{r}\frac{\phi_{j,i}}{\omega_i^2}\Gamma_i \tag{4.64}$$

This last equation can be derived if the general equation of each component of the deflection (Eq. 4.7) is evaluated for the mass proportional load. By comparing Eq. (4.64) and Eq. (4.7), it is also evident that, by considering a mass proportional load, the term $c_{p,i} = \sum_{k=1}^{n} p_k\,\phi_{k,i}$, present in Eq. (4.7), is substituted in Eq. (4.64) by a constant term a (which is equal to one) and by the modal participation factor $\Gamma_i =$

$\sum_{k=1}^{n} m_k \, \phi_{k,i}$. This property is valid because, as already mentioned, mass-normalized mode shapes are considered.

One important observation must be made on the relationship between the mass proportional load and the approach for truncation errors analysis based on the load participation factor that is proposed in the first part of this chapter. In fact, if a mass proportional load is considered, then the approach based on the load participation factor is equivalent to the approach based on the mass participation factor that was mentioned in the work by [Zhang & Aktan, 1998]. This is evident if the load participation factor (LPF) related to the *i*-th mode (Eq. 4.24) is evaluated by considering a mass proportional load (MPL). In such case the quantity that is obtained is termed mass proportional load participation factor (MPL-PF) and is defined as follows

$$\chi_{m,(i)} = \frac{c_{m,i} \, \Gamma_i}{\boldsymbol{c_m^T} \, \boldsymbol{\Gamma}} = \frac{{\Gamma_i}^2}{\boldsymbol{\Gamma^T} \, \boldsymbol{\Gamma}} = \mu_{(i)} \tag{4.65}$$

Due to the fact that, as already mentioned, the term $c_{p,i}$ evaluated for the mass proportional load is equivalent to the modal participation factor Γ_i and as evident in Eq. (4.65), this mass proportional load participation factor $\chi_{m,(i)}$ is equal to the mass participation factor $\mu_{(i)}$ (Eq. 4.1).

In the same way, if the cumulative load participation factor (Eq. 4.31) is calculated for the mass proportional load (i.e. a quantity that is termed cumulative MPL-PF), then the cumulative mass participation factor of the first *r* modes (μ_r) is obtained

$$\chi_{m,r} = \sum_{i=1}^{r} \chi_{m,(i)} = \frac{\sum_{i=1}^{r} c_{m,i} \, \Gamma_i}{\boldsymbol{c_m^T} \, \boldsymbol{\Gamma}} = \frac{\sum_{i=1}^{r} {\Gamma_i}^2}{\boldsymbol{\Gamma^T} \, \boldsymbol{\Gamma}} = \sum_{i=1}^{r} \mu_{(i)} = \mu_r \tag{4.66}$$

Two observations can be formulated on the mass proportional load participation factor. As evident in Eq. (4.65), the MPL-PF $\chi_{m,(i)}$ is a quantity that is always positive. This means that, for all the possible values of *r*, the cumulative MPL-PF $\chi_{m,r}$ is always in the following range: $0 \leq \chi_{m,r} \leq 1$. Of course, these properties are the same properties valid for the mass participation factor and the cumulative mass participation factor. It is worth noting, however, that these conditions are not always fulfilled for generic loads, including the uniform load (as shown later in the numerical analyses).

A second observation can be formulated by considering the specific case of the shear building structures. According to Eq. (4.47), it was shown in Section 4.2.1 that the truncation errors on the first DOF displacement of a shear building due to a generic load is explicitly related to the cumulative load participation factor $\chi_{p,r}$. In this section, it is also shown that when considering a mass proportional load, the proposed cumulative load participation factor is equal to the cumulative mass participation factor μ_r. From these two properties, a third property can be derived: for the specific case of a shear building structure and by considering its first DOF displacement of the modal flexibility-based deflections due to a mass proportional load, the truncation errors are explicitly related to the cumulative mass participation factors. Moreover, referring to the application of a mass proportional load on a plane shear building, it is worth noting that this load is implicitly a positive shear inspection load (as defined in the work by [Koo et al., 2010]).

As already mentioned at the beginning of this section, the mass proportional load is investigated and applied as an alternative to the uniform load. However, if one evaluates the structural deflections due to such two loads, in general the displacements that are obtained in the two cases are not of the same order of magnitudes. This is evident because the mass proportional load is a vector composed by the masses of the structure, while the uniform load, as defined in the work by [Zhang & Aktan, 1998], is a vector whose components are equal to one. In order to make these two loads more comparable, a scaled version of the uniform load can be considered. This modified uniform load is defined as $\boldsymbol{p^u} = m^* \, \boldsymbol{a}$, where $m^* = \frac{1}{n}\sum_{j=1}^{n} m_j$ is the average mass of the MDOF structure. By adopting this load, each j-th modal flexibility-based displacement is equal to Eq. (4.5) scaled by the factor $a\, m^*$, where a is a unitary acceleration.

To conclude this section, the expression of the load participation factor specified for a uniform load is reported, and this expression will be adopted in the numerical analysis presented in next section. The load participation factor (Eq. 4.24) evaluated for the uniform load and for the i-th mode is termed uniform load participation factor (UL-PF) and is defined as follows

$$\chi_{u,(i)} = \frac{c_{u,i}\,\Gamma_i}{\boldsymbol{c_u^T}\,\boldsymbol{\Gamma}} = \frac{s_i\,\Gamma_i}{\boldsymbol{s^T}\,\boldsymbol{\Gamma}} \tag{4.67}$$

Two observations can be formulated on this last equation. First of all, since in general the load participation factor is a quantity that represents the normalized contribution of one mode to the modal flexibility-based deflection, the uniform load participation factor is independent from any scaling operation that is performed on the uniform load. Secondly, it can be proven, using a demonstration very similar to the one shown in Section 4.2 to prove Eq. (4.26), that if mass normalized mode shapes are considered, then the following relationship is valid: $\mathbf{s}^{\boldsymbol{T}}\,\boldsymbol{\Gamma} = n$, where n is the total number of the DOFs of the structure.

In the same way, the cumulative load participation factor (Eq. 4.31) can be evaluated for the uniform load and for the first r modes to obtain a quantity (termed cumulative UL-PF) that is defined as follows

$$\chi_{u,r} = \sum_{i=1}^{r} \chi_{u,(i)} = \frac{\sum_{i=1}^{r} c_{u,i}\,\Gamma_i}{\boldsymbol{c_u^T}\,\boldsymbol{\Gamma}} = \frac{\sum_{i=1}^{r} s_i\,\Gamma_i}{\mathbf{s}^{\boldsymbol{T}}\,\boldsymbol{\Gamma}} \tag{4.68}$$

4.4.2 Numerical analyses on structures with mass irregularities: comparison between the mass proportional and the uniform loads

In the present section, the numerical analyses that were carried out to compare the truncation errors on the modal flexibility-based deflections calculated by applying the mass proportional load with those of the uniform load are presented.

These numerical analyses were performed on the same shear building structure that was used in Section 4.3.1 to verify the proposed approach for truncation error analysis based on the load participation factor. As already mentioned, this structure is a six-story reinforced concrete (RC) plane frame building modeled as a shear building structure (Fig. 4.1), which is characterized by a uniform distribution of the story stiffness (the story stiffness is equal to k_j=2.29×10^5 kN/m for each story).

To perform the truncation error analysis presented in this section and to compare the results obtained for the mass proportional and the uniform loads, various structural configurations of the shear building characterized by different and irregular distributions of the story masses were considered. The distributions of the structural masses considered in the present analysis are similar to the ones analyzed in Section 4.3.1. Thus, configurations characterized by both moderate and strong mass

irregularities were considered also in the present analysis to have a complete insight of the tendencies of the results. It is worth noting, however, that while in Section 4.3.1 random distributions of the structural masses were considered in the Monte Carlo simulation, in the present analysis the distributions of the structural masses were chosen at the beginning of the calculations and they are not generated randomly. In particular, twelve configurations with irregular distributions of the masses were considered, and they are reported from case 1 to case 12 in Table 4.2. In this table, the mass distributions are expressed in terms of the story mass ratios, and the coefficient γ can assume the following values: 1, 2, 3, 4, 5. This coefficient γ was used to impose increasing amounts of mass irregularities on the analyzed structural configurations, and each increased mass at the *j*-th DOF of the structure is $m_j = \gamma\ m_{ref}$, where, as already defined in Section 4.3.1, $m_{ref} = 100$ kN s^2/m. It is worth noting that, of course, if the building structure has a uniform distribution of the story masses, the mass proportional load is a uniform load. This particular case is obtained when the coefficient γ is equal to one.

j-th DOF	1	2	3	4	5	6	7	8	9	10	11	12
6	γ	1	1	1	1	1	γ	1	1	1	γ	1
5	1	γ	1	1	1	1	1	γ	1	1	1	γ
4	1	1	γ	1	1	1	γ	1	γ	1	γ	1
3	1	1	1	γ	1	1	1	γ	1	γ	1	γ
2	1	1	1	1	γ	1	1	1	γ	1	γ	1
1	1	1	1	1	1	γ	1	1	1	γ	1	γ

Table 4.2. Structural configurations of the shear building structure expressed in terms of the story mass ratios (γ =1,2,3,4,5) [Bernagozzi et al., 2017a]

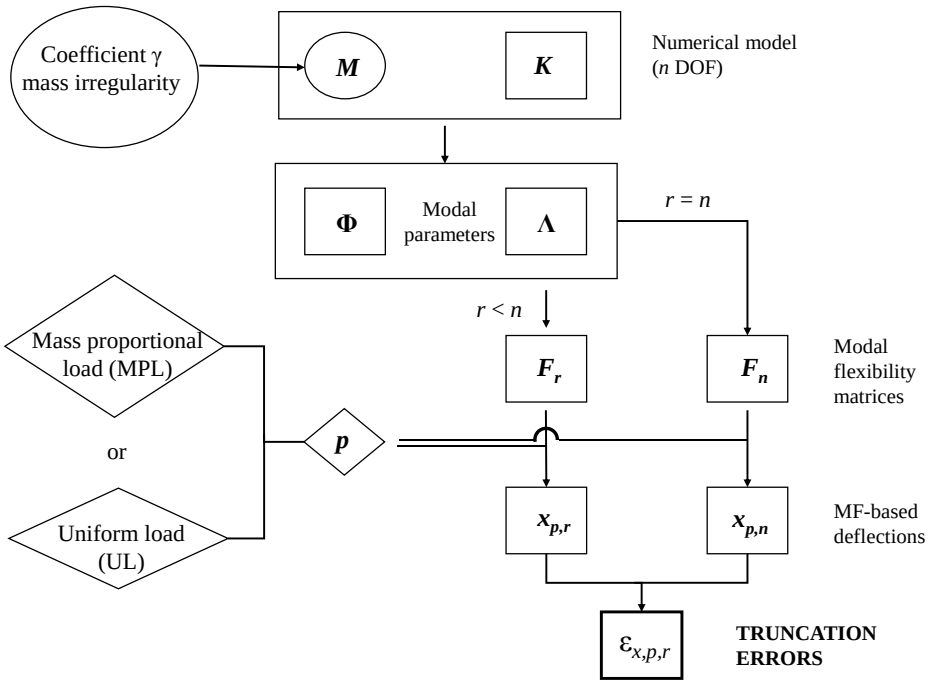

Figure 4.14. Flow chart of the analysis carried out to compare the mass proportional load and the uniform load by evaluating the corresponding truncation errors (adapted from [Bernagozzi et al., 2017a])

The calculations that were performed to compare the mass proportional load and the uniform load (by evaluating the corresponding truncation errors) are reported in the flow chart of Fig. 4.14. At first, for each structural configuration (reported in Table 4.2) an undamped numerical model of the shear building structure was assembled. The stiffness matrix **K** of the structure is defined by Eq. (4.48), mentioned in Section 4.3.1. The mass matrix is defined by Eq. (4.49), but the coefficient δ_j reported in this equation are substituted by the coefficients reported in the columns of Table 4.2 for the different structural configurations. Then, an analytical modal analysis was performed on the structural model, and the modal flexibility matrices were assembled using all the possible subsets of modes included in the calculations (i.e. $r = 1 \ldots n$, where $n = 6$ for the considered structure). Then, the deflection profiles of the structure were calculated by applying both the mass proportional load and the scaled version of the uniform load, as defined in Section 4.4.1. As already done in Section 4.3.1, the deflections evaluated for a number of modes equal to r = n were considered as the exact or target deflections and were used to calculate the errors that affect the

truncated deflections (evaluated for $r = 1 \ldots n - 1$). Both for the mass proportional load and the uniform load, the relative truncation errors on the components of the modal flexibility-based deflections were evaluated by applying Eq. (4.2). The mass proportional load and the uniform load were also compared in terms of the overall truncation errors that affect the whole deflections. To perform this operation, the overall truncation error was evaluated as the root-mean-square value of the errors related to the single components of the deflections (Eq. 4.3).

The analysis of the shear building structure with the different distributions of the structural masses reported in Table 4.2 can be considered as a parametric study, where the main variables are the position (i.e. the DOF) of the structure were the mass irregularity is imposed and the amount of the mass irregularity. This last parameter, as already mentioned, is defined by the coefficient γ which assumes the following values 1-2-3-4-5. Referring to the DOFs where the mass irregularities were imposed and as evident in Table 4.2, both single and multiple locations were considered. In fact, from configurations 1 to 6 the coefficient γ is applied on one DOF, from configurations 7 to 10 the coefficient γ is present on two DOFs, and finally for configurations 11 and 12 the coefficient γ is applied on three DOFs. In each of these three groups of the configurations, the positions where the mass irregularities are imposed using the coefficient γ are varied, trying to consider as much combinations as possible.

The results of this parametric study are presented in this section using the following strategy. At first, the results are shown for one structural configuration (i.e. configuration 7, as described in Table 4.2) with a mass irregularity that is imposed by selecting γ=3. Then, the results of the analyses performed on the same structural configuration (i.e. configuration 7) are presented by considering increasing amounts of the mass irregularities (i.e. for γ = 1, 2, 3, 4, 5). Finally, the results of the analyses are presented for all the structural configurations from 1 to 12 of the shear building structure and for a fixed mass irregularity (which is imposed again by selecting γ=3).

The results of the truncation error study performed on configuration 7 and by considering a mass irregularity that is imposed as γ=3 are presented in Figs. 4.15, 4.16, and 4.17. In particular, Fig. 4.15 shows the modal flexibility-based deflections

of the structure (configuration 7) calculated by applying both the mass proportional load and the uniform load and by considering all the possible subsets of included modes – as indicated by the parameter r, which is varied from 1 to 6. The deflections evaluated using the uniform load are reported in Fig. 4.15a, while the deflections evaluated using the mass proportional load are reported in Fig. 4.15b. As evident, in Fig. 4.15a the uniform load deflection obtained using only the first mode (i.e. r=1) shows the major discrepancies with respect to the other deflections and with respect to the exact solution obtained for r=6. On the contrary, the deflections due to the mass proportional load (reported in Fig. 4.15b) are almost overlapped. These qualitative and preliminary observations are confirmed by the analysis of the modal truncation errors. The percent error on each component of the truncated modal flexibility-based deflection was evaluated with respect to the target solution (r=n) and the outcomes are reported in terms of absolute values in Fig. 4.16. In particular, Fig. 4.16a shows the truncation errors related to the uniform load, while Fig. 4.16b shows the errors related to the mass proportional load. First of all, it is worth noting that, as expected and as already discussed in previous section, for both the two loads the displacements of the first DOF of the structure are affected by the maximum truncation errors. The second and more important observation that can be formulated on the results is the following: the truncation errors on the deflections calculated using the mass proportional load (Fig. 4.16b) are lower than the uniform load errors (Fig. 4.16a). For instance, considering the displacement of the first DOF (j=1) and including only the first mode in the calculations (i.e. r=1) the errors are 21.1% and 9.8% for the uniform load and the mass proportional load, respectively. For the same DOF and including the first two modes in the calculations (i.e. r=2) the truncation error related to the application of the uniform load is 12.1%, while the error related to the mass proportional load is 5.3%.

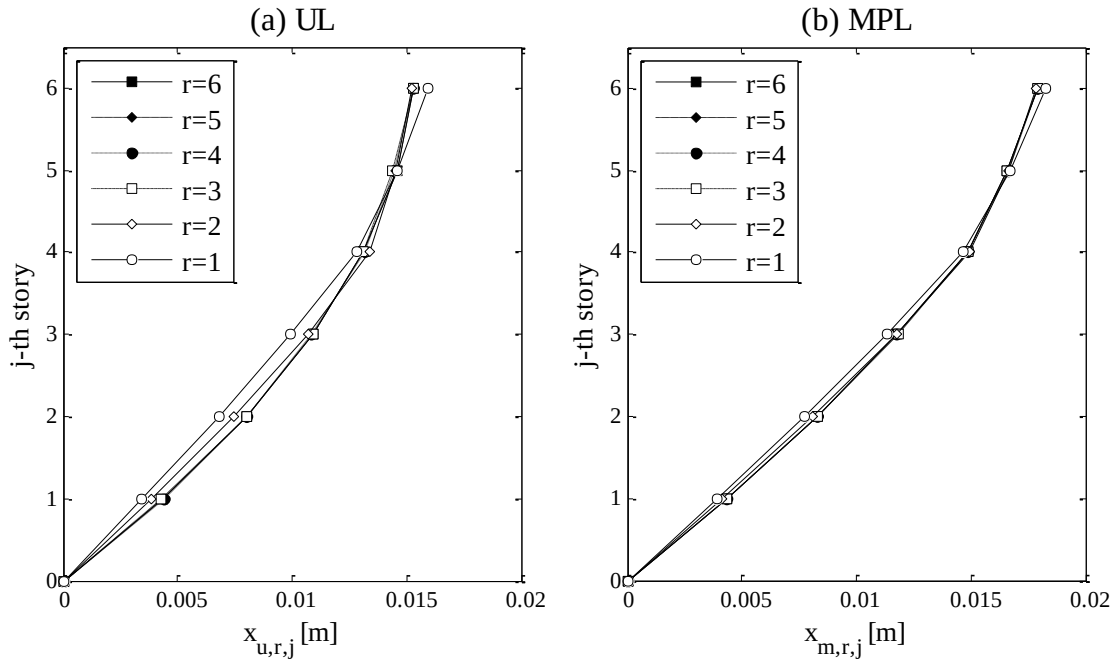

Figure 4.15. Modal flexibility-based deflections of the shear building structure (case 7; γ=3): (a) uniform load; (b) mass proportional load

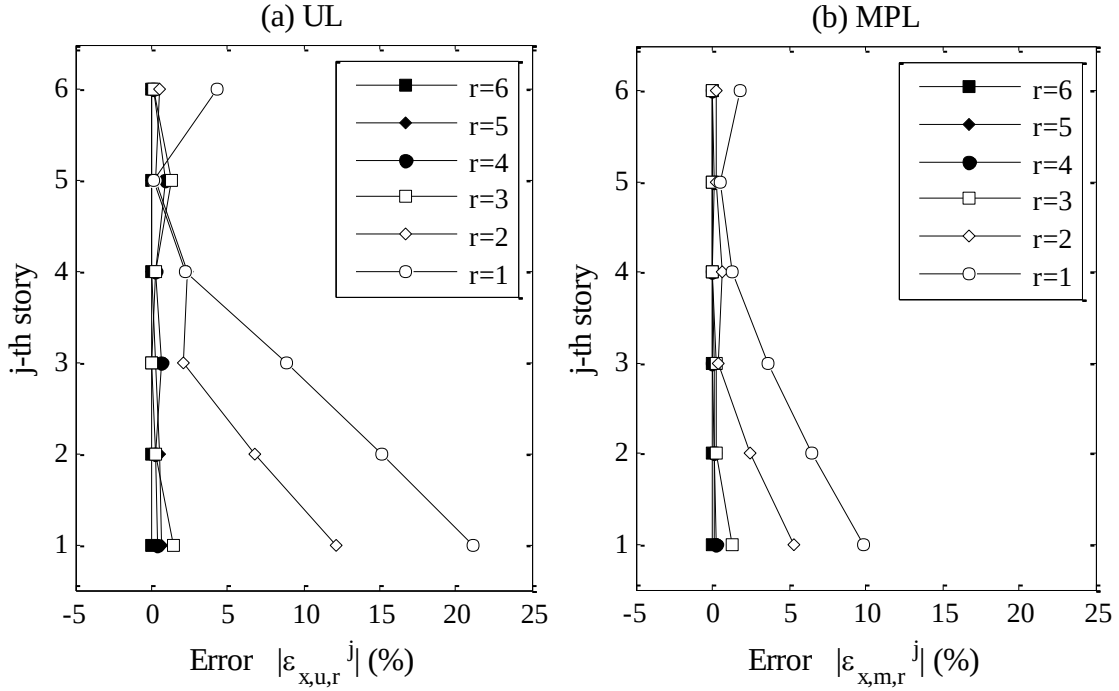

Figure 4.16. Truncation errors on the displacements of the shear building structure (case 7; γ=3): (a) uniform load; (b) mass proportional load [Bernagozzi et al., 2017a]

The values of the truncation errors related to the uniform and the mass proportional loads that are shown in Fig. 4.16 by highlighting the trend of such errors as a function of the DOFs of the structure are also plotted in Fig. 4.17 using a different strategy. In this last figure, the errors are plotted for each DOF separately, and the trends of the truncation errors are presented as a function of the number of the modes included in the calculations (i.e. the parameter *r*). One observation that can be formulated is that, as expected, the higher the number of the included modes, the lower the single-DOF truncation error for both the uniform and the mass proportional loads. However, as already discussed referring to Fig. 4.16, the results show that the errors related to the mass proportional load are lower than the ones related to the uniform load for the majority of the DOFs and the values of the parameter *r*, with only two exceptions (i.e. the 5th DOF for *r*=1 and the 3rd DOF for *r*=3). As already mentioned, both for the uniform load and the mass proportional load the errors decrease if higher values of the parameter *r* are considered. However, it can be observed that these decreasing trends of the errors related to the mass proportional load are more regular than the ones related to the uniform load, as evident for example in Fig. 4.17b for *j*=5.

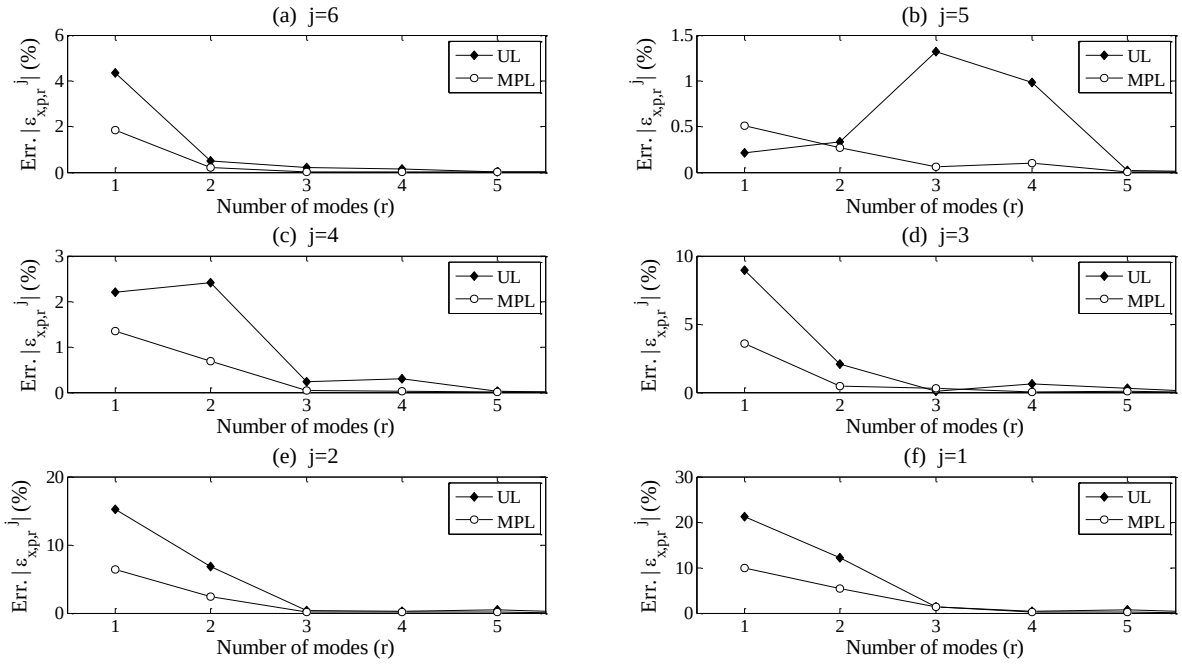

Figure 4.17. Truncation errors on the *j*-th DOF displacement of the shear building structure (case 7; γ=3) – comparison between the UL and the MPL [Bernagozzi et al., 2017a]

The results of the truncation error study performed on configuration 7 of the shear building structure and by considering increasing amounts of mass irregularities (i.e. γ =1, 2, 3, 4, 5) are presented in Figs. 4.18, 4.19, and 4.20. For such configurations characterized by increasing amounts of mass irregularities, an estimation of the overall truncation errors on the whole modal flexibility-based deflections was carried out by evaluating the root-mean-square error of the errors related to the single-DOFs. The results are reported in Fig. 4.18 by plotting the RMS errors as a function of the different number of included modes (parameter *r* reported on the x axis) and by comparing the uniform load (Fig. 4.18a) with the mass proportional load (Fig. 4.18b). Each of the different curves reported in the figure is related to one value of the parameter γ, which is used to model the amount of the mass irregularity. The results show that the RMS errors related to the mass proportional load (Fig. 4.18b) are lower than or equal to the errors related to the uniform load (Fig. 4.18a) for all the analyzed cases. For example, by including only the first mode in the calculation of the deflections (i.e. for r=1) and for a value of the coefficient γ equal to 3, the RMS error related to the uniform load is equal to 11.4%, while the RMS error related to the mass proportional load is 5.1%. It is worth noting that, of course, when the building structure has a uniform distribution of the story masses (i.e. when the coefficient γ is equal to one), the results obtained by applying the uniform load are equal to the ones related to the mass proportional load.

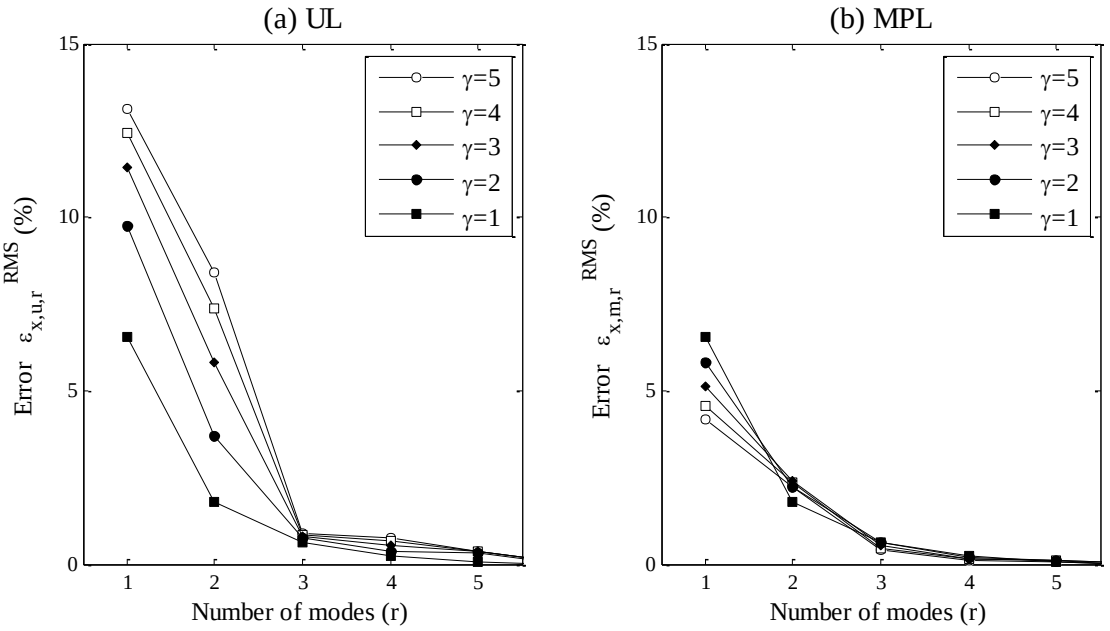

Figure 4.18. RMS truncation errors on the displacements of the shear building structure (case 7) for different mass irregularities: (a) uniform load; (b) mass proportional load [Bernagozzi et al., 2017a]

Further investigations were carried out on this configuration of the shear building structure (i.e. configuration 7) characterized by increasing amounts of mass irregularities (i.e. for γ =1, 2, 3, 4, 5) to provide an interpretation on the results of the comparison between the mass proportional load and the uniform load (in terms of the truncation errors).

As pointed out in the work by [Zhang & Aktan, 1998] and as already mentioned in this chapter, the term s_i, which is the summation of the components of the i-th mode shape (i.e. $s_i = \sum_{k=1}^{n} \phi_{k,i}$), can be considered as the weighting term of each mode in Eq. (4.5), which is related to the modal flexibility-based deflection due to the uniform load. In the same way, the modal participation factor $\Gamma_i = \sum_{k=1}^{n} m_k \, \phi_{k,i}$ can be considered as the weighting term of each mode in Eq. (4.64), which is related to the modal flexibility-based deflection due to the mass proportional load.

The terms Γ_i and s_i were evaluated for configuration 7 of the structure and for all the increasing amounts of mass irregularities, and these coefficients are reported in terms of absolute values in Fig. 4.19. In this figure, the coefficients s_i are scaled by m^* since, as defined in Section 4.4.1, a scaled version of the uniform load is considered

in the analyses. The results show that an increase in the coefficient γ lead to an increase in the parameter $m^*|s_i|$, especially for the high-order modes (i.e. the 3rd and the 5th modes). On the contrary, the modifications induced by the mass variations on the participation factors $|\Gamma_i|$ of all the high-order modes are lower than the previous case. This means that for these configurations characterized by mass irregularities, the contribution of the high-order modes of the structure to the uniform load deflection is higher than the contribution of the same modes to the mass proportional load deflections. This implies, in turn, that when the modal flexibility-based deflections are evaluated without including in the calculations such high-order modes, the truncation errors on the uniform load deflections are higher than the errors on the mass proportional load deflections.

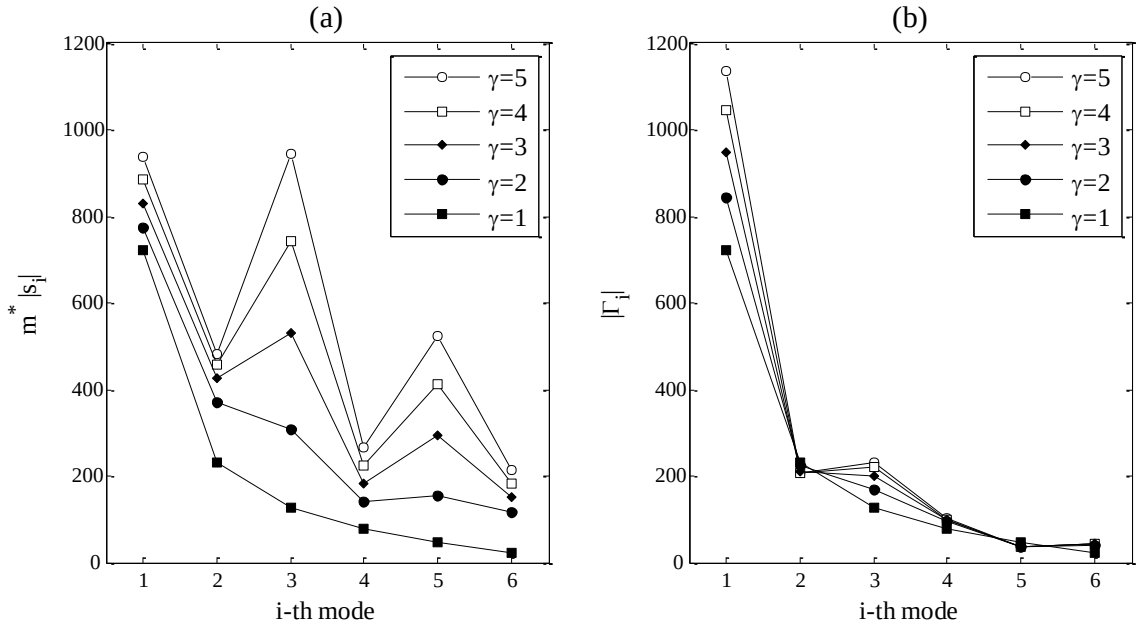

Figure 4.19. Single-mode participation factors of the shear building structure (case 7) for different mass irregularities: (a) $m^*|s_i|$; (b) $|\Gamma_i|$ [Bernagozzi et al., 2017a]

According to the approach for truncation error analysis proposed in Section 4.2, the cumulative load participation factors were also evaluated both for the uniform and the mass proportional loads (i.e. using Eqs. 4.66, 4.68). The values of these load participation factors are reported in Fig. 4.20, where Fig. 4.20a refers to the uniform load, while Fig. 4.20b refers to the mass proportional load. By adopting the same

representation used in Fig. 4.18 (for the RMS truncation errors), in Fig. 4.20 the load participation factors are plotted as a function of the different number of included modes (parameter *r* reported on the x axis) and each of the curves reported in Fig. 4.20 is related to one value of the parameter γ, which is used to model the amount of the mass irregularity.

One observation can be formulated on the values of the load participation factors obtained in the analyses (for the uniform and the mass proportional loads) to confirm the general properties that were discussed in Section 4.4.1. An asymptotic convergence to one of the cumulative mass proportional load-participation factors (cumulative MPL-PFs) for increasing values of *r* can be noticed in Fig. 4.20b. This means that, as already discussed, the cumulative MPL-PFs (which are equal to the mass participation factors) are always in the range from 0 to 1 for each value assumed by the parameter *r*. On the contrary, the cumulative uniform load-participation factors (cumulative UL-PFs) can assume values greater than one if they are evaluated using a limited number of modes (i.e. for $r < n$). This is shown, for example, in Fig. 4.20a where the cumulative UL-PFs evaluated for r=4 is equal to 1.004.

In addition, according to the LPF-based approach for truncation error analysis proposed in Section 4.2, the cumulative load participation factors (Fig. 4.20) related to one specific load (uniform or mass proportional load) can be compared with the respective RMS truncation errors (Fig. 4.18). By performing this comparison, the following observation is evident: by considering the structures with different mass irregularities (γ=1,2,3,4,5), if the cumulative load participation factors decrease, the RMS truncation errors increase (and vice versa). This is especially evident when considering the results obtained for the lower values of the parameter *r* (e.g. r=1,2 for the uniform load and r=1 for the mass proportional load). It is worth mentioning that the load participation factors reported in Fig. 4.20 (evaluated for the uniform and the mass proportional loads) are the cumulative LPFs of the modes included in the calculation of the truncated deflections. If, instead, these cumulative LPFs are evaluated for the modes not included in the computation of the truncated deflections, then a positive correlation between the errors and the cumulative LPFs is obtained. The trends of the cumulative load participations factors and the truncation errors obtained in this section for the specific cases of the UL and the MPL loads are thus in

agreement with the LPF-based approach for truncation error analysis proposed for a generic load in Section 4.2.

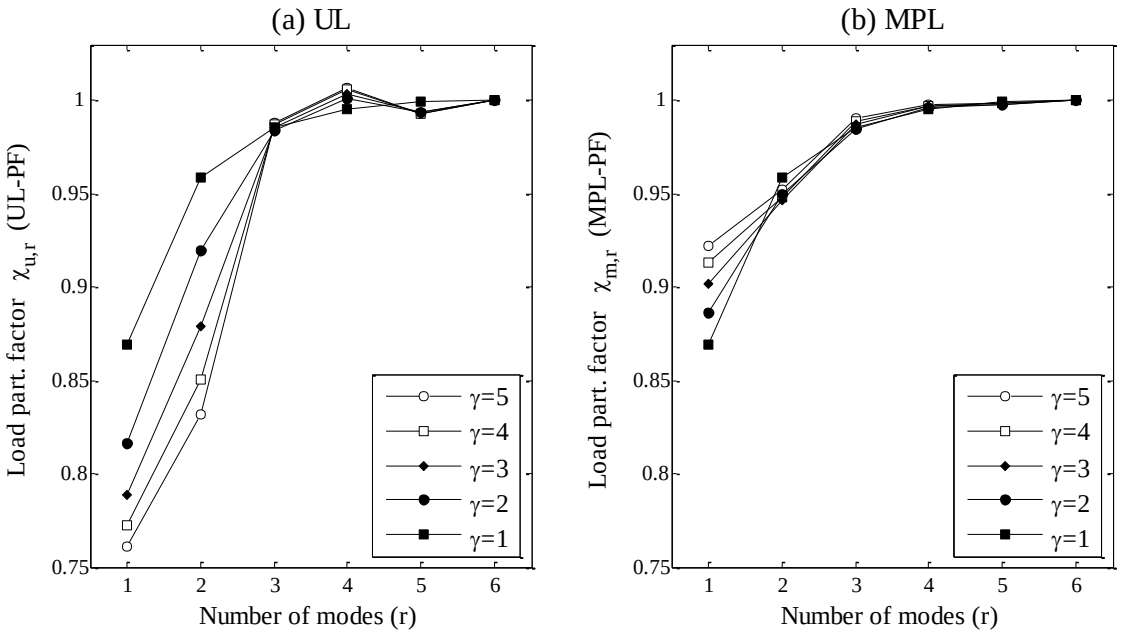

Figure 4.20. Cumulative load participation factors of the shear building structure (case 7) for different mass irregularities: (a) uniform load; (b) mass proportional load [Bernagozzi et al., 2017a].

The results of the truncation error analysis performed for all the structural configurations that were considered in the parametric study are presented in Table 4.3. This table shows the RMS truncation errors related to the modal flexibility-based deflections evaluated by applying both the uniform load and the mass proportional load and by considering the twelve configurations of the shear building structure reported in Table 4.2 (from 1 to 12) for a fixed mass irregularity (i.e. selecting γ=3). The results for each configuration are reported in each row of Table 4.3. On the contrary, each column of the table refers to calculations performed using a different subset of modes included in the evaluation of the deflections (i.e. each column refers to a different value of the parameter *r*). As already mentioned, the twelve configurations that were analyzed are characterized by different positions and different numbers of the imposed mass variations.

As shown in Table 4.3, in the 80% of the 72 analyzed cases (i.e. 12 configurations × 6 values of the parameter *r*) the mass proportional load provides RMS truncation errors that are lower than or equal to the errors related to the uniform load. Moreover, it is worth noting that for the analyzed configurations of the shear building structure, the errors related to the mass proportional load monotonically decrease if higher values of *r* are considered. On the contrary, this trend is not always evident for the uniform load.

Referring to the results obtained by including only the first mode of the structure in the calculations (i.e. r=1), it is evident in the table that the mass proportional load provides truncation errors that are lower than the errors related to the uniform load if the mass increments are applied at the upper DOFs of the shear building structure. This result was in fact obtained for the cases from 1 to 3 in the group of structures characterized by one imposed mass increment, for the cases 7 and 8 in the group of structures characterized by two imposed mass increments, and for the case 11 in the group of structures characterized by three imposed mass increments. In the other cases, where the mass modifications are applied at the lower DOFs of the structure, and again referring to results obtained using only the first mode (i.e. r=1), the uniform load provides truncation errors that are lower than the ones related to the mass proportional load. This result obtained in general for all the configurations when only the first mode is considered can be explained as follows: for a shear building structure the components of the first mode shape are higher at the upper DOFs, and this distribution is relevant in the determination of the cumulative load participation factor evaluated for the first mode (r=1). For the analyses presented in this section, the general expression of the load participation factor has to be specifically evaluated for the uniform and the mass proportional loads (Eqs. 4.66, 4.68, respectively). When evaluating such expressions for the first mode (r=1), the terms s_1 and Γ_1 are of course strongly dependent on the distribution of the components of the first mode shape, and, as already shown in this section, these terms in turn affect the truncation errors.

By considering in Table 4.3 the results obtained for higher values of the parameter *r* (i.e. by including more modes than the first one in the calculations) and especially for multiple variations of the masses (i.e. cases from 7 to 12), it is evident that the RMS truncation errors are reduced by applying the mass proportional load

instead of the uniform load. In the few cases where this reduction is not present, the errors related to the mass proportional load and the uniform load are comparable.

Case	Load *p*	RMS truncation errors on displacements $\varepsilon_{x,p,r}^{RMS}$ (%)					
		r=1	r=2	r=3	r=4	r=5	r=6
1	UL	13.73	1.43	1.12	0.15	0.12	0.00
	MPL	6.90	1.72	0.58	0.20	0.05	0.00
2	UL	10.66	1.76	0.56	0.74	0.01	0.00
	MPL	5.84	1.31	0.77	0.32	0.08	0.00
3	UL	7.30	5.45	0.45	0.34	0.36	0.00
	MPL	4.82	2.16	0.67	0.14	0.13	0.00
4	UL	4.21	4.68	0.86	0.11	0.11	0.00
	MPL	4.48	2.13	0.37	0.28	0.02	0.00
5	UL	2.00	2.17	2.34	0.68	0.08	0.00
	MPL	5.96	1.14	0.93	0.15	0.01	0.00
6	UL	3.25	1.13	0.45	0.16	0.05	0.00
	MPL	9.41	1.05	0.13	0.03	0.01	0.00
7	UL	11.41	5.82	0.82	0.54	0.37	0.00
	MPL	5.11	2.42	0.55	0.15	0.10	0.00
8	UL	7.30	4.56	0.74	0.75	0.09	0.00
	MPL	4.66	1.70	0.40	0.24	0.22	0.00
9	UL	3.81	3.14	2.12	1.47	0.36	0.00
	MPL	5.13	0.99	0.79	0.21	0.01	0.00
10	UL	2.06	2.55	0.90	0.94	0.12	0.00
	MPL	6.99	2.29	0.09	0.07	0.00	0.00
11	UL	8.13	2.60	2.22	1.39	1.19	0.00
	MPL	5.97	1.33	0.66	0.27	0.07	0.00
12	UL	5.43	1.99	1.10	0.92	0.96	0.00
	MPL	7.18	2.13	0.07	0.06	0.02	0.00

Table 4.3. RMS truncation errors on the displacements of the shear building structure – different structural configurations with a fixed mass irregularity (γ = 3) [Bernagozzi et al., 2017a]

Until this point of the section, the truncation error analyses and the comparison between the mass proportional load and the uniform load have been discussed by considering the errors that affect the displacement components of modal flexibility-based deflections of shear building structures. For such structures, however, it is also of interest to evaluate the truncation errors that affect the interstory drifts calculated from the modal flexibility-based deflections. According to the Positive Shear Inspection Load method for output-only vibration-based damage detection [Koo et al., 2010] and as extensively discussed in Chapter 3, the modal flexibility-based interstory drifts of shear building structures are, in fact, important parameters that can be used to detect and localize eventual damage in such structures (i.e. these parameters are considered as damage sensitive features). By considering that in general the evaluation of the modal flexibility-based interstory drifts from an experimental vibration test on a real structure is performed using a limited number of structural modes, it is evident that reducing the modal truncation effects on such parameters is a desirable result.

To attain this objective and in addition to the previous analyses related to the displacement components of the deflections, the truncation error analyses performed on the shear building to compare the mass proportional load with the uniform load were also executed by considering the errors that affect the modal flexibility-based interstory drifts. These analyses on the interstory drifts were performed by considering the same structural configurations with mass irregularities that were analyzed in the previous study on the displacement components (i.e. the twelve configurations described in Table 4.2 for different values of the parameter γ, with γ =1, 2, 3, 4, 5).

Referring to the calculations reported in the flow chart of Fig. 4.14, few additional steps were performed to evaluate the truncation errors on the modal flexibility-based interstory drifts. The interstory drifts were evaluated starting from the modal flexibility-based deflections of the shear building assembled using all the possible subsets of included modes ($r = 1 \dots n$). Then, the interstory drifts evaluated for a number of modes equal to $r = n$ were considered as the exact (or target) solutions and were used to calculate the errors that affect the truncated interstory drifts (evaluated for $r = 1 \dots n - 1$). To obtain the relative truncation errors on the interstory drifts, Eq. (4.2) was applied by considering in such equation the drifts instead of the

displacement components. Then, the root-mean-square value of the errors on the drifts related to the different stories of the structure was calculated.

The results of the truncation error study performed on the modal flexibility-based interstory drifts are presented using the same strategy adopted for the truncation error study performed on the displacement components of the deflections. This means that, again, the structural configuration no. 7 (Table 4.2) characterized by a mass irregularity that is imposed by selecting γ=3 is considered at first. Then, the same structural configuration (i.e. configuration 7) is used to show the results obtained for increasing amounts of the mass irregularities (i.e. for γ = 1, 2, 3, 4, 5). Finally, the results related to all the structural configurations from 1 to 12 of the shear building structure characterized by a fixed mass irregularity (i.e. for γ=3) are discussed.

The modal flexibility-based interstory drifts evaluated for configuration 7 and by considering a mass irregularity that is imposed with γ=3 are presented in Fig. 4.21. In particular, the drifts evaluated using the uniform load and the mass proportional load are reported in Fig. 4.21a, 4.21b, respectively. In both figures the results are shown for the different values assumed by the parameter r (i.e. the number of included modes). For each value of the parameter r, the drifts related to the different stories of the structure are points represented by the same marker and connected by linear segments to create the curves reported in the figure. First of all, it is worth noting that, referring to the uniform load (Fig. 4.21a) and to the exact or non-truncated solution (obtained using a number of modes equal to $r = n = 6$), the interstory drifts increase linearly from the upper to the lower stories of the structure. This trend is expected since the structure is characterized by a uniform distribution of the story stiffness, and the shear-force induced on the structure by the uniform load increases linearly from the upper to the lower stories of the building. In Fig. 4.21a it is also evident that the profiles of the interstory drifts obtained using a uniform load and calculated using only the first mode or only the first two modes (i.e. r=1 or r=2) show the major discrepancies with respect to the exact solution ($r = n = 6$). On the contrary, all the profiles of the interstory drifts obtained using a mass proportional load and evaluated using the different subsets of included modes (with $r < n$) are close to the exact solution obtained for $r = n = 6$, as evident in Fig. 4.21b.

The percent truncation errors on the truncated values of the modal flexibility-based interstory drifts of each story of the structure were evaluated with respect to the target solutions (obtained for $r=n$) and the results are reported, in terms of absolute values, in Fig. 4.22. In particular, the truncation errors related to the uniform load and the mass proportional load are shown in Fig. 4.22a, 4.22b respectively. The results obtained using both the uniform load and the mass proportional load show that the errors on the interstory drifts are higher at the upper stories of the shear building structure. This is due to the fact that, for the considered structural configuration, the interstory drifts at the upper stories are lower than the drifts evaluated at the bottom of the structure. The modal truncation effects have thus a significant impact on the modal flexibility-based interstory drifts at the upper stories of the structure. As also shown in Fig. 4.22, the modal truncation errors on the drifts calculated by applying the mass proportional load are in general lower than the errors on the drifts evaluated using the uniform load. This is evident by considering the profiles of the interstory drifts evaluated for the cases r = 1,2,3,4, and especially by considering the drifts related to the upper stories of the structure.

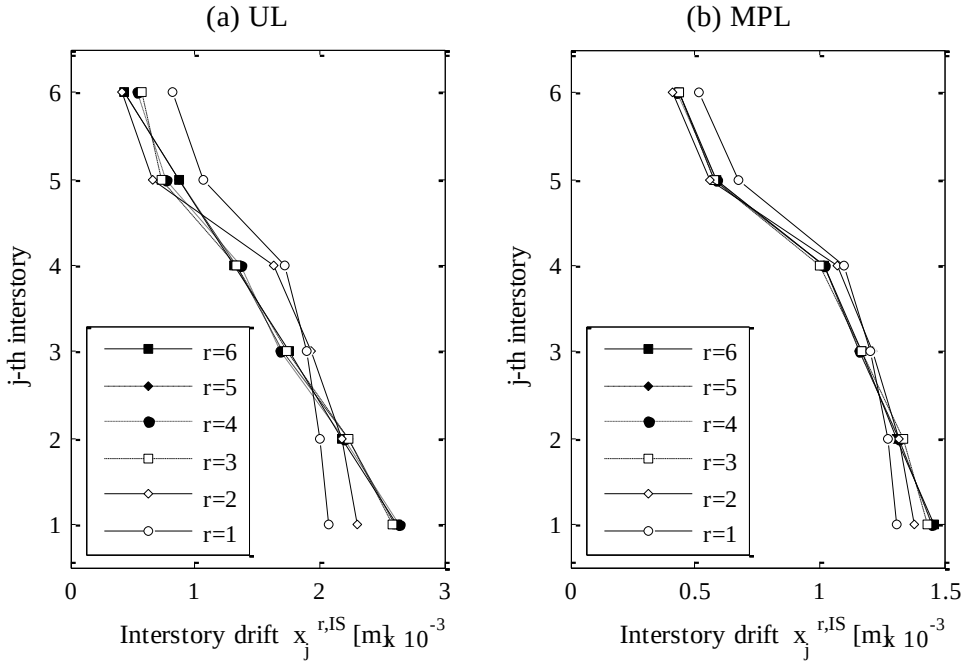

Figure 4.21. Interstory drifts evaluated on modal flexibility-based deflections of the shear building structure (case 7; γ=3): (a) uniform load; (b) mass proportional load

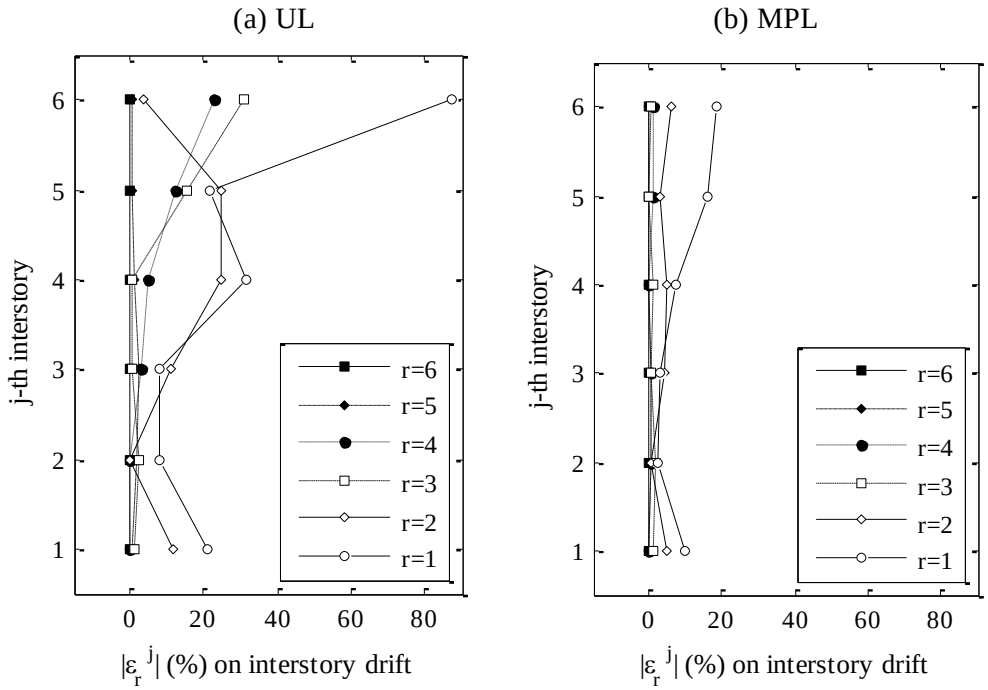

Figure 4.22. Truncation errors on the interstory drifts of the shear building structure (case 7; γ=3): (a) uniform load; (b) mass proportional load.

The root-mean-square (RMS) truncation errors on the interstory drifts evaluated for configuration 7 of the shear building structure and by considering increasing amounts of mass irregularities (i.e. γ =1, 2, 3, 4, 5) are presented in Fig. 4.23. By adopting the same representation used in Fig. 4.18 (which is, on the contrary, related to the RMS errors on the displacement components), the RMS errors on the interstory drifts are plotted as a function of the parameter *r* (reported on the x axis) and by comparing the uniform load (Fig. 4.23a) with the mass proportional load (Fig. 4.23b). Each of the different curves reported in the figure is related to one value of the parameter γ (i.e. to a different amount of the mass irregularity). Fig. 4.23 shows that, for all the analyzed cases, the RMS errors on the interstory drifts evaluated using the mass proportional load (Fig. 4.23b) are lower than or equal to the errors related to the uniform load (Fig. 4.23a). This is evident if one considers the curve of the RMS errors obtained for γ = 1 as a reference curve to compare the two graphs (as already mentioned, for γ = 1 a uniform mass distribution is considered, thus the errors related to the mass proportional load are equal to the errors related to the uniform load). Using this strategy, it is evident in Fig. 4.23 that all the RMS errors related to the uniform

load and obtained for values of the coefficient γ higher than one are located above the curve γ =1 (Fig. 4.23a). On the contrary, all the RMS errors related to the mass proportional load and obtained for values of the coefficient γ higher than one are located below the curve γ =1.

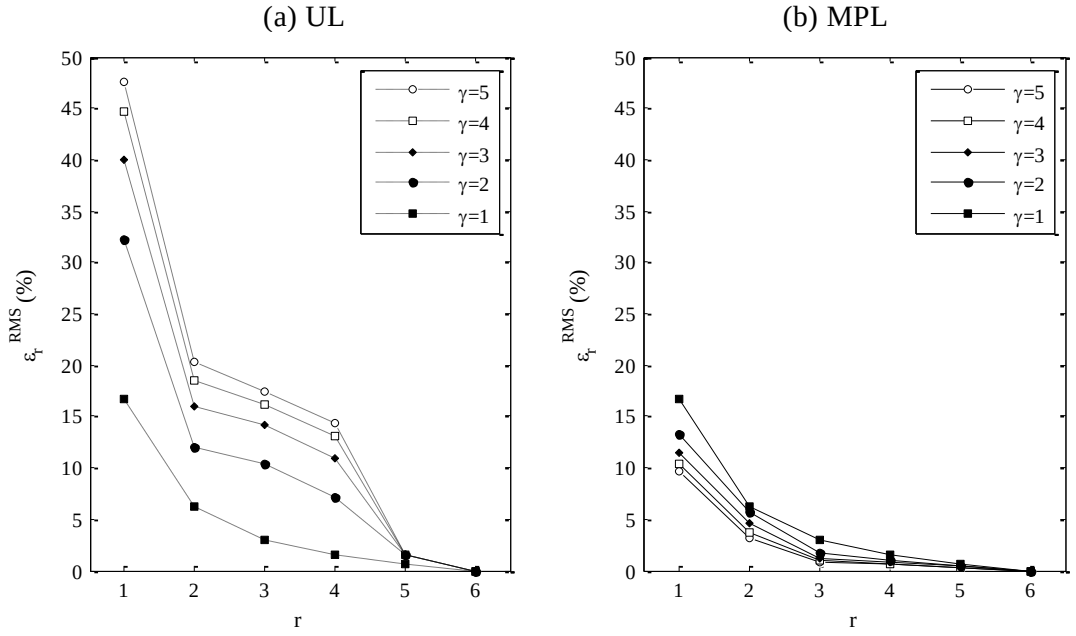

Figure 4.23. RMS truncation errors on the interstory drifts of the shear building structure (case 7) for different mass irregularities: (a) uniform load; (b) mass proportional load

The RMS truncation errors on the interstory drifts evaluated by applying both for the uniform and the mass proportional loads to all the structural configurations of the shear building reported in Table 4.2 (i.e. configurations from 1 to 12) and by considering for such configurations a mass irregularity modeled using γ=3 are shown in Table 4.4. As evident in this table, for the majority of the analyzed cases (i.e. 87.5% of the 72 analyzed cases, where the total number of cases is calculated as follows: 12 configurations × 6 values of the parameter *r*), the RMS truncation errors on the drifts calculated by applying the mass proportional load are lower than or equal to the errors related to the uniform load.

Referring to the RMS truncation errors on the displacement components of the deflections (Table 4.3) obtained by including only the first mode of the structure in the calculations (i.e. *r*=1), the results showed that the errors related to the mass

proportional load are lower than the errors related to the uniform load if the mass increments are applied at the upper DOFs of the shear building. On the contrary, when the mass increments are applied at the lower DOFs of the structure, and again considering only the first mode (i.e. r=1), the truncation errors related to the uniform load are lower than the ones related to the mass proportional load. The same results were also found by analyzing the RMS truncation errors on the drifts evaluated using only the first mode (i.e. r=1), as shown in the third column of Table 4.4. Referring to the interstory drifts, the above-mentioned observations are valid for all the configurations, except for configuration 12 (i.e. a configuration characterized by mass irregularities applied at the lower stories of the structure) for which the errors related to the uniform and the mass proportional loads are comparable. Moreover, referring again to the analyses on the displacement components of the deflections (Table 4.3) and by considering the RMS truncation errors obtained for higher values of the parameter r (i.e. for $r > 1$), it was found that the errors related to the mass proportional load are in general lower than the errors related to the uniform load. This result was obtained also for the RMS truncation errors related to the modal flexibility-based interstory drifts, as shown in Table 4.4.

Case	Load *p*	RMS truncation errors on interstory drifts $\varepsilon_{d,p,r}^{RMS}$ (%)					
		r=1	r=2	r=3	r=4	r=5	r=6
1	UL	60.58	5.98	7.73	0.86	1.05	0.00
	MPL	12.31	3.68	1.57	0.74	0.31	0.00
2	UL	27.82	24.29	7.87	3.64	0.04	0.00
	MPL	11.60	4.59	5.28	1.07	0.38	0.00
3	UL	17.31	23.49	5.81	5.46	1.51	0.00
	MPL	12.57	9.61	1.79	0.94	0.52	0.00
4	UL	10.66	9.18	11.15	2.54	2.30	0.00
	MPL	16.28	4.90	2.76	0.84	0.62	0.00
5	UL	5.74	6.20	4.42	7.08	1.50	0.00
	MPL	22.04	3.74	2.15	2.29	0.12	0.00
6	UL	12.26	4.29	3.29	1.65	0.67	0.00
	MPL	24.67	7.39	1.40	0.37	0.10	0.00
7	UL	40.06	15.91	14.11	10.88	1.52	0.00
	MPL	11.44	4.52	1.20	0.83	0.37	0.00
8	UL	20.74	21.72	9.71	9.48	0.27	0.00
	MPL	13.30	3.45	5.85	0.74	0.58	0.00
9	UL	16.43	18.20	7.03	6.91	9.43	0.00
	MPL	17.07	5.73	1.45	1.49	0.52	0.00
10	UL	10.64	8.52	6.67	4.12	2.90	0.00
	MPL	22.10	11.73	0.81	0.42	0.04	0.00
11	UL	33.84	11.56	13.24	10.40	12.26	0.00
	MPL	15.57	4.88	1.11	1.18	0.58	0.00
12	UL	19.69	20.63	18.34	8.46	8.04	0.00
	MPL	17.79	7.25	0.85	0.33	0.24	0.00

Table 4.4. RMS truncation errors on the interstory drifts of the shear building structure – different structural configurations with a fixed mass irregularity ($\gamma = 3$).

Chapter 5

Damage detection on 3D building structures using modal flexibility (MF) based deflections

This chapter presents the research investigations that were carried out in an attempt to extend the Positive Shear Inspection Load (PSIL) method for damage detection [Koo et al., 2010; Koo et al., 2011; Sung et al., 2012], which as shown in Chapter 3 was originally formulated to be applied on building structures that can be modeled as plane structures, to the case of more complex building structures[1]. As already mentioned in Section 1.3 of Chapter 1 (where the objectives of the thesis are outlined), this problem represents the second main problem that is addressed in the thesis.

As already discussed in Chapter 1, the authors that proposed the Positive Shear Inspection Load (PSIL) method verified the methodology by performing vibration tests on frame building structures with symmetric configurations (both in the pristine and in the damaged states). These vibration tests were performed using uniaxial

[1] Some of the contents presented in the first part of this chapter (Section 5.1) are published in a paper co-authored with Prof. Ventura, Dr. Allahdadian, Dr. Kaya, Dr. Landi, and Prof. Diotallevi. This paper is published in the journal Procedia Engineering, and it was also presented at the X International conference on Structural Dynamics – EURODYN, 2017, Rome (Italy), 10-13 Sept. 2017.

Bernagozzi G, Ventura CE, Allahdadian S, Kaya Y, Landi L, Diotallevi PP. Application of modal flexibility-based deflections for damage diagnosis of a steel frame structure. In: Vestroni F, Gattulli V, Romeo F (editors), *Procedia Engineering, X International Conference on Structural Dynamics, EURODYN 2017*. Volume 199, Pages 2026-2033. DOI: 10.1016/j.proeng.2017.09.468

excitations in shaking table tests [Koo et al., 2010; Koo et al., 2011] or shaker tests [Sung et al., 2012]. The types of structures that are considered in this chapter are simple rectangular "box type" 3D building structures, characterized either by plan-symmetric configurations or by plan-asymmetric configurations. Modifications are introduced in the original formulation of the Positive Shear Inspection Load (PSIL) method to deal with such structures. It is worth noting that in the present chapter and for the sake of brevity, these structures will be indicated as 3D building structures. As already mentioned in Chapter 1, it is of interest for practical applications to have a damage detection technique that can be applied on 3D building structures. On one side, in fact, real-life building structures can be characterized, for example, by a generic distribution of the stiffness and the mass of the different stories. On the other side, even if the structure considered in the damage detection process as the undamaged structure is plan symmetric (i.e. the structure can be theoretically modeled as a plane structure), the structure can then experience damage (e.g. a stiffness reduction) in a generic position. In general, the damaged structure can thus be a plan asymmetric structure, which can not be modeled as a plane structure.

Experimental tests were planned and performed to investigate the above-mentioned damage detection problem (i.e. the problem of dealing with 3D building structures). In particular, a steel frame structure was tested under ambient vibrations by considering various structural configurations with imposed stiffness reductions. These stiffness reductions were imposed in generic positions of the considered 3D structure to obtain structural configurations that are characterized by either plan-symmetric or plan-asymmetric distributions of the story stiffness. This structure is located at the Earthquake Engineering Research Facility of the University of British Columbia (Vancouver, Canada), and the tests were performed in September 2016[2].

[2] The ambient vibration tests were performed in September 2016 during a study and research period that the writer spent at the University of British Columbia (Vancouver, Canada) under the supervision of Prof. Carlos Ventura. The writer had the opportunity to be included into an experimental research program that was on going at that time and that was carried out by other members of the research group of Prof. Ventura. The writer would like to thank Prof. Ventura for his guidance during the study period, his suggestions, and for the above-mentioned great opportunity. Moreover, the writer would like to thank Dr. Saeid Allahadadian (which was the reference person for the above-mentioned experimental program) for his collaboration and for his great support. The writer would also like to thank Dr. Yuxin Pan for his assistance during the tests.

Some observations must be made on the experimental tests that were performed to apply the Positive Shear Inspection Load method on a 3D building structure and, in general, on the analyses presented in this chapter. First of all, the structure that was considered in the experimental tests is the same structure that was tested on August 2002 by the IASC-ASCE Task Group in the context of the benchmark studies for Structural Health Monitoring [Dyke et al., 2003; Ventura et al., 2003; Dyke, 2011] (see Chapter 4).

Secondly, as already mentioned in Chapter 1, the application of a technique which is almost equivalent to the PSIL method on the data of the above-mentioned IASC-ASCE benchmark studies for SHM was found in the work by [Zhang et al., 2013]. In this last work a technique based on the estimation of modal flexibility-based deflections, which as already mentioned is almost equivalent to the PSIL method for damage detection, is thus applied on a 3D building structure. There are, however, some differences between the work by [Zhang et al., 2013] and the analyses presented in this chapter that must be highlighted:

(1) in the work by [Zhang et al., 2013] the analyses on the 3D building structure were performed by estimating (from the vibration data) modal flexibility matrices that describe the behavior of the structure only in one direction, and by repeating the analyses for the two prevalent directions of the structure. Differently from the above-mentioned work, in the present chapter the calculations are performed on modal flexibility matrices that describe the behavior of the whole 3D structure (by considering simultaneously the behavior of the structure in the two prevalent directions and the torsional behavior).

(2) in the work by [Zhang et al., 2013] the analyses were performed to localize the damage on the 3D building structure. In the present chapter the calculations are carried out not only to the step of the damage localization but also to the step of the quantification of the damage (adopting criteria that are similar to the ones adopted in the original formulation of the PSIL method [Koo et al., 2010]).

(3) as already mentioned in Chapter 1, the tests performed by the IASC-ASCE Task Group in August 2002 on the steel frame structure were executed using different types of excitations (shaker, impact hammer, and ambient vibrations). The damage detection analyses reported in the work by [Zhang et al., 2013] were carried out using

the data of the impact hammer tests executed in the context of the benchmark studies for SHM and using an input-output modal identification technique. Differently from the above-mentioned work, in the present chapter the calculations are performed starting from ambient vibration data and using an output-only modal identification technique (ambient vibrations, in fact, are the excitations considered in the experimental tests performed on the structure in September 2016).

5.1 Application of the PSIL method to "box type" 3D building structures

5.1.1 Methodology and analytical formulation

This section presents the methodology and the analytical formulation that was adopted to apply the Positive Shear Inspection Load method for damage detection on a 3D building structure that was tested under ambient vibrations. In particular, the methodology presented in this section was formulated starting from the original formulation of the Positive Shear Inspection Load (PSIL) method. The original formulation of the method was adapted and extended to deal with 3D building structures.

As already mentioned, the types of structures that are considered in this chapter are simple rectangular "box type" 3D building structures, and the methodology presented in this section can be applied under two main assumptions: 1) the n-story building structure can be reasonably modeled as a $3n$-DOF shear-type 3D building structure, and each floor of the building structure has a rigid-body in-plane behavior; 2) an estimate of the system mass matrix of the structure is available. It is worth noting that this last assumption is the same assumption that is made in the original formulation of the PSIL method [Koo et al., 2010].

In the original formulation of the PSIL method, as shown in Chapter 3, acceleration measurements have to be available at all the stories of the structure. This requirement has to be also guaranteed in the methodology presented in this section. Of course, since the investigated approach is an attempt to generalize the original method from the case of plane building structures to 3D building structures, more acceleration measurements are needed for each story of the structure.

Referring to simple rectangular "box type" 3D building structures and as already mentioned in Chapter 2, only the two horizontal displacements and the rotations (around the vertical axis) of the mode shapes of the building are usually estimated when these structures are subjected to ambient vibration tests, while the vertical modal displacements are usually neglected [Brincker & Ventura, 2015]. Under the assumption of having floors with a rigid-body in-plane behavior, this operation can be performed by considering at least three measurements of horizontal accelerations (in different directions and locations) at each floor of the building structure. In this way, the dynamic behavior of the structure can be captured by estimating mode shape vectors that are characterized by horizontal components in two directions and rotational components (Fig. 5.1).

According to typical measurement plans for simple rectangular "box type" buildings, the sensors can be located in the corners (or in general on the perimeter) of each floor of the building. To obtain measurements at all the stories of the building, if one performs the ambient vibration test by acquiring only one data set, the number of the sensors should be equal to three times the number of the stories. However, as already mentioned in Chapter 2, in case of ambient vibrations multiple data sets can be also acquired by adopting both reference and roving sensors [Brincker & Ventura, 2015] (i.e. fixed and moving sensors). In this last situation, the number of the sensors can thus be lower than three times the number of the stories.

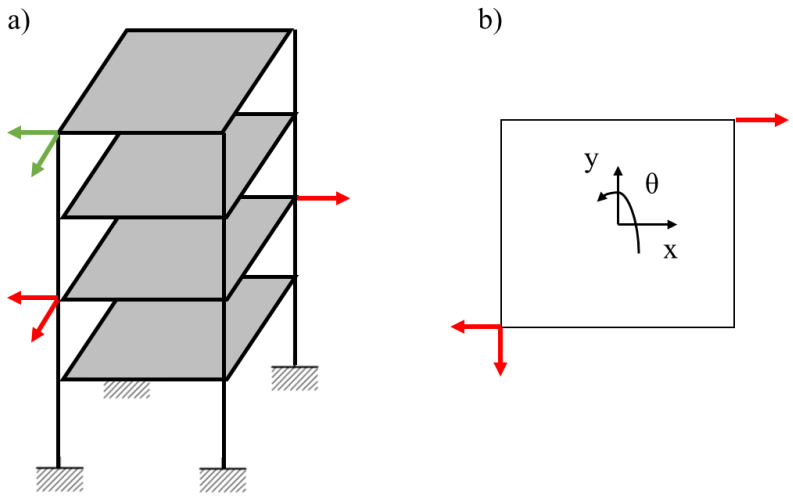

Figure 5.1. Schematic overview of a "box type" 3D building structure with a generic sensor layout.

The steps that were performed to apply the Positive Shear Inspection Load method for damage detection on a 3D building structure tested under ambient vibrations are the following:

1) Ambient vibration tests were performed on the 3D building structure, and the measurements of the output acceleration responses due to ambient inputs were acquired both for the undamaged and the possibly damaged structural configurations. A detailed description of the considered structural configurations and of the experimental test setup will be presented in next section. The acquired data were then analyzed according to the other steps described in this section. Before going further, it is worth noting that the calculations described at the steps from no. 2 to no. 5 were performed on the data related to both the undamaged and the possibly damaged structural configurations.

2) An operation modal analysis technique was applied on the recorded ambient vibration data to obtain the modal parameters of the structure (for the analyses presented in this chapter the Enhanced Frequency Domain Decomposition method [Brincker, Ventura & Andersen, 2001] was applied, as shown in next sections). After having extracted the modal parameters using the OMA technique, the components of the mode shapes were defined with reference to the geometric center of each story of the 3D building structure. It is worth noting that for the considered structures (i.e. simple rectangular "box type" 3D building structures) the geometric center of the structure can be in general assumed as the center of mass of the structure. The components of the mode shapes were collected in $3n \times 1$ vectors defined as follows

$$\boldsymbol{\psi_i} = \begin{pmatrix} \{\boldsymbol{\psi_{x,i}}\} \\ \{\boldsymbol{\psi_{y,i}}\} \\ \{\boldsymbol{\psi_{\theta,i}}\} \end{pmatrix}_{3nx1} = \begin{pmatrix} \psi_{x,i,n} \\ \vdots \\ \psi_{x,i,1} \\ \\ \psi_{y,i,n} \\ \vdots \\ \psi_{y,i,1} \\ \\ \psi_{\theta,i,n} \\ \vdots \\ \psi_{\theta,i,1} \end{pmatrix} \tag{5.1}$$

where *n* is the number of the stories of the 3D building structure. In the mode shape vector reported in Eq. (5.1) there are *n* components that are related to the x direction, *n* components that are related to the y direction, and *n* components that are rotational components of the mode shape (Fig. 5.1).

3) Starting from the identified modal parameters of the structure (i.e. natural frequencies and mode shapes), the modal flexibility matrices $\boldsymbol{F_r}$ of the 3D building structure were assembled as follows

$$\boldsymbol{F}_{\boldsymbol{r}\,3n\times 3n} = \boldsymbol{\Psi_r}\,\boldsymbol{\Lambda_r^{-1}}(\boldsymbol{\Psi_r^T}\,\mathbf{M}\,\boldsymbol{\Psi_r})^{-1}\,\boldsymbol{\Psi_r^T} \tag{5.2}$$

where $\boldsymbol{\Psi}_{\boldsymbol{r}\ 3n\times r}$ is the arbitrarily-scaled mode shape matrix, $\boldsymbol{\Lambda}_{\boldsymbol{r}\,r\times r}$ is a matrix with the square of the natural circular frequencies ω_i^2 on the main diagonal, $\boldsymbol{M}_{3n\times 3n}$ is the mass matrix of the structure, and *r* is the number of the modes included in the calculations. As already mentioned, the mass matrix of the structure was estimated a-priori and used to normalize the mode shapes extracted from the data using the output-only modal identification (this strategy is the same strategy adopted in the original formulation of the PSIL method [Koo et al., 2010]).

4) The operation of evaluating the modal flexibility-based deflections of the 3D building structure was performed by considering two different and separate analyses, one for each of the two prevalent directions of the structure (i.e. the x direction and the y direction, Fig. 5.2). In the first of the two above-mentioned analyses, inspection loads were applied in the x direction of the structure, then in the other analysis inspection loads were applied in the y direction. The inspection loads that were adopted are indicated as $\boldsymbol{p_x}$ and $\boldsymbol{p_y}$, and these loads are defined as follows

$$\boldsymbol{p_x} = \begin{pmatrix}\{\mathbf{1}\}\\ \{\mathbf{0}\}\\ \{\mathbf{0}\}\end{pmatrix}_{3nx1} = \begin{pmatrix}1\\ \vdots\\ 1\\ \\ 0\\ \vdots\\ 0\\ \\ 0\\ \vdots\\ 0\end{pmatrix} \quad ; \quad \boldsymbol{p_y} = \begin{pmatrix}\{\mathbf{0}\}\\ \{\mathbf{1}\}\\ \{\mathbf{0}\}\end{pmatrix}_{3nx1} = \begin{pmatrix}0\\ \vdots\\ 0\\ \\ 1\\ \vdots\\ 1\\ \\ 0\\ \vdots\\ 0\end{pmatrix} \tag{5.3}$$

It is worth noting that such loads $\boldsymbol{p_x}$ and $\boldsymbol{p_y}$ can be considered as uniform loads that are applied in the x and the y directions of the structure, respectively. The modal flexibility-based deflections of the structure due to the loads $\boldsymbol{p_x}$ and $\boldsymbol{p_y}$ were then calculated as follows

$$\boldsymbol{x_x} = \boldsymbol{F_r}\,\boldsymbol{p_x} \tag{5.4}$$

$$\boldsymbol{x_y} = \boldsymbol{F_r}\,\boldsymbol{p_y} \tag{5.5}$$

where $\boldsymbol{x_x}$ and $\boldsymbol{x_y}$ are $3n \times 1$ vectors that contain the components of the modal flexibility-based deflections. It is worth noting that, according to the adopted formulation, the components of the MF-based deflections were evaluated with reference to the geometric center of the structure (similarly to the components of the mode shapes).

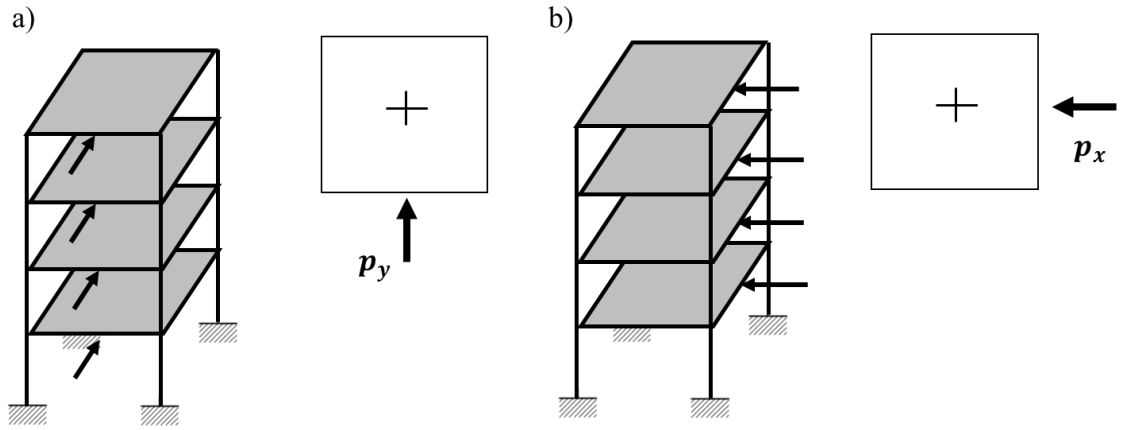

Figure 5.2. Application of PSIL loads in the prevalent directions of a "box type" 3D building structure: a) PSIL load in y direction; b) PSIL load in x direction.

5) After having evaluated the modal flexibility-based deflections of the structure due to the inspection loads in the x and the y directions, the interstory drifts were calculated by considering, respectively, the components of the deflections in the x and the y directions

$$\boldsymbol{d_x} = \boldsymbol{T_x}\,\boldsymbol{x_x} \tag{5.6}$$

$$\boldsymbol{d_y} = \boldsymbol{T_y}\,\boldsymbol{x_y} \tag{5.7}$$

where $\boldsymbol{d_x}$ and $\boldsymbol{d_y}$ are $n \times 1$ vectors of the interstory drifts. The vector $\boldsymbol{d_x}$ (or $\boldsymbol{d_y}$) contains the interstory drifts related to the deflection of the structure due to the inspection load $\boldsymbol{p_x}$ (or $\boldsymbol{p_y}$), and such interstory drifts are evaluated in the geometric centre of the structure in x (or y) direction. The matrices $\boldsymbol{T_x}$ and $\boldsymbol{T_y}$ are two $n \times 3n$ transformation matrices defined as follows

$$\boldsymbol{T_x} = [\boldsymbol{T} \quad \boldsymbol{0} \quad \boldsymbol{0}] = \begin{bmatrix} 1 & -1 & 0 & \cdots & 0 & 0 & \cdots & \cdots & \cdots & 0 & 0 & \cdots & \cdots & \cdots & 0 \\ 0 & 1 & -1 & \ddots & \vdots & \vdots & \ddots & \ddots & \ddots & \vdots & \vdots & \ddots & \ddots & \ddots & \vdots \\ \vdots & \ddots & \ddots & \ddots & 0 & \vdots & \ddots & \ddots & \ddots & \vdots & \vdots & \ddots & \ddots & \ddots & \vdots \\ \vdots & \ddots & \ddots & \ddots & -1 & \vdots & \ddots & \ddots & \ddots & \vdots & \vdots & \ddots & \ddots & \ddots & \vdots \\ 0 & \cdots & \cdots & 0 & 1 & 0 & \cdots & \cdots & \cdots & 0 & 0 & \cdots & \cdots & \cdots & 0 \end{bmatrix} \tag{5.8}$$

$$\boldsymbol{T_y} = [\boldsymbol{0} \quad \boldsymbol{T} \quad \boldsymbol{0}] = \begin{bmatrix} 0 & \cdots & \cdots & \cdots & 0 & 1 & -1 & 0 & \cdots & 0 & 0 & \cdots & \cdots & \cdots & 0 \\ \vdots & \ddots & \ddots & \ddots & \vdots & 0 & 1 & -1 & \ddots & \vdots & \vdots & \ddots & \ddots & \ddots & \vdots \\ \vdots & \ddots & \ddots & \ddots & \vdots & \vdots & \ddots & \ddots & \ddots & 0 & \vdots & \ddots & \ddots & \ddots & \vdots \\ \vdots & \ddots & \ddots & \ddots & \vdots & \vdots & \ddots & \ddots & \ddots & -1 & \vdots & \ddots & \ddots & \ddots & \vdots \\ 0 & \cdots & \cdots & \cdots & 0 & 0 & \cdots & \cdots & 0 & 1 & 0 & \cdots & \cdots & \cdots & 0 \end{bmatrix} \tag{5.9}$$

where $\boldsymbol{T}$ is the $n \times n$ transformation matrix already defined in Chapter 3

$$\boldsymbol{T} = \begin{bmatrix} 1 & -1 & 0 & \cdots & 0 \\ 0 & 1 & -1 & \ddots & \vdots \\ \vdots & \ddots & \ddots & \ddots & 0 \\ \vdots & \ddots & \ddots & \ddots & -1 \\ 0 & \cdots & \cdots & 0 & 1 \end{bmatrix} \tag{5.10}$$

6) As already mentioned, the calculations described in the steps from no. 2 to no. 5 were performed both for the undamaged and the possibly damaged structures. Then, the vectors of the interstory drifts $\boldsymbol{d_x}$ and $\boldsymbol{d_y}$ were used to localize and quantity the damage by adopting the same criteria of the original formulation of the Positive Shear Inspection Load method (i.e. the z-index for damage localization and the damage severity α_s for damage quantification). These two criteria have been already described in Chapter 3, where the original formulation of the PSIL method is presented by considering a plane shear building structure.

Referring to the generic *j*-th story of the 3D building structure, two values of the z index were thus evaluated. One was evaluated starting from the interstory drifts contained in the vector $\boldsymbol{d_x}$, the other was evaluated using the interstory drifts contained in the vector $\boldsymbol{d_y}$. Of course, to evaluate the z index the interstory drifts related to the possibly damaged structure (inspection phase) were compared with respect to the drifts related to the undamaged structure (baseline state)

$$z_{x,j} = \frac{d_{I,x,j} - \bar{d}_{B,x,j}}{s(d_{B,x,j})} \tag{5.11}$$

$$z_{y,j} = \frac{d_{I,y,j} - \bar{d}_{B,y,j}}{s(d_{B,y,j})} \tag{5.12}$$

According to the original formulation of the PSIL method described in Chapter 3, the values of the z index related to the x or the y directions were compared with respect to the threshold value (z^{TH}). For each story of the 3D building structure two statistical tests were thus performed to classify the story as healthy or damaged and to identify which prevalent direction of the structure has been affected by the damage (i.e. the x direction, the y direction, or both). It is worth mentioning that for the analyses presented in this chapter a slight modification was introduced in the original procedure used for performing the statistical z-index test according to the PSIL method. As discussed and suggested in [Koo et al., 2010; Sung et al., 2012], the value of the threshold is a user choice, and a threshold $z^{TH} = 2.5$ was selected in the above-mentioned works. However, as also suggested in [Koo et al., 2010], higher values of the z-index threshold decrease the probability of detecting false positives. On the contrary, lower values of the threshold decrease the probability of detecting false negatives. In general, there is thus always a trade off in the detection of false positives and false negatives. With reference to the mentioned indications, a threshold equal to $z^{TH} = 3$ was considered in the analyses presented in this chapter.

In the same way, two values of the damage severity α_s were evaluated for the generic *j*-th story of the 3D building structure. Again, the damage severity in x direction was evaluated starting from the interstory drifts contained in the vector $\boldsymbol{d_x}$, while the damage severity in y direction was evaluated using the interstory drifts contained in the vector $\boldsymbol{d_y}$

$$\alpha_{s,x,j} = \frac{d_{I,x,j} - \bar{d}_{B,x,j}}{d_{I,x,j}} \tag{5.13}$$

$$\alpha_{s,y,j} = \frac{d_{I,y,j} - \bar{d}_{B,y,j}}{d_{I,y,j}} \tag{5.14}$$

A general observation on the calculations presented in this section is the following. The equations of the original formulation of the Positive Shear Inspection Load method were modified in an attempt to have an approach that can deal with a

3D shear building structure characterized by 3*n* DOFs (instead of a plane shear building structure characterized by *n* DOFs). The equations presented in this section can be considered as the multidimensional version of the original equations of the PSIL method, but substantial modifications were not introduced in the approach. In fact, the inspection loads considered in this section are basically the same inspection loads applied in the original formulation of the PSIL method (i.e. translational uniform loads). The only differences between the two approaches are the following: (1) in this section modal flexibility matrices with dimensions $3n \times 3n$ are considered instead of matrices with dimensions $n \times n$ (i.e. the ones considered in the original PSIL method); (2) two separate analyses are performed by considering the two prevalent directions of the 3D building structure (instead of considering only one direction, according to the original PSIL method). Of course, if the structure has a plan-symmetric configuration and can be modeled as a plane structure, the methodology presented in this section is theoretically equivalent to the original formulation of the PSIL method.

5.1.2 Experimental application on a 3D steel frame structure tested under ambient vibrations

5.1.2.1 Description of the ambient vibration tests

The damage detection methodology that is outlined in previous section was applied on a steel frame structure that was tested under ambient vibrations. The structure is located outside the Earthquake Engineering Research Facility (EERF) of the University of British Columbia (UBC), Vancouver, Canada, and the ambient vibration tests were performed in September 2016. As already mentioned at the beginning of this chapter, this structure is the same structure that was tested by the IASC-ASCE Task Group for Structural Health Monitoring [Dyke et al., 2003; Ventura et al., 2003; Dyke, 2011] in August 2002 using different types of excitations (including ambient vibrations). This means that the structure considered in this chapter to perform the damage detection analysis is basically the same structure that has been already considered in Chapter 4 to verify the proposed approach for modal truncation error

analysis (this verification was, in fact, conducted using the data of the above-mentioned benchmark study).

This section presents a description of the geometry of the structure and the description of the ambient vibration tests that were performed in September 2016. It is worth noting that this section presents a description of the geometry of the structure that is more detailed with respect to the description provided in Chapter 4. In Chapter 4, in fact, only a brief description of the structure is reported, and this description was formulated on the basis of the information that was made available to the community by the IASC-ASCE Task Group for SHM [Dyke et al., 2011]. On the contrary, the description of the structure reported in this chapter and related to the tests performed in September 2016 was outlined on the basis of a geometric survey that was performed on the structure. Other information about the geometry of the structure was taken from the following references [Dyke et al., 2001; Kharrazi & Ventura, 2001; Ventura et al., 2003; Turek & Ventura, 2005]. Some differences between the structure that was tested in August 2002 by the IASC-ASCE Task Group for SHM and the structure that was tested in September 2016 are also highlighted in this section. Of course, the two tests were performed using different experimental setups.

A photo of the steel frame structure used in this chapter to perform the damage detection analysis is reported in Fig 5.3. The structure is a one-third scale four-story two-bay by two-bay structure. The interstory height of the building is equal to 0.9 m, and the bay width is 1.25 m (as reported in the structural drawings reported in Fig. 5.4).

The members of the frame are hot rolled grade 300W steel with a nominal yield stress equal to 300 MPa. The dimensions of the cross sections of the structural members are reported in Fig. 5.5 and in Table 5.1. The columns and the beams of the structure are double T sections (B100×9 and S75×11, respectively). Some floor braces are also positioned at each floor of the structure (Fig. 5.4a), and these elements are characterized by box sections (HSS 51×51×6.4). It is worth noting that the principal directions of the structure can be defined with reference to the orientation of the column sections (as reported in Fig. 5.4a): the X axis is aligned to the weak direction of the frame (West-East direction), while the Y axis is aligned to the strong direction

of the structure (North-South direction). All the members of the frame are connected using bolted connections, and the bolts of the structure are A325 high strength bolts for structural steel joints.

Figure 5.3. Steel frame structure (EERF laboratory, UBC) [Bernagozzi et al., 2017 b]

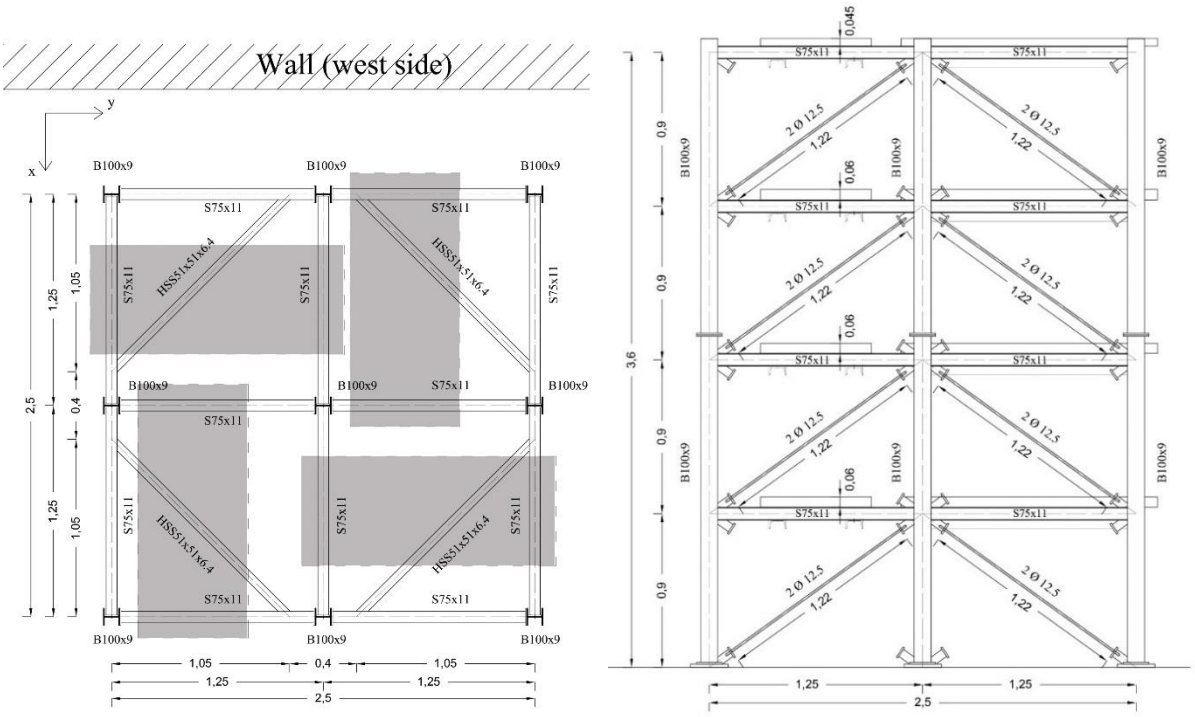

a) b)

Figure 5.4. Geometry of the steel frame structure: a) plan view; b) lateral view of the south face

As shown in Fig. 5.4b, diagonal wall braces are present in each bay of the structure. These elements can be easily removed, and this is a characteristic that makes the structure absolutely suitable for performing a damage detection analysis. In the experimental tests, in fact, damaged configurations were created by removing one or more diagonal elements from the wall bracing system of the structure (in other words, stiffness reductions were thus imposed on the structure). A detailed description of all the configurations that were tested is provided later in this section. The wall bracing system of the structure is composed as follows: in the portion of the structure that can be identified by considering a generic story and a generic bay two threaded tie-rods with a diameter equal to 12.5 mm are present. Such elements are pre-tensioned elements, and in the experimental test the tie-rods were put in tension using an adjustable-click-type torque wrench (whose head width is equal to ¾ inches): the tightening torque selected to close the bolts positioned between the wall braces and the rest of the structure was 22.5 N m (equal to 200 LB IN).

Four steel plates are located at each level of the structure (as reported in Fig. 5.4a), and these plates are positioned on the structure to make the floor masses reasonably realistic. At the top floor (i.e. the 4th floor) the mass of each plate is equal to 342 kg and the dimensions of each plate are 1,5 × 0,65 × 0,045 m; at the other floors (i.e. 1st, 2nd, and 3rd floor) the mass of each plate is equal to 454 kg with dimensions equal to 1,5 × 0,65 × 0,06 m. Two C-shaped profiles are positioned beneath each plate to fix the plate to the frame. As evident in Fig. 5.4, the plates aligned to the north-south direction are positioned in a symmetric configuration, while the plates aligned to west-east direction were shifted towards south direction. It is worth noting that the structure that was tested in September 2016 is different from the structure that was tested in August 2002 in the context of the IASC ASCE benchmark studies for SHM. In fact, in the tests that were performed by the IASC ASCE Task Group for SHM the plates of the steel frame structure aligned to the west-east direction were shifted towards north direction [Dyke et al., 2003].

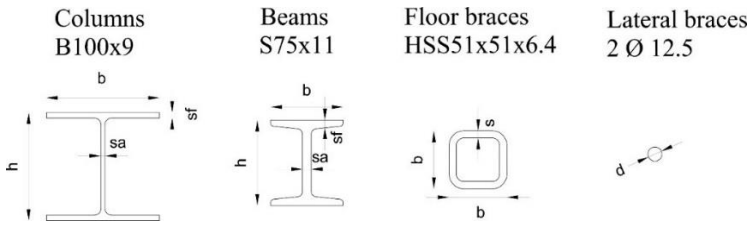

Figure 5.5. Cross sections of the members of the steel frame structure

Element	Characteristics
Columns B100×9 (mm × kg/m)	b = 100 mm h = 95 mm sf = 4.76 mm sa = 3.2 mm mass 9 kg/m
Floor braces HSS 51×51×6.4 (mm × mm × mm)	b = 51 mm s = 6.35 mm mass 8 kg/m
Beams S75×11 (mm × kg/m)	b = 64 mm h = 76 mm sf = 6.6 mm sa = 8.9 mm mass 11 kg/m
Wall braces (two threaded steel rods)	d = 12.5 mm

Table 5.1. Characteristics of the members of the steel frame structure (referred to the cross sections shown in Fig. 5.5)

The description of the experimental test setup used in the ambient vibration tests performed on the steel frame structure is reported herein. A dynamic monitoring system with 15 channels of acceleration sensors was installed on the steel frame structure and was used to collect the responses of the structure under ambient vibrations. Information about the instrumentations used during the ambient vibration tests was collected in the laboratory and from the following reference [Turek & Ventura, 2002]. The sensors are force balance accelerometers, and two types of sensors were used: Kinemetrics FBA-11, which is a uniaxial accelerometer, and Kinemetrics EPI sensor (model FBA ES-T), which is a triaxial accelerometer [Kinemetrics]. These two sensors are indicated as sensor types a) and b), respectively, and they are reported in Fig. 5.7. Both sensors have a full-scale range equal to ± 0.5 g and a sensitivity equal to 5 V/g; other specifications of the sensors are reported in Table 5.2. Three acceleration sensors were positioned on each floor of the structure (in the middle of the south, the west, and the north sides, respectively). The position and the orientation of the sensors are indicated by the arrows reported in Fig. 5.6. It is worth noting that the locations of the sensors adopted in the ambient vibration tests performed in September 2016 are different from the locations of the sensors adopted in the tests that were performed in August 2002 in the context of the IASC ASCE benchmark studies for SHM (as described in Chapter 4).

The ambient vibration measurements were acquired using a custom-built data acquisition system, which is composed by commercially available products (Fig. 5.8). The main component of the system is the IO Tech DAQ Book/216 [Measurement Computing], which includes an analog-to-digital converter (ADC) with a 16-bit resolution. The data acquisition system is also integrated with some DBK expansion cards [Measurement Computing]: four DBK18 cards, which are 4-channel low-pass filter and amplifier cards, and one DBK13 card, which is 16-channel programmable low- and high- gain analog input card. In the tests the DBK18 expansion cards were used by selecting an amplification gain equal to 10. The software for data acquisition used in the test is Dasy Lab version 11.0 [DASYLab; Measurement Computing].

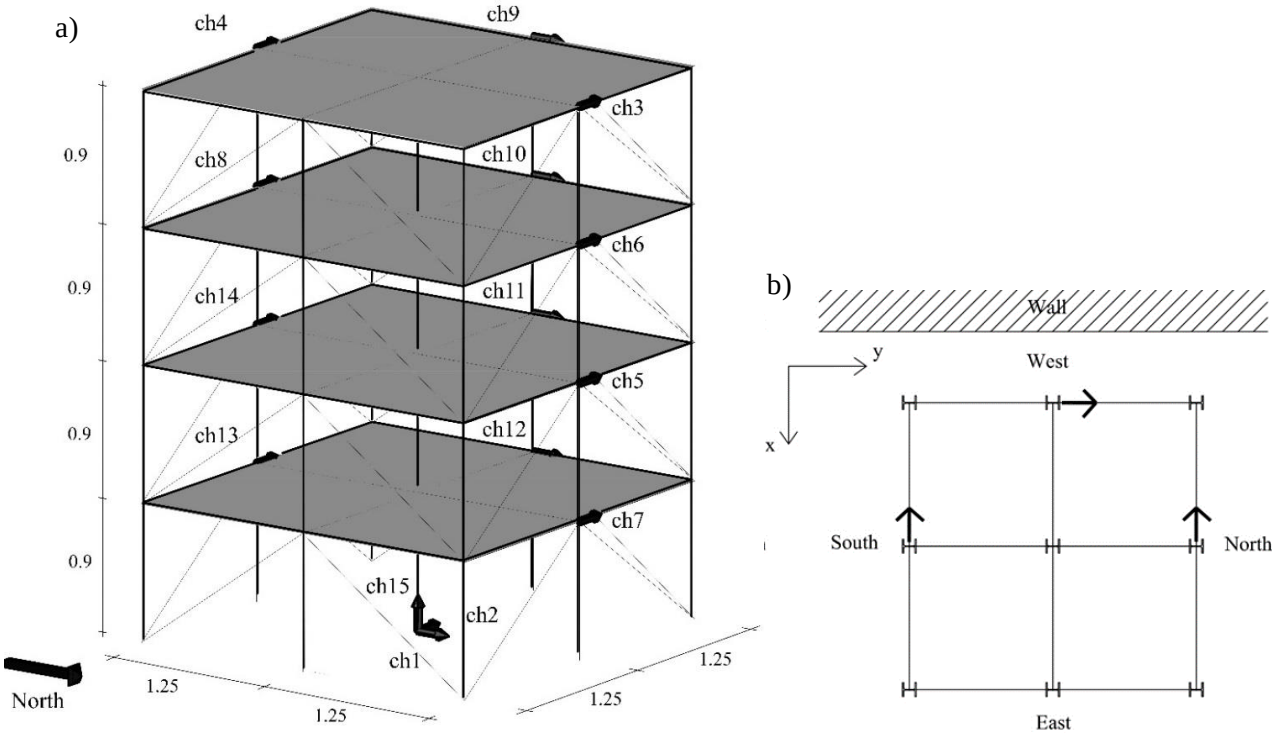

Figure 5.6. Layout of the sensors used in the ambient vibration tests:
a) 3D view; b) plan view

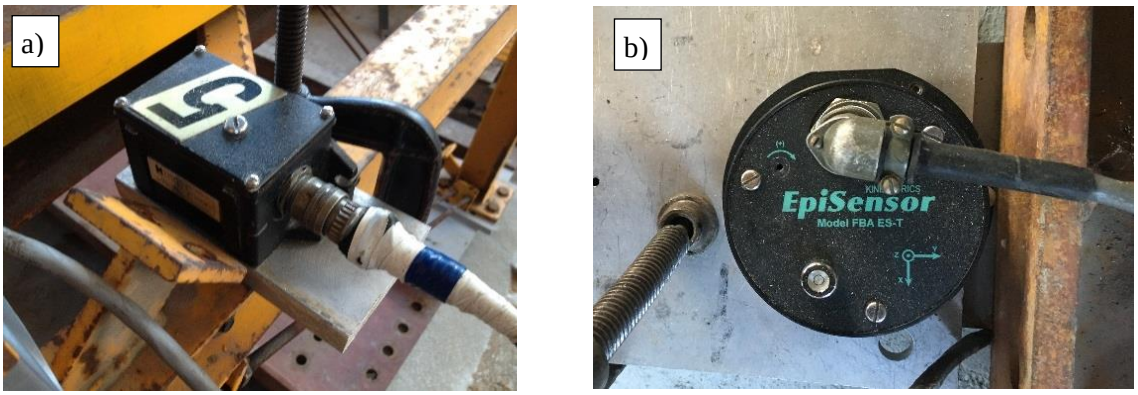

Figure 5.7. Acceleration sensors (EERF laboratory, UBC): type a); type b)

	Sensor Type (a)	Sensor Type (b)
Full scale range	± 0.5 g	± 0.5 g
Sensitivity	5 V/g	5 V/g
Dynamic range	~ 135 dB+	155 dB+
Frequency range	0.01 Hz to 50 Hz	DC – 200 Hz
Noise level	2.5 μV (0.01 Hz to 50 Hz)	10^{-15} g^2/Hz (PSD) (0.06 Hz to 50 Hz)

Table 5.2. Main specifications of the acceleration sensors (source: [Kinemetrics])

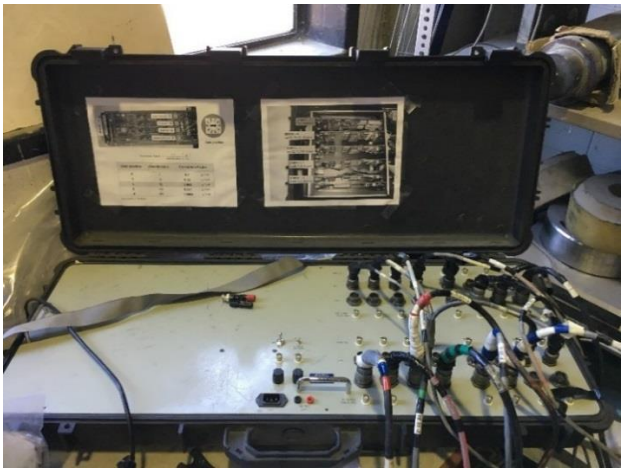

Figure 5.8. Custom-built data acquisition system (EERF laboratory, UBC)

As already mentioned, the ambient vibration tests were performed on the steel frame structure for damage detection purposes. Thus, at first the structure in the original configuration was tested by acquiring ambient vibration data using the dynamic monitoring system. This configuration is also indicated as the fully braced structure or configuration C1, and it is considered as the undamaged structure in the damage detection process. Then, modifications were introduced on the structure, and the ambient vibration tests were repeated. As already mentioned in this section, the damaged configurations were created by removing one or more diagonal braces from the wall bracing system of the structure. In other words, stiffness reductions were imposed on the structure by removing the diagonal braces. The total number of the damaged configurations that were tested is equal to twenty, and such configurations are indicated as configurations C2, C3, … C21. The ambient vibration measurements were acquired with a sampling frequency equal to 1000 Hz. The length of time of the measurements was approximately 3 hours for the fully braced or undamaged structure (i.e. configuration C1) and approximately 30 minutes for each damaged configuration (i.e. configurations from C2 to C21). It is worth mentioning that the length of time of the measurements for the damaged configurations (i.e. 30 minutes) is the length of time that approximately can be determined using the criterion suggested by the "Guidelines for the Measurement of Vibrations and Evaluation of Their Effects on Buildings" [ANSI S2.47, 1990]. This criterion has been already described in Section 2.2.1 of Chapter 2, and it was applied by assuming that the considered steel frame

structure has a first structural mode that is characterized approximately by a natural frequency equal to 10 Hz and a modal damping ratio equal to 1%. The estimates of such modal parameters were performed before the execution of the ambient vibration tests.

The description of all the structural configurations that were tested (from configuration C1 to configuration C21) is reported in Table 5.3. Information about the diagonal braces that were removed for each configuration and with respect to the original structure is reported in the table. In particular, the indication of the diagonal braces that were removed is provided using acronyms that include the following information: the story where the brace is removed (from the first to the fourth story); the bay where the brace is removed (using the nomenclature of the bays of the structure that is reported in Fig. 5.9 and that was defined according to the orientation of the structure); the number of the braces removed in the selected story and in the selected bay of the structure (i.e. one or two rods removed). With reference to this last point, it is worth mentioning again that, as schematically reported in Fig. 5.9, two tie-rods are present in the portion of the original structure that can be identified by considering a generic story and a generic bay. The acronyms reported in Table 5.3 are thus composed as: "story – bay – no. of braces removed".

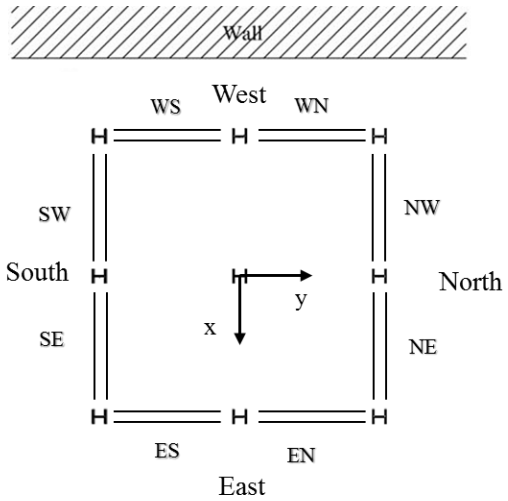

Figure 5.9. Schematic plan-view with the nomenclature adopted for each bay of the structure. Adapted from [Bernagozzi et al., 2017 b].

Configurations	Braces removed	Type (S: sym. / A: asym.)
C1 *	none	S
C2	1-SW-2; 1-SE-2	A
C3	C2 + 1-NW-2; 1-NE-2	S
C4	all braces removed at the first story	S
C5	C2 + 1-WS-2; 1-WN-2	A
C6	C2 + 1-NW-1; 1-NE-1	A
C7	1-SE-2	A
C8	1-SW-1; 1-SE-1	A
C9	3-WS-1; 3-WN-1	A
C10	4 -WS-1; 4-WN-1; 2-SW-1; 2-SE-1	A
C11	4-WS-1; 4-WN-1; 2-WN-1; 2-WS-1	A
C12	half braces removed on the west side	A
C13	half braces removed at the first story	S
C14	3-SE-2; 3-SW-2	A
C15	C14 + 2-WS-2; 2-WN-2	A
C16	2-WS-2; 2-WN-2	A
C17 *	2-WS-1; 2-NW-1; 2-ES-1; 2-SW-1	S
C18 *	C17 + 2-WN-1; 2-NE-1; 2-EN-1; 2-SE-1	S
C19 *	C18 + 2-WS-1; 2-NW-1; 2-ES-1; 2-SW-1	S
C20 *	C19 + 2-WN-1; 2-NE-1; 2-EN-1; 2-SE-1	S
C21	2-SW-2; 2-SE-2; 2-WS-1; 2-WN-1; 2-NW-1;2-NE-1	A

* progressive damage test

Table 5.3 Structural configurations considered in the ambient vibration tests. Adapted from [Bernagozzi et al., 2017 b]

The tested configurations include both single- and multiple- damage states. In other words, the stiffness reductions were imposed on the steel frame structure in one story or in more than one story. In addition, configurations with either a plan-symmetric or a plan-asymmetric distribution of the story stiffness at the damaged levels were considered (as indicated in the last column of Table 5.3). For example, configurations C17, C18, C19 and C20 have a plan-symmetric distribution of the stiffness of each story, and these configurations were tested consecutively and by progressively increasing the stiffness reductions imposed on the 2nd story. As shown in Fig. 5.10, in fact, these configurations were created by progressively increasing the number of the braces that were removed in both directions of the structure. It is worth

noting that in the present chapter the configurations C1, C17, C18, C19, and C20 (considered in this order) are also indicated as configurations that belong to a "progressive damage test".

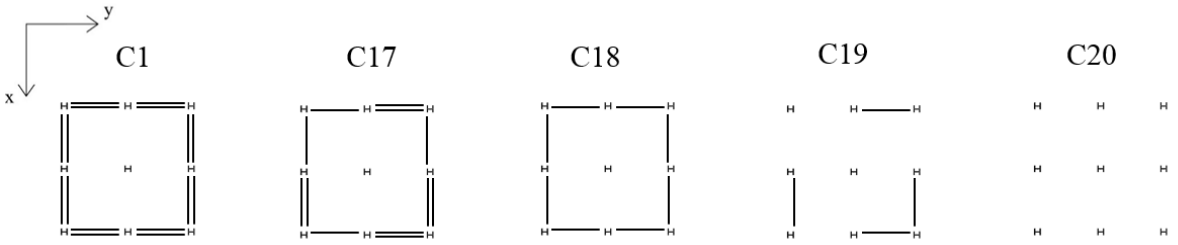

Figure 5.10. Progressive damage test: symmetric configurations with braces removed only at the 2nd story of the structure

An example of a damaged configuration with a plan-asymmetric distribution of the story stiffness is reported in Figure 5.11. In this configuration two tie-rods were removed at the first story and on the south face of the structure. It is worth noting that in such case the stiffness reduction was imposed only in the weak direction of the structure (i.e. the x or west-east direction). Other configurations are characterized by a distribution of the stiffness at the damaged level that is strongly asymmetric. For example, in configuration C2 four rods were removed at the first story and on the south face of the structure (as indicated in Table 5.3).

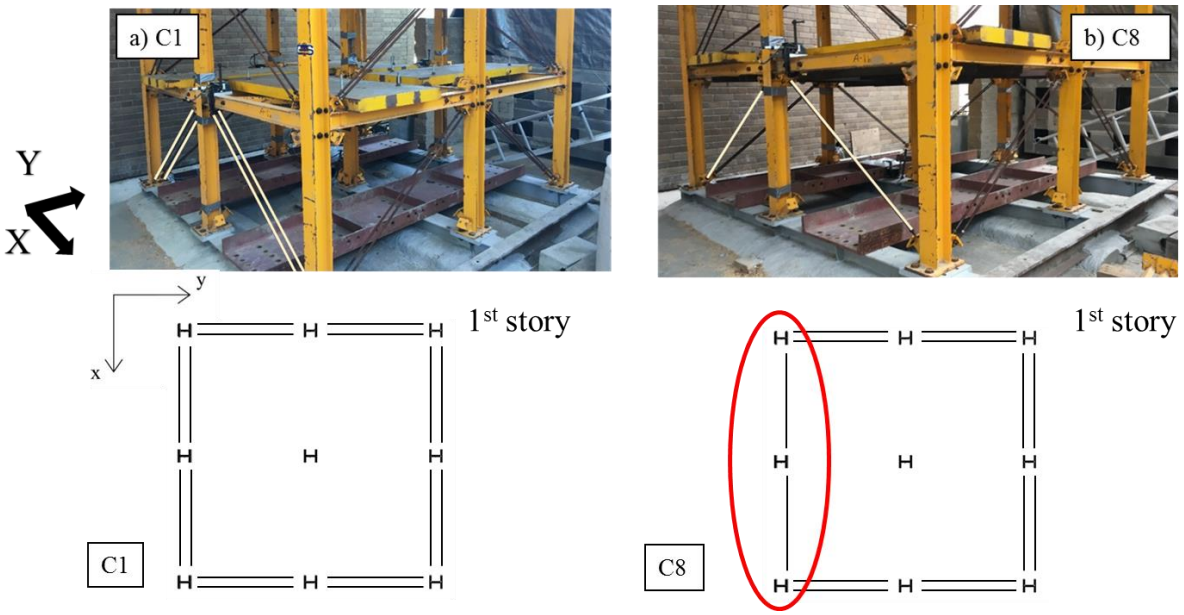

Figure 5.11. Examples of configurations considered in the ambient vibration tests: a) conf. C1 (undamaged); b) conf. C8 (damaged)

5.1.2.2 Results of the operational modal analysis

The quality of the recorded ambient vibration data was checked just after the data acquisition using the criteria that are suggested in [Brincker & Ventura, 2015] (some of these criteria have been already introduced in Section 2.2.1 of Chapter 2). This check of the data quality[3] was performed with the objective of evaluating if the recorded signals (i.e. random responses of the structure due to the natural excitations) are signals with an approximately Gaussian distribution. In particular, in the analysis the probability density functions and some statistical parameters of the recorded signals were evaluated. One of the considered statistical parameters is the so-called kurtosis. By considering a generic signal $x(t)$, the kurtosis is the fourth statistical moment of the signal, and it is defined as follows

$$\gamma = \frac{E[\,(x(t)-\mu)^4\,]}{\sigma^4} \tag{5.15}$$

where μ and σ are the mean and the standard deviation of the signal and E [·] is the operator used to indicate the expected value. The kurtosis of a random signal with Gaussian distribution is theoretically equal to 3. According to the criteria suggested in [Brincker & Ventura, 2015] to check the data quality, the kurtosis was calculated on portions of the ambient vibration measurements (i.e. windows of the signals) that have a length of time equal to the memory time of the structure. For the considered steel frame structure, the memory time of the structure was estimated as T_{mem} = 5 s. This parameter was calculated using the expression of the memory time that has been already defined in Section 2.2.1 of Chapter 2, and by assuming, again, that the first mode of the structure is characterized approximately by a natural frequency equal to 10 Hz and a modal damping ratio equal to 1%.

An example of the results of the analysis performed to check the quality of the data is reported in Figs. 5.12 and 5.13. In particular, the results are shown for a signal recorded in the test performed on the undamaged structure and recorded using channel 3 (i.e. an accelerometer positioned at the top story and aligned to the weak direction of the structure, as shown in Fig. 5.6). The acquired ambient vibration data are

[3] The check of the data quality was executed by developing a Matlab [MATLAB] code that uses some external functions of the OMA toolbox available in [Brincker & Ventura, 2015].

approximately in the range ± (1-2) mg, as shown in Fig. 5.12a. The values assumed by the kurtosis evaluated on portions of the signal with a length of time of 5 s are reported in Fig. 5.12b. As shown in this figure, the kurtosis evaluated on the ambient vibration signal is, on average, approximately close to 3, which is the theoretical value of the kurtosis that is obtained if a signal with an exact Gaussian distribution is considered. The probability density function (PDF) and the cumulative distribution function (CDF) of the selected signal (obtained using channel 3) are reported in Fig. 5.13. As shown in the figure, these functions are very similar to the functions that can be obtained if a signal with an exact Gaussian distribution is considered.

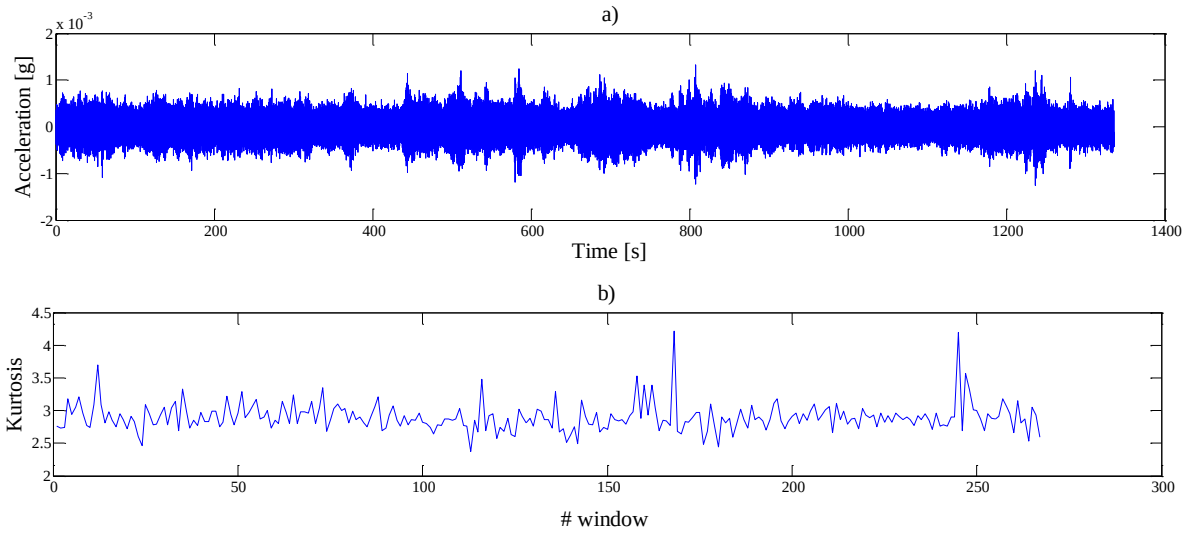

Figure 5.12. Data quality check on the raw measurements – conf. C1 channel 3:
a) time history; b) kurtosis

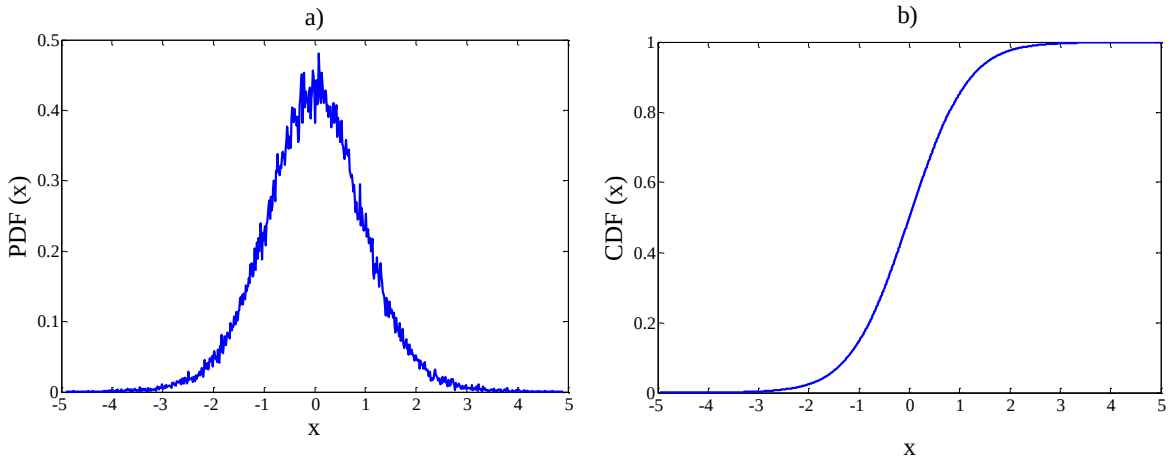

Figure 5.13. Data quality check on the raw measurements – conf. C1 channel 3:
a) probability density function (PDF); b) cumulative distribution function (CDF)

Before applying the output-only modal identification, the signals related to the ambient vibration measurements were decimated in the frequency range 0-50 Hz and detrended (i.e., any linear trend eventually present in the signals was removed to force the signals to have a zero mean). Moreover, the data recorded for the fully braced structure (C1) were segmented into non-overlapping data segments with a length of time of 30 minutes each.

The operational modal analysis[4] (i.e. the output-only modal identification) was performed on the ambient vibration data using the Enhanced Frequency Domain Decomposition method [Brincker, Zhang & Andersen, 2001; Brincker, Ventura & Andersen, 2001], which, as already discussed in Chapter 2, is one of the most common OMA techniques among the techniques that work in frequency domain. According to the EFDD method, the spectral density functions were estimated starting from the ambient vibration data. Then, a singular value decomposition was performed on the matrix of the spectral density functions estimated for all the measured channels. Two auto spectral density (ASD) functions estimated from the measurements are reported, for example, in Fig. 5.14. Such ASD functions are related to channels 9 and 3 and to the test performed on the undamaged structure (configuration C1). An example of a plot of the singular values (SV) computed from the cross spectral density (CSD) matrix is reported in Fig. 5.15. Again, the results shown in this last figure are related to the data recorded for the configuration C1, and two observations can be formulated on the plot of the singular values. First of all, it can be argued that the test was characterized by multiple inputs. This is because, as shown in Fig. 5.15, there are peaks not only in the curve of the first singular values, but also in the curves related to the other singular values. In general, it can be observed in the figure that at least the first three singular values raise above the noise level. Secondly, there is a good signal-to-noise ratio at least in the first half of the analyzed frequency band (i.e. in the range 0-25 Hz). As shown in the plot reported in Fig. 5.15, in this frequency range there are some clear peaks. According to [Brincker & Ventura, 2015], a measure of the signal-to-noise ratio can

[4] The modal extraction was performed using the EFDD method implemented in ARTeMIS software [ARTeMIS]. As a complementary tool for the analyses, a Matlab code [Matlab] that implements the FDD method was also developed and adopted.

be, in fact, obtained as the distance between the maximum values of the peaks in the singular value plot and the singular values that are related to the noise level.

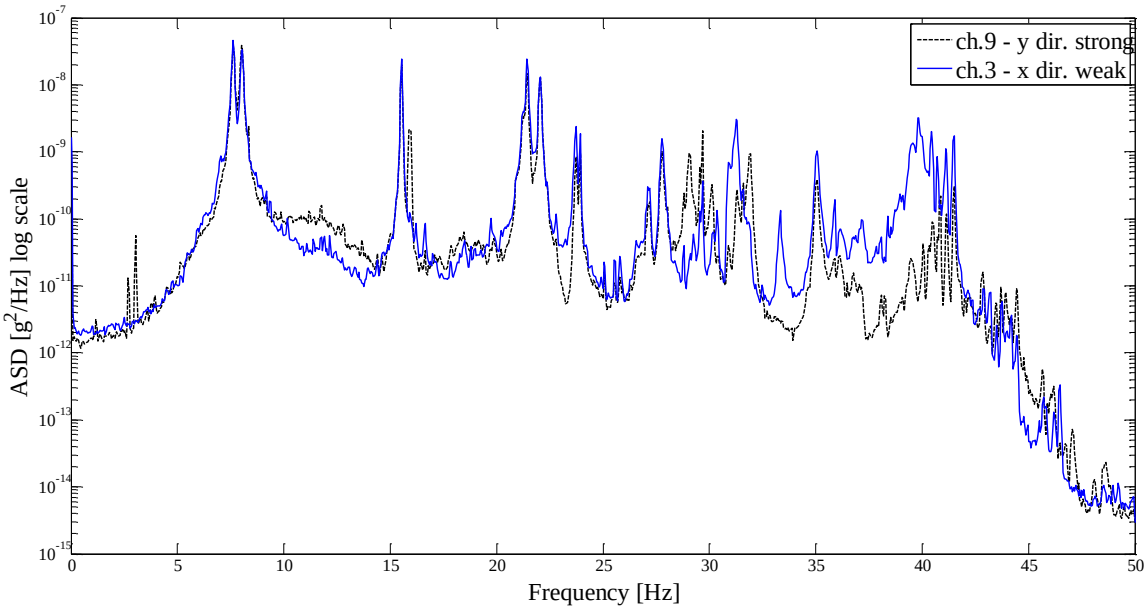

Figure 5.14. Auto spectral densities (ASD) related to channels 9 and 3 – conf. C1.

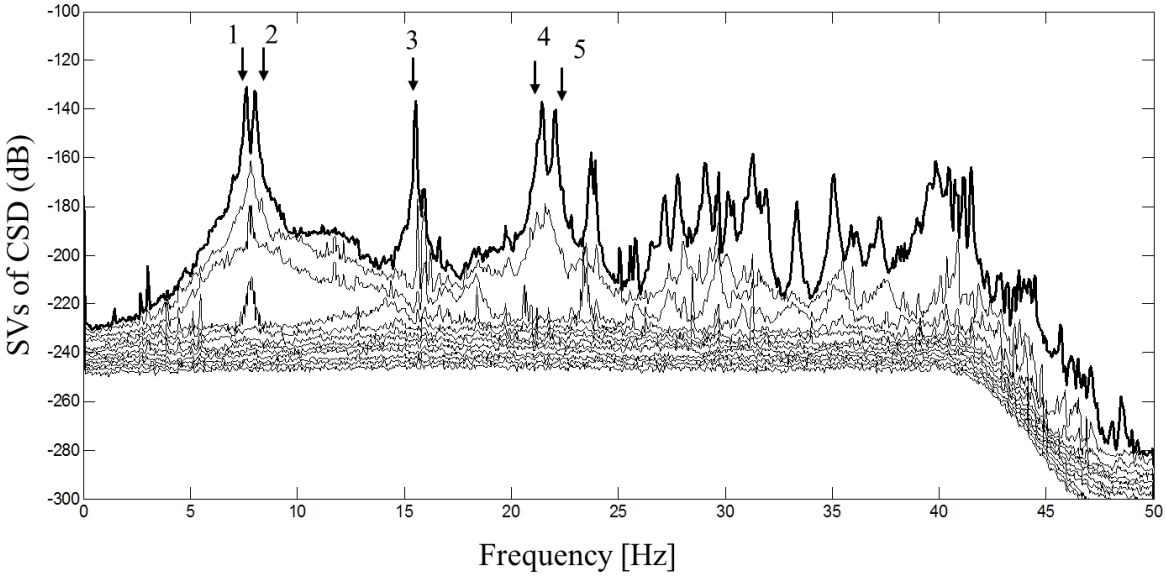

Figure 5.15. Singular values (SV) computed from the cross spectral density (CSD) matrix – conf. C1

According to the EFDD method, the structural modes were manually identified by analyzing the peaks in the plot of the singular values computed from the spectral density matrix. In general, by analyzing the ambient vibration data related to the different structural configurations that were tested (i.e. configurations from C1 to C21) it was possible to identify, on average and for each structural configuration, from eight to ten peaks that can be associated to structural modes. For example, referring to the results obtained for configuration 1, ten peaks that can be associated to structural modes were found in the plot of the singular values (shown in Fig. 5.15). The modal parameters, in terms of natural frequencies and modal damping ratios, of the ten modes that were identified for configuration 1 are reported in Table 5.4. However, only the first five modes of the structure were considered for assembling the modal flexibility matrices and for carrying out the damage detection analysis according to the steps described in Section 5.1.1. The high-order modes were, on the contrary, not included in the calculations, and this operation was done for all the tested configurations.

It is important to mention that the choice of considering only the first five low-order modes of the structure was motivated by two main reasons. First of all, for all the tested configurations the high-order modes are characterized by very high values of the Modal Complexity Factor (MCF). For example, referring to the results obtained for configuration 1, the values of the modal complexity factor are reported for each mode in the last column of Table 5.4. The modal complexity factor is an index that can be used for modal validation, and the analytical formulation of such index is described in detail in Section A.3 of Appendix A. The MCF index is evaluated on each complex-value identified mode shape, and theoretically it is equal to zero if the considered mode shape is associated to a structure that is proportionally damped (in such case, the real and the imaginary parts of the identified mode shape are proportional). However, as reported in [Brincker & Ventura, 2015], even if the structure has a proportionally damped behavior, some complexity can be present in the identified mode shapes due to the random errors that always occur in the identification process[5]. Referring to the steel frame structure that was tested under ambient vibrations, a proportional damping model can be considered in general as a reasonable model that

[5] This point is more extensively discussed in Section A.3 of Appendix A.

describes the behavior of the structure. Thus, in light of this assumption, the values of the modal complexity factor related to the identified modes suggest that the higher modes are affected by more uncertainties than the lower ones.

Secondly, the choice of considering only the first five low-order modes in the damage detection analysis was also done to have the guarantee that modes which are of the same type are included in the modal flexibility matrices estimated for all the tested configurations. In particular, for all the configurations the following modes of the steel frame structure were considered: the two first longitudinal modes, the torsional mode, and the two second longitudinal modes. For all the tested configurations, such modes are the first five peaks that can be found in the singular value plots. Referring to the results obtained for configuration 1, these five modes are highlighted by the arrows reported in the plot of the singular values shown in Fig. 5.15. As evident in the figure, such modes are related to the highest peaks in the singular value plot.

Mode no.	Type of mode shape	Configuration C1		
		Frequency f_i [Hz]	Damping ζ_i (%)	Modal complexity factor (MCF_i) (%)
1	1° mode – longitudinal (XY)	7.62	0.65	6.46
2	1° mode – longitudinal (XY)	8.04	0.72	4.35
3	1° mode – torsional (T)	15.53	0.22	19.98
4	2° mode – longitudinal (XY)	21.46	0.27	38.12
5	2° mode – longitudinal (XY)	22.05	0.23	39.33
6	3° mode – longitudinal (XY)	27.16	0.28	51.88
7	3° mode – longitudinal (XY)	29.07	0.30	62.24
8	2° mode – torsional (T)	31.27	0.27	75.80
9	4° mode – longitudinal (X)	33.33	0.21	48.79
10	3° mode – torsional (T)	35.05	0.21	85.13

Table 5.4 Modal parameters identified using the EFDD method for configuration C1 (fully-braced or undamaged structure). Adapted from [Bernagozzi et al., 2017 b]

The mode shapes that were identified using the EFDD method have, of course, components that are defined at the sensor locations. A transformation was then applied

on the identified mode shapes to obtain mode shapes whose components are defined with respect to the geometric center of the structure. This transformation was performed using the following equations

$$\psi_{i,x,C,j} = \frac{\psi_{i,x,N,j} + \psi_{i,x,S,j}}{2} \tag{5.16}$$

$$\psi_{i,\theta,C,j} = \frac{\psi_{i,x,S,j} - \psi_{i,x,N,j}}{2\,a} \tag{5.17}$$

$$\psi_{i,y,C,j} = \psi_{i,y,W,j} + \psi_{i,\theta,C,j}\,a \tag{5.18}$$

where $\psi_{i,x,N,j}$, $\psi_{i,x,S,j}$, and $\psi_{i,y,W,j}$ are the components of the i-th mode shape identified at the j-th story and at the sensor locations (i.e. at the positions of the sensors located on the north, south, and west face of the structure, respectively, as shown in Fig. 5.6). On the contrary, the terms present in Eqs. (5.16, 5.17, and 5.18) $\psi_{i,x,C,j}$, $\psi_{i,y,C,j}$, and $\psi_{i,\theta,C,j}$ are the components of the i-th mode shape defined with respect to the geometric center of the structure (Fig. 5.16). The letter a is used to indicate the width of each bay of the structure. The above-mentioned equations are valid under the simplified assumption of considering that each floor of the 3D building structure has a rigid-body in-plane behavior. Moreover, the amplitudes of the components of the identified mode shapes are small with respect to the dimensions of the structure. In such situation negligible errors are obtained using the following approximation $\sin\psi_{i,\theta,C,j} \approx \psi_{i,\theta,C,j}$, as implicitly assumed in Eq. (5.17).

The mode shapes obtained by performing a modal identification on one portion of the ambient vibration data recorded for configuration C1 (i.e. the undamaged structure) are reported in Table 5.5. The components of the mode shapes reported in this table are expressed with reference to the geometric center of the structure. It is worth noting that each longitudinal mode (i.e. all the modes except mode no. 3, which is a torsional mode) has components in x direction that are of the same order of magnitude of the components in y direction. This means that the modal displacements of the mode shapes associated to the longitudinal modes of the undamaged structure are approximately aligned to the diagonals of the plan of the structure (in other words, the modal displacements are not aligned to the x or the y directions).

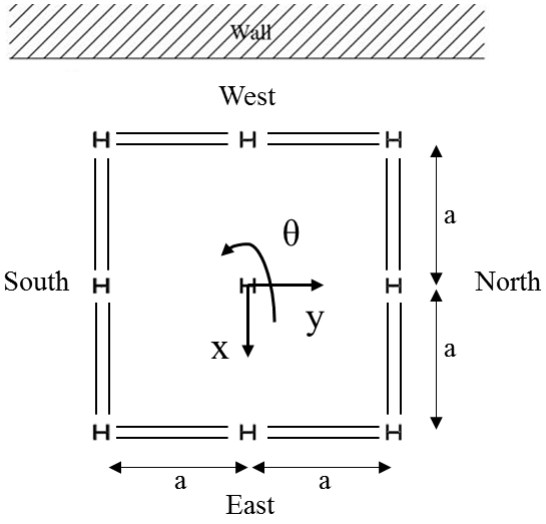

Figure 5.16. Schematic plan-view with indication of the coordinates used to define the mode shapes in the geometric center of the structure.

DOF	Mode shape components $\psi_{i,C,\,DOF}$				
	Mode #1	Mode #2	Mode #3	Mode #4	Mode #5
x_4	0.395	0.395	0.028	0.395	-0.378
x_3	0.332	0.325	0.022	0.050	-0.029
x_2	0.236	0.241	0.023	-0.309	0.312
x_1	0.131	0.121	0.012	-0.311	0.283
y_4	-0.385	0.406	-0.009	-0.343	-0.363
y_3	-0.332	0.332	0.004	-0.022	0.011
y_2	-0.228	0.247	-0.001	0.320	0.361
y_1	-0.137	0.144	0.012	0.396	0.438
θ_4	0.005	-0.015	0.300	0.017	0.007
θ_3	0.002	-0.010	0.263	-0.011	-0.050
θ_2	-0.003	-0.001	0.205	-0.049	-0.076
θ_1	0.004	-0.005	0.108	-0.051	-0.084

Table 5.5 Mode shape components for configuration C1 (defined in the geometric center of the structure)

The natural frequencies of the structural configurations that were considered in the progressive damage test are reported in Table 5.6 (i.e. configurations C1, C17, C18, C19, and C20). As shown in the table, a progressive decrease of the natural frequencies related to the different configurations can be observed, especially for the first three structural modes.

Mode no.	Natural frequency f_i [Hz]				
	C1	C17	C18	C19	C20
1	7.62	6.98	6.58	6.04	4.92
2	8.04	7.20	6.87	6.53	6.08
3	15.53	14.44	12.74	11.28	9.14
4	21.46	21.31	21.32	21.35	21.37
5	22.05	21.91	21.89	21.87	21.79

Table 5.6. Natural frequencies related to the configurations of the progressive damage test

5.1.2.3 Results of the damage localization and quantification

This section presents the results of the analyses that were carried out to localize and quantify the damage in the steel frame structure using the procedure that is outlined in Section 5.1.1. According to the above-mentioned procedure, after having performed the ambient vibration tests and the operational modal analysis (steps no. 1 and no. 2), the modal flexibility matrices of the 3D building structure were assembled (step no. 3). To perform this operation and as already mentioned in Section 5.1.1, the system mass matrix of the structure was estimated a-priori and used to normalize the mode shapes that were identified using the output-only modal identification technique. This strategy for assembling modal flexibility matrices from output-only vibration data is the same strategy that was adopted in the original formulation of the PSIL method [Koo et al., 2010].

The mass matrix that was used to normalize the identified mode shapes is the mass matrix of a 3*n*-DOF lumped-mass model of the structure (where *n*=4, i.e. the number of the stories). This mass matrix of the structure was generated using the "Acceleration Responses Generation Program for the Benchmark Problem of the

ASCE Task Group on Structural Health Monitoring", which is a MATLAB-based finite element analysis code that was made available by the IASC-ASCE Task Group [Johnson et al., 2004]. This code is able to generate the model and the acceleration responses of a structure that is similar to the steel frame structure that is located at the EERF laboratory of the University of British Columbia (Vancouver). The program was created before the execution of the experimental tests performed on the structure in August 2002 by the IASC-ASCE Task Group. It is worth noting, in fact, that these tests represent the experimental phase II of the studies conducted by the mentioned task group. In phase I, on the contrary, analytical studies were performed by the IASC-ASCE Task Group, and such studies were executed using the MATLAB code provided by [Johnson et al., 2004]. In the program two different models of the benchmark structure can be considered: a 12-DOF shear building model, where each floor of the structure is a rigid body and the degrees of freedom are the two translations and the rotation of each story; a 120-DOF model, which is a more complex model of the structure and which is not a shear-type model. The first of the two above-mentioned models was considered in the present analysis and was used to generate a 12 × 12 diagonal mass matrix $\boldsymbol{M}$ of the steel frame structure. The components of the diagonal of such matrix are reported in the following vector

$$\boldsymbol{m}_{12\times1} = \left[m_{x,4}\ m_{x,3}\ m_{x,2}\ \ m_{x,1}\ \ \ m_{y,4}\ \ m_{y,3}\ m_{y,2}\ m_{y,1}\ \ J_{\theta,4}\ J_{\theta,3}\ J_{\theta,2}\ J_{\theta,1}\right]^T \quad (5.19)$$

where $m_{x,4} = m_{y,4}$ =1583.27 kg, $m_{x,3} = m_{x,2} = m_{x,1} = m_{y,3} = m_{y,2} = m_{y,1}$ = 2079.24 kg, $J_{\theta,4}$ =1823.66 kg m^2, and $J_{\theta,3} = J_{\theta,2} = J_{\theta,1}$ = 2403.02 kg m^2.

It is worth noting that some modifications were applied to the original FEM model provided by [Johnson et al., 2004] to obtain a mass matrix that can describe the mass distribution of the structure that was tested in September 2016 (i.e. the above-mentioned mass matrix $\boldsymbol{M}$). Similarly to the real structure located at the University of British Columbia, the structure modeled using the original FEM code by [Johnson et al., 2004] has four plates added at each floor. In the model of this original FEM code the values of the masses of the plates related to the first, second, third, and four floors are, respectively, 800 kg, 600 kg, 600 kg, and 400 kg. Such values of the plate masses were substituted with the values of the plate masses related to the structure that was tested in September 2016. As already mentioned in Section 5.1.2.1, such values of the

masses of the plates are 454 kg, 454 kg, 454 kg, and 342 kg (for the first, second, third, and four floors, respectively). Moreover, in the original FEM model by [Johnson et al., 2004], the diagonal wall braces of the structure are L-shape profiles. In the modified version of the FEM model used in the present analysis to generate the mass matrix of the structure, such elements were substituted with the elements that are present in the structure that was tested in September 2016 (i.e. diagonal wall braces that are tie-rods).

The mass matrix considered in the analysis is a diagonal matrix. This means that the calculations were performed under the simplified assumption of neglecting the small eccentricity that is present in the distribution of the masses of the tested steel frame structure. In fact, as already mentioned in Section 5.1.2.1, the plates positioned at each floor of the structure and aligned to the west-east direction were shifted towards south direction. Referring to Fig. 5.4, the distances between the center of mass of the two floor plates aligned to the west-east direction and the geometric center of the structure are approximately 0.8 m and 0.5 m (for the plates located in the south-west bay and the north-east bay, respectively). If one performs a simple calculation using these distances and the values of the plate masses, the distance along the y direction between the geometric center and the center of mass of the whole structure can be estimated approximately as 0.06 m. This value of the eccentricity related to the center of mass of the structure is small with respect to the dimension of the structure (i.e. 2.5 m). Under the simplified assumption of neglecting this small eccentricity of the center of mass of the structure, the calculations were performed using a diagonal mass matrix.

After having assembled the modal flexibility matrices of the structure, the modal flexibility-based deflections and interstory drifts were computed according to the steps that are outlined in Section 5.1.1. In particular, as already mentioned in Section 5.1.1, two separate analyses were performed to evaluate the MF-based deflections of the structure due to the uniform inspection loads $\boldsymbol{p_x}$ and $\boldsymbol{p_y}$ applied in the X and the Y directions, respectively (Eq. 5.3). The damage localization and the damage quantification were then performed by evaluating the z-indices (Eqs. 5.11, 5.12) and the parameters of the damage severity (Eqs. 5.13, 5.14) starting from the modal flexibility-based interstory drifts of the structure. The procedure was applied

for each damaged configuration that was tested. This means that all the structural configurations from C2 to C21 were compared with respect to the configuration assumed as the baseline structure (i.e. configuration C1).

The results of the damage localization are presented in Fig. 5.18 for one damaged configuration. In particular, the results are presented in this figure for configuration C13, which is compared against configuration C1 (undamaged). As shown in Fig. 5.17, to create configuration C13 eight tie-rods were removed at the first story of the original structure. In particular, two tie-rods were removed from each side of the structure, and the stiffness reductions were imposed both in the weak direction of the structure (x direction) and in the strong direction (i.e. y direction). The configuration C13 is thus a configuration characterized by a plan-symmetric distribution of the story stiffness at all the stories (including the damaged story). According to the observations formulated at the end of Section 5.1.1, this means that the results of the damage localization obtained for such configuration C13 are basically the same results that can be obtained by applying the original formulation of the PSIL method (which, as already mentioned, was developed for plane structures).

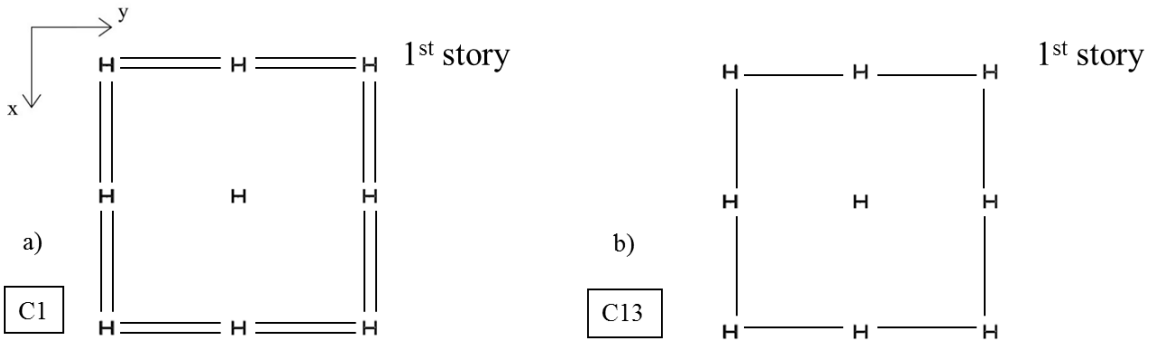

Figure 5.17. Examples of configurations considered in the ambient vibration tests:
a) conf. C1 (undamaged); b) conf. C13 (damaged)

The components in X direction of the modal flexibility-based deflections of the structure due to the inspection load $\boldsymbol{p_x}$ are reported in Fig. 5.18a both for the undamaged configuration C1 (blue continuous line) and the damaged configuration C13 (red dashed line), while the components in Y direction of the modal flexibility-based deflections of the structure due to the inspection load $\boldsymbol{p_y}$ are reported in Fig. 5.18b. The interstory drifts related to the two above-mentioned deflections are reported in Fig. 5.18c, 5.18d, which are related to the X and the Y directions, respectively. As shown in these figures, variations of the interstory drifts between the undamaged and the possibly damaged states are present only at the first story (which, as already mentioned, is the damaged story). Moreover, these variations are present in the results of the analyses both in the X and the Y directions, as also shown in Fig. 5.18e where such variations are plotted (i.e. the damage-induced interstory drifts related both to the X and the Y directions). As already mentioned, in fact, in configuration C13 the braces were removed both in the weak and in the strong direction of the structure. The results of the z-index tests are reported in Fig. 5.18f. As evident in this figure, the damage detection procedure correctly localizes the damage that was imposed at the first story and both in the X and the Y directions of the structure.

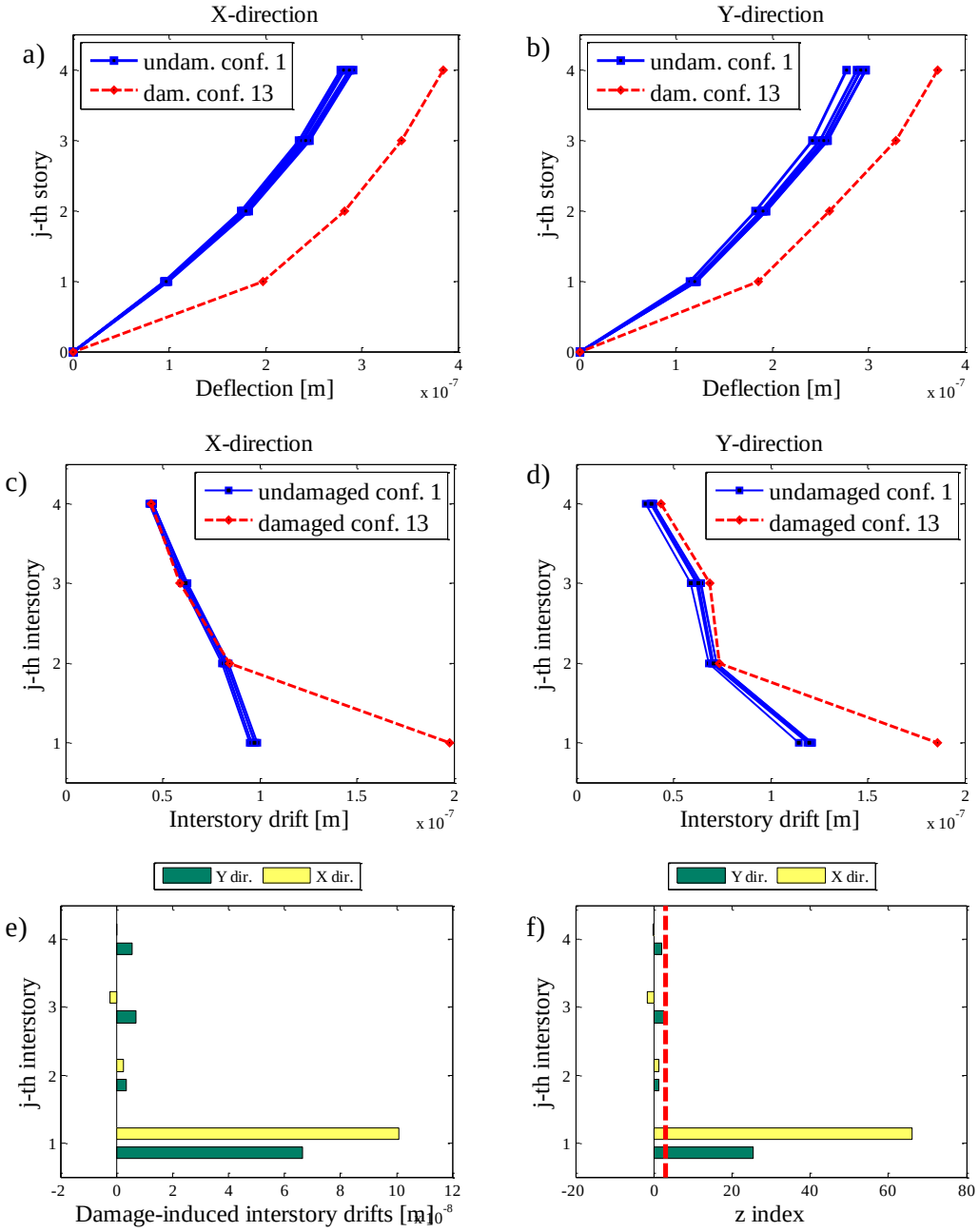

Figure 5.18. Damage localization on configuration C13: (a) deflections in X direction due to load $\boldsymbol{p_x}$; (b) deflections in Y direction due to load $\boldsymbol{p_y}$; (c) interstory drifts in X direction due to load $\boldsymbol{p_x}$; (d) interstory drifts in Y direction due to load $\boldsymbol{p_y}$; (e) damage-induced interstory drifts; (f) z-index tests.

The results of the damage localization are also presented for configuration C8 (damaged), which is compared against configuration C1 (undamaged) in Fig. 5.19. To create configuration C8 two tie-rods were removed at the first story and from the south face of the original structure (as shown in Fig. 5.11). In this way, the stiffness

reduction was imposed on the weak direction of the structure (i.e. the x direction), and this configuration is thus characterized by a plan-asymmetric distribution of the story stiffness at the damaged story. Fig. 5.19 (related to configuration C8) shows the results of the same analyses that are presented in Fig. 5.18 for configuration C13. As evident in Fig. 5.19f, the z-index tests performed for configuration C8 correctly localize the damage that was imposed at the first story and in the X direction of the structure.

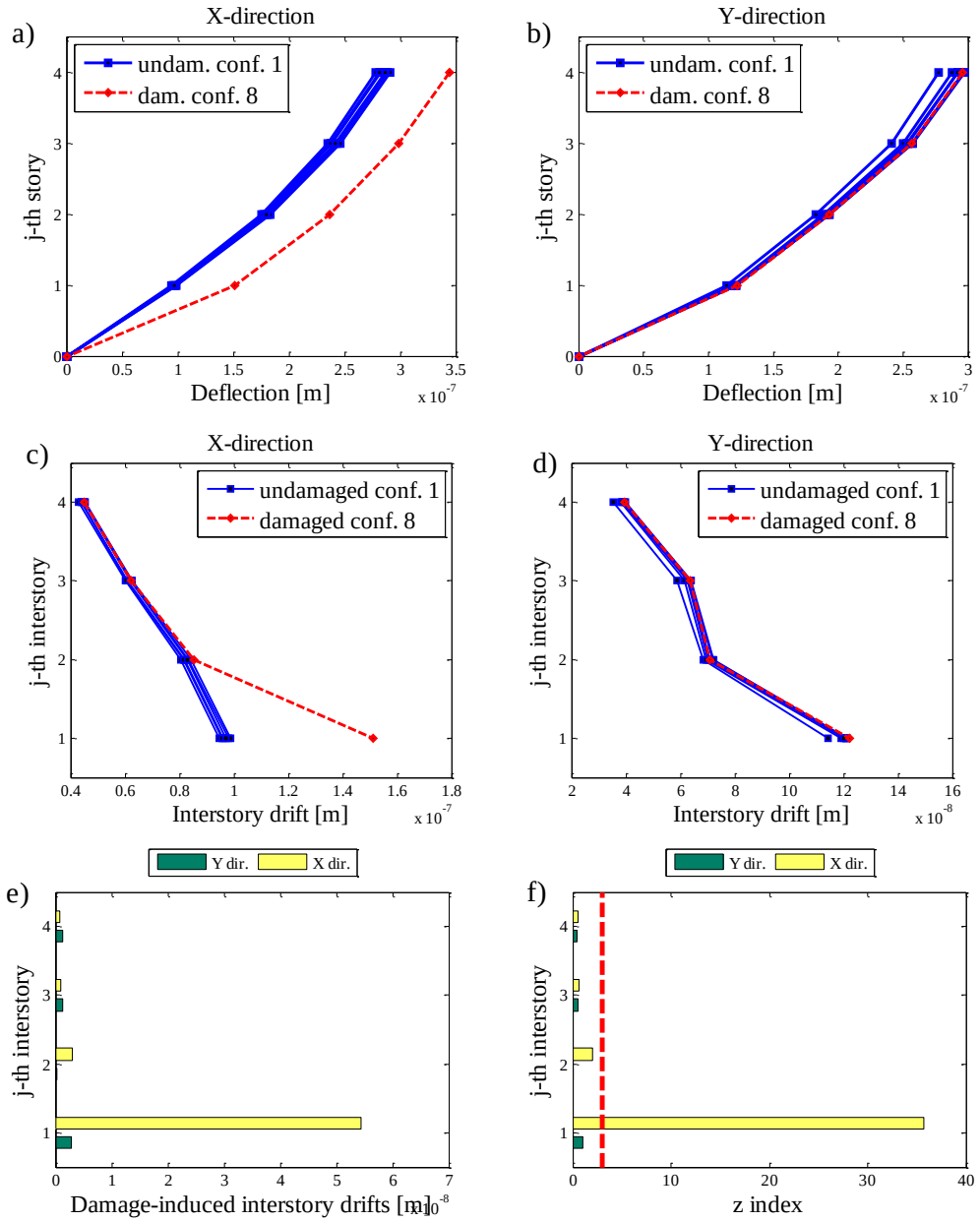

Figure 5.19. Damage localization on configuration C8: (a) deflections in X direction due to load $\boldsymbol{p_x}$; (b) deflections in Y direction due to load $\boldsymbol{p_y}$; (c) interstory drifts in X direction due to load $\boldsymbol{p_x}$; (d) interstory drifts in Y direction due to load $\boldsymbol{p_y}$; (e) damage-induced interstory drifts; (f) z-index tests. Adapted from [Bernagozzi et al., 2017 b]

The results of the damage localization are presented herein for all the configurations that were tested (i.e. configurations from C2 to C21). In particular, the values of the z-index are reported in Table 5.7 for each direction of the structure (i.e. X or Y direction) and for each story (from the 1st to the 4th story). The values of the z-index were compared against the threshold $z^{TH} = 3$ (as defined in Section 5.1.1) to evaluate if the structure, in the considered direction and at the selected story, is damaged or not. At the end, the effectiveness of the procedure used for damage localization was evaluated by comparing the outcomes of the z-index tests with the expected outcomes. Such expected outcomes were defined on the basis of the knowledge of the positions of the braces that were removed in the different configurations (i.e. the knowledge of the story and the direction of the structure that have been affected by the damage). The number of cases that were falsely detected is reported in the last two columns of Table 5.7, where a distinction is made between false positives and false negatives. A false positive damage indication is an indication of damage when the damage is not present, while a false negative damage indication means that there is no indication of damage when, on the contrary, damage is present [Farrar & Worden, 2013].

Conf.	Dir.	z-index				FP*	FN*
		z_4	z_3	z_2	z_1		
C2	x	0.90	0.15	2.36	58.66	0	0
	y	-2.59	-3.42	-3.33	-0.74	0	0
C3	x	-0.21	-2.69	3.96	140.41	1	0
	y	-0.89	-1.14	-0.94	-0.49	0	0
C4	x	-3.14	-6.42	1.42	136.04	0	0
	y	-4.96	-4.48	-0.71	81.69	0	0
C5	x	0.57	1.36	1.86	64.81	0	0
	y	-7.70	-5.79	-7.31	41.80	0	0
C6	x	0.70	0.08	3.15	85.61	1	0
	y	-0.10	-0.82	-0.38	1.39	0	0
C7	x	0.13	0.00	0.78	13.12	0	0
	y	0.56	0.09	-0.43	0.90	0	0
C8	x	0.29	0.39	1.19	20.81	0	0
	y	0.47	0.52	0.08	1.08	0	0
C9	x	1.51	1.38	1.23	1.37	0	0
	y	-0.25	7.16	-0.58	-1.19	0	0
C10	x	0.81	1.27	17.11	0.77	0	0
	y	5.58	2.60	0.52	0.79	0	0
C11	x	1.86	1.58	1.78	2.08	0	0
	y	0.98	-0.36	12.81	-5.40	0	1
C12	x	-2.11	-2.33	-1.87	-3.36	0	0
	y	-1.80	5.95	10.32	8.20	0	1
C13	x	-0.11	-0.94	0.82	38.56	0	0
	y	2.01	2.56	1.20	25.42	0	0
C14	x	3.88	37.54	2.84	2.72	1	0
	y	3.98	-0.02	2.83	3.32	2	0
C15	x	2.95	35.79	2.21	1.02	0	0
	y	-5.19	-5.73	32.03	-7.47	0	0
C16	x	1.72	1.27	2.05	1.60	0	0
	y	-6.70	-3.37	30.86	-6.55	0	0
C17	x	3.36	3.58	13.06	5.12	3	0
	y	2.00	2.79	6.31	2.52	0	0
C18	x	1.41	1.98	32.58	1.87	0	0
	y	0.09	2.87	16.30	2.95	0	0
C19	x	-0.15	1.56	57.18	0.02	0	0
	y	-0.38	3.68	28.45	3.71	2	0
C20	x	-0.88	3.68	128.21	-0.02	1	0
	y	-2.27	4.31	47.95	4.20	2	0
C21	x	2.45	5.05	81.34	4.68	2	0
	y	2.30	5.24	9.77	4.49	2	0

* FP = false positive; FN = false negative

Table 5.7 Damage localization using the z-index tests (results for all the tested configurations). [Bernagozzi et al., 2017 b]

The total number of false positives and false negatives obtained using the modal flexibility-based methodology for damage localization is equal to 19. This number was compared to the total number of the z-index tests performed for damage localization. This last number is equal to t = 160 and was calculated as follows

$$t = c \times n \times d \tag{5.20}$$

where c is the total number of the analyzed damaged configurations (i.e. c = 20), n is the number of the stories of the steel frame structure (i.e. n = 4), and d is the number of the analyzed directions (i.e. d = 2, since the analyses were performed in the X and the Y directions). By comparing the total number of false positives and false negatives (i.e. 19) against the total number of the z-index tests (i.e. 160), the failure rate in damage localization can be evaluated and it is equal to 11.87 %. A success rate of 88.13 % was thus obtained in the damage localization when the procedure outlined in Section 5.1.1 was applied on the tested configurations.

If one considers the cases that were falsely detected, it is evident from Table 5.7 that most of these cases are false positives (i.e. 17 cases). In such cases, the statistical z-index test fails in the classification of the story as undamaged (i.e. there is an indication of damage when the damage is not present in the story). By analyzing the results reported in Table 5.7, it can be observed that the values of the z-index obtained for the false positive cases are, in general, slightly higher than the selected threshold. On the contrary, the values of the z-index that are related to the localization of a story that is effectively damaged are, in general, remarkably higher than the threshold. For example, this is evident in Table 5.7 if the configuration C3 and the z-index values related to the X direction are considered: z_1 =140.41 is the value of the z-index that correctly localizes the damage imposed at the first story and in the x direction, while z_2 = 3.96 represents a false positive case.

False negative results in the damage localization were obtained in two cases. These two cases were obtained for configurations C11 and C12 in the localization of a damage that, for both configurations, was imposed at the fourth story of the structure in the strong or Y direction. These errors in the localization of the damage could be due to modal truncation errors[6] that are introduced on the modal flexibility-based interstory drifts when only a limited number of modes is included in the calculations. This is the case for the present analysis, since, as already mentioned in the previous paragraphs of this section, only the first five modes of the structure were included in the calculation of the damage sensitive features, while the higher modes affected by more uncertainties were excluded. Referring to this point, it is evident that the higher the number of modes included in the computation of the modal flexibility matrices and the MF-based deflections, the closer these estimated quantities are with respect to the static or target values. However, it is also clear that if the higher modes are affected by significant uncertainties and are included in the analysis, then these uncertainties are also introduced on the modal flexibility matrices and on the deflections.

The quantification of the damage was then carried out for the different configurations and, specifically, for each story that is labelled as damaged by the z-index test. The operation of quantifying the damage was performed by evaluating the damage severity index, and, as already done in the damage localization, the analyses were performed separately for the X and the Y directions (i.e. the weak and the strong directions of the structure).

Referring to the damage quantification, it is of interest to consider at first the results of the progressive damage test (i.e. configurations C17, C18, C19, and C20). As shown in Fig. 5.10, these configurations were tested by progressively increasing the number of the braces that were removed at the 2nd story. Moreover, these configurations are characterized by a plan-symmetric distribution of the story stiffness at all the stories (including the damaged story). This means that the results of the damage quantification obtained for the configurations C17, C18, C19, and C20 are basically the same results that can be obtained by applying the original formulation of

[6] A discussion on the effect of the modal truncation errors on the damage sensitive features and the metrics used in damage detection is presented also in Section 6.4.2.2. of Chapter 6.

the PSIL method. The modal flexibility-based deflections and the interstory drifts evaluated in the two prevalent directions of the structure for these damaged configurations and for the undamaged configuration C1 are reported in Fig. 5.20. The red dashed lines reported in Fig. 5.20a, 5.20b, 5.20c, 5.20d and considered from the left-hand side to the right-hand side of the figure correspond to the configurations C17, C18, C19, and C20, respectively. By considering the results presented in Fig. 5.20c, 5.20d (i.e. the interstory drifts related to the analyses in the X and the Y directions, respectively), it is evident that the higher the number of the braces removed at the 2nd story of the structure, the higher the interstory drifts related to that story. On the contrary, the interstory drifts related to the other stories are in general not affected by the damage. In other words, the stiffness reductions imposed at the 2nd story both in the X and the Y directions do not substantially alter the interstory drifts of the original structure at the 1st, the 3rd, and the 4th stories. The damage severity indices related to the analyses performed in the X and the Y directions ($\alpha_{s,x}$ and $\alpha_{s,y}$) were evaluated for the configurations C17, C18, C19, and C20 starting from the values of the interstory drifts that were obtained at the 2nd story of the structure. The results are shown in Fig. 5.21. This figure shows that the higher the number of the braces removed at the 2nd story of the structure, the higher the damage severity index both for the X and the Y directions.

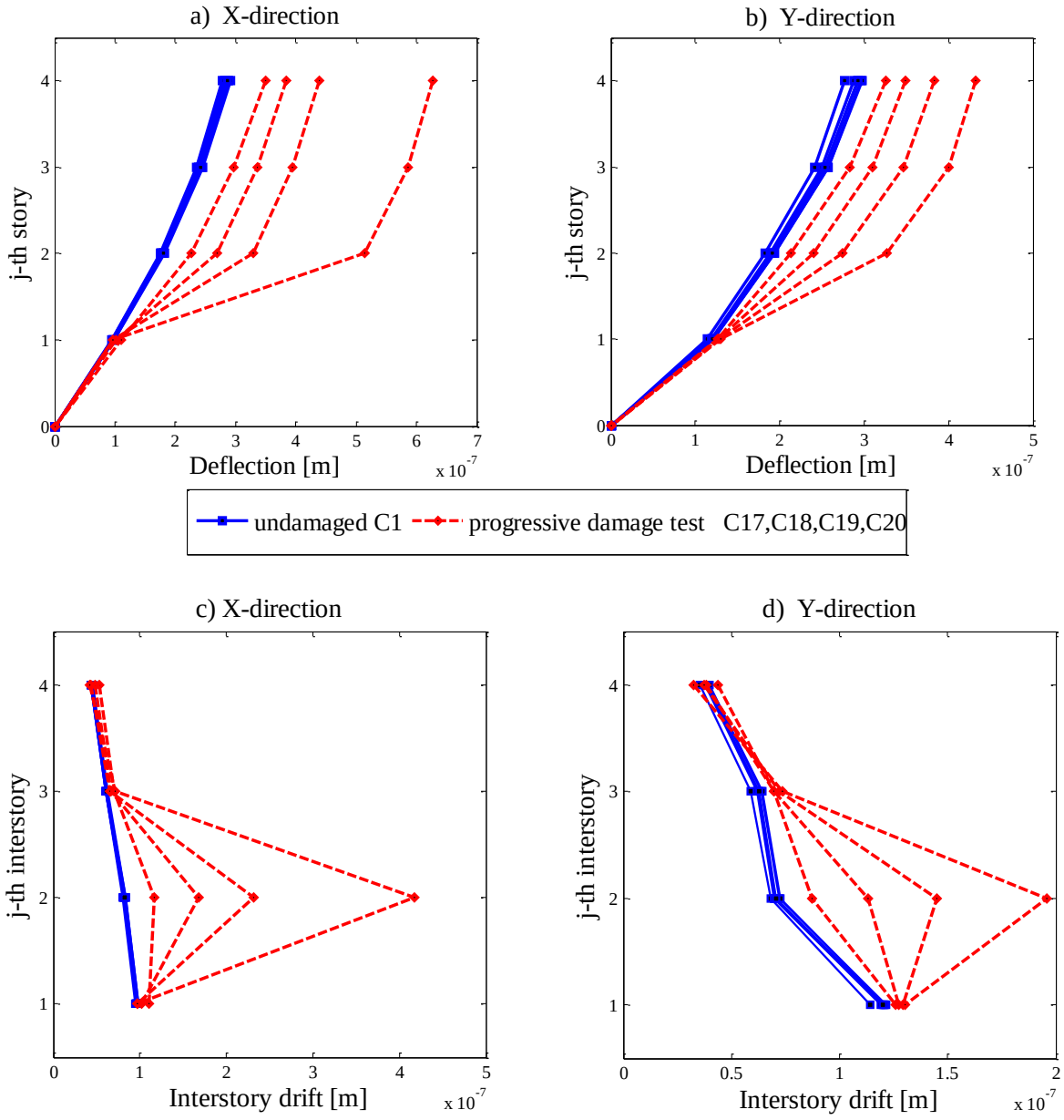

Figure 5.20. Progressive damage test on plan-symmetric configurations: (a) deflections in X direction due to load $\boldsymbol{p_x}$; (b) deflections in Y direction due to load $\boldsymbol{p_y}$; (c) interstory drifts in X direction due to load $\boldsymbol{p_x}$; (d) interstory drifts in Y direction due to load $\boldsymbol{p_y}$. Adapted from [Bernagozzi et al., 2017 b].

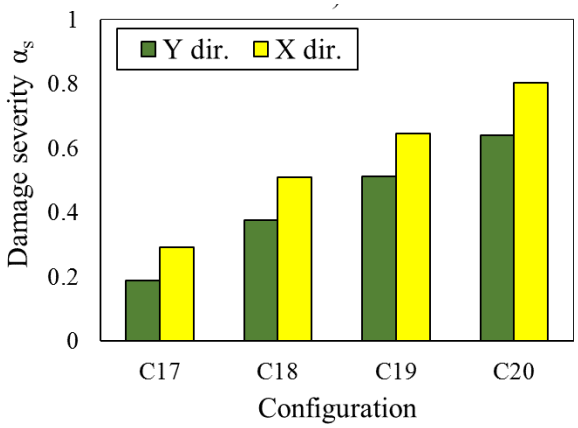

Figure 5.21. Damage quantification for the progressive damage test (plan-symmetric configurations) - damage severity evaluated at the 2nd story of the structure. Adapted from [Bernagozzi et al., 2017 b].

Some observations can be formulated on the values of the damage severity that were obtained for the structural configurations considered in the progressive damage test. As already mentioned in Chapter 3, the damage severity index quantifies the relative portion of the story stiffness that is lost due to the damage. This index, in fact, is a relative index in the range $0 \leq \alpha_s < 1$.

If one considers the configuration C20 (which is the last configuration shown in Fig. 5.10), the following result is obtained: by removing all the sixteen braces from one story of the structure (i.e. the 2nd story in such case), the damage severity is approximately equal to 0.65 and 0.8 for the y direction and the x direction, respectively (i.e. the strong and the weak direction of the structure). In other words, this means that by performing this operation (i.e. removing all the braces in one story) the 65% and the 80% of the story stiffness (in the y and x directions) of the original structure is lost. By analyzing these values of the damage severity, it is clear that most of the contribution to the story stiffness of the structure is due to the diagonal wall braces, which as already mentioned in Section 5.1.2.1, are pre-tensioned elements. The contribution of all the diagonal braces to the story stiffness is thus much higher than the contribution of the columns of the structure.

A second observation can be formulated by comparing the values of the damage severity that were obtained by performing the analyses in the X direction or

in the Y direction. For each configuration (i.e. C17, C18, C19, or C20), two different values of the damage severity were obtained in the two directions, and the damage severity in x direction is higher than the damage severity in y direction. This result was obtained by removing the same number of braces in the x and the y directions of the structure (i.e. for each direction two, four, six, and eight braces were removed for the configurations C17, C18, C19, and C20, respectively). This result is expected and can be explained as follows. The columns of the structure are double T sections, and thus the contribution to the story stiffness of the columns is different in the two directions. In the y direction (i.e. the strong direction according to the orientation of the column sections) the columns have a relative contribution to the story stiffness that is higher then the contribution of the columns in the x direction (i.e. the weak direction). This explains the fact that, by removing the same number of braces in the two directions, higher values of the damage severity were obtained in the x direction (with respect to the y direction).

A final comment must be done on the values of the damage severity that were obtained from the experimental test. The damaged configurations are characterized by amounts of damage (i.e. stiffness reductions imposed on the original structure) that correspond in some cases to realistic situations, while other cases can be more rare in practical situations. In any case, configurations that are characterized by very high values of the damage severity (for example, configurations with completely unbraced stories, such as configuration C20) were considered to have a complete insight of the tendencies of the damage quantification results.

As already mentioned, the diagonal wall braces have a very high contribution to the story stiffness, and such braces are present at all the stories of the structure. Of course, the contribution of the columns to the story stiffness might be slightly different if one takes into account the different stories. For example, it is expected that the contributions of the columns to the story stiffness at the second and the third stories are very similar. While it is expected that slightly different contributions are present at the fourth and the first stories (on one side because the fourth story is the top story of the structure, on the other side because at the first story the structure is connected to a grid of beams positioned at the base of the structure). In any case, since the contribution of the diagonal braces to the story stiffness is dominating with respect to

the contribution of the columns (especially for the weak direction of the structure), it is expected that the above-mentioned differences in the contributions of the columns (to the story stiffness) at the different stories are small. It is thus expected that similar values of the damage severity are obtained for configurations characterized by the same number of braces removed in a generic story even if this generic story is different for the mentioned configurations. For example, it is expected that the damage severity obtained for a configuration that is completely unbraced at the 2nd story is similar to the damage severity for a configuration that is completely unbraced at the 3rd story.

This last observation is confirmed by the results presented in Fig. 5.22, where, for all the tested configurations, the damage severity indices are plotted against the number of the braces removed in one story of the structure, without considering at which story the braces were removed. In particular, the results presented in Fig. 5.22a, 5.22b are related to the analyses performed in the X and the Y directions, respectively. One important aspect that must be highlighted is the following. The blue points in Fig. 5.22 are related to damaged configurations with a plan-symmetric distribution of the story stiffness at all the stories (including the damaged stories). On the contrary, the red points in Fig. 5.22 are related to damaged configurations with a plan-asymmetric distribution of the story stiffness at the damaged stories (of course, at the undamaged stories of the damaged configurations the distribution of the story stiffness is equal to the one of the original structure and thus is plan symmetric).

As already mentioned in Section 5.1.1, the results that are obtained using the considered damage detection procedure on structures with a plan-symmetric distribution of the stiffness at all the stories are basically the same results that can be obtained by applying the original formulation of the PSIL method (which was developed for plane structures). On the basis of this premise, the values of the damage severity obtained from the experimental test for configurations with a plan-symmetric distribution of the story stiffness (i.e. blue points in Fig. 5.22) can be considered as the true (or target) values of the damage severity (obtained for a certain number of braces removed and for a certain direction).

If one considers the results presented in Fig. 5.22 and considers a certain number of braces removed, it is evident that the red points (related to plan-asymmetric

configurations) are, in general, located above the blue points, which are related to plan-symmetric configurations. By considering the blue points as the target values of the damage severity, it is clear that the damage severity is slightly overestimated when configurations with a plan-asymmetric distribution of the story stiffness at the damaged stories are considered. For example, referring to Fig. 5.22a (i.e. x direction) and considering the case in which four braces were removed in the weak direction of the structure, the damage severity obtained when such braces were removed by creating a plan-symmetric configuration is approximately equal to 0.5. On the contrary, the damage severity obtained when four braces were removed in the x direction of the structure by creating a plan-asymmetric configuration is approximately equal to 0.6.

A final observation can be formulated on the results presented in Fig. 5.22. Referring to the blue points, a sort of an approximately proportional trend can be observed between the damage severity α_s and the number of braces that were removed (both for the X and the Y directions). On the contrary, the reds points tend, in general, to be not aligned with this proportional trend.

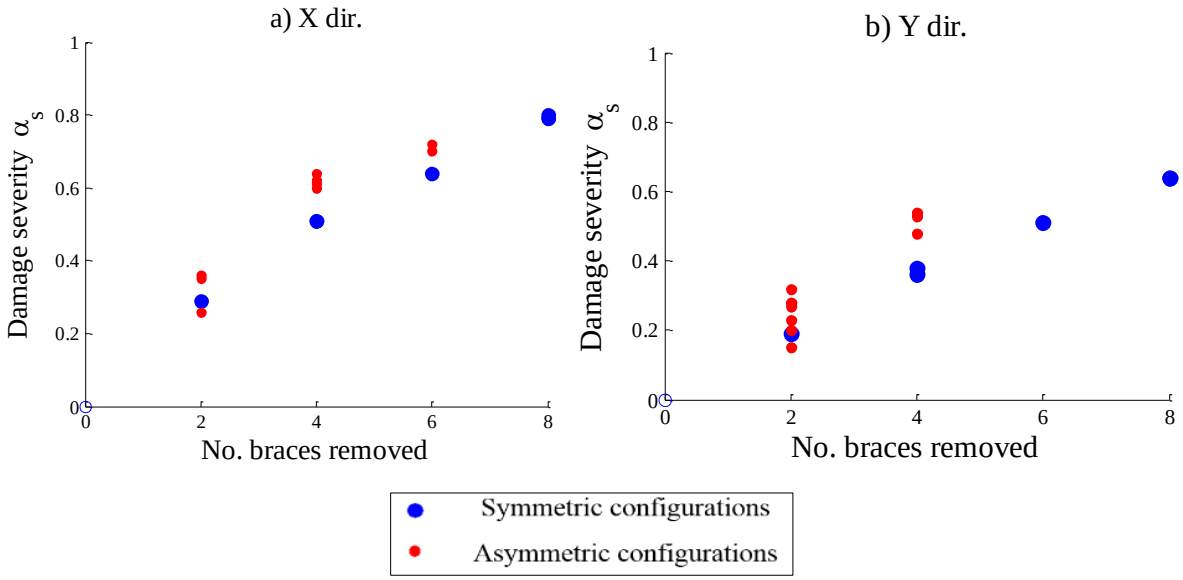

Figure 5.22. Damage quantification (results plotted for all the tested configurations): (a) damage severity in X direction; (b) damage severity in Y direction. Adapted from [Bernagozzi et al., 2017 b].

From the results of the analyses performed using the damage detection procedure outlined in Section 5.1.1 on the data of a steel frame structure that was tested under ambient vibrations (by considering structural configurations characterized by either plan-symmetric or plan-asymmetric distributions of the story stiffness), the following partial conclusions can be drawn. For the considered steel frame structure very good results were obtained in the localization of the damaged stories (the success rate in damage localization is, in fact, very high). Referring to the damage quantification, the damage severity is slightly overestimated when configurations with a plan-asymmetric distribution of the story stiffness at the damaged stories are considered.

5.2 An attempt to extend the PSIL method to account for plan-asymmetry in "box type" 3D building structures

The results presented in previous section have highlighted the necessity of modifying and improving the damage detection procedure that has been applied on a "box type" 3D building structure tested under ambient vibrations. The main purpose is to correct the slight overestimations that were obtained in the damage quantification for the configurations considered in the experimental test that are characterized by a plan-asymmetric distribution of the story stiffness at the damage stories. The research investigations that were carried out in an attempt to attain this objective are described in this section.

5.2.1 Analytical formulation

The types of structures that are considered in this section (similarly to Section 5.1.1) are simple rectangular "box type" *n*-story 3D building structures that can be modeled as 3*n*-DOF shear-type building structures. However, for the sake of simplicity, in the present section the analytical formulation is developed, at first, by considering models of 1-story shear-type 3D building structures. Then, the analytical formulation developed for the 1-story shear building structures will be applied to each story of the

n-story shear building structures, and thus the analytical formulation is generalized to the case of such *n* story structures (Fig. 5.23).

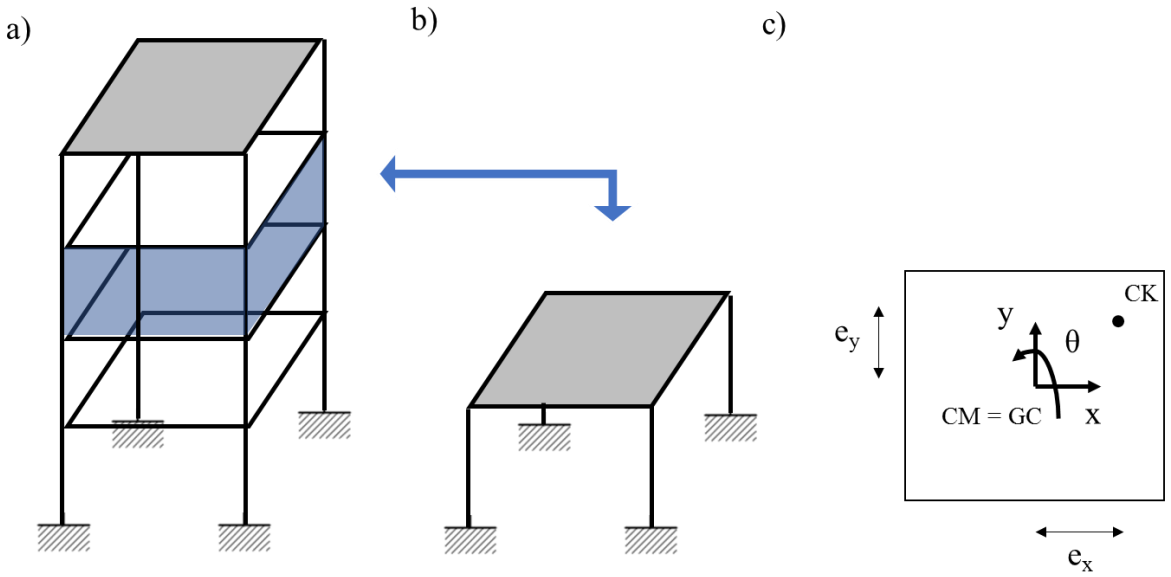

Figure 5.23. Building models: a) *n*-story shear-type building model; b) 1-story shear-type building model; c) plan view of the structure.

The stiffness matrix of a 1-story shear-type 3D building structure (i.e. a structure that can be modeled using 3 DOFs) can be in general expressed as follows

$$\boldsymbol{K} = \begin{bmatrix} k_x & 0 & -k_x e_y \\ 0 & k_y & k_y\, e_x \\ -k_x e_y & k_y\, e_x & k_\theta + k_x e_y^2 + k_y\, e_x^2 \end{bmatrix} \tag{5.21}$$

where k_x, k_y, and k_θ are, respectively, the uncoupled stiffness of the structure in x-, y-, and θ directions [Wang et al., 2013]. The parameters e_x and e_y represent the distance (projected on the x and the y axes, respectively) between the generic center of rigidity (i.e. the center of stiffness CK) and the geometric center of the structure (GC). Such parameters e_x and e_y are indicated in this section as the eccentricities in x and y directions, respectively. It is worth noting, that, as already mentioned in Section 5.1.1, for the considered structures (i.e. simple rectangular "box type" 3D building structures) the geometric center of the structure can be assumed as the center of mass (CM) of the structure.

Using a formulation similar to the one adopted in Eq. (5.21), the flexibility matrix of a 1-story shear-type 3D building structure can be expressed as follows

$$\boldsymbol{F} = \begin{bmatrix} f_x + f_\theta e_y^2 & -f_\theta e_x e_y & f_\theta e_y \\ -f_\theta e_x e_y & f_y + f_\theta e_x^2 & -f_\theta e_x \\ f_\theta e_y & -f_\theta e_x & f_\theta \end{bmatrix} \tag{5.22}$$

where f_x, f_y, and f_θ are, respectively, the uncoupled flexibility of the structure in x-, y-, and θ directions.

The simple models of a 1-story shear building structure expressed by Eqs. (5.21, 5.22) are used in this section to show the main reason for which the approach adopted in Section 5.1 can provide results in the damage quantification (i.e. values of the damage severity) that are theoretically not correct when structures with a plan-asymmetric distribution of the story stiffness are considered. These simple models are also used to derive a possible strategy that can be used to correct the results of the damage quantification for such structures (for example, to correct the slight overestimations that were obtained, as shown in Section 5.1.2.3, in the values of the damage severity related to the plan-asymmetric configurations).

Thus, let us consider such simple models of 1-story shear building structures, and let us evaluate the deflections (i.e. the two displacements in x and y directions and the rotation of the structure) by applying inspection loads. For example, an inspection load applied only in x direction can be considered. For the considered structure such load is defined as follows

$$\boldsymbol{p} = \begin{bmatrix} 1 \\ 0 \\ 0 \end{bmatrix} \tag{5.23}$$

The deflection of the structure can be evaluated by multiplying the flexibility matrix (Eq. 5.22) and the inspection load (Eq. 5.23)

$$\boldsymbol{x} = \boldsymbol{F}\,\boldsymbol{p} = 1 \times \begin{bmatrix} f_x + f_\theta e_y^2 \\ -\left(f_\theta e_x e_y\right) \\ f_\theta e_y \end{bmatrix} \tag{5.24}$$

Then, the considered analytical models are specified for structures that are undamaged or damaged[7]. Let us consider a structure that is undamaged, and that is characterized by a plan-symmetric distribution of the story stiffness. In such case the eccentricities $e_{x,B}$ and $e_{y,B}$ are equal to zero. The deflection of such undamaged structure due to the inspection load applied in x direction (Eq. 5.23) is thus

$$\boldsymbol{x_{B,sym}} = 1 \times \begin{bmatrix} f_{x,B} \\ 0 \\ 0 \end{bmatrix} \tag{5.25}$$

Then, a structure that is damaged is considered and, specifically, two different configurations of such structure are taken into account. In the first configuration the damaged structure has a plan-symmetric distribution of the story stiffness (i.e. $e_{x,I} = 0$ and $e_{y,I} = 0$), and the deflection due to inspection load in x direction is

$$\boldsymbol{x_{I,sym}} = 1 \times \begin{bmatrix} f_{x,I} \\ 0 \\ 0 \end{bmatrix} \tag{5.26}$$

In the second configuration the damaged structure has the same value of the uncoupled stiffness $k_{x,I}$ (or flexibility $f_{x,I}$) in x direction but it is characterized by a plan-asymmetric distribution of the story stiffness. For example, the center of stiffness is in a position for which $e_{y,I} \neq 0$ and $e_{x,I} = 0$. In such case the deflection of the structure due to the inspection load applied in x direction is

$$\boldsymbol{x_{I,asym}} = 1 \times \begin{bmatrix} f_{x,I} + f_{\theta,I}\, e_{y,I}^2 \\ 0 \\ f_{\theta,I}\, e_{y,I} \end{bmatrix} \tag{5.27}$$

The first components of the vectors reported in Eqs. (5.25, 5.26, and 5.27) are the displacements of the structure in x direction. It is trivial that, since the considered structures are 1-story shear buildings, the displacements in x or y directions are thus the drifts of the single story of the structures. These displacements can thus be used to evaluate the damage severity according to the criteria reported in Section 5.1.1.

[7] The undamaged and damaged structures are indicated, according to the notation used in the rest of the thesis, with the subscript B and I, respectively. Such subscripts stand for “baseline” state and “inspection” stage.

If hypothetically the damage severity in x direction is evaluated for the two above-mentioned configurations of the damaged structure (i.e. the plan-symmetric and the plan-asymmetric configurations) the following result is obtained. The damage severity evaluated for the damaged structure with a plan-symmetric configuration is

$$\alpha_{s,x,sym} = \frac{1 \times (f_{x,I} - f_{x,B})}{1 \cdot f_{x,I}} \tag{5.28}$$

On the contrary, the damage severity evaluated for the damaged structure with a plan-asymmetric configuration is

$$\alpha_{s,x,asym} = \frac{1 \times (f_{x,I} + f_{\theta,I}\, e_{y,I}^2 - f_{x,B})}{1 \times (f_{x,I} + f_{\theta,I}\, e_{y,I}^2)} \tag{5.29}$$

As evident in Eqs. (5.28, 5.29), the values of the damage severity evaluated for the damaged structure in the two configurations are different. In fact, in Eq. (5.29) there is an additional contribution (with respect to Eq. 5.28) that is represented by the term $f_{\theta,I}\, e_{y,I}^2$.

At this point it is important to consider again that in this chapter an attempt is made to extend the Positive Shear Inspection Load method [Koo et al., 2010], originally formulated for structures that can be modeled as plane structures, to the case of structures with a generic distribution of the story stiffness. The general objective that should guide the development of the extended approach is thus to obtain, using the damage severity parameters (related to the x and y directions of the structure), information about the reductions in the uncoupled story stiffness (related, respectively, to the x and y directions) that the structure has experienced due to the damage. It is clear that for the analytical models of the two configurations of the damaged structure considered in this section it is desirable to obtain the same damage severity in x direction. This is because it has been assumed that the two configurations of the damaged structure are characterized by the same uncoupled stiffness $k_{x,I}$ (or flexibility $f_{x,I}$) in x direction. In light of this premise, the expression of the damage severity related to the plan-asymmetric structure (Eq. 5.29) can not be considered as a correct way for quantifying the damage.

An important observation that can be formulated if one compares the deflections obtained for the two damaged configurations of the 1-story building

structure (i.e. Eqs. 5.26, 5.27, respectively) is the following. The deflection of the damaged structure with a plan-asymmetric configuration is characterized by a story rotation induced by the inspection load applied in x direction (Eq. 5.23). On the contrary, in the deflection related to the structure with a plan-symmetric configuration the story rotation is equal to zero. On the basis of this observation, the strategy adopted in an attempt to achieve a correct quantification of the damage (i.e. a correct evaluation of the damage severity) was developed by investigating the applicability of inspection loads that are able to make the story rotation of the structure equal to zero, even if the considered story is characterized by a plan-asymmetric distribution of the story stiffness. This problem was analyzed again by considering the simple analytical model of the 1-story shear building structure.

For a generic 1-story shear-type 3D building structure with a generic distribution of the story stiffness (either plan-symmetric or plan-asymmetric), the load that applied to the structure induces, for example, a deflection characterized by a unitary translation in x direction

$$\boldsymbol{x} = \begin{bmatrix} 1 \\ 0 \\ 0 \end{bmatrix} \tag{5.30}$$

can be evaluated as follows

$$\bar{\boldsymbol{p}}_{\boldsymbol{x}} = \boldsymbol{K}\,\boldsymbol{x} = \begin{bmatrix} k_x & 0 & -k_x e_y \\ 0 & k_y & k_y\, e_x \\ -k_x e_y & k_y\, e_x & k_\theta + k_x e_y^2 + k_y\, e_x^2 \end{bmatrix} \begin{bmatrix} 1 \\ 0 \\ 0 \end{bmatrix} = k_x \begin{bmatrix} 1 \\ 0 \\ -1 \cdot e_y \end{bmatrix} \tag{5.31}$$

This load is basically the first column of the stiffness matrix $\boldsymbol{K}$ of the structure. In order to define an inspection load that is independent as much as possible from parameters that are structure-dependent, let us consider a scaled version of the load reported in Eq. (5.31). This scaled version of the load is independent from the value of the uncoupled stiffness in x direction, and it has the component related to the x direction that is equal to one

$$\boldsymbol{p}_{\boldsymbol{x}}^{*} = \begin{bmatrix} 1 \\ 0 \\ -1 \cdot e_y \end{bmatrix} \tag{5.32}$$

The load $\boldsymbol{p}_{\boldsymbol{x}}^{*}$ has thus the following property: if this load is applied to the 1-story shear building structure, this load does not induce a story rotation. To check this property, the flexibility matrix of the structure (Eq. 5.22) can be multiplied by the load $\boldsymbol{p}_{\boldsymbol{x}}^{*}$ (Eq. 5.32)

$$\boldsymbol{x} = \boldsymbol{F}\,\boldsymbol{p}_{\boldsymbol{x}}^{*} = \begin{bmatrix} f_x + f_\theta e_y^2 & -f_\theta e_x e_y & f_\theta e_y \\ -f_\theta e_x e_y & f_y + f_\theta e_x^2 & -f_\theta e_x \\ f_\theta e_y & -f_\theta e_x & f_\theta \end{bmatrix} \begin{bmatrix} 1 \\ 0 \\ -1 \cdot e_y \end{bmatrix} = 1 \times \begin{bmatrix} f_x \\ 0 \\ 0 \end{bmatrix} \tag{5.33}$$

As shown in Eq. (5.33), the deflection of the structure due to the load $\boldsymbol{p}_{\boldsymbol{x}}^{*}$ has only one non-zero component in x direction. Moreover, such component is basically the uncoupled flexibility of the structure in x direction (this is because the load $\boldsymbol{p}_{\boldsymbol{x}}^{*}$ has been normalized in a way that the first component is equal to one).

Thus, by considering the hypothetical case in which the flexibility matrix of the structure has been estimated from a vibration test, the above-mentioned load can be a good candidate to be applied as an inspection load for the purpose of dealing with a generic (either plan-symmetric of plan-asymmetric) building structure. It is worth noting that the formulation that is derived herein for a 1-story shear building structure can be easily generalized to the case of an *n*-story building structure, as done later in this section.

In the same way, by considering again the analytical model of the 1-story shear building structure, the hypothetical inspection load that should be applied for performing the analysis in the y direction is defined as follows

$$\boldsymbol{p}_{\boldsymbol{y}}^{*} = \begin{bmatrix} 0 \\ 1 \\ 1 \cdot e_x \end{bmatrix} \tag{5.34}$$

If such load is applied to the structure, the resulting deflection has only one non-zero component in y direction, and such component is basically the uncoupled flexibility of the structure in y direction. The following calculations show the above-mentioned property

$$\boldsymbol{x} = \boldsymbol{F}\,\boldsymbol{p}_{\boldsymbol{y}}^{*} = \begin{bmatrix} f_x + f_\theta e_y^2 & -f_\theta e_x e_y & f_\theta e_y \\ -f_\theta e_x e_y & f_y + f_\theta e_x^2 & -f_\theta e_x \\ f_\theta e_y & -f_\theta e_x & f_\theta \end{bmatrix} \begin{bmatrix} 0 \\ 1 \\ 1 \cdot e_x \end{bmatrix} = 1 \times \begin{bmatrix} 0 \\ f_y \\ 0 \end{bmatrix} \tag{5.35}$$

The approach of adopting inspection loads that have the form of the ones derived in this section using the simple 1-story building model (Eqs. 5.32, 5.34) can be, of course, applied in practical situations (when one has to deal with modal flexibility matrices assembled from a vibration test) only if the values of the eccentricities of the structure can be estimated from the data of the experimental test. In other words, the position of the center of stiffness of each story of the structure has to be known to assemble the considered inspection loads.

Performing some specific operations on the modal flexibility matrices (for example, estimated from the vibration test) is a possible way to obtain the values of the eccentricities of the building structures[8]. The theoretical formulation of this approach is shown herein considering again the analytical model of the 1-story shear building structure. Then, the approach will be extended to deal with an *n*-story shear building structure.

Let us consider the deflection of the 1-story shear building structure obtained by applying a load that consists only of a unitary torque (i.e. a moment of torsion equal to one). This deflection can be evaluated as follows

$$\boldsymbol{x} = \boldsymbol{F}\,\boldsymbol{p_\theta} = \begin{bmatrix} f_x + f_\theta e_y^2 & -f_\theta e_x e_y & f_\theta e_y \\ -f_\theta e_x e_y & f_y + f_\theta e_x^2 & -f_\theta e_x \\ f_\theta e_y & -f_\theta e_x & f_\theta \end{bmatrix} \begin{bmatrix} 0 \\ 0 \\ 1 \end{bmatrix} = 1 \times \begin{bmatrix} f_\theta e_y \\ -f_\theta e_x \\ f_\theta \end{bmatrix} \tag{5.36}$$

If one analyzes the components of the deflection reported in Eq. (5.36), it can recognize that the ratios between each displacement (in the x or y direction) and the story rotation are equal to the values of the eccentricity e_x and e_y.

This simple example suggests that, in theory, if one has assembled a modal flexibility matrix of a building structure (for example, from the data of a vibration test), then the deflection of the structure due to a load that has the form of the one considered in Eq. (5.36) contains information about the eccentricities of the structure.

Referring again to the model of the 1-story shear building, if the flexibility matrix $\boldsymbol{F}$ is known (or at least an estimate of such matrix is known) then the eccentricities e_x and e_y can be obtained as follows

[8] This problem was also investigated in the work by [Bernal & Gunes, 2004].

$$\begin{bmatrix} u \\ \mathrm{v} \\ \theta \end{bmatrix} = \boldsymbol{F} \begin{bmatrix} 0 \\ 0 \\ 1 \end{bmatrix} \tag{5.37}$$

where the displacements in x-, y-, and θ directions are here indicated, for the sake of convenience, as u, v, and θ, respectively. The eccentricities in x and y directions are, respectively

$$e_x = -\frac{v}{\theta} \tag{5.38}$$

$$e_y = \frac{u}{\theta} \tag{5.39}$$

The fundamental equations of the analytical formulation presented until this point of the section for a 1-story 3D shear building structure are now extended to the case of an n-story 3D shear building structure and then used to integrate the damage detection procedure defined in previous section (i.e. Section 5.1.1) and that have been applied on the data of the ambient vibrations tests performed on the steel frame structure. This integrated version of the procedure is defined in an attempt to have a method that can provide a correct quantification of the damage severity for structures characterized by a plan-asymmetric distribution of the story stiffness.

In the integrated version of the damage detection procedure the first three steps already defined in Section 5.1.1 are unaltered. These first three steps are the following: 1) execution of the ambient vibration test; 2) estimation of the modal parameters of the structure using any output-only modal identification technique; 3) estimation of the modal flexibility matrix of the 3D building structure.

Then, differently from the procedure outlined in Section 5.1.1, an additional step is introduced in the integrated version of the methodology. This step is indicated as step no. 3b, and it is the step related to the estimation of the position of the center of stiffness (i.e. the values of the eccentricities) for each story of the building structure. This operation is performed by applying to the structure (i.e. to the experimentally-derived modal flexibility-based model of the structure estimated using Eq. 5.2) a load defined as follows

$$\boldsymbol{p_\theta} = \begin{pmatrix} \{\mathbf{0}\} \\ \{\mathbf{0}\} \\ \{\mathbf{1}\} \end{pmatrix}_{3nx1} = \begin{pmatrix} 0 \\ \vdots \\ 0 \\ \\ 0 \\ \vdots \\ 0 \\ \\ 1 \\ \vdots \\ 1 \end{pmatrix} \tag{5.40}$$

This load $\boldsymbol{p_\theta}$ consists of moments of torsion with unitary values that are applied at all the stories. In other words, this load can be considered as a uniform load applied in the direction θ. The modal flexibility-based deflection of the structure due to such load $\boldsymbol{p_\theta}$ can be calculated as follows

$$\boldsymbol{x_\theta} = \boldsymbol{F_r}\, \boldsymbol{p_\theta} \tag{5.41}$$

where $\boldsymbol{x_\theta}$ is a $3n \times 1$ vector that contains the components of the modal flexibility-based deflection. For the sake of convenience and clarity, in the present formulation the components of the vector $\boldsymbol{x_\theta}$ are indicated as

$$\boldsymbol{x_\theta} = \begin{pmatrix} \{\boldsymbol{u}\} \\ \{\boldsymbol{v}\} \\ \{\boldsymbol{\theta}\} \end{pmatrix}_{3nx1} = \begin{pmatrix} u_n \\ \vdots \\ u_1 \\ \\ v_n \\ \vdots \\ v_1 \\ \\ \theta_n \\ \vdots \\ \theta_1 \end{pmatrix} \tag{5.42}$$

The values of the eccentricities (in x and y directions) can then be estimated for each story of the structure as follows

$$e_{x,j} = \begin{cases} -\frac{v_j - v_{j-1}}{\theta_j - \theta_{j-1}} & for\ j = 2 \dots n \\ -\frac{v_j}{\theta_j} & for\ j = 1 \end{cases} \tag{5.43}$$

$$e_{y,j} = \begin{cases} \frac{u_j - u_{j-1}}{\theta_j - \theta_{j-1}} & for\ j = 2 \dots n \\ \frac{u_j}{\theta_j} & for\ j = 1 \end{cases} \tag{5.44}$$

Such values of the eccentricities are then used to define the inspection loads. Similarly to the procedure outlined in Section 5.1.1, the inspection loads are applied in the x and the y directions of the structure to perform two separate analyses. However, the inspection loads that are presented at the fourth step of Section 5.1.1 (i.e. the loads reported in Eqs. 5.3) are substituted, according to the improved procedure, with inspection loads that have the same form of the inspection loads that have been derived in this section for the 1-story shear building structure (i.e. Eqs. 5.32, 5.34). In the improved procedure the inspection loads are defined as follows

$$\boldsymbol{p}_{\boldsymbol{x}}^{*} = \begin{pmatrix} \{\mathbf{1}\} \\ \{\mathbf{0}\} \\ \{\boldsymbol{M}_{\boldsymbol{z,x}}\} \end{pmatrix}_{3nx1} = \begin{pmatrix} 1 \\ \vdots \\ 1 \\ \\ 0 \\ \vdots \\ 0 \\ \\ M_{z,x,n} \\ \vdots \\ M_{z,x,1} \end{pmatrix} \quad ; \quad \boldsymbol{p}_{\boldsymbol{y}}^{*} = \begin{pmatrix} \{\mathbf{0}\} \\ \{\mathbf{1}\} \\ \{\boldsymbol{M}_{\boldsymbol{z,y}}\} \end{pmatrix}_{3nx1} = \begin{pmatrix} 0 \\ \vdots \\ 0 \\ \\ 1 \\ \vdots \\ 1 \\ \\ M_{z,y,n} \\ \vdots \\ M_{z,y,1} \end{pmatrix} \tag{5.45}$$

where $M_{z,x,j}$ and $M_{z,y,j}$ (for $j = 1 \dots n$) are moments of torsion applied at the j-th story of the structure that are defined as

$$M_{z,x,j} = \begin{cases} -1 \cdot \ e_{y,j} & for\ j = n \\ -((n-j+1)\ e_{y,j} - (n-j)\ e_{y,j+1}) & for\ j = 1 \dots (n-1) \end{cases} \tag{5.46}$$

$$M_{z,y,j} = \begin{cases} 1 \cdot e_{x,j} & for\ j = n \\ (n-j+1)\ e_{x,j} - (n-j)\ e_{x,j+1} & for\ j = 1 \dots (n-1) \end{cases} \tag{5.47}$$

Differently from the case of the 1-story shear building, some coefficients that multiply the values of the eccentricities are introduced in the expressions of the moments of torsion $M_{z,x,j}$ and $M_{z,y,j}$ related to the n-story building structure. Such coefficients depend on the story shear that is induced in each story of the shear building structure by the translational uniform load (in x and y directions, respectively). The modal

flexibility-based deflections of the structure are then evaluated for the inspection loads reported in Eq. (5.45)

$$\boldsymbol{x_x} = \boldsymbol{F_r}\, \boldsymbol{p_x^*} \tag{5.48}$$

$$\boldsymbol{x_y} = \boldsymbol{F_r}\, \boldsymbol{p_y^*} \tag{5.49}$$

and, then, the vectors of the interstory drifts of the structure are determined using the criterion that has been already defined in the step no. 5 in Section 5.1.1 (i.e. using Eqs. 5.6, 5.7).

Similarly to the procedure outlined in Section 5.1.1, all the steps from no. 1 to no. 5 (including in such case the step no. 3b) have to be performed both for the undamaged and the possibly damaged structures. Finally, to conclude the description of the integrated version of the damage detection procedure outlined in this section, the step no. 6, which have been already defined in Section 5.1.1, can be applied. In particular, for the purposes of the analyses presented in this section the damage severity related to the x and y directions of the structure will be evaluated using Eqs. (5.13, 5.14).

To conclude this section, the main difference between the approach presented in this section and the approach presented in Section 5.1.1 is summarized. In Section 5.1.1 the inspection loads have only translational components which are equal to one (Eq. 5.3). On the contrary, the inspection loads considered in the present section include, in addition to the translational uniform components, torsional components (i.e., moments of torsion) that depend on the values of the eccentricities (Eq. 5.45). It is important to underline again that, when the modal flexibility-based deflections are evaluated, such moments of torsion should in theory avoid relative rotations between the stories of the structure.

In next sections the results obtained in the damage quantification using the two different types of inspection loads are compared, and the loads are indicated using the following terminology. The inspection loads defined in this section are indicated with the acronym “UL+M” (i.e. uniform load + moments of torsion), while the inspection loads that are defined in Section 5.1.1 are indicated as “UL” loads. A schematic exemplification of the two different types of inspection loads is reported in Fig. 5.24.

In Fig. 5.24a an example of a "UL+M" load applied to the building structure in the y direction is reported, while Fig. 5.24b shows an example of a "UL" load applied to the structure in y direction.

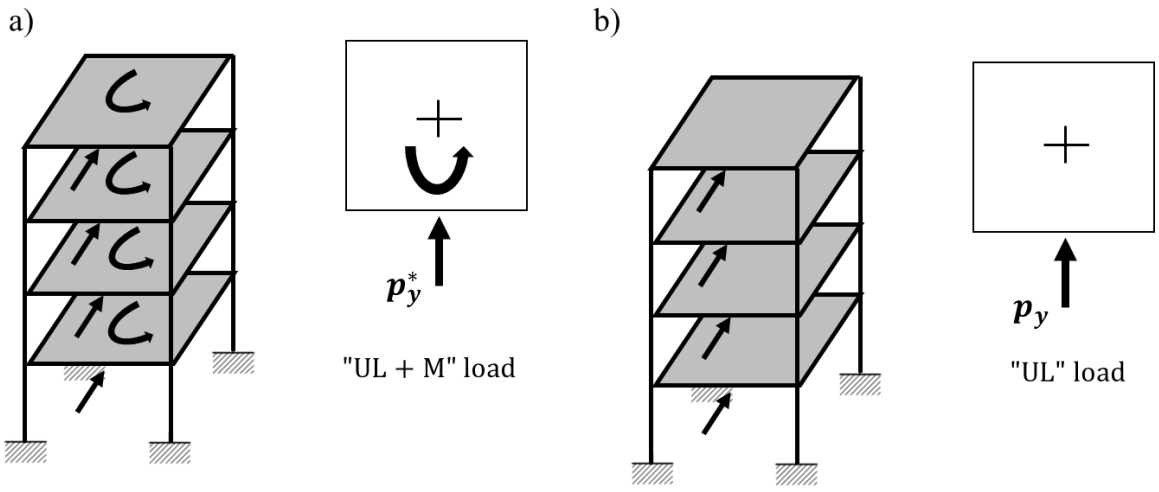

Figure 5.24. Inspection loads applied to the building structure in y direction:
a) UL+M load (Eq. 5.45); b) UL load (Eq. 5.3)

5.2.2 Verification using a numerical model of a 4-story building structure

In this section the analytical formulation of the damage detection procedure presented in previous section (i.e. Section 5.2.1) is tested and verified on a numerical model of a 4-story building structure. The numerical model of this building structure was created using the MATLAB-based finite element analysis code that was made available by the IASC-ASCE Task Group [Johnson et al., 2004]. This code has been already described in Section 5.1.2.3, and, as already mentioned in that section, is able to generate a model of a structure that is similar to the steel frame structure that is located at the EERF laboratory of the University of British Columbia (Vancouver)[9]. The model created using this code is thus a model of a 4-story 3D building structure that is similar to the one that was tested under ambient vibrations, as described in previous sections of this chapter.

[9] As already mentioned in Section 5.1.2.3, the program provided by [Johnson et al., 2004] was used in the context of the analytical studies (phase I) performed by the IASC-ASCE Task Group.

Three important observations have to be formulated on the numerical model that was considered in the analyses presented in this section. Firstly, as already mentioned in Section 5.1.2.3, in the program provided by [Johnson et al., 2004] two different models of the benchmark structure can be considered (i.e. a 12-DOF shear building model or a more complex 120-DOF model). To perform the analyses presented in this section the 12-DOF shear building model was considered. Secondly, it is important to mention that the code developed by [Johnson et al., 2004] can be used to create user-defined damaged configurations of the structure. This operation can be performed in the program using a graphic user interface where one can specify the elements (for example, wall braces of the structure) that want to remove from the model. The program was thus used to create both undamaged and damaged configurations of the structure. Thirdly, for performing the analyses presented in this section the original version of the program provided by [Johnson et al., 2004] was used. Modifications in the parameters that define the characteristics of the structure were not applied to the program[10].

The model considered in the present section has thus the same geometry and the same structural elements of the structure that was tested under ambient vibrations. Referring to the structural elements, the only difference between the numerical model and the real structure is that in the numerical model L-shape profiles (L 25×25×3) are present in the wall bracing system (instead of tie rods). Referring to the structural masses, the numerical model considered in the present section is characterized by a plan-symmetric distribution of the masses. In particular, in the numerical model provided by [Johnson et al., 2004] the structure has four plates that are added at each floor (similarly to the real structure). In the model the values of the masses of the plates related to the first, second, third, and four floors are, respectively, 800 kg, 600 kg, 600 kg, and 400 kg.

The program provided by [Johnson et al., 2004] was thus used to create 12-DOF shear-type models of a 4-story building structure similar to the one that was tested under ambient vibrations. In particular, the program was used to create the

[10] This operation was done, on the contrary, in the context of the experimental analyses, as described in Section 5.1.2.3, to obtain an estimate of the mass matrix of the structure tested under ambient vibrations.

models related to three different configurations of the structure. In the first configuration the structure is fully braced (i.e. the L-shape profiles are present in each bay and in each story of the structure). This configuration represents the undamaged structure (configuration U reported in Fig. 5.25a). The second and the third configurations are, on the contrary, damaged configurations, and these configurations are indicated as configurations D1 and D2, respectively. Both configurations D1 and D2 were created by removing braces at the first story of the structure. Moreover, both the two configurations are characterized by the same number of braces removed in the two main directions of the structure (i.e., two braces are removed from the model at first story in x direction, and two braces are removed at the same story in y direction). However, in configuration D1 the braces were removed by creating a plan-symmetric distribution of the story stiffness at the damaged level (Fig. 5.25b), while in configuration D2 the braces were removed by creating a plan-asymmetric distribution of the story stiffness at the damaged level (Fig. 5.25c). The two considered damaged configurations were thus specifically created to test the proposed approach (Section 5.2.1) based on inspection loads that should be able to deal with plan-asymmetric configurations and to provide a correct estimate of the damage severity for such structures.

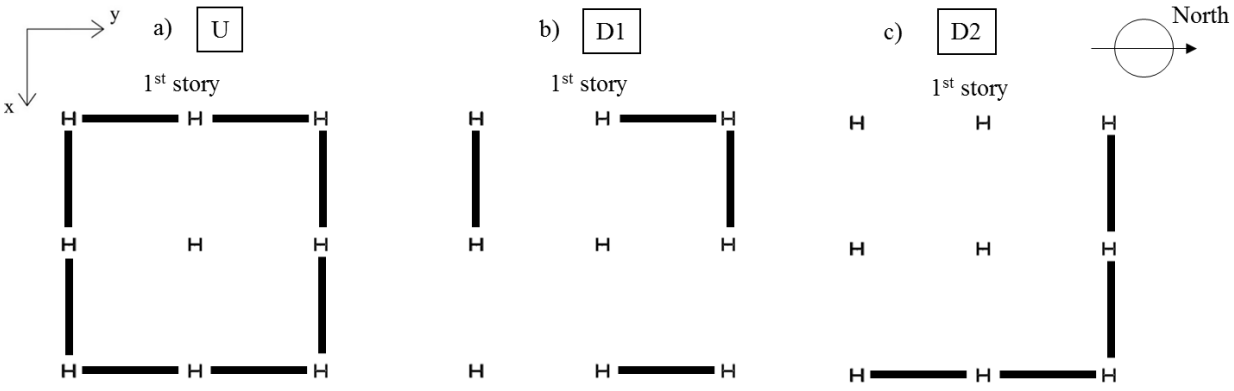

Figure 5.25. Configurations of the building structure generated using the FE code by [Johnson et al., 2004]: a) configuration U; b) configuration D1; c) configuration D2.

For each of the three considered configurations (Fig. 5.25), the FE code provided by [Johnson et al., 2004] was used to define an undamped model of the structure. This model consists of stiffness and mass matrices, which are both 12 × 12 matrices. Such matrices were used to perform an eigenvalue analysis to define the modes of the structural configurations (defined in terms of natural frequencies and mode shapes). The first nine natural frequencies of the three considered 12-DOF models are reported in Table 5.8. The mode shapes are defined with respect to the geometric center of the structure (which is also the center of mass), and these mode shapes were normalized using the mass matrix of the structure. Then, the mass-normalized mode shapes and the natural circular frequencies of the first nine structural modes were used to assemble the modal flexibility matrices related to the three different structural configurations. It is worth mentioning that the analyses presented in this section were carried out using modal flexibility matrices assembled after performing an eigenvalue analysis on the numerical models and by considering a subset of the modal parameters. The modal flexibility matrices are thus not affected by uncertainties (differently from modal flexibility matrices estimated, for example, from vibration data)[11]. This simple approach was used to test the validity of the analytical formulation related to the damage detection procedure outlined in Section 5.2.1. On the contrary, the application of the procedure on the experimental data of the ambient vibration tests performed on the steel frame structure (described in Section 5.1.2.1) is presented in next section. It is worth noting that the simple approach of verifying the analytical formulation of the methodology using "exact" modal flexibility matrices is an approach that was adopted (before verifying the procedure using experimental data) also in the work by [Koo et al., 2010], where the original formulation of the Positive Shear Inspection Load method was presented.

[11] A possible strategy to introduce uncertainties on the modal flexibility matrices assembled after performing an eigenvalue analysis on a numerical model is discussed and adopted in the damage detection analyses presented in Chapter 6.

Mode no.	Natural frequency f_i [Hz]		
	Conf. U	Conf. D1	Conf. D2
1	9.41	8.34	7.78
2	11.79	11.02	10.67
3	16.38	14.73	14.62
4	25.54	23.64	23.56
5	32.01	30.53	30.31
6	38.66	37.95	37.70
7	44.64	41.63	42.03
8	48.01	47.85	47.90
9	48.44	47.91	48.01

Table 5.8. Natural frequencies related to the configurations of the building structure generated using the FE code by [Johnson et al., 2004].

After having assembled the modal flexibility matrices of the three structural configurations, the procedure outlined in Section 5.2.1 for estimating the positions of the centers of stiffness (i.e. the values of the eccentricities) was applied. According to the procedure, the deflections of the three different structures were evaluated using Eq. (5.41) and by applying the load $\boldsymbol{p_\theta}$, which is a load that consists of unitary moments of torsion at all the stories (Eq. 5.40). Then, starting from the components of such deflections, the values of the eccentricities were determined using Eqs. (5.43, 5.44). Values of the eccentricities approximately equal to zero were obtained at all the stories both for the undamaged configuration U and the damaged configuration D1. Such configurations, in fact, are both characterized by a plan-symmetric distribution of the story stiffness at all the stories (including the damaged story in configuration D1). For configuration D2 the values of the eccentricities are approximately equal to zero at the undamaged stories (2^{nd}, 3^{rd}, and 4^{th} stories) and different from zero at the first story, where the damage has been imposed in a plan-asymmetric configuration.

The positions of the centers of stiffness related to the first story are reported in the plan view of the structure presented in Fig. 5.26 for the different configurations. In particular, in each figure the center of stiffness related to the undamaged configuration is plotted together with the center of stiffness related to the damaged

configuration (in other words, Fig. 5.26a is related to configurations U and D1, while Fig. 5.26b is related to configurations U and D2). As evident in Fig. 5.26a, the centers of stiffness are positioned in the geometric center of the structure both for configurations U and D1. On the contrary, in Fig, 5.26b the center of stiffness is in the origin for configuration U and then moves towards east-north direction when the configuration D2 is considered. This is expected since in configuration D2 the wall braces were removed on the south and the west faces of the structure.

As reported in the work by [Wang et al., 2013], where a damage detection methodology not based on the modal flexibility-based approach was applied on the experimental data of the IASC-ASCE benchmark studies (phase II), the centers of stiffness related to the undamaged and the damaged structures give useful indications for the localization in the plan of the structure of the region that most probably has experienced major damage. Referring to Fig. 5.26b, the region that most probably has experienced the damage can be individuated by the segment that connects the two centers of stiffness (related to the undamaged and the damaged structures, respectively). Of course, this region is located on the opposite side with respect to the center of stiffness related to the damaged structure. By considering the interpretation proposed by [Wang et al., 2013], it is clear, referring to the results shown in Fig. 5.26b, that if the center of stiffness moves towards east-north direction, one can suppose that the region of the structure that most probably has experienced major damage is located approximately in the south-west corner.

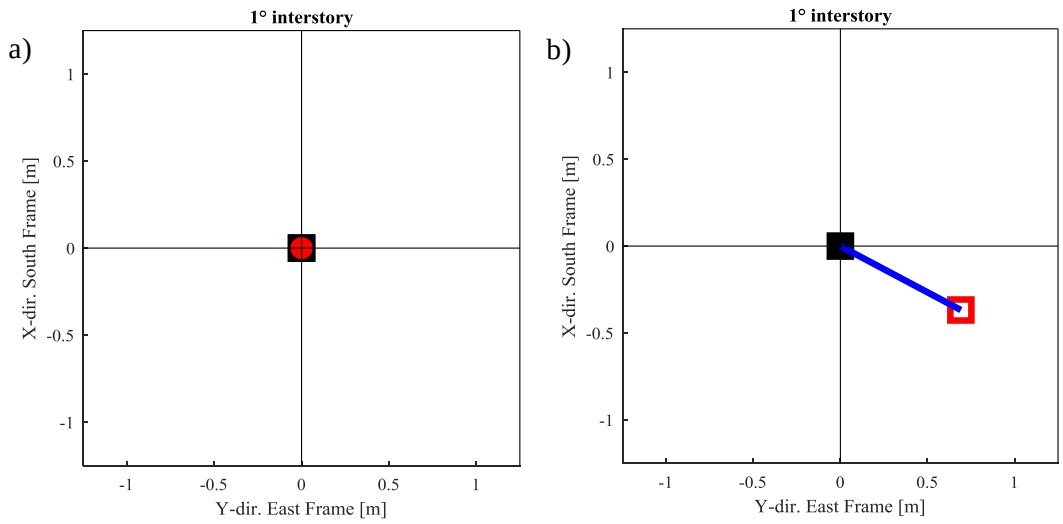

Figure 5.26. Positions of the centers of stiffness for the undamaged configuration (black marker) and the damaged configuration (red marker) - analytical model: a) U vs D1 (1st story); b) U vs D2 (1st story).

The values of the eccentricities determined from the modal flexibility matrices were then used to assemble the "UL+M" inspection loads defined in Eq. (5.45) (i.e. the inspection loads, that include, in addition to translational uniform loads, the moments of torsion that depend on the values of the eccentricities). The "UL+M" inspection loads were then applied to the modal flexibility-based models of the considered configurations (U, D1, D2) by performing, according to the general approach presented in this chapter, two different analyses. One inspection load $\boldsymbol{p}_{\boldsymbol{x}}^{*}$ is applied in x direction (Eq. 5.48), while the other inspection load $\boldsymbol{p}_{\boldsymbol{y}}^{*}$ is applied in y direction (Eq. 5.49). Starting from each deflection, the interstory drifts of the structure were evaluated in the direction of the corresponding applied load (using Eqs. 5.6, 5.7). The above-mentioned calculations were performed not only using the "UL+M" inspection loads, but also using the "UL" loads (Eq. 5.3), and at the end the results obtained using the two types of loads were compared.

The damage-induced interstory drifts that were obtained when the plan-asymmetric damaged configuration D2 was compared against the undamaged configuration U are reported in Fig. 5.27. In particular, in such figure the results of the analyses performed using the UL inspection loads are compared with the results

obtained using the UL+M inspection loads. Fig. 5.27a is related to the analysis in x direction, while Fig. 5.27b is related to the analysis in y direction. As evident in Fig. 5.27, using either the UL+M loads or the UL loads and for both the two directions, the damage-induced interstory drifts are non-zero at the first story. This is expected since in configuration D2 the stiffness reductions were applied at the first story (by removing braces in the two directions). This means that, in general, both the two loads can provide useful information for the damage localization (in terms of the story and the direction where the damage was applied). However, the values of the damage-induced interstory drifts at the first story obtained using the UL+M inspection loads are different from the damage-induced interstory drifts obtained using the UL inspection loads. This is evident both for the analysis performed in x direction and for the analysis performed in y direction. These differences obtained in the damage-induced interstory drifts using the two loads have a direct implication on the values of the damage severity, as shown in next paragraph. According to Eqs. 5.13, 5.14, in fact, the parameter used for evaluating the damage severity is basically the ratio between the damage-induced interstory drift and the drift related to the damaged structure.

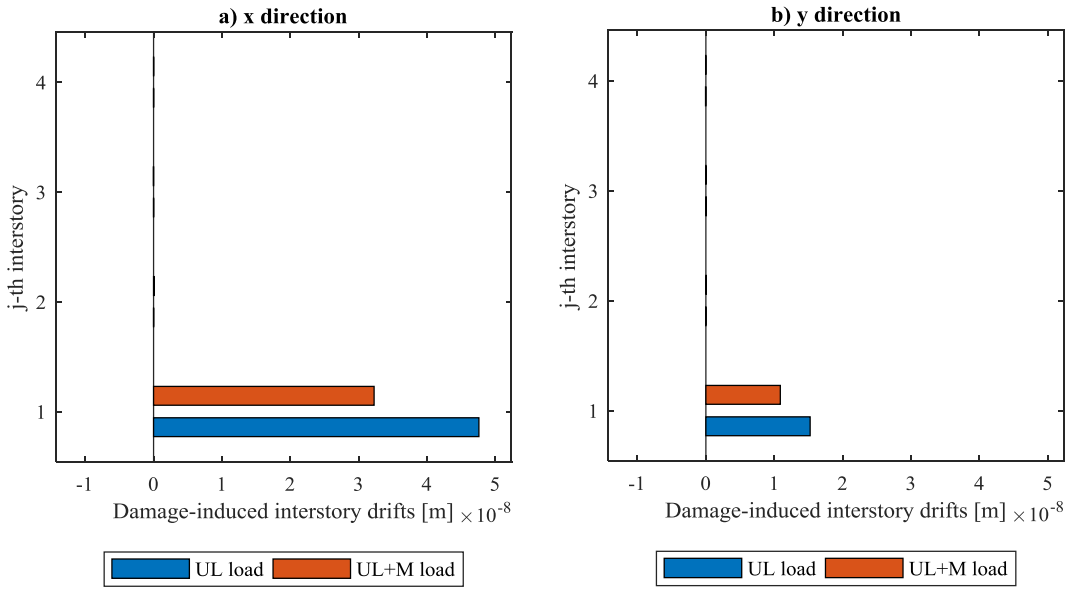

Figure 5.27. Damage-induced interstory drifts - configuration U vs D2 (analytical model) – comparison between the UL load and the UL+M load: a) x direction; b) y direction.

The results of the quantification of the damage (i.e. the evaluation of the damage severity parameters $\alpha_{s,x}$ and $\alpha_{s,y}$) are reported in Fig. 5.28 for the two damaged configurations D1 and D2. Again, the results obtained by applying the UL+M inspection loads are compared with the results obtained using the UL inspection loads. For configuration D2 (plan-asymmetric) the damage severity in x direction obtained using the UL inspection load is $\alpha_{s,x} = 0.45$, while the value of the damage severity obtained using the UL+M inspection load is $\alpha_{s,x} = 0.35$. Referring to the same configuration, the damage severity in y direction obtained using the UL inspection load is $\alpha_{s,y} = 0.29$, while the value of the damage severity obtained using the UL+M inspection load is $\alpha_{s,y} = 0.22$. In general, for the considered plan-asymmetric configuration (D2) the damage severities (in both directions) obtained using the UL+M inspection loads are thus lower than the corresponding ones obtained using the UL inspection loads. However, the important result that must be highlighted is that (both in the x and the y directions) the damage severities calculated using the UL+M inspection loads for the plan-asymmetric configuration (D2) are equal to the damage severities obtained for the plan-symmetric configuration (D1) using the same inspection loads. As already mentioned in this section, the configurations D1 and D2 were created by removing the same number of braces at the first story and in both directions, but the former has plan-symmetric distribution of the story stiffness, while the latter has a plan-asymmetric distribution of the story stiffness. Obtaining the same values of the damage severity is thus the result that is desirable for the two configurations.

The above-mentioned result obtained by performing a simple numerical analysis on models of a shear building structure confirms that, when a structure with a plan-asymmetric distribution of the story stiffness at the damaged story is considered, the UL+M inspection loads (applied instead of the UL inspection loads) can lead to the correct values of the damage severity. Of course, when the structure is plan-symmetric, the damage severity obtained using the UL+M inspection load is equal to the damage severity obtained using the UL load (as shown in Fig. 5.28 for configuration D1). In such case, in fact, the moments of torsion present in the UL+M inspection load are equal to zero, and this load is equal to the UL load.

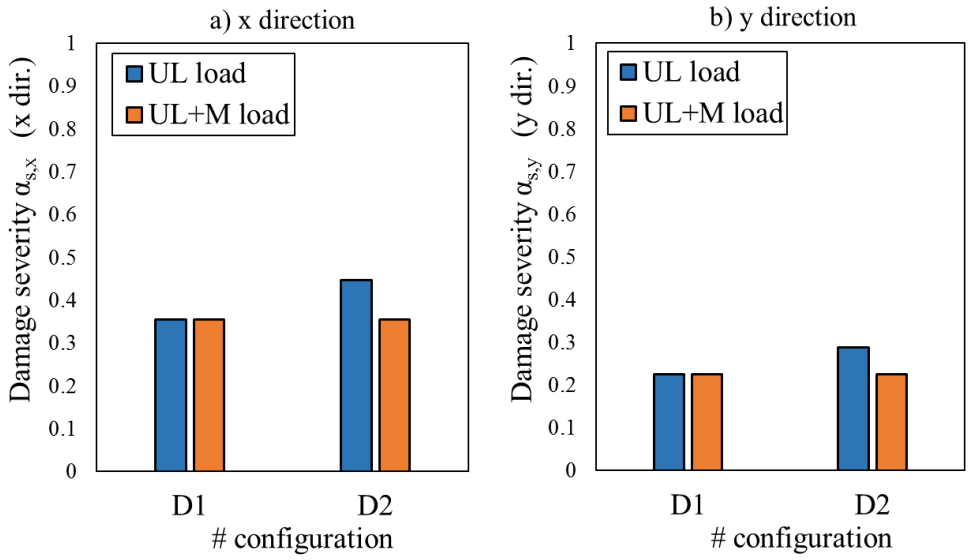

Figure 5.28. Damage severity evaluated on the analytical model - comparison between the UL load and the UL+M load for configurations D1 (plan-symmetric) and D2 (plan-asymmetric): a) x direction; b) y direction.

5.2.3 Application to the 3D steel frame structure tested under ambient vibrations

In this section the results of the application of the damage quantification procedure based on the so-called "UL+M" inspection loads to some of the structural configurations of the steel frame structure tested under ambient vibrations are presented and discussed. In particular, the results of the procedure based on the "UL+M" inspection loads (Section 5.2.1) are compared with the results of the procedure based on the "UL" inspection loads (Section 5.1.1). As already mentioned in Section 5.1.2.1, the above-mentioned steel frame structure is located at the EERF laboratory of the University of British Columbia (Vancouver) and the ambient vibration tests were performed in September 2016.

As shown in previous sections of this chapter, the measured responses of the structure under ambient vibrations were analyzed by means of an output-only modal identification technique (i.e. the Enhanced Frequency Domain Decomposition method [Brincker, Zhang & Andersen, 2001; Brincker, Ventura & Andersen, 2001]). Identified

natural frequencies and mode shapes normalized with respect to the mass matrix[12] of the structure were used to assemble the modal flexibility matrices.

The procedure for estimating the position of the centers of stiffness at the different stories of the steel frame structure (step no. 3b described in Section 5.2.1) was then applied starting from the experimentally-derived modal flexibility matrices of the structure. However, when this methodology, whose theoretical formulation is shown in Section 5.2.1 and whose validity has been demonstrated in Section 5.2.2 using a numerical model, was applied on the modal flexibility matrices of the steel frame structure tested under ambient vibrations, results that were considered, on the basis of engineering judgment, as not accurate were obtained. For example, the centers of stiffness that were obtained for the undamaged configuration C1 (which is a configuration with a plan-symmetric distribution of the story stiffness at all the stories, see Table 5.3) are located at not negligible distances with respect to the geometric center of the structure (which is, in theory, the center of stiffness for this configuration). In other cases, for some structural configurations with a plan-asymmetric distribution of the story stiffness, the centers of stiffness (estimated using the procedure described at the step 3b of Section 5.2.1) are located in positions that were judged as unreliable positions (for example, in some cases the centers of stiffness are located outside of the structural plan of the building, which is a result that is clearly not accurate).

One of the main motivations for which the above-mentioned not accurate results were obtained in the estimation of the centers of stiffness might be related to the fact that the modal flexibility matrices were assembled using only a limited number of structural modes. As already mentioned in Section 5.1.2.2, in fact, such matrices were assembled by considering only the first five modes of the 4-story steel frame structure, and such matrices are thus affected by modal truncation errors. Similar observations on this problem are also reported in the work by [Bernal & Gunes, 2004]. In this work the authors performed numerical analyses for damage detection purposes in the context of the analytical phase (phase I) of the IASC-ASCE

[12] The description of how the mass matrix of the steel frame structure was determined is reported in Section 5.1.2.3.

benchmark studies. The structure considered in the work by [Bernal & Gunes, 2004], using a numerical model, is thus similar to the building structure that is considered in this chapter. In particular, the authors applied the Damage Locating Vector (DLV) method for damage localization purposes, while for damage quantification purposes the stiffness coefficients and the centers of stiffness of the building structure were estimated from modal flexibility matrices assembled from vibration data. In the above-mentioned work based on numerical analyses the authors were able to estimate accurately the positions of the centers of stiffness of the structure. However, in the work it is also reported that the approach may be difficult to be applied and scaled to field conditions (i.e. for ambient vibration tests on real-life structures) because the effects of the modal truncation errors might not allow to obtain accurate estimates of physical parameters of the structures such as the positions of the centers of stiffness [Bernal & Gunes, 2004].

In an attempt to reduce the modal truncation errors on the modal flexibility matrices, which in general negatively affect the accuracy of the procedure for estimating the centers of stiffness, these matrices were also assembled by including the high-order modes of the steel frame structure. Such high-order modes were excluded at the beginning of the analyses because, by evaluating the values of the Modal Complexity Factors (MCF) associated to the identified modes (see Table 5.4 for conf. C1 and discussion in Section 5.1.2.2), such modes were considered as affected by uncertainties that are higher than the ones associated with the low-order modes. However, the results obtained in the determination of the centers of stiffness by considering modal flexibility matrices that include also the high-order modes are even worse than the case of considering only the low-order modes. This effect might be due to the fact that, even if the truncation errors are reduced when considering the high-order modes, the uncertainties on such high-order modes negatively affect the accuracy of the procedure for estimating the centers of stiffness, as well.

An alternative procedure for obtaining the positions of the centers of stiffness of the steel frame structure from modal flexibility matrices was investigated. As shown later in this section, this procedure, even if it is based on some simplifying assumptions and even if represents an approximated approach for the considered steel frame structure, showed that it is a suitable approach to investigate the behavior and

the condition of the structure at least in one direction (i.e. in the weak or x direction of the steel frame structure). In particular, this procedure can be applied on configurations of the considered steel frame structure that have the following two characteristics: 1) the configuration is characterized by a generic (either plan-symmetric or plan-asymmetric) distribution of the story stiffness with respect to the x axis (weak direction); 2) the configuration is characterized by a plan-symmetric distribution of the story stiffness with respect to the y axis (strong direction).

For configurations that have the above-mentioned characteristics the approximated procedure was thus used to determine the positions of the centers of stiffness and the related values of the eccentricity along the y direction starting from modal flexibility matrices estimated from the ambient vibration data. In particular, the approximated procedure was applied instead of the exact procedure described in Section 5.2.1, which, on the contrary, provided not accurate results when applied in the experimental case study. Then, according to the procedure outlined in Section 5.2.1, such values of the eccentricity along the y direction were used to assemble the UL+M inspection loads $\boldsymbol{p}_{\boldsymbol{x}}^{*}$. These loads applied in the weak or x direction of the structure were used to investigate the condition of the structure and to quantify the damage in that direction. At the end, the results of the analyses performed in the weak or x direction for quantifying the damage using the UL+M inspection loads were compared with the same results obtained by applying the UL inspection loads.

To demonstrate the applicability on the steel frame structure of the approximated approach for evaluating the positions of the centers of stiffness and to compare the results of the UL+M and the UL inspection loads, three structural configurations of the steel frame structure tested under ambient vibrations were considered (Fig. 5.29). According to the description and the nomenclature of all the tested configurations provided in Section 5.1.2.1 and in Table 5.3, these three configurations are configurations C1, C2, and C13. As already mentioned in Section 5.1.2.1, configuration C1 is the fully braced structure that is assumed as the undamaged configuration. On the contrary, configurations C13 and C2 are damaged configurations. These two damaged configurations were selected because they have the following characteristics. Both in configurations C13 and C2 the braces were removed at the first story of the structure, and, as shown in Fig. 5.29b, 5.29c, these

configurations are characterized by the same number of braces removed in the weak or x direction (i.e. four tie rods removed in the x direction). However, in configuration C13 the braces were removed by creating a plan-symmetric distribution of the story stiffness with respect to the x axis (weak direction), while in configuration C2 the braces were removed by creating a plan-asymmetric distribution of the story stiffness with respect to the x axis. As already done in Section 5.2.2 where numerical analyses are presented, these two configurations were thus specifically selected because the application of UL+M inspection loads on such two configurations (i.e. C13 and C2) should, in theory, provide the same amount of damage severity in the x direction. Finally, it is worth mentioning that these configurations are characterized by a distribution of the story stiffness for all the stories that is plan-symmetric with respect to the y axis (strong direction). As shown later in this section, this is a requirement that is necessary for applying the approximated approach for estimating the positions of the centers of stiffness.

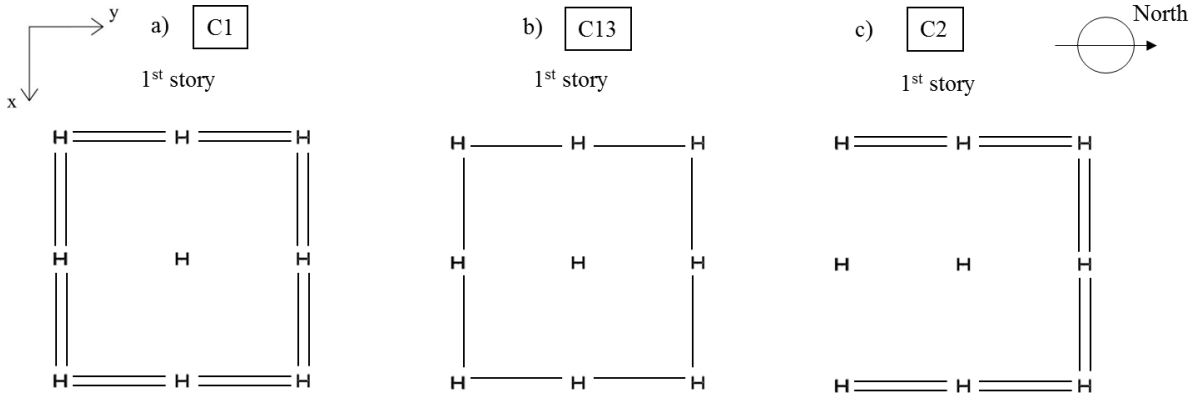

Figure 5.29. Configurations of the steel frame structure tested under ambient vibrations analyzed in this section: a) undamaged conf. C1; b) damaged conf. C13; c) damaged conf. C2.

The approximated approach, used for estimating the positions of the centers of stiffness of the three considered configurations (Fig. 5.29), was developed by investigating at first the static behavior of a very simple model of a 2-DOF system. Then, later in this section it will be shown how this approximated and simplified

approach can be applied on the 4-story steel frame structure (specifically, for each story of that structure).

Let us assume to have a very simple 2-DOF system that is composed by two generic structural elements located at a certain distance (as shown in Fig. 5.30). These two elements resist to lateral forces only in z direction (i.e. the contribution, in term of stiffness, of the two elements is only in z direction - Fig. 5.30a). The stiffness of the element located on the left-hand side is indicated as k_L, while the stiffness of the element located on the right-hand side is k_R. It is assumed that these two elements are linked by a rigid connection, and these two elements thus form a 2-DOF system that can be described, for example, by one translation in z direction and one rotation at the origin[13]. Finally, let us assume that $k_L > k_R$, and thus the center of stiffness of the system (CK) is located on the left-hand side of the origin of the system (0) at a distance that is measured by the variable e (i.e. the eccentricity).

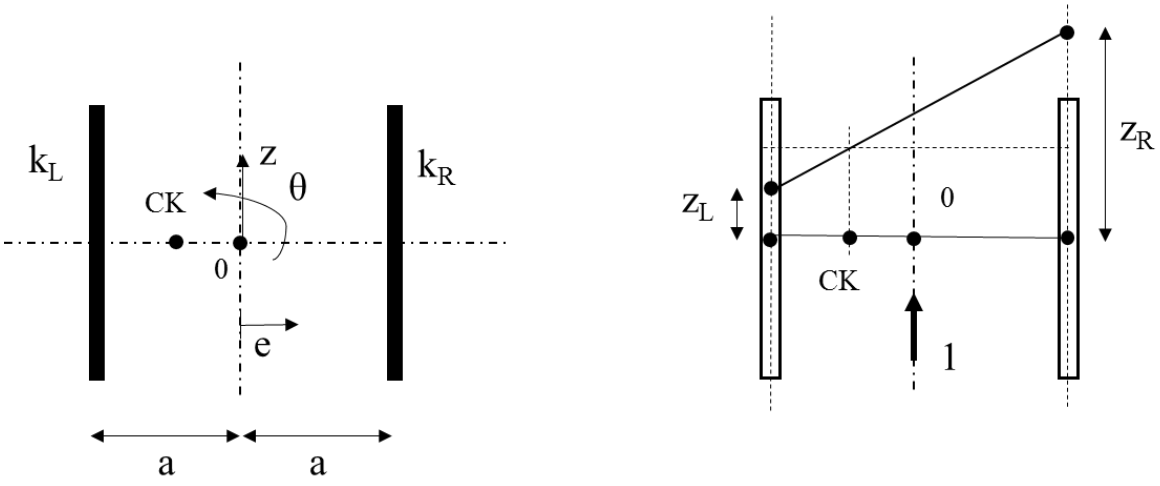

Figure 5.30. Model of a 2-DOF system: a) geometry; b) application of a unitary translational load.

This simple 2-DOF system has the interesting property that follows. The position of the center of stiffness can be univocally determined starting from the knowledge of the displacements of the two elements of the system due to a unitary

[13] The system can also be thought of as composed by two springs that are connected by a rigid element.

load applied in the origin and in z direction (Fig. 5.30b). Of course, the eccentricity can be also estimated starting from the displacements of the two elements due to a unitary rotation applied to the system (i.e. the approach valid for a more general class of structural systems, as shown in Section 5.2.1). However, the 2-DOF system is specifically considered herein to investigate an approach that is alternative with respect to the one shown in Section 5.2.1.

Using simple static equilibrium considerations, the displacements of the two elements of the 2-DOF system due to a unitary load applied in the origin and in z direction are as follows

$$z_L = \frac{1}{2\,k_L} \tag{5.50}$$

$$z_R = \frac{1}{2\,k_R} \tag{5.51}$$

where z_L, z_R are the displacements of the elements on the left-hand side and the right-hand side, respectively. As evident in Eqs. (5.50, 5.51), the displacements are inversely proportional to the values of the stiffness.

The position of the center of stiffness of the considered simple 2-DOF system can be evaluated using the following expression

$$e = \frac{-k_L\,a + k_R\,a}{k_L + k_R} \tag{5.52}$$

where a is the distance between each structural element and the origin of the system (Fig. 5.30). Then, by substituting Eqs. (5.50, 5.51) into Eq. (5.52) the eccentricity can be expressed as a function of the displacements of the two elements of the system due to a unit load applied in the geometric center of the system

$$e = a\,\frac{z_L - z_R}{z_L + z_R} \tag{5.53}$$

The approximated procedure, used for estimating the positions of the centers of stiffness of the three considered configurations of the steel frame structure (reported in Fig. 5.29), is based on the principle for which the mechanical behavior of each story of the structure in the weak or x direction can be modeled through the 2-DOF system described in previous paragraphs. This very simplified approach can be considered as a valid approach due to the three assumptions and observations on the characteristics

of the structure that are discussed in next paragraphs. Then, later in this section the analytical formulation of this approximated approach will be presented.

Firstly, it is assumed, as already done since the beginning of this chapter, that the steel frame structure can be modeled approximately as a shear-type building structure[14]. This is a fundamental assumption for which the behavior of each story can be analyzed separately from the other stories, for example using the model of the 2-DOF system.

Secondly, for the considered configurations of the steel frame structure the response due to inspection loads applied in the geometric center of the structure and in the x direction is approximately uncoupled with respect to the response of the structure due to inspection loads applied in the geometric center and in the y direction. The considered configurations, in fact, are characterized by a generic (either plan-symmetric or plan-asymmetric) distribution of the story stiffness with respect to the x axis (weak direction) and by a plan-symmetric distribution of the story stiffness with respect to the y axis (strong direction).

Thirdly, the two external frames of the structure in the weak or x direction provide most of the lateral stiffness of the structure in that direction, while the contribution to the lateral stiffness in x direction of the internal frame is very low. Differently from the external frames, in the internal frames of the structure there are, in fact, no bracing elements, and, as already discussed in Section 5.1.2.3, the contribution to the story stiffness of the braces is much higher than the contribution of the columns. Thus, under the simplifying assumption of neglecting the contribution of the internal frame in x direction, the behavior of each story of the structure in x direction was analyzed using the model of the simple 2-DOF system analyzed in previous paragraphs. In this simple 2-DOF model, in fact, the elements that provide a contribution to the lateral stiffness are concentrated in two points diametrically opposed with respect to the geometric center of the system (similarly to the two external frames of the steel frame structure).

[14] This assumption is also made in the work by [Bernal & Gunes, 2004], which, as already mentioned, deals with the benchmark steel frame structure.

A general observation must be made on the approximated and simplified approach of modeling the behavior of each story of the steel frame structure using the model of the simple 2-DOF system. This approximated criterion applied by considering the weak or x direction of the structure is much more valid than the same criterion applied by considering the strong or y direction. In other words, if configurations that are plan-asymmetric with respect to the y direction and plan-symmetric in x direction are considered, then the approximated approach based on the 2-DOF system leads in general to results (in terms of the positions of the centers of stiffness) that are less accurate than the ones obtained for the configurations considered in this section (which are, on the contrary, configurations that can be either plan-asymmetric or plan-symmetric with respect to the x direction and that are plan-symmetric in y direction). These last statements can be explained and justified as follows. As also reported in the work by [Bernal & Gunes, 2004], both in the x and y directions the two external frames of the benchmark steel frame structure resist to most of the lateral forces in the two directions, respectively. However, it is clear that, due to the different orientation of the cross sections of the columns in the two directions (as shown in Fig. 5.29), the above-mentioned characteristic of the structure, discussed also in the work by [Bernal & Gunes, 2004], is more valid for the x direction (weak direction) with respect to the y direction (strong direction).

The positions of the centers of stiffness (i.e. the values of the eccentricity in y direction) of the three configurations of the steel frame structure considered in this section (Fig. 5.29), were determined as follows. After having estimated the modal flexibility matrices from the ambient vibration data, the modal flexibility-based deflections of such configurations due to a translational uniform load (UL) applied in x direction were determined. As already shown in Section 5.1.1, such deflections can be obtained using the following expression

$$\boldsymbol{x_x} = \boldsymbol{F_r}\,\boldsymbol{p_x} \tag{5.54}$$

where the UL load in x direction is

$$\boldsymbol{p_x} = \begin{pmatrix} \{\mathbf{1}\} \\ \{\mathbf{0}\} \\ \{\mathbf{0}\} \end{pmatrix}_{3nx1} = \begin{pmatrix} 1 \\ \vdots \\ 1 \\ \\ 0 \\ \vdots \\ 0 \\ \\ 0 \\ \vdots \\ 0 \end{pmatrix} \tag{5.55}$$

It is worth noting that, for the sake of convenience and clarity, the components of the vector $\boldsymbol{x_x}$ are indicated with the following notation

$$\boldsymbol{x_x} = \begin{pmatrix} \{\boldsymbol{u}\} \\ \{\boldsymbol{v}\} \\ \{\boldsymbol{\theta}\} \end{pmatrix}_{3nx1} = \begin{pmatrix} u_n \\ \vdots \\ u_1 \\ \\ v_n \\ \vdots \\ v_1 \\ \\ \theta_n \\ \vdots \\ \theta_1 \end{pmatrix} \tag{5.56}$$

Then, starting from the components reported in Eq. (5.56), which are defined with respect to the geometric center of the structure, the displacements of the modal flexibility-based deflections were evaluated in the x direction and for the external frames of the structure that are aligned to that direction (i.e. the frames on the south and the north sides of the structure). According to the coordinate reference system reported in Fig. 5.16 and under the simplified assumption of considering each floor of the structure with a rigid-body in-plane behavior, such displacements were calculated as follows

$$u_{S,j} = u_j + \theta_j \; a \tag{5.57}$$

$$u_{N,j} = u_j - \theta_j \; a \tag{5.58}$$

where $u_{S,j}$ and $u_{N,j}$ are, respectively, the displacements (in x direction and at the j-th story) of the south and the north frame of the structure, a is the bay width of the

structure, and $j = 1\ldots n$. The interstory drifts related to the two external frames were then evaluated as follows

$$d_{S,j} = \begin{cases} u_{S,j} - u_{S,j-1} & \text{for } j=2\ldots n \\ u_{S,j} & \text{for } j=1 \end{cases} \tag{5.59}$$

$$d_{N,j} = \begin{cases} u_{N,j} - u_{N,j-1} & \text{for } j=2\ldots n \\ u_{N,j} & \text{for } j=1 \end{cases} \tag{5.60}$$

where $d_{S,j}$ and $d_{N,j}$ are the interstory drifts of the modal flexibility-based deflection due to the inspection load $\boldsymbol{p}_x$ evaluated for the south and the north frames, respectively. Finally, the value of the eccentricity in y direction for the generic j-th story of the structure was estimated as follows

$$e_{y,j} = a \ \frac{d_{S,j} - d_{N,j}}{d_{S,j} + d_{N,j}} \tag{5.61}$$

This equation has the same structure of the equation derived for the simple 2-DOF system to obtain the eccentricity (Eq. 5.53). However, in Eq. (5.53) the displacements of the two elements that form the 2-DOF system are considered, while in such case Eq. (5.61) is applied for each story of the 4-story steel frame structure using the values of the modal flexibility-based interstory drifts related to the external frames.

Fig. 5.31 shows the positions of the centers of stiffness related to the first story of the structural configurations C1, C13, and C2. The positions of such centers of stiffness were defined by evaluating the values of the eccentricity in y direction according to the approximated approach shown in this section and using Eq. (5.61). Similarly to Fig. 5.26, the center of stiffness related to the undamaged configuration is plotted together with the center of stiffness related to a damaged configuration in each graph reported in Fig. 5.31. In other words, the centers of stiffness of configurations C1 and C13 are reported in Fig. 5.31a, while Fig. 5.31b is related to configurations C1 and C2. The centers of stiffness at the first story are positioned in the geometric center of the structure for the two plan-symmetric configurations C1 and C13 (Fig. 5.31a). On the contrary, the center of stiffness at the first story for configuration C2 is shifted, with respect to the origin, towards the north direction (Fig. 5.31b). This is expected since in configuration C2 the bracing elements were removed on the south face of the structure. Referring to the other stories (i.e. 2nd, 3rd, and 4th

stories) of the three structural configurations (i.e. C1, C13, and C2), values of the eccentricity in y direction approximately equal to zero were obtained.

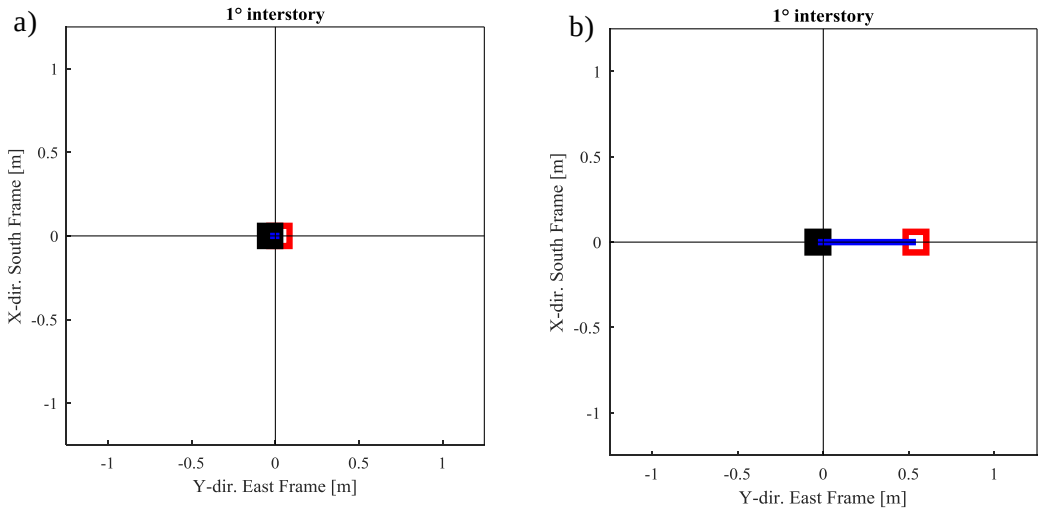

Figure 5.31. Positions of the centers of stiffness estimated using the approximated approach for the undamaged configuration (black marker) and the damaged configuration (red marker) – eccentricities in y direction: a) C1 vs C13 (1st story); b) C1 vs C2 (1st story).

The values of the eccentricities, even if estimated from the modal flexibility matrices using the alternative and approximated approach adopted in this section, were used to assemble the UL+M inspection loads to be applied in the weak or x direction of the structure (Eq. 5.45). The UL+M inspection loads related to the x direction were then applied to the modal flexibility-based models of the considered structural configurations (C1, C13, and C2), and the deflections were evaluated using Eq. (5.48). Finally, starting from each modal flexibility-based deflection due to the UL+M load, the interstory drifts of the structure were estimated in the geometric center of the structure and in x direction (i.e. the direction of the applied load) using Eq. (5.6). These calculations were also performed by adopting UL inspection loads in x direction (Eq. 5.3), to compare the results obtained using such loads with the results obtained using the UL+M inspection loads.

The differences between the interstory drifts obtained for the plan-asymmetric damaged configuration C2 and the interstory drifts related to the undamaged configuration C1 (i.e. the damage-induced interstory drifts) are reported in Fig. 5.32.

In particular, in such figure the results of the analysis performed using the UL+M inspection load in x direction are compared with results obtained using the UL inspection load in x direction. As evident in Fig. 5.32, using either the UL+M load or the UL load values of the damage-induced interstory drifts remarkably different from zero occur only at the first story (this information represents useful information for the damage localization). This story, in fact, is the story of configuration C2 where the wall braces were removed (i.e. where the stiffness reductions were imposed). However, the value of the damage-induced interstory drift at the first story obtained using the UL inspection load is different from the one obtained using the UL+M inspection load. This is the same result that was obtained in Section 5.2.2 where numerical analyses were performed on a model of a structure similar to the one considered in the experimental test. As already discussed in that section, obtaining differences in the damage-induced interstory drifts evaluated using the two loads implies in general that also different values of the damage severity are obtained using the UL+M load or the UL load.

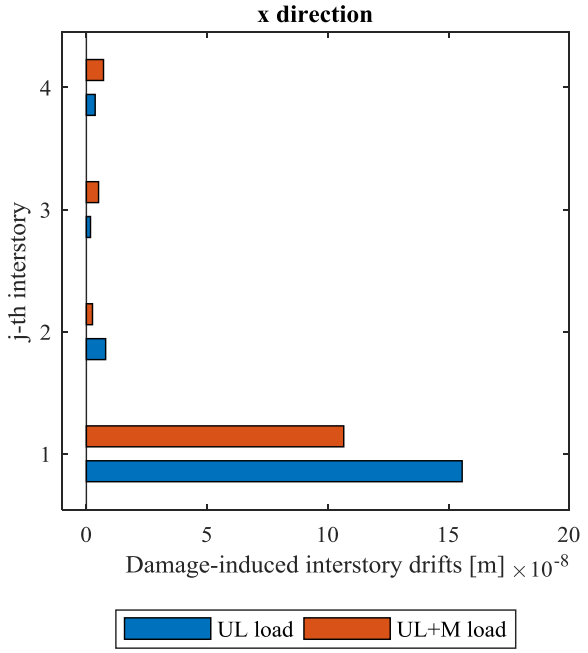

Figure 5.32. Damage-induced interstory drifts – configuration C1 vs C2 – comparison between the UL load and the UL+M load in x direction.

The results obtained in the quantification of the damage by evaluating the damage severity in x direction ($\alpha_{s,x}$) are reported in Fig. 5.33 for the two damaged configurations C13 and C2. Similarly to Fig. 5.32, the results obtained by applying the UL inspection load in x direction are compared with the results obtained using the UL+M inspection load defined for the same direction. Referring to configuration C2, which is a configuration with a plan-asymmetric distribution of the story stiffness at the damaged level, the damage severity in x direction obtained using the UL inspection load is $\alpha_{s,x} = 0.62$, while the value of the damage severity obtained using the UL+M inspection load is lower and it is equal to $\alpha_{s,x} = 0.53$. For configuration C13, which is a configuration with a plan-symmetric distribution of the story stiffness at the damaged level, the damage severity in x direction obtained using the UL load is, as expected, equal to the damage severity obtained using the UL+M load (i.e. $\alpha_{s,x} = 0.52$). The important result that is observed is the following. When the UL load is applied, the damage severity obtained for the plan-asymmetric configuration (C2) is different from the damage severity obtained for the plan-symmetric configuration (C13). On the contrary, when considering the UL+M load, the damage severity for configuration C2 is very similar to the damage severity obtained for configuration C13. The last result is the correct result that should be obtained in the damage quantification process applied on the two configurations, since, as already mentioned in this section, the configurations C13 and C2 were created by removing the same number of braces (i.e. four tie-rods) in the weak or x direction of the structure and at the first story. The only difference between the two configurations is that in configuration C13 the braces were removed by creating a plan-symmetric distribution of the story stiffness at the damaged level, while in configuration C2 the braces were removed by creating a plan-asymmetric distribution of the story stiffness.

The above-mentioned result obtained for the steel frame structure tested under ambient vibrations confirms the findings of the numerical analyses performed on a model of a structure similar to the one considered in the experimental test. In the experimental case study, in fact, even if the positions of the centers of stiffness were estimated from the modal flexibility matrices using an approximated and simplified approach that is valid for some configurations of the steel frame structure with certain characteristics, the UL+M inspection load has provided damage quantification results

that are more consistent than the results obtained using the UL inspection load. For example, by considering a configuration characterized by a plan-asymmetric distribution of the story stiffness at the damage level, the UL+M inspection load is able to correct the slight overestimation that is obtained when, on the contrary, the damage severity of such plan-asymmetric configuration is evaluated using the UL inspection load.

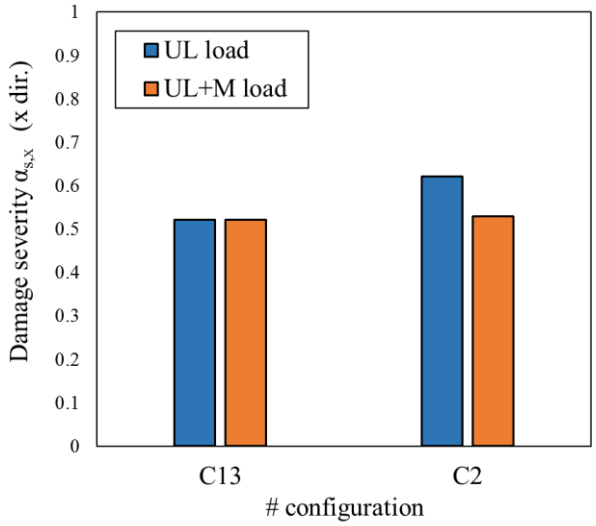

Figure 5.33. Damage severity in x direction - comparison between the UL load and the UL+M load for configurations C13 (plan-symmetric) and C2 (plan-asymmetric).

Chapter 6

Damage detection using proportional MF-based deflections with minimal or no a-priori information on the structural masses

In this chapter of the thesis a modal-flexibility based approach for output-only damage detection in building structures that can be applied with minimal or no a-priori information on the structural masses is presented and discussed[1]. The research investigations on this topic and the development of this proposed approach were performed after identifying a research gap that, as already discussed in Chapter 1, is indicated as the "third problem" considered in the thesis, and that is related to the Positive Shear Inspection Load method for damage detection. This research gap and the approach that is proposed as a possible strategy to address the problem can be summarized as follows.

As shown in Chapter 3, modal flexibility matrices can be assembled only when mass-normalized mode shapes are available. However, starting from ambient vibration data and applying the techniques of operational modal analysis (or output-

[1] Some of the contents of this chapter (i.e. the contents of this chapter related to the integration of the procedure defined by Bernal [2001] into the proposed methodology for damage detection) are presented in a paper co-authored with Dr. Suparno Mukhopadhyay, Prof. Raimondo Betti, Dr. Luca Landi, and Prof. Pier Paolo Diotallevi that was submitted to the journal Engineering Structures and it is currently under review.

only modal identification), only arbitrarily-scaled mode shapes can be obtained. It is thus clear that for the case of ambient vibrations, modal flexibility matrices can not be estimated using only the results of the modal identification (i.e. natural frequencies and arbitrarily-scaled mode shapes of the structure). In the work by [Koo et al., 2010; Koo et al., 2011; Sung et al., 2012], where the formulation of the Positive Shear Inspection Load (PSIL) method for output-only damage detection in building structures is presented, the mass normalization of identified mode shapes was carried out using an a-priori estimate of the system mass matrix.

In the literature, however, there exist techniques that were developed to obtain the flexibility matrices in the context of an output only vibration test and that do not require an a-priori estimate of the mass matrix of the structure. These techniques, as already mentioned in Chapter 1, are presented in the works by [Bernal, 2001; Bernal & Gunes, 2002; Duan et al., 2005; Duan et al., 2007] and were developed in the context of another damage detection method, which is the Damage Locating Vector (DLV) method [Bernal, 2002]. When such techniques are applied together with the DLV method, the damage detection is carried out using only the output vibration responses of the structures and by estimating flexibility matrices (termed proportional flexibility matrices or PFMs) that are proportional to the corresponding true flexibility matrices. Detecting damage using the proportional flexibility matrices (instead of the true flexibility matrices) is an operation that is possible because in damage detection are not of interest the values assumed by the components of the flexibility matrices but the variations of such components. It is thus clear that, as indicated in [Bernal, 2001], mapping changes in flexibility (which might be due to the damage) can be done both considering the true flexibility matrices or the proportional flexibility matrices.

The approach proposed in this chapter was developed on the basis of the theory behind the PSIL method [Koo et al., 2010], and it is an attempt to make the damage detection process based on the modal flexibility-based deflections independent as much as possible from an a-priori estimate of the mass matrix of the structure, as required on the contrary in the PSIL method. According to the proposed approach, two techniques defined, respectively, in the work by [Bernal, 2001] and in the work by [Duan et al., 2005] are integrated in the framework of the PSIL method for damage detection in building structures. Such techniques are used to obtain proportional

flexibility matrices from output-only data, and then, according to the proposed approach, modal flexibility-based deflections that are proportional to the corresponding true deflections can be estimated. Such proportional modal flexibility-based deflections can be used to detect the existence of damage in building structures, and, in this way, the calculations are performed using output-only vibration data without the need to estimate a-priori the mass matrix of the structure.

The chapter is organized as follows. Section 6.1 is an introductory section that presents the original formulation of the two Proportional Flexibility Matrix (PFM) techniques that were defined, respectively, in the work by [Bernal, 2001] and in the work by [Duan et al., 2005]. Then, Sections 6.2 and 6.3 are dedicated to the description of the proposed modal flexibility-based approach for output-only damage detection with minimal or no a-priori information on the structural masses. In Section 6.2 it is shown at first how the two above-mentioned PFM techniques can be integrated in the proposed approach, and then the steps for the estimation of proportional modal flexibility-based deflections of building structures are outlined. In Section 6.3, two indices that can be evaluated starting from the proportional MF-based deflections of shear building structures and that can be used for damage detection are presented. Finally, Section 6.4 is dedicated to the verification of the proposed damage detection approach. This verification was conducted using both numerical simulations on shear building structures and the data of experimental vibration tests performed on a steel frame structure.

6.1 Estimation of Proportional Flexibility Matrices (PFM) in the literature

In recent years some researches have been dedicated to solving the problem of modal scaling in output-only identification with the specific purpose of obtaining modal flexibility matrices directly from output-only vibration data.

For example, the Damage Locating Vector method [Bernal, 2002], which, as already mentioned in Chapter 1, is a damage detection method based on a decomposition of the change-in-flexibility matrix, was originally formulated to be applied starting from input-output vibration data. Then, the method has been extended

and enhanced so that it can be applied in the output-only case using the approaches proposed in the works by [Bernal, 2001; Bernal & Gunes, 2002; Duan et al., 2005; Duan et al., 2007].

One characteristic of all these approaches is that they do not aim to find the correct way of scaling the mode shapes used to assemble the flexibility matrices (i.e. to obtain mode shapes normalized to the mass matrix of the structure). These approaches aim to normalize the mode shapes in a consistent manner and to use such normalized mode shapes to assemble flexibility matrices that are proportional to the corresponding real flexibility matrices. Thus, these approaches, which, for the sake of convenience, are indicated in the present dissertation as Proportional Flexibility Matrix (PFM) techniques according to the terminology used in [Duan et al., 2005; Duan et al., 2007], do not require that the mass matrix of the structure is known. The general strategy adopted in the PFM techniques is to estimate directly from the vibration data a mass matrix that is proportional to the corresponding true mass matrix (indicated as Proportional Mass Matrix - PMM).

For example, according to the procedure defined in the work by [Bernal, 2001] and as shown later in this section, this operation, is performed starting from arbitrarily-scaled mode shapes (identified from output-only vibration data) and using the equations that are offered by the modal orthogonality relationships of the mode shapes with respect to the mass matrix of the structure. Then, the proportional mass matrix is used to normalize the mode shapes, which are, in turn, adopted to obtain the proportional flexibility matrix.

A proportional flexibility matrix $\boldsymbol{F}_{\boldsymbol{r}}^{*}$ is a matrix that differs from the true flexibility matrix $\boldsymbol{F}_{\boldsymbol{r}}$ by a scalar multiplier α_f

$$\boldsymbol{F}_{\boldsymbol{r}}^{*} = \alpha_f \, \boldsymbol{F}_{\boldsymbol{r}} \tag{6.1}$$

In Eq. (6.1) the proportional flexibility matrix $\boldsymbol{F}_{\boldsymbol{r}}^{*}$ is indicated using a star as a superscript, and in this way, it is distinguishable from the flexibility matrix $\boldsymbol{F}_{\boldsymbol{r}}$. It is worth noting that this notation (i.e. using a star as a superscript) is adopted in this chapter to denote all the parameters that are proportional to the corresponding true values (e.g. proportional flexibility matrices, proportional mass matrices, proportional modal flexibility-based deflections etc.).

As already mentioned and according to the approach proposed in this chapter, two PFM techniques defined, respectively, in the work by [Bernal, 2001] and in the work by [Duan et al., 2005] are considered and integrated in the framework of the PSIL method. The main steps and the analytical formulation related to these two techniques are presented in the next two sections. Then, in Section 6.1.3 of this chapter some important aspects that have to be considered when the proportional flexibility matrices (PFM) are used for damage detection purposes will be presented.

6.1.1 Bernal's [2001] procedure

In this section, the procedure defined in the work by [Bernal, 2001] to assemble proportional flexibility matrices (PFM) from output-only vibration data is presented. The procedure is developed for a generic *n*-DOF structure and assumes that the components of the experimental mode shapes are available at all the DOFs of the structure with a significant translational inertia. The vectors of the mode shapes have thus to be spatially complete, while, on the contrary, not all the modes of the structure are required to apply the procedure. There is, however, a minimum number of modes required to apply the procedure defined by Bernal [2001], and this is an aspect that is discussed at the end of this section.

The first step of the procedure is to obtain a proportional mass matrix (PMM) of the structure, and this operation is performed using the equations related to the modal orthogonality relationships of the mode shapes with respect to the mass matrix. These relationships can be expressed as follows

$$\boldsymbol{\Psi}_{\mathbf{r}}^{T}\,\mathbf{M}\,\boldsymbol{\Psi}_{\mathbf{r}} = \mathbf{M}_{\boldsymbol{\mu}} \tag{6.2}$$

where $\mathbf{M}_{\,n\times n}$ is the mass matrix of the structure, which is assumed diagonal, $\boldsymbol{\Psi}_{n\times r}$ is the arbitrarily-scaled mode shape matrix composed by mode shape vectors related to the first *r* modes, and $\mathbf{M}_{\boldsymbol{\mu}\,r\times r}$ is a diagonal matrix which contains the modal masses μ_i related to each of the considered *r* modes. Eq. (6.2) can be specified as follows by highlighting all the different terms present in the equation

$$\begin{bmatrix} \cdots & \cdots & \cdots & \cdots & \cdots \\ \psi_{ni} & \cdots & \psi_{ji} & \cdots & \psi_{1i} \\ \cdots & \cdots & \cdots & \cdots & \cdots \end{bmatrix} \begin{bmatrix} m_n & 0 & \cdots & \cdots & 0 \\ 0 & \ddots & \ddots & \ddots & \vdots \\ \vdots & \ddots & m_j & \ddots & \vdots \\ \vdots & \ddots & \ddots & \ddots & 0 \\ 0 & \cdots & \cdots & 0 & m_1 \end{bmatrix} \begin{bmatrix} \vdots & \psi_{nk} & \vdots \\ \vdots & \vdots & \vdots \\ \vdots & \psi_{jk} & \vdots \\ \vdots & \vdots & \vdots \\ \vdots & \psi_{1k} & \vdots \end{bmatrix} = \begin{bmatrix} \mu_1 & 0 & \cdots & \cdots & 0 \\ 0 & \ddots & \ddots & \ddots & \vdots \\ \vdots & \ddots & \mu_i & \ddots & \vdots \\ \vdots & \ddots & \ddots & \ddots & 0 \\ 0 & \cdots & \cdots & 0 & \mu_r \end{bmatrix} \tag{6.3}$$

with $j = 1 \dots n$ and $i, k = 1 \dots r$. By re-arranging the equations related to the off-diagonal terms in the modal mass matrix (e.g. the equations related to the zeros in the upper triangular part of the matrix $\mathbf{M_\mu}$), the orthogonality relationships can be expressed as

$$\boldsymbol{E}\,\mathbf{m} = \mathbf{0} \tag{6.4}$$

where $\boldsymbol{E}_{\frac{r\,(r\,-1)}{2}\times n}$ is a rectangular matrix formed by mode shape components and $\mathbf{m}_{n\times 1}$ is a vector formed by the diagonal values of the mass matrix $\boldsymbol{M}$. The terms contained in Eq. (6.4) can be specified as

$$\begin{bmatrix} \cdots & \cdots & \cdots & \cdots & \cdots \\ \psi_{ni}\psi_{nk} & \cdots & \psi_{ji}\psi_{jk} & \cdots & \psi_{1i}\psi_{1k} \\ \cdots & \cdots & \cdots & \cdots & \cdots \end{bmatrix} \begin{pmatrix} m_n \\ \dots \\ m_1 \end{pmatrix} = \begin{pmatrix} 0 \\ \dots \\ 0 \end{pmatrix} \tag{6.5}$$

where ψ_{ji}, ψ_{jk} are the *j*-th components of the *i*-th and the *k*-th mode shapes, respectively. Each element of one row of $\boldsymbol{E}$ is composed by multiplying one component of the *i*-th mode with the corresponding one of the mode *k* (with $i \neq k$). Alternatively, in a more compact notation Eq. (6.5) can be expressed as

$$\sum_{j=1}^{n} \psi_{ji}\psi_{jk}\; m_j = 0 \qquad \forall\, i,k \in [1,\dots,r], with\; i \neq k \tag{6.6}$$

where again ψ_{ji}, ψ_{jk} are the *j*-th components of the *i*-th and the *k*-th mode shapes, respectively, and m_j is the generic component of the diagonal of the mass matrix.

The system described through Eqs. (6.4, 6.5, 6.6) can be assembled using identified mode shapes and can be solved to obtain an estimate from the experimental data (and specifically from experimental mode shapes) of the vector **m**.

If the exact values of the mode shape components are considered in Eq. 6.4 (assuming, for example, that the identification is performed on noiseless data, which is an ideal case), the vector **m** belongs to the null space or kernel of the matrix $\boldsymbol{E}$. Since in general any vector that belongs to the kernel of a matrix is defined to within a scalar multiplier, the relationship between the vector **m** and the kernel of the matrix $\boldsymbol{E}$ (indicated as ker $\boldsymbol{E}$) can be expressed as follows

$$\mathbf{m} = \frac{1}{\alpha_m}\;\; \ker \boldsymbol{E} \tag{6.7}$$

where α_m is an arbitrary scalar. By assembling the matrix $\boldsymbol{E}$ using experimental mode shapes, a vector $\mathbf{m}^*$ proportional to the vector **m** (i.e. proportional to the diagonal values of the mass matrix $\boldsymbol{M}$) can thus be determined as the null space of $\boldsymbol{E}$. It is worth noting

that this vector $\mathbf{m}^*$ is a vector that describes the distribution of the masses of the structure, while, of course, in Eq. (6.7) the constant α_m is undetermined.

As reported in [Bernal, 2001], the approach can be applied if a sufficient number of modes is considered – i.e. if the following condition is fulfilled

$$r\,(r-1) \geq 2(n-1) \tag{6.8}$$

where, as already mentioned, *r* is the number of the identified modes which are included in Eq. (6.4) and *n* is the number of the DOFs of the structure. The condition expressed by Eq. (6.8) and the assumption of dealing with structural systems with a diagonal mass matrix guarantee that a unique solution is obtained by solving Eq. (6.4) and when estimating the mass proportional vector $\mathbf{m}^*$. In fact, if exact components of the mode shapes are considered, in the above-mentioned situation (i.e. the condition expressed by Eq. 6.8 is fulfilled and the system has a diagonal mass matrix) the dimension of the null space or kernel of the matrix $\boldsymbol{E}$ is equal to one (i.e. the rank deficiency of $\boldsymbol{E}$ is equal to one). In such case a unique solution is obtained by solving Eq. (6.4).

The problem of dealing with mode shape components that are affected by uncertainties and the specific technique that has been adopted in the approach proposed in this chapter to obtain the mass proportional vector $\mathbf{m}^*$ is discussed later in Section 6.2.1.1. Of course, in such situation (i.e. when the components of the matrix $\boldsymbol{E}$ are affected by uncertainties) the kernel of the matrix $\boldsymbol{E}$ is always empty, and thus a numerical solution has to be adopted to have an estimate of the vector $\mathbf{m}^*$.

After having estimated the vector $\mathbf{m}^*$, the proportional mass matrix $\boldsymbol{M}^*$ of the structure can be assembled and used to compute the normalized mode shapes and the proportional flexibility matrix [Bernal, 2001]. The proportional flexibility matrix $\boldsymbol{F}^*_{\boldsymbol{r}\,n\times n}$ of the structure can be assembled from the arbitrarily-scaled mode shapes, the natural frequencies, and the proportional mass matrix as follows

$$\boldsymbol{F}^*_{\boldsymbol{r}} = \boldsymbol{\Psi}_{\boldsymbol{r}}\,\boldsymbol{\Lambda}_{\boldsymbol{r}}^{-1}(\boldsymbol{\Psi}_{\boldsymbol{r}}^{T}\,\mathbf{M}^{*}\,\boldsymbol{\Psi}_{\boldsymbol{r}})^{-1}\,\boldsymbol{\Psi}_{\boldsymbol{r}}^{T} \tag{6.9}$$

It is worth noting that this equation is similar to the equation that has been already presented in Chapter 3 referring to the procedure used to estimate the modal flexibility matrix of the structure according to the Positive Shear Inspection Load method. There is, however, an important difference between the two equations. One of the terms present in

the equation reported in Chapter 3 is the mass matrix of the structure, while in Eq. (6.9) presented in this chapter the calculations are performed starting from the proportional mass matrix $\mathbf{M}^*$.

6.1.2 Duan et al.'s [2005] procedure

As already mentioned, there exists in the literature another technique that can be used to extract the proportional flexibility matrix from output-only vibration data. This technique is presented in the work by [Duan et al., 2005]. The procedure proposed by Duan et al. [2005], similarly to the procedure defined by Bernal et al. [2001], was developed for a generic *n*-DOF structure and assumes that the vectors of the mode shapes are spatially complete. On the contrary, not all the modes of the structure are required to apply the procedure.

In the procedure developed by Duan et al. [2005] the problem of constructing the proportional flexibility matrix of a structure from output-only vibration data is solved by defining a second structure (termed "dummy structure"), which is not equal to the real physical structure but has a well-defined relationship with the real structure. The passages outlined in the work by Duan et al. [2005] to define the characteristics of the dummy structure and to justify the choice of considering in the approach this dummy structure are summarized herein. Let us consider at first the equation of the flexibility matrix of the real structure

$$\boldsymbol{F_r} = \sum_{i=1}^{r} \frac{\boldsymbol{\phi}_i \boldsymbol{\phi}_i^T}{\omega_i^2} \tag{6.10}$$

where $\boldsymbol{\phi}_i$ and ω_i are, respectively, the *i*-th mass normalized mode shape and the *i*-th natural circular frequency of the real structure. As already mentioned in Chapter 3, the relationship between any mass normalized mode shape vector $\boldsymbol{\phi_i}$ and the corresponding arbitrarily-scaled mode shape vector $\boldsymbol{\psi_i}$ is

$$\boldsymbol{\phi_i} = \frac{1}{\sqrt{\mu_i}} \boldsymbol{\psi_i} \tag{6.11}$$

where μ_i is the *i*-th modal mass. By substituting Eq. (6.11) in Eq. (6.10), the flexibility matrix expressed in terms of the arbitrarily-scaled mode shapes is

$$\boldsymbol{F_r} = \sum_{i=1}^{r} \frac{\boldsymbol{\psi}_i \boldsymbol{\psi}_i^T}{\mu_i \omega_i^2} \tag{6.12}$$

At this point the concept of the dummy structure, as defined in [Duan et al., 2005], is introduced. According to the approach proposed in [Duan et al., 2005], a term $\omega_{i,D}$ (which as shown later in this section is the natural circular frequency of the dummy structure) is introduced

$$\omega_{i,D} = \sqrt{\mu_i}\, \omega_i \tag{6.13}$$

On the basis of this last equation (Eq. 6.13), the expression of the flexibility matrix of the real structure assembled using arbitrarily-scaled mode shapes (Eq. 6.12) can be reformulated as

$$\boldsymbol{F_r} = \sum_{i=1}^{r} \frac{\boldsymbol{\psi}_i \boldsymbol{\psi}_i^T}{\omega_{i,D}^2} \tag{6.14}$$

Eq. (6.10) can be compared with Eq. (6.14) by considering that using both equations the same flexibility matrices are obtained. From this comparison the following observations can be formulated. All the quantities in the first equation (Eq. 6.10) are related to the real structure and the equation contains mode shapes that are normalized with respect to the mass matrix of the real structure. On the contrary, Eq. (6.14) can be considered as an expression related to a structure (i.e. the dummy structure) that has the same stiffness/flexibility matrix of the real structure but a mass matrix different from the mass matrix of real structure. In fact, the arbitrarily-scaled mode shapes of the real structure that are present in Eq. (6.14) can be considered as mode shape vectors that are normalized with respect to the mass matrix of the dummy structure (of course, by considering in Eq. 6.14 the terms $\omega_{i,D}$ as the natural circular frequencies of the dummy structure, which are modified with respect to the natural circular frequencies of the real structure according to Eq. 6.13).

As discussed in [Duan et al., 2005], two different structures (i.e. the real and the dummy structures) are thus considered. The properties of such structures can be summarized as follows. These structures have the same stiffness/flexibility matrix and the same mode shapes, while they have different mass matrices and different natural frequencies. However, both the mass matrix and the natural frequencies of the dummy structure can be related to the corresponding quantities of the real structure.

The main idea behind the approach is that, as already mentioned, the mass matrix of the dummy structure is defined in a way that the arbitrarily-scaled mode shapes of the real structure are mass orthogonal and mass normalized with respect to such mass matrix of the dummy structure. This important point can be expressed using an analytical formulation as follows

$$\boldsymbol{\Psi}_{\mathbf{r}}^{T}\,\mathbf{M_D}\,\boldsymbol{\Psi}_{\mathbf{r}} = \boldsymbol{I} \tag{6.15}$$

where $\mathbf{M_D}_{\,n\times n}$ is the mass matrix of the dummy structure, $\boldsymbol{\Psi}_{n\times r}$ is the arbitrarily-scaled mode shape matrix composed by mode shape vectors related to the first *r* modes (which are equal for the real and the dummy structures), and $\boldsymbol{I}_{r\times r}$ is the identity matrix. According to [Duan et al., 2005], Eq. (6.15) can be solved to obtain the mass matrix $\mathbf{M_D}$ of the dummy structure. This mass matrix can be assumed symmetric and contains n $(\mathrm{n}-1)/2$ unknows, while the number of the linear equations available in Eq. (6.15) is r $(\mathrm{r}-1)/2$. The system can thus be solved if *r* = *n* (i.e. if all the structural modes of the structure are included in the calculations). However, for a truncated set of mode shapes (i.e. for *r* < *n*) and according to [Duan et al., 2005], a least-square solution can be obtained by means of the Moore-Penrose inverse operation. The mass matrix $\mathbf{M_D}$ of the dummy structure can thus be derived as follows

$$\mathbf{M_D} = (\boldsymbol{\Psi}_{\mathbf{r}}^{T})^{+}\,\boldsymbol{I}\,\boldsymbol{\Psi}_{\mathbf{r}}{}^{+} \tag{6.16}$$

where the symbol $^{+}$ denotes the pseudo-inverse operation.

Of course, the use of the Moore-Penrose inverse operation leads to inevitable approximations in the calculations. This is true especially if the calculations are performed using a very limited number of structural modes (i.e. using only the first modes of the structure). However, differently from the procedure defined by Bernal [2001], in the procedure by Duan et al. [2005] there is not a condition that imposes a minimum number of modes required to perform the calculations. This is an important aspect that was considered for the development of the approach proposed in this chapter (as shown in later sections).

As shown in [Duan et al., 2005], after determining the mass matrix of the dummy structure, the second fundamental step of the procedure is to relate the mass matrix of the dummy structure $\mathbf{M_D}$ and the mass matrix of the real structure **M**. This

operation is done by considering the dynamic characteristic equations of the two undamped structures (i.e. the real and the dummy structures).

These dynamic characteristic equations for the real and the dummy structures are, respectively

$$\mathbf{K}\,\boldsymbol{\psi}_i = \omega_i^2\ \mathbf{M}\,\boldsymbol{\psi}_i \tag{6.17}$$

$$\mathbf{K}\,\boldsymbol{\psi}_i = \omega_{i,D}^2\ \mathbf{M_D}\,\boldsymbol{\psi}_i \tag{6.18}$$

where **K** is the stiffness matrix, which is equal for the two structures. By comparing the two equations (Eqs. 6.17, 6.18) and by considering the relationship between the natural frequencies of the real and dummy structures (Eq. 6.13), the mass matrix of the dummy structure $\mathbf{M_D}$ and the mass matrix of the real structure **M** can be related according to the following equation [Duan et al., 2005]

$$\left(\mathbf{M_D} - \frac{1}{\mu_i}\,\boldsymbol{M}\right)\boldsymbol{\psi}_i = \mathbf{0} \tag{6.19}$$

where $\boldsymbol{\psi}_i$ and $\mathbf{M_D}$ are known quantities, while μ_i and $\boldsymbol{M}$ are unknowns to be calculated.

According to [Duan et al., 2005], the mass matrix of the real structure can be assumed as diagonal, and under this assumption the problem expressed in Eq. (6.19) is characterized by *n* equations and *n*+1 unknows. Notwithstanding the fact that the number of unknowns is higher than the number of equations, in the paper by Duan et al. [2005] it is shown that Eq. (6.19) can be solved to obtain the minimum amount of information required to assemble the proportional flexibility matrix of the structure – i.e. the ratios between each modal mass μ_i and the first modal mass μ_1 of the structure.

This operation is performed by normalizing the mass matrix of the real structure in a way that a designated element of the diagonal of the matrix is equal to one. This normalized mass matrix $\bar{\boldsymbol{M}}$ can be defined as

$$\boldsymbol{M} = \frac{1}{c}\,\bar{\boldsymbol{M}} \tag{6.20}$$

where *c* is a constant value. Then, Eq. (6.20) is substituted in Eq. (6.19), and Eq. (6.19) is reformulated as

$$\left(\mathbf{M_D} - \frac{1}{\eta_i}\,\bar{\boldsymbol{M}}\right)\boldsymbol{\psi}_i = \mathbf{0} \tag{6.21}$$

where the term η_i is defined as

$$\eta_i = c\,\mu_i \tag{6.22}$$

Using the above-mentioned normalization on the mass matrix of the structure, Eq. (6.21) is composed by *n* equations and *n* unknows. Thus, for each modal vector $\boldsymbol{\psi}_i$ a unique solution can be determined by calculating the parameter η_i and the components of the matrix $\bar{\boldsymbol{M}}$ that are unknown. As already mentioned, this last matrix is a proportional mass matrix with a designated element of the main diagonal that is equal to one.

Then, the ratio γ_i between each modal mass μ_i and the first modal mass μ_1 of the real structure can be obtained as follows

$$\gamma_i = \frac{\eta_i}{\eta_1} = \frac{\mu_i}{\mu_1} \tag{6.23}$$

As already mentioned, the equation that was considered before performing the normalization of the mass matrix (i.e. Eq. 6.19) is characterized by *n* equations and *n*+1 unknows. Thus, using the above-mentioned strategy only the ratios between each modal mass μ_i and the first modal mass μ_1 can be determined, and the first modal mass of the structure is undetermined.

These ratios γ_i between the modal masses are then used to assemble the proportional flexibility matrix $\boldsymbol{F}_{\boldsymbol{r}}^{*}$ (or PFM). In fact, by introducing Eq. (6.23) into Eq. (6.12), the flexibility matrix of the structure can be expressed as

$$\boldsymbol{F}_{\boldsymbol{r}} = \frac{1}{\mu_1}\sum_{i=1}^{r}\frac{\boldsymbol{\psi}_i\,\boldsymbol{\psi}_i^T}{\gamma_i\,\omega_i^2} = \frac{1}{\mu_1}\,\boldsymbol{F}_{\boldsymbol{r}}^{*} \tag{6.24}$$

where the proportional flexibility matrix is

$$\boldsymbol{F}_{\boldsymbol{r}}^{*} = \sum_{i=1}^{r}\frac{\boldsymbol{\psi}_i\,\boldsymbol{\psi}_i^T}{\gamma_i\,\omega_i^2} \tag{6.25}$$

This proportional flexibility matrix $\boldsymbol{F}_{\boldsymbol{r}}^{*}$ differs from the real flexibility $\boldsymbol{F}_{\boldsymbol{r}}$ to within a scalar unknown multiplier, which is theoretically equal to the first modal mass of the structure [Duan et al., 2005]. In other words, according to the approach proposed by Duan et al. [2005] the coefficient α_f reported in Eq. (6.1) is equal to μ_1.

6.1.3 Compatibility of the unknown scaling factors related to the PFMs in the damage detection methods based on changes in flexibility

One important aspect that has to be considered when applying the techniques proposed in the works by Bernal [2001] and Duan et al. [2005] to estimate the proportional flexibility matrices and when using such matrices for damage detection is the following. The proportional flexibility matrices in the undamaged and in the possibly damaged states have to be scaled in a consistent manner to perform the damage detection. As discussed in [Bernal, 2001] and as shown in this section, in fact, the two matrices in the undamaged and in the possibly damaged states have to be scaled with respect to the true flexibility matrices by a common scaling factor.
In such condition the scaling factors on the proportional flexibility matrix are comparable.

This important aspect can be investigated by remembering that the Proportional Flexibility Matrix (PFM) techniques [Bernal, 2001; Duan et al. 2005] were developed to be integrated in the framework of the Damage Locating Vector (DLV) approach [Bernal, 2002]. In particular, the techniques were used to extend the DLV methodology, originally developed to be applied in the context of an input-output identification, to the output-only case. As already mentioned in Chapter 1, the Damage Locating Vector method is a modal flexibility-based method that is based on a decomposition of the change-in-flexibility matrix. It is thus clear that evaluating the change-in-flexibility matrix is one of the steps of the Damage Locating Vector method. The Positive Shear Inspection Load is also a method that can be considered as a method based on the evaluation of the change-in-flexibility matrix. This is because, as shown by the analytical formulation presented in Section 3.3.2 of Chapter 3, there is a direct relationship between the damage-induced deflection and the change-in-flexibility matrix. For this reason, the problem of the compatibility of the scaling factors on the PFMs that was discussed in the works by [Bernal, 2001; Duan et al. 2005] referring to the change-in-flexibility matrix, which has to be calculated according to the Damage Locating Vector method, is an important aspect that has to be considered also in the approach presented in this chapter, which was developed on the basis of the Positive Shear Inspection Load method.

The change-in-flexibility matrix can be evaluated starting from the true modal flexibility matrices as follows

$$\Delta \boldsymbol{F} = \boldsymbol{F_I} - \boldsymbol{F_B} \tag{6.26}$$

where $\boldsymbol{F_B}$ and $\boldsymbol{F_I}$ are the flexibility matrices assembled in the original or baseline state and in the inspection phase, respectively. These matrices are usually assembled using the same number of identified modes (i.e. $r_I = r_B = r$). Under this assumption and for the sake of convenience the subscript r has been omitted in Eq. (6.26).

According to [Bernal, 2001; Duan et al. 2005] and when the proportional flexibility matrices are estimated using the procedures defined in Sections 6.1, the change-in-flexibility matrix is evaluated as

$$\boldsymbol{\Delta F}^* = \boldsymbol{F}_{\boldsymbol{I}}^* - \boldsymbol{F}_{\boldsymbol{B}}^* \tag{6.27}$$

which is properly a "proportional change-in-flexibility".

By evaluating Eq. (6.1) both for the structure in the baseline state and for the structure in the inspection phase, and by substituting such equations in Eq. (6.27), the proportional change-in-flexibility matrix can be reformulated as

$$\boldsymbol{\Delta F}^* = \alpha_{f,I}\, \boldsymbol{F_I} - \alpha_{f,B}\, \boldsymbol{F_B} \tag{6.28}$$

where the scalar multipliers related to the two states are indicated as $\alpha_{f,I}$ and $\alpha_{f,B}$. At this point the problem that must be addressed is to ensure that the PFMs both for the undamaged and the possibly damaged structures are adequately scaled [Bernal, 2001; Duan et al. 2005]. In fact, it is evident in Eq. (6.28) that only if the proportional flexibility matrices of the undamaged and the possibly damaged structures differ from the true flexibilities by the same scalar (i.e. $\alpha_{f,I} = \alpha_{f,B} = \alpha_f$), then also the change-in-flexibility $\Delta \boldsymbol{F}^*$ is proportional to the real $\Delta \boldsymbol{F}$, i.e.

$$\boldsymbol{\Delta F}^* = \alpha_f\, (\boldsymbol{F_I} - \boldsymbol{F_B}) = \alpha_f\, \Delta \boldsymbol{F} \tag{6.29}$$

In this way (i.e. by ensuring the compatibility of the scaling factors) changes in flexibility that can be due to the damage can be detected using the proportional flexibility matrices instead of the true flexibility matrices.

According to the procedure defined by Bernal [2001], if the structural masses are unchanged before and after damage, the use of the same proportional mass matrix

to normalize the mode shapes in the undamaged and the possibly damaged states implies that the compatibility of the scaling factors related to the PFMs is fulfilled.

According to the procedure defined by Duan et al. [2005], the proportional flexibility matrix theoretically differs from the true flexibility matrix by a scaling factor that is equal to the first modal mass. It is thus clear that using this method when comparing the proportional flexibility matrices for damage detection purposes, some additional scaling operations must be applied to the estimated matrices (even in the case in which the masses of the structure are unchanged before and after damage). A possible damage (such a stiffness reduction) can lead to a change in the mode shapes of the structure and thus a change in the first modal mass. Moreover, in the work by Duan et al. [2005] the general case in which the structural masses can change before and after damage is considered. As indicated in [Duan et al., 2005], the compatibility of the scalar multipliers related to the undamaged and the possibly damaged states can be guaranteed if there exists in the mass matrix of the structure at least one element that is unchanged before and after damage.

The problem of detecting damage when the mass of the original structure is different from the mass of the possibly damaged structure has been investigated also in other researches [Figueiredo et al., 2009; Mei & Gül, 2015; Villalpando et al., 2016], where the damage detection was not carried out using modal flexibility-based approaches. Such mass modifications can be present in structures that experience changing operational conditions (for example, due to the variability of the payloads) [Farrar & Worden, 2013]. These effects are always present in civil structures, such as bridges or building structures. The resulting mass changes are in general not related to a damaged state, but they affect the dynamics of the system (e.g. the modal properties). It is thus important to ensure that the indices used for damage detection are not sensitive to such changes [Farrar & Worden, 2013].

In this chapter and specifically in later sections, where numerical and experimental analyses will be presented, the damage detection process will be carried out by considering both the situation in which the masses of the structure are unchanged before and after damage and the situation in which mass variations are present between the two structural states.

6.2 Proposed approach for the estimation of the proportional MF-based deflections in building structures

The damage detection method described in Chapter 3 (i.e. the Positive Shear Inspection Load method) is based on the estimation of modal flexibility-based deflections and interstory drifts of shear building structures. The interstory drifts are considered as damage sensitive features (DSFs), and the methodology was verified starting from output-only vibration data and by assuming the system mass matrix of the structure as known [Koo et al., 2010; Koo et al., 2011; Sung et al., 2012]. On the contrary, the two procedures developed by [Bernal, 2001; Duan et al. 2005] (described in previous sections of this chapter) are able to extract proportional mass matrices and proportional flexibility matrices of the structures from output-only vibration data.

The damage detection approach proposed in this chapter aims to integrate the Proportional Flexibility Matrix techniques into the framework of the damage detection methodology based on modal flexibility-based deflections (i.e. the framework of the Positive Shear Inspection Load method). It is worth noting that, according to the original formulation of the PSIL method, the approach proposed in this chapter is developed by considering plane shear building structures.

The integration of the PFM techniques into the framework of the Positive Shear Inspection Load (PSIL) method is theoretically possible because the assumptions made in the PFM techniques are compatible with the ones related to the PSIL method. Firstly, in the two PFM procedures the mass matrix of the structure is assumed to be diagonal, and under this assumption a mass matrix that is proportional to the true mass matrix can be obtained. Dealing with a diagonal mass matrix is also the case of the Positive Shear Inspection Load method, which has been developed for plane shear building structures. Secondly, both the two PFM techniques can be applied using a limited number of structural modes, while modal vectors that are spatially complete are considered. These last two assumptions are the same assumptions that are made in the works by Koo et al. [2010, 2011] and Sung at al. [2012] where the Positive Shear Inspection Load method is presented.

One important aspect that must be underlined and justified about the proposed approach is that both the two PFM techniques (defined by Bernal [2001] and Duan et

al. [2005]) are integrated in the framework of the PSIL method. The reason for this choice is evident if one considers the main characteristics and differences between the two PFM techniques. When dealing with exact modal parameters (for example, the modal identification is performed ideally on noiseless data) and considering a limited number of modes, the approach by Bernal [2001] leads to an exact solution (i.e. an exact proportional mass matrix and an exact proportional flexibility matrix are obtained). However, to apply the PFM procedure proposed by Bernal [2001] the condition expressed by Eq. (6.8) has to be fulfilled. This condition, as already mentioned, fixes a minimum number of modes that have to be identified and considered to apply the procedure. On the contrary, if the condition expressed by Eq. (6.8) is not fulfilled, the approach proposed by Bernal [2001] can not be applied. In other words, this means that if exact modal parameters are considered, an exact solution is obtained for any subset of modes that satisfies the condition expressed by Eq. (6.8).

Referring to the technique proposed by Duan et al. [2005], if the exact values of the mode shape components are considered, this procedure provides an exact solution only if all the modes are included in the calculation (i.e. $r=n$). If a limited number of modes is considered, the approach by Duan et al. [2005] provides an approximated solution in the estimation of the proportional mass matrix. This is due to the fact that pseudo inverse operations are performed on the truncated mode shape matrices reported in Eqs. (6.15, 6.16). However, the authors of the work [Duan et al., 2005] do not mention any condition that imposes a minimum number of modes that have to be considered to apply the procedure. Thus, the technique can be theoretically applied for any subset of r modes included in the calculations.

In light of these premises, it is clear that a convenient approach, which is the approach adopted in the damage detection methodology proposed in this chapter, is the following: apply the PFM technique defined by Bernal [2001] if the condition expressed by Eq. (6.8) is fulfilled (i.e. apply the procedure by Bernal whenever possible); apply the PFM technique defined by Duan et al. [2005] in all the cases in which the procedure by Bernal [2001] is not applicable (i.e. if the above-mentioned condition expressed by Eq. 6.8 is not fulfilled).

In the attempt to combine the two techniques in a unified framework, another important aspect must be considered and addressed. As already mentioned, if the two techniques are applied considering noiseless data and all the structural modes, both techniques provide an exact proportional mass matrix (and thus an exact proportional flexibility matrix). However, as evident in Section 6.1, the two techniques adopt different strategies to assemble the proportional flexibility matrices. In the procedure defined by Bernal [2001] the proportional mass matrix is used to normalize the mode shapes as shown in Eq. (6.9). On the contrary, in the procedure defined by Duan et al. [2005] the ratios between each modal mass of the structure and the first modal mass are included in the expression of the proportional flexibility matrix, as shown in Eq. (6.25). Consequently, even when applied considering noiseless data and all the structural modes, the scalar multipliers on the proportional flexibility matrices obtained using the two techniques are not the same. This problem related to the scaling factors on the proportional flexibility matrices (unknown in output-only identification) in an important aspect that is addressed later in this section.

According to the proposed approach, the first objective is thus to define modified implementations of the two PFM procedures [Bernal, 2001; Duan et al., 2005] and to find a way for which both the two procedures can be integrated into the framework of the PSIL method. This is an aspect that is addressed in next section (i.e. Section 6.2.1). Then, the two techniques will be integrated into a procedure that is able to obtain proportional modal flexibility-based deflections of shear building structures from output-only vibration data. The steps of this proposed procedure are presented in Section 6.2.2.

6.2.1 Implementation of the PFM techniques in a unified framework

6.2.1.1 Implementation of Bernal's [2001] procedure

In the proposed methodology, the proportional mass matrix estimated from the data is used to normalize the mode shapes that are considered to assemble the proportional flexibility matrix. This is the same approach that is adopted in the procedure defined by Bernal [2001]. This means that basically the procedure by Bernal [2001] is kept unaltered in the proposed approach, while modifications are introduced in the

procedure defined by Duan et al. [2005] to make the results obtained using this approach comparable with respect to the results of the procedure by Bernal [2001].

The procedure defined in [Bernal, 2001] is, however, complemented by defining some steps that, according to the proposed approach, should be a continuation of the calculations presented in Section 6.1.1. First of all, the numerical technique that is used in the present chapter to estimate the mass proportional vector $\mathbf{m}^*$ and to solve Eq. (6.4) when the data are affected by uncertainties is presented. Secondly, referring to the structures that are considered in the original formulation of the PSIL method (i.e. plane shear buildings) an approach is proposed to provide a physical interpretation on the value assumed by the missing scaling factors on the proportional flexibility matrices. This approach implies that the mass proportional vector $\mathbf{m}^*$ estimated using the procedure by Bernal [2001] is normalized in a certain way, as shown later in this section.

Of course, when the modal identification is applied on real data, the identified modal parameters are always affected by uncertainties. This means that if Eq. (6.4) is solved in the experimental case, the mode shape components present in such equation will be always affected by uncertainties. To deal with such uncertainties and to obtain an estimate of the mass distribution of the structure (i.e. the vector $\mathbf{m}^*$) using the procedure defined by Bernal [2001], a singular value decomposition (SVD) of the matrix $\boldsymbol{E}$ – Eq. (6.4) – is considered in the analyses presented in this chapter

$$\boldsymbol{E} = \boldsymbol{U}\,\boldsymbol{\Sigma}\,\boldsymbol{V}^{\boldsymbol{T}} \tag{6.30}$$

The vector $\boldsymbol{m}^*$ is then determined as the singular vector of the right-hand-side eigenvector matrix $\boldsymbol{V}$ which is associated to the smallest singular value of $\boldsymbol{E}$. It is worth noting that, due to the property of the singular value decomposition, the singular vectors contained in the matrices $\boldsymbol{U}$ and $\boldsymbol{V}$ are orthonormal vectors. These vectors have a 2-norm[2] equal to one, and thus the vector $\boldsymbol{m}^*$ estimated using such approach has a

[2] If a generic vector is indicated with the letter **v**, its 2-norm is defined as follows

$$\|\mathbf{v}\|_2 = \sqrt{\sum_{j=1}^{n} v_j^2}$$

where *n* is the dimension of the vector **v**.

2-norm equal to one, as well. This is an important aspect because the normalization of the vector $\boldsymbol{m}^*$ plays a fundamental role in the proposed approach, as discussed in the following.

Before presenting how the mass proportional vector $\boldsymbol{m}^*$ is normalized, according to the proposed approach, some observations must be presented on the relationship between the scaling factors on the proportional flexibility matrices and the scaling factors on the proportional mass matrices. In general, by applying the PFM procedure defined by Bernal [2001] and as shown in Section 6.1.1, a proportional mass matrix $\boldsymbol{M}^*$ can be estimated from output-only vibration data. Using the same notation adopted in Eq. (6.7), the scaling factor (unknown in output-only identification) between the proportional mass matrix and the true mass matrix is indicated as α_m. The relationship between the two matrices can thus be expressed as follows

$$\boldsymbol{M}^* = \alpha_m \boldsymbol{M} \tag{6.31}$$

By substituting Eq. (6.31) in Eq. (6.9), Eq. (6.9) can be reformulated as

$$\boldsymbol{F}_r^* = \boldsymbol{\Psi}_r \boldsymbol{\Lambda}_r^{-1} (\boldsymbol{\Psi}_r^T \alpha_m \mathbf{M} \boldsymbol{\Psi}_r)^{-1} \boldsymbol{\Psi}_r^T \tag{6.32}$$

At this point the expression of the true flexibility matrix, that was defined in Chapter 3, is considered

$$\boldsymbol{F}_r = \boldsymbol{\Psi}_r \boldsymbol{\Lambda}_r^{-1} (\boldsymbol{\Psi}_r^T \mathbf{M} \boldsymbol{\Psi}_r)^{-1} \boldsymbol{\Psi}_r^T \tag{6.33}$$

By comparing Eq. (6.33) with Eq. (6.32) and by considering that α_m is a scalar, then the relationship between the proportional and the true flexibility matrices is

$$\boldsymbol{F}_r^* = \frac{1}{\alpha_m} \boldsymbol{F}_r \tag{6.34}$$

Finally, by comparing Eq. (6.34) with Eq. (6.1), it turns out that the scaling factor on the proportional mass matrix is the inverse with respect to the scaling factor on the proportional flexibility matrix

$$\alpha_f = \frac{1}{\alpha_m} \tag{6.35}$$

This in an important point, because the scaling factor on the proportional mass matrix can be controlled or modified adopting different normalizations on the mass

proportional vector $\boldsymbol{m}^*$, and this operation then has an implication on the scaling factor on the proportional flexibility matrix. By adopting this strategy and according to the proposed approach, the scaling factor α_f on the proportional flexibility matrices of the structures considered in the present chapter (i.e. plane shear buildings with a diagonal mass matrix) is imposed as equal to the total mass of the structure. The analytical passages used to show this important characteristic of the approach are the following.

The scaling factor α_f on the proportional flexibility matrices of structures with a diagonal mass matrix can be expressed as the ratio between the 1-norm of the vector $\boldsymbol{m}$ and the 1-norm of the vector $\boldsymbol{m}^*$

$$\alpha_f = \frac{\|\boldsymbol{m}\|_1}{\|\boldsymbol{m}^*\|_1} \tag{6.36}$$

where $\|\cdot\|_1$ is the 1-norm of a generic vector. If the generic vector is indicated with the letter **v**, its 1-norm is defined as

$$\|\mathbf{v}\|_1 = \sum_{j=1}^{n} |v_j| \tag{6.37}$$

where *n* is the dimension of the vector **v**.

This formulation is derived firstly by substituting in Eq. (6.31) the diagonal mass matrices $\boldsymbol{M}$ and $\boldsymbol{M}^*$ with the 1-norm of the vectors $\boldsymbol{m}$ and $\boldsymbol{m}^*$, respectively. Then, this modified version of Eq. (6.31) is substituted into Eq. (6.35). Of course, the operation is valid only if structures with a diagonal mass matrix are considered.

Among the different norms that can be chosen and applied on the mass proportional vectors $\boldsymbol{m}$ and $\boldsymbol{m}^*$ to define the scaling factor α_f, this definition adopted in Eq. (6.36) and which uses the 1-norm of the mass proportional vectors was selected due to its practical applicability. In fact, for the structures considered in the present chapter, which are structures with a diagonal mass matrix, the term $\|\boldsymbol{m}\|_1$ is the total mass of the structure $m_{tot} = \sum_{j=1}^{n} m_j$. Of course, the masses of the stories of the structure are always positive quantities, and thus the total mass can be evaluated as the 1-norm of the vector $\boldsymbol{m}$ (which is the vector formed by the diagonal components of the mass matrix).

The main idea behind the proposed approach is the following: if the mass proportional vector $\boldsymbol{m}^*$ estimated using the PFM technique (in such case the PFM

technique proposed by Bernal [2001]) is scaled in a way that its 1-norm is equal to one (i.e. $\|\boldsymbol{m}^*\|_{\mathbf{1}} = 1$), then, according to Eq. (6.36), the scaling factor on the proportional flexibility matrix is theoretically equal to the total mass of the structure

$$\alpha_f = \|\boldsymbol{m}\|_{\mathbf{1}} = m_{tot} \tag{6.38}$$

In this way a physical interpretation is provided on the scaling factor of the proportional flexibility matrix which is unknown in output-only identification and damage detection. According to the proposed approach, the mass proportional vector estimated by performing a singular value decomposition of the matrix $\boldsymbol{E}$ (Eq. 6.30), is thus normalized in a way that its 1-norm is equal to one (i.e. $\|\boldsymbol{m}^*\|_{\mathbf{1}} = 1$).

6.2.1.2 Implementation of Duan et al.'s [2005] procedure

As already mentioned, in the approach proposed in this chapter the strategy adopted in the procedure by Bernal [2001] to assemble the proportional flexibility matrices (PFMs) is considered. On the contrary, a different strategy used to assemble the PFMs is considered in the procedure by Duan et al. [2005]. To make the technique defined by Duan et al. [2005] applicable in the framework of a unified strategy to assemble the proportional flexibility matrices, some modifications of the original procedure defined by Duan et al. [2005] are proposed and are presented in this section. In any case, the proposed implementation of the procedure by Duan et al. [2005] does not substantially alter the fundamental equations of the original methodology. The main goal that the proposed implementation aims to achieve is to modify the scaling factors on the proportional mass matrices and the proportional flexibility matrices that are obtained using the procedure by Duan et al. [2005].

According to the original formulation of the procedure defined in the work by [Duan et al., 2005], the mass matrix of the dummy structure $\boldsymbol{M_D}$ can be obtained by solving Eq. (6.15). Moreover, the relationship between the mass matrix of the dummy structure and the true mass matrix is expressed by Eq. (6.19). According the proposed implementation, this equation can be specified for the first structural mode (i.e. by considering the first mode shape $\boldsymbol{\psi}_1$ and the first modal mass) as follows

$$\left(\mathbf{M_D} - \frac{1}{\mu_1}\boldsymbol{M}\right)\boldsymbol{\psi}_1 = \mathbf{0} \tag{6.39}$$

The choice of considering the first mode of the structure is done because of two main reasons: firstly, of course, if a limited number of modes is extracted from the data, it is assumed that at least the first mode is identified; secondly, it is assumed that, among the different modes, the first mode shape is presumably affected by uncertainties that are lower than the ones associated with the other modes.

As discussed in Section 6.1.2, the first modal mass is theoretically the scalar multiplier on the proportional flexibility matrices obtained according to the procedure by [Duan et al., 2005]. By having in mind this property and by considering both the definition of the proportional mass matrix (Eq. 6.31) and the relationship between the scaling factors on the proportional mass and flexibility matrices (Eq. 6.35), it can be recognized that a proportional mass matrix $\boldsymbol{M}^*$ can be introduced in Eq. (6.39).

$$\mathbf{M_D}\,\boldsymbol{\psi}_1 = \mathbf{M}^*\,\boldsymbol{\psi}_1 \tag{6.40}$$

This proportional mass matrix $\boldsymbol{M}^*$ has the property that if used to assemble the proportional mass matrices using the strategy adopted by Bernal [2001] (Eq. 6.9) (i.e. by normalizing the mode shapes included in the PFM with respect to the PMM, which is the strategy considered in the proposed approach), then the scaling factor on the PFM is equal to $\alpha_f = \mu_1$. This value of the scaling factor is the value that can be obtained using the original approach by Duan, which on the contrary adopts a different strategy to assemble the PFMs, as shown in Section 6.1.2.

In Eq. (6.40) there are *n* equations and *n* unknowns, and thus Eq. (6.40) can be solved to obtain the proportional mass matrix $\boldsymbol{M}^*$. Of course, the scalar multiplier α_m on the proportional mass matrix is undetermined. It is worth noting that by performing a matrix/vector manipulation in Eq. (6.40) an explicit formula can also be obtained to derive the vector $\boldsymbol{m}^*$ (which is formed by the diagonal components of the proportional mass matrix). If one considers the terms on the right-hand side of Eq. (6.40), the unknowns are contained in the diagonal matrix $\boldsymbol{M}^*$ while the vector $\boldsymbol{\psi}_1$ is known. However, these two mentioned elements can be rearranged by introducing the vector $\boldsymbol{m}^*$ unknown (in place of the vector $\boldsymbol{\psi}_1$) and a diagonal matrix $\boldsymbol{\Psi}_{d(\boldsymbol{\psi}_1)}$ that has the first modal vector on the main diagonal (in place of the matrix $\boldsymbol{M}^*$). Eq. (6.40) can thus be reformulated as

$$\mathbf{M_D}\,\boldsymbol{\psi}_1 = \boldsymbol{\Psi}_{d(\boldsymbol{\psi}_1)}\,\boldsymbol{m}^* \tag{6.41}$$

and then the system can be solved to obtain the mass proportional vector $\boldsymbol{m}^*$ as follows

$$\boldsymbol{m}^* = \boldsymbol{\Psi}_{d(\boldsymbol{\psi}_1)}^{-1} \, \mathbf{M_D} \, \boldsymbol{\psi}_1 \tag{6.42}$$

The vector obtained using Eq. (6.42) is arbitrarily scaled. However, according to the proposed approach, this mass proportional vector $\boldsymbol{m}^*$ is normalized in a way that its 1-norm is equal to one (i.e. $\|\boldsymbol{m}^*\|_\mathbf{1} = 1$). This is the same operation that was applied at the end of the procedure described in the previous section. The normalized vector $\boldsymbol{m}^*$ is used to form the proportional mass matrix $\boldsymbol{M}^*$, which is then used to normalize the mode shapes and to estimate the proportional flexibility matrices using the same strategy adopted in the PFM procedure by Bernal [2001] – i.e. Eq. (6.9).

In the modified implementation of the procedure by Duan et al. [2005], the theoretical unknown scaling factor on the proportional flexibility matrices, which is equal to the first modal mass according to the original procedure proposed by Duan et al. [2005], is equal to the total mass of the structure (i.e. the same theoretical scaling factor that is obtained using the implementation of the procedure by Bernal [2001] described in previous section).

Referring to the procedure by Duan et al. [2005] and as already mentioned in Section 6.2, some approximations are introduced when the mass matrix of the dummy structure is calculated using a limited number of modes. This is because pseudo inverse operations are performed on the truncated mode shape matrices (as shown in Eq. 6.16). Thus, using the proposed normalization of the mass proportional vector $\boldsymbol{m}^*$, the unknow scaling factor is theoretically equal to the total mass of the structure if all the modes are considered in the determination of the dummy mass matrix. If a limited number of modes is considered in the calculations than approximations are inevitably introduced, as shown in the numerical and experimental analyses presented in this chapter. Of course, using the proposed approach the unknow scaling factor is exactly equal to the total mass of the structure also if exact mode shapes components are considered. In fact, both in the PFM technique defined by Duan et al. [2005] and in the PFM technique by Bernal [2001], the uncertainties that affect the mode shapes components lead to inevitable uncertainties that affects also the mass proportional vector $\boldsymbol{m}^*$.

6.2.2 Steps for the estimation of the proportional MF-based deflections

In previous sections it has been shown how the two PFM techniques proposed respectively by Bernal [2001] and Duan et al. [2005] can be implemented in a unified framework. While, as already mentioned, the final objective of the approach proposed in this chapter is to integrate such techniques into a damage detection methodology that is developed on the basis of the theory behind the Positive Shear Inspection Load method.

By integrating the PFM techniques into the PSIL method, the fundamental operation that is performed according to the proposed approach is to estimate deflections of shear building structures that are proportional to the corresponding true modal flexibility-based deflections. These proportional modal flexibility-based deflections are then used for damage detection (according to the criterion that will be discussed in Section 6.3).

This section describes the approach that is proposed for the estimation of proportional modal flexibility-based deflections and interstory drifts of shear building structures from output-only vibration data. The steps that have to be done according to the proposed approach are summarized in the flow chart reported in Fig. 6.1. Before presenting in detail each step, it is worth noting that the implementation of the PFM techniques (discussed in previous sections) are included into this flow chart (i.e. steps no. 2 and 3).

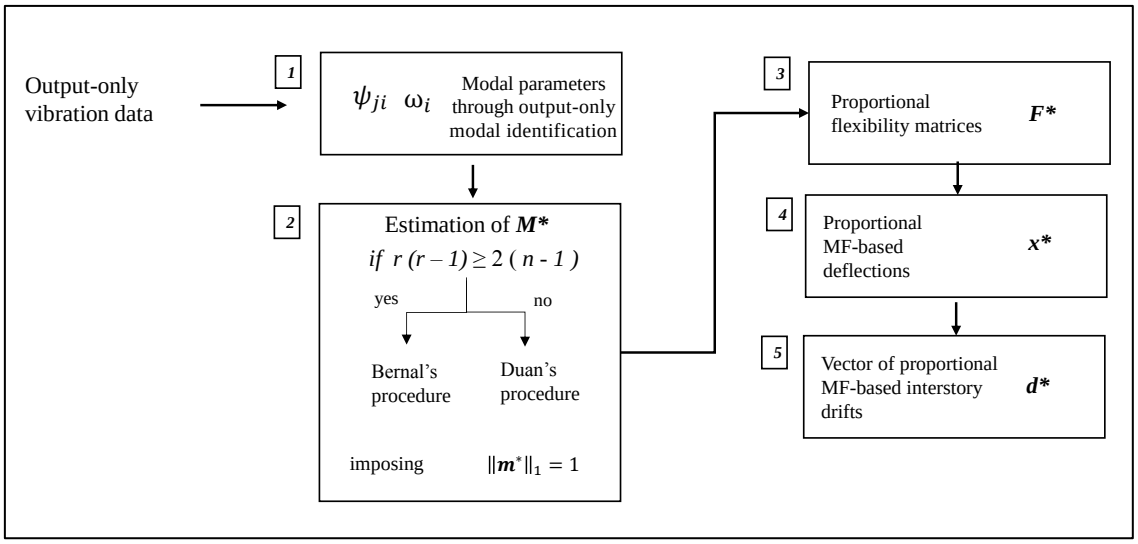

Figure 6.1. Flow chart of the procedure adopted to estimate proportional modal flexibility-based deflections of shear building structures

The steps that, according to the proposed approach, have to performed to estimate proportional modal flexibility-based deflections and interstory drifts of shear building structures are the following:

1. Apply any output-only modal identification technique to extract the modal parameters of the *n*-DOF structure from output-only vibration data;

2. Use arbitrarily-scaled mode shapes to apply the proposed implementation of the PFM techniques originally defined by Bernal [2001] and Duan et al. [2005] to obtain the distribution of the masses of the structure, which is defined by the mass proportional vector $\boldsymbol{m}^*$. As already mentioned, according to the proposed approach, the choice of using one or the other PFM technique depends on the number of structural modes that have been identified (i.e. the parameter *r*). Specifically, the choice is done by evaluating if the condition expressed by Eq. (6.8) is fulfilled or not. This condition is here reported again for the sake of clarity, and the criterion related to the choice of one or the other approach is the following:

- Apply the proposed implementation of the procedure originally formulated by Bernal [2001] if $r\,(r-1) \geq 2(n-1)$

- Apply the proposed implementation of the procedure originally formulated by Duan et al. [2005] if $r\,(r-1) < 2(n-1)$

Both procedures (according to the proposed implementation) provide an estimate of the vector of the mass distribution $\boldsymbol{m}^*$, and according to the proposed approach, this vector is then normalized in a way that that its 1-norm is equal to one – i.e. $\|\boldsymbol{m}^*\|_{\mathbf{1}} = 1$. By adopting this normalization on the vector $\boldsymbol{m}^*$, as shown in previous sections, the unknown scaling factor on the proportional flexibility matrices is theoretically the total mass of the structure. The normalized vector $\boldsymbol{m}^*$ is used to assemble the proportional mass matrix $\mathbf{M}^*$.

3. Use the identified arbitrarily-scaled mode shapes, the identified natural frequencies, and the proportional mass matrix $\mathbf{M}^*$ (obtained at step no. 2) to estimate the proportional flexibility matrix $\boldsymbol{F}^*_{\boldsymbol{r}\,n\times n}$ of the shear building structure as follows

$$\boldsymbol{F}^*_{\boldsymbol{r}} = \boldsymbol{\Psi}_{\boldsymbol{r}}\, \boldsymbol{\Lambda}_{\boldsymbol{r}}^{-1} (\boldsymbol{\Psi}_{\boldsymbol{r}}^T\, \mathbf{M}^*\, \boldsymbol{\Psi}_{\boldsymbol{r}})^{-1}\, \boldsymbol{\Psi}_{\boldsymbol{r}}^T \tag{6.43}$$

The estimation of the modal flexibility matrix is performed using the strategy proposed by Bernal [2001], which is also the strategy adopted in the proposed implementation of the procedure originally formulated by Duan et al. [2005], as shown in Section 6.2.1.2.

4. Calculate the proportional modal flexibility-based deflection $\boldsymbol{x}^*_{n\times 1}$ of the shear building by applying the Positive Shear Inspection Load (PSIL) $\boldsymbol{p}$

$$\boldsymbol{x}^* = \boldsymbol{F}^*_{\boldsymbol{r}}\, \boldsymbol{p} \tag{6.44}$$

where the vector $\boldsymbol{p}_{n\times 1}$ is a uniform load vector $\boldsymbol{p} = [1 \;\; 1 \;\; \ldots \;\; 1]^T$. This is the same load that is adopted in the original work that proposed the PSIL method for damage detection in building structures [Koo et al., 2010] (as discussed in Chapter 3).

5. Calculate the vector of the proportional modal flexibility-based interstory drifts $\boldsymbol{d}^*_{n\times 1}$ starting from the modal flexibility-based deflection of the shear building structure using the following equation

$$\boldsymbol{d}^* = \boldsymbol{T}\,\boldsymbol{x}^* \tag{6.45}$$

where $\boldsymbol{T}_{n\times n}$ is a transformation matrix defined as follows

$$\boldsymbol{T} = \begin{bmatrix} 1 & -1 & 0 & \cdots & 0 \\ 0 & 1 & -1 & \ddots & \vdots \\ \vdots & \ddots & \ddots & \ddots & 0 \\ \vdots & \ddots & \ddots & \ddots & -1 \\ 0 & \cdots & \cdots & 0 & 1 \end{bmatrix} \tag{6.46}$$

It is worth noting that in the vector $\boldsymbol{d}^*$ the interstory drifts are ordered from the top story of the structure to the bottom story, and the matrix $\boldsymbol{T}$ was assembled accordingly. The vector of the proportional MF-based interstory drifts is assumed as the damage sensitive feature (DSF), as shown in Section 6.3.

By performing the above-mentioned steps proportional modal flexibility-based deflections and vectors of proportional modal flexibility-based interstory drifts of shear building structures can be calculated. It is clear that the scaling factors on such quantities, as well as the scaling factors on the proportional flexibility matrices, are undetermined when the procedure is applied starting from output-only modal identification.

Moreover, the scaling factor between the proportional flexibility matrices and the flexibility matrices is kept unaltered when the flexibility coefficients are combined to obtain the structural deflections. This means that the scaling factor between the proportional and the true flexibility matrices is the same scaling factor that is present between the proportional and the true deflections. This an important property that allows the integration of the PFM techniques in the framework of the PSIL method, and that can be easily shown as follows.

By post-multiplying both sides of Eq. (6.1) by the PSIL load $\boldsymbol{p}$, the term on the right-hand side is the true modal flexibility-based deflection $\boldsymbol{x}$, while the term on the

left-hand side is the proportional modal flexibility-based deflection $\boldsymbol{x}^*$ (according to Eq. 6.44). The relationship between the proportional MF-based deflection and the MF-based deflection is thus

$$\boldsymbol{x}^* = \alpha_f \, \boldsymbol{x} \tag{6.47}$$

Moreover, it can be shown that the operation of evaluating the proportional MF-based interstory drifts of the structure is an operation that does not alter the scaling factor that relates proportional and true deflections. By pre-multiplying both sides of Eq. (6.47) by the transformation matrix $\boldsymbol{T}$, the term on the right-hand side is the vector of the modal flexibility-based interstory drifts $\boldsymbol{d}$, while the term on the left-hand side is the vector of the proportional modal flexibility-based interstory drifts $\boldsymbol{d}^*$ (according to Eq. 6.45). The relationship between the two vectors is

$$\boldsymbol{d}^* = \alpha_f \, \boldsymbol{d} \tag{6.48}$$

It is evident that the scaling factor on the proportional modal flexibility-based deflections and on the vectors of proportional MF-based interstory drifts is equal to the scaling factor on the proportional flexibility matrices (in the remainder of the chapter this scaling factor is indicated with the symbol α). Moreover, according to Eq. (6.38), it was shown in previous sections that if the proportional vector $\boldsymbol{m}^*$ (estimated using the PFM techniques) is scaled in a way that $\|\boldsymbol{m}^*\|_{\boldsymbol{1}} = 1$, then, the scaling factor on the proportional flexibility matrices is theoretically equal to the total mass of the structure. The final property that derives from the two above-mentioned observations is that, adopting the proposed normalization of the mass proportional vector and the proportional mass matrix, the scaling factor on the proportional modal flexibility-based deflections of shear building structures is theoretically equal to the total mass of the structure (i.e. $\alpha = \|\boldsymbol{m}\|_{\boldsymbol{1}} = m_{tot}$).

6.3 Damage detection in building structures using proportional modal flexibility-based deflections

In this section the proportional modal flexibility-based deflections, obtained according to the procedure defined in previous sections, are employed for damage

detection purposes using an approach that is developed on the basis of the theory behind the Positive Shear Inspection Load (PSIL) method.

According to the original formulation of the PSIL method [Koo et al., 2010; Koo et al., 2011; Sung et al., 2012] and as shown in Chapter 3, the modal flexibility-based interstory drifts of each story of a shear building are considered as the damage sensitive features, and used to evaluate if such story is damage or not (which is an operation that leads to the localization of the damage).

On the contrary, according to the approach proposed in this chapter, the vectors of the proportional MF-based interstory drifts of the structure are considered as the damage sensitive features, and they are used to detect the existence of the damage in the whole shear building structure. This means that, according to the different achievement levels in damage detection that are defined in [Farrar & Worden, 2013], in the proposed approach a level one of achievement was selected (i.e. detecting the existence of the damage, instead of localizing the damage, as done on the contrary in the original formulation of the PSIL method).

The choice is motivated by the fact that, differently from the original PSIL method, in the proposed approach the distribution of the masses is estimated directly from the vibration data and the calculations are performed with minimal or no a-priori information about the masses of the structures. These operations may introduce additional uncertainties in the damage detection process and thus a level one of achievement was selected[3].

6.3.1 Compatibility of the scalar multipliers related to proportional modal flexibility-based deflections

Referring to the original formulation of the PSIL method, it was shown in Chapter 3 that there exists an explicit relationship between the vector of the damage-

[3] Investigations on the potential use of the proposed approach (based on the estimation of proportional modal flexibility-based deflections of shear buildings and applicable with minimal or no a-priori information on the masses) for damage localization may be the object of future developments of the research, as discussed in Chapter 7.

induced deflection of the shear building structure $\Delta\boldsymbol{x}$ and the change-in-flexibility matrix $\Delta\boldsymbol{F}$

$$\Delta\boldsymbol{x} = \boldsymbol{x_I} - \boldsymbol{x_B} = (\boldsymbol{F_I} - \boldsymbol{F_B})\,\boldsymbol{p} = \Delta\boldsymbol{F}\;\boldsymbol{p} \tag{6.49}$$

Moreover, according to the PSIL method the damage sensitive features are the modal flexibility-based interstory drifts of the structure, and the variations of these interstory drifts are used to localize the damage. In Chapter 3 it was also shown that there exists an explicit relationship between the vector of the damage-induced interstory drifts $\boldsymbol{\Delta d}$ of the shear building structure and the change-in-flexibility matrix $\Delta\boldsymbol{F}$

$$\boldsymbol{\Delta d} = \boldsymbol{d_I} - \boldsymbol{d_B} = \boldsymbol{T}\,(\boldsymbol{F_I} - \boldsymbol{F_B})\,\boldsymbol{p} = \boldsymbol{T}\,\Delta\boldsymbol{F}\,\boldsymbol{p} \tag{6.50}$$

In the present chapter, proportional modal flexibility-based deflections and vectors of proportional MF-based interstory drifts are considered instead of the real quantities since the calculations are performed from output-only vibration data using the Proportional Flexibility Matrix techniques [Bernal, 2001; Duan et al., 2005]. The vector of the proportional damage-induced interstory drifts $\boldsymbol{\Delta d}^*$, i.e. the vector difference between the vectors of the proportional MF-based interstory drifts related to the possibly damaged and the undamaged structures, can be thus expressed as

$$\boldsymbol{\Delta d}^* = \boldsymbol{d_I^*} - \boldsymbol{d_B^*} \tag{6.51}$$

The previous equation (Eq. 6.51) is reformulated using the following operations: Eq. (6.44) is substituted in Eq. (6.45), and then Eq. (6.45) evaluated both for the undamaged and the possibly damaged structures is substituted in Eq. (6.51).

$$\boldsymbol{\Delta d}^* = \boldsymbol{T}\,(\boldsymbol{F_I^*} - \boldsymbol{F_B^*})\,\boldsymbol{p} = \boldsymbol{T}\,\Delta\boldsymbol{F}^*\,\boldsymbol{p} \tag{6.52}$$

The vector of the proportional damage-induced interstory drifts is thus expressed as a function of the matrix $\Delta\boldsymbol{F}^*$. It is evident from this formulation that the core of the calculations is to evaluate the change-in-flexibility matrix $\Delta\boldsymbol{F}^*$, and then some algebraic operations are performed on this matrix (i.e. multiplying the change-in-flexibility matrix by an inspection load $\boldsymbol{p}$, which is a uniform vector of all ones, and then transforming the vector of the deflection to the vector of the interstory drifts using the transformation matrix $\boldsymbol{T}$).

As already discussed in Section 6.1.3, when the change-in-flexibility matrix is evaluated using proportional flexibility matrices instead of the true flexibility matrices, it is important to ensure the compatibility between the scaling factors related to such proportional quantities.

In light of these premises, it is clear that if the vector of the damage-induced interstory drifts is evaluated by considering proportional quantities instead of true values (i.e. using the vector of proportional MF-based interstory drifts instead of the true vector of MF-based interstory drifts), then the problem of ensuring the compatibility on the scalar multipliers related to the proportional quantities is a problem that has to be addresses also in this case (where vectors of interstory drifts are considered instead of modal flexibility matrices).

The vectors of the proportional MF-based interstory drifts related to the baseline and the possibly damaged states ($\boldsymbol{d_I^*}$ and $\boldsymbol{d_B^*}$) are calculated using the procedure proposed in Section 6.2.2, and they can be related with the corresponding true quantities as expressed by Eq. (6.48). This equation can be evaluated both for the baseline and the possibly damaged states and then substituted in Eq. (6.51)

$$\boldsymbol{\Delta d}^* = \alpha_I \, \boldsymbol{d_I} - \alpha_B \, \boldsymbol{d_B} \tag{6.53}$$

As shown in Section 6.2.2 and according to the proposed approach related to the normalization of the mass proportional vectors $\boldsymbol{m}^*$, the scaling factor on the vectors of the proportional MF-based interstory drifts is theoretically equal to the total mass of the structure. In general, the two scaling factors α_B and α_I can thus be different ($\alpha_B \neq \alpha_I$) in the case in which mass variations are present before and after damage. However, it is clear that the vector of the proportional damage-induced interstory drifts $\boldsymbol{\Delta d}^*$ can be appropriately evaluated only if the compatibility between the scaling factors is guaranteed (i.e. some scaling operations are performed to ensure that $\alpha_B = \alpha_I = \alpha$). In such case the vector of the proportional damage-induced interstory drifts differs from the vector of the true damage-induced interstory drifts to within a unique scalar α

$$\boldsymbol{\Delta d}^* = \alpha \, (\boldsymbol{d_I} - \boldsymbol{d_B}) = \alpha \, \boldsymbol{\Delta d} \tag{6.54}$$

According to the approach proposed in this chapter, the compatibility between the scaling factors on the vectors $\boldsymbol{d_I^*}$ and $\boldsymbol{d_B^*}$ is guaranteed by performing an additional

scaling operation on the vector of the proportional modal flexibility-based interstory drifts related to the possibly damage state $\boldsymbol{d}_{\boldsymbol{I}}^{*}$. This operation is done by correcting Eq. (6.52), and by evaluating the vector of the proportional damage-induced interstory drifts as follows

$$\boldsymbol{\Delta d}^{*} = \frac{1}{w}\,\boldsymbol{d}_{\boldsymbol{I}}^{*} - \boldsymbol{d}_{\boldsymbol{B}}^{*} = \alpha_B\,(\boldsymbol{d}_{\boldsymbol{I}} - \boldsymbol{d}_{\boldsymbol{B}}) = \alpha_B\,\boldsymbol{\Delta d} \tag{6.55}$$

where the parameter *w* is defined as

$$w = \frac{\|\boldsymbol{m}_{\boldsymbol{I}}\|_1}{\|\boldsymbol{m}_{\boldsymbol{B}}\|_1} = \frac{m_{I,tot}}{m_{B,tot}} \tag{6.56}$$

In this last equation $\|\boldsymbol{m}_{\boldsymbol{I}}\|_1$ is the total mass of the possibly damaged structure, and $\|\boldsymbol{m}_{\boldsymbol{B}}\|_1$ is the total mass of the undamaged structure. The parameter *w* is thus indicated in the present chapter as "total-mass-ratio". By performing this additional scaling operation on the vector $\boldsymbol{d}_{\boldsymbol{I}}^{*}$, the scaling factor in the possibly damaged state is imposed as equal to $\alpha_B = \|\boldsymbol{m}_{\boldsymbol{B}}\|_1$, which is the scaling factor related to the structure in the baseline condition. In this way, the compatibility between the scaling factors on the vectors of the proportional MF-based interstory drifts is guaranteed – i.e. the scaling factors in the baseline and in the possibly damaged states are the same. It is worth noting that having the knowledge of the ratio *w* means basically to know the eventual relative modification of the total mass of the structure between the undamaged and the possibly damaged states.

6.3.2 Proposed indices for damage detection using proportional MF-based deflections

According to the proposed approach and as already mentioned in previous sections, the vectors of the interstory drifts evaluated from the proportional modal flexibility-based deflections of shear building structures are considered as damage sensitive features (DSFs). In this section two damage indices that can be calculated starting from these damage sensitive features and that can be used for detecting the existence of damage in shear building structures are presented and discussed.

As shown in detail in this section, the first index is based on the evaluation of the Mahalanobis distance [Barnett & Lewis, 1994] between the vectors assumed as

DSFs, while the second proposed index is based on the evaluation of the degree of correlation between the vectors of the proportional modal flexibility-based interstory drifts. It is important to underline that the application of both two indices was investigated in the present dissertation because such indices are characterized by two different strategies for evaluating the differences or the similarities between the vectors assumed as damage sensitive features. In other words, the two indices can be considered as two completely different metrics that can be used to perform the damage detection.

As shown later in this section, the fundamental difference between the two indices is the following. Referring to the first index (Mahalanobis distance), the core of the calculations related to this proposed index is the evaluation of the vector of the proportional damage-induced interstory drifts $\boldsymbol{\Delta d}^*$, and this means that, as shown in previous section, when applying this index particular care should be taken to ensure that the scalar multipliers on the damage sensitive features (DSFs) are comparable.

On the contrary, the second index is based on the evaluation of the degree of correlation between the vectors assumed as the DSFs. This means that a completely different strategy is adopted in this second index to compare the damage sensitive features, and the main advantage of the proposed second index is that, as demonstrated in the following, it is not sensitive to the scaling factors on the vectors of the proportional modal flexibility-based interstory drifts.

6.3.2.1 Damage index based on Mahalanobis distance

The damage index that is presented in this section is based on the evaluation of the Mahalanobis distance (MD) [Barnett & Lewis, 1994] between the vectors that are assumed as the damage sensitive features.

In the original formulation of the Positive Shear Inspection Load method [Koo et al., 2010], an index z_j is considered and used to perform a statistical test for the localization of the damaged stories in shear building structures using the modal flexibility-based interstory drifts. This statistical test based on a z-score is a widely used criterion in the field of univariate outlier analysis [Barnett & Lewis, 1994; Farrar & Worden, 2013]. As already discussed in Chapter 3, this index z_j is defined as

$$z_j = \frac{d_{j,I} - \bar{d}_{j,B}}{s(d_{B,j})} \tag{6.57}$$

where $\bar{d}_{j,B}$ and $s(d_{j,B})$ are, respectively, the sample mean and the sample standard deviation of the interstory drifts $d_{j,B,i}$ of the j-th story of the structure calculated for the baseline state (for $i = 1 \ldots p$), and $d_{j,I}$ is the interstory drift estimated in the inspection phase.

The index proposed in this section is the multi-dimensional counterpart of the z-score that is considered in the original formulation of the PSIL method. This multi-dimensional criterion is based on the calculation of the Mahalanobis distance (MD) between the vectors of the proportional modal flexibility-based interstory drifts – i.e. the DSFs. Evaluating Mahalanobis distance and then performing a statistical test is a widely used criterion in the field of multivariate outlier analysis [Barnett & Lewis, 1994]. The criterion has been also used in the context of structural damage detection by considering damage sensitive features different from the ones adopted in the present chapter [Worden et al., 2000; Farrar & Worden, 2013; Balsamo & Betti, 2015; Ubertini et al., 2016].

The Mahalanobis distance evaluated between the DSFs extracted for the baseline state and for the state related to the inspection phase is defined as

$$MD_{id}^{*} = \sqrt{\left(\boldsymbol{d}_{\boldsymbol{I,w}}^{*} - \bar{\boldsymbol{d}}_{\boldsymbol{B}}^{*}\right)^{\boldsymbol{T}} \boldsymbol{S}_{\boldsymbol{B}}^{*\,-1} \left(\boldsymbol{d}_{\boldsymbol{I,w}}^{*} - \bar{\boldsymbol{d}}_{\boldsymbol{B}}^{*}\right)} \tag{6.58}$$

where $\bar{\boldsymbol{d}}_{\boldsymbol{B}}^{*}$ and $\boldsymbol{S}_{B}^{*}$ are, respectively, the sample mean vector and the unbiased sample covariance matrix of the vectors of the proportional modal flexibility-based interstory drifts $\boldsymbol{d}_{\boldsymbol{B,i}}^{*}$ (where $i = 1 \ldots p$) calculated for the baseline state and using the training data set; $\boldsymbol{d}_{\boldsymbol{I,w}}^{*}$ represents the potential outlier, and it is defined as

$$\boldsymbol{d}_{\boldsymbol{I,w}}^{*} = \frac{1}{w}\,\boldsymbol{d}_{\boldsymbol{I}}^{*} \tag{6.59}$$

i.e. $\boldsymbol{d}_{\boldsymbol{I,w}}^{*}$ is the vector of the interstory drifts extracted from the testing data set $\boldsymbol{d}_{\boldsymbol{I}}^{*}$ that is normalized and scaled by the factor $1/w$, using the criterion defined in Section 6.3.1.

The number of DSFs related to the baseline state is equal to p. Each DSF is a vector of proportional MF-based interstory drifts which is calculated starting from the vibration data related to the training data set and through the approach defined in

Section 6.2.2. To evaluate the proposed index (Eq. 6.58) it is assumed that p is large enough so that adequate estimates of the true (and unknown) mean vector and covariance matrix of the interstory drift vectors are obtained using the sample counterparts. This requirement is important especially for the sample covariance matrix which needs to be numerically inverted in the formula of the index MD_{id}^{*} (Eq. 6.58). If a sufficient number of DSFs is not considered, then the covariance matrix may be ill-conditioned, and problems may arise in the computation of the inverse matrix [Balsamo & Betti, 2015].

Several observations can be formulated on the proposed index. First of all, let us consider the differences between the proposed index based on Mahalanobis distance and the z-index that is adopted in the original formulation of the PSIL methods. The first main difference is that in the latter the true interstory drifts of the shear building structure are considered, while in the former (i.e. the proposed approach) the calculations are performed using the proportional modal flexibility-based interstory drifts. This is because in the proposed approach the Proportional Modal Flexibility techniques are integrated in the calculations. Moreover, both the two indices (Mahalanobis distance and z-index) are scalar quantities. However, the second important difference between the two indices is the following: the z index is evaluated for each story of the structure by considering the interstory drifts related to that story in the possibly damaged and in the undamaged states; on the contrary, in the approach based on Mahalanobis distance the calculations are performed on vectors that are formed by all the proportional MF-based interstory drifts of the structure. In this way, a parameter that quantifies for the whole structure eventual changes in the vectors of the proportional MF-based interstory drifts (when comparing the undamaged and the possibly damaged states) is obtained.

The second observation is that if the covariance matrix present in the equation of Mahalanobis distance (Eq. 6.58) is assumed equal to the identity matrix (i.e. $\boldsymbol{S}_{\boldsymbol{B}}^{*} = \boldsymbol{I}$), then the proposed index is equivalent to the calculation of the Euclidean distance (ED_{id}^{*}) between the vectors of the proportional MF-based interstory drifts related to the undamaged and the possibly damaged states. This concept can be exemplified using the following equation

$$ED_{id}^{*} = \sqrt{\left(\boldsymbol{d}_{\boldsymbol{I,w}}^{*} - \boldsymbol{d}_{\boldsymbol{B}}^{*}\right)^{\boldsymbol{T}} \left(\boldsymbol{d}_{\boldsymbol{I,w}}^{*} - \boldsymbol{d}_{\boldsymbol{B}}^{*}\right)} = \|\boldsymbol{\Delta d}^{*}\|_{\boldsymbol{2}} \tag{6.60}$$

where $\boldsymbol{\Delta d}^{*} = \boldsymbol{d}_{\boldsymbol{I,w}}^{*} - \boldsymbol{d}_{\boldsymbol{B}}^{*}$.

By comparing Eq. (6.60) and Eq. (6.58), it is clear that, as reported in [Balsamo & Betti, 2015], the Mahalanobis distance can be interpreted as an Euclidean distance where the components of the feature vectors (i.e. the components of $\boldsymbol{\Delta d}^{*}$ in this specific case) are weighted by the covariance matrix. In Eq. (6.60) it is also highlighted that this operation of evaluating the Euclidean distance is equivalent to the calculation of the 2-norm of the vector of the proportional damage-induced interstory drifts $\boldsymbol{\Delta d}^{*}$.

The third observation is that the total mass ratio *w* (present in Eq. 6.58 and defined in Section 6.3.1) is the sole parameter that has to be known a-priori to perform the damage detection using the index based on Mahalanobis distance and starting from output-only vibration data. The vectors of the proportional MF-based interstory drifts, in fact, are evaluated using the procedure outlined in Section 6.2.2, without any a-priori information on the structural masses. Then, the ratio *w* is required to guarantee that the scaling factors on the vectors related to the undamaged and the possibly damaged states are comparable. Of course, if the masses of the structure are unchanged before and after damage, the ratio *w* is equal to one. However, imposing *w* =1 is an a-priori information that has to be known, as well.

To classify the structure considered in the inspection phase as damaged or undamaged a discordancy test has to be performed. This test implies the comparison of the value of Mahalanobis distance obtained using Eq. (6.58) against a threshold value, which is indicated as $MD_{id}^{*\,TH}$. Then, the structure in the inspection phase is considered as damaged if $MD_{id}^{*} > MD_{id}^{*\,TH}$, while the structure in the inspection phase is considered as undamaged if $MD_{id}^{*} \leq MD_{id}^{*\,TH}$.

The evaluation of the threshold value when considering the types of metrics shown in this section is a problem that in the literature has been addressed by considering the Mahalanobis-squared distance. However, it is clear that, as shown later in this section, the value of the threshold for the Mahalanobis distance (which is the metric used in the proposed approach) can then be easily determined.

As reported in [Farrar & Worden, 2013] and under the assumption that the feature vectors used in the calculation of Mahalanobis-squared distance follow a multivariate normal distribution, the threshold value for Mahalanobis-squared distance can be obtained in terms of the chi-squared-statistic. In fact, under the assumption of having data that are multivariate normal distributed, the Mahalanobis-squared distance evaluated for a large number of *n*-dimensional feature vectors tends to follow approximately a χ^2 distribution with *n* degrees of freedom. The threshold can thus be theoretically determined using this statistical distribution (for example, considering the *k*-th percentile of a χ^2 distribution with *n* degrees of freedom, where the value of *k* is in the range 95-99) [Farrar & Worden, 2013; Balsamo & Betti, 2015].

However, as also suggested in [Farrar & Worden, 2013], an option that is preferable to obtain the threshold for Mahalanobis-squared distance is to have a numerical method that can be used to obtain the value of the threshold. This method is described in the works by [Worden et al., 2000; Farrar & Worden, 2013], where metrics based on Mahalanobis-squared distance were applied on damage sensitive features different from the ones considered in the present chapter. The approach defined by [Worden et al., 2000; Farrar & Worden, 2013] is the approach that has been adopted in the analyses presented in this chapter for the calculation of the threshold related to the proposed index based on Mahalanobis distance (Eq. 6.58).

The method is based on a Monte Carlo simulation: the threshold is calculated as a function of the dimension of the feature vectors (*n*) and the number of the feature vectors (*p*), and the calculations are performed on feature vectors composed by normally-distributed random numbers. The threshold value is thus not calculated from the training data set used for the damage detection, but it is calculated from the random numbers generated in the Monte Carlo simulation.

The main steps of the procedure, reported in [Farrar & Worden, 2013], that is able to calculate numerically the threshold for Mahalanobis-squared distance are summarized herein:

1. At first a $p \times n$ matrix $\mathbf{X}$ is assembled. The components of such matrix are numbers that are randomly generated from a univariate normal distribution with a zero mean and a standard deviation equal to one. The mean vector $\bar{\boldsymbol{x}}$ and the

covariance matrix $\boldsymbol{S}$ of the feature vectors that are represented by each row of the matrix **X** are calculated. These feature vectors (i.e. each row of $\boldsymbol{X}$) are indicated as $\boldsymbol{x}(i)$ for $i = 1 .. p$.

2. The Mahalanobis-squared distance is calculated between each row $\boldsymbol{x}(i)$ of the matrix $\boldsymbol{X}$ and the whole data set (by considering in the calculation the mean vector $\bar{\boldsymbol{x}}$ and the covariance matrix $\boldsymbol{S}$ calculated at step 1)

$$MD^2(i) = (\boldsymbol{x}(i) - \bar{\boldsymbol{x}})\ \boldsymbol{S}^{-1}\ (\boldsymbol{x}(i) - \bar{\boldsymbol{x}})^T \tag{6.61}$$

   The maximum value of the Mahalanobis-square distance $MD^2(i)$ obtained for the different vectors $\boldsymbol{x}(i)$ is stored. It is worth noting that each vector $\boldsymbol{x}(i)$ is included in the calculation of the mean vector $\bar{\boldsymbol{x}}$ and the covariance matrix $\boldsymbol{S}$. This means that inclusive measures of the Mahalanobis-squared distance are calculated.

3. The steps from 1 to 2 are repeated for a number of trials that is at least equal to 1000, and at the end the maximum value of the Mahalanobis-squared distance obtained for each trial is collected in a vector $\boldsymbol{t}$.

4. The critical value is obtained as the *k*-th percentile of the values contained in the vector $\boldsymbol{t}$ (i.e. the maximum values of the Mahalanobis-squared distance obtained for the different trials). The value of *k* is typically selected as 95 or 99 [Farrar & Worden, 2013], and $k = 99$ was selected for the analyses presented in this chapter.

5. The value obtained at step 4 represents an inclusive threshold (T_{inc}), and in order to obtain an exclusive threshold (T_{exc}), the following formula can be adopted

$$T_{exc} = \frac{(p-1)\,(p+1)^2 T_{inc}}{p\,(p^2-(p+1)\,T_{inc})} \tag{6.62}$$

As already mentioned, the procedure described in [Farrar & Worden, 2013] was developed to obtain the threshold for the Mahalanobis-square distance, while the proposed index (Eq. 6.58) is based on the evaluation of the Mahalanobis distance between the damage sensitive features. A final step, which is not reported in [Farrar

& Worden, 2013] and that is needed to calculate the threshold value for the proposed index based on Mahalanobis distance is the following

$$MD_{id}^{*\,TH} = \sqrt{T_{exc}} \tag{6.63}$$

It is worth noting that step no. 5 of the procedure described by [Farrar & Worden, 2013] is a step that is required because the Mahalanobis distance (Eq. 6.58) evaluated on the feature vectors considered in the proposed approach (i.e. the vectors of the proportional modal flexibility-based interstory drifts) is calculated as an exclusive measure. On the contrary, in the numerical procedure proposed by [Farrar & Worden, 2013] and as already mentioned at step no. 2 inclusive measures are considered. Referring to Eq. (6.58), evaluating Mahalanobis distance as an exclusive measure means that the feature vector $\boldsymbol{d}_{I,w}^{*}$ is not included in the data set used to calculate the mean vector $\overline{\boldsymbol{d}}_{\boldsymbol{B}}^{*}$ and the unbiased covariance matrix $\boldsymbol{S}_{B}^{*}$. As observed in [Farrar & Worden, 2013], in fact, in structural health monitoring and damage detection the potential outlier (i.e. $\boldsymbol{d}_{I,w}^{*}$ in this case) is in general always known beforehand, and thus it is not meaningful to include this potential outlier in the calculation of the statistics related to the baseline state (i.e. the mean vector $\overline{\boldsymbol{d}}_{\boldsymbol{B}}^{*}$ and the unbiased covariance matrix $\boldsymbol{S}_{B}^{*}$).

6.3.2.2 Damage index based on Modal Assurance Criterion

In this section another index that can be adopted for damage detection on shear building structures using the vectors of the proportional modal flexibility-based interstory drifts as damage sensitive features is presented. This index was derived starting from the definition of the Modal Assurance Criterion (MAC) [Allemang & Brown, 1982].

As already mentioned in Chapter 1, the Modal Assurance Criterion is a criterion that, in the original formulation, is used to evaluate the degree of correlation or similarity between mode shape vectors. The criterion can be used to compare analytical and experimental modal vectors for model validation and updating [Ewins, 2000], or to compare mode shapes of the undamaged structure and mode shapes in the possibly damaged structure in the context of vibration-based damage detection [Farrar & Worden, 2013]. The Modal Assurance Criterion is defined as

$$MAC = \frac{(\boldsymbol{\psi_i}^T \boldsymbol{\psi_j})^2}{(\boldsymbol{\psi_i}^T \boldsymbol{\psi_i})(\boldsymbol{\psi_j}^T \boldsymbol{\psi_j})} \tag{6.64}$$

where $\boldsymbol{\psi_i}$ and $\boldsymbol{\psi_j}$ are experimental or analytical mode shapes related to the *i*-th mode and the *j*-th mode. The parameter is evaluated by considering modes related to any mode index $i, j \in [1 \dots r]$, where *r* is the total number of the considered modes. The value of the MAC matrix is in the range $0 \leq \text{MAC} \leq 1$, and in case of a good correlation between the two considered mode shapes the value of the MAC is close to one. As reported in [Farrar & Worden, 2013], the type of metric used in the Modal Assurance Criterion can be applied to compare not only mode shape vectors. This metric can be applied to compare any feature vector considered in the context of vibration-based damage detection as damage sensitive feature (DSF).

The index that is proposed in this section has the same formulation of the Modal Assurance Criterion developed for mode shape vectors, and it is adopted to evaluate the degree of correlation between the vectors of the proportional modal flexibility-based interstory drifts (which are assumed, as already mentioned, as DSFs). The proposed index is termed Modal Assurance Criterion on interstory drifts (MAC_{id}^*), and it is defined as follows

$$MAC_{id}^* = \frac{\left(\boldsymbol{d_I^{*T}}\ \boldsymbol{d_B^*}\right)^2}{\left(\boldsymbol{d_I^{*T}}\ \boldsymbol{d_I^*}\right)\left(\boldsymbol{d_B^{*T}}\ \boldsymbol{d_B^*}\right)} \tag{6.65}$$

The correlation is performed between vectors of proportional modal flexibility-based interstory drifts evaluated for the structural state considered in the inspection phase $\boldsymbol{d_I^*}$ and for the baseline state $\boldsymbol{d_B^*}$. Such vectors are calculated using the procedure described in Section 6.2.2.

To show some important properties of the index MAC_{id}^*, the Modal Assurance Criterion evaluated on the true vectors of MF-based interstory drifts (instead of the proportional vectors) has to be considered. This index is defined as

$$MAC_{id} = \frac{(\boldsymbol{d_I^T}\ \boldsymbol{d_B})^2}{(\boldsymbol{d_I^T}\ \boldsymbol{d_I})(\boldsymbol{d_B^T}\ \boldsymbol{d_B})} \tag{6.66}$$

where $\boldsymbol{d_I}$ and $\boldsymbol{d_B}$ are the true vectors of MF-based interstory drifts related to the inspection phase and to the baseline state, respectively. If the proportional vectors of

interstory drifts present in Eq. (6.65) are substituted by the corresponding true vectors using Eq. (6.48), Eq. (6.65) can be reformulated as follows

$$MAC_{id}^{*} = \frac{(\alpha_I \ \alpha_B \quad \boldsymbol{d}_I^T \boldsymbol{d}_B)^2}{(\alpha_I^2 \quad \boldsymbol{d}_I^T \boldsymbol{d}_I)(\alpha_B^2 \quad \boldsymbol{d}_B^T \boldsymbol{d}_B)} = \frac{(\boldsymbol{d}_I^T \boldsymbol{d}_B)^2}{(\boldsymbol{d}_I^T \boldsymbol{d}_I)(\boldsymbol{d}_B^T \boldsymbol{d}_B)} = MAC_{id} \qquad \forall\, \alpha_B, \alpha_I \qquad (6.67)$$

It is evident in Eq. (6.67) that the MAC_{id}^{*} evaluated on the vectors of the proportional interstory drifts is equal to the MAC_{id} evaluated on the vectors of the true interstory drifts independently from the values assumed by the scalar multipliers α_I , α_B, which are related to the two states involved in the damage detection process. In fact, as evident in Eq. (6.67), for any value of the scaling factors α_I , α_B, these factors cancel out.

The values assumed by the MAC_{id}^{*} are in the range $0 \leq MAC_{id}^{*} \leq 1$ (similarly to the original MAC). If the structure considered in the inspection phase is undamaged, then the value of the MAC_{id}^{*} is theoretically equal to 1, which means that there is a perfect correlation between the vectors assumed as damage sensitive features. The parameter MAC_{id}^{*} assumes values that are lower than one if there are changes in the vectors of the proportional modal flexibility-based interstory drifts, and such changes can be in general associated to a damaged state. Of course, having a value of the MAC_{id}^{*} equal to 1 for a structure in the inspection phase that is undamaged is a theoretical result that is obtained if exact modal parameters and all the structural modes (i.e. r=n) are considered when the proportional modal flexibility matrices are assembled. Dealing with damage sensitive features affected by uncertainties and with a limited number of modes is considered in the numerical and experimental analyses, presented in next sections.

The first observation that can be formulated on the proposed index derives from the fact that, as shown in the Eq. (6.67), the MAC_{id}^{*} is independent from the scalar multipliers α_B , α_I related to the vectors of the proportional MF-based interstory drifts. The operation of ensuring the compatibility of such scalar factors, as described in Section 6.3.1, and which is based on a-priori information on the relationship between the structural masses in the undamaged and in the possibly damaged states (i.e. the parameter w "total-mass-ratio") is thus not required. For this reason, it is clear that according to the proposed approach for output-only damage detection, where the

distribution of the masses of the structures is extracted directly from the vibration data and specifically from arbitrarily-scaled mode shape vectors, the proposed index MAC_{id}^{*} can be calculated without any a-priori information on the structural masses. This property will be also demonstrated in the numerical and experimental analyses presented in this section, and it is one of the main advantages of the proposed index. The proposed index MAC_{id}^{*} is thus a modal flexibility-based index that can be adopted for damage detection using exclusively output-only vibration data.

A second observation that can be formulated on the proposed index is the following. Due to the formulation of the MAC_{id}^{*} which is based on evaluating the degree of correlation between the vectors assumed as damage sensitive features, this index is suitable for the detection of the existence of localized damage in the building structures. On the contrary, in the ideal case in which the damage pattern is uniformly distributed along the height of the shear building, for example in the case in which all the stories of the structure are characterized by the same interstory stiffness reduction, the MAC_{id}^{*} is theoretically insensitive to such type of damage. This means that, in this particular case, the correlation between the vectors of the modal flexibility-based interstory drifts (either the true or the proportional vectors of the interstory drifts) is equal to one even if the structure is damaged.

This property can be shown analytically by considering the parameter that, according to the original formulation of the PSIL method [Koo et al., 2010] and as discussed in Chapter 3, is indicated as the damage severity. This parameter evaluated for the *j*-th story is as follows

$$\alpha_{s,j} = \frac{d_{j,I} - d_{j,B}}{d_{j,I}} \tag{6.68}$$

Eq. (6.68) can then be reformulated as

$$d_{j,B} = d_{j,I} \left(1 - \alpha_{s,j}\right) \tag{6.69}$$

If the damage severity is uniform along the height of the building (i.e. each story is characterized by the same stiffness reduction that is due to the damage) then $\alpha_{s,j} = \alpha_s$ for each story. This means that Eq. (6.69) can be reformulated in a vector representation as follows

$$\boldsymbol{d_B} = \boldsymbol{d_I} \left(1 - \alpha_s\right) \tag{6.70}$$

When considering the above-mentioned particular situation, the vector of the drifts in the undamaged and in the possibly damaged states are collinear vectors, as shown in Eq. (6.70), and thus the correlation between such vectors is equal to one for each value assumed by the damage severity α_s.

In light of these premises, it is clear that the damage that is detectable using the proposed index MAC_{id}^{*} can be either a single- or multiple- damage, but theoretically a uniform stiffness reduction in all the stories of the shear building structure is not detectable. This limitation is however not so restrictive as it may appear, since in general having a uniform damage is not a common situation in practice. On the contrary, damage in structures is in general localized. Finally, it is worth noting that the traditional Modal Assurance Criterion index evaluated on mode shape vectors is also affected by the same limitation. In fact, a uniform stiffness reduction in all the stories of a shear building structure does not theoretically alter the mode shapes, and thus the traditional Modal Assurance Criterion is not sensitive to a damage pattern that is uniformly distributed along the height of the building, as well.

Two modifications have to be applied to the proposed index MAC_{id}^{*} to obtain an index that can be useful in practical applications. These two modifications derive from the following two considerations.

First of all, the metrics used for damage detection aim in general to measure the departure of the damage sensitive features extracted in the testing or inspection phase from the DSFs obtained in the training phase (or baseline state). It is thus of interest to have metrics that are zero or very close to zero if the structure related to the inspection phase is undamaged, and metrics that become different from zero in presence of some structural modifications that can be associated to a damaged state. Referring to this point, the index reported in Eq. (6.65) is based, on the contrary, on the determination of the similarity between the DSFs. For this reason, it is more convenient to consider as the damage index the error in the MAC_{id}^{*} with respect to 1 instead of the MAC_{id}^{*}. This metric is indicated as $eMAC_{id}^{*}$.

Secondly, it is trivial that uncertainties affect the damage sensitive features (i.e. the vectors of proportional MF-based interstory drifts) extracted from real vibration data. To deal with such uncertainties it is assumed that, as already done to

derive the index based on Mahalanobis distance, the number of the damage sensitive features that have to be estimated for the baseline state and considered in the calculations is equal to p. These DSFs are the vectors of the proportional MF-based interstory drifts $\boldsymbol{d}_{\boldsymbol{B},\boldsymbol{i}}^{*}$ calculated using the training data set (where $i = 1 \ldots p$), and then the mean vector $\bar{\boldsymbol{d}}_{\boldsymbol{B}}^{*}$ of such damage sensitive features is considered in the evaluation of the index $eMAC_{id}^{*}$.

In light of these two observations and starting from Eq. (6.65), the final expression of the index that is proposed in this section – i.e. the error on the MAC_{id}^{*} – is as follows

$$eMAC_{id}^{*} = 1 - MAC_{id}^{*} = 1 - \frac{\left(\boldsymbol{d}_{\boldsymbol{I}}^{*\boldsymbol{T}}\ \bar{\boldsymbol{d}}_{\boldsymbol{B}}^{*}\right)^{2}}{\left(\boldsymbol{d}_{\boldsymbol{I}}^{*\boldsymbol{T}}\ \boldsymbol{d}_{\boldsymbol{I}}^{*}\right)\left(\bar{\boldsymbol{d}}_{\boldsymbol{B}}^{*\boldsymbol{T}}\ \bar{\boldsymbol{d}}_{\boldsymbol{B}}^{*}\right)} \tag{6.71}$$

To label the structure considered in the inspection phase as damaged or undamaged, a statistical test has to be performed on the values of $eMAC_{id}^{*}$ calculated from the vibration data. Of course, to perform this statistical test a threshold value for $eMAC_{id}^{*}$ is required. Differently from the index defined in Section 6.3.2.1 (i.e. Mahalanobis distance) where a statistical model was assumed, it is not assumed to have a statistical model behind the calculations related to the index $eMAC_{id}^{*}$. For this reason, the threshold for $eMAC_{id}^{*}$ is calculated empirically using the training data set. This represents one difference with respect to the index based on Mahalanobis distance where, on the contrary, the threshold is determined independently from the training data set.

To calculate the threshold for the index $eMAC_{id}^{*}$ the approach presented in [Balsamo & Betti, 2015], which was developed by considering damage sensitive features different from the ones considered in the present dissertation and a damage index different from the one presented in this section, was considered. The approach presented in [Balsamo & Betti, 2015] was adapted and adjusted so that it can be applied on the proposed index $eMAC_{id}^{*}$.

The threshold for the damage index $eMAC_{id}^{*}$ is calculated through the following steps:

1. At first, the value of the metric is evaluated for the generic *i*-th feature vector $\boldsymbol{d}_{\boldsymbol{B},\boldsymbol{i}}^{*}$ extracted from the training data set

$$eMAC_{id}^{*}\left(\boldsymbol{d}_{\boldsymbol{B},\boldsymbol{i}}^{*}\right) = 1 - \frac{\left(\boldsymbol{d}_{\boldsymbol{B},\boldsymbol{i}}^{*\,T}\ \bar{\boldsymbol{d}}_{\boldsymbol{B},(\boldsymbol{i})}^{*}\right)^{2}}{\left(\boldsymbol{d}_{\boldsymbol{B},\boldsymbol{i}}^{*\,T}\ \boldsymbol{d}_{\boldsymbol{B},\boldsymbol{i}}^{*}\right)\left(\bar{\boldsymbol{d}}_{\boldsymbol{B},(\boldsymbol{i})}^{*\,T}\ \bar{\boldsymbol{d}}_{\boldsymbol{B},(\boldsymbol{i})}^{*}\right)} \qquad \text{for } i = 1 \ldots p \quad (6.72)$$

   where $\bar{\boldsymbol{d}}_{\boldsymbol{B},(\boldsymbol{i})}^{*}$ is the mean vector of all the feature vectors related to the baseline state excluding the *i*-th sample $\boldsymbol{d}_{\boldsymbol{B},\boldsymbol{i}}^{*}$. It is worth noting that the evaluation of the metric $eMAC_{id}^{*}\left(\boldsymbol{d}_{\boldsymbol{B},\boldsymbol{i}}^{*}\right)$ in the procedure to determine the threshold is thus performed by considering an exclusive measure of the departure of $\boldsymbol{d}_{\boldsymbol{B},\boldsymbol{i}}^{*}$ from $\bar{\boldsymbol{d}}_{\boldsymbol{B},(\boldsymbol{i})}^{*}$. Considering an exclusive measure is the same strategy that is considered in the evaluation of the damage index $eMAC_{id}^{*}$ and, as already discussed in Section 6.3.2.1, is the strategy adopted for the majority of the metrics that are considered in damage detection.

2. The step no. 1 is repeated for each DSF extracted from the training data set (i.e. for $i = 1 \ldots p$) and in each case the value of $eMAC_{id}^{*}\left(\boldsymbol{d}_{\boldsymbol{B},\boldsymbol{i}}^{*}\right)$ is stored.

3. The threshold for the damage index $eMAC_{id}^{*}$ (which is indicated as $eMAC_{id}^{*\,TH}$) is obtained as the *k*-th percentile of the values of $eMAC_{id}^{*}\left(\boldsymbol{d}_{\boldsymbol{B},\boldsymbol{i}}^{*}\right)$ calculated for $i = 1 \ldots p$. The value of *k* is typically selected in the range from 95 to 99 [Balsamo & Betti, 2015], and $k = 99$ was considered for the analyses presented in this chapter.

At the end, the statistical test is performed to label the structure considered in the inspection phase as damaged or undamaged: the structure in the inspection phase is considered as damaged if $eMAC_{id}^{*} > eMAC_{id}^{*\,TH}$, while the structure in the inspection phase is considered as undamaged if $eMAC_{id}^{*} \leq eMAC_{id}^{*\,TH}$.

6.4 Verification of the proposed approach for damage detection using proportional MF-based deflections

The proposed approach for output-only damage detection in shear building structures, which is based on the estimation of proportional MF-based deflections and which is applicable with minimal or no a-priori information on the structural masses, was verified using both numerical simulations and experimental vibration data. In next section, the validity of the methodology is demonstrated using a numerical model of a shear building structure, while the experimental verification is presented in Section 6.4.2.

Both the numerical and the experimental verifications were conducted considering two different cases: in the first case, the masses of the structure are unchanged before and after damage; in the second case, mass variations are present between the two states involved in the damage detection process. As already mentioned, such mass variations can be present in real-life structures that experience changing operational conditions [Farrar & Worden, 2013]. Moreover, as shown in previous sections and according to the proposed approach, there is a relationship between the total mass of the structure and the unknown scaling factors on the proportional MF-based deflections. The choice of considering the above-mentioned second case, in which there are mass variations between the two states involved in the damage detection, was thus made specifically to test the methodology in the case in which the scaling factors related to the undamaged and the possibly damaged states are varied and theoretically not comparable.

6.4.1 Numerical verification

6.4.1.1 First numerical analysis: damage detection without mass variations

The structure used in the numerical verification is a 6-story shear-type frame building structure that can be modeled using 6 DOFs (Fig. 6.2), and this structure is similar to the structure that was used for the analyses presented in Chapter 4. The structure considered in the present section is characterized by a generic mass distribution, and the floor masses are: m_6 = 50 kN s^2/m, $m_5 = m_4 = m_2$ = 100 kN s^2/m and $m_3 = m_1 =$

150 kN s^2/m. The interstory stiffness of each story of the structure is equal to k_j = 2.29 × 10^5 kN/m. Such parameters were used to define the diagonal mass matrix $\mathbf{M_{ref}}$ and the stiffness matrix $\mathbf{K_{ref}}$ of the structure. Moreover, it is assumed that the system is classically damped with a modal damping ratio equal to ζ_i = 0.01 for all the modes. Such values of the modal damping ratios and the undamped modes of the structure (obtained by performing an eigenvalue analysis using the matrices $\mathbf{M_{ref}}$ and $\mathbf{K_{ref}}$) were used to assemble the damping matrix of the structure as follows

$$\boldsymbol{C_{ref}} = \boldsymbol{\Phi}^{-T}\,\boldsymbol{\Theta}\,\boldsymbol{\Phi}^{-1} \tag{6.73}$$

where $\boldsymbol{\Theta} = \text{diag}\{2\,\zeta_i\,\omega_i\}$ with $i = 1,\ldots, n$ [Alvin et al., 2003].

In this way, a second-order analytical model of the structure was obtained, by defining the mass, stiffness and damping matrices. This model represents the original or baseline structure for damage detection purposes. This second order model is then transformed to a first order state space model [De Angelis et al., 2002], according to the formulation that is presented in Section A.1.1 of Appendix A. This first order state space model of the structure was used for the simulation of the vibration data, i.e. for the generation of the training data set that is used in the damage detection process, and the calculations were performed using the Matlab command "lsim" [Matlab].

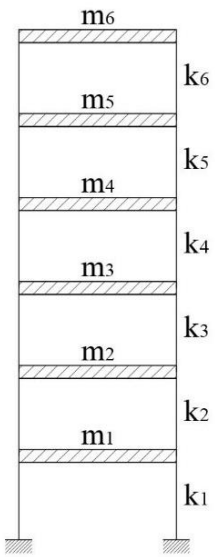

Figure 6.2. Six story shear-type frame building structure

The structure was excited by white noise inputs at all the degrees of freedom to mimic the excitations that can be present in real structures that are tested under ambient vibrations. The white noise inputs considered in the analysis have a duration of 1000 s, and the sampling frequency is assumed as f_s = 100 Hz. The vibration responses of the structure due to such inputs were obtained, and white noise was added on the data to model the measurement noise that is present on real data. The Root-Mean-Square (RMS) amplitude of the added noise is equal to the 5% of the RMS amplitude of the response signals.

The calculations described in the previous paragraph were repeated for a number of times equal to p = 30 to obtain the vibration response data that are considered as the training data set in the numerical simulation of the damage detection process. It is worth noting that the input signals were not included in the training data set since the proposed methodology works in output-only conditions.

Then, structural configurations that represent testing configurations (i.e. possibly damaged structures) were considered, and these configurations are described in Table 6.1. In this table, the first three configurations (U1a, U2a, U3a) are equal to the structure used for the simulation of the training data set and are thus indicated as undamaged configurations. The configurations from D1a to D4a were obtained by imposing interstory stiffness reductions on the undamaged model of the structure (as described in the table), and these configurations from D1a to D4a are thus indicated as damaged configurations. It is worth noting that all the testing configurations considered in this section and reported in Table 6.1 have the same mass distribution of the baseline structure. This means that, referring to the considered configurations, the masses of the structure are unchanged before and after damage.

The simulation of the vibration responses due to the white noise inputs was repeated for each of the configurations that are reported in Table 6.1, to obtain the testing data set. In this case only one simulation of the vibration responses due to white noise inputs with a duration of 1000 s was performed for each testing configuration.

Configurations	State	Description
U1a, U2a, U3a	Undamaged	Baseline condition
D1a	Damaged	15% stiffness reduction at 2nd story
D2a	Damaged	15% stiffness reduction at 3rd story
D3a	Damaged	30% stiffness reduction at 2nd story
D4a	Damaged	30% stiffness reduction at 3rd story

Table 6.1. Testing configurations with description of damage scenarios (numerical simulation)

The vibration response data that were generated in the numerical simulation and that represent the training and the testing data set were used to extract the proportional modal flexibility-based deflections of the structure, according to the steps that are outlined in Section 6.2.2. Then, the damage sensitive features (i.e. the vectors of the proportional modal flexibility-based interstory drifts) obtained for the testing configurations were compared with the DSFs related to the baseline structure using the damage indices proposed in Section 6.3.2 (i.e. the index based on Mahalanobis distance and the error on the MAC^*_{id}).

The output-only modal identification was applied on the structural responses, both for the training and the testing data set, using the Natural Excitation technique (NExT) [James et al., 1993] combined with the Eigensystem Realization Algorithm (ERA) [Juang & Pappa, 1985]. Six modes were identified for each structural configuration but only the first four modes of the structure were considered in the calculations related to the proposed damage detection approach. This means that both for the baseline state and for the state related to the possibly damaged structure the number of modes included in the calculations is $r_B = r_I = r = 4$. The choice of considering a limited number of modes mimics the situation that can be obtained in practical applications, where usually not all the modes of real-life structures can be identified. The results, in terms of natural frequencies and mode shapes (normalized to a maximum value of unity), of the output-only modal identification executed usign the NExT-ERA algorithm, are reported in Table 6.2 for an undamaged configuration and for a damaged configuration. On the left-hand side of the table the results are presented for configuration U1a (undamaged), while on the right-hand side of Table 6.2 the results are presented for configuration D3a (damaged). If one compares the natural frequencies related to these two configurations, a reduction in the frequencies

of the damaged configuration can be observed with respect to the frequencies of the undamaged configuration, as expected.

	Undamaged (U1a)				Damaged (D3a)			
Mode	1st	2nd	3rd	4th	1st	2nd	3rd	4th
f_i [Hz]	1.90	5.41	8.15	11.32	1.79	5.39	7.91	10.84
ψ_{ji}	1.00	1.00	0.78	1.00	1.00	1.00	1.00	1.00
	0.97	0.75	0.33	-0.11	0.97	0.75	0.47	-0.01
	0.88	0.12	-0.49	-0.98	0.89	0.12	-0.58	-1.00
	0.73	-0.57	-0.76	0.31	0.76	-0.57	-0.99	0.04
	0.52	-0.83	0.28	0.57	0.57	-0.83	0.19	0.96
	0.27	-0.66	1.00	-0.43	0.25	-0.61	1.59	-0.50

Table 6.2. Identified modal parameters for configurations U1a and D3a (numerical simulation)

The arbitrarily-scaled mode shapes obtained from the output-only modal identification were then used to apply the proposed implementation of the Proportional Flexibility Matrix techniques originally formulated by Bernal [2001] and Duan et al. [2005]. In the remainder of the chapter these techniques will be indicated, for the sake of simplicity, as the PFM procedures defined by Bernal [2001] and Duan et al. [2005]. However, it goes without saying that in the present chapter all the analyses were performed using the proposed implementation of these techniques, as described in Section 6.2.1. In particular, both the two techniques were applied on two different subsets of structural modes. On one side, the identified mode shapes related to the modes from the 1st to the 4th were used to apply the PFM technique defined by Bernal [2001]. It is worth noting that, according to the condition expressed by Eq. (6.8), a limited number of modes equal to $r = 4$ represents the minimum number of modes that can be considered for the application of the PFM procedure defined by Bernal [2001]. This is evident if Eq. (6.8) is evaluated by considering $r = 4$ and $n = 6$. On the other side, the identified mode shapes related to the modes from the 1st to the 3rd were used to apply the PFM technique defined by Duan et al. [2005]. Of course, in such case ($r = 3$) and as evident if Eq. (6.8) is evaluated by considering $r = 3$ and $n = 6$, the PFM technique proposed by Bernal [2001] can not be applied.

In the analyses, and according to the proposed approach, the mass proportional vectors $\boldsymbol{m}^*$ estimated using both the procedures by Bernal [2001] and Duan et al. [2005], were normalized in a way that the 1-norm of such vectors is equal to one. Then, the proportional mass matrices were used to mass normalize the mode shapes and to assemble the proportional flexibility matrices. Starting from the PFMs and according to the steps defined in Section 6.2.2, the proportional MF-based deflections due to a uniform inspection load were calculated, and then the vectors of the proportional MF-based interstory drifts, which are assumed as damage sensitive features, were computed.

Before performing the damage detection, some statistical properties related to the vectors of the proportional modal flexibility-based interstory drifts estimated for the baseline state and using the training data set were evaluated. Two statistical checks were made to evaluate if the statistical assumptions, which were discussed in Section 6.3.2.1 referring to the application of the proposed damage index based on Mahalanobis distance, are fulfilled for the damage sensitive features considered in the analysis presented in this section. The threshold value for the index based on Mahalanobis distance is, in fact, calculated using the procedure originally formulated by [Worden et al., 2000; Farrar & Worden, 2013]. This procedure assumes that the feature vectors extracted from the measured data are characterized by a multivariate normal distribution[4], and, under this assumption, the calculation of the threshold value is not executed from these feature vectors but using vectors composed by normally distributed random numbers. The results of the two statistical checks are presented herein referring to the proportional interstory drifts obtained using the first four structural modes (r=4) and the PFM procedure by Bernal [2001] (however, similar results can be obtained using a number of modes r=3 and the procedure by Duan et al. [2005]).

[4] I would like to thank Dr. Suparno Mukhopadhyay for his constructive comments and suggestions on this point.

The first statistical check was made on the single components of the vectors of the proportional modal flexibility-based interstory drifts estimated using the training data set (i.e. on the drifts related to each story of the structure) to check if the distribution of such quantities is normal. The calculations were performed using the Matlab command "normplot" [Matlab], and the results, in terms of normal probability plots, are shown in Fig. 6.3. This command makes a correlation between the quantiles of the sample data considered in the analysis (in such case the proportional MF-based interstory drifts) and the quantiles of a normal distribution. As reported in the figure, the drifts related to each story are sorted in ascending order and plotted on the x-axis, while the y-axis represents the quantiles of the normal distribution that have been converted into the corresponding values of the probability (it is worth noting that the scaling on the y-axis is not linear). The command makes also a reference line that passes through the first and third quartiles of the sample data. This line can be used to evaluate the linearity of the plot (i.e. to evaluate if the distribution of the sample data is normal). As shown in Fig. 6.3, the points in each plot are in general aligned to the line that have been fitted into the data. This means that the considered sample data can be reasonably assumed as normally distributed.

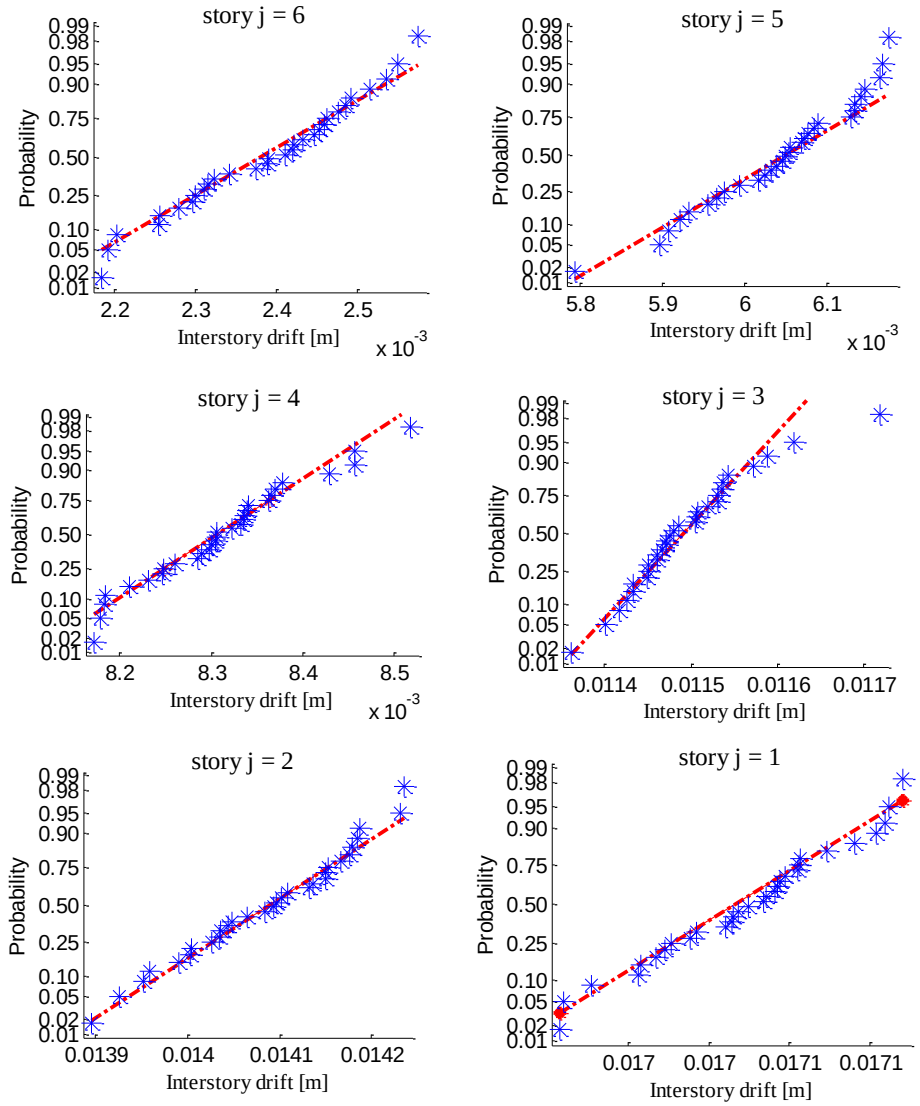

Figure 6.3. Normal probability plots of the proportional MF-based interstory drifts obtained from the training data set (for each story j = 1 … 6)

A second statistical check was performed by evaluating the Mahalanobis-squared distance between each feature vector (i.e. vector of proportional MF-based interstory drifts) calculated from the training data set and the whole set of the feature vectors related to the training data set. As already mentioned in Section 6.3.2.1, under the assumption that the feature vectors used in the calculation of Mahalanobis-squared distance follow a multivariate normal distribution, the values of Mahalanobis-squared distance tend to follow approximately a χ^2 distribution. By ideally inverting this statement, it is clear that if the values of Mahalanobis-squared distance tend to follow

a χ^2 distribution, then it can be concluded that the distribution of the data considered in the calculations is multivariate normal.

The Mahalanobis-squared distance was evaluated for each damage sensitive feature extracted from to the training data set by applying a modified version of the damage index based on Mahalanobis distance presented in Eq. (6.58). This modified version of Eq. (6.58) is as follows

$$MD_{i\ id}^{2\ *} = \left(\boldsymbol{d}_{\boldsymbol{B,i}}^{*} - \overline{\boldsymbol{d}}_{\boldsymbol{B}}^{*}\right)^{\boldsymbol{T}} \boldsymbol{S}_{\boldsymbol{B}}^{*\ -1} \left(\boldsymbol{d}_{\boldsymbol{B,i}}^{*} - \overline{\boldsymbol{d}}_{\boldsymbol{B}}^{*}\right) \tag{6.74}$$

In this modified version of Eq. (6.58), the vector $\boldsymbol{d}_{\boldsymbol{I,w}}^{*}$ (related to the inspection phase) is substituted by the vector $\boldsymbol{d}_{\boldsymbol{B,i}}^{*}$ which is related to the baseline state. Moreover, the Mahalanobis-squared distance was evaluated as the square of the Mahalanobis distance. By evaluating Eq. (6.74) for $i = 1 \ldots p$, p values of Mahalanobis-squared distance were thus determined. Probability density estimation was then carried out for such sample data (i.e. for the values of Mahalanobis-squared distance) using the Matlab command "ksdensity" [Matlab]. The estimated probability density function (PDF) is compared in Fig. 6.4a with the probability density function of a χ^2 distribution with 6 degrees of freedom. The number of the DOFs in the χ^2 distribution was selected as equal to 6 because the dimension of the considered feature vectors (i.e. the vectors of the proportional MF-based interstory drifts) is equal to 6 (in fact, n=6 where n is the number of the DOFs/stories of the considered shear building structure). As evident in Fig. 6.4a, the plots of the probability density function estimated from the values of Mahalanobis-squared distance and the probability density function of the χ^2 distribution are almost overlapped.

This good match between the two distributions was also assessed by making a comparison between the quantiles related to the two probability density functions. In particular, the values of the quantiles related to these two probability density functions (i.e. the PDF estimated from the values of Mahalanobis-squared distance and the PDF of the χ^2 distribution) were evaluated for each order α_q where α_q assumes the following values $\alpha_q = 0.01, 0.02, \ldots 1$ (i.e. for 100 values in the range from 0 to 1). The values of the quantiles related to Mahalanobis-squared distance are plotted on the y-axis in Fig. 6.4b, while the values of the quantiles related to the χ^2 distribution are plotted on the x-axis. As evident in the figure, the resulting points are almost aligned on the

bisection of the plot, which is the red dashed line reported in Fig. 6.4b. This means that a good correlation was found between the quantiles of the distribution estimated from the values of Mahalanobis-squared distance and the quantiles of the χ^2 distribution.

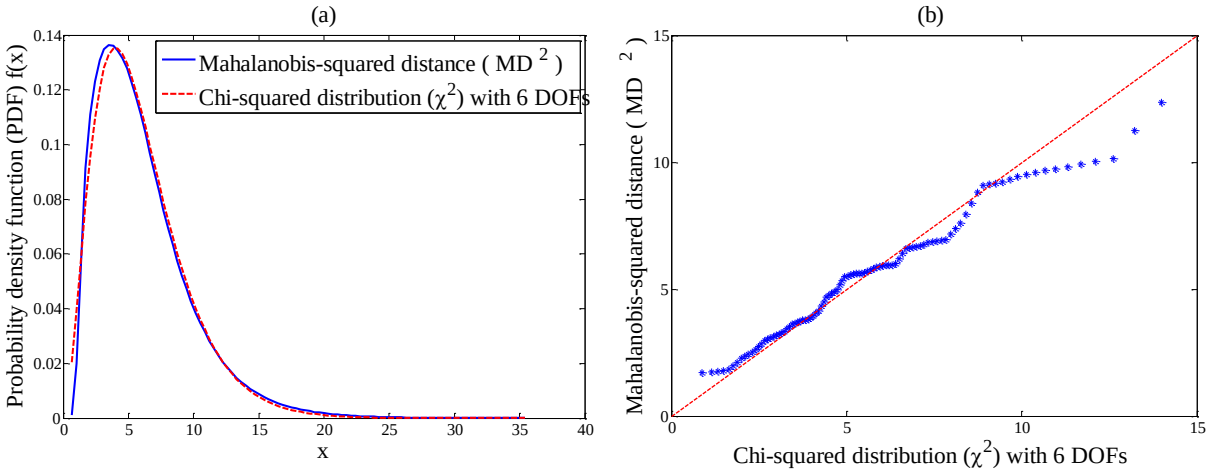

Figure 6.4. Comparison between the distribution of the Mahalanobis-squared distance obtained using the training data set and the χ^2 distribution: a) probability density functions; b) quantile-quantile plot.

In the numerical simulation presented in this section the damage detection was carried out by calculating for each testing configuration reported in Table 6.1 the two damage indices proposed in Section 6.3.2 – i.e. the index based on Mahalanobis distance and the error on the MAC_{id}^{*}. It is worth noting again that in this numerical simulation the masses of the structure are unchanged before and after damage, and thus the first index based on Mahalanobis distance (MD_{id}^{*}) was calculated by assuming in Eq. (6.58) a total-mass-ratio w=1 (as defined in Eq. 6.56). On the contrary, the $eMAC_{id}^{*}$ was calculated without any a-priori information on the structural masses (and on their relationship between the undamaged and the possibly damaged states).

The results of the damage detection carried out using a number of modes included in the calculations equal to *r*=4 and by applying the PFM procedure by Bernal [2001] are reported in Fig. 6.5, where the horizontal red lines represent the threshold values for the two damage indices calculated as outlined in Section 6.3.2. As shown in the figure, both indices are able detect and label the configurations from D1a to D4a as damaged, while the values of both the MD_{id}^{*} and the $eMAC_{id}^{*}$ for the configurations U1a, U2a, U3a are below the thresholds. These configurations are thus classified as undamaged. The same results were obtained when the damage detection was carried out using a number of modes included in the calculations equal to r = 3 and by applying the PFM procedure by Duan et al. [2005], as shown in Fig. 6.6.

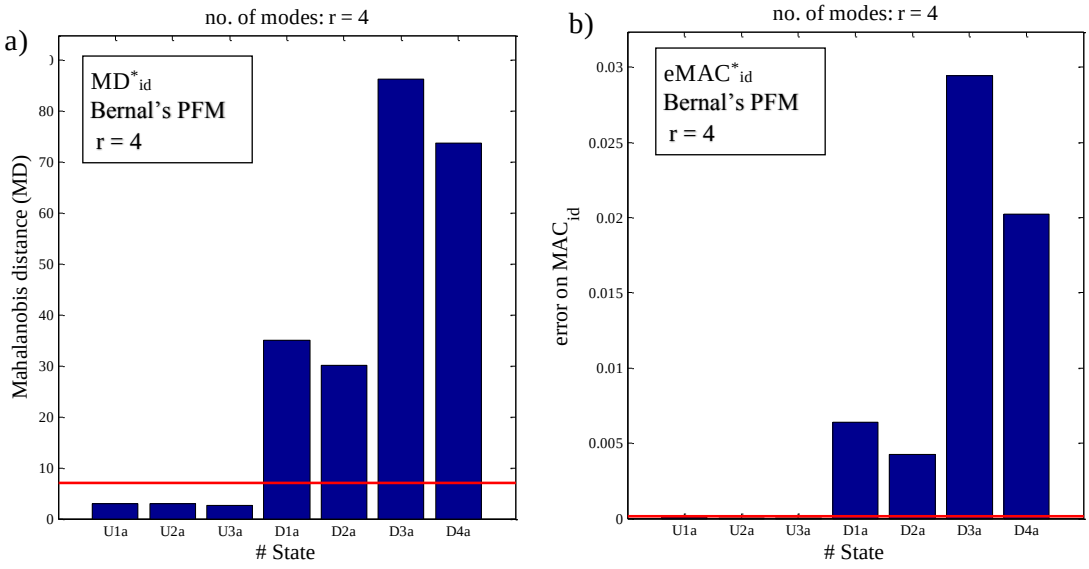

Figure 6.5. Damage detection (Bernal's PFM ; r = 4): a) Mahalanobis distance; b) error on MAC^{*}_{id}

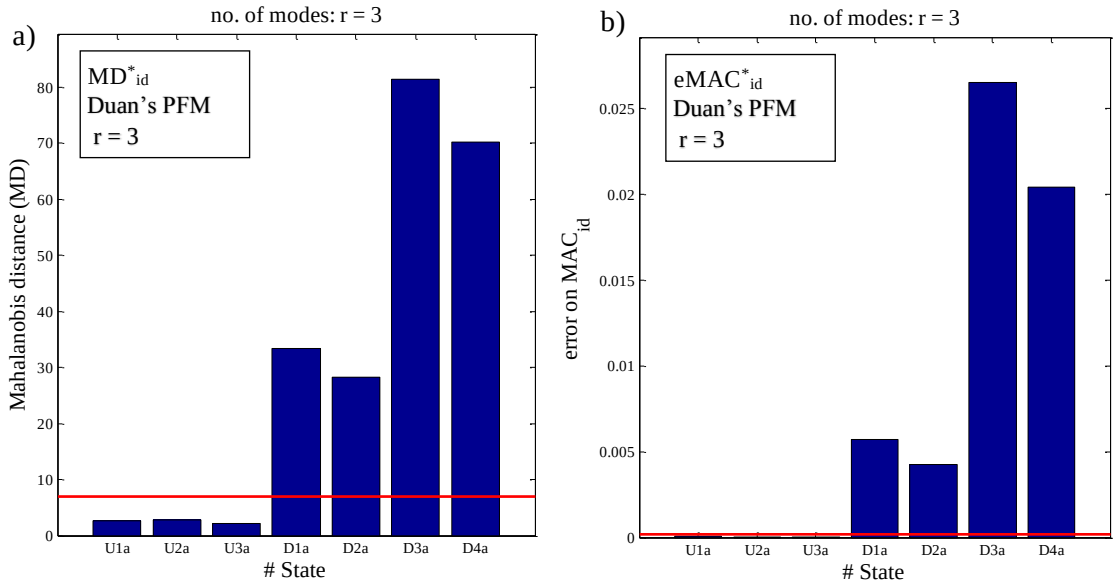

Figure 6.6. Damage detection (Duan's PFM ; r = 3): a) Mahalanobis distance; b) error on MAC^*_{id}

6.4.1.2 Second numerical analysis: damage detection with mass variations

This section deals with the problem of detecting damage in the general case in which the masses of the structure related to the baseline state can be different from the masses of the structure related to the inspection phase. As shown in previous section and according to the proposed approach, the theoretical scaling factor on the vectors of the proportional MF-based interstory drifts (i.e. the damage sensitive features) is equal to the total mass of the structure. In this section the two proposed indices for damage detection – i.e. the index based on Mahalanobis distance and error on the MAC^*_{id} – are thus applied and tested in the general situation in which the damage sensitive features, related to the two states involved in the damage detection and obtained from the procedure described in Section 6.2.2 and Fig. 6.1, are characterized by different scaling factors.

To consider several configurations related to the inspection stage that are characterized by different distributions of the masses and thus characterized by different variations of the masses with respect to the original structure, the numerical analyses presented in this section were performed using a Monte Carlo simulation.

The structure considered in this simulation is the same structure used in previous section – i.e. a 6-story shear building structure.

In the Monte Carlo simulation the modal parameters used to assemble the proportional flexibility matrices were not obtained through a modal identification on the simulated vibration data (as done in previous section). The modal parameters in the Monte Carlo simulation were computed from an eigenvalue analysis on the numerical model of the structure, and random variables were added on the modal parameters to mimic the uncertainties that can derive from the identification process applied on real noisy data. This approach for modeling the uncertainties on the modal parameters has been adopted in other works related to both structural identification [Mukhopadhyay et al., 2012, Aenlle & Brincker, 2013] and damage detection [Fan & Qiao, 2011; Yan & Ren, 2014; Yang & Mosalam, 2016].

The natural circular frequencies $\widehat{\omega}_i$ and mode shapes $\hat{\psi}_{ji}$ affected by uncertainties were obtained as follows

$$\widehat{\omega}_i = \omega_i \, (1 + \gamma_\omega \, \varepsilon_\omega) \tag{6.75}$$

$$\hat{\psi}_{ji} = \psi_{ji} \, (1 + \gamma_\phi \, \varepsilon_\phi) \tag{6.76}$$

where ε_ω, ε_ϕ are random variables extracted from a normal distribution with a zero mean and a standard deviation equal to one, and γ_ω, γ_ϕ are coefficients that are related to the amount of uncertainties that are added on the exact natural circular frequencies (ω_i) and mode shape components (ψ_{ji}), respectively. The values of the coefficients were selected as γ_ω = 0.1% and γ_ϕ = 1%. It is worth noting that in this section the superscript $\widehat{\ }$ is used to indicate quantities that are affected by uncertainties. For example, this symbol is used to distinguish modal parameters affected by uncertainties ($\widehat{\omega}_i$, $\hat{\psi}_{ji}$) from exact modal parameters (ω_i , ψ_{ji}) obtained using an eigenvalue analysis on the undamped model of the structure. By adopting the above-mentioned criteria to model the uncertainties on the modal parameters (i.e. by adding random variables with a normal distribution on the modal parameters to model the uncertainties, instead of performing a modal identification on simulated vibration data) a large number of structural configurations were considered in the Monte Carlo simulation, as shown later in this section, without having high computational efforts in the algorithm that was implemented in Matlab [Matlab].

The calculations that are performed in each run of the Monte Carlo simulation are reported in the flow chart of Fig. 6.7. The procedure described in this flow chart is able to define one damage sensitive feature, i.e. one vector of the proportional modal flexibility-based interstory drifts. The procedure was thus adopted at first to the define the damage sensitive features related to the structure that is assumed as the original structure (to mimic the results that can be obtained from the training data set), and then it was repeated for the possibly damaged structural configurations related to the inspection phase (to mimic the results that can be obtained from the testing data set).

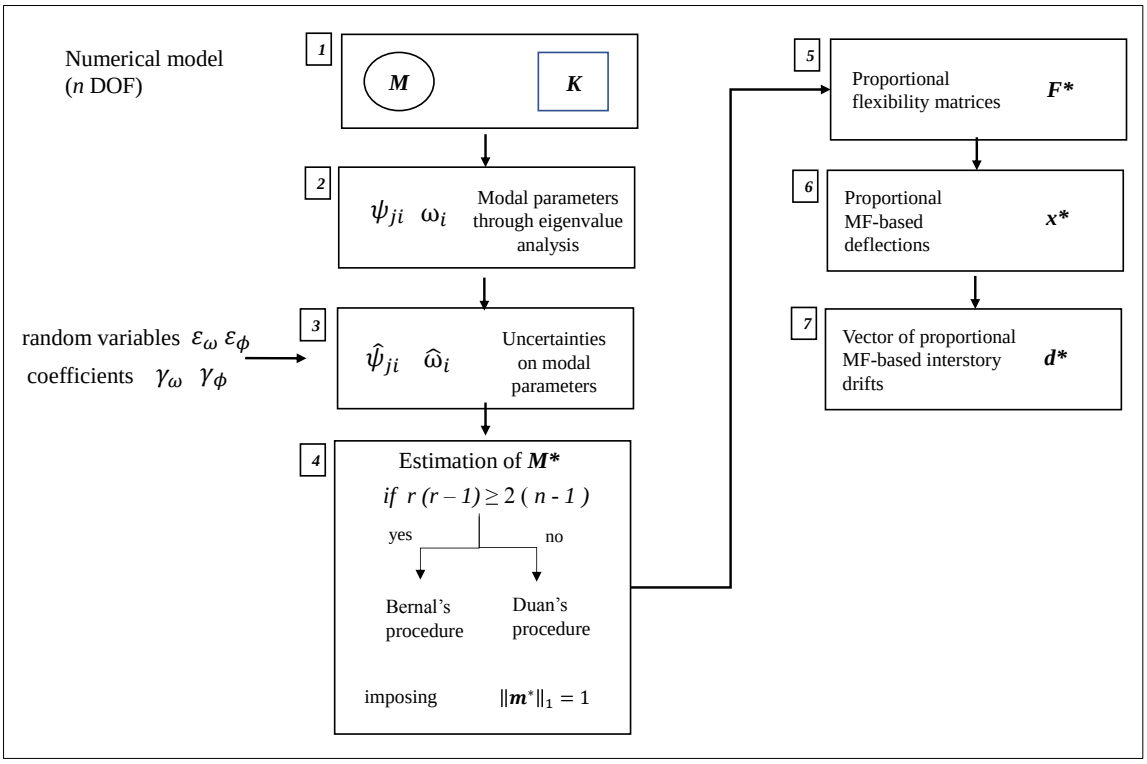

Figure 6.7. Flow chart used in the Monte Carlo simulation to obtain the DSFs

The following steps were performed to define one damage sensitive feature related to the baseline structure, according to the procedure outlined in Fig. 6.7. In the 1st step, an analytical second-order undamped model of the structure was assembled, where the mass matrix is $\mathbf{M_B} = \mathbf{M_{ref}}$ and the stiffness matrix is $\mathbf{K_B} = \mathbf{K_{ref}}$ (as defined in previous section). In the 2nd step, the modal parameters of the structure were computed through an eigenvalue analysis on the undamped model assembled in the

1st step. Then, the random variables ε_ω, ε_ϕ were generated using the MATLAB command "randn" [Matlab], and the modal parameters affected by uncertainties were computed using Eqs. (6.75, 6.76) (3rd step). It is worth noting that these first three steps of the flow chart adopted in the Monte Carlo simulation generate modal parameters of the structure that are affected by uncertainties. These three steps thus mimic the results that can be obtained by applying an output-only modal identification algorithm on real vibration data. The steps from the 4th to the 7th can then be adopted to complete the flow chart presented in Fig. 6.7 and to obtain one damage sensitive feature (i.e. one vector of the proportional MF-based interstory drifts $\boldsymbol{d}^*$). It is worth noting that these steps from the 4th to the 7th of the flow chart used in the Monte Carlo simulation (Fig. 6.7) are equivalent to the steps from the 2nd to the 5th of the procedure shown in Section 6.2.2 and Fig. 6.1 proposed to estimate the proportional modal flexibility-based deflections starting from real vibration data. According to these steps, the proportional mass matrix (PMM) is estimated from arbitrarily-scaled mode shapes using the proposed implementation of one of the two PFM procedures originally defined by Bernal [2001] and Duan et al. [2005]. Then, the proportional flexibility matrix (PFM) is assembled, and subsequently the proportional MF-based deflection and the vectors of proportional MF-based interstory drifts are calculated.

In the Monte Carlo simulation to deal with the uncertainties that affect the modal parameters (and all the quantities that are obtained from the modal parameters) and to obtain a sufficient number of damage sensitive features related to the original or baseline structure, the calculations described in Fig. 6.7 were repeated for a number of times equal to p (where p is assumed equal to 30 in the simulation). It is worth noting that in each of these p runs of the Monte Carlo simulation executed for the baseline structure both the stiffness matrix and the mass matrix assumed at the beginning of the simulation (1st step in Fig. 6.7) are fixed.

The flow chart presented in Fig. 6.7 was also used to consider structural configurations that are testing configurations (i.e. related to the inspection phase of the damage detection process) and used for the generation of the damage sensitive features related to such structural configurations. The structures considered in the inspection phase can be either undamaged or damaged. Moreover, such structures are also characterized by mass variations with respect to the structure that is considered

as the original or baseline structural configuration. Referring to the inspection phase, the number of testing configurations that were considered is equal to 200. This means that the Monte Carlo simulation executed through the steps of the flow chat reported in Fig. 6.7 was repeated for a number of times equal to 200. Each of these runs of the Monte Carlo simulation creates one sample of the damage sensitive features in the inspection phase and each run is related to a different structural configuration.

The 200 runs of the Monte Carlo simulation related to the inspection phase were performed by considering two groups of structures (indicated as group A and group B):

- Group A: the structures that belong to group A are undamaged configurations and for these structures the stiffness matrix is equal to the stiffness matrix of the original or baseline structure $\mathbf{K_I} = \mathbf{K_{ref}}$. This first group of structural configurations (group A) corresponds to the first half of the 200 Monte Carlo simulations (simulations from 1 to 100).

- Group B: the structures that belong to group B are damaged configurations. For these structures and starting from the original baseline model, a 30% reduction of the interstory stiffness was applied at the third story. The stiffness matrix $\mathbf{K_I}$ of these structures was derived by modifying the original matrix $\mathbf{K_{ref}}$ and by imposing the above-mentioned stiffness reduction. This second group of structural configurations (group B) corresponds to the second half of the 200 Monte Carlo simulations (simulations from 101 to 200).

As already mentioned, the structures related to the inspection phase are characterized by mass variations with respect to the structure that is considered as the original or baseline structural configuration. In the Monte Carlo simulation the mass matrices related to the structures considered in the inspection phase are thus characterized by variations with respect to the mass matrix assumed for the baseline state. For each run of the Monte Carlo simulation (i.e. for all the configurations from 0 to 200, and thus both for group A and group B) the mass matrix of the structure is $\boldsymbol{M_I} = \boldsymbol{\beta}\, \boldsymbol{M_{ref}}$ where $\boldsymbol{\beta}_{n \times n}$ is a diagonal matrix, and each element $\beta_{j,j}$ of the main

diagonal of such matrix is a random variable extracted from a normal distribution with a mean equal to one and a standard deviation $\sigma = 0.2$.

The calculations performed for the structural configurations considered in the inspection phase were thus performed using the flow chart of Fig. 6.7, and each run of the Monte Carlo simulation was executed starting from an analytical undamped model of the structure formed by the stiffness matrix $\mathbf{K_I}$ and the mass matrix $\boldsymbol{M_I}$, as described in the previous paragraphs.

As shown in Fig. 6.7, the Monte Carlo simulation can be performed for any subset of modes of the structure, which is in such case a 6-story shear building structure. However, as already done in Section 6.4.1.1, the analyses are presented in this section by considering two specific subsets of structural modes (i.e. two different cases). At first, the calculations were performed for the case $r = 4$ (i.e. the first four modes of the 6-story shear building structure were considered) by applying the PFM technique defined by Bernal [2001]. Then, the calculations were repeated for the case $r = 3$ (i.e. the first three modes of the 6-story shear building structure were considered) by applying the PFM technique defined by Duan et al. [2005]. As already mentioned in Section 6.4.1.1, for the selected structure the case $r = 4$ represents the minimum number of modes that can be considered to apply the PFM procedure defined by Bernal [2001].

In the calculations described in this section and performed using a simulation approach the analytical models of the considered structural configurations are, of course, known. For this reason, the Monte Carlo simulation was used not only to obtain the final results of the damage detection process, but also to check the intermediate steps of the damage detection process based on modal flexibility-based deflections of shear buildings. In particular, the main goal was to evaluate if the proportional quantities that are estimated according to the procedures described in the flow chart of Fig. 6.7 (for example, mass proportional vectors and vectors of proportional MF-based deflections) are accurate and effectively proportional to the corresponding true and scaled quantities (which are known in the simulation approach). The mode shape components, which are used to extract the distribution of the structural masses according to the PFM techniques, are affected in fact by

uncertainties, and thus the proportional mass matrices obtained from the data are affected by uncertainties as well. These uncertainties then propagate to proportional flexibility matrices and its derivatives (i.e. structural deflections and vectors of MF-based interstory drifts).

To check if the mass proportional vectors and the vectors of the proportional MF-based interstory drifts estimated in the calculations are effectively proportional with respect to the corresponding true vectors, one geometrical property of collinear vectors is considered. This geometric property is as follows: the cosine of the angle between two collinear vectors (i.e. two vectors that differ by a scalar multiplier) is equal to one. This property can be derived from the definition of the scalar product between two generic vectors $\boldsymbol{a}$ and $\boldsymbol{b}$

$$\boldsymbol{a} \circ \boldsymbol{b} = \|\boldsymbol{a}\|_2 \, \|\boldsymbol{b}\|_2 \, cos\, \theta \tag{6.77}$$

where the symbol $\circ$ denotes the operator of the scalar product and $\| \cdot \|_2$ is the 2-norm of a generic vector. By reformulating Eq. (6.77) and by expressing the scalar product using a vector notation, the cosine of the angle between the two vectors can be expressed as

$$cos\, \theta = \frac{\boldsymbol{a}^T \boldsymbol{b}}{\|\boldsymbol{a}\|_2 \, \|\boldsymbol{b}\|_2} \tag{6.78}$$

It is clear that if the two vectors are collinear (i.e. $\boldsymbol{a} = c\, \boldsymbol{b}$, where c is an arbitrary constant), then the cosine of the angle between the two vectors is equal to one.

In the analyses, the cosine of the angle between the vectors related to the mass distribution was evaluated as follows

$$\cos \hat{\theta}_m = \frac{\boldsymbol{m}^T \hat{\boldsymbol{m}}^*}{\|\boldsymbol{m}\|_2 \, \|\hat{\boldsymbol{m}}^*\|_2} \tag{6.79}$$

where $\hat{\boldsymbol{m}}^*$ is the mass proportional vector estimated using the proposed implementation of the two PFM procedures originally defined by Bernal [2001] and Duan et al. [2005], and $\boldsymbol{m}$ is the true mass vector (i.e. the diagonal of the mass matrix, known in the simulation). If the two vectors are proportional, the cosine of the angle should be approximately equal to one.

The same calculation presented in Eq. (6.79) was performed also for the vectors of the modal flexibility-based interstory drifts

$$\cos \hat{\theta}_d = \frac{\boldsymbol{d}^T \, \widehat{\boldsymbol{d}}^*}{\|\boldsymbol{d}\|_2 \, \|\widehat{\boldsymbol{d}}^*\|_2} \tag{6.80}$$

where $\widehat{\boldsymbol{d}}^*$ is the vector of the proportional MF-based interstory drifts affected by uncertainties and estimated using the steps reported in Fig. 6.7, and $\boldsymbol{d}$ is the vector of the true interstory drifts calculated by assembling modal flexibility matrices using exact modal parameters and an exact mass matrix (which are quantities that are all known in the simulation). Of course, the two vectors of the interstory drifts ($\widehat{\boldsymbol{d}}^*$ and $\boldsymbol{d}$) present in Eq. (6.80) were determined using the same number of modes included in the calculation of the modal flexibility matrices. In this way, eventual discrepancies between the two vectors (which may lead to values of the cosine of the angle that are lower than one) are only due to uncertainties that affect the vector $\widehat{\boldsymbol{d}}^*$. These eventual discrepancies are, on the contrary, not due to modal truncation errors that would have been introduced by evaluating $\widehat{\boldsymbol{d}}^*$ and $\boldsymbol{d}$ using a different number of modes to assemble the modal flexibility matrices.

The results of the above-mentioned calculations are shown in Fig. 6.8, where the check of the collinearity between proportional and true vectors is shown, for example, by considering the structures that belong to group A (i.e. the testing configurations that are undamaged and related to the simulations from 0 to 100, as defined in this section). The cosine of the angle between the mass vectors and the vectors of the MF-based interstory drifts were calculated using Eqs. (6.79, 6.80), respectively. Fig. 6.8a shows the results obtained for the case r = 4 by applying the PFM technique defined by Bernal [2001], while Fig. 6.8b shows the results obtained for the case r = 3 by applying the PFM technique defined by Duan et al. [2005].

Referring to the case r = 4 (Bernal's PFM) and as shown in the Fig. 6.8a, values of the cosine of the angle that are very close to one were obtained both for the mass vectors and for the vectors of the MF-based interstory drifts. On the contrary, referring to the case r = 3 (Duan's PFM) and as shown in Fig. 6.8b, the values of the cosine of the angle between the mass vectors are lower than the corresponding values obtained for the case r = 4 (Bernal's PFM). This means that the mass proportional vectors estimated using the procedure defined by Duan et al. [2005] for the case r = 3 are characterized by uncertainties that are higher than the uncertainties that affect the

mass proportional vectors estimated using the procedure defined by Bernal [2001] for the case $r = 4$. This result is expected and can be explained by the two following motivations: first of all, it is trivial that the calculations related to the case $r = 3$ are performed using a number of modes that is lower than the number of modes considered in the case $r = 4$; secondly, more uncertainties are in general expected in the mass proportional vectors obtained using the procedure by Duan et al. [2005] because, as already discussed, pseudo inverse operations are performed on the truncated mode shape matrices reported in Eqs. (6.15, 6.16) to have an estimate of the mass matrix of the dummy structure. Of course, when applying pseudo inverse operations in the procedure by Duan et al. [2005] an approximated solution is obtained. These operations are not present, on the contrary, in the procedure by Bernal. In any case, the uncertainties that were obtained on the mass proportional vectors estimated using the procedure by Duan et al. [2005] seem not to have a great impact on the vectors of the proportional MF-based interstory drifts. As shown in Fig. 6.8b, in fact, the values of the cosine of the angle obtained for the vectors of the MF-based interstory drifts are very close to one. The results obtained for the interstory drifts vectors in the case $r = 3$ by applying the PFM procedure by Duan et al. [2005] are thus very similar to the results obtained for the same quantities in the case $r = 4$ by applying the PFM procedure by Bernal [2001].

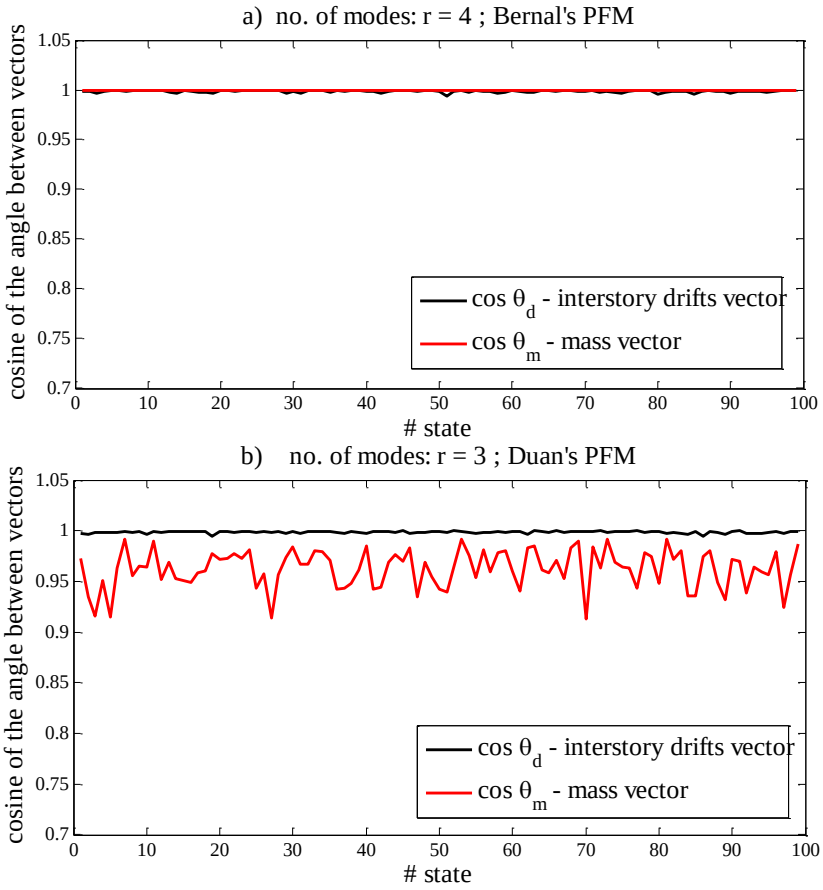

Figure 6.8. Check of the collinearity between true and proportional vectors. Calculation of the cosine of the angle between: mass vectors using Eq. (36), interstory drifts vectors using Eq. (37). Results for group A. (a) *r* = 4, Bernal's PFM; (b) *r* = 3, Duan's PFM.

According to the approach proposed in Section 6.2.2 for the estimation of the vectors of the proportional MF-based interstory drifts of shear buildings, the scaling factor on such quantities is theoretically equal to the total mass of the structure. This result is obtained by normalizing the mass proportional vector estimated using the PFM techniques in a way that its 1-norm is equal to one. Of course, when dealing with both modal parameters and mass proportional vectors that are affected by uncertainties, inevitable discrepancies are present between the theoretical scaling factor and the scaling factor that is effectively related to the vectors of the proportional MF-based interstory drifts of shear buildings. To address this problem, a second analysis was executed in the Monte Carlo simulation to check the accuracy related to the damage sensitive features (before performing the damage detection process).

In the analyses the theoretical scaling factor, known in the simulation, was evaluated using Eq. (6.38), and it is indicated as α_{true} (this factor is the total mass of the structure). The scaling factor α_{true} was compared with respect to the scaling factor that is effectively related to the vectors of the proportional MF-based interstory drifts $\widehat{\boldsymbol{d}}^*$ (which are affected by uncertainties). This last scaling factor is indicated as $\hat{\alpha}_{effective}$, and it is calculated as follows

$$\hat{\alpha}_{effective} = \frac{\|\widehat{\boldsymbol{d}}^*\|_1}{\|\boldsymbol{d}\|_1} \tag{6.81}$$

where $\boldsymbol{d}$ is the vector of the true interstory drifts, known in the simulation, and $\widehat{\boldsymbol{d}}^*$ is the vector of the proportional MF-based interstory drifts affected by uncertainties and estimated using the steps of the flow chart reported in Fig. 6.7. As already done in Eq. (6.80), the two interstory drift vectors were calculated using the same number of modes (i.e. r = 4 or r = 3 in this simulation).

As already done in Fig. 6.8 (where the degree of collinearity between proportional and true vectors was checked), the results of the comparison between the true and the effective scaling factors are presented by considering the structures that belong to group A (i.e. the testing configurations that are undamaged and related to the simulations from 0 to 100). The results of this comparison are presented in Fig. 6.9, where the parameters α_{true} and $\hat{\alpha}_{effective}$ are reported on the x-axis and the y-axis, respectively. In particular, Fig. 6.9a shows the results obtained for the case r = 4 by applying the PFM technique defined by Bernal [2001], while Fig. 6.9b shows the results obtained for the case r = 3 by applying the PFM technique defined by Duan et al. [2005]. In general, for both cases and as shown in the figure, the points of this correlation analysis are positioned on the bisection of the plot, and this means that the effective scaling factors on the proportional MF-based interstory drifts estimated using Eq. (6.81) are close to the true scaling factors (i.e. the values of the total mass of the structure). The only difference between Figs. 6.9a and 6.9b is that the points obtained for the case r = 4 using the procedure by Bernal [2001] (Fig. 6.9a) are in general slightly closer to the bisection of the plot than the points obtained in the case r = 3 using the procedure by Duan et al. [2005] (Fig. 6.9b).

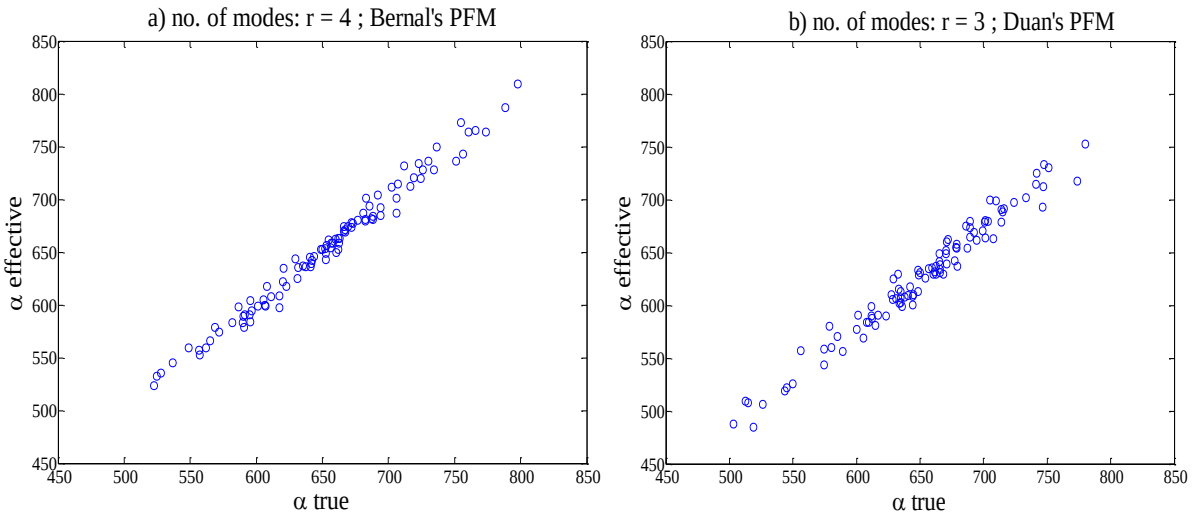

Figure 6.9. Correlation analysis between the true and the effective scaling factors. Results for group A. (a) *r* = 4, Bernal's PFM; (b) *r* = 3, Duan's PFM.

The results of the damage detection analyses carried out on the 6-story shear building structure using the Monte Carlo simulation are presented herein. The damage indices proposed in Section 6.3.2 (i.e. the index based on Mahalanobis distance and the error on the MAC_{id}) were calculated to compare the damage sensitive features obtained for the baseline structure with the damage sensitive features obtained for each of the 200 structural configurations that are considered in the inspection phase.

As already mentioned, the structures considered in this simulation as possibly damaged structures (inspection phase) have a distribution of the masses that is different with respect to the mass distribution of the baseline structure. This means that, according to the proposed approach and using the procedure outlined in Section 6.2.2, the scaling factors on the DSFs (i.e. the vectors of proportional MF-based interstory drifts) related to the possibly damaged structures are different from the scaling factors related to the same quantities in the baseline condition. However, as shown in Section 6.3.1, the scaling factors on the damage sensitive features related to the undamaged and the possibly damaged states can be made comparable by performing an additional scaling operation on one DSF (for example, the DSF related to the inspection phase). As already mentioned in Section 6.3.1, this operation can be done if the ratio between the total mass of the structure in the two states involved in

the damage detection process is known a-priori (i.e. if the parameter *w* defined in Eq. 6.56 is known).

To demonstrate the validity of the proposed approach and the effectiveness of the two proposed damage indices, in the simulation presented herein the damage detection process was carried out by considering two different situations. The first situation is an attempt to make the scaling factors on the proportional MF-based interstory drifts related to the undamaged and the possibly damaged states comparable. This attempt was made by considering the total-mass-ratio *w* as known, and this situation is indicated as "DSFs scaled by total-mass-ratio *w*". In the second case, the damage detection was carried out using DSFs that are characterized by their original scaling factors (and thus different scaling factors were obtained between the undamaged and the possibly damage states). This second situation is indicated as "DSFs with original scaling", and the calculations were performed without any a-priori information on the structural masses.

The results of the damage detection carried out on the 6-story shear building structure by considering a number of modes equal to $r = 4$ and by applying the PFM procedure proposed by Bernal [2001] are reported in Fig. 6.10. In particular, the results obtained in the first situation (i.e. "DSFs scaled by total-mass-ratio *w*") are presented on the left-hand side of the figure (Fig. 6.10a, 6.10c, 6.10e), while the results related to the second situation (i.e. "DSFs with original scaling") are reported on the right-hand side of the figure (Fig. 6.10b, 6.10d, 6.10f). In Fig. 6.10a, 6.10b the scaling factors related to the DSFs used to calculate the damage indices for the 200 structural configurations considered in the inspection phase are reported. Such scaling factors are known in the simulation approach. As shown in Fig. 6.10a, the scaling factors have been made comparable using the additional scaling operation based on the total-mass-ratio *w*. Of course, as also evident in Fig. 6.10a the scaling factors in the inspection phase are not exactly equal to the scaling factor related to the baseline state (which is a constant value). This effect is due to the fact that the effective scaling factors on the vectors of the proportional MF-based interstory drifts are reported in the figure (not the theoretical scaling factors), and the effective scaling factors are affected by uncertainties, as well as the damage sensitive features. On the contrary, as

shown in Fig. 6.10b, in the second situation the scaling factors on the DSFs are not comparable.

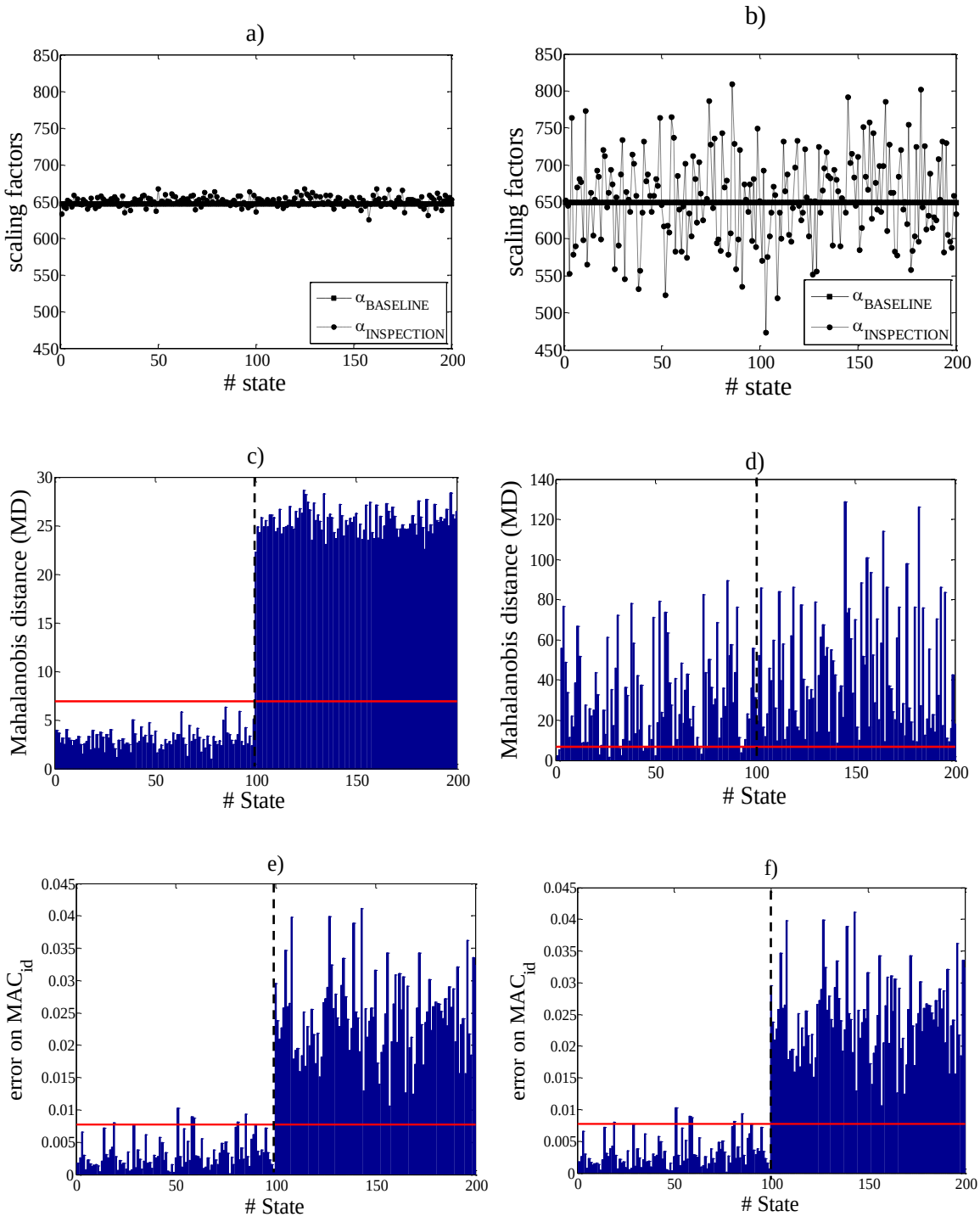

Figure 6.10. Damage detection for the case r = 4 using Bernal's PFM. Analyzed situations: a),c),e) DSFs scaled by the total-mass-ratio w; b),d),f) DSFs with original scaling. Parameters: a,b) scaling factors; c,d) Mahalanobis distance; e,f) error on MAC_{id}

The results obtained using the damage index based on Mahalanobis distance are presented in Fig. 6.10c, 6.10d. To obtain the results presented in Fig. 6.10c the proposed formulation of the index MD_{id}^{*} was applied (i.e. Eq. 6.58) and the total-mass-ratio *w* is assumed to be known (first situation "DSFs scaled by ratio *w*"). As shown in Fig. 6.10c, the damage index based on Mahalanobis distance is able to identify and separate the group of structures that are damaged (group B, configurations related to the simulations from #101 to #200) from the group that is undamaged (group A, configurations related to the simulations from #0 to #100). To obtain the results presented in Fig. 6.10d the Mahalanobis distance was calculated using Eq. (6.58) but forcing the ratio *w* to be equal to one (even if this parameter is in theory different from one). In this way, the additional scaling operation is not applied on the DSFs (second situation "DSFs with original scaling"), and the DSFs related to the undamaged and the possibly damaged states are not adequately scaled (as shown in Fig. 6.10b). In this last case the index based on Mahalanobis distance is not able to perform correctly the damage detection process (as shown in the Fig. 6.10d).

The results obtained using the error in the Modal Assurance Criterion evaluated on the vectors of the proportional MF-based interstory drifts ($eMAC_{id}^{*}$) are presented in Fig. 6.10e, 6.10f. In particular, the results presented in Fig. 6.10f were obtained by applying the proposed formulation of $eMAC_{id}^{*}$ (i.e. Eq. 6.71). In this proposed formulation it is not necessary to perform the additional scaling operation on the DSFs using the ratio *w* (second situation "DSFs with original scaling"). On the contrary, the results presented in Fig. 6.10e are related to the first situation ("DSFs scaled by ratio *w*") and were obtained by considering a modified version of the proposed damage index $eMAC_{id}^{*}$ (i.e. Eq. 6.71). In this modified version of the index the scaled version of the DSF in the inspection phase $\boldsymbol{d}_{\boldsymbol{I},\boldsymbol{w}}^{*}$ (defined in Section 6.3.1) was considered instead of the vector $\boldsymbol{d}_{\boldsymbol{I}}^{*}$. As shown in Fig. 6.10e, 6.10f, the $eMAC_{id}^{*}$ is able to separate the group of undamaged structures (group A, simulations from #0 to #100) from the group of damaged structures (group B, simulations from #101 to #200) both when the scaling factors are comparable (Fig. 6.10e) and when they are not comparable (Fig. 6.10f). Moreover, the same values of $eMAC_{id}^{*}$ were obtained in the two situations, and this confirms that this parameter, which is based on the evaluation

of the degree of correlation between the DSFs, is not sensitive to the scaling factors on the vectors of the proportional MF-based interstory drifts.

The results of the damage detection carried out for the different configurations of the shear building structure by considering a number of modes equal to $r = 3$ and by applying the PFM procedure proposed by Duan et al. [2005] are reported in Fig. 6.11. This figure has the same format and presents the same type of results that are shown in Fig. 6.10 – i.e. the results on the left-hand side are related to the first situation "DSFs scaled by ratio w" (Fig. 6.11a, 6.11c, 6.11e), and the results on the right-hand side are related to the second situation "DSFs with original scaling" (Fig. 6.11b, 6.11d, 6.11f). In general, the results obtained for the case $r = 3$ by applying the PFM technique by Duan et al. [2005] (Fig. 6.11) are similar to the results obtained for the case $r = 4$ by applying the PFM technique by Bernal [2001] (Fig. 6.10). There are, however, some differences between the results obtained in the two cases that must be discussed. First of all, if one compares Fig. 6.11a and Fig. 6.10a it is clear that, referring to the first situation ("DSFs scaled by ratio w"), the discrepancies between the scaling factors in the inspection phase and the scaling factors in the baseline state obtained for $r = 3$ using the Duan's PFM are higher than the discrepancies between the same quantities obtained for $r = 4$ using the Bernal's PFM. A general observation on the above-mentioned result is the following. As already shown by the previous analyses presented in this section (Figs. 6.8, 6.9), the uncertainties on the proportional mass vectors and the effective scaling factors obtained for the case $r = 3$ using the Duan's PFM are higher than the ones obtained on the same quantities for the case $r = 4$ using the Bernal's PFM. In light of this consideration, it is clear that better results are obtained in the latter case (with respect to the former case) when one tries to retrieve and guarantee the compatibility between the scaling factors, related to the two states involved in the damage detection, using the additional scaling operation based on the total-mass-ratio w.

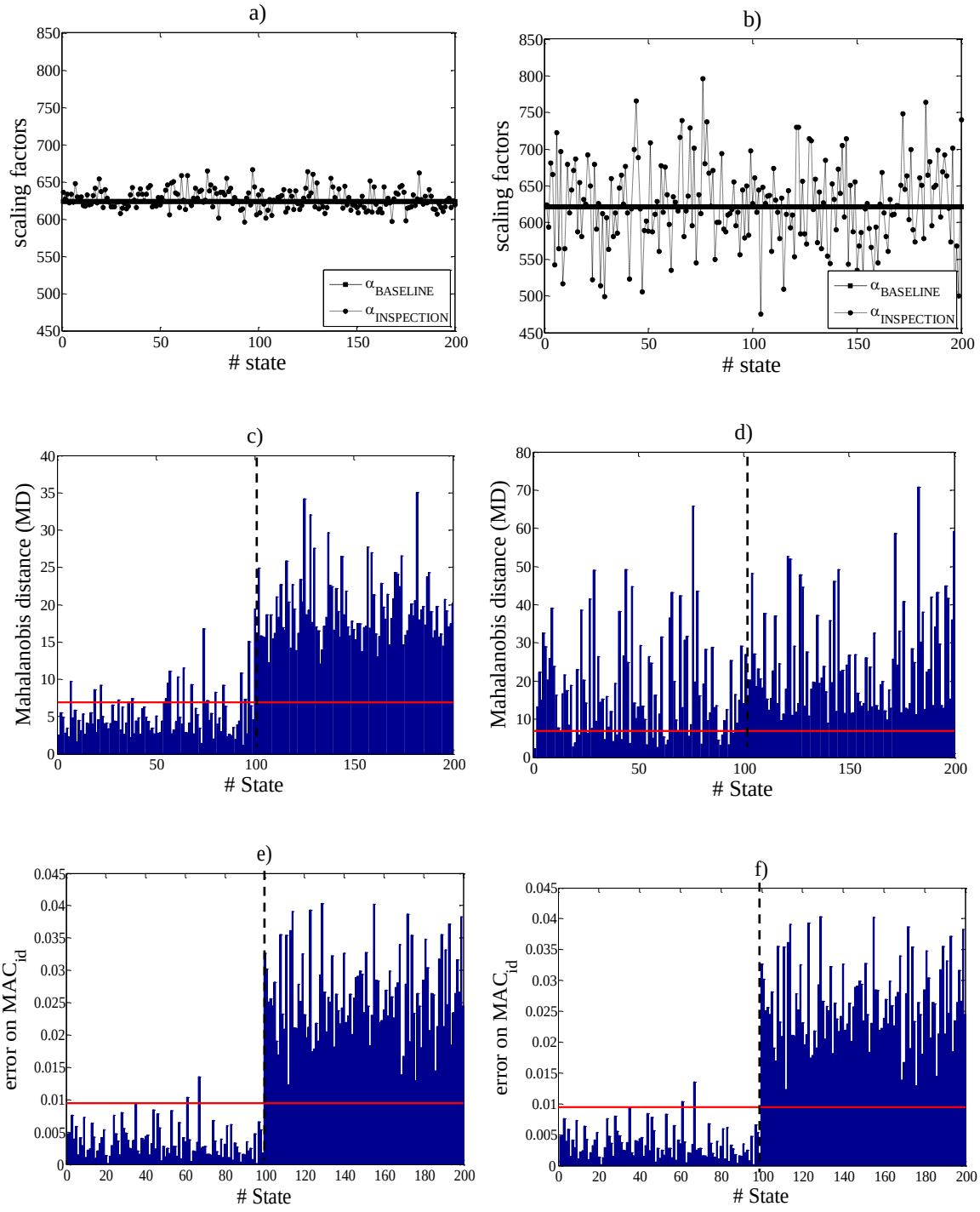

Figure 6.11. Damage detection for the case r = 3 using Duan's PFM. Analyzed situations: a),c),e) DSFs scaled by the total-mass-ratio w; b),d),f) DSFs with original scaling. Parameters: a,b) scaling factors; c,d) Mahalanobis distance; e,f) error on MAC_{id}.

Referring to the case $r = 3$ (Duan's PFM), the discrepancies that were obtained between the scaling factors in the undamaged and in the possibly damage states (even if the scaling operation based on the ratio w is applied - Fig. 6.11a) affect the results of the damage index based on Mahalanobis distance. For the present simulation and as shown in Fig. 6.11c, this index evaluated in the situation "DSFs scaled by ratio w" is in general able to separate the first group of undamaged structures (group A) from the second group of damaged structures (group B). However, if one compares Fig. 6.11c ($r = 3$) and Fig. 6.10c ($r = 4$), it is clear that the number of false positives obtained in the results of the index based on Mahalanobis distance calculated using the Duan's PFM ($r = 3$) is higher than the number of false positives obtained in the results of the same index evaluated using the PFM procedure by Bernal ($r = 4$).

The other results presented in Fig. 6.11 (i.e. Fig. 6.11d, 6.11e, 6.11f) and related to the case $r = 3$ (Duan's PFM) confirm the findings that have been already discussed for the corresponding plots presented in Fig. 6.10 and related to the case $r = 4$ (Bernal's PFM).

6.4.2 Experimental verification

In this section the experimental verification of the modal flexibility-based approach proposed in this chapter for detecting damage in building structures using minimal or no a-priori information on the structural masses is presented. Vibration tests were performed on a steel frame structure to verify the proposed damage detection approach. This first part of the chapter describes the structure and the experimental setup that were considered in the tests. Then, in next sections the tested structural configurations and the experimental results of two different damage detection tests will be presented. The first test was planned to perform the damage detection in the case in which the structural masses are unchanged before and after damage; in the second test, structural configurations that are characterized both by stiffness reductions and mass modifications with respect to the baseline structure were considered.

The structure that was considered in the vibration tests is located at the Carleton Laboratory of Columbia University, New York, USA[5], and it is a one sixth scale four-story one-bay by one-bay frame structure (Figs. 6.12, 6.13). This frame structure is characterized by the following dimensions: the inter-story height is equal to 533 mm, and the dimensions of the floor plates are 610 × 457 × 12.7 mm. Four columns are located at each story of the structure, and such columns have rectangular cross sections with dimensions 50.8 × 9.5 mm. As evident in Figs. 6.12, 6.13, the structure is diagonally braced in the north-south direction, while it is unbraced in the west-east direction. The diagonal braces have rectangular cross sections with dimensions 50.8 × 6.4 mm. All the members of the structure are A36 steel, and they are connected using bolted connections.

Two prevalent directions can be easily identified to characterize the mechanical and the dynamic behavior of the structure: the north-south direction (i.e. x direction) is the strong direction of the structure, while the west-east direction (i.e. z direction) is the weak direction of the structure. This characteristic of the structure is evident for two main reasons. On one side, the diagonal braces are present only in the bays of the structure that are aligned to the north-south direction (i.e. the strong direction). On the other side, the rectangular cross-sections of the columns (with dimensions 50.8 × 9.5 mm) are oriented in a way that their longest side is aligned to the north-south direction of the structure (i.e. the strong direction).

[5] The vibration tests were performed during a study and research period that the writer spent at Columbia University, New York, USA under the supervision of Prof. Raimondo Betti. The vibration tests were performed by the writer with the assistance of Prof. Betti. The writer would like to thank Prof. Betti for his guidance during the study period, for his suggestions, and for his great support during the vibration tests. The writer would also like to thank all the other people that provided their assistance during the vibration tests performed at the Carleton Laboratory of Columbia University (NY), especially Adrian Brügger and Matthew Sloane.

Figure 6.12. Four story steel frame structure used for the experimental verification (Carleton Laboratory, Columbia University).

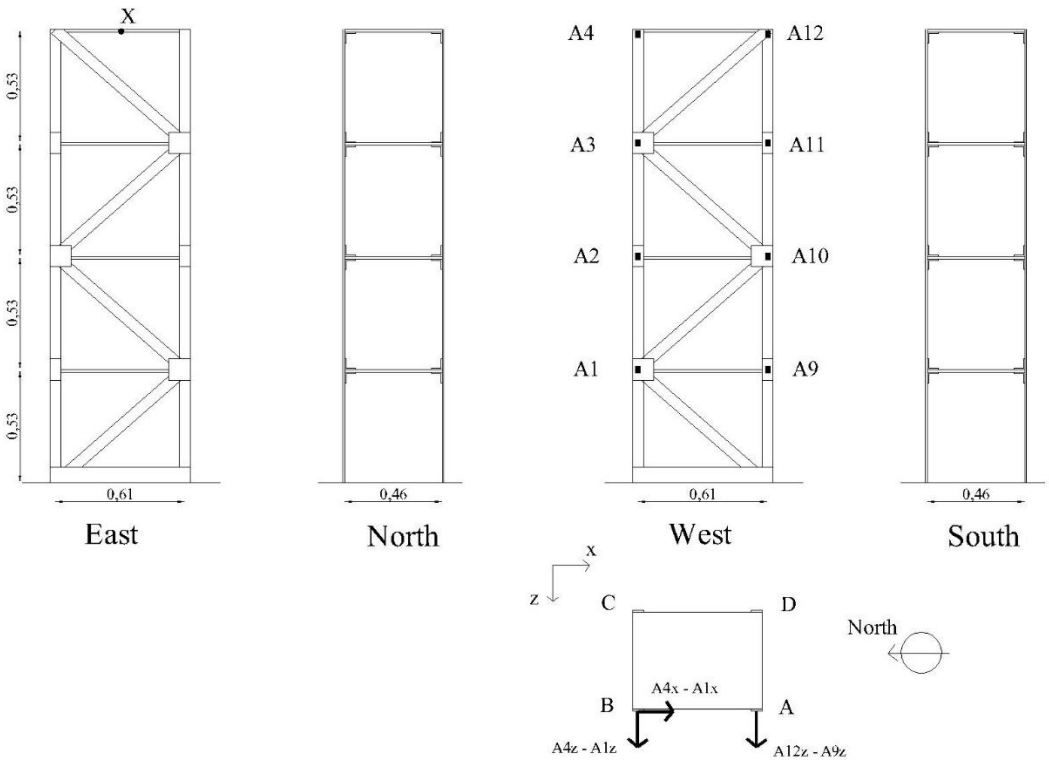

Figure 6.13. Geometry of the steel frame structure (dimensions in m) and location of the accelerometric sensors.

In the planning phase of the vibration tests different ways for exciting the structure were considered. After examining the different options that were available in the laboratory, it was decided to excite the structure using an impact hammer. Performing hammer tests is a rapid way of testing structures, and using such type of excitation several vibration tests were performed on the structure in a relatively limited amount of time. Before presenting the experimental test setup, one important aspect must be clarified. When performing impact hammer tests both the input forces and the output vibration responses are in general available. On the contrary, the approach presented in this chapter of the thesis was developed for detecting damage in structures starting from output-only vibration measurements. In this last situation, in fact, it is not possible to obtain information on the modal masses of the structure, and only arbitrarily-scaled mode shapes can be identified. For this reason, the following approach was adopted in the experimental verification of the proposed approach. The structure was excited by the impact of the hammer, and both the input force, produced by the hammer, and the structural responses, in terms of floor accelerations, were measured. Then, in the damage detection process only the output vibration responses of the structure were considered (i.e. the input was not included in the training and testing data sets used for the damage detection). In this way, it was not possible to have from the vibration data information on the modal masses of the structure, and the Proportional Flexibility Matrix techniques [Bernal, 2001; Duan et al. 2005] were applied on arbitrarily-scaled mode shapes.

The hammer that was used in the tests is a sledgehammer model PCB 086B50 [PCB Piezotronics], which is able to measure the input force that is applied in the impact. This hammer has a measurement range of ± 22240 N and a sensitivity equal to 0.23 mV/N. Moreover, this hammer can be used by considering two different types of the tips positioned in the head of the instrument (a soft tip or a hard tip). After having evaluated how the hammer with one or the other tip excites the structure, all the tests were performed using a soft tip.

The vibration responses of the structure due to the impact of the hammer were measured using eight accelerometers. In particular, two different types of accelerometers were used in the tests: four accelerometers are Crossbow CXL04LP3 [Crossbow Technology] and they are triaxial accelerometers with a measurement

range of ± 4g and a sensitivity of 500 mV/g (Fig. 6.14a); four accelerometers are PCB 353B34 [PCB Piezotronics] and they are uniaxial accelerometers with a measurement range of ± 50g and a sensitivity equal to 100 mV/g (Fig. 6.14b). The four accelerometers that belong to the first group (i.e. triaxial accelerometers) were positioned at the intersection between the columns located in the north-west corner of the structure (position B in Fig. 6.13) and each floor plate. These accelerometers are indicated as sensors A1-A2-A3-A4. The four accelerometers that belong to the second group of accelerometers (i.e. uniaxial accelerometers) are indicated as sensors A9-A10-A11-A12 and they were positioned on the west-south columns (position A in Fig. 6.13).

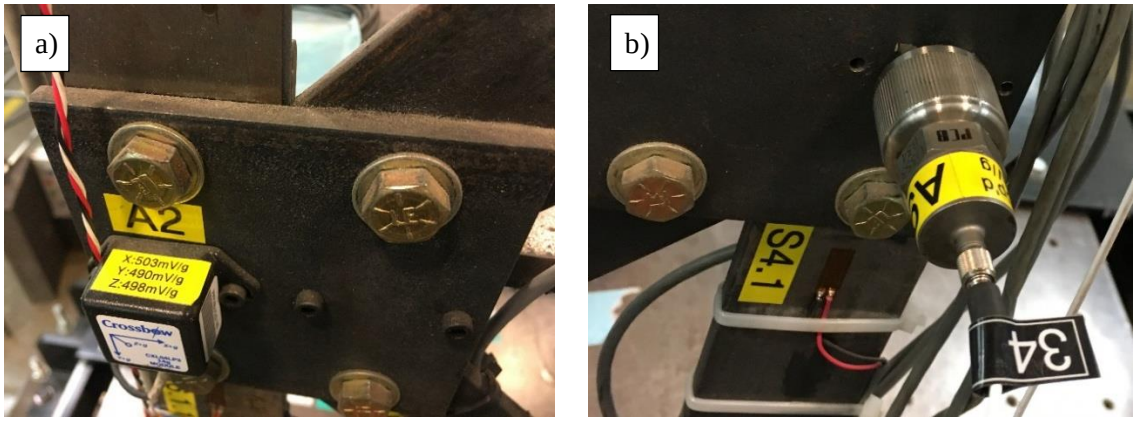

Figure 6.14. Accelerometers used in the vibration test (Carleton Laboratory, Columbia University): a) triaxial accelerometer positioned on north-west columns; b) uniaxial accelerometer positioned on west-south columns.

All the sensors were connected to a data acquisition system that was controlled by an application that was developed in the computer software LabVIEW 2014 [LabVIEW]. Thirteen channels were used in the data acquisition system: one channel was used to measure the input signal (i.e. the input force) produced by the hammer, and twelve channels were used to measure the signals from the accelerometers. The channels that were connected to the accelerometers of a generic floor of the structure are schematically represented in the plan view of Fig. 6.13. In particular, three channels were used to measure the accelerations of each floor of the structure: one channel was used to measure the accelerations in the west-east direction (i.e. z

direction) near the column located at the west-south corner of the structure (position A); two channels were used to measure the accelerations near the west-north column (position B) in the west-east and north-south directions, respectively.

The structure was tested in different configurations, and examples of these configurations are reported in Fig. 6.15. The types of structural modifications that were applied on the frame during the vibration tests are described herein, while a detailed description of all the configurations that were tested in the two series of tests that were performed for damaged detection purposes will be presented in next section.

Several vibration tests were performed on the structure in the original configuration (Fig. 6.15a). As shown later in this section, this configuration will be considered as the undamaged structure. Other tests were performed on structural configurations characterized by reductions (with respect to the original structure) in the interstory stiffness, and these configurations will be considered as damaged configurations (Fig. 6.15b). To obtain such configurations, one or more columns of the frame structure were replaced with other columns with reduced cross-sections. The dimensions of the cross-sections of the columns introduced in these damaged configurations are 50.8 × 7 mm, while, as already mentioned, the dimensions of the cross sections of the columns in the original structure are 50.8 × 9.5 mm. Replacing one column with another one with a reduced cross-section results in imposing approximately a 15% reduction in the inter-story stiffness of one story of the structure. If, for example, as shown in Fig. 6.15b, two columns are replaced with other columns with reduced cross-sections, then approximately a 30% reduction is imposed on the inter-story stiffness. Of course, when one column of the structure is replaced with another column, the bolts of the connections located near that column have to be opened and then positioned again on the structure with the replaced column. After each structural modification that implied the substitution of the columns, the bolts were closed using an adjustable-click-type torque wrench. This instrument was used to close the bolts with a tightening torque of 81.35 N m (equivalent to 60 ft lb), and the tightening torque was maintained fixed during all the tests. Using this procedure all the tested configurations have bolts that theoretically work with the same tension.

The structure was also tested with added masses (Fig 6.15c). The increase in the floor masses was created by positioning on the structure some metallic bricks which were connected to the plates of the frame through metallic clamps. The masses that were added on the structure in different configurations, as shown in next sections, are the following: two bricks with dimensions 20 × 14 × 5 cm and one brick with dimensions 23 × 16.5 × 5 cm. The weight of each of the first two bricks is 12.7 kg (including the weight of the clamp), while the weight of the third brick is 16.3 kg (including the weight of the clamp).

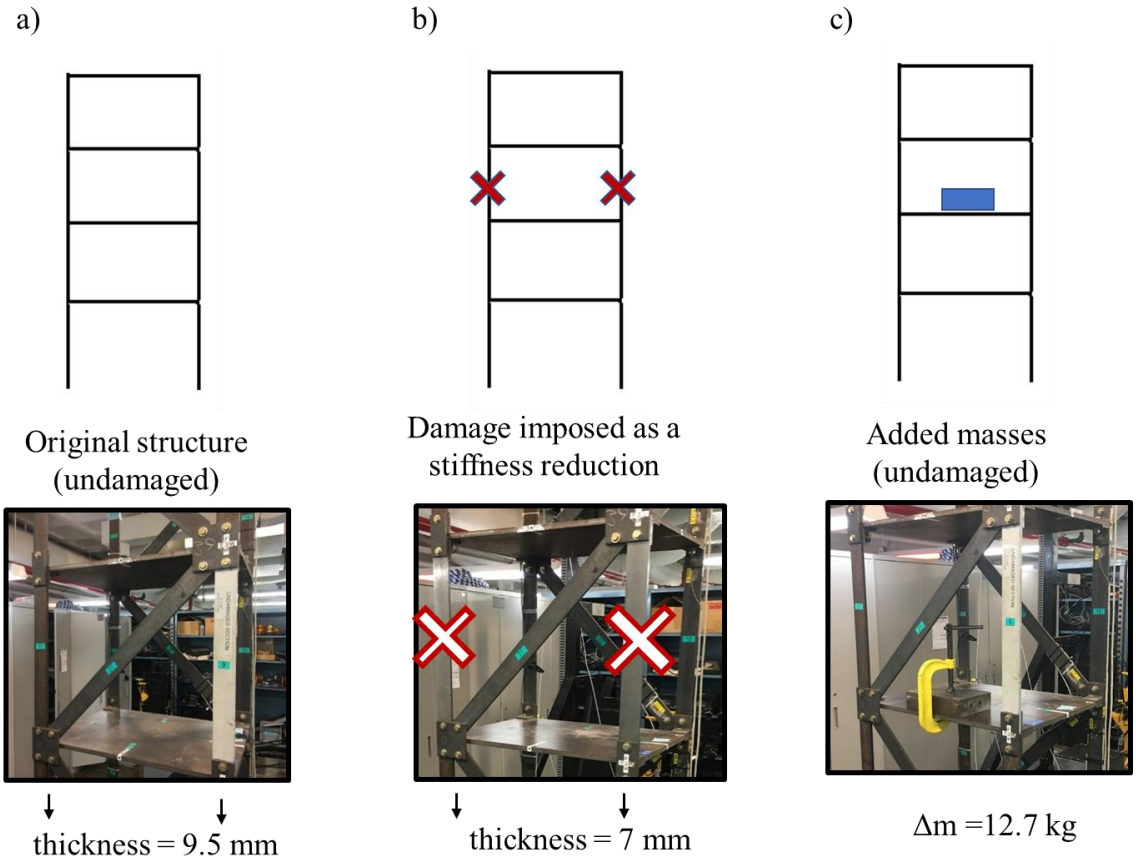

Figure 6.15. Examples of tested configurations (Carleton Laboratory, Columbia University): a) original structure; b) modified structure with an imposed inter-story stiffness reduction; c) modified structure with added masses.

The damage detection approach proposed in this chapter was developed for plane shear building structures, which are the structures that are considered in the work by [Koo et al., 2010] where the original formulation of the Positive Shear

Inspection Load was presented. For this reason, in the experimental verification the frame structure was tested only in one direction. In particular, the frame was tested in the west-east direction, which, as already mentioned, is the weak direction of the structure. All the vibration tests were performed by hitting the structure through the hammer at the fourth story in the geometric center of the floor (which is also the center of mass and the center of stiffness). The point of the impact is indicated with the letter X in the schematic drawings of the structure reported in Fig. 6.13, and it is also indicated by the arrow in Fig. 6.16. The choice of hitting the structure at the fourth floor was done to avoid locations that can be possible nodes of the mode shapes of the structure in the weak direction (impact locations at the intermediate stories of the structure were thus not considered in the tests). Moreover, the choice of considering the geometric center of the floor as the impact location was done to minimize the torsional effects and to test the structure only in one direction, which is the weak direction.

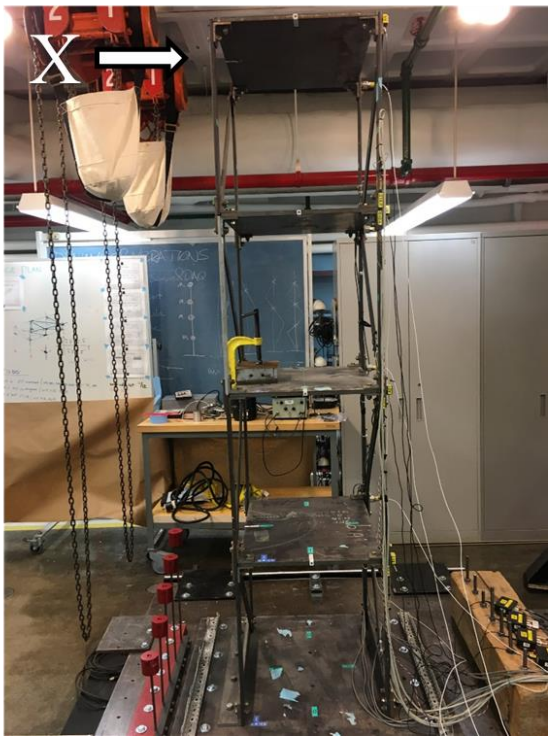

Figure 6.16. North face of the structure with indication of the impact location (Carleton Laboratory, Columbia University)

All the measurements were acquired by considering a sampling frequency equal to 1000 Hz. For each vibration measurement that was recorded using the data acquisition system, the structure was excited by five hits of the hammer. An example of the data acquired for a vibration test performed on the original structure is reported in Fig. 6.17.

a)

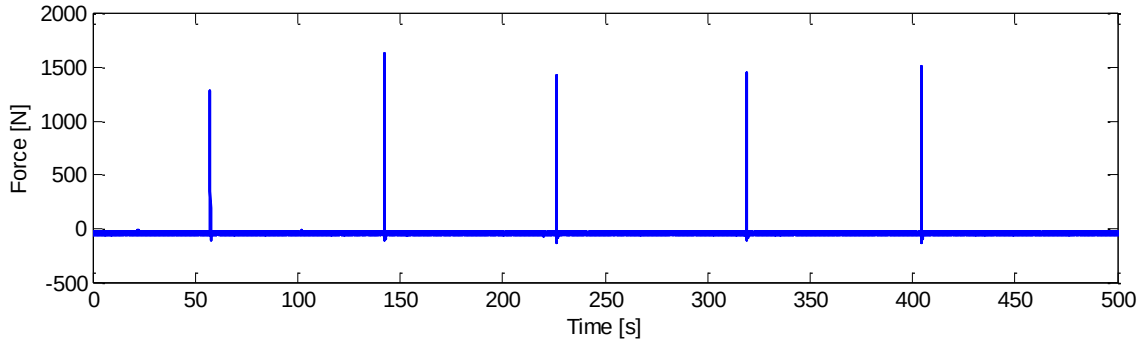

b)

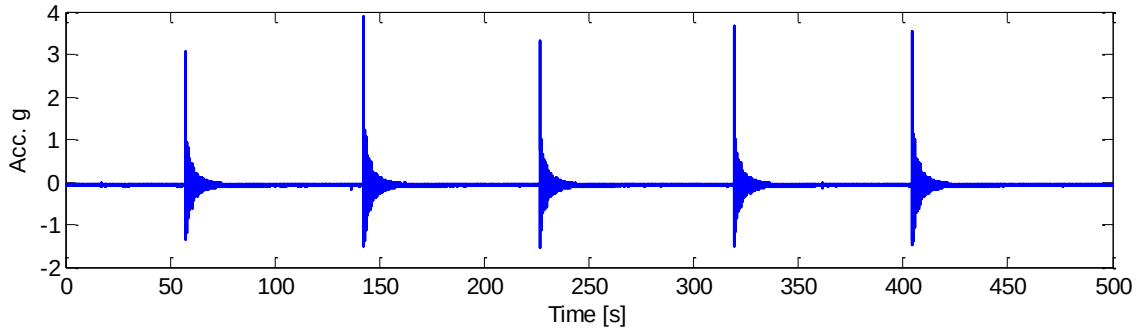

Figure 6.17. Vibration measurements acquired for the original structure: a) input force; b) vibration responses measured through channel A12z.

As already mentioned, the damage detection analyses on the experimental data were performed using only the output vibration responses of the structure. However, during the tests and just after the data acquisition the Frequency Response Functions (FRF) were evaluated using both the input force and the output responses. This operation was done to check the data quality and to check that the structural modes were adequately excited. Examples of drive point Frequency Response Functions (FRFs) are reported in Fig. 6.18, together with the related coherence function. The functions reported in this figure were evaluated for a vibration test performed on the

original structure and for five hits of the hammer. The drive point FRFs were evaluated by considering the input force and the output response measured through channel A12z (which is positioned at the top story). First of all, clear peaks that can be associated to structural modes are evident in the plot of the magnitude of the FRFs. This means that the structure was adequately excited by the hammer in the considered frequency range (i.e. 0-50 Hz). Moreover, the FRFs obtained for each of the five different hits of the hammer are almost overlapped, as shown in Fig 6.18. This good agreement between the five FRFs is also confirmed by the values of the coherence function, which are in general close to one. Only some drops in the values of the coherence function were obtained at the frequencies related to the antiresonances.

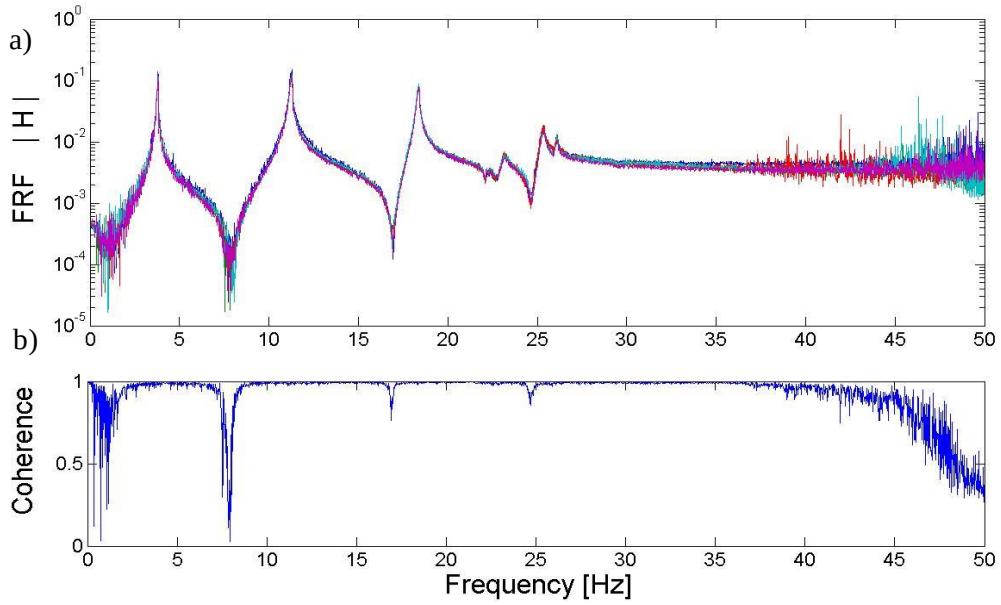

Figure 6.18. Drive point Frequency Response Functions (FRFs): a) magnitude of FRFs; b) coherence function.

6.4.2.1 First experimental test: damage detection without mass variations

This section presents the structural configurations and the results of a first experimental test performed on the steel frame structure for damage detection purposes. This test was planned to apply the damage detection methodology in the case in which the structural masses are unchanged before and after damage.

In this first experimental test, the structure was tested at first in the original configuration, which is assumed as the baseline condition for the damage detection process. To obtain the training data set, 30 vibration tests were performed on the structure in the baseline condition (i.e. six different vibration measurements were acquired, where five hits of the hammer compose each measurement). Then, the structure was tested again to obtain the testing data set related to the inspection phase of the damage detection process. Seven structural configurations were considered and tested to obtain the testing data set, and these configurations are reported in Table 6.3. The first three configurations (U1c-U3c) are equal to the original structure (i.e. these configurations are undamaged). The last four configurations are damaged configurations (D1c-D4c) and were obtained by replacing one or more columns of the structure with other columns with reduced cross-sections. For each configuration reported in Table 6.3 one vibration measurement was acquired (as already mentioned, each measurement is composed by five hits of the hammer).

Configurations	State	Description
U1c, U2c, U3c	Undamaged	Baseline condition
D1c	Damaged	15% stiffness reduction at 3rd story
D2c	Damaged	30% stiffness reduction at 3rd story
D3c	Damaged	D2c + 15% stiffness reduction at 2nd story
D4c	Damaged	D2c + 30% stiffness reduction at 2nd story

Table 6.3. Testing configurations related to the first experimental test

In the damage detection analyses, as already mentioned, the input force produced by the hammer was not considered, and only the output acceleration responses of the structure were taken into account. Moreover, in the analyses only the eight channels that measured the accelerations in the west-east direction were considered and used to estimate the proportional flexibility matrices and the proportional modal flexibility-based deflections of the different configurations in the weak direction of the structure. According to Fig. 6.13 the channels considered in the analyses are A4z, A3x, A2z, A1z and A12z, A11z, A10z, A9z. Performing a 2D analysis is considered as a valid approach since the structure is characterized by a plan-symmetric distribution of both the story stiffness and the structural masses at

each floor. Moreover, due to the presence of the diagonal braces only in the x direction and due to the orientation of the column sections (Fig. 6.13), the structure is characterized by structural modes that are well separated in the two main directions. The structure both in the original configuration and in all the testing configurations is characterized by the above-mentioned dynamic behavior. It is worth noting that only the configurations D1c and D3c are characterized by a distribution of the story stiffness that is slightly plan-asymmetric at the damaged stories (i.e. the stories where the stiffness reductions were imposed). These two configurations were in fact created by substituting only one column (i.e. the column in position C - Fig. 6.13) with another column with a reduced cross section at the damaged stories. These two configurations are thus different from configurations D2c and D4c, which were, on the contrary, created by substituting two original columns with other two columns with reduced cross sections (configurations D2c and D4c are perfectly symmetric configurations, where the damaged columns were introduced in positions C, D - Fig. 6.13). The coupling effects on the structural modes related to configurations D1c and D3c are, however, very small. Under the simplified assumption of neglecting the mentioned small coupling effects, the configurations D1c and D3c were also considered in the 2D analyses that were carried out to verify the damage detection approach proposed for plane structures.

The acceleration responses of the structure due to the impact of the hammer can be considered as free decay signals, and they were used to perform an output-only modal identification of the structure through the Eigensystem Realization Algorithm (ERA) [Juang & Pappa, 1985]. Considering the data from the eight channels in the west-east direction (i.e. the weak direction of the structure) and using the Eigensystem Realization Algorithm, four structural modes were identified. If one assumes that the behavior of the structure in the weak direction can be described through a simplified modeling, such as a 4-DOF shear-type modeling, then it is clear that in such case all the prevalent longitudinal modes of the structure in the considered direction were identified. The components of the mode shapes were identified using the Eigensystem Realization Algorithm at the sensor locations (i.e. the positions indicated with the letters A, B in Fig. 6.13). Then, under the simplifying assumption of considering each floor of the structure with a rigid-body in-plane behavior, the components of the mode

shapes in the direction considered in the test and in the geometric center of the structure were determined (the obtained mode shapes are thus characterized by four components). The results of the modal identification, in terms of natural frequencies and mode shape components (normalized to a maximum value equal to unit), are reported, for example, for the configurations U1c and D4c in Table 6.4.

	Undamaged (U1c)				Damaged (D4c)			
Mode	1st	2nd	3rd	4th	1st	2nd	3rd	4th
f_i [Hz]	3.77	11.23	18.32	26.05	3.46	10.83	17.24	22.48
ψ_{ji}	1.00	1.00	0.72	0.30	1.00	1.00	0.78	0.38
	0.84	-0.12	-0.93	-0.67	0.86	-0.06	-0.90	-0.77
	0.61	-0.77	0.01	1.00	0.61	-0.92	-0.03	1.00
	0.30	-0.66	1.00	-0.86	0.25	-0.70	1.00	-0.96

Table 6.4. Identified modal parameters for configurations U1c and D4c (first experimental test)

Starting from the identified modal parameters (i.e. natural frequencies and arbitrarily-scaled mode shapes), the calculations were performed according to the steps defined in Section 6.2.2 to obtain the vectors of the proportional MF-based interstory drifts. Then, the damage detection was carried out by calculating the damage indices proposed in Section 6.3.2 (i.e. the index based on Mahalanobis distance and the error on the MAC_{id}).

The results of the damage detection are presented at first for the cases in which the PFM technique by Bernal [2001] was applied. In these cases, the calculations were performed by considering a number of modes equal to both $r = 3$ and $r = 4$. The case $r = 3$ represents the minimum number of modes that has to be considered for the application of the PFM procedure defined by Bernal. This is evident if Eq. (6.8) is evaluated for $r = 3$ and $n = 4$. For a number of modes that is lower than $r = 3$ (i.e. $r = 2,1$) the PFM procedure by Bernal can not be applied. It is worth noting that the case $r = 4$ means that all the prevalent longitudinal modes of the structure in the considered direction were included in the calculations. The values of the damage index based on Mahalanobis distance evaluated for the different configurations described in Table 6.3

are reported in Fig. 6.19. As already done in the numerical analyses presented in Section 6.4.1.1, this index was calculated by considering in Eq. (6.58) a total-mass-ratio w=1 (Eq. 6.56). This is because in the first experimental test the masses of the structure are unchanged before and after damage. The results obtained using the error on the MAC_{id} are reported in Fig. 6.20, and this index was calculated, on the contrary, without any a-priori information on the structural masses. As shown in Figs. 6.19 and 6.20, both the two indices are able to classify as damaged the configurations that are characterized by stiffness reductions with respect to the structure in the baseline state (i.e. D1c-D4c) both for the cases r = 4 and r = 3. On the contrary, the damage indices related to the configurations that are equal to the baseline state (i.e. U1c-U3c) are below the thresholds both using the index MD_{id}^{*} and the index $eMAC_{id}^{*}$ and both for r = 4 and r = 3. These configurations are correctly classified as undamaged.

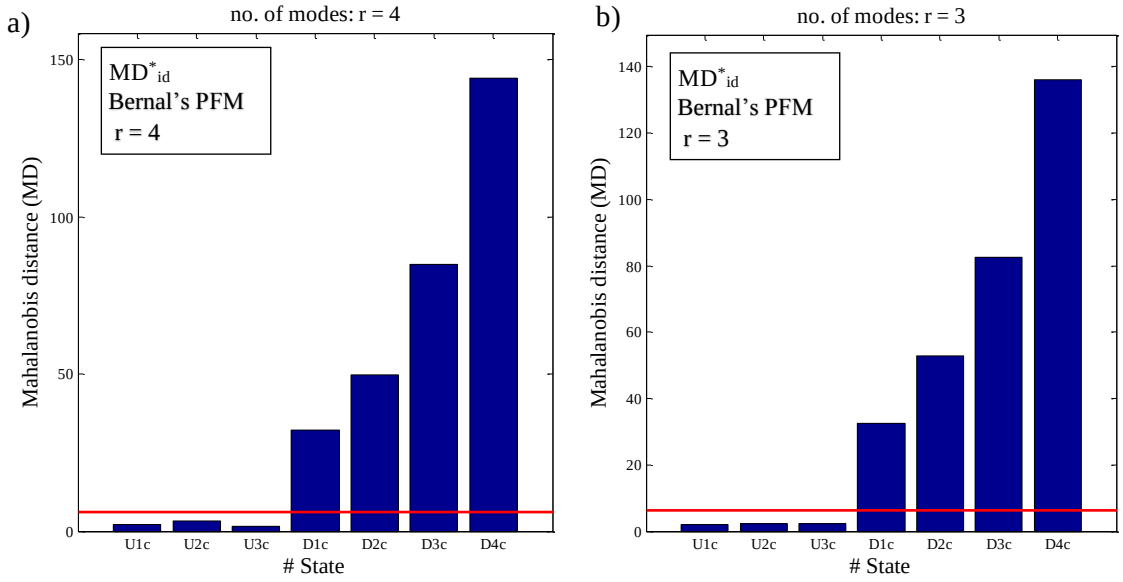

Figure 6.19. Damage detection using Mahalanobis distance (first experimental test - Bernal's PFM): a) r = 4; b) r = 3.

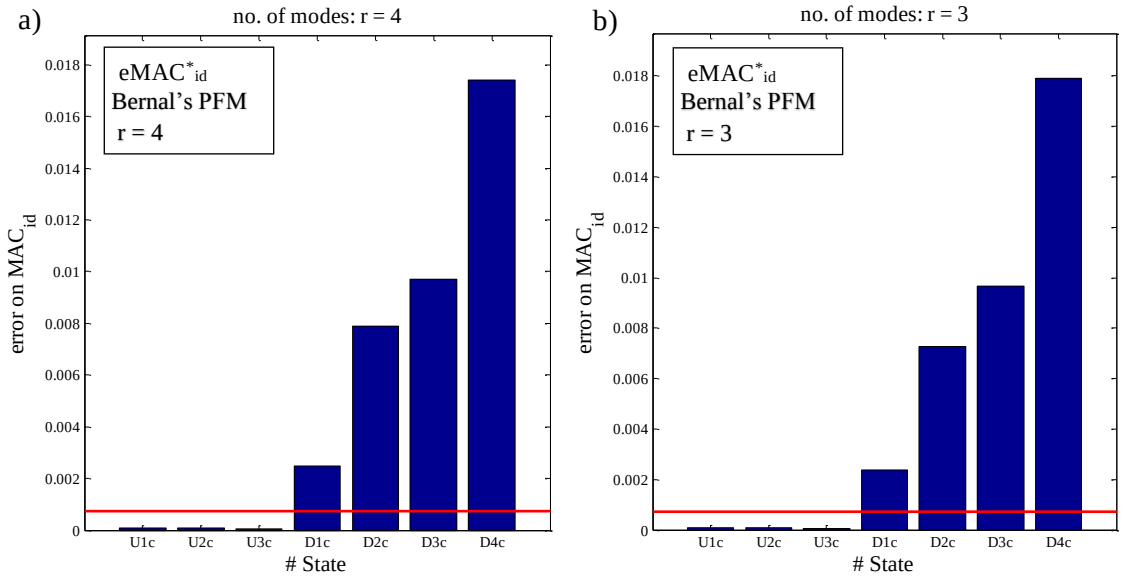

Figure 6.20. Damage detection using the error on MAC_{id} (first experimental test – Bernal's PFM): a) r = 4; b) r = 3.

The results of the damage detection are now presented for the cases in which the PFM procedure by Duan et al. [2005] was applied. It is worth noting that, referring to the experimental test, the results of the damage detection using the Duan's PFM are presented for all the possible subsets of modes of the structure (i.e. for r = 4,3,2,1, where r is the number of modes included in the calculations). This means that, using the data of the experimental test, the procedure by Duan et al. [2005] was also adopted in the cases r = 3,4. These last two cases, as shown in previous paragraphs, are cases where the procedure by Bernal [2001] can be applied and this procedure is the preferred option. The reason for performing the analyses using the Duan's PFM technique also in the cases r = 3,4 will be clarified in next section, where the results of the first test (in which the masses are unchanged before and after damage) will be compared with the results of the second test (in which mass variations are present between the undamaged and the possibly damaged states).

Referring to the first experimental test and considering the Duan's PFM technique in the calculations, the results of the damage detection using the index based on Mahalanobis distance are reported in Fig. 6.21, while the results obtained using the error on the MAC_{id} are reported in Fig. 6.22. As shown in Figs. 6.21 and 6.22, for this experimental test (where the masses are unchanged before and after damage) both

indices evaluated using the Duan's PFM and for all the possible subsets of modes included in the calculations (i.e. r = 4,3,2,1) are able to separate the group of structures that are undamaged (i.e. U1c-U3c) from the group of structures that are damaged (i.e. D1c-D4c). This means that for the considered structure and for the considered configurations (which are all characterized by the same structural masses) the results of the damage detection obtained using the proposed approach with the PFM procedure by Duan et al. [2005] do not depend in general on the number of modes included in the calculations. This is an important observation that will be considered also in next section.

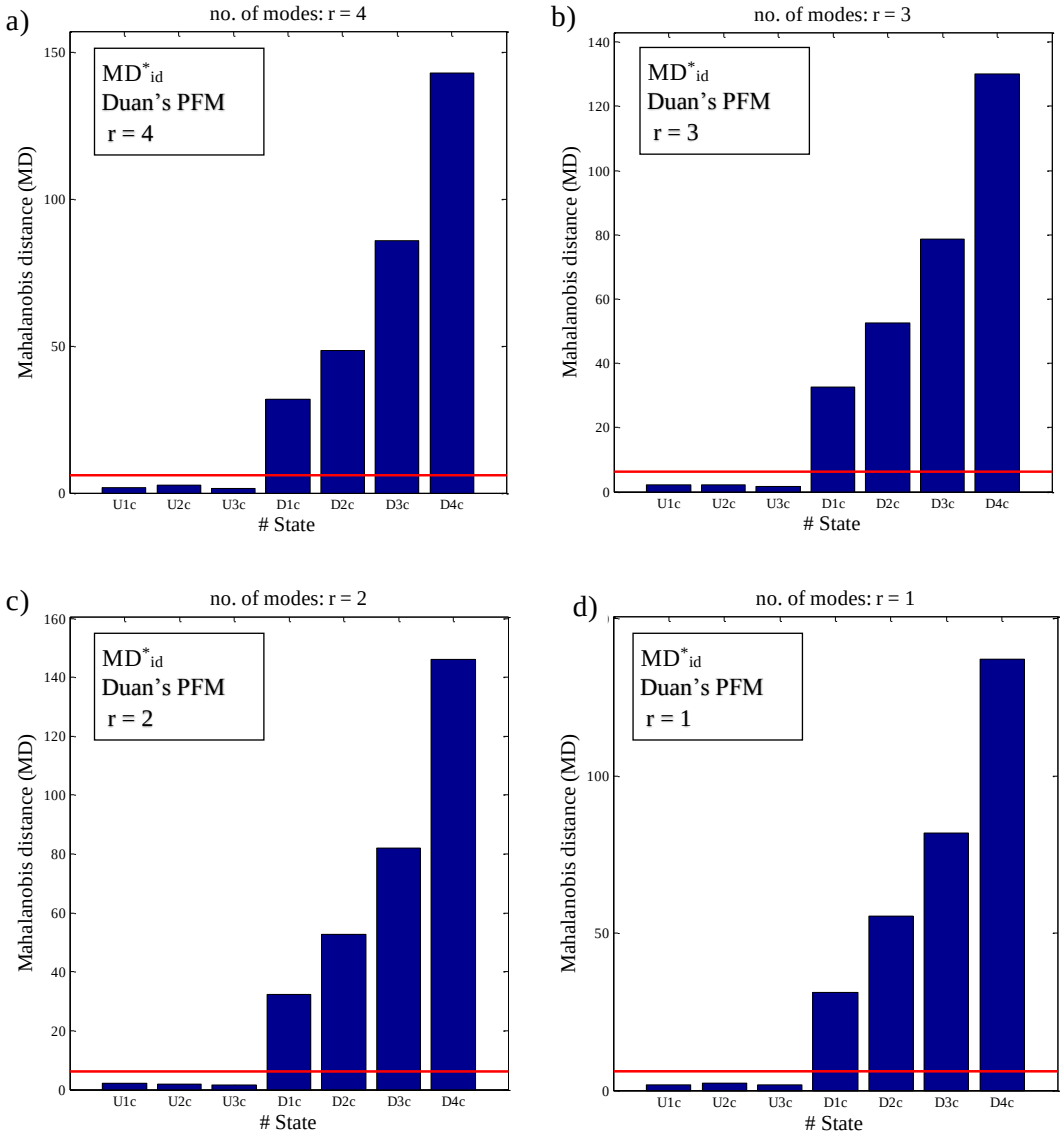

Figure 6.21. Damage detection using Mahalanobis distance (first experimental test - Duan's PFM): a) r = 4; b) r = 3; c) r = 2; d) r = 1.

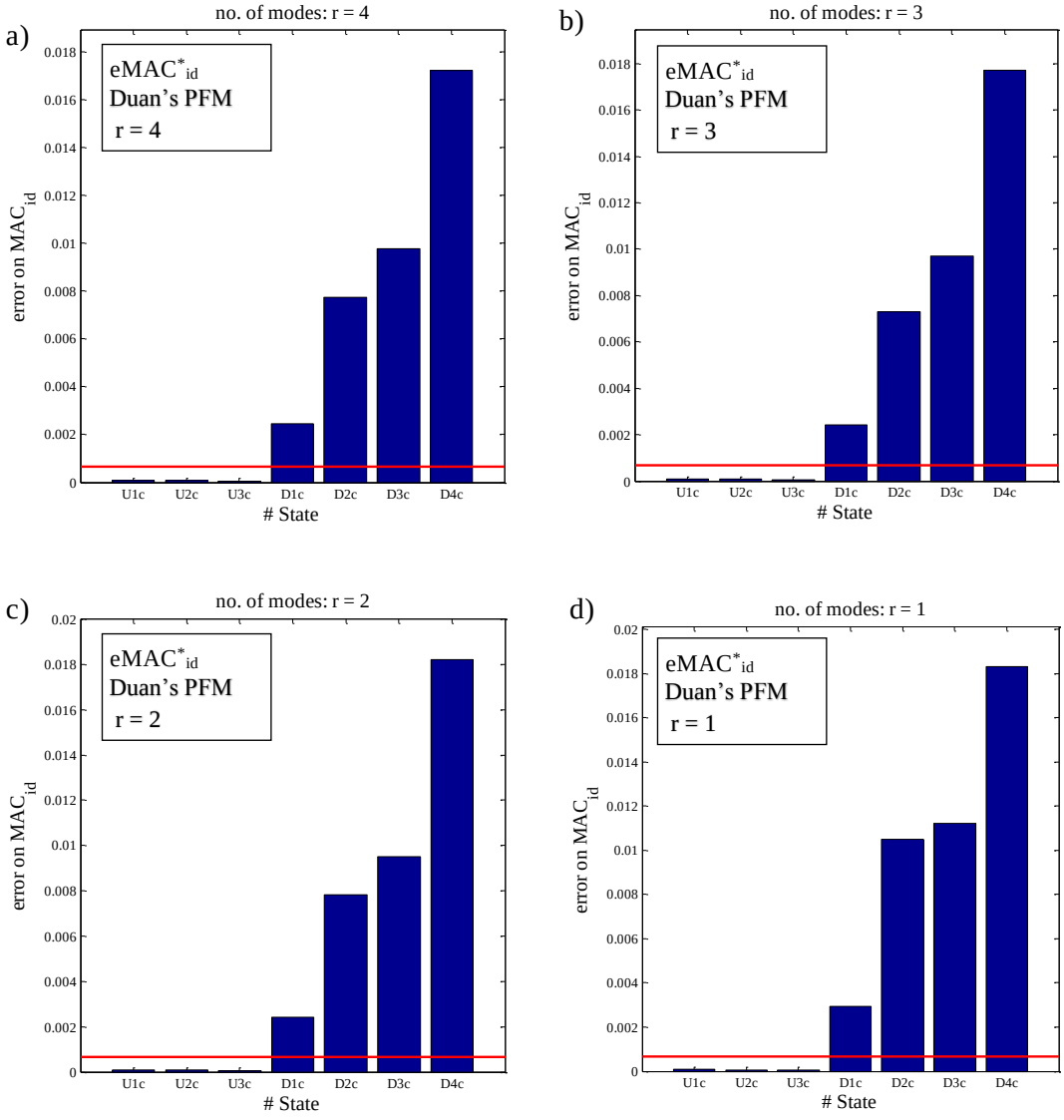

Figure 6.22. Damage detection using the error on MAC_{id} (first experimental test – Duan's PFM): a) $r = 4$; b) $r = 3$; c) $r = 2$; d) $r = 1$.

6.4.2.2 Second experimental test: damage detection with mass variations

In this section, the results of a second vibration test that was performed to apply the proposed damage detection approach are presented and discussed. This second test was performed on the same structure considered in the first test (i.e. the steel frame structure located at the Carleton Laboratory of Columbia University, New York, USA), using the same test setup and the same excitation (i.e. the impact of an hammer). However, the testing configurations (i.e. the configurations related to the

inspection phase) considered in the second test are different from the configurations related to the first test. In fact, the majority of the testing configurations in the second test are characterized by mass modifications with respect to the structural configuration that is assumed as the baseline state. Of course, similarly to the first experimental test, some of the testing configurations in the second test are also characterized by stiffness modifications with respect to the baseline structure. The second experimental test was thus planned and executed to apply the proposed damage detection approach in the case in which the masses of the structure are varied before and after damage.

Similarly to the first test, the training data set was obtained by performing 30 vibration tests on the original or baseline structure using the hammer. Then, the frame was tested again, and sixteen configurations were considered as possibly damaged structures. These configurations are described in Tables 6.5, 6.6. It is worth mentioning that Table 6.5 describes the structural configurations in terms of the stiffness distribution, while Table 6.6 describes the structural configurations in terms of the mass distribution. According to Table 6.5, the first eight configurations (U0, U1, U2, U3, U4, U5, U6, U7) are undamaged configurations. For such configurations the stiffness of each story is equal to the corresponding story stiffness in the structure assumed as the baseline state. The remaining eight configurations (D0, D1, D2, D3, D4, D5, D6, D7) are damaged configurations. These configurations were obtained by replacing two columns at the third story of the structure with other two columns with reduced cross sections (referring to Fig. 6.13, these columns are in positions C, D). As already mentioned, this modification is approximately equivalent to the operation of reducing by 30% the story stiffness of the original structure at the third story.

Configurations	State	Description
U0, U1, U2, U3, U4, U5, U6, U7	Undamaged	No stiffness reductions
D0, D1, D2, D3, D4, D5, D6, D7	Damaged	30% stiffness reduction at 3rd story

Table 6.5. Testing configurations related to the second experimental test.

Conf.	U0*,D0*	U1,D1	U2,D2	U3,D3	U4,D4	U5,D5	U6,D6	U7,D7
m_4	34.52	59.92	34.52	34.52	34.52	59.92	34.52	34.52
m_3	42.82	42.82	68.22	42.82	42.82	42.82	68.22	84.52
m_2	42.82	42.82	42.82	68.22	42.82	59.12	42.82	42.82
m_1	42.82	42.82	42.82	42.82	68.22	42.82	59.12	42.82
m_{TOT}	162.98	188.38	188.38	188.38	188.38	204.68	204.68	204.68

* configuration with a mass distribution equal to the one of the structure used to obtain the training data set

Table 6.6. Distribution of the structural masses [kg] related to the testing configurations considered in the second experimental test.

Each configuration indicated by a different number in the acronym (i.e. 0,1,2,3,4,5,6,7) is characterized by a different distribution of the structural masses, as described in Table 6.6. The configurations U0 and D0 have the same mass distribution of the structure assumed as the baseline structure, while the other configurations were tested with additional masses. As already mentioned in Section 6.4.2, the increase in the structural masses was created by adding on the structure some metallic bricks. It is important to underline that, for all the tested configurations, the added masses were positioned on the different floors of the structure in a configuration that is plan-symmetric with respect to the z direction (Fig. 6.13). This direction is the weak direction of the structure and the direction considered in the vibration tests. The masses of each story of the structure were measured and determined in the laboratory, and these story masses are reported in Table 6.6 to describe the configurations that were tested. Of course, in the calculations for damage detection the values of the floor masses were assumed as unknown, and the mass distributions were extracted from the data using the proposed implementation of the PFM procedures originally defined by Bernal [2001] and Duan et al. [2005]. It is worth noting that the majority of the tested configurations are characterized by additional masses with respect to the original structure. Therefore, the scaling factors on the vectors of the proportional MF-based interstory drifts related to the inspection phase (theoretically equal to the total mass of the structure, according to the approach proposed for the estimation of the proportional deflections) are in general different from the scaling factors on the damage sensitive features related to the baseline state. The scenario analyzed in this

second experimental test is thus similar to the scenario that was analyzed in Section 6.4.1.2 using the numerical model of a shear building structure and the Monte Carlo simulation. The values of the total mass for the testing configurations considered in the second experimental test are reported in the last row of Table 6.6.

As already done for the first experimental test, the vectors of the proportional MF-based interstory drifts were calculated using the procedure described in Section 6.2.2. The damage indices proposed in Section 6.3.2 (i.e. the index based on Mahalanobis distance and the error on the MAC_{id}) were then calculated for each configuration that is described in Tables 6.5, 6.6.

The results of the output-only damage detection are presented at first for the cases in which the PFM technique by Bernal [2001] was applied. As already done in the analyses related to the first experimental test, the proposed approach and the Bernal's PFM technique were applied for a number of modes included in the calculations equal to $r = 3$ and $r = 4$ (where again the case $r = 3$ represents the minimum number of modes that has to be considered to apply the Bernal's PFM technique, while in the case $r = 4$ all the prevalent longitudinal modes of the structure in the direction considered in the analyses were taken into account).

The results obtained by calculating the damage index based on Mahalanobis distance (using the PFM procedure by Bernal) are presented in Fig. 6.23. In this figure, the bar plot on the left-hand side is related to the results obtained for the case $r = 4$ (Fig. 6.23a), while the bar plot reported on the right-hand side is related to calculations performed using a number of modes $r = 3$ (Fig. 6.23b). The damage index based on Mahalanobis distance was calculated using Eq. (6.58). It is worth noting that according to the proposed approach the relationship between the masses in the undamaged and in the possibly damaged states has to be known to apply the index based on Mahalanobis distance. According to Eq. (6.58), the calculations were thus performed using the total-mass-ratio w (minimal a-priori information) to scale the vectors of the proportional MF-based interstory drifts related to the inspection phase. By performing this operation, the scaling factors on the DSFs related to the undamaged and the possibly damaged states (which are initially different because the masses are varied before and after damage in this experimental test) were made

comparable. Otherwise, if this operation is not performed the index based on Mahalanobis distance can not be correctly applied, as already demonstrated in the numerical analysis based on Monte Carlo simulation presented in Section 6.4.1.2. As evident in Fig. 6.23, the damage index based on Mahalanobis distance is able to separate the group of the undamaged structures (U0-U7) from the group of the damaged structures (D0-D7) both considering a number of modes r = 4 (Fig. 6.23a) and r = 3 (Fig. 6.23b). It is worth noting that, referring to the case r = 3 (i.e. when considering a limited number of modes), some false positive results were obtained. This is evident in Fig. 6.23b where, referring to some configurations that were tested with added masses and that are undamaged, the values of the damage index based on Mahalanobis distance are slightly higher than the threshold (indicated by the red line in the bar plot). In any case, the values of the index obtained for such false positives are remarkably lower than the values of the index obtained for the damaged configurations, as shown in Fig. 6.23b.

The results obtained by calculating the error on the Modal Assurance Criterion applied on the vectors of proportional MF-based interstory drifts (using the PFM procedure by Bernal) are presented in Fig. 6.24. Again, in this figure, the bar plot on the left-hand side is related to the results obtained for the case r = 4 (Fig. 6.24a), while the bar plot reported on the right-hand side is related to calculations performed using a number of modes r = 3 (Fig. 6.24b). Both for the cases r = 4 and r = 3, the $eMAC_{id}^{*}$ is able to identify and separate the group of configurations that are damaged (D0-D7) from the undamaged configurations (U0-U7). This result was obtained by calculating the $eMAC_{id}^{*}$ according to the formulation presented in Section 6.3.2.2, and the calculations were performed without any a-priori information on the structural masses and without any information on the relationship between the masses in the undamaged and the possibly damaged states. It is worth noting that two false positive results were obtained using $eMAC_{id}^{*}$ for the case r = 3 (Fig. 6.24b) – i.e. for configurations U3 and U5. The values of $eMAC_{id}^{*}$ related to configurations U3 and U5 calculated for r = 3 are, however, very close to the threshold, and they are remarkably lower than the values of $eMAC_{id}^{*}$ obtained for the damaged configurations. The results obtained using the index $eMAC_{id}^{*}$ (calculated for the cases r =4,3 using the Bernal's PFM technique – Fig. 6.24) can be compared with the corresponding results obtained using the index

based on Mahalanobis distance (6.23). For the case r = 4 (i.e. using all the modes in the calculations) no false positives were obtained both for the index $eMAC_{id}^{*}$ (Fig. 6.24a) and the index based on Mahalanobis distance (6.23a). For the case r = 3 (i.e. using a limited number of modes in the calculations), the number of the false positives obtained using the error on the MAC_{id}^{*} (Fig. 6.24b) is lower than the number of the false positives obtained using the index based on Mahalanobis distance (Fig. 6.23b).

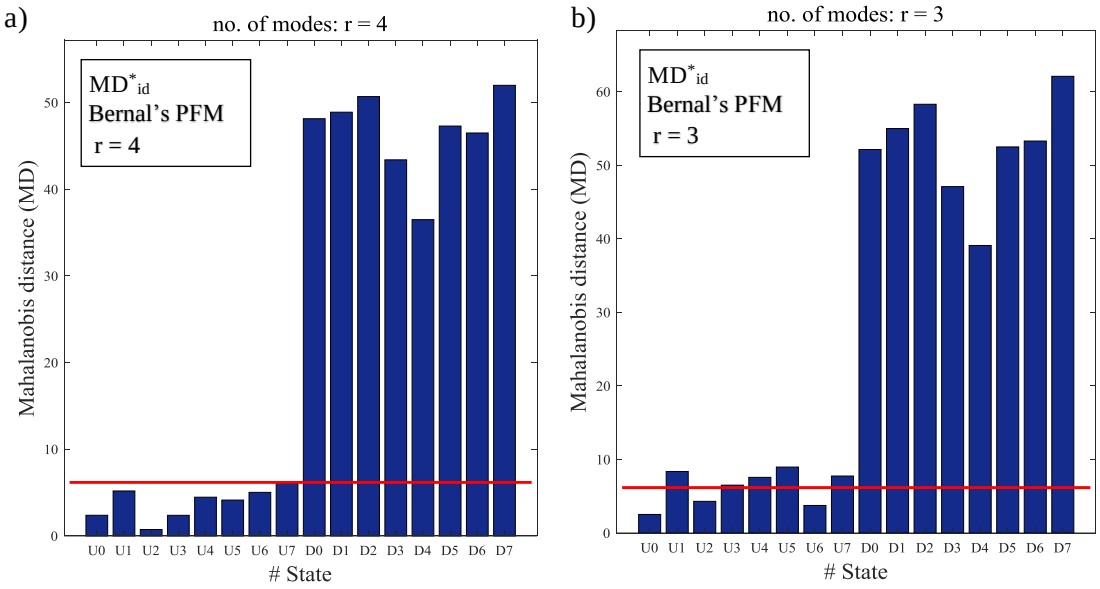

Figure 6.23. Damage detection using Mahalanobis distance (second experimental test - Bernal's PFM): a) r = 4; b) r = 3.

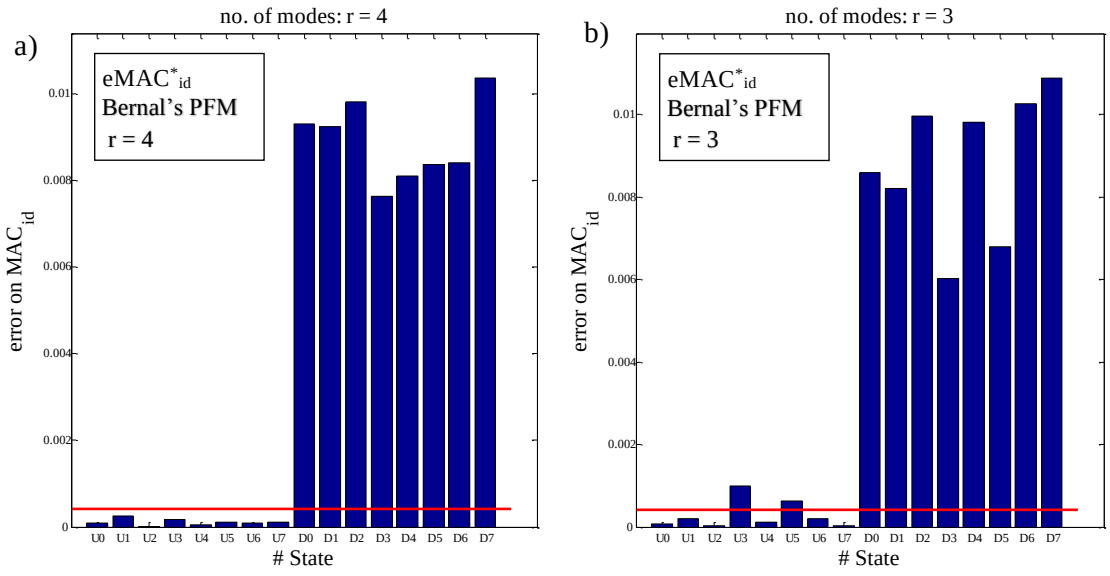

Figure 6.24. Damage detection using the error on MAC_{id} (second experimental test - Bernal's PFM): a) r = 4; b) r = 3.

The results of the damage detection for the cases in which the PFM procedure by Duan et al. [2005] was applied are presented herein. It is worth noting that, referring to the second experimental test characterized by mass variations before and after damage and as already done for the first test, the damage detection using the Duan's PFM technique was performed for all the possible subsets of structural modes of the steel frame structure (i.e. for r = 4,3,2,1, where r is the number of modes included in the calculations).

The results obtained using the damage index based on Mahalanobis distance (and the Duan's PFM technique) are reported in Fig. 6.25, where each plot is related to a different case (r = 4, r = 3, r = 2, or r = 1). The evaluation of the damage index based on Mahalanobis distance was performed using the additional scaling operation on the DSFs that is based on the knowledge of the total-mass-ratio w (according to Eq. 6.58). This was done in an attempt to guarantee the compatibility between the scaling factors on the vectors of the proportional MF-based interstory drifts related to the undamaged and the possibly damaged states. As shown in Fig. 6.25, a separation between the undamaged configurations (U0-U7) and the damaged configurations (D0-D7) is evident only when all the modes of the structure are considered (i.e. for r = 4, Fig. 6.25a). In Fig. 6.25a, in fact, all the configurations from D0 to D7 are classified as damaged, and only one false positive result was obtained (i.e. the damage index related to configuration U4 is slightly higher than the threshold value). On the contrary, referring to the cases in which the calculations were performed using a limited number of modes (i.e. cases r = 3,2,1 reported in Fig. 6.25b, 6.25c, and 6.25d, respectively) there is not a clear separation between the undamaged and the damaged configurations. A possible interpretation on the results that were obtained in such cases will be provided later in this section after presenting the results of the damage detection using the index $eMAC_{id}^{*}$. At this point the results obtained for the cases r = 4,3 using the Duan's PFM technique can be compared with the corresponding results obtained using the Bernal's PFM technique. For the case r = 4 no false positives were obtained using the index MD_{id} and the Bernal's PFM technique (Fig. 6.23a), while only one false positive was obtained using the Duan's PFM technique (Fig. 6.25a). For the case r = 4 thus similar results were obtained using either one technique or the other. On the contrary, for r = 3 clear benefits are evident when considering the

Bernal's PFM technique (Fig. 6.23b) instead of the Duan's PFM procedure (Fig. 6.25b).

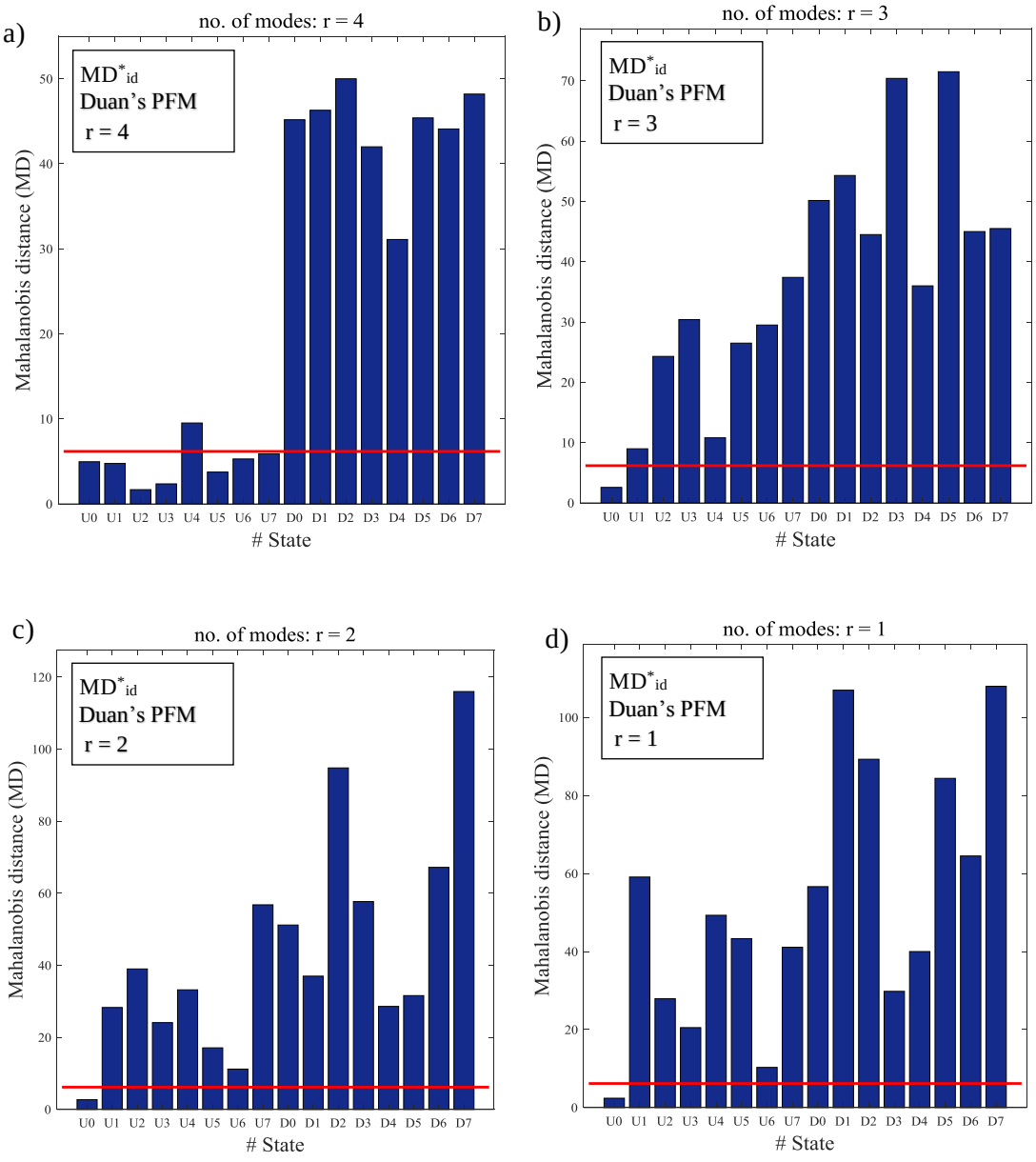

Figure 6.25. Damage detection using Mahalanobis distance (second experimental test - Duan's PFM): a) $r = 4$; b) $r = 3$; c) $r = 2$; d) $r = 1$.

The results of the damage detection performed using the damage index $eMAC_{id}^{*}$ and by considering the Duan's PFM technique are reported in Fig. 6.26 (for the different cases r = 4, r = 3, r = 2, or r = 1). According to the proposed approach, the index $eMAC_{id}^{*}$ was calculated without any a-priori information on the structural masses. As shown in Fig. 6.26, the index $eMAC_{id}^{*}$ is able to clearly separate the undamaged and the damaged configurations when all the structural modes of the steel frame structure are considered (i.e. for r = 4, Fig. 6.26a), and good results were also obtained using a number of modes equal to r = 3 (Fig. 6.26b). Then by considering the cases r = 2 and r = 1 (Fig. 6.26c, 6.26d, respectively), it is clear that reducing the number of modes included in the calculations the separation between the undamaged and the damaged configurations tends to be lost. It is worth noting, however, that for the case r = 2 all the damage indices evaluated for the damaged configurations (D0-D7) are higher than the indices related to the undamaged configurations (U0-U7). On the contrary, this is not true for the case r = 1 (Fig. 6.26d) where some values of the index $eMAC_{id}^{*}$ related to undamaged configurations are equal or higher than some values of the index related to damaged configurations. A possible interpretation on the above-mentioned results that were obtained for the cases r = 2,1 will be provided in next paragraphs. At this point the results obtained using the index $eMAC_{id}^{*}$ and the Duan's PFM technique for the cases r = 4,3 can be compared with corresponding results obtained with the Bernal's PFM technique. For r = 4 very similar results were obtained using the two PFM techniques (as shown in Fig. 6.24a and Fig. 6.26a). For r = 3 the number of false positives obtained using the index $eMAC_{id}^{*}$ and the Bernal's PFM technique (Fig. 6.24b) are lower than the ones obtained with the Duan's PFM technique (Fig. 6.26b). Finally, the results obtained using the index $eMAC_{id}^{*}$ and the Duan's PFM technique for the cases r = 2,1 (which are cases where the Bernal's PFM technique can not be applied) can be compared with corresponding results obtained using the index based on Mahalanobis distance. For the case r = 2, the separation between the undamaged and the damaged configurations is more clear using the index $eMAC_{id}^{*}$, as evident if one compares Fig. 6.26c with Fig. 6.25c. On the contrary, for the case r = 1 the separation between the two groups of structural configurations (undamaged and damaged) is not evident using both indices.

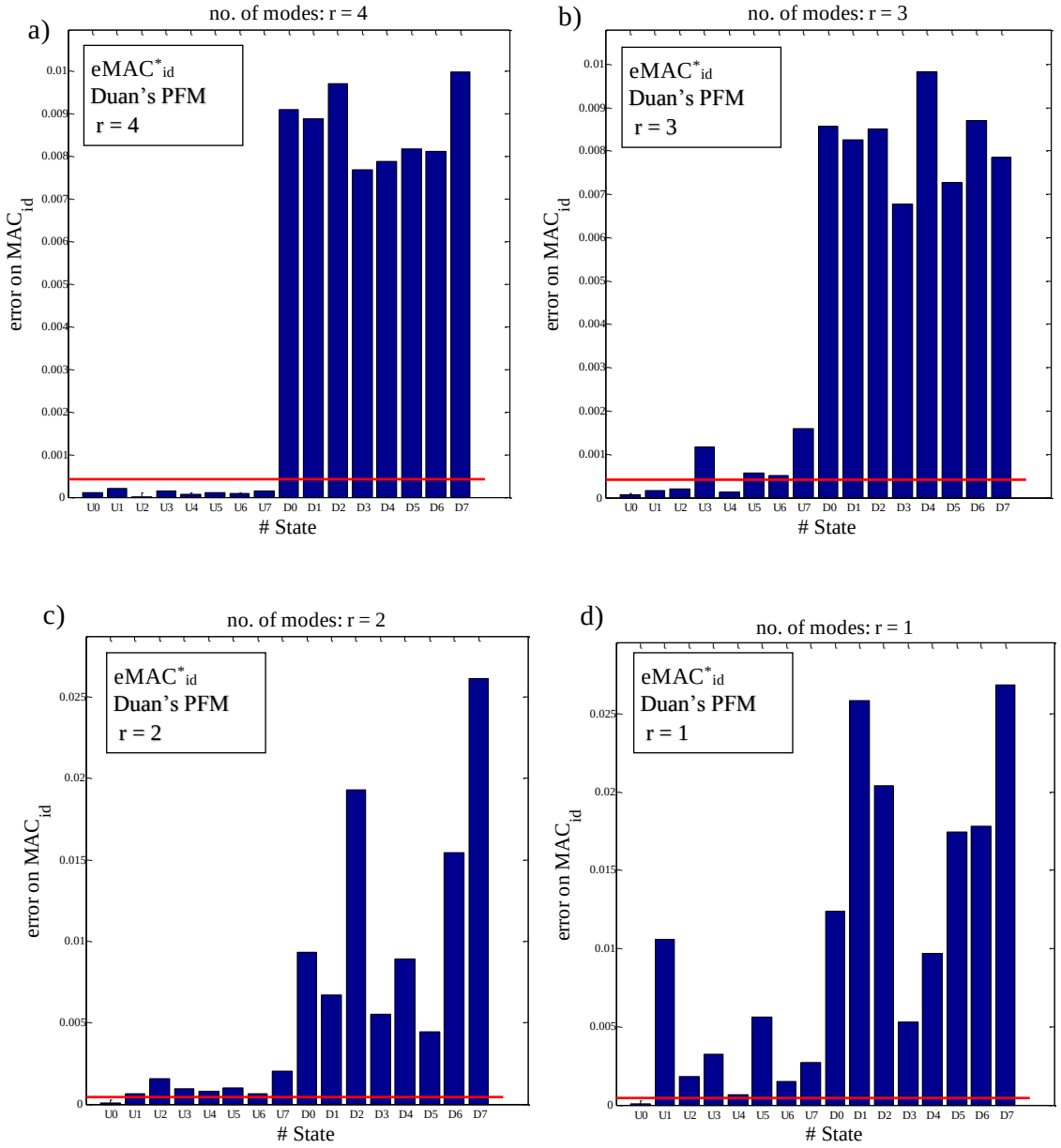

Figure 6.26. Damage detection using the error on MAC_{id} (second experimental test – Duan's PFM): a) $r = 4$; b) $r = 3$; c) $r = 2$; d) $r = 1$.

The results of the damage detection obtained using the two proposed indices and the Duan's PFM technique on the data of the second experimental test (with mass variations before and after damage) can be summarized as follows. Good results were obtained in the damage detection when all the structural modes of the steel frame structure were included in the calculations, i.e. $r = 4$. In such case the results obtained

with the Duan's PFM technique are comparable with the corresponding results obtained with the Bernal's PFM technique. When a limited number of modes is considered and both the two PFM's techniques can be applied, better results were obtained using the Bernal's PFM technique instead of the Duan's PFM procedure (this observation is evident especially for the damage index based on Mahalanobis distance). For the cases in which the procedure by Duan et al. [2005] is the only option that can be applied (i.e. when the condition expressed by Eq. 6.8 is not fulfilled because a very limited number of modes is considered, and thus the PFM technique by Bernal [2001] can not be applied) a clear separation between the undamaged and the damaged configurations was not found by evaluating both damage indices (MD_{id}^{*} and $eMAC_{id}^{*}$) for this experimental test with mass variations. It is important to underline that this last result was obtained in the second experimental test where mass variations are present between the undamaged and the possibly damaged structures. This result was not found, on the contrary, in the first experimental test where the structural masses are unchanged before and after damage. As shown in Section 6.4.2.1, in fact, both the two damage indices evaluated using the Duan's PFM technique on the data of the first experimental test provided a correct identification of the damaged configurations for all the different cases (r = 4,3,2,1) characterized by different subsets of modes included in the calculations (Figs. 6.21 and 6.22). The differences that were obtained in the results related to the two experimental tests can be explained by considering the two following effects.

The first effect is related to the fact that, as already mentioned in Section 6.2.1, an approximated estimate of the proportional mass matrix (PMM) is obtained when the Duan's PFM technique is applied on a truncated set of modal parameters (i.e. using a limited number of structural modes). In general, the lower the value of the parameter r, the higher the approximations that are introduced on the estimated PMM. This is because, as already discussed in Section 6.2.1, according to the Duan's PFM procedure pseudo inverse operations are performed on truncated mode shape matrices to obtain the mass matrix of the dummy structure. Then, it has to be considered that having approximations in the proportional mass matrix estimated from the data (which is used to normalize the mode shapes that are included in the calculations of the modal flexibility matrices) leads to the following effect. The higher the approximations on

the proportional mass matrix, the higher the approximations introduced on the effective scaling factors related to the vectors of the proportional MF-based interstory drifts (i.e. the damage sensitive features). This means that both for the undamaged and the possibly damaged structures the effective scaling factors are approximated with respect to the theoretical scaling factors (which, according to the proposed approach, are equal to the total mass of the structure). Of course, the procedure adopted to guarantee the compatibility between the scaling factors related to the DSFs in the two states involved in the damage detection process (i.e. performing an additional scaling operation on the DSFs using the total-mass-ratio w) works adequately if the approximations on the effective scaling factors are low. Otherwise, if higher approximations affect the effective scaling factors on the DSFs, then problems may arise when the procedure to ensure the compatibility of such scaling factors is applied. It is considered that this effect is the main reason for which a clear separation between the undamaged and the damaged configurations of the second experimental test (with mass variations) was not found using the damage index based on Mahalanobis distance and the Duan's PFM technique in the cases characterized by a limited number of modes (i.e. the cases r = 3,2,1, shown in Fig. 6.25).

A second effect must be considered to interpret and understand the results obtained for the second experimental test (with mass variations before and after damage). Of course, the problem described in the previous paragraph (i.e. the problem related to the compatibility of the scaling factors on the DSFs) does not affect the results obtained using the index $eMAC_{id}$. As already shown both in the analytical formulation and in the numerical analyses, this index in fact is not sensitive to the scaling factors on the DSFs. However, both the index based on Mahalanobis distance and the index based on the evaluation of the error in the MAC_{id} are subjected to the effects of the modal (or flexibility) truncation errors when the calculations are performed using a limited number of modes (i.e. for $r < n$, where n is the total number of DOFs of the MDOF structure). This is because, by considering two structures (one undamaged and one that is potentially damaged) any damage metric evaluated in the modal flexibility-based approach by considering a number of structural modes equal to r (with $r < n$) can be in general different from the same metric evaluated using all the structural modes (i.e. $r = n$). The difference between the metric evaluated for $r <$

n and the metric evaluated for $r = n$ can be considered as a modal truncation error on the damage metric. The modal truncation effects on the damage metrics are, of course, related to the modal truncation errors that were discussed in Chapter 4. However, one important difference between the truncation effects considered in Chapter 4 and the ones related to this chapter must be highlighted. In Chapter 4 the truncation errors were evaluated on quantities obtained in the modal flexibility approach (e.g. MF-based deflections and interstory drifts) that are related to a single structural state (as shown in Chapter 4, the errors were evaluated between a truncated solution obtained for $r < n$ and the exact solution – i.e. $r = n$). When considering, on the contrary, the damage metrics the modal truncation effects are generated by the fact that the metric is computed considering two structural states and two damage sensitive features, and each DSF represents a truncated solution calculated using a limited number of modes.

This premise on the modal truncation errors related to the damage metrics can be used to interpret the results obtained for the two experimental tests using the index $eMAC_{id}$ and considering all the possible subsets of modes included in the calculations $r = 3,2,1$ (when the Duan's PFM technique was applied). The effects of the modal truncation errors on the considered damage index are clearly evident in Fig. 6.26, where the results of the damage detection performed on the data of the second experimental test (characterized by mass variations before and after damage) are presented. As evident in the figure, the effects of the modal truncation errors increase by considering lower values of the parameter *r*, and for the case $r = 1$ the separation between the undamaged and the damaged configurations is lost. On the contrary, as shown in Fig. 6.22, the modal truncation effects on the damage metric are much less evident in the results of $eMAC_{id}$ obtained for the first experimental test (where the masses of the structure are unchanged before and after damage). In such case, the values of the damage index obtained for $r = 3,2,1$ are similar to the corresponding values obtained for the case $r = 4$, and using the damage index the undamaged configurations can be clearly distinguished from the damaged ones for any value of the parameter *r*. The modal truncation errors have thus negatively affected the considered damage metric only in the case in which there are mass variations before and after damage.

One final observation on the truncation errors related to the damaged metrics must be made to conclude this section. Of course, modal truncation effects are also present in the damage detection results obtained using the proposed approach and the Bernal's PFM technique on the data of the second experimental test. However, the Bernal's PFM technique can only be applied when a sufficient number of modes is considered (i.e. when the condition expressed by Eq. 6.8 is fulfilled), and thus in such case the effects of the modal truncation errors are relatively low.

Chapter 7

Conclusions

The present dissertation has been developed in the area of research that deals with the application of the vibration-based structural health monitoring and damage detection techniques on civil structures. Such techniques can be conveniently applied on civil structures that are tested, for example, under ambient vibrations and during their normal operating conditions. The types of structures that have been considered in the thesis are mainly building structures. This choice was done since the number of the damage detection studies that have been carried out in the literature for such structures is lower than the number of studies related to other structures, such as bridge structures [Koo et al., 2010].

Modal flexibility (MF)-based approaches for damage detection are the methods that have been considered in the dissertation. Specifically, the thesis has focused on a subclass of such modal flexibility (MF)-based methods where the main operation that has to be performed in the damage detection process is to determine the modal flexibility-based deflections of the structures. Such deflections are calculated starting from modal flexibility-models of the structures estimated from vibration tests and by applying loads that are termed “inspection loads”. The modal flexibility-based deflections are considered as important sources of information for detecting and localizing damage.

The Uniform Load Surface method [Zhang, 1993; Zhang & Aktan, 1995; Zhang & Aktan, 1998] and the method proposed by [Koo et al., 2010; Koo et al., 2011; Sung et al., 2012], which in the present thesis is referred to as Positive Shear Inspection Load (PSIL) method, are the modal flexibility-based methods that represent the theoretical background for the dissertation. The first approach was applied mainly on bridge structures. On the contrary, the second method was specifically developed for building structures, and the thesis has thus focused mainly on this second method. The fundamental characteristics of the PSIL method, extensively described in Chapters 1 and 3, are briefly summarized herein. a) The method is formulated for building structures that can be modeled as shear building structures. b) The modal flexibility-based deflections of the building structures have to be calculated by applying special loads termed Positive Shear Inspection Loads (PSIL). Such loads are loads that induce positive shear forces in all the stories of the shear building structure [Koo et al., 2010], and, among all the potential PSIL loads, the authors suggest using a uniform load as the inspection load (which is the same load adopted in the Uniform Load Surface method [Zhang & Aktan, 1998]). c) The parameters considered as damage sensitive features in the PSIL method are the interstory drifts computed from the modal flexibility-based deflections.

The dissertation has focused on three main problems, which have been defined and analyzed after having recognized potential research gaps in the literature. Research investigations have been carried out and approaches have been proposed in an attempt to address the three above-mentioned problems. The main conclusions drawn for each of the three analyzed problems are reported in the following.

7.1 Conclusions on the three main problems analyzed in the thesis

7.1.1 Problem no. 1: Truncation error analysis on modal flexibility-based deflections

The first problem, considered in the thesis, has concerned the study of the truncation errors that are introduced on modal flexibility-based deflections of building structures when such deflections are estimated using only a subset of structural modes. Having

the necessity of dealing with a limited number of modes is, in fact, a common situation that occurs in practical applications of modal testing on real-life structures. Referring to the topic of truncation errors analysis on modal flexibility-based deflections, the research investigations were carried out in the thesis to attain two general purposes: predicting or reducing the truncation effects on the modal flexibility-based deflections of building structures.

Prediction of the modal truncation effects

In the thesis an approach for truncation error analysis has been proposed to have an indication of the truncation effects expected on the modal flexibility-based deflections of building structures evaluated for inspection loads with generic distributions. The definition of an index termed load participation factor (LPF) is the fundamental aspect that characterizes the proposed approach. In particular, the approach was investigated to continue the research presented in the work by [Zhang & Aktan, 1998], where truncation error studies were performed on structural deflections evaluated for a uniform inspection load and where a criterion based on mass participation factor (MPF) is reported.

The index defined as load participation factor (LPF) represents basically the relative contribution of each mode of the considered structure to the modal flexibility-based deflection. The expression of the load participation factor was deduced analytically by performing simple algebraic and matrix operations on the relationships between the modal flexibility matrices, the vectors of the modal flexibility-based deflections, and the vectors of the applied loads (as shown in Section 4.2). According to the expression of the load participation factor, this index evaluated for one mode depends on the mode shape of that mode, on the load applied to evaluate the deflection, and on the distribution of the structural masses.

The main idea behind the proposed approach is that by calculating the contribution (i.e. the cumulative load participation factor) of the modes included in the truncated deflection, the relative contribution of the missing modes (i.e. the modes not included in the calculations) can be then determined. This is done by considering the simple principle for which the sum of the two contributions related, respectively,

to the modes included in the calculations and to the missing modes is equal to one. Finally, the cumulative load participation factor of the modes not included in the truncated deflection can be used to obtain an a-priori indication of the truncation effects expected on the modal flexibility-based deflection.

The proposed approach for truncation error analysis based on the load participation factor was verified using both numerical analyses and an experimental case study. Referring to the former, the analyses were conducted on numerical models of plane shear building structures, and a Monte Carlo simulation was adopted to consider in the analyses several structural cases where both the masses of the structure and the applied inspection loads are characterized by generic distributions. The truncation errors were computed by directly comparing truncated and non-truncated deflections using different criteria (e.g. single-DOF errors, maximum or root-mean-square values related to the errors in the single components of the deflections). On the contrary, according to the proposed approach, the load participation factors were computed only for the modes used for calculating the truncated deflection (i.e. a limited subset of modes). The results showed that the proposed load participation factors are highly correlated with the truncation errors on the modal flexibility-based deflections. On the contrary, for the considered structural cases no correlations were found between the truncation errors and the mass participation factors.

The above-mentioned result does not imply that the approach reported in the work by [Zhang & Aktan, 1998] and based on the mass participation factor is not correct. The important point that must be highlighted is that in the study presented in this dissertation a more general situation than the one presumably analyzed by [Zhang & Aktan, 1998] has been taken into account. Here the observation is made in hypothetical terms because, as already mentioned in Chapter 4, the criterion based on mass participation factor is mentioned in the work by [Zhang & Aktan, 1998] but it is not applied in the numerical analyses performed by the authors. For example, if one considers a structure with a uniform mass distribution (such as a simple bridge structure with a uniform cross section, as the one considered in [Zhang & Aktan, 1998]) and the deflections due to a uniform load, then the criterion based on mass participation factor is perfectly suitable for performing the truncation error study. However, in a more general case in which the distribution of the masses of the

structure is different from the distribution of the applied load, then one should refer to the load participation factor to perform the truncation error study, instead of the mass participation factor. The load participation factor, in fact, is an index for which the contribution related to the applied load and the contribution related to the structural masses are clearly separated and identifiable (as evident if one analyzes the analytical formulation of the LPF index, see Section 4.2). This is, of course, not true for the mass participation factor which depends exclusively on the structural masses and does not depend on the load that is applied to calculate the modal flexibility-based deflection. Referring to the topic of truncation error study on modal flexibility-based deflections, the proposed criterion based on load participation factor can thus be seen as a generalization of the criterion based on mass participation factor [Zhang & Aktan, 1998].

An important feature of the investigated LPF-based approach was found when the criterion has been applied in the numerical analyses. When considering plane shear building structures and the modal flexibility-based deflections of such structures due to positive shear inspection loads with random distributions, the LPF-based approach can be used not only to have an indication of the amount of the truncation effects expected on the modal flexibility-based deflections. The approach can be also used to have a quantitative measure (i.e. an a-priori estimate) of the maximum value of the single-DOF truncation errors expected on the deflections. Referring to this point, it is worth noting that adopting an index that has to be evaluated for each structural mode to obtain such a-priori estimate of the truncation errors is an aspect that was not considered in the work by [Zhang & Aktan, 1998]. In fact, the criterion based on mass participation factor is suggested by [Zhang & Aktan, 1998] only to have an indication of the amount of the modal truncation effects.

The property of the load participation factor mentioned in previous paragraph can be explained as follows. As shown in Chapter 4, the load participation factor was developed at first by considering the general expression of the modal flexibility matrix of a generic structural system with a diagonal mass matrix (Section 4.2). Then, after having derived the analytical expressions for calculating the truncation errors on the modal flexibility-based interstory drifts of shear building structures (Section 4.2.1), it was found that the expression of the truncation error related to the lower DOF of the

structure is equivalent to the expression of the load participation factor. As shown in the analyses presented in Chapter 4, when considering plane shear building structures and the modal flexibility-based deflections of such structures due to positive shear inspection loads, the truncation errors have a significant impact on the displacement of the lower DOF. In other words, in most of the cases the maximum value of the truncation errors on the single components of the deflections occur at the first DOF, and thus the load participation factor can be used to obtain a prediction of such maximum error. The validity of the LPF-based approach and of the use of such approach to predict the maximum truncation errors on the modal flexibility-based deflections of shear building structures was also confirmed using the data of an ambient vibration test that was performed on a steel frame structure[1].

As a final remark, it should be mentioned that the LPF-based approach proposed for truncation error analysis on modal flexibility-based deflections has been applied in the thesis on building structures that can be modeled as plane shear building structures. In future studies, this approach can be applied, for example, on more complex building structures. Moreover, the application of the LPF-based approach to other types of structures may be also considered in the future.

Reduction of the modal truncation effects

Referring to the topic of truncation error analysis, research investigations were also carried out in an attempt to reduce the truncation errors on the modal flexibility-based deflections of plane shear building structures evaluated for a uniform inspection load. As shown by the numerical analyses presented in Chapter 4, such truncation errors can not be in general considered as negligible especially for structures with mass irregularities. The attempt to reduce the above-mentioned truncation errors was pursued by considering inspection loads different from the uniform load.

As discussed in Section 4.4.1, among the different alternative loads that were taken into account in the initial phase of the research, a load that is proportional to the

[1] The considered data belong to the experimental phase of the benchmark studies for vibration-based damage detection that were sponsored by the IASC-ASCE Task Group for Structural Health Monitoring [Dyke et al., 2003; Ventura et al., 2003; Dyke, 2011].

mass distribution of the structure showed interesting results. In the thesis this load is referred to as mass proportional load (MPL), and it has a special property. If the proposed approach for truncation error analysis based on load participation factor (LPF) is applied by considering a mass proportional load, then the expression of the load participation factor is equal to the expression of the mass participation factor (MPF). As already mentioned in previous section, this last index is the one adopted in the criterion for truncation error analysis mentioned in the work by [Zhang & Aktan, 1998].

In the numerical analyses presented in Section 4.4.2, various configurations of models of plane shear building structures with increasing amounts of mass irregularities were considered, and the truncation errors on the components of the deflections due to the mass proportional load (MPL) were compared with the errors on the deflections due to the uniform load (UL). The analyses were also performed by comparing the truncation errors on the interstory drifts related to such modal flexibility-based deflections. Referring to both the two types of truncation errors (i.e. the errors on the components of the modal flexibility-based deflections and the errors on the interstory drifts), the results showed that for the large majority of the analyzed configurations, the truncation errors due to the mass proportional load are lower compared to those related to the uniform load. In the few cases where the result was not found, the errors related to the two loads were comparable.

The results of the comparison between the mass proportional load and the uniform load suggest that in principle in real-life applications of structural identification and damage detection for structures with mass irregularities, a mass proportional load might be considered as an alternative to the uniform load, with the aim of reducing the truncation errors on the modal flexibility-based deflections. In the analyses performed in the present dissertation, however, the application of a mass proportional load in the damage detection procedures based on modal flexibility-based deflections has not been considered and investigated because some inherent limitations related to such potential approach have been recognized.

For example, in the thesis one case where the effects of the modal truncation errors have affected the results of the damage detection for structures with mass

irregularities has been shown in Section 6.4.2.2 of Chapter 6. For the considered steel frame structure and only in the experimental test where mass variations are present before and after damage, the modal flexibility-based indices for damage detection evaluated for a very limited number of the modes have been negatively affected by modal truncation errors. In such case, one might question whether the use of a mass proportional load (MPL) as the inspection load would have reduced the effects of the modal truncation errors on the damage metrics. This potential approach was considered but not applied because of the following limitation of the mass proportional load. A mass proportional load is a potential inspection load that is system dependent. Thus, in the general case in which mass variations are present before and after damage, the potential mass proportional inspection loads are different for the two states involved in the damage detection process. However, a basic assumption in the original formulation of the Positive Shear Inspection Load (PSIL) method [Koo et al., 2010] for damage detection is that the same inspection load (for example, a uniform load) has to be applied both to the undamaged and to the possibly damaged structures. This requirement, as shown in Chapter 3, guarantees that for shear building structures eventual changes in the modal flexibility-based deflections can be associated to the presence and the location of the damage. On the contrary, if the inspection loads are varied for the two states involved in the damage detection process, changes in the modal flexibility-based deflections might be due not only to eventual damage present in the structure, but also due to the variations in the loads. This is, of course, an undesirable situation that might lead to misleading results in the damage detection process.

7.1.2 Problem no. 2: Damage detection on 3D building structures using modal flexibility (MF) based deflections

In the context of the second main problem considered in the thesis, research investigations were carried out in an attempt to extend the Positive Shear Inspection Load (PSIL) method for damage detection [Koo et al., 2010], originally formulated to be applied on building structures that can be modeled as plane structures, to the case of more complex building structures. These research investigations were carried out by considering simple

rectangular "box type" 3D building structures, characterized by either plan-symmetric or plan-asymmetric distributions of the story stiffness.

At first, the original formulation of the Positive Shear Inspection Load method was modified to define an approach that can be applied on 3D shear building structures, instead of plane shear building structures. According to the investigated methodology, modal flexibility matrices of 3D building structures are estimated from ambient vibration measurements. Then, the modal flexibility-based deflections of the considered building structure are evaluated by performing two separate analyses and by applying inspection loads in the two prevalent directions of the considered structure (which, as already mentioned, is a simple rectangular "box type" structure). The considered inspection loads are translational uniform loads (UL) applied in one or in the other direction of the building structure, and they are thus the same type of loads applied in the original formulation of the PSIL method. The components of the modal flexibility-based deflections related to one or the other direction of the structure are used for damage localization and quantification using the same criteria of the original formulation of the PSIL method.

The above-mentioned methodology was applied on a one-third scale four-story steel frame structure that was tested under ambient vibrations. One of the main characteristics of the structure is the presence of diagonal wall braces (i.e. tie-rods) in each bay and at each story of that structure, and these elements can be easily removed to impose reductions in the story stiffness. The experimental tests were thus planned and performed for damage detection purposes, and the diagonal wall braces were removed from the structure in different structural configurations to simulate damaged conditions. The diagonal wall braces were removed in generic positions of the considered steel frame structure (i.e., at different stories and in different directions of the structure). Moreover, structural configurations that are characterized by either plan-symmetric or plan-asymmetric distributions of the story stiffness at the damaged levels were considered. The results of the analyses performed using the modified version of the Positive Shear Inspection Load method showed that the damage can be localized by identifying the stories and the directions where the stiffness reductions have been applied. The effectiveness of the methodology was also evaluated by analyzing the results obtained for all the structural configurations that were tested, and a high success rate in damage localization was attained. Referring to the damage quantification, the results showed that

the amount of damage estimated for each damaged story and for a certain direction of the structure (using the damage severity index) is slightly overestimated when configurations with plan-asymmetric distributions of the story stiffness at the damaged stories are considered. This result was observed when the damage severity obtained for a plan-asymmetric configuration with a certain number of braces removed in one direction was compared with the damage severity obtained for a plan-symmetric configuration with the same number of braces removed in the same direction. In particular, in the comparison the result obtained for the plan-symmetric configuration was considered as the target value of the damage severity since in such case (i.e. when considering a plan-symmetric structure) the adopted methodology is basically equivalent to the original formulation of the PSIL method.

To correct the slight overestimations that were obtained in the damage quantification for the plan-asymmetric configurations, an attempt was made to develop an improved version of the damage detection methodology applicable on simple rectangular "box type" 3D building structures. In this improved version of the methodology the vectors of the applied inspection loads (indicated as "UL+M" loads) include not only translational components with unitary values applied in the prevalent directions of the structure (similarly to the uniform loads "UL"), but also torsional components (i.e., moments of torsion). Such moments of torsion are specifically introduced in the "UL+M" inspection loads to avoid relative rotations between the stories in the modal flexibility-based deflections of the structures, and they can be determined after having estimated the centers of stiffness of each story of the structure. This last operation, as also shown in the work by [Bernal & Gunes, 2004], is an operation that can be performed using information contained in the modal flexibility matrices estimated for the building structure. The improved version of the methodology was applied by performing numerical analyses on a model of a structure that is similar to the one considered in the ambient vibration tests. For structural configurations of that model characterized by a generic plan-asymmetric distribution of the story stiffness at the damaged story, the results showed that the methodology based on "UL+M" inspection loads can provide estimates of the damage severity that are more accurate than the ones obtained using the "UL" inspection loads.

The improved methodology based on "UL+M" inspection loads was also applied on the experimental data of the steel frame structure tested under ambient vibrations. In such case, however, the procedure for estimating the centers of stiffness of each story of the structure (successfully applied, on the contrary, in the numerical analyses) provided not accurate results. This drawback, as discussed in Section 5.2.3, is most likely due to the modal truncation effects and the uncertainties that affect the modal flexibility matrices of the considered structure tested under ambient vibrations. Notwithstanding this drawback, the improved damage detection methodology based on "UL+M" inspection loads was applied, in any case, on the data of the ambient vibration tests by adopting an approximated and simplified approach to estimate the positions of the centers of stiffness of the structure from the modal flexibility matrices. This approximated approach is valid under certain simplifying assumptions and only for some configurations of the steel frame structure with certain characteristics (as shown in Section 5.2.3). For such configurations characterized by a plan-asymmetric distribution of the story stiffness at the damaged level, the results showed that the improved procedure based on "UL+M" inspection loads can correct the slight overestimations that are obtained, on the contrary, in the damage quantification when the "UL" inspection loads are applied.

As a final remark, it should be mentioned that the research investigations related to the second problem analyzed in the thesis were carried out for simple rectangular "box type" 3D building structures by assuming that the geometric center of such structures is also the center of mass. Moreover, both in the experimental and in the numerical analyses the considered structural configurations have a plan-asymmetric distribution of the story stiffness only at the damaged levels. In other words, at the undamaged stories of the damaged configurations and at all the stories of the undamaged configurations, the considered structures are characterized by a plan-symmetric distribution of the story stiffness. Analyses for damage localization (and, eventually, for the more challenging problem of the damage quantification) on more complex structures may be considered in the future. Such more complex structures can be, for example, generic 3D building structures with generic positions of the centers of mass and the centers of stiffness both in the undamaged and in the damaged configurations.

7.1.3 Problem no. 3: Damage detection using proportional MF-based deflections with minimal or no a-priori information on the structural masses

In the context of the third main problem considered in the thesis, a modal flexibility-based approach for output-only damage detection in building structures that can be applied with minimal or no a-priori information about the masses of the structures has been investigated. This proposed approach has been developed on the basis of the theory behind the Positive Shear Inspection Load method [Koo et al., 2010; Koo et al., 2011; Sung et al., 2012]. In particular, the proposed approach has been investigated because in the above-mentioned works, where the original formulation of the PSIL method is presented, the mass normalization of the mode shapes obtained from output-only modal identification was carried out using an a-priori estimate of the system mass matrix. The proposed approach is thus an attempt to make the output-only damage detection process based on modal flexibility-based deflections independent as much as possible from an a-priori estimate of the mass matrix of the building structure.

The problem of obtaining modal flexibility matrices directly from output-only vibration data was also investigated and solved by some authors [Bernal, 2001; Bernal & Gunes, 2002; Duan et al., 2005; Duan et al., 2007] in the context of another damage detection method - i.e. the Damage Locating Vector (DLV) method [Bernal, 2002]. In particular, two procedures were defined, respectively, in the works by [Bernal, 2001; Duan et al., 2005] to extract the distribution of the structural masses (i.e. a proportional mass matrix) and to assemble proportional flexibility matrices from output-only vibration data. These two procedures, originally formulated for the DLV method and indicated in the present thesis as Proportional Flexibility Matrix (PFM) techniques, were adapted and integrated into the framework of the proposed approach for damage detection. As discussed in Chapter 6, both the two PFM techniques were considered because, according to the proposed approach, the choice of using one or the other technique depends on the number of structural modes that are identified from the vibration test. Theoretically, if a limited number of modes is considered the

procedure by Bernal [2001] is more accurate than the procedure by Duan et al. [2005][2]. However, the procedure by Bernal [2001] can be applied only if a certain minimum number of modes is considered, while the procedure by Duan et al. [2005] can be theoretically applied using any subset of modes. The approach adopted in the proposed damage detection methodology is thus to use the procedure by Bernal [2001] if applicable, otherwise the procedure by Duan et al. [2005] is considered. Moreover, since the two techniques adopt different strategies to assemble the proportional flexibility matrices, the following approach was considered in the proposed methodology. To assemble the proportional flexibility matrices the strategy used in the procedure by Bernal [2001] was considered (this procedure is unaltered with respect to the original formulation). On the contrary, a modified implementation of the procedure by Duan et al. [2005] (which, in any case, does not substantially alter the fundamental equations of the original procedure) was adopted in the proposed approach to have a unified strategy to assemble the proportional flexibility matrices.

The main steps of the approach proposed for output-only damage detection in building structures that can be modeled as plane shear building structures are briefly summarized herein. The PFM techniques [Bernal, 2001; Duan et al., 2005] are used to estimate proportional flexibility matrices of the building structures from output-only vibration data. Then, uniform inspection loads are applied to calculate modal flexibility-based deflections that are proportional with respect to the corresponding true and scaled deflections. Starting from these proportional modal flexibility-based deflections vectors that contain the interstory drifts[3] of the structures are determined, and such vectors are considered as damage sensitive features (DSFs). Finally, to detect the existence of damage in shear building structures, two damage indices have been investigated and proposed. In particular, both the two indices were considered because such indices are characterized by two different criteria to evaluate the differences or

[2] This is because in the procedure by Duan et al. [2005] pseudo-inverse operations are performed on truncated mode shape matrices, while this operation, which inevitably introduces approximations, is not present in the procedure by Bernal [2001]. The statement reported in the text is also confirmed by the results of numerical analyses shown in Chapter 6.

[3] Considering the interstory drifts of shear building structures as damage sensitive features is an operation that is also performed in the original formulation of the Positive Shear Inspection Load (PSIL) method [Koo et al., 2010].

the similarities between the vectors assumed as damage sensitive features. The first index is based on the evaluation of the Mahalanobis distance (MD) between the vectors assumed as damage sensitive features. The second index (indicated in the thesis as MAC_{id}^{*}) is based on the evaluation of the degree of correlation between the vectors assumed as DSFs. This damage index has the same formulation of the Modal Assurance Criterion [Allemang & Brown, 1982], which is traditionally applied on mode shape vectors, but, according to the proposed approach, the criterion is applied on vectors of proportional MF-based interstory drifts.

One important aspect that should be mentioned is the fact that, as shown in Section 6.2, the procedure proposed to estimate the proportional modal flexibility-based deflections was also developed with the objective of providing a physical interpretation on the value assumed by the scaling factor between the proportional and the true deflections. This scaling factor is, of course, undetermined since the calculation of the proportional deflections is performed from output-only vibration data without any a-priori information on the mass matrix of the structure. However, for the considered structures (i.e. shear buildings with a diagonal mass matrix), it has been shown in Chapter 6 that using an appropriate normalization on the proportional mass matrix estimated from the data using the PFM technique, the missing scaling factor on the proportional deflections is theoretically equal to the total mass of the structure.

The effectiveness of the proposed approach and of the two damage indices has been evaluated considering both simulations on a numerical model of a 6-story shear-type frame structure and experimental vibration tests conducted on a 4-story steel frame structure. In both cases, damaged configurations were created by imposing stiffness reductions at one or more stories of the structure. Moreover, both in the numerical and in the experimental validation, the approach has been tested in two different situations: firstly, the case in which the masses of the structure are unchanged before and after damage was considered; secondly, the case in which mass variations are present between the two structural states involved in the damage detection process was analyzed. Such mass variations mimic changing operational conditions that the structures can experience in practice [Farrar & Worden, 2013] and structural modifications that are not related to a damaged state. In particular, this second case

(where the structural masses are varied before and after damage) was analyzed to test the proposed approach and the two damage indices in the general case in which the unknown scaling factors on the vectors of the proportional MF-based interstory drifts (related to the undamaged and to the possibly damaged states) are theoretically different.

The results of the numerical and experimental analyses have demonstrated the effectiveness of the two proposed damage indices. Moreover, the analyses have confirmed the main difference between the two indices. According to the proposed approach, the first index based on the Mahalanobis distance (MD) can be applied if the ratio between the total mass of the structure in the undamaged and in the possibly damaged states is known. This is the sole parameter that has to be known a-priori to perform the damage detection using this index and starting from output-only vibration data. The parameter is required to guarantee the compatibility of the scaling factors related to the damage sensitive features. On the contrary, the second index MAC_{id}^{*} (i.e. the one based on the evaluation of the degree of correlation between the DSFs) is not sensitive to the scaling factors on the vectors of the proportional MF-based interstory drifts. Due to this property, this second index can be calculated not only by estimating the distribution of the masses of the structure from the data - using the procedures defined by Bernal [2001] and Duan et al. [2005] - but also without the need of an additional parameter (known a-priori) that provides information on the relationship between the structural masses in the two states involved in the damage detection process (as required, on the contrary, in the calculations related to the first index based on Mahalanobis distance).

In the framework of the proposed approach for output-only damage detection, the second index MAC_{id}^{*} has thus shown more promising results than the index based on Mahalanobis distance. The index MAC_{id}^{*}, in fact, is a modal flexibility-based index that can be calculated starting from the results of any output-only modal identification technique, in terms of natural frequencies and arbitrarily-scaled mode shapes, and without any a-priori information on the masses of the building structure. In other words, the proposed approach when used with the second index MAC_{id}^{*}, is a modal flexibility-based approach for damage detection applicable starting from output-only vibration response data of building structures that is completely data-driven.

As a final remark on the third problem considered in the thesis, it is important to mention that the original formulation of the Positive Shear Inspection Load (PSIL) method [Koo et al., 2010] was developed for localizing (or quantifying) the damage in building structures. On the contrary, the proposed approach has focused on detecting the existence of the damage. This choice was made to start developing a modal flexibility-based approach applicable from output-only vibration data with minimal or no a-priori information about the masses of the structures that aims to reach an achievement (i.e. detecting the existence of damage) that is simpler than other more complex achievements (such as damage localization or damage quantification). To continue the investigations related to the third problem analyzed in the thesis, a natural next step is thus to extend the proposed modal flexibility-based approach so that it can be used to localize (or eventually quantify) damage in building structures. Preliminary thoughts on such more complex problem suggest that proportional modal flexibility-based deflections of shear building structures calculated by estimating the distribution of the structural masses directly from the data can be employed for damage localization and quantification. In particular, in the general case in which the masses of the structure are varied before and after damage, it is expected that a correct localization (or quantification) of the damage can be obtained by adapting the criteria of the original PSIL method applicable on true/scaled deflections to the case of the proportional deflections and if a parameter that defines the relationship between the masses in the two structural states is known a-priori (for example, the ratio between the total mass of the structure in the undamaged and in the possibly damaged states, as adopted in the thesis for evaluating the damage index based on Mahalanobis distance). Referring on the contrary to the scenario considered in the thesis when evaluating the index MAC_{id}^{*} for damage detection (i.e. mass variations can be present before and after damage, but such variations are unknown and the calculations are performed without any a-priori information on the masses), it is presumed that localizing and quantifying damage may be much more complex tasks.

7.2 Concluding remarks and directions for future research

The main conclusions and potential directions for future research related to each of the three main problems considered in the thesis have been discussed in previous sections. This section presents some concluding remarks common to all the three analyzed problems and discusses potential directions for future research that derive mainly from the limitations of the research carried out in the dissertation.

First of all, the general problem of vibration-based damage assessment in building structures has been considered both in the second and the third problems analyzed in the thesis and, specifically, using the following strategy. Referring to the second problem, the modal flexibility-based approach for damage assessment starting from output-only vibration measurements has been investigated by considering "box type" 3D building structures and by assuming that an a-priori estimate of the system mass matrix of the structure is available. On the contrary, in the context of the third problem, the modal flexibility-based approach for output-only damage assessment has been developed by considering building structures that can be modeled as plane structures and information on the structural masses are extracted directly from the vibration data (specifically, from mode shape vectors). A natural next step for future research may be to combine the second and the third problems in an attempt to develop an approach for vibration-based damage assessment (based on the evaluation of modal flexibility-based deflections due to inspection loads) that can be applied on "box type" 3D building structures and with minimal or no a-priori information on the structural masses.

Secondly, in all the modal flexibility-based approaches investigated in the thesis it is assumed that vibration measurements are available at all the stories of the building structure (and, specifically, at all the prevalent DOFs of the structure). This is an assumption that is also made in the original formulation of the Positive Shear Inspection Load method [Koo et al., 2010]. As shown in several passages of the thesis, obtaining vibration measurements at all the stories of the building structure is not necessarily related to the requirement of having sensors simultaneously at all the stories. For example, as discussed in Sections 2.2.1 and 5.1.1 of the thesis, in ambient vibration tests on building structures multiple data sets can be acquired using both

reference and roving sensors, and in such case the number of the sensors to be used in the test can be lower than the number of the DOFs to be measured. However, performing this operation on medium- and high- rise building structures may be time consuming or may increase the cost of the experimental test, and in many practical cases having measurements available at all the stories of the structure is a condition that is seldom satisfied. Thus, the situation of dealing with measurements available at a limited number of stories of the building structure should be considered in the future. As suggested in the work by [Bernal & Gunes, 2004], model updating approaches can be conveniently applied in such case, and, of course, one can use directly information contained in the updated model to perform the damage detection. An alternative potential approach that is based on the general idea adopted in the thesis (i.e. trying to use as much information as possible derived from the experimental test) is the following. After having defined a reliable model of the structure (for example, using model updating, if needed), modal expansion techniques, such as the ones described in [Brincker & Ventura, 2015], can be used to expand experimental mode shapes defined only at the measured DOFs. In this way, mode shapes defined at all the prevalent DOFs of the building structure can be obtained, and such mode shapes may be considered for assembling modal flexibility matrices and for estimating modal flexibility-based deflections of the structure.

Appendix A

Output-only modal identification techniques adopted in the thesis and applications

This appendix presents the main steps of the two output-only modal identification techniques that are applied in the present dissertation. These two techniques are the Eigensystem Realization Algorithm (ERA) [Juang & Pappa, 1985], applied in the output-only case according to the Natural Excitation technique (NExT) [James et al., 1993], and the Frequency Domain Decomposition (FDD) [Brincker, Zhang & Andersen, 2001]. The first method (i.e. the NExT procedure based on ERA) is a time domain identification method, while the second technique works in frequency domain. In the final part of this appendix some numerical and experimental case studies are also presented, and in these case studies the two above-mentioned output-only modal identification techniques were applied.

A.1 Eigensystem Realization Algorithm (ERA)

As already mentioned in Chapter 2, the Eigensystem Realization Algorithm (ERA) is a time-domain modal identification method that was developed in the framework of the system and control theory. In these fields the systems are generally and conveniently modeled using a state space formulation (in other words, state space models are adopted). For this reason, before presenting the steps of the ERA identification method (Section A.1.2), it is shown (in next section) how the

fundamental equation of motion of a generic multi-degree-of-freedom (MDOF) structural system [Clough, 1975; Chopra, 2000] can be transformed into the equivalent state space formulation [Juang, 1994; Alvin et al., 2003].

A.1.1 Dynamics of an MDOF structure in the state space formulation

The continuous-time second-order equation of motion of an n-DOF damped structure under forced excitations is expressed as

$$\boldsymbol{M}\,\ddot{\boldsymbol{v}}(t) + \boldsymbol{C}\,\dot{\boldsymbol{v}}(t) + \boldsymbol{K}\,\boldsymbol{v}(t) = \widehat{\boldsymbol{B}}\;\boldsymbol{u}(t) \tag{A.1}$$

where $\boldsymbol{v}(t)_{n\times 1}$ is the displacement vector, $\boldsymbol{u}(t)_{i\times 1}$ is the input force vector, $\widehat{\boldsymbol{B}}_{n\times i}$ is the input-state influence matrix, i is the number of the inputs, and $\boldsymbol{M}_{n\times n}$, $\boldsymbol{C}_{n\times n}$, $\boldsymbol{K}_{n\times n}$ are the mass, damping and stiffness matrices, respectively. It is worth noting that the notation used in this appendix for quantities like displacements and forces is different from the notation used in previous chapters of the thesis. The notation adopted in this appendix follows the original formulation presented in the works of [Juang, 1994; Alvin et al., 2003].

To obtain a state space model of the structural system, it is introduced, in addition to Eq. (A.1), an observation or output transform equation, which is defined as follows

$$\boldsymbol{y}(t) = \boldsymbol{\Xi}_a\,\ddot{\boldsymbol{v}}(t) + \boldsymbol{\Xi}_v\,\dot{\boldsymbol{v}}(t) + \boldsymbol{\Xi}_d\,\boldsymbol{v}(t) \tag{A.2}$$

where $\boldsymbol{y}(t)_{o\times 1}$ is the observation vector, o is the number of the outputs, and $\boldsymbol{\Xi}_a$, $\boldsymbol{\Xi}_v$, $\boldsymbol{\Xi}_d$ are the $o\times n$ state-output influence matrices which relate the accelerations, velocities, and displacements of some DOFs of the structure with the measured outputs contained in the vector $\boldsymbol{y}(t)$. A physical displacement-velocity (PDV) model [Alvin et al., 2003] is considered to define the so-called state vector $\boldsymbol{x}(t)$

$$\boldsymbol{x}(t) = \begin{bmatrix}\boldsymbol{v}(t)\\ \dot{\boldsymbol{v}}(t)\end{bmatrix}_{2n\times 1} \tag{A.3}$$

which is a $2n\times 1$ vector. Using this vector, the state space representation of the structural system can be then derived, and this representation is formed by the two first-order matrix differential equations that follows

$$\begin{cases} \dot{\boldsymbol{x}}(t) = \boldsymbol{A}\,\boldsymbol{x}(t) + \boldsymbol{B}\,\boldsymbol{u}(t) \\ \boldsymbol{y}(t) = \boldsymbol{C}\,\boldsymbol{x}(t) + \boldsymbol{D}\,\boldsymbol{u}(t) \end{cases} \tag{A.4}$$

This last equation (Eq. A.4) is obtained by appropriately modifying both Eqs. (A.1, A.2) and by introducing the state vector $\boldsymbol{x}(t)$. In particular, the relationships between the terms present in Eq. (A.4) and the terms present in Eqs. (A.1, A.2) are the following

$$\boldsymbol{A} = \begin{bmatrix} \boldsymbol{0} & \boldsymbol{I} \\ -\boldsymbol{M}^{-1}\boldsymbol{K} & -\boldsymbol{M}^{-1}\boldsymbol{C} \end{bmatrix}_{2n\times 2n} \tag{A.5}$$

$$\boldsymbol{B} = \begin{bmatrix} \boldsymbol{0} \\ \boldsymbol{M}^{-1}\widehat{\boldsymbol{B}} \end{bmatrix}_{2n\times i} \tag{A.6}$$

$$\boldsymbol{C} = \begin{bmatrix} \boldsymbol{\Xi}_d - \boldsymbol{\Xi}_a\boldsymbol{M}^{-1}\boldsymbol{K} & \boldsymbol{\Xi}_v - \boldsymbol{\Xi}_a\boldsymbol{M}^{-1}\boldsymbol{C} \end{bmatrix}_{o\times 2n} \tag{A.7}$$

$$\boldsymbol{D} = \begin{bmatrix} \boldsymbol{\Xi}_a\boldsymbol{M}^{-1}\widehat{\boldsymbol{B}} \end{bmatrix}_{o\times i} \tag{A.8}$$

According to the terminology used for a generic state space model (Eq. A.4), $\boldsymbol{A}$ is the dynamic system matrix, $\boldsymbol{B}$ is the input influence matrix, $\boldsymbol{C}$ is the output influence matrix, and $\boldsymbol{D}$ is the direct-transmission or feed-through matrix. One of the advantages of the first-order state space formulation when used to represent the dynamics of structural systems is that the formulation is more suitable, with respect to the second-order formulation, to deal with structures characterized by a generic damping (for example, non-proportional or non-classical damping). In addition, a great advantage of the state space formulation, when applied to any dynamic system, is that all the dynamics is embedded into the system matrix $\boldsymbol{A}$ [Alvin et al., 2003].

The solution $\boldsymbol{x}(t)$ of the equation of motion in the state space form is as follows

$$\boldsymbol{x}(t) = \mathrm{e}^{\boldsymbol{A}(t-t_0)}\,\boldsymbol{x}(t_0) + \int_{t_0}^{t} \mathrm{e}^{\boldsymbol{A}(t-\tau)}\,\boldsymbol{B}\,\boldsymbol{u}(\tau)\,d\tau \tag{A.9}$$

where $\boldsymbol{x}(t_0)$ is the initial state of the system at time $t = t_0$ and where the matrix exponential approach is adopted[1].

[1] The matrix exponential for a generic square matrix $\mathbf{W}$ is defined as follows

$$\mathrm{e}^{\boldsymbol{W}} = \sum_{k=0}^{\infty} \frac{1}{k!}\boldsymbol{W}^k$$

The discrete-time representation of the continuous-time state space model can be obtained by substituting the sampled time $t_0 = k\,\Delta t$ and $t = (k+1)\,\Delta t$ in the solution of the equation of motion (Eq. A.9) and in the second equation of the system described in Eq. A.4

$$\begin{cases} \boldsymbol{x}[(k+1)\,\Delta t] = \mathrm{e}^{\boldsymbol{A}\,\Delta t}\,\boldsymbol{x}(k\,\Delta t) + \int_{k\,\Delta t}^{(k+1)\,\Delta t} \mathrm{e}^{\boldsymbol{A}\,[(k+1)\,\Delta t - \tau]}\,\boldsymbol{B}\,\boldsymbol{u}(\tau)\,d\tau \\ \boldsymbol{y}(k\,\Delta t) = \boldsymbol{C}\,\boldsymbol{x}(k\,\Delta t) + \boldsymbol{D}\,\boldsymbol{u}(k\,\Delta t) \end{cases} \tag{A.10}$$

Then, a change of the integration variable $\sigma = (k+1)\,\Delta t - \tau$ is introduced in Eq. (A.10), and, according to the steps presented in [Juang, 1994], the discrete-time first-order matrix difference equation of the state space system is obtained

$$\begin{cases} \boldsymbol{x}_{k+1} = \boldsymbol{A}_d\,\boldsymbol{x}_k + \boldsymbol{B}_d\,\boldsymbol{u}_k \\ \boldsymbol{y}_k = \boldsymbol{C}\,\boldsymbol{x}_k + \boldsymbol{D}\,\boldsymbol{u}_k \end{cases} \tag{A.11}$$

where the discrete form of the dynamic system matrix $\boldsymbol{A}_d$ and the input influence matrix $\boldsymbol{B}_d$ are, respectively

$$\boldsymbol{A}_d = \mathrm{e}^{\boldsymbol{A}\,\Delta t} \tag{A.12}$$

$$\boldsymbol{B}_d = \int_0^{\Delta t} \mathrm{e}^{\boldsymbol{A}\,\sigma}\,\boldsymbol{B}\,d\sigma \tag{A.13}$$

It is worth noting that the matrices $\boldsymbol{C}$ and $\boldsymbol{D}$ are not indicated with the subscript d (which is used to denote "discrete-time") because these matrices are equal both for the discrete- and the continuous- time systems.

For a generic initial state $\boldsymbol{x}_0$ and for a generic input $\boldsymbol{u}_k$ applied to the system, both the state and the response of the system at a generic instant of time can be determined using the discrete-time state space model presented in Eq. (A.11). In particular, as shown in [Juang, 1994; Juang & Phan, 2001], the state of the system at the generic time $t = k\,\Delta t$ is expressed by the following equation

$$\boldsymbol{x}_k = \boldsymbol{A}_d^{\,k}\,\boldsymbol{x}_0 + \sum_{h=1}^{k} \boldsymbol{A}_d^{\,h-1}\boldsymbol{B}_d\,\boldsymbol{u}_{k-h} \tag{A.14}$$

In a similar way, the output response of the system at the generic time $t = k\,\Delta t$ is expressed by the following equation

$$\boldsymbol{y}_k = \boldsymbol{C}\,\boldsymbol{A}_d^{\,k}\,\boldsymbol{x}_0 + \sum_{h=1}^{k} \boldsymbol{C}\,\boldsymbol{A}_d^{\,h-1}\boldsymbol{B}_d\,\boldsymbol{u}_{k-h} + \boldsymbol{D}\,\boldsymbol{u}_k \tag{A.15}$$

Among the different inputs that can be applied to the structural system, one that is of particular relevance, both in the theory and for practical applications, is the unit pulse input [Juang & Phan, 2001]. In particular, the response of the system can be evaluated by considering a zero initial condition $\boldsymbol{x}_0 = 0$ and by applying a unit pulse at the generic *j*-th input. In such case the input sequence is defined as

$$\boldsymbol{u}_0 = \begin{bmatrix} 0 \\ \vdots \\ 0 \\ 1_j \\ 0 \\ \vdots \\ 0 \end{bmatrix}_{i \times 1} \tag{A.16}$$

$$\boldsymbol{u}_1 = \boldsymbol{u}_2 = \ldots = \boldsymbol{u}_k = \{\boldsymbol{0}\}_{i \times 1} \tag{A.17}$$

with $k = 1, 2...$ and where the vector $\boldsymbol{u}_0$ is a vector of all zeros except for a unit value at the *j*-th position that corresponds to the *j*-th input of the system. If the response of the structure is evaluated for such input sequence, a sequence of response vectors $\boldsymbol{y}_0, \boldsymbol{y}_1, \boldsymbol{y}_2 \ldots \boldsymbol{y}_k$ is obtained (each vector has dimensions $o \times 1$). This operation can be performed by considering input sequences where each sequence is characterized by a unit pulse for a different input (i.e. for $j = 1 \ldots i$). The responses of the system that are obtained can be then assembled into pulse response matrices $\boldsymbol{Y}_0, \boldsymbol{Y}_1, \boldsymbol{Y}_2, \ldots \boldsymbol{Y}_k$ which have dimensions $o \times i$. As shown in [Juang, 1994; Juang & Phan, 2001], it can be demonstrated that the sequence of such pulse response matrices is as follows

$$\boldsymbol{Y}_0 = \boldsymbol{D} \tag{A.18}$$

$$\boldsymbol{Y}_k = \boldsymbol{C}\, \boldsymbol{A_d}^{k-1}\, \boldsymbol{B_d} \tag{A.19}$$

with $k = 1, 2...$. The sequence of such $o \times i$ matrices is also known in the literature as the sequence of the system Markov parameters.

As shown in Eqs. (A.18, A.19), the matrices that describe the state space model of the structural system are included implicitly into the sequence of the Markov parameters [Juang & Phan, 2001]. This suggests that if the Markov parameters for a generic system are known, they can be used to identify the discrete-time state space model of that system (Eq. A.11). In other words, they can be used to determine the four matrices $\boldsymbol{A_d}$, $\boldsymbol{B_d}$, $\boldsymbol{C}$, and $\boldsymbol{D}$ [Juang, 1994]. In particular, as shown in Eq. (A.18),

the matrix $\boldsymbol{D}$ is directly related to the first Markov parameter, thus only the matrices $\boldsymbol{A_d}$, $\boldsymbol{B_d}$, and $\boldsymbol{C}$ have to be determined. Obtaining four matrices starting from the Markov parameters that satisfies the system described in Eq. A.11 is an operation that is usually referred to as the operation of obtaining a realization of the system [Ho & Kalman, 1966].

A general observation must be made on the realization problems and on their relationship with the identification problems. In a realization problem it is assumed to deal with quantities (for example, input/output sequences or pulse response sequences) that are generated by a model (such as the one expressed by Eq. A.11), and thus such quantities are not affected by errors and noise. On the contrary, in an identification problem one has usually to deal with experimental data (for example, measurements of input forces and output responses) that are affected by errors and noise. In the identification problem the characteristics of the system have to be determined starting from the measured data. However, the technique adopted in the context of a system realization problem can also be adapted to the context of a system identification problem. This, in fact, is the main idea that is behind the Eigensystem Realization Algorithm (ERA), which is an algorithm that was developed for structural system identification and, specifically, for modal identification.

A.1.2 Steps of the Eigensystem Realization Algorithm (ERA)

The Eigensystem Realization Algorithm (ERA) [Juang & Pappa, 1985] can be applied starting from the pulse response-histories (i.e. the Markov parameters) of a structural system. Such quantities may have been measured directly during a free-decay vibration test or may have been computed starting from experimental vibration measurements of input forces and output responses. It is worth noting that this section presents the original formulation of the ERA method (i.e. the version of the methodology that can be applied in the context of a traditional vibration test). On the contrary, next section explains how the methodology can be applied in the context of an output-only vibration test.

Let us assume that the discrete sequence of the pulse responses is assembled into matrices ***Y(k)*** with dimensions $o \times i$ and for $k = 0,1,2 \ldots$ As already mentioned, i is the number of the inputs and o is the number of the outputs of the structural system. In the first step of the ERA method these pulse response matrices are arranged in the so-called block Hankel matrix[2] as follows

$$\boldsymbol{H}(k)_{or \times is} = \begin{bmatrix} \boldsymbol{Y}(k+1) & \boldsymbol{Y}(k+2) & \boldsymbol{Y}(k+3) & \ldots & \boldsymbol{Y}(k+s+1) \\ \boldsymbol{Y}(k+2) & \boldsymbol{Y}(k+3) & \ldots & \ldots & \boldsymbol{Y}(k+s+2) \\ \boldsymbol{Y}(k+3) & \ldots & \ldots & \ldots & \ldots \\ \ldots & \ldots & \ldots & \ldots & \ldots \\ \boldsymbol{Y}(k+r+1) & \boldsymbol{Y}(k+r+2) & \ldots & \ldots & \boldsymbol{Y}(k+r+s+1) \end{bmatrix} \tag{A.20}$$

where k refers to the sampled time and r,s are the row and column indices, respectively, of the single block or submatrix ***Y(k)***. When the Hankel matrix is assembled according to [Juang & Phan, 2001], it is important to guarantee that the following condition is fulfilled: $(s \times i) \geq (r \times o)$.

At first, Eq. (A.20) is evaluated for $k = 0$, and the block Hankel matrix $\boldsymbol{H}(0)$ is obtained. It is worth noting that the first Markov parameter $\boldsymbol{Y}(0)$ is not included in the matrix $\boldsymbol{H}(0)$. The block Hankel matrix $\boldsymbol{H}(0)$ is then processed through a singular value decomposition (SVD) as follows

$$\boldsymbol{H}(0) = \boldsymbol{R}\,\boldsymbol{\Sigma}\,\boldsymbol{S}^T \tag{A.21}$$

where the matrices $\boldsymbol{R}$ and $\boldsymbol{S}$ are formed by columns that are orthonormal vectors, and the matrix $\boldsymbol{\Sigma}$ is a rectangular matrix

$$\boldsymbol{\Sigma} = \begin{bmatrix} \boldsymbol{\Sigma}_{n^*} & \boldsymbol{0} \\ \boldsymbol{0} & \boldsymbol{0} \end{bmatrix} \tag{A.22}$$

In Eq. (A.22), the matrix $\boldsymbol{\Sigma}_{n^*}$ is a diagonal matrix with elements in a monotonically decreasing order, and the parameter n^* is theoretically the true order of the system (i.e. the theoretical dimension of the state space model that describes the system). Due to the fact that theoretically only one portion of the matrix reported in Eq. (A.22) is non-zero, the block Hankel matrix $\boldsymbol{H}(0)$ can be also expressed as follows

[2] A Hankel matrix is a matrix where each secondary diagonal (i.e. each skew diagonal) has constant values. A block Hankel matrix is a matrix where the above-mentioned rule is valid if block (or submatrices) are considered instead of the single components of the matrix. This characteristic of the block Hankel matrix is evident in Eq. (A.20).

$$\boldsymbol{H}(0) = \boldsymbol{R}_{n*}\boldsymbol{\Sigma}_{n*}\boldsymbol{S}_{n*}^{T} \quad \text{where} \quad \boldsymbol{R}_{n*}^{T}\boldsymbol{R}_{n*} = \boldsymbol{I}_{n*} = \boldsymbol{S}_{n*}^{T}\boldsymbol{S}_{n*} \tag{A.23}$$

where the matrices $\boldsymbol{R}_{n*}$ and $\boldsymbol{S}_{n*}$ are matrices formed by the first n^* columns of the matrices $\boldsymbol{R}$ and $\boldsymbol{S}$, respectively [Juang & Phan, 2001].

As already mentioned, n^* is the theoretical true order of the system, and it can be determined according to Eq. (A.22) using the SVD if the Markov parameters used to assemble the block Hankel matrix are exact (i.e. not affected by errors and generated by a state space model of order n^*). Of course, when the procedure is applied by considering a real structure and starting from experimental data (affected by noise), it is much more difficult to determine the order of the system (this is a common drawback in any identification problem). In such case, the matrix $\boldsymbol{H}(0)$ will be in general full rank. In practical applications it is appropriate, however, to consider values of the parameter n^* such that the diagonal elements present in Eq. (A.22) but not included in Eq. (A.23) are very small. It is worth noting that in the ideal unnoisy case if a structural system characterized by n DOFs is considered (for example, the one discussed in Section A.1.1), then the parameter n^* should be theoretically equal to $2n$ (i.e. the dimension of the state space model that describes an n-DOF structural system).

Then, Eq. (A.20) is evaluated for $k = 1$, and the shifted block Hankel matrix $\boldsymbol{H}(1)$ is assembled. Finally, to identify the matrices $\boldsymbol{A}_d$, $\boldsymbol{B}_d$, $\boldsymbol{C}$, and $\boldsymbol{D}$ that describe the state space model of the considered structural system the following equations are applied[3]

$$\boldsymbol{A}_d = \boldsymbol{\Sigma}_{n*}^{-1/2}\,\boldsymbol{R}_{n*}^{T}\boldsymbol{H}(1)\,\boldsymbol{S}_{n*}\boldsymbol{\Sigma}_{n*}^{-1/2} \tag{A.24}$$

$$\boldsymbol{B}_d = \text{the first } i \text{ columns of } \boldsymbol{\Sigma}_{n*}^{1/2}\boldsymbol{S}_{n*}^{T} \tag{A.25}$$

$$\boldsymbol{C} = \text{the first } o \text{ rows of } \boldsymbol{R}_{n*}\boldsymbol{\Sigma}_{n*}^{1/2} \tag{A.26}$$

$$\boldsymbol{D} = \boldsymbol{Y}(0) \tag{A.27}$$

As reported in [Juang, 1994], when considering data that is not affected by excessive noise, the order of the system n^* can be taken as the true order of the structural system.

[3] A rigorous mathematical proof of Eqs. (A.24, A.25, A.26, A.27) can be found in the work by [Juang, 1994].

Thus, the matrices $\boldsymbol{A}_d$, $\boldsymbol{B}_d$, $\boldsymbol{C}$, and $\boldsymbol{D}$ can be considered as a minimal realization. It is important to underline that the matrices $\boldsymbol{A}_d$, $\boldsymbol{B}_d$, and $\boldsymbol{C}$ depend on the coordinates used in the identified state space model [Juang & Phan, 2001]. However, one important property of a minimal realization, which is relevant especially in the context of a modal identification problem, is the following: if a realization is minimal, its eigenvalues and eigenvectors do not depend on the coordinates that are adopted in the state space model [Juang, 1994].

In light of this premise, the identified modal parameters of the structure can be determined using the following steps. First of all, the eigenvalue problem associated to the discrete system matrix $\boldsymbol{A}_d$ has to be solved

$$\boldsymbol{A}_d \, \boldsymbol{\chi}_{s,i} = \lambda_{d,i} \, \boldsymbol{\chi}_{s,i} \tag{A.28}$$

where $\lambda_{d,i}$, $\boldsymbol{\chi}_{s,i}$ are complex eigenvalues (i.e. the poles) and complex eigenvectors, respectively, of the discrete-time system in the state space coordinates. The former are collected in the spectral diagonal matrix $\boldsymbol{\Lambda}_d = \text{diag}\{\lambda_{d,i}\}$ for $i = 1 \dots n^*$, while the latter form the modal matrix $\mathbf{X}_s = [\boldsymbol{\chi}_{s,1}, \dots, \boldsymbol{\chi}_{s,j}, \dots, \boldsymbol{\chi}_{s,n^*}]$. Then, the eigenvalues λ_i related to the continuous-time system matrix $\boldsymbol{A}$ can be obtained using the following equation

$$\lambda_i = \frac{\ln(\lambda_{d,i})}{\Delta t} = \sigma_i \pm j \, \omega_{D,i} \tag{A.29}$$

where σ_i and $\omega_{D,i}$ are the real and imaginary parts of the complex eigenvalue λ_i and j is the imaginary unit. In Eq. (A.29) it is also highlighted and assumed that the identified poles occur in complex conjugate pairs. This is true for the structural systems that are considered in the present dissertation, which are underdamped structural systems. The necessity of applying the transformation reported in Eq. (A.29) is justified by the fact that the matrix $\boldsymbol{A}_d$ and the matrix $\boldsymbol{A}$ are related through the matrix exponential function (as shown in Eq. A.12).

The eigenvectors contained in the matrix $\mathbf{X}_s$ are not estimates of the mode shapes of the structure at sensor locations [Brincker & Ventura, 2015], because the realization is expressed in the state space coordinates (which are not the physical coordinates). It is thus necessary to introduce a transformation to obtain the mode

shapes at sensor locations. The complex value mode shapes defined at sensor locations can be obtained as

$$\boldsymbol{C}^m = \boldsymbol{C}\ \mathbf{X}_s \tag{A.30}$$

where $\boldsymbol{C}$ is the identified output matrix of the state space model. The matrix $\boldsymbol{C}^m$ contains the complex value mode shapes defined at sensor locations, and, for the sake of convenience, it is also indicated in the present appendix as the matrix $\mathbf{X}$. The matrix $\boldsymbol{C}^m = \mathbf{X} = [\ \ldots, \Re(\boldsymbol{\chi}_i) \pm j\ \Im(\boldsymbol{\chi}_i), \ldots\ ]$ is an o × n^* matrix, and each complex value mode shape $\boldsymbol{\chi}_i$ of the structure is reported in one column of such matrix. It is worth noting that the transformation reported in Eq. (A.30) is a transformation of the output matrix from the state space to the modal coordinates. In fact, the superscript *m* has been introduced in Eq. (A.30) to indicate that modal coordinates are adopted. According to [Juang, 1994; Alvin et al., 2003], the identified continuous-time state space model, expressed in modal coordinates, of the structural system is as follows

$$\begin{cases} \dot{\boldsymbol{x}}^m = \boldsymbol{\Lambda}\ \boldsymbol{x}^m + \boldsymbol{B}^m\ \boldsymbol{u} \\ \boldsymbol{y} = \boldsymbol{C}^m\ \boldsymbol{x}^m + \boldsymbol{D}\ \boldsymbol{u} \end{cases} \tag{A.31}$$

where $\boldsymbol{\Lambda}$ is the spectral diagonal matrix $\boldsymbol{\Lambda}$ = diag$\{\lambda_i\}$ for $i = 1 \ldots n^*$, $\boldsymbol{B}^m = \mathbf{X}_s^{-1}\boldsymbol{B}$ is the input matrix in modal coordinates and $\boldsymbol{B}$ is the continuous-time transform of the discrete-time matrix $\boldsymbol{B}_d$ obtained using ERA, and, as already mentioned, $\boldsymbol{C}^m = \mathbf{X}$ is the output matrix in modal coordinates (i.e. the matrix of the damped mode shapes of the structure).

At this point, the continuous-time complex eigenvalues and the complex mode shapes of the damped structure have been obtained. According to [Alvin et al., 2003] and under the assumption of considering the identified structure as proportionally damped, the complex or damped modes can be related to the real or normal modes. Under this assumption, the normal modes of the structure can thus be estimated starting from the modes identified usign the ERA algorithm. The natural circular frequency ω_i of the undamped system and the modal damping ratio ζ_i for the generic mode *i* can be obtained as follows

$$\omega_i = \sqrt{\sigma_i^2 + \omega_{D,i}^2} \tag{A.32}$$

$$\zeta_i = -\frac{\sigma_i}{\omega_i} \tag{A.33}$$

starting from the complex eigenvalues of the damped system. To obtain an estimate of the real mode shapes from complex mode shapes, the Standard technique (ST) [Imregun & Ewins, 1993; Alvin et al., 2003] can be applied. According to the technique, the complex mode shape $\boldsymbol{\chi}_i$ of the *i*-th mode is interpreted as a vector which is characterized by a magnitude $\bar{\chi}_{i,j}$ and a phase $\alpha_{i,j}$ at each *j*-th component

$$\bar{\chi}_{i,j} = \sqrt{\Re(\chi_{i,j})^2 + \Im(\chi_{i,j})^2} \tag{A.34}$$

$$\alpha_{ij} = \text{atan}\left(\frac{\Im(\chi_{i,j})}{\Re(\chi_{i,j})}\right) \tag{A.35}$$

According to [Alvin et al., 2003], if the structural modes are almost proportionally damped, the phase angles are clustered around the value $\alpha_{0,i} \pm \frac{\pi}{2}$, where $\alpha_{0,i}$ is an arbitrary angle that depends on the scaling of the modes. The technique assumes that the mode shape components are purely in phase. According to the Standard technique, in fact, the difference between the effective phase values of the mode shapes and the theoretical value ($\alpha_{0,i} \pm \frac{\pi}{2}$), which is valid in the ideal case of a proportionally damped system, are neglected. The component ψ_{ij} of the undamped real-value mode shape can be estimated using the following equation [Alvin et al., 2003]

$$\psi_{ij} = \bar{\chi}_{i,j} \ \text{sgn}(j) \tag{A.36}$$

where sgn (*j*) is a sign function that assumes the values ± 1 and depends on the location of the *j*-th component of the mode shape.

One important aspect that has to be considered in modal identification, especially when a parametric method in time domain is applied (for example, the ERA method), is the fact that not all the poles of the identified model correspond necessarily to structural modes. In general, some of the poles of the identified model will be related to structural modes, while, on the contrary, other poles will not be physical. The modes associated to these non-physical poles are generated by the presence of noise and uncertainties on the measurements and are indicated as noise or computational modes. It is thus important in modal identification to separate the true structural modes from the noise modes. To perform this operation, one of the most common approaches in time-domain modal identification is to use the technique of

the so-called stabilization diagram. According to this technique, the modal identification is performed by considering different and increasing values of the order of the identified model. Referring to the case of the ERA method and to the calculations described in this section, this means to perform and repeat the identification for increasing values of the parameter n^*. For each identified model, all the poles are estimated and considered, and the corresponding modal parameters are determined (natural frequencies, modal damping ratios, and mode shapes). Then, the modal parameters related to models with a different order are compared with each other to determine which are the poles that are stable and approximately independent from the order of the model. In general, in fact, the modal parameters that are associated to a true structural mode are approximately independent from the order of the model. On the contrary, the above-mentioned property is not valid for noise modes. This simple principle is thus adopted to distinguish the structural modes from the noise modes.[4]

When the ERA method is applied, another strategy (alternative or complementary to the stabilization diagram) can be adopted to distinguish between the true modes and the noise modes. In particular, two modal indices can be adopted for this purpose, as shown in [Juang, 1994]. To derive such indices, let us consider, according to [Juang, 1994], the identified discrete-time state space model, expressed in modal coordinates, of the structural system

$$\begin{cases} \boldsymbol{x}_{k+1}^{m} = \boldsymbol{\Lambda_d}\ \ \boldsymbol{x}_k{}^{m} + \boldsymbol{B_d}{}^{m}\, \boldsymbol{u_k} \\ \boldsymbol{y_k} = \boldsymbol{C}^{m}\ \ \boldsymbol{x}_k{}^{m} + \boldsymbol{D}\, \boldsymbol{u_k} \end{cases} \tag{A.37}$$

where $\boldsymbol{\Lambda_d}$ is the spectral diagonal matrix $\boldsymbol{\Lambda_d} = \mathrm{diag}\{\lambda_{d,i}\}$ for $i = 1 \ldots n^*$, $\boldsymbol{B_d}{}^{m} = \mathbf{X}_s^{-1}\boldsymbol{B}_d$ is the discrete-time input matrix in modal coordinates, and, as already mentioned, $\boldsymbol{C}^{m} = \mathbf{X}$ is the output matrix in modal coordinates. It is worth noting that the model expressed in Eq. (A.37) is equivalent to the model expressed by Eq. (A.31) with the only difference that the latter is formulated for the continuous-time case.

The sequence of the identified Markov parameters, which do not depend on the adopted coordinates, can be expressed as a function of the system matrix, the input

[4] An extensive description of the technique based on the stabilization diagram can be found in [Rainieri & Fabbrocino, 2014; Brincker & Ventura, 2015].

influence matrix, and the output influence matrix expressed in the modal space as follows

$$\boldsymbol{Y}_k = \boldsymbol{C}^m \boldsymbol{\Lambda}_{\boldsymbol{d}}^{k-1} \boldsymbol{B_d}^m = \sum_{i=1}^{n^*} \boldsymbol{c}_i \lambda_{d,i}^{k-1} \boldsymbol{b}_i \tag{A.38}$$

where $\boldsymbol{c}_i$ is the i-th column of the output matrix in modal coordinates (i.e. $\boldsymbol{C}^m$), $\boldsymbol{b}_i$ is the i-th row of the discrete-time input matrix in modal coordinates (i.e. $\boldsymbol{B_d}^m$), $\lambda_{d,i}$ is the i-th complex eigenvalue of the discrete state space matrix (i.e. $\boldsymbol{A}_d$), and $k = 1 \ldots p$ with a number of Markov parameters equal to p. As evident in Eq. (A.38), each modal coordinate has a sequence of Markov parameters

$$\left[\boldsymbol{c}_i \boldsymbol{b}_i \quad \boldsymbol{c}_i \lambda_{d,i} \boldsymbol{b}_i \quad \boldsymbol{c}_i \lambda_{d,i}^2 \boldsymbol{b}_i \quad \ldots \quad \boldsymbol{c}_i \lambda_{d,i}^{p-2} \boldsymbol{b}_i\right] \tag{A.39}$$

According to [Juang, 1994], the following sequence can be defined

$$\hat{\boldsymbol{q}}_i = \left[\boldsymbol{b}_i \quad \lambda_{d,i} \boldsymbol{b}_i \quad \lambda_{d,i}^2 \boldsymbol{b}_i \quad \ldots \quad \lambda_{d,i}^{p-2} \boldsymbol{b}_i\right] \tag{A.40}$$

This sequence is the so-called Modal Amplitude time history for the i-th mode. This sequence represents the contribution, expressed as a time history, of the i-th mode to the sequence of the identified Markov parameters.

On the basis of this premise, the two above-mentioned modal indices can be defined. The first modal index is the so-called Modal Amplitude Coherence (MAmC) [Juang, 1994]. This index is defined as the coherence function between the Modal Amplitude time history $\hat{\boldsymbol{q}}_i$ (Eq. A.40) and the same time history $\bar{\boldsymbol{q}}_i$ obtained directly from the experimental data (by performing a decomposition of the block Hankel matrix $\boldsymbol{H}(0)$, as shown in [Juang, 1994]). The MAmC index is thus expressed as follows

$$MAmC_i = \frac{\left|\bar{\boldsymbol{q}}_i \hat{\boldsymbol{q}}_i^*\right|}{\left(\left|\bar{\boldsymbol{q}}_i \bar{\boldsymbol{q}}_i^*\right| \left|\hat{\boldsymbol{q}}_i \hat{\boldsymbol{q}}_i^*\right|\right)^{1/2}} \tag{A.41}$$

where * stands for transpose and complex conjugate. The second modal index is the so-called Mode Singular Value (MSV), which is defined for the generic i-th mode as follows

$$MSV_i = \sqrt{|\boldsymbol{c}_i| \left(1 + \left|\hat{\lambda}_{d,i}\right| + \left|\hat{\lambda}_{d,i}^2\right| + \ldots + \left|\hat{\lambda}_{d,i}^{p-2}\right|\right) |\boldsymbol{b}_i|} \tag{A.42}$$

This index determines the relative contribution of each identified mode to the sequence of the identified Markov parameters of the system (i.e. the "identified model pulse response history" [Juang, 1994]). In general, both the two above-mentioned indices (MAmC and MSV) evaluated for a true structural mode are higher than the corresponding indices obtained for a noise mode. These two indices can thus be used to distinguish the true structural modes from the noise modes.

A schematic representation of the main steps that can be applied in a modal identification process based on the Eigensystem Realization Algorithm (ERA) are reported in Fig. A.1.

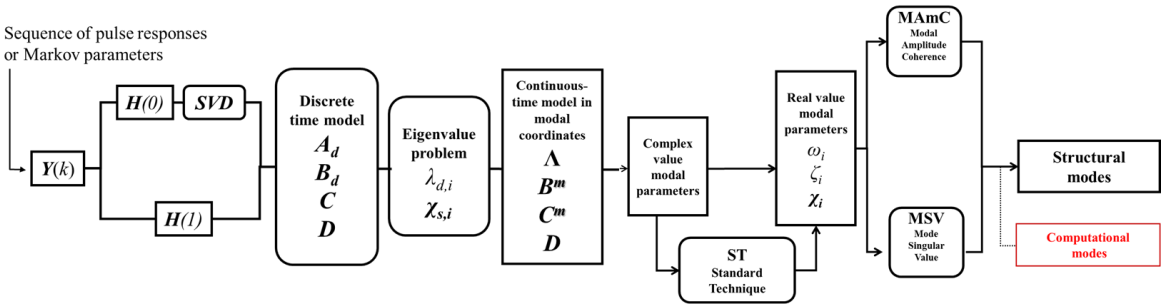

Figure A.1. Main steps of the modal identification process based on Eigensystem Realization Algorithm (ERA)

A.1.3 Natural Excitation technique (NExT)

In this section it is shown how the Eigensystem Realization Algorithm (ERA), originally developed to work starting from experimentally-derived free decays of structures, can be adopted as an output-only modal identification technique and applied, for example, on ambient vibration data. One of the earliest works where the ERA method was applied starting from output-only vibration data is the work of [James et al., 1993], where the Natural Excitation technique (NExT) was presented.

According to the NExT technique, the first operation that has to be performed on the measured vibration responses is to estimate the correlation functions. Then, such functions are assumed as the free decays of the structure and used to apply the

ERA method. Adopting this approach is a valid approach because of the following property of the correlation functions, which is demonstrated in the work of [James et al., 1993]. The correlation functions evaluated starting from the responses of a structural system due to random white noise inputs can be expressed as a summation of decaying sinusoids. In particular, each of these decaying sinusoids is characterized by a damped natural frequency and a damping ratio that are equal to the corresponding quantities related to one of the structural modes [James et al., 1993]. Due to this property the correlation functions can thus be considered as free vibration responses.

To show how the ERA method can be applied starting from output-only vibration data, let us assume that we have recorded the acceleration response measurements of a generic structure from a number of channels equal to o. Among these different channels of accelerations, one is selected as a reference channel and used to calculate the cross-correlation functions. Such cross-correlation functions are evaluated between each channel and the reference channel. As suggested in [Caicedo, 2011], in the selection of the reference channel it is important to choose a channel whose signal amplitudes are higher with respect to the other channels and with a low noise-to-signal ratio. Moreover, it is important to avoid channels that are related to nodal points (i.e. positions where a generic identified mode shape of the structure has components that are approximately equal to zero).

The cross-correlation function $R_j(k)$ between the generic j-th channel of accelerations $y_j(l)$ and the reference one $y_R(l+k)$ is thus evaluated. This cross-correlation function can be calculated, for example, using the direct procedure as follows

$$R_j(k) = \frac{1}{L-k} \sum_{l=1}^{L-k} y_j(l)\, y_R(l+k) \tag{A.43}$$

This last equation is expressed in discrete-time, and the terms present in Eq. (A.43) are the following: L is the total number of sampled points, the parameter k in the discrete-time formulation corresponds to a time lag $\tau = k\,\Delta t$ in the corresponding continuous-time formulation, where Δt is the time step. In the same way, in the discrete-time formulation the notation $y_j(l)$ corresponds to the notation $y_j(t)$ in the continuous-time formulation, where $t = l\,\Delta t$.

The cross-correlation functions are evaluated for the different channels of accelerations (for $j = 1 \ldots o$ and using Eq. A.43). Then, for each value of k (i.e. the index used to define the time lag) the cross-correlation functions are assembled in matrices $\boldsymbol{R}(k)$ with dimension $o \times 1$. Such matrices are the quantities that are processed using the Eigensystem Realization Algorithm (ERA). In fact, the matrices $\boldsymbol{R}(k)$ can be used to assemble the block Hankel matrix (Eq. A.20), instead of using the pulse response histories or Markov parameters - which are, according to the notation used in previous section, contained in the matrices $\boldsymbol{Y}(k)$.

Then, according to the steps outlined in previous section the Eigensystem Realization Algorithm (ERA) can be applied to identify a model of the structure. There is, however, one important difference between applying ERA using input-output data and using output-only data that must be mentioned. When ERA is applied using input-output data, the realization consists in the determination of the matrices $\boldsymbol{A}_d$, $\boldsymbol{B}_d$, $\boldsymbol{C}$, and $\boldsymbol{D}$ (which are the matrices that describe the deterministic model reported in Eq. A.11). On the contrary, when ERA is applied using output-only data, the system matrix $\boldsymbol{A}_d$ and the output influence matrix $\boldsymbol{C}$ have to be determined (using Eqs. A.24, A.26, respectively) [Caicedo, 2011] to identify a stochastic state space model, where the input is considered as a zero-mean stationary white noise process. After having identified the matrices $\boldsymbol{A}_d$ and $\boldsymbol{C}$, the modal parameters of the structure (i.e. natural frequencies, modal damping ratios, and arbitrarily scaled mode shapes) can be estimated using the criteria described in previous section (Eqs. A.32, A.33, A.36). However, Eqs. (A.25, A.27) related to the original formulation of the ERA method can be still applied when the method is adopted in the output-only case starting from the output correlations (according to NExT), to identify two matrices indicated herein as $\boldsymbol{G}_d$ and $\boldsymbol{R}(0)$. These matrices substitute, respectively, the matrices $\boldsymbol{B}_d$ and $\boldsymbol{D} = \boldsymbol{Y}(0)$ obtained in the original formulation of the ERA method. This operation can be considered as a valid approach because, by transposing to the context of the ERA method the interpretation and the property related to the stochastic identification problem discussed in [Van Overschee and De Moor, 1996], the output correlations (i.e. the output covariances for signals with a zero mean) can be considered as the Markov parameters of a deterministic linear time-invariant system formed by the matrices $\boldsymbol{A}_d$, $\boldsymbol{G}_d$, $\boldsymbol{C}$, and $\boldsymbol{R}(0)$. Under this interpretation all the steps of the ERA method

presented in previous section, including the approach of evaluating the indices of the Modal Amplitude Coherence (MAmC) and the Mode Singular Value (MSV), can thus be transposed to the output-only case and applied starting from the output correlations. An example in the literature where the criterion of the original formulation of the ERA method based on the evaluation of the MAmC index is extended to the output-only case and applied in numerical simulations on structures loaded by white noise is reported in the work of [Zhang et al., 2001].

The validity of the approach that considers the correlation functions instead of the free decays of the structure can be also demonstrated, as done in the works of [Caicedo et al., 2004; Caicedo, 2011], by showing that the correlation functions satisfy the equation of motion of a damped MDOF system under free vibrations. The main steps of the above-mentioned proof, reported in [Caicedo et al., 2004], are summarized herein.

Let us consider the equation of motion of a generic MDOF structural system under forced vibrations

$$\mathbf{M}\,\ddot{\mathbf{x}}(t) + \boldsymbol{\mathcal{C}}\,\dot{\mathbf{x}}(t) + \mathbf{K}\,\mathbf{x}(t) = \mathbf{f}(t) \tag{A.44}$$

If we assume that both the input forces and the response quantities are stationary random processes, Eq. (A.44) can be rewritten as follows

$$\mathbf{M}\,\ddot{\mathbf{X}}(t) + \boldsymbol{\mathcal{C}}\,\dot{\mathbf{X}}(t) + \mathbf{K}\,\mathbf{X}(t) = \mathbf{F}(t) \tag{A.45}$$

where $\mathbf{X}(t), \dot{\mathbf{X}}(t), \ddot{\mathbf{X}}(t), \mathbf{F}(t)$ are the vectors of the stochastic processes related, respectively, to displacements, velocities, accelerations and forces. Eq. (A.45) is then reformulated by post multiplying both sides of the equation through a scalar response process $X_i(t+\tau)$, where τ is the time lag

$$\mathbf{M}\,\ddot{\mathbf{X}}(t)\,X_i(t+\tau) + \boldsymbol{\mathcal{C}}\,\dot{\mathbf{X}}(t)\,X_i(t+\tau) + \mathbf{K}\,\mathbf{X}(t)\,X_i(t+\tau) = \mathbf{F}(t)\,X_i(t+\tau) \tag{A.46}$$

Then, the expected value of both sides of Eq. (A.46) is evaluated

$$\mathbf{M}\,E\left[\ddot{\mathbf{X}}(t)\,X_i(t+\tau)\right] + \boldsymbol{\mathcal{C}}\,E\left[\dot{\mathbf{X}}(t)\,X_i(t+\tau)\right] + \mathbf{K}\,E[\mathbf{X}(t)\,X_i(t+\tau)] = E[\mathbf{F}(t)\,X_i(t+\tau)] \tag{A.47}$$

Under the assumption that the excitation has white noise characteristics, it is possible to recognize that the input $\mathbf{F}(t)$ is uncorrelated with the response $X_i(t+\tau)$ for $\tau > 0$,

and thus $E[\mathbf{F}(t)\, X_i(t+\tau)] = \mathbf{0}$. Moreover, according to the definition of the correlation function that has been already mentioned in Chapter 2, the vectors of correlation functions $\mathbf{R}_{\ddot{\mathbf{X}}\, X_i}(\tau)$, $\mathbf{R}_{\dot{\mathbf{X}}\, X_i}(\tau)$, and $\mathbf{R}_{\mathbf{X}\, X_i}(\tau)$ are introduced in Eq. (A.47), which is reformulated as follows

$$\mathbf{M}\, \mathbf{R}_{\ddot{\mathbf{X}}\, X_i}(\tau) + \boldsymbol{\mathcal{C}}\, \mathbf{R}_{\dot{\mathbf{X}}\, X_i}(\tau) + \mathbf{K}\, \mathbf{R}_{\mathbf{X}\, X_i}(\tau) = \mathbf{0} \tag{A.48}$$

The expression reported in Eq. (A.48) can then be reformulated by considering one property of the processes that can be assumed as stationary. As discussed in [Caicedo et al., 2004] and as shown more in detail in [Bendat & Piersol, 2000], by considering two stationary processes A(t) and B(t) the following property is valid

$$\mathbf{R}_{A^{(m)}\, B}(\tau) = \mathbf{R}^{(m)}{}_{A\, B}(\tau) \tag{A.49}$$

where $A^{(m)}$ denotes the *m*-th derivative of A(t) with respect to the variable t (i.e. time) and $\mathbf{R}^{(m)}{}_{A\, B}$ denotes the *m*-th derivative of $\mathbf{R}_{A\, B}$ with respect to the variable τ (i.e. the time lag). By applying the property expressed in Eq. (A.49) on the quantities reported in Eq. (A.48), this last equation can be reformulated as follows

$$\mathbf{M}\, \ddot{\mathbf{R}}_{\mathbf{X}\, X_i}(\tau) + \boldsymbol{\mathcal{C}}\, \dot{\mathbf{R}}_{\mathbf{X}\, X_i}(\tau) + \mathbf{K}\, \mathbf{R}_{\mathbf{X}\, X_i}(\tau) = \mathbf{0} \tag{A.50}$$

Eq. (A.50) shows that the correlation functions evaluated starting from the displacements of the structure, which are assumed as stationary random processes, satisfy the equation of motion of the damped free vibrations of the system [Caicedo et al., 2004]. The same result, as also discussed in [Caicedo et al., 2004] and as shown more in detail in [Beck et al., 1994], is obtained if the correlation functions are evaluated starting from acceleration signals, which are stationary random processes, i.e.

$$\mathbf{M}\, \ddot{\mathbf{R}}_{\ddot{\mathbf{X}}\, \ddot{X}_i}(\tau) + \boldsymbol{\mathcal{C}}\, \dot{\mathbf{R}}_{\ddot{\mathbf{X}}\, \ddot{X}_i}(\tau) + \mathbf{K}\, \mathbf{R}_{\ddot{\mathbf{X}}\, \ddot{X}_i}(\tau) = \mathbf{0} \tag{A.51}$$

When dealing with ambient vibrations and when applying the techniques of the Operational Modal Analysis (OMA), as shown in Chapter 2, it is assumed that the measured responses have approximately the characteristics of stationary random processes. On the basis of this assumption and by considering the analytical formulation shown at the end of this section, it is more evident the reason for which the correlation functions evaluated from ambient vibration measurements of a generic

structure can be interpreted as the free decays of that structure. This is the main idea that is behind the Natural Excitation technique (NExT), and, more generally as already mentioned in Chapter 2, is one of the fundamental aspects in OMA [Brincker & Ventura, 2015].

A.2 Frequency Domain Decomposition (FDD)

In this section the main steps of the Frequency Domain Decomposition method [Brincker, Zhang & Andersen, 2001] are briefly described, following closely the formulation presented in [Brincker & Ventura, 2015].

As already mentioned in Chapter 2, the main operation that has to be done according to the FDD method, it to perform a singular value decomposition of the spectral density matrix estimated from the response measurements (i.e. the output-only vibration data). The validity of the approach can be easily explained through the following steps, which are more extensively discussed in [Brincker & Ventura, 2015].

Let us consider a vector of measured responses $\boldsymbol{y}(t) = \{y_1(t), \dots , y_o(t)\}^T$ with dimensions o × 1, where o is the number of the responses. The matrix $\boldsymbol{R}_y(\tau)$ of the cross-correlation functions evaluated among all the measured responses can be calculated as follows

$$\boldsymbol{R}_y(\tau) = E\,[\boldsymbol{y}(t)\,\boldsymbol{y}(t+\tau)^T] \tag{A.52}$$

The measured responses can be related to the time histories expressed in modal coordinates using the normal modes

$$\boldsymbol{y}(t) = \boldsymbol{\Psi}\,\boldsymbol{q}(t) \tag{A.53}$$

where $\boldsymbol{\Psi} = [\boldsymbol{\psi_1}, \boldsymbol{\psi_2}, \dots]$ is the mode shape matrix, which contains each modal vector $\boldsymbol{\psi_i}$, and $\boldsymbol{q}(t) = \{q_1(t), \dots , q_o(t)\}^T$ is the vector of the time histories expressed in modal coordinates. By substituting Eq. (A.53) in Eq. (A.52), the matrix of the cross-correlation functions can be reformulated as

$$\boldsymbol{R}_y(\tau) = \boldsymbol{\Psi}\,E\,[\boldsymbol{q}(t)\,\boldsymbol{q}(t+\tau)^T]\boldsymbol{\Psi}^{\mathbf{T}} = \boldsymbol{\Psi}\,\boldsymbol{R}_q(\tau)\boldsymbol{\Psi}^{\mathbf{T}} \tag{A.54}$$

where $\boldsymbol{R}_q(\tau)$ is the matrix of the cross-correlation functions evaluated on the time histories expressed in modal coordinates. According to [Brincker & Ventura, 2015], if one takes the Fourier transform of both sides of Eq. (A.54), this equation can be reformulated in the frequency domain

$$\boldsymbol{G}_y(f) = \boldsymbol{\Psi}\, \boldsymbol{G}_q(f) \boldsymbol{\Psi}^{\mathbf{T}} \tag{A.55}$$

where $\boldsymbol{G}_y(f)$ and $\boldsymbol{G}_q(f)$ are, respectively, the Spectral Density (SD) matrices of the measured responses and of the time histories expressed in modal coordinates. Under the assumption that the responses in modal coordinates are uncorrelated, both the correlation and the spectral density matrices of such responses are diagonal matrices. Thus, under this assumption Eq. (A.55) can be reformulated as follows

$$\boldsymbol{G}_y(f) = \boldsymbol{\Psi}\ [g_n^2(f)]\ \boldsymbol{\Psi}^{\mathbf{H}} \tag{A.56}$$

where the terms $g_n^2(f)$ are the diagonal elements of the matrix $\boldsymbol{G}_q(f)$ (i.e. these terms are the values of the auto spectral density functions). Moreover, the Hermitian operator ($\cdot^{\mathbf{H}}$) is introduced in Eq. (A.56) instead of the transpose operator ($\cdot^{\mathbf{T}}$) because in general the spectral density matrix is an Hermitian matrix[5] and the mode shapes have components that are complex values [Brincker & Ventura, 2015].

In light of the above-mentioned formulation, it is evident that performing a Singular Value Decomposition (SVD) of the spectral density matrix evaluated from the ambient vibration measurements can be a convenient approach to obtain a decomposition of such matrix similar to the one reported in Eq. (A.56). According to the FDD method, the spectral density matrix estimated from the vibration data is thus processed through the SVD as follows

$$\boldsymbol{G}_y(f) = \boldsymbol{U}\, \boldsymbol{S}\, \boldsymbol{U}^{\boldsymbol{H}} = \boldsymbol{U}\, [s_n^2]\, \boldsymbol{U}^{\boldsymbol{H}} \tag{A.57}$$

where the diagonal values of the matrix $\boldsymbol{S}$ and the columns of the matrix $\boldsymbol{U}$ are interpreted, respectively, as the auto spectral densities of the time histories expressed in modal coordinates and the mode shapes of the structure. Of course, as extensively discussed in [Brincker & Ventura, 2015], the decomposition presented in Eq. (A.57)

[5] A Hermitian matrix is a square matrix whose components are complex numbers and that is equal to its own conjugate transpose matrix.

is not exactly equivalent to the decomposition that is reported in Eq. (A.56). This means that the results obtained using the FDD method are in general approximated solutions. Notwithstanding the fact that approximated solutions are provided by the methodology, the results, in terms of modal parameters, that can be obtained by applying the FDD method are accurate, as extensively demonstrated in the literature through a comparison between the FDD and other OMA techniques [Brincker & Ventura, 2015].

According to the FDD method [Brincker, Zhang & Andersen, 2001], the structural modes can be determined through the analysis of the singular values computed from the SVD of the spectral density matrix. According to the method, such singular values are conveniently plotted as a function of the frequency, and, among the different singular values related to a certain frequency, one has in general to consider the first singular value (i.e., the highest singular value). The value of the frequency that corresponds to a peak in the plot of the first singular values is considered as the natural frequency related to an identified structural mode. While, the mode shape of such identified mode is estimated as the singular vector that corresponds to the first singular value found at the above-mentioned peak in the plot. The mode shapes estimated using the FDD method are complex-value mode shapes and are related to damped modes. Then, the mode shapes associated to the normal modes of the structure can be obtained using the Standard technique [Alvin et al., 2003] (using the procedure that has been already presented in Section A.1.2).

As already mentioned in Chapter 2, by using the basic version of the FDD method, it is not possible to have an estimate of the modal damping ratios. Moreover, the values of the natural frequencies of the structure that can be estimated using the basic version of the FDD are conditioned by the frequency resolution of the spectral density functions.

To overcome these shortcomings, an improved version of the method was presented in [Brincker, Ventura & Andersen, 2001]. The method is indicated as the Enhanced Frequency Domain Decomposition (EFDD). The method is able to identify the auto spectral density functions of the single-degree-of-freedom (SDOF) systems that correspond to each of the structural modes. Each SDOF spectral density function

is composed by singular values that are located near a peak in the singular value plot and that are associated to similar singular vectors [Rainieri & Fabbrocino, 2014]. According to the EFDD method, each SDOF-equivalent spectral density function is transformed from the frequency domain to the time domain using an inverse Fourier transform. In this way, a correlation function associated to each SDOF equivalent system and to each structural mode is obtained. Starting from these estimated SDOF-equivalent correlation functions the natural frequencies and the modal damping ratios of the considered structural modes are determined.

A.3 Modal validation

Modal validation is the operation of checking the results (i.e. the modal parameters, in terms of natural frequencies, mode shapes, and modal damping ratios) that have been estimated from a vibration test using the techniques of the modal identification. In this operation the engineering judgement can play a major role. In the majority of the cases, for example, it is possible to have an idea of the values of the natural frequencies expected for the structure, or to evaluate if the values of the identified modal damping ratios are reasonable values. Moreover, just animating and observing an identified mode shape is also a good way to understand if the related mode is a structural mode or not.

There are, however, some specific techniques that can be adopted in the stage of the modal validation of any modal identification process. In particular, two of the most common indices used for modal validation are described in this section. These indices are the Modal Phase Collinearity (MPC) and the Modal Assurance Criterion (MAC), and they are both evaluated on identified mode shapes.

The Modal Phase Collinearity (MPC) [Alvin et al., 2003] is a modal index that evaluates the linear dependence between the real and the imaginary parts of complex-value (or damped) mode shapes. This index is defined as follows

$$MPC_i = \frac{\left(S_{xx}-S_{yy}\right)^2+4\,S_{xy}^2}{\left(S_{xx}+S_{yy}\right)^2} \tag{A.58}$$

where the terms S_{xx}, S_{yy}, and S_{xy} are respectively

$$S_{xx} = \mathfrak{R}(\boldsymbol{\chi_i})^{\mathrm{T}}\ \mathfrak{R}(\boldsymbol{\chi_i}) \tag{A.59}$$

$$S_{yy} = \mathfrak{I}(\boldsymbol{\chi_i})^{\mathrm{T}}\ \mathfrak{I}(\boldsymbol{\chi_i}) \tag{A.60}$$

$$S_{xy} = \mathfrak{R}(\boldsymbol{\chi_i})^{\mathrm{T}}\ \mathfrak{I}(\boldsymbol{\chi_i}) \tag{A.61}$$

and $\boldsymbol{\chi_i}$ is the vector of the *i*-th complex-value identified mode shape. The Modal Phase Collinearity (MPC) is also closely related to the Modal Complexity Factor (MCF), which is a modal index defined as follows

$$MCF_i = 1 - MPC_i \tag{A.62}$$

The values of both the MPC index and the MCF index are in the range from 0 to 1. In particular, the MPC is one or very close to one (i.e. the MCF is zero or very close to zero), if the considered mode shapes are related to a structure that is proportionally (or classically) damped. In such case, the real and the imaginary parts of the identified mode shapes are approximately proportional. This is a result that is in general expected for most of the civil structures that are subjected to a vibration modal test. For such structures, in fact, a proportional damping model is considered in general as a reasonable model. However, when the modal identification techniques are applied on vibration data of real structures (including civil structures), it is not unusual to identify modes that are characterized by a certain degree of complexity (i.e. the MPC for some of the mode shapes is not close to one, or, equivalently, the MCF is not close to zero). In such cases, the resulting modal complexity can be due to the two following effects. On one side, a non-proportional damping behavior can effectively characterize the structure. On the other side, the structure might have a proportionally damped behavior, but complex mode shapes are estimated due to the random errors that always occur in the identification process [Brincker & Ventura, 2015] or due to a low quality of the response measurements (for example, in case of low values of the signal-to-noise ratio) [Rainieri & Fabbrocino, 2014]. If one expects to deal with a proportionally-damped structure, these indices (i.e. the MPC and the MCF) can be thus considered as indicators of the quality of the mode shape estimates and indicators of the quality of the modal identification process.

The second index that can be used in the stage of the modal validation is the Modal Assurance Criterion (MAC) [Allemang & Brown, 1982]. As already mentioned in

Chapter 6, the Modal Assurance Criterion is a criterion that is used to evaluate the degree of correlation or similarity between mode shape vectors, and it is defined as follows

$$MAC = \frac{\left(\boldsymbol{\psi}_{A,i}{}^{T}\ \boldsymbol{\psi}_{B,j}\right)^{2}}{\left(\boldsymbol{\psi}_{A,i}{}^{T}\ \boldsymbol{\psi}_{A,i}\right)\left(\boldsymbol{\psi}_{B,j}{}^{T}\ \boldsymbol{\psi}_{B,j}\right)} \tag{A.63}$$

where $\boldsymbol{\psi}_{A,i}$ and $\boldsymbol{\psi}_{B,j}$ are mode shapes related to the i-th mode of the modal model "A" and the j-th mode of the modal model "B", respectively. As already mentioned in Chapter 6, the MAC can be evaluated for mode shapes related to any mode index $i, j \in [1 \dots r]$, where r is the total number of the considered modes, and the value of the MAC is in the range $0 \leq \text{MAC} \leq 1$. In case of a good correlation between the two considered mode shapes the value of the MAC is close to one.

In the stage of the modal validation the MAC index can be mainly adopted in two different ways. First of all, the MAC can be calculated by considering a modal model obtained through a modal identification technique and by comparing this modal model with itself (i.e., the modal models "A" and "B" reported in Eq. A.63 are the same). In such case, the MAC is indicated in the literature as "auto MAC", and it has in general the following properties: when the mode indices are the same (i.e. $i = j$), a value of the auto MAC equal to one is obtained (i.e., each mode shape has, of course, a perfect correlation with itself); on the contrary, it is expected that the values of the auto MAC calculated for $i \neq j$ are approximately equal to zero. This last property derives from the fact that different mode shapes are mutually orthogonal, for example, with respect to the mass matrix of the structure. This also means that the degree of correlation between different mode shapes of the same structure is in general very low.

The Modal Assurance Criterion can be also adopted to compare mode shapes related to two different modal models, and, in such case, it is indicated in the literature as "cross MAC". For example, the mode shapes identified through a certain modal identification technique (modal model "A") can be compared with the mode shapes obtained using a different modal identification technique (modal model "B"). In such situation, it is expected that the results obtained using the two different modal identification techniques are similar. This means that it is expected to have values of

the cross MAC that are close to one if the mode indices are equal (i.e. $i = j$), and values of the cross MAC that are close to zero if the mode indices are different (i.e. $i \neq j$).

It is worth noting that the cross MAC can be also used to compare the experimental mode shapes identified through a modal identification technique (modal model "A") with the corresponding eigenvectors that derive from an analytical or a FEM model (modal model "B"). In the same way, for example, the natural frequencies obtained from the experimental test can be compared with respect to the natural frequencies calculated from the analytical or FEM model. In general, such operations can not be considered as part of the modal validation process when the modal identification is applied on real vibration data. However, such operations can be conveniently applied when the modal identification is performed on vibration data obtained through numerical simulations.

A.4 Applications of output-only modal identification

This section presents a numerical case study (see Section A.4.1) and an experimental case study (see Section A.4.2) where the output-only modal identification techniques described in previous sections were applied. Both in the numerical and in the experimental case studies the analyses were performed starting from the output vibration responses of frame building structures.

A.4.1 Output-only modal identification applied on simulated vibration data

This section[6] presents the application of the output-only modal identification on the simulated vibration responses of a numerical model of a frame building structure. Applying a modal identification technique in the framework of a simulation approach means basically that the exact modal properties of the considered structural system are known, and thus these properties can be compared with the modal parameters extracted from the simulated vibration data through the modal identification technique. As reported in [Brincker & Ventura, 2015], the possibility of doing this comparison (between the exact and the identified modal properties) makes the simulation approach an important tool for investigating the accuracy and the reliability of the modal identification technique. In the analyses presented in this section the considered output-only modal identification technique is the Natural Excitation technique (NExT) [James et al., 1993] combined with the Eigensystem Realization Algorithm (ERA) [Juang & Pappa, 1985]. The application performed using a simulation approach and presented in this section thus aims to investigate the effectiveness and the accuracy of the adopted implementation of the NExT-ERA

[6] Some of the contents of this section are presented in the conference papers co-authored with Dr. Landi and Prof. Diotallevi, published in the following conference proceedings:

Landi L., Bernagozzi G., Diotallevi P.P., Operational modal analysis of a plan-asymmetric RC frame structure subjected to a simulated random ground motion along different directions. *Proceedings of the XVI conference "L'Ingegneria sismica in Italia" ANIDIS 2015*, L'Aquila, Italy, September 13-17, 2015.

Bernagozzi G., Landi L., Diotallevi P.P., On the application of output-only modal identification to base excited frame structures. *Proceedings of the 16th World Conference on Earthquake Engineering (WCEE)*, Chile, January 9-13, 2017.

method[7]. It is worth noting that this technique and the related implementation have been also used a tool for extracting the modal properties of the structural systems in the analyses related to some of the modal flexibility-based approaches that are presented in other chapters of the thesis.

The numerical model that is considered in the present section is the model of a reinforced concrete (RC) building structure (Fig. A.2). The structure is a three story one-bay by one-bay frame building structure, and it is characterized by a bay width equal to 6 m and an interstory height equal to 3.2 m (as shown in Fig. A.2). Moreover, the elastic modulus of the concrete is equal to 20000 N/mm^2 and the mass of each story of the structure is equal to 43200 kg. Four columns with a rectangular cross section are present at each story of the structure. In particular, at each floor three columns have a rectangular cross section of 30×40 cm, while the column located in the point where the origin of the coordinate reference system is positioned has a rectangular cross section of 40×50 cm (Fig. A.2b). The structure is thus characterized by a plan-asymmetric distribution of the story stiffness. The center of stiffness of a generic story of the structure is indicated in Fig. A.2b with the letter C, while the center of mass is indicated with the letter G. It is worth noting that for the considered structure, which is a simple rectangular "box type" building structure, it was made the simplified assumption of considering the center of mass as located in the geometric center of the floor plan.

[7] The computations related to the application of the NExT-ERA method were performed in the Matlab programming system [Matlab].

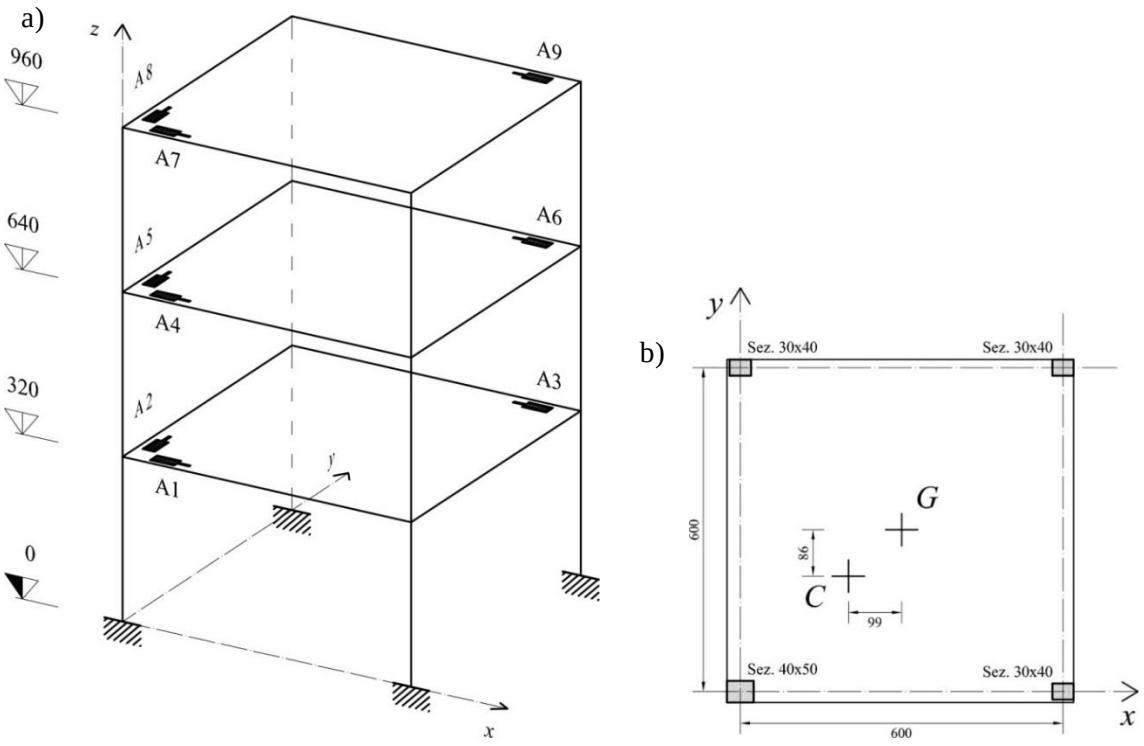

Figure A.2. Frame structure: a) 3D view with simulated layout of the sensors; b) plan view. Adapted from [Landi et al., 2015]

The numerical model considered in the analyses is a shear-type model that is characterized by nine DOFs. It is assumed that the beams of the structure are infinitely stiff in comparison to the columns and that each floor of the structure has a rigid-body in-plane behavior. The numerical model was created by defining the mass and the stiffness matrices of the building structure (such matrices have dimensions 9 × 9). Then, this undamped model of the structure was used to perform an eigenvector analysis, and the natural frequencies and the mode shapes of the structure were determined. The natural frequencies of the structure are reported in Table A.2 (which is shown later in this section together with the modal parameters extracted through the output-only modal identification), while the mode shapes related to the analytical model of the structure are reported in Fig. A.3. As shown in this figure, each mode shape can be easily associated to a predominant direction (for example, to the direction related to the *y*-axis, to the direction related to the *x*-axis, or to the direction that corresponds to the rotations around the *z*-axis).

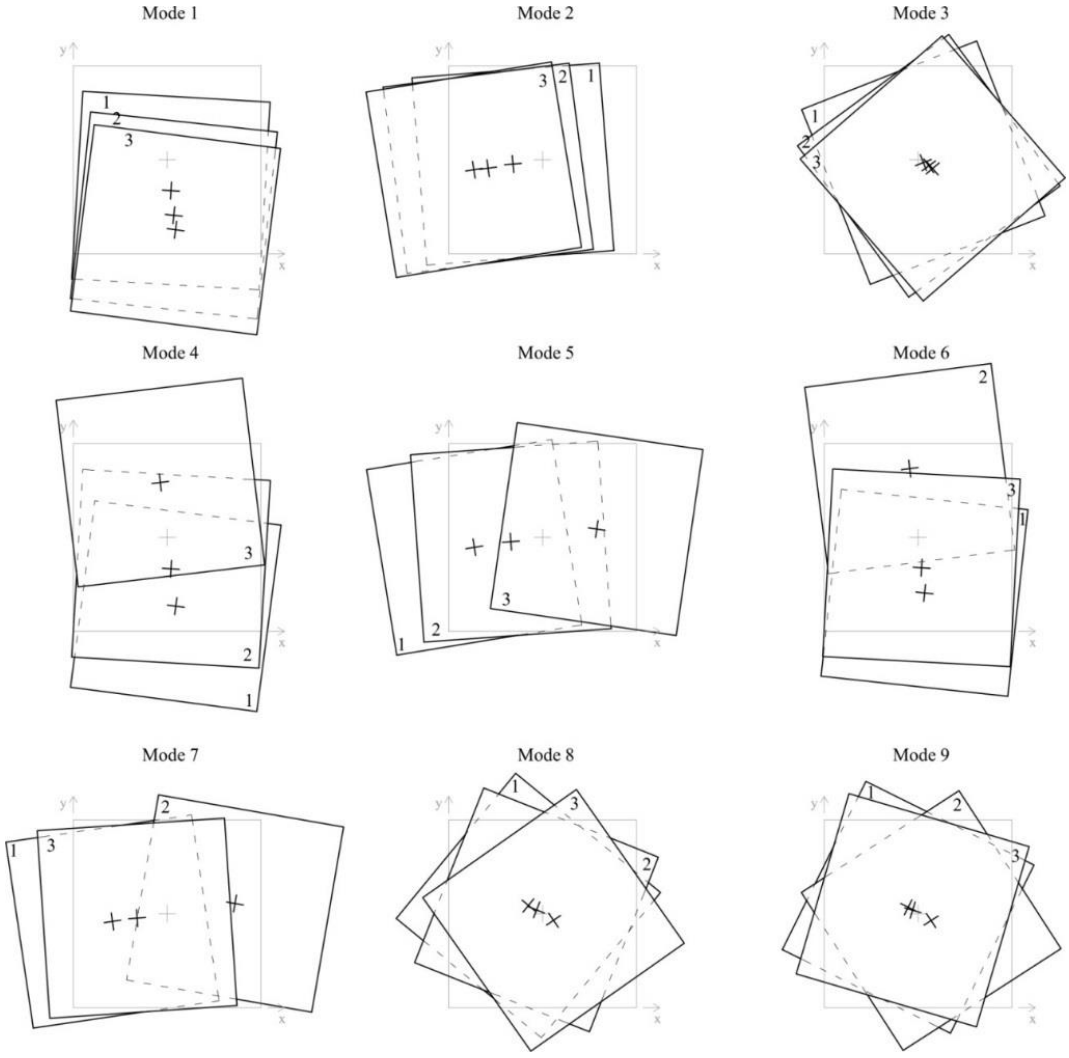

Figure A.3. Plan view of the analytical mode shapes of the structure [Landi et al., 2015]

Referring to the numerical model of the structure, it was also assumed that the modal damping ratio related to each mode of the structure is equal to $\zeta_i = 0.05$, and the vibration responses of the structure were determined by applying a white noise input at the base of the structure. This white noise input used in the simulation has a duration of 500 s, and it was applied in the direction that is orthogonal with respect to the segment that connects the center of mass and the center of stiffness of each story of the structure (i.e. the segment that connects the points G and C in Fig. A.2b). It is worth noting that the input used in this simulation (i.e. a single input) is not the ideal type of input that one expects to have when considering real-life structures that are tested under ambient vibrations (where, as already mentioned in Chapter 2, multiple inputs in general act simultaneously on the structure). In the present simulation, however, this simplified

approach of exciting the structure using the considered white noise input was in any case suitable to excite all the modes of the building structure (which, as already mentioned, is a plan-asymmetric frame building structure). The vibration responses due to the applied input were determined at all the DOFs of the structure, and, specifically, in the points and in the directions that are highlighted in Fig. A.2a. This figure shows the layout of the hypothetical sensors that have been used to collect the vibration responses of the structure. After having determined the vibration responses of the structure, white noise signals were added on the data to model measurement noise that can be present on real vibration data. The Root-Mean-Square (RMS) amplitude of the added noise is equal to the 10% of the RMS amplitude of the response signals.

The simulated vibration responses of the considered building structure were adopted to perform the output-only modal identification using the Natural Excitation technique (NExT) [James et al., 1993] combined with the Eigensystem Realization Algorithm (ERA) [Juang & Pappa, 1985] (Section A.1). According to the NExT method, outlined in Section A.1.3, the correlation functions were evaluated between all the vibration responses of the structure and the response associated to a reference channel. In particular, in the analysis channel A7 was selected as the reference channel. As shown in Fig. A.2a, this channel is assumed in the numerical simulation as the channel that measures the response of the structure at the top story (i.e. the third story) and in the x direction. After having determined the correlation functions, the ERA method was applied. In the analysis the dimension of the state space model that has to be identified was selected as equal to four times the number of the expected structural modes, according to the indication reported in [Caicedo, 2011]. For the considered building structure, which is modeled as a 9-DOF structural system, the number of the expected structural modes is equal to nine, and, thus, the dimension of the state space model was selected as equal to thirty-six. Using the output-only version of the ERA method, as described in Sections A.1.2 and A.1.3, the system matrix $\boldsymbol{A}_d$ of the identified stochastic state space model was determined. Then, an eigenvalue analysis was performed on the identified system matrix, and thirty-six poles of the model were obtained.

The selection of the structural modes, among all the poles that were estimated using the modal identification technique, was performed, by evaluating the indices of the Modal Amplitude Coherence (MAmC) and the Mode Singular Value (MSV) (described

in Section A.1.2 and extended to the output-only case as discussed in Section A.1.3). Such indices were evaluated for each of the modes identified using the ERA method and by considering a dimension of the state space model equal to thirty-six, and the results are reported in Table A.1. In this table, the identified modes are ordered with respect to the Mode Singular Value (MSV), from the largest to the smallest ones. Moreover, since, as already mentioned in Section A.1.2, when an underdamped structure is considered, the identified poles occur in complex conjugate pairs, in the table the results are shown by selecting only one mode among the two modes that form each complex conjugate pair. The selection of the structural modes was then performed through the analysis of the values of the Modal Amplitude Coherence (MAmC). The first nine modes that are associated to the highest values of the modal amplitude coherence are highlighted in Table A.1, and, as shown later in this section through a comparison between the identified and the analytical modes, they correspond to the nine structural modes of the considered building structure.

Frequency (Hz)	Damping Ratio	Mode Singular Value (MSV)	Modal Amplitude Coherence (MAmC)
2.66[a]	0.050	1.000	0.997
2.06[a]	0.043	0.746	0.989
5.70[a]	0.049	0.375	0.987
7.42[a]	0.052	0.301	0.995
4.32[a]	0.042	0.296	0.997
9.85	0.711	0.169	0.876
8.29[a]	0.063	0.147	0.999
3.63	0.124	0.145	0.600
10.61[a]	0.048	0.120	0.974
12.71	0.145	0.120	0.646
11.18	0.092	0.118	0.964
12.22[a]	0.055	0.103	0.971
6.54	0.061	0.098	0.389
15.50	0.051	0.054	0.566
17.61[a]	0.066	0.048	0.999
18.36	0.029	0.043	0.310
21.38	0.025	0.042	0.703
24.02	0.021	0.016	0.375

[a] : identified structural mode

Table A.1. Modes identified using the NExT-ERA method. Adapted from [Bernagozzi et al., 2017c].

After having identified the structural modes of the considered building structure, some of the criteria for modal validation that have been described in Section A.3 were applied. First of all, the modal complexity associated to the complex-value mode shapes of the identified structural modes was determined by evaluating the index of the Modal Phase Collinearity (MPC). All the identified structural modes and, especially, the first structural modes are characterized by values of the modal phase collinearity that are approximately close to one. This result is expected since in the present numerical simulation the model of the building structure is proportionally damped. The polar plots of the complex-value mode shapes related to the first four identified structural modes are reported in Fig. A.4, and in such figure the values of the modal phase collinearity are also reported. It is worth noting that among the first four modes, the third mode (M3-ϕ), which is a torsional mode, shows an amount of modal complexity that is higher with respect to the other modes (for which, on the contrary, the amount of the modal complexity is practically equal to zero, as shown by the values of the MPC index). This effect, of course, is not related to the dynamics of the structure, but it is only due to the presence of noise on the vibration data and due to the uncertainties that derive from the identification process.

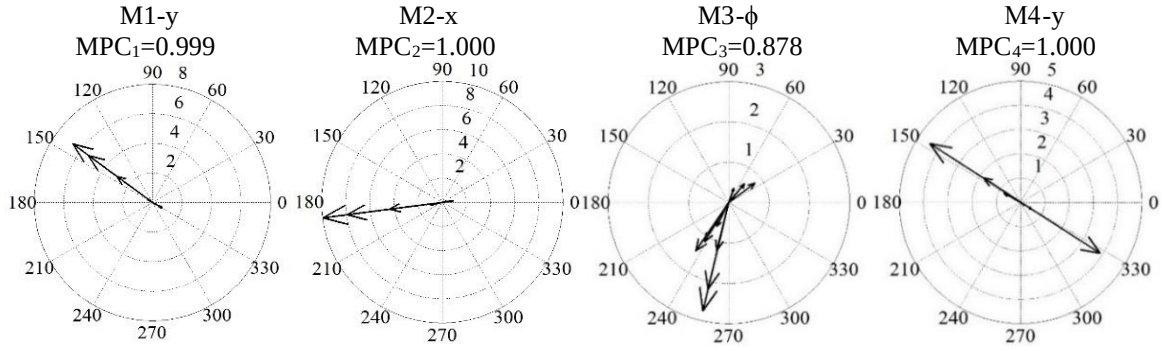

Figure A.4. Polar plots of identified complex-value mode shapes [Bernagozzi et al., 2017c].

The Modal Assurance Criterion (MAC) was also evaluated by comparing each identified mode shape of the structure with respect to all the other identified mode shapes (according to the description of the modal validation approach based on the MAC provided in Section A.3, in such case the auto MAC values associated to the identified mode shapes were determined). In particular, the MAC criterion was applied on the mode

shapes of the real (or normal) modes of the structure, which were obtained starting from the complex (or damped) identified modes using the Standard Technique [Alvin et al., 2003] (described in Section A.1.2). A graphical representation of the matrix that contains the values of the auto MAC is reported in Fig. A.5. As expected and as already discussed in Section A.3, the diagonal elements of this matrix are equal to one, because each mode is, of course, perfectly correlated with itself. On the contrary, small values (i.e. values that are approximately close to zero) were obtained in the off-diagonal components of the auto MAC matrix. As already discussed in Section A.3, it is expected that the degree of correlation between the different mode shapes is very low, and thus the above-mentioned result suggests that the identified modal model is consistent.

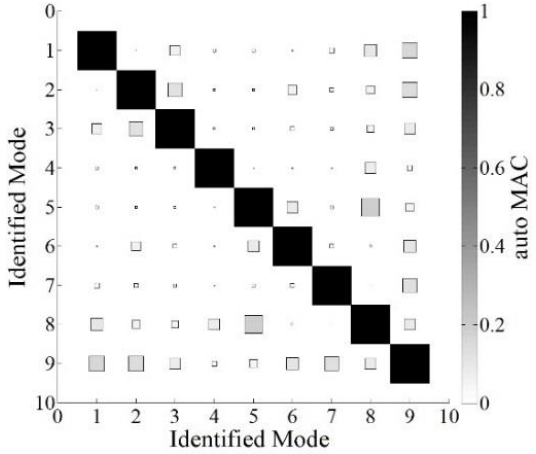

Figure A.5. Matrix of the auto MAC: identified structural modes compared with each other. Adapted from [Bernagozzi et al., 2017c].

Finally, to conclude the analyses performed in the framework of the numerical simulation, the identified modal parameters were compared with the true modal parameters related to the analytical model of the structure. The results are reported in Table A.2, where the natural frequencies and the modal damping ratios of the structural modes identified using the NExT-ERA method are compared with respect to the natural frequencies and the modal damping ratios of the analytical model. Moreover, in the last column of the table the values of the Modal Assurance Criterion evaluated between the identified and the analytical mode shapes are reported (as discussed in Section A.3 these values are termed cross MAC). It is worth noting that such values of the cross MAC reported in the last column of Table A.2 correspond to the

diagonal components of the cross MAC matrix evaluated between the identified and the analytical mode shapes (a graphical representation of this cross MAC matrix is reported in Fig. A.6). Referring to the natural frequencies, as shown in Table A.2, a very good agreement was found between the identified and the analytical natural frequencies of the structure. A good agreement was also found between the identified and the analytical mode shapes of the structure. This statement is supported by the fact that the values of the cross MAC reported in Table A.2 are close to one, especially for the first structural modes. Referring to the modal damping ratios, it is evident in Table A.2 that the discrepancies between the identified and the analytical values of the damping are in general higher than the discrepancies present between the identified and the analytical natural frequencies. In any case, the identified modal damping ratios are not far from the value of the damping $\zeta_i = 0.05$, which was assumed as the value of the modal damping ratio related to each structural mode in the numerical model.

Structural mode	Natural frequency (Hz)		Modal Damping Ratio		Cross MAC_{ii} (/)
	Identified	Analytical	Identified	Analytical	
M1-y	2.06	2.05	0.045	0.05	1.000
M2-x	2.66	2.63	0.050	0.05	0.997
M3-ϕ	4.32	4.34	0.042	0.05	0.999
M4-y	5.70	5.75	0.049	0.05	0.993
M5-x	7.42	7.38	0.052	0.05	0.990
M6-y	8.29	8.30	0.063	0.05	0.885
M7-x	10.61	10.66	0.048	0.05	0.968
M8-ϕ	12.22	12.15	0.055	0.05	0.850
M9-ϕ	17.61	17.56	0.066	0.05	0.664

Table A.2. Comparison between identified and analytical modal parameters. Adapted from [Bernagozzi et al., 2017c].

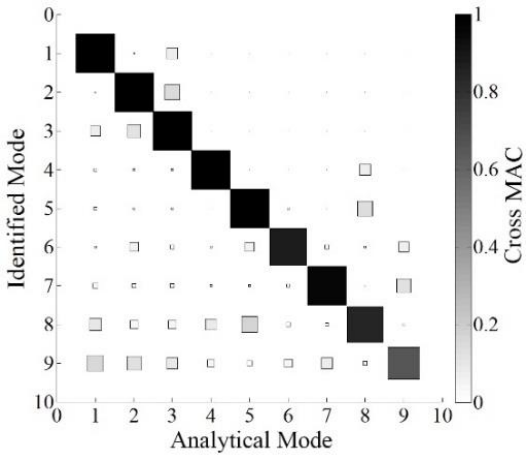

Figure A.6. Matrix of the cross MAC: comparison between identified modes and analytical modes. Adapted from [Bernagozzi et al., 2017c].

A.4.2 Output-only modal identification applied on real vibration data

This section[8] presents the application of the output-only modal identification on the experimental vibration data of an Operational Modal Analysis (OMA) test that was performed on a steel frame structure. As reported in [Brincker & Ventura, 2015], when dealing with experimental data, a convenient approach to perform the OMA identification is to apply both frequency and time domain techniques, trying to validate the identification process by comparing the results obtained in the two domains. Following the above-mentioned indication reported in [Brincker & Ventura, 2015], in the analysis presented in this section the output-only modal identification was performed using both the Enhanced Frequency Domain Decomposition (EFDD) [Brincker, Zhang & Andersen, 2001; Brincker, Ventura & Andersen, 2001] and the Eigensystem Realization Algorithm [Juang & Pappa, 1985] combined with the Natural Excitation technique [James et al., 1993] (NExT-ERA). As already mentioned in Chapter 2 and in previous sections of this

[8] Some of the contents of this section are presented in a conference paper co-authored with Prof. Ventura, Dr. Kaya, Dr. Landi, and Prof. Diotallevi, published in the following conference proceedings:

Bernagozzi G, Ventura CE, Kaya Y, Landi L, Diotallevi PP, Comparison of OMA techniques and effect of added masses on the modal properties of a small steel frame. *Proceedings of the 7th International Operational Modal Analysis Conference (IOMAC)*, Ingolstadt, Germany, 10-12 May 2017.

appendix, the former (i.e. the EFDD method) is a frequency domain technique, while the latter (i.e. the NExT-ERA method) is a technique that works in time domain. At the end, the modal parameters obtained using the two above-mentioned techniques were compared.

The structure that was considered in the Operational Modal Analysis (OMA) test [9] is a scaled steel frame structure (Fig. A.7) that is located in the laboratory of the Polytechnic School of Engineering in Gijón (Spain). The structure is a two-story, 1-bay-by-1-bay frame, and it is characterized by the following dimensions: each floor has dimensions equal to 0.42 m × 0.28 m, and the height of the structure is 1 m (as shown in Fig. A.7b where a schematic representation of the geometry of the frame structure is reported). The structure is composed by four columns that have hollow rectangular cross sections with dimensions equal to 20 mm × 15 mm and a thickness equal to 1.5 mm. The steel plates that create the two floors of the structure have a thickness equal to 5 mm. The structure is plan-symmetric with respect to two prevalent directions, and due to the orientation of the cross sections of the columns (Fig. A.7b) the weak direction of the structure is the Y direction, while the strong direction of the frame is the X direction.

[9] The vibration test was performed on May 11, 2015 during the pre-conference Operational Modal Analysis course held by Prof. Carlos Ventura and Prof. Svend Gade at the 6-th International Modal Analysis Conference (IOMAC) in Gijon, Spain. The test was executed by the participants of the mentioned OMA course (which was attended by the writer). The writer would like to thank Prof. Ventura and Prof. Gade for their assistance during the test. The writer would also like to thank Prof. Manuel López Aenlle and Dr. Pelayo Fernández Fernández for their support in the execution of the vibration test. Finally, the writer gratefully acknowledges the collaboration of all the participants of the OMA course that were involved in the OMA test (especially the collaboration of Oscar Ramírez and Guillermo Fernandez-Lorenzo).

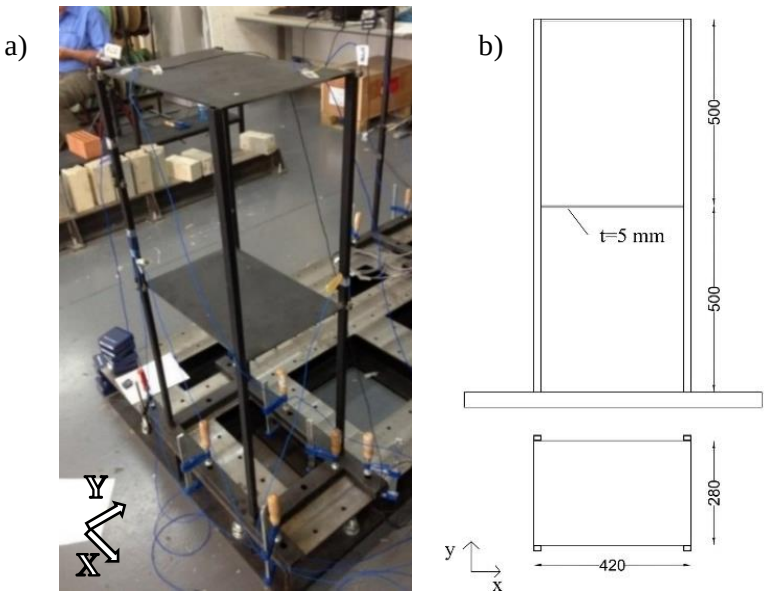

Figure A.7. Tested steel frame structure: a) photo (Polytechnic School of Engineering, Gijón); b) geometry. Adapted from [Bernagozzi et al., 2017d].

The structure was excited by artificial inputs that aim to simulate the type of inputs that acts on real-life structures that are tested under ambient vibrations (i.e. random, multiple, and uncorrelated inputs at different spatial locations). In particular, the structure was tested in the laboratory under human-hand-induced vibrations. In other words, during the operational modal analysis test the structure was excited by the inputs produced by several people that randomly, continuously, and lightly hit the structure in different spatial locations using the hands. Due to the type of the applied inputs, the test should be thus a suitable case study for the application of the OMA identification techniques. Only the output vibration responses of the structure due to the applied random inputs were recorded during the test using piezoelectric uniaxial accelerometers (Fig. A.8a). The sensors used in the test are PCB Model 333B32 [PCB Piezotronics], which are characterized by a sensitivity equal to 100 mV/g and a measurement range equal to ±50g. The vibration responses of the structure were recorded with a sampling frequency equal to 200 Hz, and the length of time of the measurements was approximately 10 minutes. In the test eight sensors were installed on the structure, but only the measurements obtained from six sensors were considered in the data analysis (i.e. the measurements obtained from three sensors for each story

of the structure). The locations and the orientations of these six sensors (i.e. uniaxial accelerometers) are shown in Fig. A.8b.

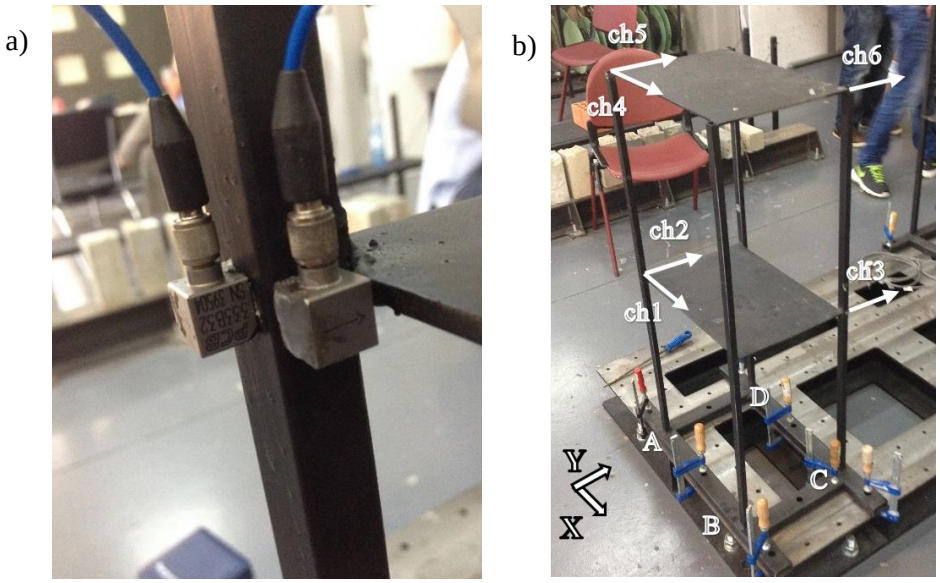

Figure A.8. Test setup: a) accelerometric sensors; b) schematic layout of the channels used in the data analysis (Polytechnic School of Engineering, Gijón). Adapted from [Bernagozzi et al., 2017d].

The output-only modal identification was performed at first using the Enhanced Frequency Domain Decomposition (EFDD) method [10] [Brincker, Zhang & Andersen, 2001; Brincker, Ventura & Andersen, 2001], using the steps that are described in Section A.2. According to the EFDD method, the spectral density functions were estimated starting from the measured vibration responses of the steel frame structure (i.e. the data acquired using the six channels reported in Fig. A.8b), and then a singular value decomposition was performed on the matrix of the spectral density functions. An example of the Auto Spectral Density (ASD) functions estimated from the measurements is shown in Fig. A.9, where the ASD functions evaluated for the signals acquired using channel 4 and channel 5 are reported. These two channels were used in the test to measure the accelerations at the second story of the structure near the column indicated with the letter A in Fig. A.8b, but channel 4 is oriented in X direction

[10] The EFDD method implemented in ARTeMIS software [ARTeMIS] was adopted, and as a complementary tool for performing the analyses in frequency domain, a Matlab code [Matlab] that implements the FDD method was also developed and used.

(i.e. the strong direction of the frame) while channel 5 is oriented in Y direction (i.e. the weak direction). The plot of the singular values computed from the matrix of the spectral density functions is reported in Fig. A.10. First of all, if one considers the first singular values (black line reported in Fig. A.10), it is evident that, in the analyzed frequency range (from 0 to 100 Hz), there are some clear peaks that can be associated to structural modes. Moreover, it is worth noting that some peaks are also present in the plots of the other singular values (reported as gray lines in Fig. A.10). According to [Brincker & Ventura, 2015], this characteristic of the plot of the singular values can be considered as an indication of the fact that the vibration test has been effectively performed by applying a multiple input excitation. According to the EFDD method, the structural modes were manually identified by analyzing the peaks in the plot of the first singular values, and six structural modes were identified. The peaks in the plot of the singular values associated to these six structural modes are highlighted in Fig. A.10, and the peaks correspond, respectively, to the following structural modes:

- first longitudinal mode in weak direction (1Y)
- first longitudinal mode in strong direction (1X)
- first torsional mode (1T)
- second longitudinal mode in weak direction (2Y)
- second longitudinal mode in strong direction (2X)
- second torsional mode (2T).

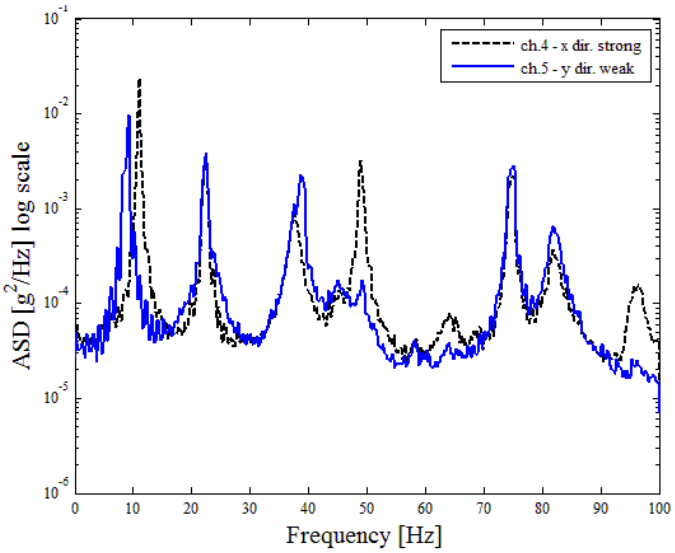

Figure A.9. Magnitude of the auto spectral density functions related to channels 4, 5. Adapted from [Bernagozzi et al., 2017d].

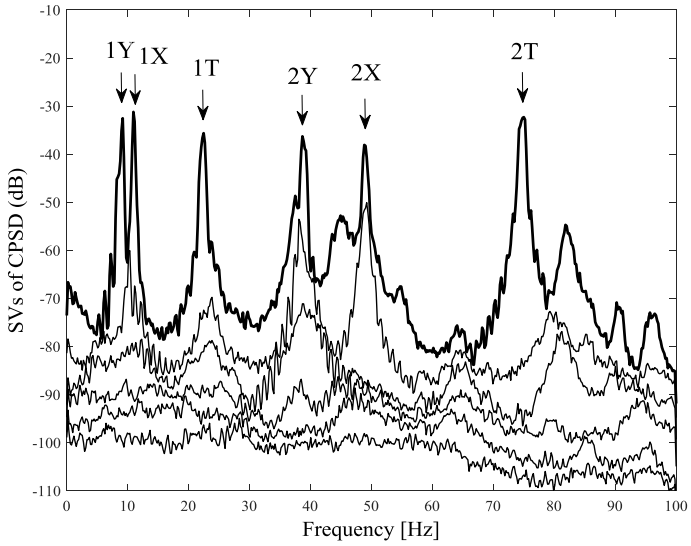

Figure A.10. Singular values computed from spectral density functions. Adapted from [Bernagozzi et al., 2017d].

The natural frequencies and the modal damping ratios of the steel frame structure identified using the EFDD method are reported in Table A.3, while the identified mode shapes of the structure are reported in Fig. A.11. Of course, the components of the mode shapes were identified at the sensor locations, and then to create the graphical representation of the identified mode shapes shown in Fig. A.11, it was made the simplifying assumption of considering each floor of the structure as a rigid body. The output-only modal identification was also applied in time domain using the Eigensystem Realization Algorithm (ERA) [Juang & Pappa, 1985] combined with the Natural Excitation technique (NExT) [James et al., 1993]. According to the steps reported in Sections 6.1.2 and 6.1.3, the correlation functions were estimated starting from the measured vibration responses of the steel frame structure (NExT procedure), and then the ERA method was applied [11]. The natural frequencies and the modal damping ratios related to the six prevalent modes of the structure identified using the NExT-ERA method are reported in Table A.3, while the identified mode shapes are reported in Fig. A.12. In Table A.3 the modal parameters identified using the EFDD method (in terms of natural frequencies, modal damping ratios, and mode shapes) are

[11] The computations related to the application of the NExT-ERA method were performed in the Matlab programming system [Matlab].

thus compared with the modal parameters identified using the NExT-ERA method. It is worth noting that, while the natural frequencies and the modal damping ratios are directly compared in Table A.3, the mode shapes identified using the EFDD method were compared with the mode shapes identified using the NExT-ERA method through the Modal Assurance Criterion (i.e. the cross MAC, as described in Section A.3). The values of the cross MAC obtained for the six modes identified using the two OMA techniques are reported in the last column of Table A.3. Referring to the natural frequencies of the structure, a very good agreement was found between the frequencies identified using the EFDD method and the corresponding frequencies identified using the NExT-ERA method. Moreover, all the values of the cross MAC evaluated on the identified mode shapes are close to one (as shown in Table A.3), and thus a very good agreement was also found between the two OMA techniques in the estimation of the mode shapes of the structure. Referring to the modal damping ratios, a good agreement between the two OMA identification techniques was observed, especially for the first two structural modes.

Mode number	Mode type	Natural frequency [Hz]		Modal damping ratio (%)		Cross MAC
		EFDD	NExT-ERA	EFDD	NExT-ERA	
1	1Y	9.20	9.10	1.65	1.68	0.999
2	1X	11.00	11.04	1.51	1.41	0.988
3	1T	22.34	22.60	1.67	0.91	0.994
4	2Y	38.76	38.78	0.69	0.66	0.989
5	2X	48.95	49.00	0.60	0.27	0.967
6	2T	74.75	74.51	0.57	0.37	0.999

Table A.3. Identified modal parameters – comparison between the EFDD method and the NExT-ERA method. Adapted from [Bernagozzi et al., 2017d].

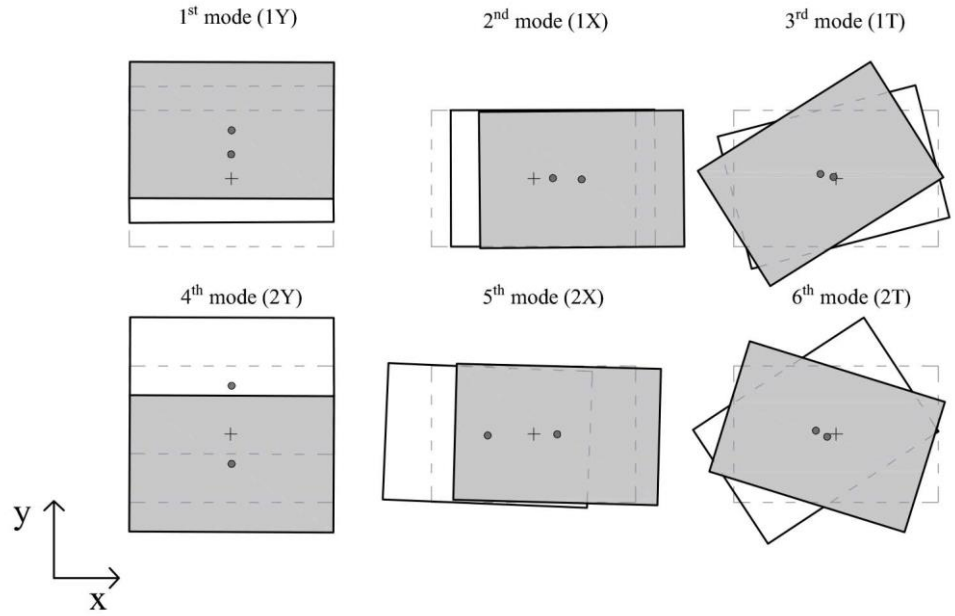

Figure A.11. Plan view of the mode shapes identified using the EFDD method.

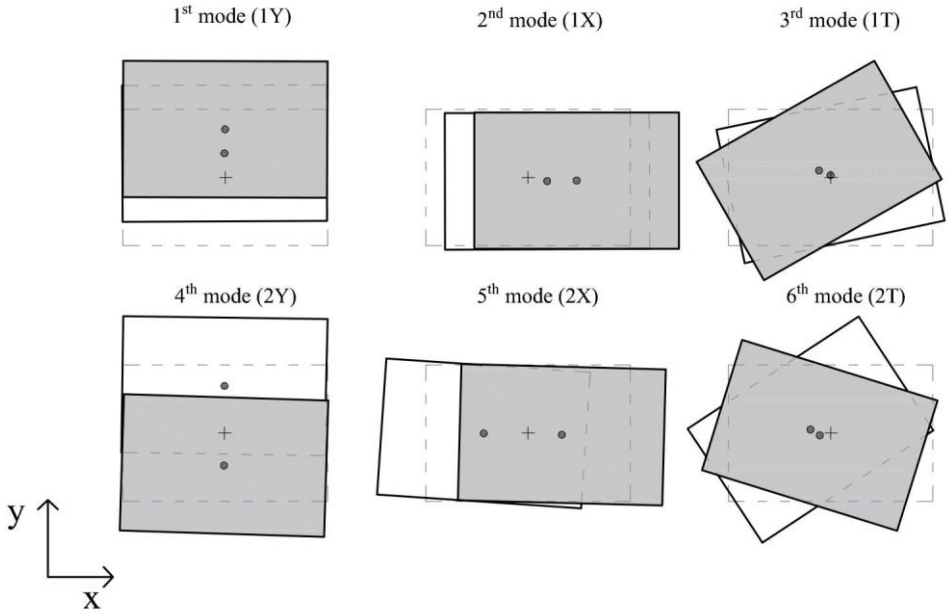

Figure A.12. Plan view of the mode shapes identified using the NExT-ERA method. Adapted from [Bernagozzi et al., 2017d].

Bibliography

Aenlle ML, Brincker R, Canteli AF (2005). Some Methods to Determine Scaled Mode Shapes in Natural Input Modal Analysis. *Proceedings of the International Modal Analysis Conference (IMAC-XXIII): A Conference & Exposition on Structural Dynamics*. Society for Experimental Mechanics.

Aenlle ML, Fernández P, Brincker R, Fernández-Canteli A (2010). Scaling-factor estimation using an optimized mass-change strategy. *Mechanical Systems and Signal Processing*; 24 (5):1260-1273.

Aenlle ML, Brincker R, Pelayo F, Canteli AF (2012). On exact and approximated formulations for scaling-mode shapes in operational modal analysis by mass and stiffness change. *Journal of Sound and Vibration*; 331 (3): 622–637.

Aenlle ML, Brincker R (2013). Modal scaling in operational modal analysis using a finite element model. *International Journal of Mechanical Sciences*; 76: 86-101.

Allemang RJ, Brown DL (1982). A correlation coefficient for modal vector analysis. *Proceedings of the 1st International Modal Analysis Conference (IMAC)*, Kissimmee, FL, USA, 1982, pp. 110–116.

Alvin FK, Robertson AN, Reich GW, Park KC (2003). Structural system identification: from reality to model. *Computers and Structures*; 81, 1149-1176.

ANSI S2.47 (1990). Guidelines for the Measurement of Vibrations and Evaluation of Their Effects on Buildings. *American National Standard, Vibration of Buildings, R2001*.

American Society of Civil Engineers - ASCE (2013). Structural Identification of Constructed Systems: Approaches, Methods, and Technologies for Effective Practice of St-Id. Çatbas FN, Kijewski-Correa T, Aktan AE (editors).

ARTeMIS software, Structural Vibration Solutions, http://www.svibs.com/

Asmussen JC, Ibrahim R, Brincker R (1998). Random Decrement: Identification of Structures subjected to Ambient Excitation. *Proceedings of the 16th International Modal Analysis Conference*, February 2-5, Santa Barbara, California, USA.

Balsamo L, Betti R (2015). Data-based structural health monitoring using small training data sets. *Structural Control and Health Monitoring*; 22 (10): 1240-1264.

Barnett V, Lewis T (1994). *Outliers in Statistical Data*. 3rd ed. Chichester, UK: John Wiley & Sons.

Beck JL, Vanik MW, Katafygiotis LS (1994). Determination of model parameters from ambient vibration data for structural health monitoring. *Proceedings of the 1st World Conference on Structural Control*, Pasadena, California.

Bendat JS, Piersol AG (2000). *Random data: Analysis and measurement procedures*. Wiley, New York.

Berman A, Flannelly WG (1971). Theory of Incomplete Models of Dynamic Structures. *AIAA Journal*; 9 (8): 1481-1487.

Bernagozzi G, Landi L, Diotallevi PP (2017 a). Truncation error analysis on modal flexibility-based deflections: application to mass regular and irregular structures. *Engineering Structures*; 142 (1): 192–210. DOI: 10.1016/j.engstruct.2017.03.057

Bernagozzi G, Ventura CE, Allahdadian S, Kaya Y, Landi L, Diotallevi PP (2017 b). Application of modal flexibility-based deflections for damage diagnosis of a steel frame structure. In: Vestroni F, Gattulli V, Romeo F (editors), *Procedia Engineering, X International Conference on Structural Dynamics, EURODYN 2017*. Volume 199, Pages 2026-2033. DOI: 10.1016/j.proeng.2017.09.468

Bernagozzi G, Landi L, Diotallevi PP (2017 c). On the application of output-only modal identification to base excited frame structures. *Proceedings of the 16th World Conference on Earthquake Engineering (WCEE*), Chile, January 9-13, 2017.

Bernagozzi G, Ventura CE, Kaya Y, Landi L, Diotallevi PP (2017 d). Comparison of OMA techniques and effect of added masses on the modal properties of a small steel frame. *Proceedings of the 7th International Operational Modal Analysis Conference (IOMAC)*, Ingolstadt, Germany, 10-12 May 2017.

Bernal D (2001). A subspace approach for the localization of damage in stochastic systems. In: Chang FK, editor. *Structural Health Monitoring: The Demand and Challenges - Proceedings of the 3rd International Workshop in Structural Health Monitoring*. Boca Raton, FL, USA: CRC Press; p. 899-908.

Bernal D (2002). Load Vectors for Damage Localization. *Journal of Engineering Mechanics*; 128 (1): 7-14.

Bernal D, Gunes B (2002). Damage localization in output-only systems: A flexibility based approach. *Proc. SPIE - The International Society for Optical Engineering*, 4753 II, pp. 1185-1191.

Bernal D (2004). Modal scaling from known mass perturbations. *Journal of Engineering Mechanics*, 2004; 130 (9): 1083 -1088.

Bernal D, Gunes B (2004). Flexibility Based Approach for Damage Characterization: Benchmark Application. *Journal of Engineering Mechanics*; 130 (1): 61-70.

Bishop RED, Gladwell GML (1963). An Investigation Into The Theory Of Resonate Testing. *Philosophical Trans. of the Royal Society of London*; 255 (1055): 241-280.

Brincker R, Ventura CE, Andersen P (2001). Damping Estimation by Frequency Domain Decomposition. *Proceedings of the 19th International Modal Analysis Conference (IMAC)*, Orlando, Florida, 2001.

Brincker R, Zhang L, Andersen P (2001). Modal identification of output-only systems using frequency domain decomposition. *Smart Materials and Struc*tures; 10 (3): 441-445.

Brincker R, Ventura C, Andersen P (2003). Why Output Only Modal Analysis is a Desirable Tool for a Wide Range of Practical Applications. *Proceedings of the 21st International Modal Analysis Conference*, February 3-6, Kissimmee, Florida, USA.

Brincker R, Andersen P (2003). A way of getting scaled mode shapes in output only modal analysis. *Proceedings of the International Modal Analysis Conference (IMAC XXI)*, Orlando, USA, 2003.

Brincker R, Andersen P (2006). Understanding Stochastic Subspace Identification. *Proceedings of the International Modal Analysis Conference (IMAC-XXIV), A Conference & Exposition on Structural Dynamics*. Society for Experimental Mechanics.

Brincker R, Ventura C (2015). *Introduction to OPERATIONAL MODAL ANALYSIS*. 1st ed. Chichester, UK: John Wiley & Sons.

Brincker R, Aenlle ML (2015). Mode shape sensitivity of two closely spaced eigenvalues. *Journal of Sound and Vibratio*n; 334: 377–387.

Brincker R (2015). Implications of closely spaced modes in OMA. *Proceedings of the 6th International Operational Modal Analysis Conference (IOMAC)*, Gijón, Spain, May 12-14, 2015.

Brown DL, Allemang RJ, Zimmerman R, Mergeay M (1979). Parameter Estimation Techniques For Modal Analysis. *SAE Technical Paper 790221*.

Caicedo JM, Dyke SJ, Johnson EA (2004). Natural Excitation Technique and Eigensystem Realization Algorithm for Phase I of the IASC-ASCE Benchmark Problem: Simulated Data. *Journal of Engineering Mechanics*; 130 (1): 49-60

Caicedo JM (2011). Practical guidelines for the natural excitation technique (NExT) and the eigensystem realization algorithm (ERA) for modal identification using ambient vibration, *Experimental Techniques*, 35 (4), 52-58.

Catbas FN, Brown DL, Aktan AE (2006). Use of modal flexibility for damage detection and condition assessment: Case studies and demonstrations on large structures. *Journal of Structural Engineering*; 132 (11): 1699-1712.

Catbas FN, Gul M, Burkett JL (2008). Damage assessment using flexibility and flexibility-based curvature for structural health monitoring. *Smart Materials and Structures*; 17 (1): 015024.

Cawley P, Adams R (1979). The locations of defects in structures from measurements of natural frequencies. *Journal of Strain Analysis*, 14 (2), 49–57.

Chang FK, Prosser WH, Schulz MJ (2002). Editorial: Letter of Introduction from the Editors of Structural Health Monitoring. *Structural Health Monitoring*, Vol. 1 (1), pp. 3-4.

Ching J, Beck JL (2004). Bayesian Analysis of the Phase II IASC–ASCE Structural Health Monitoring Experimental Benchmark Data. *Journal of Engineering Mechanics*; 130 (10): 1233-1244.

Chopra AK (2000). *Dynamics of structures: Theory and Applications to Earthquake Engineering*. Prentice Hall: New Jersey, USA.

Clough RW, Penzien J (1975). *Dynamics of structures*. McGraw-Hill.

Cole HA (1973). On-line failure detection and damping measurements of aerospace structures by random decrement signature. *Report NASA CR-2205*.

Crossbow Technology, San Jose, CA, USA

Cunha A, Caetano E (2005). From Input-Output to Output-Only Modal Identification of Civil Engineering Structures. *Proceedings of the 1st International Operational Modal Analysis Conference*, April 26-27, Copenhagen, Denmark.

DASYLab software, Measurement Computing, https://www.mccdaq.com/products/DASYLab.aspx

De Angelis M, Luş H, Betti R, Longman RW (2002). Extracting Physical Parameters of Mechanical Models From Identified State-Space Representations. *Journal of Applied Mechanics*; 69 (5): 617-625.

De Schutter B (2000). Minimal state-space realization in linear system theory: An overview. *Journal of Computational and Applied Mathematics*, Special Issue on Numerical Analysis in the 20th Century, Vol. I: Approximation Theory; 121(1–2): 331–354.

Doebling SW, Farrar CR, Prime MB, Shevitz DW (1996). *Damage Identification and Health Monitoring of Structural and Mechanical Systems from Changes in their Vibration Characteristics: A Literature Review*. Report LA-13070-MS, Los Alamos National Laboratory, Los Alamos, NM, USA.

Doebling SW, Peterson LD, Alvin KF (1996). Estimation of reciprocal residual flexibility from experimental modal data. *AIAA Journal*; 34 (8): 1678-1685.

Doebling SW, Farrar CR, Aktan AE, Beck J, Cornwell P, Helmicki A, Safak E, Yao J (2000). The State of the Art in Structural Identification of Constructed Facilities. A report by the ASCE committee on Structural Identification of Constructed Facilities.

Duan Z, Yan G, Ou J, Spencer BF (2005). Damage localization in ambient vibration by constructing proportional flexibility matrix. *Journal of Sound and Vibration*; 284: 455-466.

Duan Z, Yan G, Ou J, Spencer BF (2007). Damage detection in ambient vibration using proportional flexibility matrix with incomplete measured DOFs. *Structural Control and Health Monitoring*; 14 (2): 186-196.

Dyke SJ, Bernal D, Beck J, Ventura CE (2001). An experimental benchmark problem in structural health monitoring. In: Chang FK (editor), *Structural Health Monitoring: The Demand and Challenges - Proc. of the 3rd International Workshop in Structural Health Monitoring*, CRC Press, Boca Raton, FL, 2001, pp. 488-497.

Dyke SJ, Bernal D, Beck J, Ventura CE (2003). Experimental Phase II of the Structural Health Monitoring Benchmark Problem. *Proceedings of the 16th ASCE Engineering Mechanics Conference*, Seattle, Washington, USA, July 16-18, 2003.

Dyke SJ (2011). Report on the Building Structural Health Monitoring Problem Phase 2 Experimental. Network for Earthquake Engineering Simulation (database), https://nees.org/resources/2412.

Dynamic Testing Agency (1993). *Handbook on Guidelines to Best Practice: Modal Testing v. 3*. Dynamic Testing Agency, Cranfield.

Ewins DJ (2000). *Modal testing: theory, practice and application*. 2nd ed. Philadelphia, PA, USA: Research Studies Press Ltd.

Fan W, Qiao P (2011). Vibration-based Damage Identification Methods: A Review and Comparative Study. *Structural Health Monitoring*; 10 (1): 83-111.

Farrar R, Worden K (2013). *Structural health monitoring: A machine learning perspective*. 1st ed. Chichester, UK: John Wiley & Sons.

Felber AJ (1993). *Development of a hybrid bridge evaluation system*. PhD thesis, University of British Columbia, Vancouver, Canada.

Figueiredo E, Park G, Figueiras J, Farrar C, Worden K (2009). *Structural Health Monitoring Algorithm Comparisons Using Standard Data Sets*. Report LA-14393, Los Alamos National Laboratory, Los Alamos, New Mexico, USA, March 2009.

Friswell MI, Mottershead JE (1995). *Finite Element Model Updating in Structural Dynamics*. Springer.

Gao Y, Spencer Jr BF (2002). Damage localization under ambient vibration using changes in flexibility. *Earthquake Engineering and Engineering Vibration*; 1 (1): 136 -144.

Gersch W. (1970). Estimation of The Autoregressive Parameters of A Mixed Autoregressive Moving-Average Time Series. *IEEE Trans. on Automatic Control*; 15 (5): 583-588.

Guidorzi R (2003). *Multivariable System Identification. From observations to models*. Bologna, Italy. Bononia University Press.

He J, Fu ZF (2001). *Modal analysis*. Butterworth-Heinemann.

Ho BL, Kalman RE (1966). Effective construction of linear state-variable models from input/output functions. *Regelungstechnik*, 14: 545-548.

Hogue TD, Ahmet E, Aktan AE, Hoyos A (1991). Localized Identification of Constructed Facilities. *Journal of Structural Engineering*; 117 (1): 128-148.

Ibrahim SR, Mikulcik EC (1973). A Time Domain Modal Vibration Test Technique. *The Shock and Vibration Bulletin*; 43 (4): 21-37.

Ibrahim SR, Mikulcik EC (1977). A Method for the Direct Identification of Vibration Parameters from the Free Response. *The Shock and Vibration Bulletin*; 47 (4): 183-198.

Ibrahim SR (1977). Random decrement technique for modal identification of structures. *Journal of Spacecraft and Rockets*; 14: 696–700.

Ibrahim SR, Asmussen JC, Brincker R (1996). Modal parameter identification from responses of general unknown random inputs. *Proceedings of the 14th International Modal Analysis Conference - IMAC XIV*, 1996.

Imregun M, Ewins DJ (1993). Realisation of complex mode shapes. *Proceedings of the 11th Annual International Modal Analysis Conference*, February 1993, p. 1303–9.

James III GH, Carne TG, Lauffer PJ (1993). The Natural Excitation Technique (NExT) for Modal Parameter Extraction From Operating Wind Turbines. *The International Journal of Analytical and Experimental Modal Analysis*, 10(4), 260-277.

Johnson EA, Lam HF, Katafygiotis LS, Beck JL (2004). Phase I IASC-ASCE Structural Health Monitoring Benchmark Problem Using Simulated Data. *Journal of Engineering Mechanics*, 130 (1): 3-15.

Juang JN, Pappa RS (1985). An eigensystem realization algorithm for modal parameter identification and model reduction. *Journal of Guidance, Control, and Dynamics*, 8 (5): 620-627.

Juang J, Phan M, Horta LG, Longman RW (1993). Identification of observer/Kalman filter Markov parameters - Theory and experiments. *Journal of Guidance, Control, and Dynamics*, 16 (2): 320-329.

Juang JN (1994). *Applied system identification*, Prentice Hall.

Juang JN, Phan MQ (2001). *Identification and control of mechanical systems*. Cambridge University Press.

Kennedy CC, Pancu CDP (1947). Use Of Vectors In Vibration Measurement And Analysis. *Journal of the Aeronautical Sciences*; 14 (11): 603-625.

Kharrazi MHK, Ventura CE (2001). *Experimental Benchmark Problem in Structural Health Monitoring – Results of Ambient Vibration Studies*. Report – Civil 598 Directed Studies. Department of Civil Engineering The University of British Columbia. June 2001.

Khatibi MM, Ashory MR, Malekjafarian A, Brincker R (2012). Mass-stiffness change method for scaling of operational mode shapes. *Mechanical Systems and Signal Processing*; 26: 34–59.

Kinemetrics Inc., http://www.kinemetrics.com/p-163-Home.aspx

Koo KY, Lee JJ, Yun CB, Kim JT (2008). Damage detection in beam-like structures using deflections obtained by modal flexibility matrices. *Smart Structures and Systems*; 4 (5): 605-628.

Koo KY, Sung SH, Park JW, Jung HJ (2010). Damage detection of shear buildings using deflections obtained by modal flexibility. *Smart materials and structures*; 19 (11): 115026.

Koo KY, Sung SH, Jung HJ (2011). Damage quantification of shear buildings using deflections obtained by modal flexibility. *Smart materials and structures*; 20: 045010.

LabVIEW, National Instruments, http://www.ni.com/

Landi L, Bernagozzi G, Diotallevi PP (2015). Operational modal analysis of a plan-asymmetric RC frame structure subjected to a simulated random ground motion along different directions. *Proceedings of the XVI conference "L'Ingegneria sismica in Italia" ANIDIS 2015*, L'Aquila, Italy, September 13-17, 2015.

Lieven N, Ewins, D. (1988) Spatial correlation of mode shapes: the coordinate modal assurance criterion (COMAC). *Proceedings of the 6th International Modal Analysis Conference (IMAC)*, Orlando, FL, Society for Experimental Mechanics.

Ljung L (1987). *System Identification Theory for the User*. Prentice Hall, New Jersey.

Maia, Silva, He, Lieven, Skingle, To, Urgueira (1997). *Theoretical and Experimental Modal Analysis*. Research Studies Press, UK.

Masjedian MH, Keshmiri M (2009). A review on operational modal analysis researches: classification of methods and applications. *Proceedings of the 3rd International Operational Modal Analysis Conference*, May 4-6, 2009, Portonovo, Ancona, Italy.

MATLAB, The MathWorks, Inc., Natick, Massachusetts, United States

Measurement Computing, http://www.mccdaq.com/

Mei Q, Gül M. (2015). Novel Sensor Clustering–Based Approach for Simultaneous Detection of Stiffness and Mass Changes Using Output-Only Data, *Journal of Structural Engineering*; 141 (10): 04014237.

Mukhopadhyay S, Luş H, Hong AL, Betti R (2012). Propagation of mode shape errors in structural identification. *Journal of Sound and Vibration*; 331 (17): 3961-3975.

Pandey AK, Biswas M, Samman MM (1991). Damage detection from changes in curvature mode shapes. *Journal of Sound and Vibration*; 145 (2): 321-332.

Pandey AK, Biswas M (1994). Damage Detection in Structures Using Changes in Flexibility. *Journal of Sound and Vibration*; 169 (1): 3-17.

Pandey AK, Biswas M (1995). Experimental verification of flexibility difference method for locating damage in structures. *Journal of Sound and Vibration*; 184 (2): 311-328.

Parloo E, Verboven P, Guillaume P, Van Overmeire M (2003). Force identification by means of in-operation modal models. *Journal of Sound and Vibration*; 262 (1): 161-173.

PCB Piezotronics, http://www.pcb.com/

Peeters B, De Roeck G, Pollet T, Schueremans L (1995). Stochastic subspace techniques applied to parameter identification of civil engineering structures. In: Jezequel L (editor). *Proceedings of New Advances in Modal Synthesis of Large Structures: Nonlinear, Damped and Nondeterministic Cases*, pp. 151-162, Lyon, France, 5-6 October.

Peeters B, De Roeck G (1999). Reference-based stochastic subspace identification for output-only modal analysis. *Mechanical Systems and Signal Processing*; 13 (6): 855 – 878.

Rainieri C, Fabbrocino G (2014). *Operational Modal Analysis of Civil Engineering Structures*. Springer-Verlag New York.

Ranieri C, Fabbrocino G, Cosenza E (2009). Identificazione dinamica automatica, problemi e prospettive di applicazione al monitoraggio strutturale in zona sismica. *Proceedings of the XIII Anidis conference, "L'ingegneria sismica in Italia"*, Bologna, January 2009.

Richardson MH, Formenti DL (1982). Parameter Estimation From Frequency Response Measurements Using Rational Fraction Polynomials. *Proceedings of the International Modal Analysis Conference (IMAC I)*, Orlando, Florida.

Rodrigues J, Brincker R (2005). Application of the Random Decrement Technique in Operational Modal Analysis. *Proceedings of the 1st International Operational Modal Analysis Conference*, April 26-27, 2005, Copenhagen, Denmark.

Rytter A (1993). *Vibration Based Inspection of Civil Engineering Structures*. PhD thesis. Building Technology and Structural Engineering. Aalborg University, Aalborg, Denmark.

Sabatino S, Ervin EK (2015). Comparison of Damage Diagnosis Algorithms on a Spatial Frame Using Vibration Data. *Advances in Structural Engineering*; 18 (5): 739-758.

Schmerr LW (1982). A New Complex Exponential Frequency Domain Technique For Analysing Dynamic Response Data. *Proceedings of the International Modal Analysis Conference (IMAC I)*, Orlando, Florida.

Shih CY, Tsuei YG, Allemang RJ, Brown DL (1988). Complex mode indication function and its application to spatial domain parameter estimation. *Mechanical Systems and Signal Processing*; 2 (4): 367–377.

Soderstrom T, Stoica P (2001). *System identification*. Uppsala.

Sohn H, Farrar CR, Hemez FM, Shunk DD, Stinemates SW, Nadler BR, Czarnecki JJ (2003). *A Review of Structural Health Monitoring Literature form 1996-2001*. Report LA-13976-MS, Los Alamos National Laboratory, Los Alamos, NM, USA.

Spitznogle FR, Quazi AH (1970). Representation And Analysis Of Time-Limited Signals Using A Complex Exponential Algorithm. *The Journal of The Acoustical Society of America*; 47 (5) Part l: 1150-l 155.

Stubbs N, Kim JT, Topole K (1992). An efficient and robust algorithm for damage localization in offshore structures. *Proceedings of the 10th ASCE Structures Conference*, American Society of Civil Engineers, New York, NY, pp. 543–546.

Stubbs N, Kim JT, Farrar C (1995). Field verification of a nondestructive damage localization and severity estimation algorithm. *Proceedings of the 13th International Modal Analysis Conference*, Society for Experiment, Nashville, TN, pp. 210–218.

Sung SH, Koo KY, Jung HY, Jung HJ (2012). Damage-induced deflection approach for damage localization and quantification of shear buildings: validation on a full-scale shear building. *Smart materials and structures*; 21: 115013.

Turek M, Ventura CE (2002). *Performing Ambient Vibration Tests using the UBC Earthquake Engineering Research Facility (EERF) Dynamic Structural Behaviour Assessment System (DSBAS) User's Manual*. Report – Civil 598 Directed Study Project. Department of Civil Engineering The University of British Columbia. Spring, 2002.

Turek M, Ventura CE (2005). Finite Element Model Updating of a Scale-Model Steel Frame Building. *Proceedings of the 1st International Operational Modal Analysis Conference*. April 26-27, 2005, Copenhagen, Denmark.

Ubertini F, Comanducci G, Cavalagli N (2016). Vibration-based structural health monitoring of a historic bell-tower using output-only measurements and multivariate statistical analysis. *Structural Health Monitoring*, 15 (4): 438–457.

Van Overschee P, De Moor B (1996). Subspace identification for linear systems. Kluwer Academic Publishers.

Ventura CE, Lord JF, Turek M, Sereci AM, Radulescu D, Radulescu C (2003). Experimental Studies and Remote Monitoring of IASC-ASCE Benchmark Test Frame, *Proceedings of the 21st International Modal Analysis Conference (IMAC)*, Orlando, FL, USA, February 3–6, 2003.

Vicario F, Phan MQ, Betti R, Longman RW (2015). Output-only observer/Kalman filter identification (O3KID). *Structural Control and Health Monitoring*; 22: 847–872.

Villalpando P, Meruane M, Boroschek R, Orchard M (2016). Damage Location by Maximum Entropy Method on a Civil Structure. *Proceedings of the 34th International Modal Analysis Conference*, Orlando, FL, USA, January 25-28, 2016.

Vold H, Rocklin GT (1982). The Numerical Implementation Of A Multi-Input Modal Estimation Method For Mini-Computers. *Proceedings of the International Modal Analysis Conference (IMAC I)*, Orlando, Florida.

Wang JF, Lin CC, Yen SM (2007). A story damage index of seismically-excited buildings based on modal frequency and mode shape. *Engineering Structures*; 29 (9): 2143-2157.

Wang JF, Lin CC, Lin GL, Yang CH (2013). Story Damage Identification of Irregular Buildings Based on Earthquake Records. *Earthquake Spectra*; 29 (3): 963–985.

West W (1984). *Fault Detection in Orbiter OV-101 Structure and Related Structural Test Specimens*. Loads and Structural Dynamics Branch Report, NASA-JSC, Houston, TX.

Worden K, Manson G, Fieller NRJ (2000). Damage detection using outlier analysis. *Journal of Sound and Vibration*; 229 (3): 647-667.

Worden K, Farrar CR, Manson G, Park G (2007). The fundamental axioms of structural health monitoring. *Proceedings of the Royal Society of London, Series A: Mathematical, Physical and Engineering Sciences*, 463(2082): 1639-64.

Yan WJ, Ren WX (2014). Closed-form modal flexibility sensitivity and its application to structural damage detection without modal truncation error. *Journal of Vibration and Control*; 20 (12): 1816-1830.

Yang QW, Liu JK (2009). Damage identification by the eigenparameter decomposition of structural flexibility change. *International Journal for Numerical Methods in Engineering*; 78: 444–459.

Yang Y, Mosalam KM, Liu G, Wang X (2016). Damage Detection Using Improved Direct Stiffness Calculations — A Case Study. *International Journal of Structural Stability and Dynamics*; 16 (1): 1640002.

Yuen MM (1985). A numerical study of the eigenparameters of a damaged cantilever. *Journal of Sound and Vibration*, 103: 301–310.

Zhang Z (1993). Error Study of Bridge Test. *Proceedings of the 12th International Modal Analysis Conference*, Hawaii.

Zhang Z, Aktan AE (1995). The Damage Indices for Constructed Facilities. *Proceedings of the 13th International Modal Analysis Conference*, pp. 1520–1529.

Zhang Z, Aktan AE (1998). Application of Modal Flexibility and Its Derivatives in Structural Identification. *Research in Nondestructive Evaluation*; 10 (1): 43-61.

Zhang LM, Brincker R, Andersen P (2001). Modal indicators for operational modal identification. *Proceedings of the 19th International Modal Analysis Conference (IMAC XIX)*, Kissimmee, USA, February 5-8, 2001.

Zhang L (2004). An Overview of Major Developments and Issues in Modal Identification. *Proceedings of the 22nd International Modal Analysis Conference*, January 26-29, 2004, Detroit, Michigan, USA.

Zhang L, Brincker R, Andersen P (2005). An Overview of Operational Modal Analysis: Major Developments and Issues. *Proceedings of the 1st International Operational Modal Analysis Conference*, April 26-27, 2005, Copenhagen, Denmark.

Zhao J, DeWolf J (1999). Sensitivity Study for Vibrational Parameters Used in Damage Detection. *Journal of Structural Engineering*; 125 (4): 410-416.

Zhang J, Xu JC, Guo SL, Wu ZS (2013). Flexibility-based structural damage detection with unknown mass for IASC-ASCE benchmark studies. *Engineering Structures*; 48: 486–496.